Stress Intensity Factors for Bolt Fixed Laminated Glass

Fröling, Maria; Persson, Kent

Published in:
TRITA-MEK Technical report

2010

KTH Engineering Sciences

Proceedings of NSCM-23: the 23rd Nordic Seminar on Computational Mechanics

EDITORS:
ANDERS ERIKSSON
GUNNAR TIBERT

Stockholm 2010

KTH Mechanics
Royal Institute of Technology
www.mech.kth.se

TRITA-MEK
Technical report 2010:07
ISSN 0348-467X
ISRN KTH/MEK/TR--10/07- -SE

Proceedings of NSCM-23: the 23rd Nordic Seminar on Computational Mechanics

Anders Eriksson and Gunnar Tibert (editors)

KTH Mechanics
The Royal Institute of Technology,
Stockholm, Sweden
2010

TRITA-MEK Technical report 2010:07
ISSN 0348-467X ISRN KTH/MEK/TR--10/07--SE

Sponsors:

KTH Engineering Sciences

Preface

This volume contains the extended abstracts from the presentations at the 23rd Nordic Seminar on Computational Mechanics held at KTH — The Royal Institute of Technology — in Stockholm, Sweden, 21–22 October 2010.

The Nordic Seminars on Computational Mechanics ('NSCM') are annually organized by the Nordic Association for Computational Mechanics (the NoACM). The seminars have circulated in the Nordic countries, and offered a meeting place between academics and practitioners from the participating countries. The atmosphere has always been a friendly and creative one. This year saw contributions and delegates from a more international community than ever before.

This year's seminar contained four invited lectures and 85 contributed papers, whereof four keynote lectures, divided into two plenary sessions and twelve parallel sessions. In the present volume, the invited lectures are placed first, followed by keynote and contributed papers in the order of their placement in the seminar schedule.

The editors of this volume thank all invited and keynote lecturers together with all contributors for their efforts in producing good presentations and abstracts. We thank Ms. Nina Bauer at KTH Mechanics for substantial help in the arrangements, and CIMNE, Barcelona (and, in particular, Mr. Alessio Bazzanella) for administrative support, but also ELU Konsult AB and KTH for financial support.

Stockholm in October 2010

Anders Eriksson and Gunnar Tibert

Contents

Invited lectures:

23rd Nordic Seminar on Computational Mechanics
NSCM-23
A. Eriksson and G. Tibert (Eds)

ISOGEOMETRIC ANALYSIS

TOR DOKKEN, TROND KVAMSDAL, KJELL F. PETTERSEN, AND VIBEKE SKYTT

SINTEF ICT, Forskningsveien 1, N0373, Oslo, Norway
e-mail: tor.dokken@sintef.no, web page: http://www.sintef.no/math

Key words: Isogeometric Analysis, NURBS, Locally Refined Splines.

Summary. NURBS (Non Uniform Rational B-Spline) curves and surfaces have been used extensively in Computer Aided Design (CAD) in the last two decades but not in Finite Element Analysis (FEA). Isogeometric analysis [6], introduced in 2005 by Hughes [9] proposes to replace traditional Finite Elements shape functions with volumetric NURBS. Although mathematically this seems to be a minor adjustment, it will drastically change the model life-cycle in FEA.

1 INTRODUCTION

While the theoretical basis of Finite Element Analysis was already established around 1970 [10], the basis of current CAD-technology was only developed during the 1970s and the early 1980s [1,2,5], with wide deployment in industry in the 1990s. From the start FEA and CAD were developed in separate communities, consequently there are a lot of differences between the technologies.

As integration and interoperability of systems have become more and more important in industry, the discrepancies between CAD and FEA have become evident:

- Why is it so difficult to generate a Finite Element grid from CAD-models?
- Why does not FEA keep the high precision of CAD-models for its element geometry description?
- Why is it so difficult to use feedback from FEA within CAD-systems to adjust the CAD-model?

In [5,6,9] isogeometric analysis is introduced proposing to replace traditional Finite Elements shape functions by trivariate tensor product NURBS. The obvious rationale for using NURBS representations rather than Finite Element shape functions is the possibility to represent exactly all elementary shapes from CAD (plane, sphere, cylinder, cone and torus) as well the NURBS surfaces of CAD.

Higher order finite elements have until now had limited use within FEA as they often have not performed better than lower order elements (in some cases the observed performance is even worse), for industry relevant problems (for such cases the convergence rate is usually limited by the regularity of the problem, not the polynomial order of the finite elements). The commonly prevailing line of thought that higher order elements do not provide improved solutions was challenged in [4], where it is shown for vibration analysis that higher order isogeometric NURBS perform much better than traditional Finite Elements when the

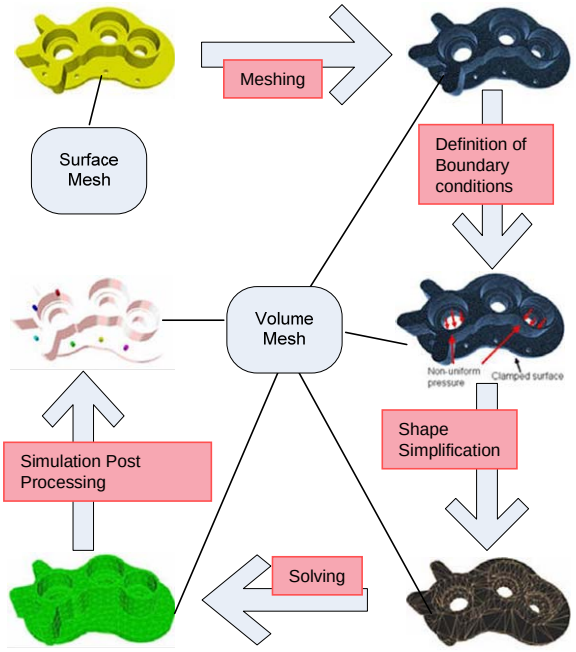

Fig.1. The AIM@SHAPE scenario related to the ontology for product design. This builds on deducting a simulation model (the surface mesh to the right at the top) from the CAD-model by approximating the CAD-surfaces by low degree surface pieces that match the representation of the volumetric Finite Elements to be generated later in the meshing process.

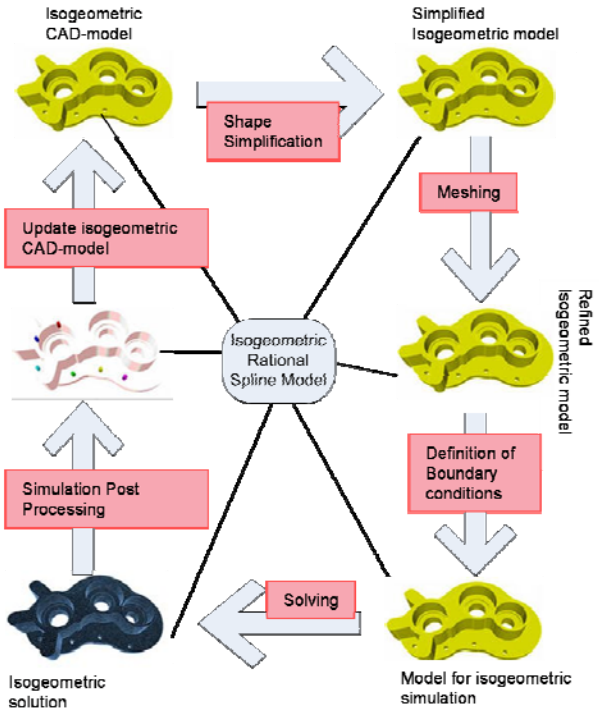

Fig. 2. A revised scenario adapted to the potential of isogeometric analysis. It should be noted that the Shape Simplification can now take place much earlier in the process, as the same shape representation is used throughout the processes, however, with gradually improving resolution with regard to the analysis to be performed. Note that an additional arrow has been added for updating the isogeometric CAD-model directly from the simulation results.

polynomial degree of the element is increased.

If one wants to make practical use of the proclaimed superiority of isogeometric analysis one should start to prepare the introduction of isogeometric analysis.

2 FROM MODEL CONVERSION TO INTEROPERABLITY OF CAD AND ANALYSIS

2.1 Isogeometric model quality

Figure 1 depicts the current state-of-the-art one way information flow from CAD to analysis, while Figure 2 illustrates the potential for interoperability between CAD and analysis introduced by using NURBS elements in analysis. However, while CAD represents volumes as a patchwork of 2-variate surfaces describing the outer and inner hulls of the objects, the isogeometric NURBS model represents the objects by structures of 3-variate volumes that match exactly along common boundaries. Adjacent surfaces in the CAD patchwork of surfaces are not required to match exactly; they are only required to meet within

tight tolerances. Thus the way from traditional CAD to an isogeometric NURBS model is not straight forward.

2.2 Scenarios for isogeometric analysis

When the AIM@SHAPE ontologies [3] were developed, scenarios and check lists of questions played a central role for validating the suitability of the scenarios. To follow this approach also for isogeometric analysis, scenarios have to be developed to support the revision of information processes triggered by isogeometric analysis. These scenarios should include aspects of:

- Creation of the analysis model from a CAD-model by successively building a phantom block structure on top of the CAD-model to assist its conversion to a volumetric rational spline model.
- Direct creation of the rational spline volumes of the analysis model through a broad range of volumetric shape operators such as ruling, sweeping, lofting, offsetting, intersection, filleting, rounding, etc.
- Simplification of the analysis model by removing shape features with little influence on the analysis result.
- Refinement of the analysis model to introduce the necessary additional degrees of freedom to produce a result of the required quality. This process is closely related to the traditional gridding. However, in contrast to traditional gridding the refinement does not change the physical shape of the model. The Locally Refined Splines will be an important spline representation to ensure the proper localization of the degrees of freedom added by the refinement.
- Visualization of analysis results. Isogeometric analysis employs rational splines for representing the result. Consequently the visualization of the results poses new challenges and possibilities. The results will have the form of scalar and vector fields represented by higher polynomial degrees than in traditional Finite Element Analysis. The calculated solution can consequently better reflect the actual physical behavior, and has the potential of modeling singularities and features that traditional Finite Element Analysis is unable to represent. Consequently the traditional visualization tools will not be well suited when visualizing the results of isogeometric analysis.
- Updating the isogeometric model by simulation results. Due to the discrepancies of CAD and FEM meshes it is very cumbersome to combine CAD-models, FEM and optimization. As the geometry representation and the simulation results now use the same spline space, simulation results can be directly applied to modify the isogeometric model and thus allow for advanced optimization processes.
- For many analysis problems there exist invariants with respect to the properties of the FEM-model. One such test, known as the patch test, ensures that calculated displacements can be directly added to the grid and provide a correct displaced grid. The scenarios must include sufficient analysis focused invariants to ensure the applicability to the scenarios.
- The scenarios should also include the potential of emerging spline technologies

such as T-Spline [10] and Locally Refined Splines (LR-Splines) [8]. While tensor product NURBS only allow global refinement of the spline space, T-splines and LR-Splines allow the introduction of local degrees of freedom where required.

3 CONCLUSION

Isogeometric analysis has the potential of drastically increasing the quality of FEA. Many challenges, however, remain to be solved, both with respect to creating analysis-suitable isogeometric models, local refinement, and to deploy the technology in industrial information processes.

REFERENCES

[1] C. de Boor C, *A Practical Guide to Splines*, Springer ,New York, (1978).

[2] I.C. Braid, Designing with volumes, *Ph.D. Thesis*, Cambridge University, UK (1974).

[3] C. Catalano, E. Camossi, R. Ferrandes, V. Cheutet, and N. Sevilmis, A product design ontology for enhancing shape processing in design workflows, *Journal of Intelligent Manufacturing* **20**, 553–567 (2009),

[4] E. Cohen., T. Lyche, and R. Riesenfeld, Discrete B-splines and subdivision techniques in computer aided geometric design and computer graphics, *Computer Graphics and Image Processing* **14,** 87–111 (1980).

[5] J.A. Cottrell, A. Reali, Y. Bazilevs, T.J.R. Hughes, Isogeometric analysis of structural vibrations, *Comput. Methods Appl. Mech. Engrg.* **195,** 5257–5296, (2006).

[6] J. A. Cottrell, T.J.R. Hughes, and Y. Bazilevs, Isogeometric Analysis: Toward Integration of CAD and FEA, Wiley, Chichester, UK., 2009

[7] T. Dokken, V. Skytt, J. Haenisch, and K. Bengtsson Isogeometric Representation and Analysis – Bridging the Gap between CAD and Analysis. *47th AIAA Aerospace Sciences Meeting Including The New Horizons Forum and Aerospace Exposition 5 - 8 January 2009*, (2009)

[8] T. Dokken, Locally Refined Splines. *Workshop on: "Non-Standard Numerical Methods for PDE's"*, Pavia, Italy, July 2, 2010, http://www-dimat.unipv.it/3indampv/

[9] T.J.R. Hughes, J.A. Cottrell, and Y. Bazilevs, Isogeometric analysis: CAD, finite elements, NURBS, exact geometry, and mesh refinement, *Computer Methods in Applied Mechanics and Engineering* **194** , 4135–4195 (2005).

[10] T. W. Sederberg, J. Zheng, A. Bakenov., and A. Nasri, T-splines and T-NURCCS. *ACM Transactions on Graphics* **22**, 477–484 (2003).

[11] G. Strang and G. J. Fix, *An Analysis of the Finite Element Method*, Prentice Hall, Englewood Cliffs, N.J, (1973).

[12] K.J. Weiler, Topological Structures for Geometric Modeling, *PhD Dissertation*, Rensselaer Polytechnic Institute, Troy, NY, (1986).

23rd Nordic Seminar on Computational Mechanics
NSCM-23
A. Eriksson and G. Tibert (Eds)

MISCONCEPTIONS IN FRACTURE TOUGHNESS DEFINITIONS REQUIRED FOR STRUCTURAL INTEGRITY ASSESSMENT

KIM. R. W. WALLIN*

* VTT Materials for Power Engineering
P.O. Box 1000, FI-02044 VTT, Espoo, Finland
Email: Kim.Wallin@vtt.fi

Key words: Fracture Toughness, Structural Integrity assessment, Estimation, Application.

Summary. The term fracture toughness can contain several misconceptions. Some of them are addressed here.

1 INTRODUCTION

Fracture mechanics is a comparatively new research field combining mechanical engineering and material science. The importance of fracture mechanics is constantly increasing, due to demand of increased structural efficiency, safety and life extension. Approximately sixty years ago, George Irwin and his co-workers laid the foundation for a one-parameter, continuum mechanics description of the fracture criteria. This description is to a large extent still in use today. Most structural integrity assessment procedures are based on this original description. The original continuum mechanics description assumes that there exists a single lower bound, geometry and specimen size independent fracture toughness value, when the crack experiences a plane-strain stress state. Deviations from pure plane-strain state, will then be seen as an increase in the structural crack resistance. This is the view adopted in classical fracture mechanical text books, still in use today. Improved understanding of material behavior has revealed that the original continuum mechanics description of the fracture criteria is insufficient and may lead to major misconceptions regarding the actual failure process. Examples of such misconceptions are the specimen size requirement, expected scatter in results, effect of stable crack propagation prior to failure, effect of time dependent fracture processes, quantification of the loss of constraint and specimen geometry effects. The improved material understanding has also opened a possibility to correct these misconceptions, which presently form the major obstacle to the widened use of fracture mechanics in design, material development, life prediction and safety assessment.

The material parameter required for the assessment of the criticality of real or postulated flaws in structures is the fracture toughness. Unfortunately, due to historical reasons and a strongly diversified research and standardization environment has led to a myriad of different fracture toughness definitions (Figure 1), some of which are directly erroneous. This multitude of parameters makes it difficult for the user to comprehend the significance of different definitions. Sometimes the chosen parameter is totally irrelevant with respect to the

desired assessment. This may lead to incorrect decisions regarding the safety or usability of the structure being assessed, resulting in either unwanted failure or unneeded repair, replacement or shut-down. There is clearly a need for a guide explaining the meaning of the different fracture toughness definitions. Also, it is important to obtain information regarding the relations between different fracture toughness definitions. Unlike mechanical properties, there is no typical standard fracture toughness for a specific material. Therefore, material data bases can only provide qualitative information and are not recommended for structural integrity assessment.

Figure 1: The multitude of fracture toughness definitions makes it difficult for the user to select the proper definition for his/her purposes.

Besides the actual fracture toughness definition, the assessment is also affected by the reliability of the test results themselves (Figure 2). Testing standards contain requirements on the test equipment and specimen dimensions. Some standards contain even indirect quality assurance criterions related to a specific test procedure. Generally applicable simple quality assurance tests related to test performance have however not been proposed until now. Also, the standards lack guidance on the test planning with regard e.g. to required displacements or crack mouth openings as a function of specimen size and expected fracture toughness level. Sometimes it is also required to apply test specimen dimensions or measuring locations, not covered by the testing standards. In such cases, guidance is needed for the analysis of the test results, to obtain comparable accuracy as with standard dimensions.

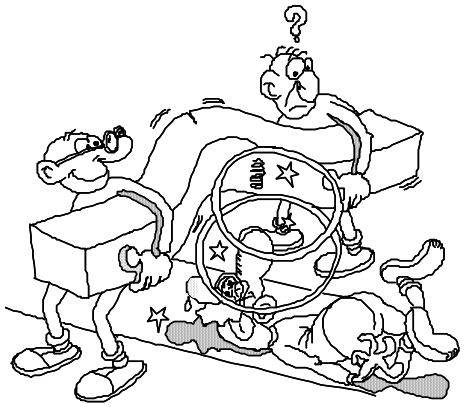

Figure 2: Uncertainties related to testing may have pronounced effects on the test result.

This presentation intends to shed some light upon the above issues, focusing on providing optimum estimates of fracture toughness values applicable in structural integrity assessment, either advising on the test procedure and suitable parameter or giving relations between other possibly available parameters.

2 ACKNOWLEDGEMENTS

This work is part of the authors Academy Professorship and is funded by the Academy of Finland decision 117700.

23rd Nordic Seminar on Computational Mechanics
NSCM-23
A. Eriksson and G. Tibert (Eds)

FATIGUE COMPUTATIONS IN ENGINE DEVELOPMENT

MATS G. DANIELSSON

Strength Analysis
Engine Development
Scania CV AB
e-mail: mats_g.danielsson@scania.com, web page: http://www.scania.com

Key words: Fatigue, Finite elements

1 INTRODUCTION

Scania is a leading manufacturer of heavy-duty trucks, buses, coaches and engines for marine and industrial applications. Since its birth in 1891, Scania has built and delivered more than 1,400,000 trucks and buses. Scania operates in around a hundred countries and employs 34,000 people of which 2,400 work in research and development, mainly in Sweden.

Scania presently produces a wide range of engines, reaching in power from 230 hp diesel engines for bus applications, to diesel engines for marine applications in excess of 1000 hp. Some five-hundred engineers and technicians work full time in the research and development of present and future engines. Ever-increasing peak cylinder pressures to address demands on fuel efficiency, as well as legally imposed limits on toxic emissions, pose great challenges to this development. From a durability point of view, engine components are subjected to vibrations and / or thermal cycling, both of which can cause fatigue. Some components are verified using traditional S/N testing while others require a “complete” engine environment due to complex displacement / temperature loading conditions. However, early on in the design phase, components may not even exist for testing purposes. Numerous concepts are usually evaluated before an actual (often expensive) first prototype is manufactured. Computational mechanics plays an important role in the design process, and is a key to saving time and effort. “Virtual test rigs” can aid in discarding bad designs early on, and overall make for rapid convergence of the design process. This lecture will describe two recent fatigue computations that were performed. The first case concerns the high cycle fatigue analysis of exhaust collectors, and the second case concerns the thermo-mechanical fatigue analysis of a cylinder head. Both results are presented in view of actual engine test results. The former case is described, in brief, below.

2 HIGH CYCLE FATIGUE OF AN EXHAUST COLLECTOR

The exhaust collectors, responsible for bringing exhaust fumes from the cylinder heads to the turbo, are mounted on the side of the engine (Figure 1). During normal operation, the engine firing causes vibrations that may lead to high cycle fatigue of the exhaust collectors. The standard work flow for this type of problem is as follows (Figure 2). The fundamental load associated with the firing is the cylinder pressure curve which gives the cylinder pressure

at a given crank angle. It is usually obtained through measurements. The curve is used as a driving force in full engine simulations, using the MBD code Excite.

Figure 1 Exhaust collectors of the V8 engine (left bank)

The size of the (coarsely meshed) FE model of the engine is in the order 3 Mdofs, but static and dynamic reductions are employed to reduce the model to some 4 kdofs for use in Excite. The results of the Excite simulation can be expanded to the original FE-model. The results are used to calculate, for example, emitted engine noise, as well as to provide excitation data for strength analyses. In the case of the analysis of an exhaust collector, displacement data (in the frequency domain) are extracted at its attachments to the cylinder heads and turbo. The displacement data, together with a detailed mesh for the exhaust collector are then used to calculate stresses in a frequency response analysis, typically performed using the FE code Nastran. The calculated stresses are analyzed using the fatigue post-processor FEMFAT, whereby a safety factor against fatigue is calculated using known fatigue data for the material. Figure 3 shows a predicted critical region, which also failed during engine testing.

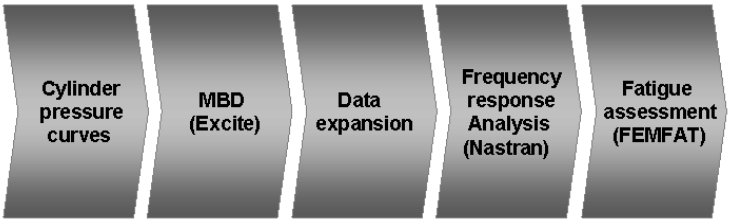

Figure 2 Work flow of a high cycle fatigue analysis

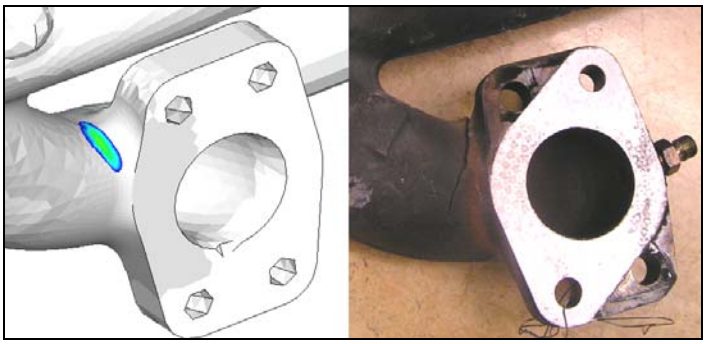

Figure 3 Prediction of region of low fatigue strength (left) and fatigue failure during engine run (right)

23rd Nordic Seminar on Computational Mechanics
NSCM-23
A. Eriksson and G. Tibert (Eds)

PARTICLE METHODS IN FLUID MECHANICS

J. H. WALTHER[†,*], H. A. ZAMBRANO[†] AND J. T. RASMUSSEN[†]

[†]Department of Mechanical Engineering
Technical University of Denmark
DK-2800 Kgs. Lyngby, Denmark

[*]Chair of Computational Science
ETH Zürich
CH-8092 Zürich
walther@inf.ethz.ch

Key words: Particle Methods, nanofluidics, molecular dynamics, adaptive, vortex methods.

Summary. We present adaptive particle methods for the simulations of fluid flow at the nano- and macroscale. The nanoscale phenomena are studied using atomistic simulations with focus on thermophoretic motion of nanodroplets confined inside carbon nanotubes. For simulations at the macroscale we present a novel adaptive particle vortex method.

1 INTRODUCTION

Particle methods is the generic title of a series of methods based on a Lagrangian formulation of discrete and continuous systems in science and engineering[1,2]. The methods enable simulations of fluid flow at all length scales[3]: from ab-initio quantum mechanics, Monte Carlo and Molecular Dynamics simulations of nanofluidic systems[4], to Dissipative Particle Dynamics, and Discrete Element Method simulations of discrete Brownian systems, to Smooth Particle Hydrodynamics[5,6], Reproducing Kernel Methods[7], Moving Least Squares[8], and Discrete Vortex Methods[9,2] for problems in continuum fluid dynamics — and beyond, to simulations of planetary systems in cosmology[10,11].

The methods share common strengths such as their inherent adaptivity, as the computational elements "go with the flow", and common weaknesses such as uniform particle size, inaccurate treatment of diffential operators, and complex boundary conditions and kinematics. The diffential operators are treated differently in the different particle methods. Thus, they are computed by exact diffentiation (if available)[12], by stochastic models[13], through diffentiation of the smoothing kernels[14], or by the method of Particle Strength Exchange[15,16]. Boundary conditions are described by various techniques such as the method of images, boundary elements, immersed boundary methods or penalization techniques[17,18]. The N-body problems associated with the kinematics of the N particles may be solved using Cell and Verlet lists for the near neighbour interactions[19], and tree data structures and fast multipole methods[20], or by hybrid particle-mesh techniques for the far-field interactions[21,22,23].

In continuum fluid dynamics the convergence of the methods has partly been ensured by a renormalization of the particle interaction[24,25] or by a reinitialization of the particles[26]. While

generally applicable, these techniques are often limited to specfic particle methods.

For fluid flow at the nanoscale, molecular dynamics simulations allow us to study the individual motion of the molecules at the solid surface and hence probe the validity of macroscale models e.g., the fundamental, but empirically founded no-slip boundary condition. Moreover, it allows us to study driving mechanisms for fluid flow at the nanoscale, where surface forces play a dominating role. One mechanism is thermophoresis[27,28,29] which we will discuss in detail at the meeting. Fig. 1 illustrates a water nanodroplets confined inside a carbon nanotube. Motion is imparted onto the droplet by imposing a thermal gradient onto the carbon nanotube[30,31].

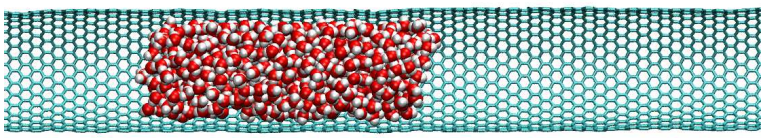

Figure 1: Flow of water in carbon nanotubes is studied using molecular dynamics simulations.

At the macroscale we study adaptive particle methods using particles of different resolution cf. Fig. 2. The adaptivity is based on the linearity of the Poisson equation governing the flow velocity and the properties of Fourier transforms. The second part of the talk will discuss this algorithm in detail.

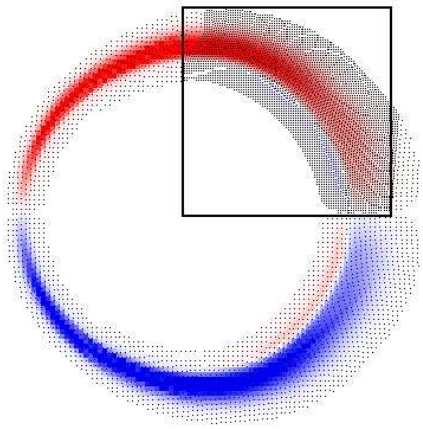

Figure 2: Schematic of the local refinement using patches in two-dimensional particle Vortex methods.

REFERENCES

[1] Hockney, R. W. & Eastwood, J. W. *Computer Simulation Using Particles* (Institute of Physics Publishing, Bristol, PA, USA, 1988), 2 edn.

[2] Cottet, G.-H. & Koumoutsakos, P. *Vortex Methods – Theory and Practice* (Cambridge University Press, New York, 2000).

[3] Koumoutsakos, P. Multiscale flow simulations using particles. *Annu. Rev. Fluid Mech.* **37**, 457–487 (2005).

[4] Koplik, J. & Banavar, J. R. Continuum deductions from molecular hydrodynamics. *Annu. Rev. Fluid Mech.* **27**, 257–292 (1995).

[5] Monaghan, J. J. Particle methods for hydrodynamics. *Comput. Phys. Rep.* **3**, 71–123 (1985).

[6] Monaghan, J. J. An introduction to SPH. *Comp. Phys. Commun.* **48**, 89–96 (1988).

[7] Liu, W. K., Jun, S. & Zhang, S. Reproducing kernel particle methods. *Int. J. for Numer. Methods In Engng.* **20**, 1081–1106 (1995).

[8] Belytschko, T., Krongauz, Y., Organ, D., Fleming, M. & Krysl, P. Meshless methods: An overview and recent developments. *Comp. Meth. Appl. Mech. & Engng.* **139**, 3–47 (1996).

[9] Leonard, A. Vortex methods for flow simulation. *J. Comput. Phys.* **37**, 289–335 (1980).

[10] Monaghan, J. J. Smoothed particle hydrodynamics. *Annu. Rev. Astron. Astrophys.* **30**, 543–574 (1992).

[11] Bertschinger, E. Simulations of structure formation in the universe. *Annu. Rev. Astron. Astrophys.* **36**, 599–654 (1998).

[12] Leonard, A. & Koumoutsakos, P. High resolution vortex simulation of bluff body flows. *J. Wind Eng. Ind. Aerodyn.* **46 & 47**, 315–325 (1993).

[13] Chorin, A. J. Numerical study of slightly viscous flow. *J. Fluid Mech.* **57**, 785–796 (1973).

[14] Fishelov, D. A new vortex scheme for viscous flows. *J. Comput. Phys.* **86**, 211–224 (1990).

[15] Degond, P. & Mas-Gallic, S. The weighted particle method for convection-diffusion equations. part 1: The case of an isotropic viscosity. *Math. Comput.* **53**, 485–507 (1989). Oct.

[16] Eldredge, J. D., Leonard, A. & Colonius, T. A general determistic treatment of derivatives in particle methods. *J. Comput. Phys.* **180**, 686–709 (2002).

[17] Goldstein, D., Handler, R. & Sirovich, L. Modeling a no-slip flow boundary with an external force field. *J. Comput. Phys.* **105**, 354–366 (1993).

[18] Coquerelle, M. & Cottet, G.-H. A vortex level set method for the two-way coupling of an incompressible fluid with colliding rigid bodies. *J. Comput. Phys.* **227**, 9121–9137 (2008).

[19] Allen, M. P. & Tildesley, D. J. *Computer Simulation of Liquids* (Clarendon Press Oxford, Oxford, 1987).

[20] Greengard, L. & Rokhlin, V. A fast algorithm for particle simulations. *J. Comput. Phys.* **73**, 325–348 (1987).

[21] Sbalzarini, I. F. *et al.* PPM – a highly efficient parallel particle-mesh library for the simulation of continuum systems. *J. Comput. Phys.* **215**, 566–588 (2006).

[22] Sbalzarini, I. F. *et al.* A software framework for portable parallelization of particle-mesh simulations. *Lect. Notes Comput. Sc.* **4128**, 730–739 (2006).

[23] Morgenthal, G. & Walther, J. H. An immersed interface method for the vortex-in-cell algorithm. *Computers & Structures* **85**, 712–726 (2007).

[24] Shankar, S. & van Dommelen, L. A new diffusion procedure for vortex methods. *J. Comput. Phys.* **127**, 88–109 (1996).

[25] Schrader, B., Reboux, S. & Sbalzarini, I. F. Discretization correction of general integral PSE operators for particle methods. *J. Comput. Phys.* **229**, 4159–4182 (2010).

[26] Koumoutsakos, P. & Leonard, A. High-resolution simulation of the flow around an impulsively started cylinder using vortex methods. *J. Fluid Mech.* **296**, 1–38 (1995).

[27] Soret, C. *Ann. Chim. Phys.* **22**, 293 (1884).

[28] Schoen, P. A. E., Walther, J. H., Poulikakos, D. & Koumoutsakos, P. Phonon assisted thermophoretic motion of gold nanoparticles inside carbon nanotubes. *Appl. Phys. Lett.* **90**, 253116 (2007).

[29] Schoen, P. A. E., Walther, J. H., Arcidiacono, S., Poulikakos, D. & Koumoutsakos, P. Nanoparticle traffic on helical tracks: Thermophoretic mass transport through carbon nanotubes. *Nano Lett.* **6**, 1910–1917 (2006).

[30] Zambrano, H. A., Walther, J. H. & Jaffe, R. L. Thermally driven molecular linear motors: A molecular dynamics study. *J. Chem. Phys.* **131**, 241104 (2009).

[31] Zambrano, H. A., Walther, J. H., Koumoutsakos, P. & Sbalzarini, I. F. Thermophoretic motion of water nanodroplets confined inside carbon nanotubes. *Nano Lett.* **9**, 66–71 (2009).

[32] Rasmussen, J. T., Hejlesen, M. M., Larsen, A. & Walther, J. H. Discrete vortex method simulations of the aerodynamic admittance in bridge aerodynamics. *J. Wind Eng. Ind. Aerodyn.* in press (2010).

[33] Bergdorf, M., Cottet, G.-H. & Koumoutsakos, P. Multilevel adaptive particle methods for convection-diffusion equations. *Multiscale Model. Simul.* **4**, 328–357 (2005).

23rd Nordic Seminar on Computational Mechanics
NSCM-23
A. Eriksson and G. Tibert (Eds)

ISOGEOMETRIC ANALYSIS AND SHAPE OPTIMISATION

JENS GRAVESEN[1], ANTON EVGRAFOV[2], ALLAN ROULUND GERSBORG[3], NGUYEN DANG MANH[4], PETER NØRTOFT NIELSEN[5]

[1,2,4,5]DTU Mathematics and [3,5]DTU Mechanical Engineering
Technical University of Denmark
email: [1]j.gravesen@mat.dtu.dk (corresponding author), [2]a.evgrafov@mat.dtu.dk,
[3]agersborg.hansen@gmail.com, [4]d.m.nguyen@mat.dtu.dk, [5]p.n.nielsen@mat.dtu.dk

Key words: shape optimisation, isogeometric analysis, parametrisation

Summary. We look at some succesfull examples of shape optimisation using isogeometric analysis. We also addresses some problems which we encountered.

1 Introduction

In isogeometric analysis the physical domain $\Omega \subseteq \mathbb{R}^2$ is parametrised by a map $\mathbf{x} : [0,1]^2 \to \Omega$. The map $\mathbf{x}$, as well as all physical fields, are given in terms of B-splines or NURBS,

$$\mathbf{x}(u,v) = \sum_{i=1}^{m}\sum_{j=1}^{n} \mathbf{c}_{i,j} M_i(u)\, N_j(v), \tag{1}$$

where $\mathbf{c}_{i,j}$ are the control points. When u or v becomes 0 or 1 we obtain the four boundary curves $\mathbf{x}_1, \ldots, \mathbf{x}_4$. The shape of Ω is determined by the boundary so shape optimisation is done by adjusting the four boundary curves or rather the boundary control points $\mathbf{c}_{0,j}, \mathbf{c}_{m,j}, \mathbf{c}_{i,0}, \mathbf{c}_{i,n}$. How the inner control points are determined is addressed in Section 4.

2 Optimisation of the frequencies of a drum

In the first example we consider the design of a drum. That is, given N required frequencies $\widehat{\lambda}_i$, $i = 1, \ldots, N$, we want to design a vibrating membrane such that the lower eigenfrequences are exactly as required. Mathematically we specify the lower eigenvalues of the Laplace operator. Not even the full spectrum of the Laplace operator determines the domain so we minimise the length of the perimeter and treat the specified eigenvalues as constraints, see [8] and references therein. If $\lambda_1 \le \lambda_2 \le \ldots$ are the eigenvalues of the Laplace operator $\triangle$, then we consider the following optimisation problem,

$$\text{minimise} \sum_{i=1}^{4} \int_0^1 \left| \frac{\mathrm{d}\mathbf{x}_i}{\mathrm{d}t} \right| \mathrm{d}t, \quad \text{such that} \quad \begin{array}{ll} \lambda_i = \widehat{\lambda}_i, & i = 1, \ldots, N, \\ \triangle f_i = \lambda_i\, f_i, & i = 1, \ldots, N. \end{array} \tag{2}$$

In the specific example shown in Figure 1 we want the first four frequencies or eigenvalues to be in the harmonic proportion $2 : 3 : 3 : 4$. The problem with the double eigenvalue is solved by replacing (2) for the case $i = 2, 3$ with $\lambda_2 + \lambda_3 = \widehat{\lambda_2} + \widehat{\lambda_2}$ and $\lambda_2\, \lambda_3 = \widehat{\lambda_2}\, \widehat{\lambda_2}$.

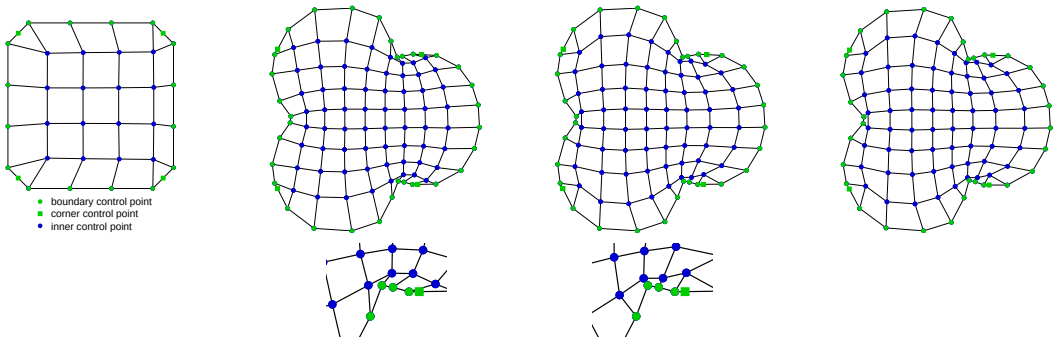

Figure 1: Minimising the perimeter of a harmonic drum. After 50 iterations the parametrisation became nearly singular and if we continued it started to fold over in the indicated area. After improving the parametrisation by using the Winslow functional the optimisation converged after another 16 iterations.

One problem we encountered during the optimisation was that the map $\mathbf{x}$ became singular, i.e., it was no longer a parametrisation. So there is the need to have an reliable method to determine the inner control points, see Section 4.

3 Optimisation of a pipe bend

In the second example we look at a 2D Stokes flow problem where a pipe bend has to be designed such that the internal energy loss is minimised under constraints on the area of the pipe bend, see [9]. If (u_1, u_2) is the velocity of the fluid the we have the following problem,

$$\text{minimise} \int_\Omega (\|\nabla u_1\| + \|\nabla u_2\|)\,\mathrm{d}x\,\mathrm{d}y \quad \text{such that} \quad \text{area}(\Omega) \le A \tag{3}$$

The optimised design, see Figure 2, is in agreement with the result obtained by topology op-

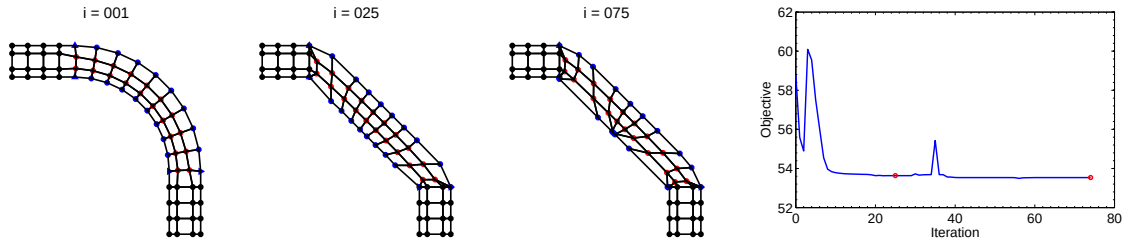

Figure 2: Optimisation of a pipe bend. After 25 iterations the geometry is determined. During the remaining iterations the optimisation only changes the parametrisation, making it worse.

timisation, c.f., [3]. We see that the design is obtained after 25 iterations. But, the optimiser continues its work, not changing the design but clustering the control points and thereby creating a poorer parametrisation. This introduces numerical errors that makes the objective function smaller. It is possible because the design contains a straight line and the control points can move freely on this line without changing the geometry. It is a well known problem in shape optimisation and has previously been dealt with by filtering techniques, extra contributions to the objective function, or extra constraints such as a minimum distance between control points,

see [1]. The latter will unfortunately also prevents the sharp corners at the inlet and outlet that are part of the design. Another solution is to detect and remove superfluous control points, in the present case eight on the inside and six on the outside of the bend.

4 Parametrisation

We now consider the parametrisation problem. That is, given a parametrisation $\mathbf{y} : \partial[0,1]^2 \to \partial\Omega$ of the boundary of a domain Ω extend it to a parametrisation $\mathbf{x} : [0,1]^2 \to \Omega$ of the whole domain. Or, in terms of the control points given boundary control points determine the inner control points, see Figure 3. The simplest way of obtaining a map $\mathbf{x}$ is by considering the control

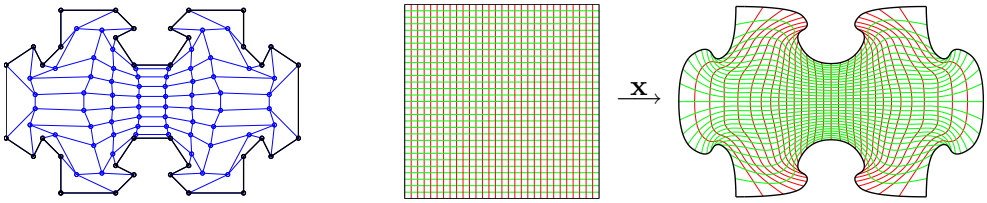

Figure 3: The parametrisation problem: Given the (black) boundary control points, determine the (blue) inner control points such that the map $\mathbf{x}$ is a parametrisation.

net as a set of springs with the same spring constant. Then every inner control points is the average of its four neighbours. This is a linear system of equations which are easily solved. By adjusting the spring constants one can make a given reference configuration in balance and then use the equilibrium equations to get the inner control points after a change of the boundary control points. One way of doing this is by using the mean value coordinates of Floater, see [4]. Another way to use a reference configuration is to demand that the configuration of an inner control point and its four neighbours should be a scaled and rotated version of the one in the reference net. This leads to an overdetermined set of equations which has to be solved in the least square sense.

The map $\mathbf{x}$ is a parametrisation if and only if the determinant of the Jacobian is non vanishing. The determinant of the Jacobian is piecewise polynomial, so we can write it in terms of B-splines

$$\det J = \sum_{i,j=1}^{m,n} \sum_{k,\ell=1}^{m,n} \det(\mathbf{c}_{i,j}, \mathbf{c}_{k,\ell})\, M_i'(u)\, N_j(v)\, M_k(u)\, N_\ell'(v) = \sum_{i,j=1}^{\widetilde{m},\widetilde{n}} d_{i,j}\, \widetilde{M}_i(u)\, \widetilde{N}_j(v), \tag{4}$$

A *sufficient* condition for the positivity of $\det J$ is the positivity of all the coefficients $d_{i,j}$. They depend quadratically on the control points $\mathbf{c}_{i,j}$. The solution to the following problem

$$\underset{\text{inner control points}}{\text{maximise}} \quad S, \quad \text{such that} \quad d_{i,j} \geq S. \tag{5}$$

gives a valid parametrisation if the control net is sufficiently refined. Even though the parametrisation is valid it need not be very good. One way to improve it is to make it as conformal as possible and this can be done by minimising the *Winslow* functional:

$$\underset{\text{inner control points}}{\text{minimise}} \int_0^1 \int_0^1 \frac{\|\mathbf{x}_u\|^2 + \|\mathbf{x}_v\|^2}{\det(\mathbf{x}_u, \mathbf{x}_v)}\, \mathrm{d}u\, \mathrm{d}v, \tag{6}$$

see [5] for details. To make sure that we have a valid parametrisation, and a positive denominator, we add the constraints, $d_{i,j} \geq \delta S_0$, where $\delta \in [0,1]$ and $d_{i,j}$ and S_0 are given by (4) and (5) respectively. If we let $\mathbf{r} = \mathbf{x}^{-1}$ be the inverse map and change variables from (u,v) to (x,y) in (6) then we obtain the following linearly constrained quadratic optimisation problem

$$\underset{\mathbf{r}}{\text{minimise}} \int_\Omega \left(\|\mathbf{r}_x\|^2 + \|\mathbf{r}_y\|^2 \right) \, \mathrm{d}x \, \mathrm{d}y, \quad \text{such that} \quad \mathbf{r}|_{\partial\Omega} = \mathbf{y}^{-1}. \tag{7}$$

It has a unique minimum realised by a pair of harmonic functions. By the Kneser-Rado-Choquet Theorem, [2, 6, 10], this is a diffeomorphism. So the original problem (6) has a unique minimum too.

If we square the numerator in (6) then we obtain the modified Liao functional which is well known from grid generation, [7], but in our experience the Winslow functional behaves better for our purpose.

It is quite expensive to solve the problems (5) and (6) so we do not do this in each optimisation cycle. If the parametrisation becomes close to singular then we do it and obtain hereby a good reference parametrisation, or control net, $\mathbf{x}_0$. We then propose to linearise the problem (6) and solve the linear equation

$$H_{\mathbf{x}_0}(\mathcal{W})\mathbf{x} = H_{\mathbf{x}_0}(\mathcal{W})\mathbf{x}_0 - \nabla_{\mathbf{x}_0}\mathcal{W}, \tag{8}$$

where $\mathcal{W}$ denotes the Winslow functional and $\nabla_{\mathbf{x}_0}\mathcal{W}$ and $H_{\mathbf{x}_0}(\mathcal{W})$ are the gradient and Hessian evaluated at $\mathbf{x}_0$, respectively.

REFERENCES

[1] K.-U. Bletzinger, M. Firl, J. Lindhard, and R. WÜchner, Optimal shapes of mechanically motivated surfaces, *Comput. Methods Appl. Mech. Engrg.* **199** (2010), 324–333.

[2] G. Choquet, Sur un type de transformation analytique généralisant la représentation conforme et définé au moyen de fonctions harmoniques, *Bull. Sci. Math.* **69** (1945), 156–165.

[3] A. Gersborg-Hansen, O. Sigmund, and R.B. Haber, Topology optimization of channel flow problems, *Structural and Multidisciplinary Optimization* **30**, (2005), 181–192.

[4] K. Hormann and M. Floater, Mean value coordinates for arbitrary polygons, *ACM Transactions on Graphics* **25**, (2006), 1424–1411.

[5] J. Gravesen, Parametrisation in isogeometric analysis. In preparation.

[6] H. Kneser, Lösung der Aufgabe 41, *Jahresber. Deutsch. Math.-Verien.* **35**, (1926), 123–124.

[7] P. Knupp and S. Steinberg, *Fundamentals of Grid Generation*, CRC Press, 1993.

[8] Nguyen D. M., A. Evgrafov, A. R. Gersborg, and J. Gravesen, Isogeometric shape optimization of vibrating membranes. Submitted (2010), 23 p.

[9] P.N. Nielsen, A.R. Gersborg, and J. Gravesen, Isogeometric analysis of 2-dimensional steady-state non-linear flow problems. In preparation.

[10] T. Radó, Aufgabe 41, *Jahresber. Deutsch. Math.-Verien.* **35**, (1926), 49.

23rd Nordic Seminar on Computational Mechanics
NSCM-23
A. Eriksson and G. Tibert (Eds)

ISOGEOMETRIC ANALYSIS TOWARD SHAPE OPTIMIZATION IN ELECTROMAGNETICS

NGUYEN DANG MANH[⋆,1], ANTON EVGRAFOV[⋆], JENS GRAVESEN[⋆], JAKOB SØNDERGAARD JENSEN[†]

[⋆]Department of Mathematics and [†]Department of Mechanical Engineering
Technical University of Denmark
e-mail: ⋆{D.M.Nguyen,A.Evgrafov,J.Gravesen}@mat.dtu.dk, †jsj@mek.dtu.dk

Key words: Isogeometric analysis, shape optimization, electromagnetics.

Summary. We use NURBS-based isogeometric analysis to investigate dependences of magnetic energy on geometry for some two-dimensional scattering problems.

1 INTRODUCTION

We consider two-dimensional electromagnetic (EM) scattering problems as depicted in Fig. 1(**a**) where the incident magnetic field intensity is given as: $\mathbf{H} = (0, 0, H_z)$. The governing equations

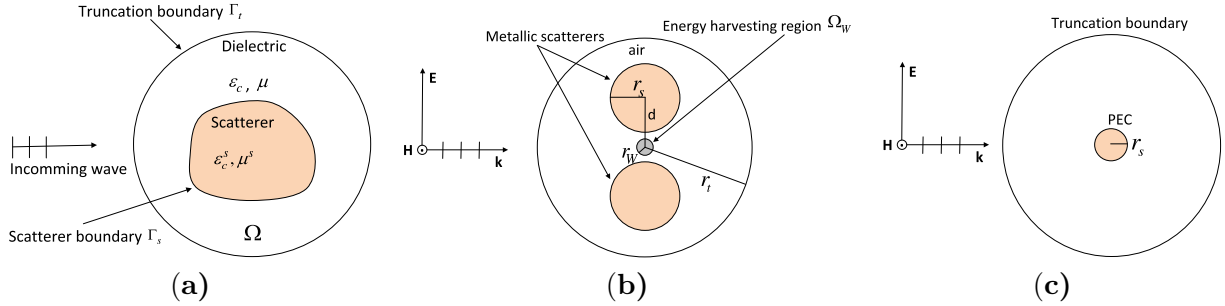

Figure 1: Various models of scattering problems

of the problem, c.f. [1], are

$$\boldsymbol{\nabla} \cdot \Big(\frac{1}{\varepsilon_{cr}} \boldsymbol{\nabla} H_z\Big) + k_0^2 \mu_r H_z = 0 \qquad \text{in } \Omega, \tag{1a}$$

$$\frac{1}{\varepsilon_{cr}} \frac{\partial H_z}{\partial \mathbf{n}} - jk_0 \sqrt{\frac{\mu_r^{\mathrm{s}}}{\varepsilon_{cr}^{\mathrm{s}}}}\, H_z = 0 \qquad \text{on } \Gamma_s, \tag{1b}$$

$$\frac{\partial H_z}{\partial \mathbf{n}} + (jk_0 + \frac{1}{2r_t}) H_z - \frac{\partial H_z^i}{\partial \mathbf{n}} - (jk_0 + \frac{1}{2r_t}) H_z^i = 0 \qquad \text{on } \Gamma_t, \tag{1c}$$

[1]Corresponding author. Tel.: +45 4525 3037; fax: +45 4588 1399.

where ε_{cr}, μ_r are the relative complex permittivity and the relative permeability of the dielectric material to the corresponding constants of free space, respectively; $\varepsilon^{\mathrm{s}}_{cr}$, μ^{s}_r are the relative complex permittivity and the relative permeability of the scatterer, respectively; r_t is the radius of the circular truncation boundary; k_0 is the wavenumber of free space. As a results of the above equations, the weak form of the scattering problem reads: Find $H_z \in H(\mathrm{div}, \Omega)$ [2] such that for every $\phi \in H(\mathrm{div}, \Omega)$:

$$\int_\Omega \frac{1}{\varepsilon_{cr}} \boldsymbol{\nabla} H_z \cdot \boldsymbol{\nabla} \phi \, \mathrm{d}V - k_0^2 \int_\Omega \mu_r H_z \, \phi \, \mathrm{d}V - jk_0 \int_{\Gamma_s} \eta^s_{cr} H_z \, \phi \, \mathrm{d}\partial + (jk_0 + \frac{1}{2r_t}) \int_{\Gamma_t} \frac{1}{\varepsilon_{cr}} H_z \, \phi \, \mathrm{d}\partial$$
$$= \int_{\Gamma_t} \frac{1}{\varepsilon_{cr}} \left(\frac{\partial H^i_z}{\partial \mathbf{n}} + (jk_0 + \frac{1}{2r_t}) H^i_z\right) \phi \, \mathrm{d}\partial. \quad (2)$$

In particular, if $H_z = H_0 e^{-jkx}$ and geometry of the problem is symmetric about the line $y = 0$, e.g. the model in Fig. 1(**b**), the problem can be solved in a half of the truncation domain with the following boundary condition along the boundary $y = 0$: $\frac{\partial H_z}{\partial y} = 0$.

2 NUMERICAL EXAMPLES

2.1 Comparison between numerical and exact solutions

We consider the problem sketched in Fig. 1(**c**), in which the scatterer is a perfect electric conductor. The exact solution of the problem, cf. [3], is

$$H_z = \sum_{n=-\infty}^{+\infty} j^{-n} \left(\mathrm{J}_n(k\rho) - \frac{\mathrm{J}'_n(kr_s)}{H^{(2)'}_n(kr_s)} H^{(2)}_n(k\rho) \right) e^{jn\phi}. \quad (3)$$

To apply isogeometric analysis to the problem, we model the problem by two patches as showed in Fig. 2(a). According to Fig. 2(d), the numerical and exact solutions agree up to 2%.

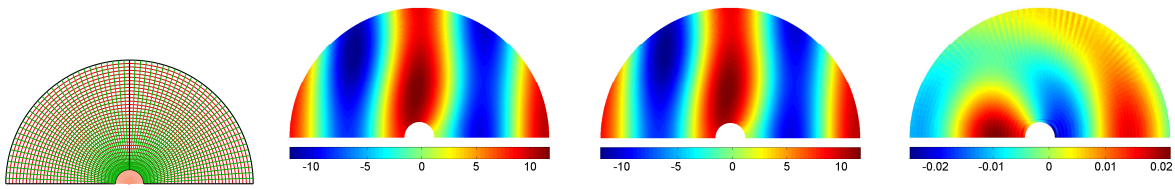

(a) (b) (c) (d)

Figure 2: Comparison between numerical and exact solutions of the scattering problem in Fig. 1(**c**). (a): The truncation domain comprised of two patches. (b): Exact solution. (c): Isogeometric analysis-based solution. (d): Relative error.

2.2 Magnetic resonator

We now want to examine dependences of magnetic energy, in terms of the quantity $W_m = \int_{\Omega_W} \lg\left(\frac{\mu |\mathbf{H}(\mathbf{u})|^2}{4 \cdot 10^{-7}}\right) \mathrm{d}V$, on geometry of the scattering problem sketched in Fig. 1(**b**). To solve the

problem, three patches are used to model its truncation domain, see Fig. 3(left). To compute W_m, we use an extended trapezoidal rule and an optimization problem to find preimages of the integrating points of the rule in the physical domain is invoked.

We first examine the dependence on the distance d between the origin and the scaterer center. The results, depicted in Fig. 3(right), shows that magnetic energy depends inversely on d.

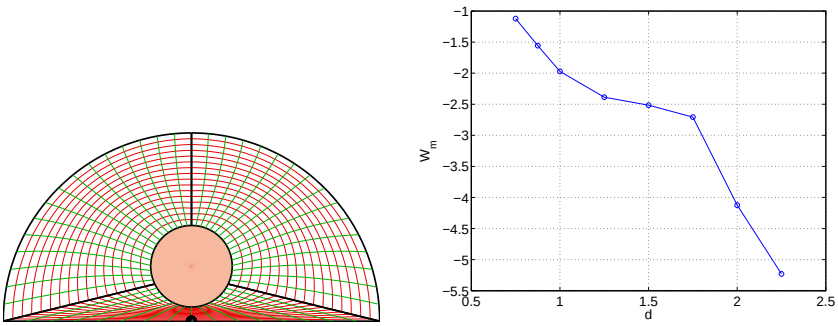

Figure 3: Left: Multiple patches used to model the scattering problem sketched in Fig. 1(**b**); Right: The dependence of magnetic energy on the distance d between the origin and the scaterer center.

Moreover, we choose the model with circular magnetic resonators as a reference model and compare models whose magnetic resonators have different shapes to the reference model. In comparison to magnetic energy of the reference model (Fig. 4(a)), magnetic energies of the models whose resonators with one deformed upper part (Fig. 4(b)) or lower part (Fig. 4(d)) are stronger.

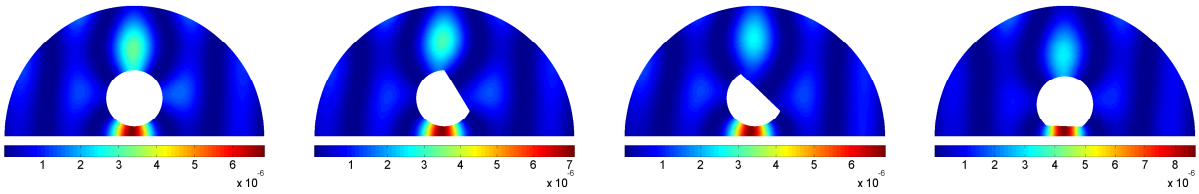

$W_m = -1.5562$ (a) $W_m = -1.5204$ (b) $W_m = -1.5821$ (c) $W_m = -1.347$ (d)

Figure 4: Magnetic energy in the presence of various magnetic resonators with different shapes

3 FUTURE WORK

We consider the following shape optimization problem

$$\underset{\boldsymbol{\rho}_b}{\text{maximize}} \quad W_m \tag{4a}$$

$$\text{where} \quad \mathbf{K}(\boldsymbol{\rho}_b)\mathbf{u} = \mathbf{f}(\boldsymbol{\rho}_b), \tag{4b}$$

where $\boldsymbol{\rho}_b$ are the control points that govern the shape of the scatterer and the equation (4b) is the discretized form of the weak form (2). This is not a new problem. It originates from recent attempts for improving wireless power transfer via coupled magnetic resonances [4]. Recently, Sigmund and his coworkers [5] have used topology optimization to find spatial distributions of two magnetic resonators. Some of their results are depicted in Fig. 3.

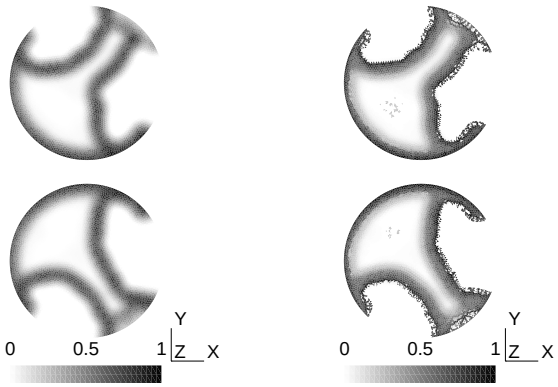

Figure 5: Results from a previous work [5], which were obtained by topology optimization, the initial designs are similar to the model in Fig. 1(**b**).

Our future work is to utilize advantages of isogeometric shape optimization [6] to enhance their results.

REFERENCES

[1] Jianming Jin. *The finite element method in electromagnetics.* John Wiley & Sons, New York, 2002.

[2] R.A. Adams. *Sobolev spaces. Pure and Applied Mathematics, Vol. 65.* Academic Press, New York-London, 1975.

[3] Constantine A. Balanis. *Advanced engineering electromagnetics.* Wiley, New York, 1989.

[4] Andre Kurs, Aristeidis Karalis, Robert Moffatt, J. D. Joannopoulos, Peter Fisher, and Marin Soljacic. Wireless power transfer via strongly coupled magnetic resonances. *Science*, 317(5834):83–86, JUL 6 2007.

[5] N. Aage, N.A. Mortensen, and O. Sigmund. Topology optimization of metallic devices for microwave applications. *International Journal for numerical methods in engineering*, 83(2):228–248, JUL 9 2010.

[6] N.D. Manh, A. Evgrafov, A.R. Gersborg, and J. Gravesen. Isogeometric shape optimization of vibrating membranes. *SUBMITTED*, 2010.

23rd Nordic Seminar on Computational Mechanics
NSCM-23
A. Eriksson and G. Tibert (Eds)

ADAPTIVE ISOGEOMETRIC ANALYSIS USING T-SPLINES

KJETIL ANDRÉ JOHANNESSEN* **AND TROND KVAMSDAL†**

*Department of Mathematical sciences
Norwegian University of Science and Technology (NTNU)
Alfred Getz vei 1, 7491 Trondheim, Norway
e-mail: kjetijo@math.ntnu.no

Key words: T-splines, Isogeometry, Finite Element Method, A posteriori error estimates.

Summary. We present an adaptive T-spline f nite element solver in an isogeomtric setting. Traditional NURBS basis functions are tensor-product, while T-splines allow for true local ref nement. This is proving superior to problems containing singularities. Moreover, T-splines is having a positive effect on smooth problems as well, since it will make the solver less prone to the choice parametrization.

1 Introduction

Hughes et al.[1] introduced the concept of isogeometric f nite element method (FEM) solvers by using non-uniform rational B-splines (NURBS) as a basis. One of the main arguments is that modern computer aided engineering (CAE) is seeing a severe bottleneck in the construction of analysis suitable geometries. Hughes reports that as much as 20 percent of the time used in a CAE pipeline is used for creating a geometric model which for analysis is *possible*, while as much as 60 percent of the time is used creating a model which is *good* for analysis purposes. This totals a 80/20 factor of geometry construction versus actual analysis. While NURBS basis functions itself might reduce the f rst 20 percent by allowing geometry construction to take place in existing computer-aided design (CAD) tools which have perfected this process for decades, there still remains to create a model which is *good* for analysis. T-splines along with adaptive ref nement through a posteriori error estimates is what is making this last step superf uous by completely automating this process, allowing the designer to ultimately focus on the task at hand, which is making a model in which analysis is *possible*.

2 T-splines

For our solutions, we will be using T-splines as introduced by Sederberg et al. in 2003[2]. T-splines allow for true local ref nement as they are not restricted to tensor product conf gurations. While you will have to add an entire new row or column to your mesh when ref ning using NURBS, the T-spline technology allows for T-joints.

3 Problems containing singularities

We will here present how the T-splines along with a posteriori error estimators perform on problems containing singularities. We will present a model problem which we will solve using the presented method. Obviously, T-splines will outperform the homogeneous ref nement strategies, but as we shall see, even more sophisticated NURBS ref nement strategies are not comparable with T-splines due to the fact that they are limited to tensor product ref nement. For our model problem containing a singularity, we are going to solve the stationary heat equation, or Laplace equation $\nabla^2 u = f$ on an L-shape geometry with appropriate boundary conditions.

3.1 A posteriori error estimator

For the adaptivity we will need an estimate on what parts of the grid is contributing the most to the global error. For this purpose, we will be using a resiudal-based a posteriori error estimator. From Ainsworth[3], we have

$$|||e|||^2 \leq C \left\{ \sum_{K \in \mathcal{P}} h_K^2 \|r\|^2_{L^2(K)} + \sum_{\gamma \in \Gamma} h_K \|R\|^2_{L^2(\gamma)} \right\}, \tag{1}$$

where R is a compact notation for the edge residual

$$R = \begin{cases} g - \frac{\partial u_h}{\partial \boldsymbol{n}}, & \text{on } \partial\Omega_N \\ \left[\frac{\partial u_h}{\partial \boldsymbol{n}}\right]_K - \left[\frac{\partial u_h}{\partial \boldsymbol{n}}\right]_L, & \text{on } \partial K \cap \partial L \ \ \forall \ \ K, L \in \mathcal{P} \\ 0, & \text{else} \end{cases} \tag{2}$$

and r is the internal residual $r = f - \nabla^2 u$. This allows us to quantify an error estimate for each element to be

$$\eta_K^2 = h_K^2 \|r\|^2_{L_2(K)} + h_K \|R\|^2_{L_2(\partial K)} \tag{3}$$

For comparison purposes, we provide three adaptivity strategies.
a) Uniform ref nement using NURBS.
b) Rule of thumb ref nement, where we recursively ref ne the element closest to the singularity using NURBS.
c) Adaptive T-splines where we use the error estimator η_K to ref ne the α percent elements with the highest contribution to the error.

3.2 Results

Due to the singularity the convergence rates of the uniform ref nement is completely ruined. However the rule-of-thumb ref nement keeps an optimal slope up until the point where the error from other parts of the grid than the singularity becomes dominant. The T-splines however gains an optimal convergence.

4 Smooth problems

In this section we take a look at a smooth problem, namely the static elasticity problem on an inf nite plate with a circular hole. For full details on the problem see[4].

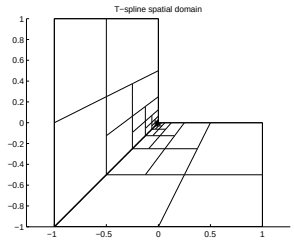

(a) T-spline grid with adaptive solver

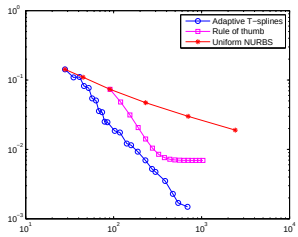

(b) Convergence rates for the three proposed ref nement strategies

Figure 1: Results obtained from the singularity problem

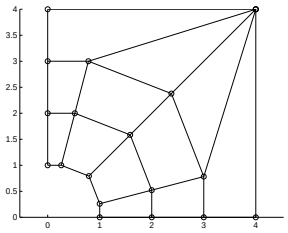

(a) The parametrization control mesh

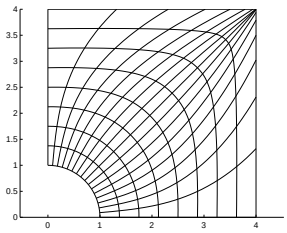

(b) The physical mapping

Figure 2: Parametrization of the hole problem

4.1 Parametrization

What is interesting here is the choice of parametrization. We will chose a particular parametrization which is given in f gure 2. The traditional way of creating sharp corners using NURBS is by making the knot vector be interpolating by creating a knot with multiplicity p where p is the degree of the NURBS. However we have created the upper right corner by stacking p control points on top of each other. Multiple control points is making the derivatives vanish, much in the same manner as multiple knots and is thus allowing us to create the sharp corner. This parametrization has some propterties which is rendering the particular error estimator presented earlier, useless. We will use the exact error for adaptation purposes and argue that given an appropriate error estimator, then T-splines will contain some remarkable properties, even for smooth problems without singularities. The problem with our choice of parametrization for the hole-problem is that it is not uniform. That is a uniform ref nement in the parametric domain, will result in a biased ref nement in the physical space. This is illustrated in f gure 2b where we have drawn one such uniform ref nement. We clearly see that the ref nements are completely biased towards the upper right corner, leaving the lower right and upper left corners with unnaturally large elements. It is however possible to bypass this by weighting the ref nement in the parametric space, but this requires hand-tailoring by the implementer, which we want to avoid as much as possible.

4.2 Refinement using T-splines

When using an adaptive T-spline ref nement strategy, this will detect the large elements that occur in the upper left and lower right corners and ref ne those as appropriate. This is a true local ref nement and will not spread out to the rest of the domain, resulting in a better ref nement. T-splines is

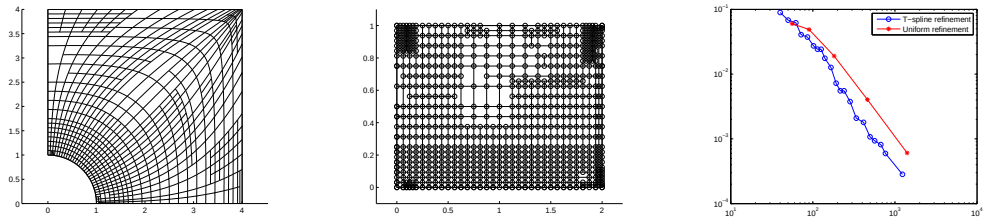

(a) Refined T-spline grid in the physical space

(b) Refined T-spline grid in the parametric space

(c) Convergence rates of T-splines versus uniform NURBS

Figure 3: Results from solving a smooth problem

as such, *negating* the effect of the bad parametrization by enforcing a true uniform refinement in the *physical* space.

This is shown in figure 3a where the physical T-mesh is illustrated. The parametric mesh corresponding to this is depicted in figure 3b where it is plotted in the parametric space.

4.3 Results

Since this problem has a smooth solution, we expect the uniform NURBS refinement to be close to optimal. As was seen, however, the (parametric) uniform refinement scheme was not uniform at all when viewed in the physical space. This is then resulting in a non-optimal refinement scheme. The adaptive T-splines countered this, and is thus providing a better convergence rate. These are shown in figure 3c.

5 Concluding remarks

T-splines shows great promise as a basis for adaptive FEM. Not only have they superior properties when it comes to true local refinement around singularities, but they also have the remarkable property of negating the effect of badly parameterized models.

REFERENCES

[1] Hughes, T. J. R., Cottrell, J. A. & Bazilevs, Y. Isogeometric analysis: Cad, finite elements, nurbs, exact geometry and mesh refinement. *Computer Methods in Applied Mechanics and Engineering* **194**, 4135–4195 (2005). URL `http://dx.doi.org/10.1016/j.cma.2004.10.008`.

[2] Sederberg, T. W., Zheng, J., Bakenov, A. & Nasri, A. T-splines and t-nurccs. In *SIGGRAPH '03: ACM SIGGRAPH 2003 Papers*, 477–484 (ACM, New York, NY, USA, 2003).

[3] Ainsworth, M. & Oden, J. T. A posteriori error estimation in finite element analysis. *Computer Methods in Applied Mechanics and Engineering* **142**, 1 – 88 (1997).

[4] Kvamsdal, T. & Okstad, K. M. Error estimation based on superconvergent patch recovery using statically admissable stress fields. *Int. J. Numer. Meth. Engng.* **42**, 443–472 (1998).

23rd Nordic Seminar on Computational Mechanics
NSCM-23
A. Eriksson and G. Tibert (Eds)

LINEAR ISOGEOMETRIC SHELL ANALYSIS IN MARINE APPLICATIONS

GEIR SKEIE*, SUSANNE STØLE-HENTSCHEL AND TORGEIR RUSTEN

*Det Norske Veritas (DNV)
Veritasveien 1, 1322, Høvik, Norway
e-mail: Geir.Skeie@dnv, web page: http://www.dnv.com/

Key words: Marine Engineering, Isogeometric Analysis, Linear Shell Formulation

Summary. Isogeometric analysis is a novel technique in Finite Element Analysis. The current paper discusses simulation in marine applications using isogeometric shell approximations.

1 INTRODUCTION

Isogeometric Analysis (IGA), Hughes *et al.* [5], is a novel approach within Finite Element Analysis (FEA) where the concept is motivated by the gap existing between Computer Aided Design (CAD) models and the FEA models. The transfer of a design model to an analysis model is a bottleneck in the current simulation based design cycle. IGA is an attempt to adapt both the analysis geometry and solution parameters to the modelling geometry found in most CAD systems in order to simplify the model transfer.

Current practise for linear analyses of thin walled structures in the marine industry includes the use lower order finite elements based on thin or moderately thick shell theory.

In CAD software spline or Non-Uniform Rational B-splines (NURBS) is used to model the geometry. Splines are defined recursively for all polynomial degrees using a knot vector. In IGA they are also used in the approximation of the displacements, thus higher order approximations are straightforward. Here an isogeometric continuum based shell element is compared to an equivalent second order element found in most finite element implementations. The current isogeometric shell implementation is based on a pure displacement formulation with no special techniques to handle out of plane shear locking or membrane locking. This is due to the fact that higher order approximations are believed to be less susceptible to locking.

The geometry model is the union of a set of patches where each patch is a tensor product NURBS surface where two patches sharing a common edge has the same parameterization. Geometry has to be generated very carefully in order to make it suitable for IGA. In particulare we note that trimmed surfaces, which are common in CAD models, are not used in IGA. Further, proper continuity in multi-patch models also pose a challenge using tensor product NURBS.

2 SHELL FORMULATION

A number of shell models are available in the literature. In the current study the shell kinematics are derived from an Isogeometric solid element formulation. This is similar to the

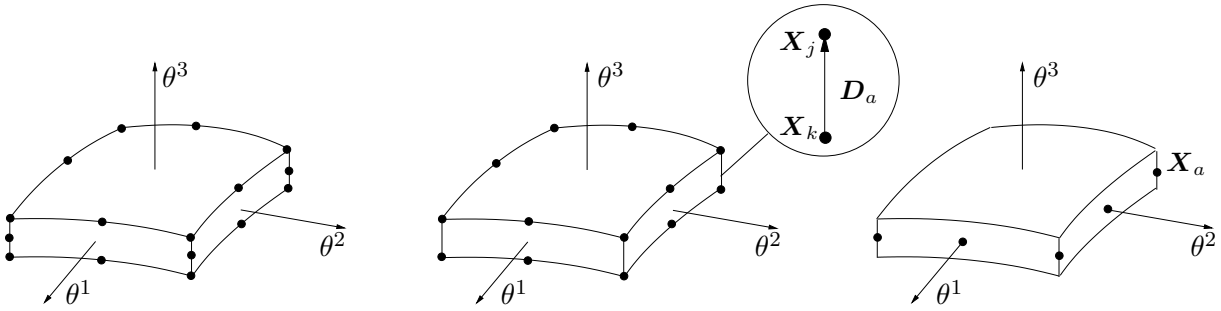

Figure 1: The degenerated solid approach illustrated in three steps: parent element, linear constraint in normal direction and midplane projection.

implementation found in SESTRA, [6], the linear finite element solver within the SESAM system. The principle approach is depicted in Figure 1.

The displacement field may be expressed using parameters defined on the shell mid surface where the through thickness in-plane displacements are expressed using midplane rotation components and the through thickness out-of-plan displacement component is constant, thus

$$\boldsymbol{u}(\theta^1, \theta^2, \theta^3) = N_a(\theta^1, \theta^2) \left(\boldsymbol{v}_a + \theta^3 t_a \boldsymbol{v}_a^d \right) \tag{1}$$

$\boldsymbol{v}_a$ denotes the midplane control point translation vector while $\boldsymbol{v}_a^d$ denotes the out-of-midplane displacement corrections. t_a is the shell thickness at the control point and θ^i are the curvilinear coordinates (parametric coordinates) and the Einstein's summation convention is used. N_a denotes the spline (in our setting NURBS) shape functions. $\boldsymbol{v}_a^d$ may be expressed using either two or three rotations where the latter include the drilling rotation;

$$\boldsymbol{v}_a^d = -\boldsymbol{D}_a \times \boldsymbol{\omega} \qquad \text{or} \qquad \boldsymbol{v}_a^d = (-\boldsymbol{A}_{a2}\Theta_{a1} + \boldsymbol{A}_{a1}\Theta_{a2}) \tag{2}$$

Θ_{ai} denotes the midplane rotation components and $\boldsymbol{A}_{a^\alpha}$ is an orthogonal local coordinate system that span the shell tangent plane. $\boldsymbol{\omega}$ denotes the three components of the global rotation vector.

The linearized strains may be expressed in the global coordinate system according to the familiar expression from linearized elasticity. The zero transverse normal stress condition $\sigma_{33} = 0$ has to be enforced in the local shell coordinate frame.

Since the formulation may include an additional unknown the formulation needs to be stabilized. One criteria for the stabilization is that is should not destroy the sparsity pattern of the patch stiffness matrix. A penalty formulation, suggested by Fox and Simo [4], is used with this in mind. The augmented potential energy functional may be expressed as

$$\Pi_\gamma(\boldsymbol{u}, \boldsymbol{\omega}) = \Pi(\boldsymbol{u}, \boldsymbol{\omega}) + \frac{\gamma}{2} \int_\Omega \left(\boldsymbol{A}_1 \cdot \frac{\partial \boldsymbol{u}}{\partial \theta^2} - \frac{\partial \boldsymbol{u}}{\partial \theta^1} \cdot \boldsymbol{A}_2 - 2\boldsymbol{A}_1 \times \boldsymbol{A}_2 \cdot \boldsymbol{\omega} \right)^2 \tag{3}$$

where $\Pi(\cdot)$ denotes the potential energy for the shell formulation and γ is the penalty parameter.

The equations above use a local coordinate triad to express the shell rotations and the local material law. A number of methods to establish the local triad at control points has been suggested in Benson *et al.* [2].

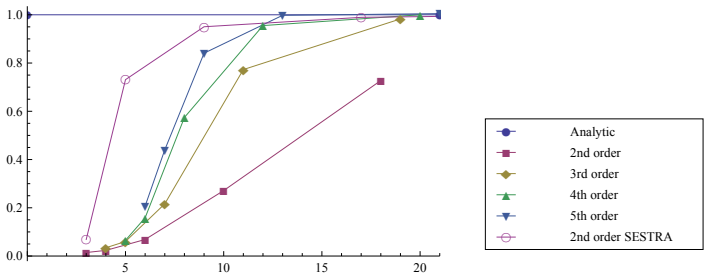

Figure 2: Pinched cylinder with diaphragms; convergence of the displacement under the load.

3 NUMERICAL EXAMPLE

3.1 Pinched cylinder

The shell obstacle course suggested by Belytschko *et al.* [1] is used to check robustness and accuracy for shell implementation in complex strain states. The problem set includes three problems, namely, the Scordelis-Lo roof, the pinched cylinder diaphragm and finally the pinched hemispherical shell. The cylinder is fully restrained by rigid diagraph at the ends and is subjected to two radial point loads alternating at 90°. The displacement in the direction of the point load is compared to the reference solution given as $|u_z| = 1.8248 \times 10^{-5}$.

The convergence curves for displacement under the load as a function of the mesh density for the spline and SESTRA formulation is shown in Figure 2.

3.2 Tubular joint

Pipe intersections occur frequently in off-shore applications. A simple two pipe model is shown in Figure 3 where the pipes meet at a right angle. The diameters are different for the two intersecting pipes, $D_1 = 2$ and $D_2 = 1$. The pipe segements are $L_1 = 10$ and $L_2 = 5$ respectively. The number of patches in the pipe model is 12.

A stress analysis is performed. The two ends of the larger pipe are fixed in all translations and rotations. The free end of the smaller pipe is subject to a line-load with a load intensity of unity in the global z-direction, that is in the longitudinal direction of the larger pipe. The geometry is not exact in this example, that is, the vertical cylinder is not a perfect cylinder in the neighborhood of the intersection.

The convergence of the displacement under the load is shown in Figure 3.

4 CONCLUSIONS

The results are comparable to the current second order shell finite element. However, the SESTRA second order shell element performs in general better than the plain Isogeometric shell implementation. The current Isogeometric shell implementation is based on a pure displacement formulation with no remedies to handle out of plane shear locking or membrane locking. This is due to the fact that higher order approximations are believed to be less susceptible to locking. IGA is in its infancy and more research is needed to tune the performance in commercial shell type applications.

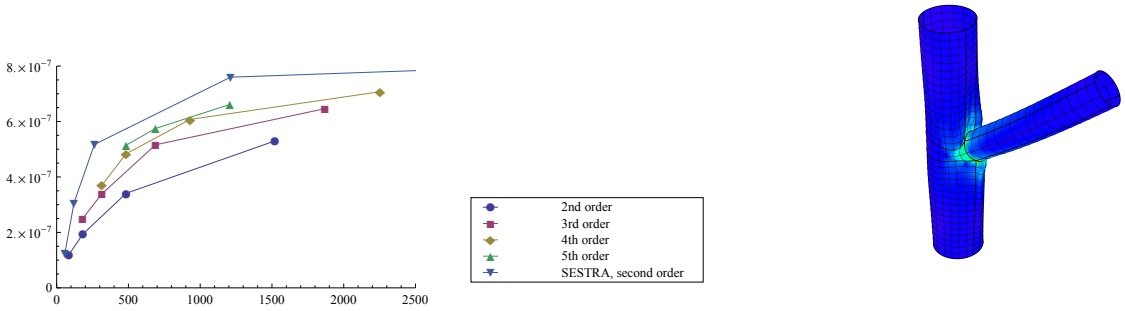

Figure 3: Two intersecting pipes; convergence of the displacement under the load. $E = 2.1 \times 10^{11}$, $\nu = 0.3$, $t = 0.02$ and $f_z = 1$.

REFERENCES

[1] Ted Belytschko, Henryk Stolarski, Wing Kam Liu, Nicholas Carpenter, and Jame S.J. Ong. Stress projection for membrane and shear locking in shell finite elements. *Computer Methods in Applied Mechanics and Engineering*, 51(1-3):221 – 258, 1985.

[2] D.J. Benson, Y. Bazilevs, M.-C. Hsu, and T.J.R. Hughes. A Large Deformation, Rotation-Free, Isogeometric Shell. Technical Report 09-37, Institute for Computational Engineering and Sciences, The University ofTexas at Austin, 201 East 24th Street, 1 University Station C0200, Austin, TX 78712, USA, 2009.

[3] J. A. Cottrell, T. J .R. Hughes, and A. Reali. Studies of Refinement and Continuity in Isogeometric Structural Analysis. Technical Report 07-05, Institute for Computational Engineering and Sciences, The University ofTexas at Austin, 201 East 24th Street, 1 University Station C0200, Austin, TX 78712, USA, 2007.

[4] D.D. Fox and J.C. Simo. A drill rotation formulation for geometrically exact shells. *Computer Methods in Applied Mechanics and Engineering*, 98(3):329 – 343, 1992.

[5] T.J.R. Hughes, J. A. Cottrel, and Y. Bazilevs. Isogeometric analysis: CAD, finite elements, NURBS, exact geometry and mesh refinement. *Computer Methods in Applied Mechanics and Engineering*, 194:4135—4195, 2005.

[6] SESTRA. *SESTRA – Super Element Structural Analysis, User's Manual*. DNV Software, Høvik, Norway, 2008.

23rd Nordic Seminar on Computational Mechanics
NSCM-23
A. Eriksson and G. Tibert (Eds)

ISOGEOMETRIC FINITE ELEMENT METHODS FOR NONLINEAR PROBLEMS

KNUT MORTEN OKSTAD*, KJELL MAGNE MATHISEN†, AND TROND KVAMSDAL*

*SINTEF ICT - Department of Applied Mathematics
NO-7465 Trondheim, Norway
E-mail: knut.morten.okstad@sintef.no, trond.kvamsdal@sintef.no
Web page: http://www.sintef.no

†Department of Structural Engineering
Norwegian University of Science and Technology
NTNU, NO-7491 Trondheim, Norway
E-mail: kjell.mathisen@ntnu.no
Web page: http://www.ntnu.no

Key words: Isogeometric analysis, NURBS, Nonlinear FEM, Finite deformation elasticity.

Summary. We are developing a framework (C++ class library) for isogeometric, nonlinear quasi-static FE analysis in structural applications, using splines and NURBS as basis functions. The work is based on the foundation developed in the project ICADA for linear analysis, but have been augmented with additional capabilities such that nonlinear analysis of finite deformation problems in solid mechanics involving material and geometrical nonlinearities may be performed. Herein, we report some preliminary findings when comparing results obtained with NURBS and classical Lagrange finite elements on a three-dimensional finite deformation elastic problem.

1 FINITE ELEMENT FORMULATION

The new paradigm of Isogeometric analysis, which was introduced by Hughes *et al.*[1,2], demonstrates that much is to be gained with respect to efficiency, quality and accuracy in analysis by replacing traditional finite elements by volumetric NURBS (Non-Uniform Rational B-Splines) elements. By using NURBS, which is standard technology employed in CAD systems, as basis functions in the finite element analysis one may transfer models from design directly to analysis without any modifications. This reduces the man-hours needed for establishing analysis-suitable finite element meshes, as well as no loss of accuracy in the geometrical description of the object at hand. Thus, use of NURBS seems to be a very appealing step forward for finite element analysis. It is therefore natural to investigate the numerical performance of NURBS compared to traditional Lagrange basis functions. We have been doing so for linear elasticity problems and obtained very promising results, and we have now started to address this for finite deformation elastic problems.

Two important features with NURBS are its capability to exactly represent conical sections (e.g. circles) and that a regular p-th order NURBS basis is $\mathcal{C}^{p-1}$ continuous. Many industrial

solid/structural mechanics problems involve objects where part of the geometry is described by circles or circle segments, and traditionally this has been represented inaccurately by means of low order Lagrange polynomials, whereas by using NURBS these inaccuracies may be eliminated. Furthermore, in elasticity we do have continuous stresses and strains except for at certain singular points, lines or surfaces, i.e. the displacement field is $\mathcal{C}^1$-continuous away from singularities. Classical finite elements based on Lagrange polynomials are only $\mathcal{C}^0$-continuous and this lack of regularity shows up in discontinuous (along inter-element boundaries) finite element stress and strain fields, whereas NURBS ($p \geq 2$) may represent this behavior qualitatively correct.

NURBS-based and classical Lagrange, finite deformation, displacement-based, solid elements of any order have been implemented into our nonlinear FE solver. Both the material and spatial formulation, based on the reference and the current configuration, respectively, have been implemented. However, as pointed out in standard references on the subject[3,4], the spatial formulation is more computational efficient on the elemental level due to the standard sparse structure of the **B**-matrix, that coincides with the sparsity of the **B**-matrix of the linear theory, compared to the full **B**-matrix for the material formulation.

Also as pointed out by Miehe[5], the formulation and the finite element implementation of finite deformation isotropic elasticity turns out to be more compact and carried out with lower computational effort when adopting the spatial configuration. As demonstrated in[5], the elasticity equations may be formulated exclusively based on the left Cauchy-Green tensor, often referred to as the Finger tensor; $\mathbf{b} = \mathbf{F}\mathbf{F}^T$, that may be be computed directly and with low computational effort for a given deformation gradient **F**. For this reason the spatial formulation is adopted in the present study.

2 NUMERICAL RESULTS

The isogeometric nonlinear solver has been tested on a geometry that cannot be represented exactly by Lagrange polynomials. It involves finite deformation analysis of a thick hollow cylinder, for which the exact initial geometry can be obtained with quadratic NURBS. Due to symmetry only one quarter of the whole problem is discretized and analyzed, and boundary conditions at the two symmetry planes are set accordingly, as shown in Figure 1. This problem was first studied by Büchter and co-workers[6] using shell elements, and later by others[7,8] considering it as a 3D continuum. The material model applied is a standard compressible Neo-Hookean model with strain energy function

$$W(J,\mathbf{b}) = \frac{1}{2}\mu(\mathrm{tr}\mathbf{b} - 3) - \mu \ln J + \frac{1}{2}\lambda(\ln J)^2 \tag{1}$$

where μ and λ are Lame's constants that may be derived from Young's modulus E and Poisson's ratio ν, J is the determinant of the deformation gradient **F** and **b** is the Finger tensor. Since Poisson's ratio $\nu = 0.4$, no volumetric locking is expected.

Herein, the cylinder is parameterized by a single NURBS patch and analyzed using quadratic and cubic NURBS as basis functions, and compared with standard quadratic Lagrange elements. Gaussian integration is used throughout all analyses applying $3\times3\times3$ Gauss points for quadratic NURBS as well as Lagrange basis functions and $4 \times 4 \times 4$ Gauss points for NURBS functions of order 3. Even though it is sufficient with quadratic basis functions in the thickness direction to capture the bending behavior, herein NURBS functions of order 3 are used in the thickness

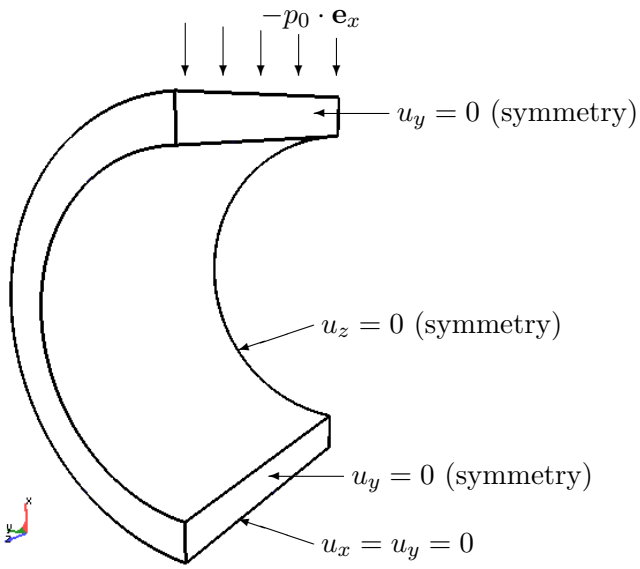

Half length	:	L	= 15.0
Outer radius	:	R_o	= 10.0
Inner radius	:	R_i	= 8.0
Young's modulus	:	E	= 16800
Poisson's ratio	:	ν	= 0.4
Load intensity	:	p_0	= 500.0

Figure 1: Compression of a thick cylinder: Geometry and properties.

direction as well for the cubic NURBS elements. In order to avoid singularities due to the concentrated loading, an equivalent constant traction is applied to the reference configuration of the top symmetry cross-section of the cylinder and kept fixed during deformation, such that the total load applied on the cylinder is 30×10^3. Therefore, we cannot expect full compliance with the results obtained in[7,8] where the load is applied as a line load along the top edge.

The results are presented in Figure 2. As expected, cubic NURBS gives a somewhat softer solution than quadratic NURBS. However it is also interesting to note that the quadratic NURBS seems to give a slightly stiffer solution than the Lagrange elements. This is believed to be an effect of inter-element continuity, since this is one of the main differences between NURBS finite elements and Lagrange finite elements. While standard Lagrange finite elements provide $\mathcal{C}^0$-continuous interpolation between elements, $\mathcal{C}^{p-1}$-continuity may be achieved with NURBS throughout an entire patch. In general it is interesting to investigate further whether such improved inter-element continuity will improve the quality of the approximate solution or not, particularly in cases where standard finite elements tend to lock.

REFERENCES

[1] T. J. R. Hughes, J. A. Cottrell, and Y. Bazilevs. Isogeometric Analysis: CAD, Finite Elements, NURBS, Exact Geometry and Mesh Refinement. *Computer Methods in Applied Mechanics and Engineering*, 194:4135–4195, 2005.

[2] J. A. Cottrell, T. J. R. Hughes, and Y. Bazilevs. *Isogeometric Analysis: Toward Integration of CAD and FEA*. John Wiley & Sons, Chichester, England, 2009.

[3] O. C. Zienkiewicz and R. L. Taylor. *The Finite Element Method for Solid and Structural Mechanics*. Elsevier Butterworth and Heinemann, Oxford, England, 6th edition, 2005.

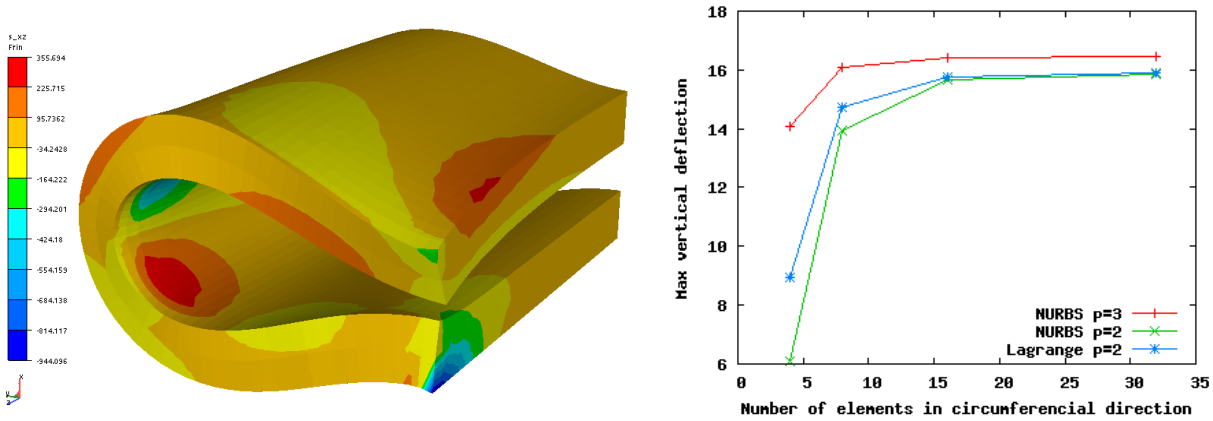

Figure 2: Compression of a thick cylinder: Deformed configuration with σ_{xz} Cauchy stress for the $32 \times 16 \times 1$ mesh with quadratic NURBS (left), and maximum vertical deflection for all meshes (right).

[4] P. Wriggers. *Nonlinear Finite Element Methods*. Springer, Berlin, Germany, 2008.

[5] C. Miehe. Aspects of the Formulation and Finite Element Implementation of Large Strain Isotropic Elastcity. *International Journal for Numerical Methods in Engineering*, 37:1981–2004, 1994.

[6] N. Büchter, E. Ramm, and D. Roehl. Three-dimensional Extension of Non-linear Shell Formulation based on the Enhanced Assumed Strain Concept. *International Journal for Numerical Methods in Engineering*, 37:2551–2568, 1994.

[7] S. Reese, P. Wriggers, and B. D. Reddy. A New Locking-free Brick Element Technique for Large Deformation Problems in Elasticity. *Computers and Structures*, 75:291–304, 2000.

[8] T. Elguedj, Y. Bazilevs, V. M. Calo, and T. J. R. Hughes. $\overline{\mathrm{B}}$ and $\overline{\mathrm{F}}$ Projection Methods for Nearly Incompressible Linear and Non-linear Elasticity and Plasticity using Higher-order NURBS Elements. *Computer Methods in Applied Mechanics and Engineering*, 197:2732–2762, 2008.

23rd Nordic Seminar on Computational Mechanics
NSCM-23
A. Eriksson and G. Tibert (Eds)

MAPPING OF STRESS, STRAIN, DISLOCATION DENSITY AND FRACTURE PROBABILITY IN SILICON MULTICRYSTALS

J. COCHARD[*], S. GOUTTEBROZE[†], M. M'HAMDI[†] AND Z.L. ZHANG[*]

[*] Department of Structural Engineering
Norwegian University of Science and Technology (NTNU)
Rich. Birkelandsvei 1ª, NO-7491 Trondheim, Norway
e-mail: julien.cochard@ntnu.no, web page: http://www.ntnu.no/kt

[†] SINTEF Materials and Chemistry
P.P. 124 Blindern, NO-0315 Oslo, Norway
e-mail: mohammed.mhamdi@sintef.no, web page: http://www.sintef.no

Key words: Crystal plasticity, Micromechanics, Silicon, Computational Methods.

Summary. We derive a novel rate-dependent, physically based constitutive model for intrinsic and oxygen-contaminated silicon monocrystals and calibrate it on experimental data covering a broad range of temperature and strain rates. This model is implemented further in a commercial Finite Elements software and used to study the evolution of stresses, strains and dislocation densities in both monocrystalline and multicrystalline silicon materials.

1 INTRODUCTION

Silicon ingots produced by directional solidification for the photovoltaic (PV) industry exhibit a multicrystalline nature (mc-Si) that makes their mechanical analysis complicated to perform. Assessing the fracture risk of a brittle material relies on probabilistic methods that request the knowledge of the stress level throughout the material[1]. Silicon being brittle below 600 °C approximately, it is of high industrial interest to predict the fracture probability of mc-Si given a thermo-mechanical loading path such as a solidification and cooling process history.

The constitutive models used until now to analyze the stress field evolution in mc-Si materials assume them to be continuum, homogeneous single crystals, and plasticity is assumed to be isotropic[2-4]. This approach provides with the thermally-induced, macroscopic stresses. However, the multicrystalline nature of directionally solidified ingots and wafers leads to additional, mesoscopic stresses owing to kinematic compatibility requirements at the grain boundaries[5,6]. Finally, the presence of inclusions and impurities in Solar-grade silicon (SoG-Si) implies stress peaks on a microscopic scale[7,8].

We introduce in section 2 a novel constitutive model for silicon materials based on the rate-dependent crystal plasticity theory, able to account for complex thermo-mechanical loading paths and the subsequent stress and dislocation density evolutions from the melting

point down to room temperature[9]. Model parameters for intrinsic and oxygen-contaminated single crystals are derived from tensile tests performed at high temperatures[10,11].

We apply this constitutive model to 3D simulations of different thermo-mechanical loadings of mc-Si samples in section 3. The evolution of stresses with time is analyzed. Stress, strain and dislocation density distributions in the final material are shown to be heterogeneous. The fracture probability map at room temperature is drawn using our experimental characterization of SoG-Si.

2 CONSTITUTIVE MODEL

The constitutive model adopted in this work is physically based on the dynamical properties of dislocations in silicon crystals. Dislocations in silicon have been studied for many decades at high temperatures and their velocity is well established[12,13] in the temperature range below roughly 1323 K as a function of temperature T and the effective stress τ_{eff}:

$$v^{(\alpha)} = v_0 \frac{\tau_{eff}^{(\alpha)}}{\tau_0} \exp\left(-\frac{U}{k_b T}\right) \tag{1}$$

Where v_0 and τ_0 are constants, U is the activation energy for dislocation motion proceeding by double kink nucleation and propagation in the considered temperature range, and k_b is Boltzmann's constant. Note that the equation is valid on any of the 12 slip systems α allowed by the diamond cubic structure. Orowan's law is used to link the microscopic dislocation mechanisms to the macroscopic plastic slip rate:

$$\dot{\gamma}_p^{(\alpha)} = \rho_m^{(\alpha)} b v^{(\alpha)} \tag{2}$$

The constitutive model is characterized by the expression of the effective stress, and the rate equations governing the evolution of the dislocation densities.

2.1 Evolution of dislocation densities and internal stress

Two dislocation density populations are distinguished on each slip system: the mobile dislocation density that carries plastic flow ρ_m and the density of immobile dislocations ρ_i that contribute to the buildup of internal stresses but do not affect the plastic slip rates. In the presence of dissolved oxygen or other fast-diffusing impurities, the dislocations are pinned by impurity atoms that have segregated at their core and the effective dislocation density actually carrying plastic flow $\rho_{m,eff}$ is a fraction of ρ_m that depends solely on the unlocking stress, stress required to free dislocations from their impurities. The temperature-dependent model equations have been derived and their parameters calibrated elsewhere[9,14].

The internal stress τ_{int} is made up of three components, one stemming from the long-range stresses generated by the mobile dislocations τ_{lr}, another one representing short-range interactions due to e.g. forest interactions τ_{sr}, the last term being due to dislocation pinning by impurities that leads to the appearance of an unlocking stress[11,15]. τ_{int} reads:

$$\tau_{eff}^{(\alpha)} = \max\left(\left|\tau^{(\alpha)}\right| - \tau_{\text{int}}^{(\alpha)}, 0\right) \tag{3}$$

Where τ is the Schmid stress, projection of the second Piola-Kirchhoff stress onto each slip system. Detailed expressions of the internal stress components are given elsewhere[9,14].

2.3 Implementation into an explicit Finite Element Software

The constitutive model is implemented into Abaqus/Explicit in a VUMAT (user material) routine working in the co-rotational coordinate system. The kinematics used in large strains crystal plasticity rely on the multiplicative decomposition of the deformation gradient, and even though plastic slip does not deform the crystal lattice it does induce a rotation of the material point, and care must be taken to correctly account for this effect[9,14].

3 FOUR-POINT BENDING OF SILICON MULTICRYSTALS

Multicrystalline silicon bars of dimensions 4x3x50mm3 are generated from smoothed EBSD scans of real specimen. In this work we consider only bars made up of 11 crystals, which orientations are randomly assigned. Figure 1 shows the mesh used for simulating the four point bending test, as well as the orientations of the different crystals.

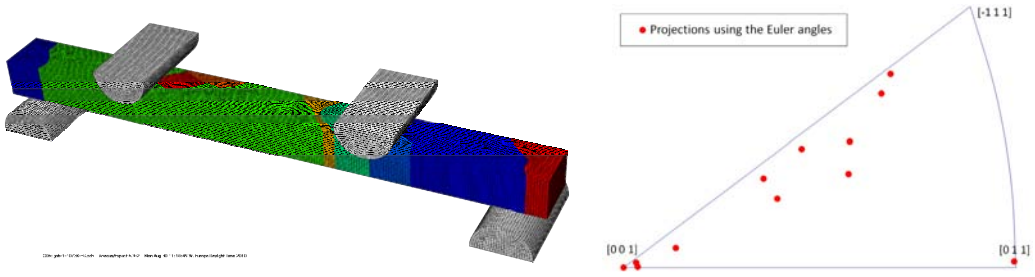

Figure 1: FE mesh used for simulation of 4PB tests of mc-Si bars (~140,000 elements) and crystal orientations

Dissolved oxygen can be incorporated into the model if required. Deformation is simulated at a strain rate of 10^{-5} s^{-1} and a temperature of 1173 K. The initial dislocation density is homogeneous and equal to $\rho_m=10^8$ m^{-2} per slip system. Deformation is stopped after the lower yield point, in the steady-state of deformation. Output clearly outlines the inhomogeneity of stresses and dislocation densities in the sample (Figure 2). Comparison can be done with the case of monocrystals loaded in similar conditions. Stress concentrations caused by kinematic compatibility at the grain boundaries and the intrinsic material anisotropy increase the failure probability at room temperature and favors the nucleation and opening of microcracks at high temperatures.

4 CONCLUSIONS

- The constitutive model successfully reproduces the behavior of intrinsic and oxygen-contaminated silicon monocrystals at high temperatures
- Application to multicrystals shows a global force-displacement behavior similar to the one of monocrystals, but reveals strong inhomogeneities at a smaller scale
- Simulations predict the development of stress concentrations and localized dislocation clusters as experimentally observed

- Coupling of these results with statistically determined fracture strength has been done

This model will be applied in the future to the case of directionally solidified ingots.

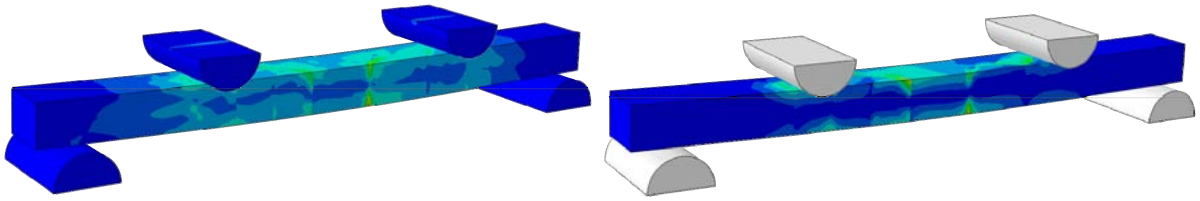

Figure 2: (left) Von Mises stress distribution (right) total density of dislocations

REFERENCES

[1] B.R. Lawn, *Fracture of brittle solids, 2nd Edition* (1993).
[2] O.W. Dillon, C.T. Tsai, R.J. De Angelis, "Dislocation dynamics during the growth of silicon ribbon", *J. Appl. Phys*. **60**, 1784 (1986)
[3] Y.K. Kim, R.J. De Angelis, C.T. Tsai, O.W. Dillon, "Dislocation motion and multiplication during the growth of silicon ribbon", *Acta Metall*. **35**, 2091 (1987)
[4] M. M'Hamdi, E.A. Meese, H. Laux, E.J. Øvrelid, "Thermomechanical analysis of directional crystallization of multicrystalline silicon ingots", *Mat. Sci. Forum* **508**, 597 (2006)
[5] F. Barbe, L. Decker, D. Jeulin, G. Cailletaud, "Intergranular and intragranular behavior of polycrystalline aggregates. Part I: F.E. model", *Int. J. Plast*. **17**, 513 (2001)
[6] K. Sai, G. Cailletaud, S. Forest, "Micromechanical modeling of the inelastic behavior of directionally solidified materials", *Mech. Mater*. **38**, 203 (2006)
[7] J. Cochard, S. Gouttebroze, S. Dumoulin, M. M'Hamdi, Z.L. Zhang, "Mechanical modeling of impure silicon materials", 24th EUPVSEC, Hamburg (2009)
[8] M. M'Hamdi, S. Gouttebroze, 24th EUPVSEC, Hamburg (2009)
[9] J. Cochard, I. Yonenaga, S. Gouttebroze, M. M'Hamdi, Z.L. Zhang, "Constitutive modeling of silicon monocrystals in easy glide", *J. Appl. Phys*. **107**, 033512 (2010)
[10] I. Yonenaga, K. Sumino, "Dislocation dynamics in the plastic deformation of silicon crystals I. Experiments", *Phys. Stat. Sol. (a)* **50**, 685 (1978)
[11] I. Yonenaga, K. Sumino, K. Hoshi, "Mechanical strength of silicon crystals as a function of the oxygen concentration", *J. Appl. Phys.* **56**, 2346 (1984)
[12] M. Imai, K. Sumino, "In-situ X-ray topographic study of the dislocation mobility in high-purity and impurity-doped silicon crystals", *Phil. Mag. A* **47**, 599 (1983)
[13] H. Siethoff, "Yield point and dislocation velocity of diamond and zincblende semiconductors in different temperature regimes", *Phil. Mag. A* **82**, 1299 (2002)
[14] J. Cochard, I. Yonenaga, S. Gouttebroze, M. M'Hamdi, Z.L. Zhang, "Constitutive modeling of intrinsic and oxygen-contaminated silicon monocrystals in easy glide", *J. Appl. Phys*., accepted for publication (2010)
[15] J.D. Murphy, S. Senkader, R.J. Falster, P.R. Wilshaw, "Oxygen transport in Czochralski silicon investigated by dislocation locking experiments", *Mat. Sci. Eng. B* **134**, 176 (2006)

23rd Nordic Seminar on Computational Mechanics
NSCM-23
A. Eriksson and G. Tibert (Eds)

A CONSTITUTIVE MODEL FOR STRAIN-RATE DEPENDENT DUCTILE-TO-BRITTLE TRANSITION

JUHA HARTIKAINEN*, KARI KOLARI† AND REIJO KOUHIA*

*Department of Structural Engineering and Building Technology
Aalto University School of Science and Technology
P.O. Box 12100, FI-00076 Aalto, Finland
e-mail: firstname.lastname@tkk.fi, web page: http://www.tkk.fi/

†VTT Technical Research Center of Finland
P.O. Box 1000, FI-02044 VTT, Finland
e-mail: firstname.lastname@vtt.fi, web page: http://www.vtt.fi/

Key words: Constitutive model, Continuum damage mechanics, Viscoplasticity, Dissipation potential, Ductile-to-brittle transition

Summary. In this paper a simple phenomenological model to describe ductile to brittle transition of rate-dependent solids is presented. The model is based on consistent thermodynamic formulation using proper expressions for the Helmholtz free energy and the dissipation potential. In the model the dissipation potential is additively split into damage and visco-plastic parts and the transition behaviour is obtained using a stress dependent damage potential. Damage is described by using a vectorial variable.

1 INTRODUCTION

Most materials exhibit rate-dependent inelastic behaviour. Increasing strain-rate usually increases the yield stress thus enlarging the elastic range. However, the ductility is gradually lost and for some materials there exist a rather sharp transition strain-rate zone after which the material behaviour is completely brittle.

In this paper a simple phenomenological approach to model ductile to brittle transition of rate-dependent solids is presented. It is an extension to the model presented in [1,2] using vectorial damage variable [3]. The model is based on consistent thermodynamic formulation using proper expressions for the Helmholtz free energy and dissipation potential. The dissipation potential is additively split into damage and visco-plastic parts and the transition behaviour is obtained using a stress dependent damage potential. The basic features of the model are discussed.

2 THERMODYNAMIC FORMULATION

The constitutive model is derived using a thermodynamic formulation, in which the material behaviour is described completely through the Helmholz free energy and the dissipation potential in terms of the variables of state and dissipation and considering that the Clausius-Duhem inequality is satisfied [4].

The Helmholtz free energy

$$\psi = \psi(\boldsymbol{\epsilon}_\mathrm{e}, \mathbf{D}) \tag{1}$$

is assumed to be a function of the elastic strains, $\boldsymbol{\epsilon}_\mathrm{e}$, and the damage vector $\mathbf{D}$. Assuming small strains, the total strain can be additively decomposed into elastic and inelastic strains $\boldsymbol{\epsilon}_\mathrm{i}$ as $\boldsymbol{\epsilon} = \boldsymbol{\epsilon}_\mathrm{e} + \boldsymbol{\epsilon}_\mathrm{i}$.

The Clausius-Duhem inequality, in the absence of thermal effects, is formulated as

$$\gamma \geq 0, \quad \gamma = -\rho\dot{\psi} + \boldsymbol{\sigma} : \dot{\boldsymbol{\epsilon}}, \tag{2}$$

where ρ is the material density. As usual in the solid mechanics, the dissipation potential

$$\varphi = \varphi(\boldsymbol{\sigma}, \mathbf{Y}) \tag{3}$$

is expressed in terms of the thermodynamic forces $\boldsymbol{\sigma}$ and $\mathbf{Y}$ dual to the fluxes $\dot{\boldsymbol{\epsilon}}_\mathrm{i}$ and $\dot{\mathbf{D}}$, respectively. The dissipation potential is associated with the power of dissipation, γ, such that

$$\gamma = \frac{\partial \varphi}{\partial \boldsymbol{\sigma}} : \boldsymbol{\sigma} + \frac{\partial \varphi}{\partial \mathbf{Y}} \cdot \mathbf{Y}. \tag{4}$$

Using definition (4) equation $(2)_2$ and defining that $\rho\partial\psi/\partial\mathbf{D} = -\mathbf{Y}$, result in equation

$$\left(\boldsymbol{\sigma} - \rho\frac{\partial \psi}{\partial \boldsymbol{\epsilon}_\mathrm{e}}\right) : \dot{\boldsymbol{\epsilon}}_\mathrm{e} + \left(\dot{\boldsymbol{\epsilon}}_\mathrm{i} - \frac{\partial \varphi}{\partial \boldsymbol{\sigma}}\right) : \boldsymbol{\sigma} + \left(\dot{\mathbf{D}} - \frac{\partial \varphi}{\partial \mathbf{Y}}\right) \cdot \mathbf{Y} = 0. \tag{5}$$

Then, if eq. (5) holds for any evolution of $\dot{\epsilon}_\mathrm{e}$, σ and Y, inequality (2) is satisfied and the following relevant constitutive relations are obtained:

$$\boldsymbol{\sigma} = \rho\frac{\partial \psi}{\partial \boldsymbol{\epsilon}_\mathrm{e}}, \qquad \dot{\boldsymbol{\epsilon}}_\mathrm{i} = \frac{\partial \varphi}{\partial \boldsymbol{\sigma}}, \qquad \dot{\mathbf{D}} = \frac{\partial \varphi}{\partial \mathbf{Y}}. \tag{6}$$

3 PARTICULAR MODEL

In the present formulation the Helmholtz free energy, ψ, is a function depending on the symmetric second order strain tensor $\boldsymbol{\epsilon}_\mathrm{e}$ and the damage vector $\mathbf{D}$, the integrity basis thus consists of the following six invariants

$$I_1 = \operatorname{tr}\boldsymbol{\epsilon}_\mathrm{e}, \quad I_2 = \tfrac{1}{2}\operatorname{tr}\boldsymbol{\epsilon}_\mathrm{e}^2, \quad I_3 = \tfrac{1}{3}\operatorname{tr}\boldsymbol{\epsilon}_\mathrm{e}^3, \quad I_4 = \|\mathbf{D}\|, \quad I_5 = \mathbf{D}\cdot\boldsymbol{\epsilon}_\mathrm{e}\cdot\mathbf{D}, \quad I_6 = \mathbf{D}\cdot\boldsymbol{\epsilon}_\mathrm{e}^2\cdot\mathbf{D}. \tag{7}$$

A particular expression for the free energy, describing the elastic material behaviour with the directional reduction effect due to damage, is given by[3]

$$\begin{aligned}\rho\psi = {} & (1 - I_4)\left(\tfrac{1}{2}\lambda I_1^2 + 2\mu I_2\right) \\ & + H(\sigma^\perp)\frac{\lambda\mu}{\lambda + 2\mu}(I_4 I_1^2 - 2I_1 I_5 I_4^{-1} + I_5^2 I_4^{-3}) + (1 - H(\sigma^\perp))(\tfrac{1}{2}\lambda I_4 I_1^2 + \mu I_5^2 I_4^{-3}) \\ & + \mu\left(2I_4 I_2 + I_5^2 I_4^{-3} - 2I_6 I_4^{-1}\right),\end{aligned} \tag{8}$$

where λ and μ are the Lamé parameters, H is the Heaviside step-function and

$$\sigma^\perp = \lambda I_1 + 2\mu\hat{\mathbf{D}}\cdot\boldsymbol{\epsilon}_\mathrm{e}\cdot\hat{\mathbf{D}}, \quad \text{and} \quad \hat{\mathbf{D}} = \mathbf{D}/I_4. \tag{9}$$

To model the ductile-to-brittle transition due to increasing strain-rate, the dissipation potential is decomposed into the brittle damage part, $\varphi_{\rm d}$, and the ductile viscoplastic part, $\varphi_{\rm vp}$, as

$$\varphi(\boldsymbol{\sigma},\mathbf{Y}) = \varphi_{\rm d}(\mathbf{Y})\varphi_{\rm tr}(\boldsymbol{\sigma}) + \varphi_{\rm vp}(\boldsymbol{\sigma}), \tag{10}$$

where the transition function, $\varphi_{\rm tr}$, deals with the change in the mode of deformation when the strain-rate $\dot{\boldsymbol{\epsilon}}_{\rm i}$ increases. Applying an overstress type of viscoplasticity[5,6,7] and the principle of strain equivalence[8,9], the following choices are made to characterize the inelastic material behaviour:

$$\varphi_{\rm d} = \frac{1}{2r+2}\frac{Y_{\rm r}}{\tau_{\rm d}(1-I_4)}H(\epsilon_1-\epsilon_{\rm tresh})\left(\frac{\mathbf{Y}\cdot\mathbf{M}\cdot\mathbf{Y}}{Y_{\rm r}^2}\right)^{r+1}, \tag{11}$$

$$\varphi_{\rm tr} = \frac{1}{pn}\left[\frac{1}{\tau_{\rm vp}\eta}\left(\frac{\bar{\sigma}}{(1-I_4)\sigma_{\rm r}}\right)^{p}\right]^{n}, \tag{12}$$

$$\varphi_{\rm vp} = \frac{1}{p+1}\frac{\sigma_{\rm r}}{\tau_{\rm vp}}\left(\frac{\bar{\sigma}}{(1-I_4)\sigma_{\rm r}}\right)^{p+1}, \tag{13}$$

where parameters $\tau_{\rm d}$, r and n are associated with the damage evolution, and parameters $\tau_{\rm vp}$ and p with the visco-plastic flow. In addition, η denotes the inelastic transition strain-rate. The damage treshold strain is $\epsilon_{\rm tresh}$ and the largest principal strain is denoted as ϵ_1. Direction of the damage vector is defined through the tensor

$$\mathbf{M} = \mathbf{n}\otimes\mathbf{n} \tag{14}$$

where $\mathbf{n}$ is the eigenvector of the elastic strain tensor corresponding to the largest principal strain ϵ_1 and $\otimes$ denotes the tensor product. The relaxation times $\tau_{\rm d}$ and $\tau_{\rm vp}$ have the dimension of time and the exponents $r, p \geq 0$ and $n \geq 1$ are dimensionless. $\bar{\sigma}$ is a scalar function of stress, e.g. the effective stress $\sigma_{\rm eff} = \sqrt{3J_2}$, where J_2 is the second invariant of the deviatoric stress. The reference values $Y_{\rm r}$ and $\sigma_{\rm r}$ can be chosen arbitrarily, and they are used to make the expressions dimensionally reasonable. Since only isotropic elasticity is considered, the reference value $Y_{\rm r}$ has been chosen as $Y_{\rm r} = \sigma_{\rm r}^2/E$, where E is the Young's modulus.

Making use of eqs. (6), choices (8)-(13) yield the desired constitutive equations.

This particular model has the following general properties:

- Elastic stiffness is reduced monotonously due to damage.
- The model does not include any specific yield stress.
- In the absence of damage evolution, the inelastic model behaves under a constant uniaxial strain-rate loading as
$$\sigma \to (\tau_{\rm vp}\dot{\epsilon}_0)^{1/p}\sigma_{\rm r} \quad \text{when} \quad t\to\infty,$$
where $\dot{\epsilon}_0$ is a prescribed strain-rate;
- In the evolution of damage, the constraint for the damage $D = I_4 = \|\mathbf{D}\|$ that $D \in [0,1]$ is satisfied automatically, since initially $D = 0$, $\dot{\mathbf{D}} \geq 0$ and $\dot{\mathbf{D}} \to 0$ as $D \to 1$;
- The transition function $\varphi_{\rm tr}$ deals with the change in the mode of deformation through the damage evolution such that

$$\varphi_{\rm tr} \geq 0 \quad \text{and} \quad \varphi_{\rm tr} \approx 0 \text{ when } \|\dot{\boldsymbol{\epsilon}}_{\rm i}\| < \eta \quad \text{and} \quad \varphi_{\rm tr} > 1 \text{ when } \|\dot{\boldsymbol{\epsilon}}_{\rm i}\| > \eta;$$

- Inequality (2) is satisfied *a priori* for any admissible isothermal process. Moreover, the dissipation potential (10) is a non-convex function with respect to the thermodynamic forces $\boldsymbol{\sigma}$ and $\mathbf{Y}$.
- The evolution of damage $(6)_3$ with the potential (11) will result in splitting damage in compression, while for tensile loading damage occurs on the plane perpendicular to the tensile stress[10].
- The form (8) of the Helmholtz free energy takes into account the directionality of damage. The crack deactivation criteria is based on the elastic normal stress acting on the damage plane.

REFERENCES

[1] Fortino, S., Hartikainen, J., Kolari, K., Kouhia, R. & Manninen, T. A constitutive model for strain-rate dependent ductile-to brittle-transition. In von Hertzen, R. & Halme, T. (eds.) *The IX Finnish Mechanics Days*, 652–662 (Lappeenranta University of Technology, Lappeenranta, 2006).

[2] Askes, H., Hartikainen, J., Kolari, K. & Kouhia, R. Dispersion analysis of a strain-rate dependent ductile-to-brittle transition model. In Mäkinen, R., Neittaanmäki, P., Tuovinen, T. & Valpe, K. (eds.) *Proceedings of The 10th Finnish Mechanics Days*, 478–489 (University of Jyväkylä, Jyväskylä, 2009).

[3] Kolari, K. Damage mechanics model for brittle failure of transversely isotropic solids - finite element implementation. VTT Publications 628, Espoo (2007).

[4] Frémond, M. *Non-Smooth Thermomechanics* (Springer, Berlin, 2002).

[5] Perzyna, P. *Fundamental problems in viscoplasticity*, vol. 9 of *Advances in Applied Mechanics*, 243–377 (Academic Press, London, 1966).

[6] Duvault, G. & Lions, L. *Inequalities in Mechanics and Physics* (Springer, Berlin, 1972).

[7] Ristinmaa, M. & Ottosen, N. Consequences of dynamic yield surface in viscoplasticity. *International Journal of Solids and Structures* **37**, 4601–4622 (2000).

[8] Lemaitre, J. & Chaboche, J.-L. *Mechanics of Solid Materials* (Cambridge University Press, 1990).

[9] Lemaitre, J. *A Course on Damage Mechanics* (Springer-Verlag, Berlin, 1992).

[10] Murakami, S. & Kamiya, K. Constitutive and damage evolution equations of elastic-brittle materials based on irreversible thermodynamics. *International Journal of Mechanical Sciences* **39**, 473–486 (1997).

23rd Nordic Seminar on Computational Mechanics
NSCM-23
A. Eriksson and G. Tibert (Eds)

ON CRACK PROPAGATION IN RAILS UNDER RCF LOADING CONDITIONS

JIM BROUZOULIS*

*Applied Mechanics
Chalmers University of Technology
Gothenburg, Sweden
e-mail: jim.brouzoulis@chalmers.se

Key words: Crack propagation, head checks, rolling contact fatigue

Summary. Three crack propagation methods (based on material forces) are compared for two test cases. From this, a crack propagation law for fatigue growth is proposed. Time integration of this propagation law allows for simulation of head check growth. This is exemplified through a 2D example where the propagation of a single surface crack is simulated for various parameters.

1 INTRODUCTION

Rolling Contact Fatigue (RCF) of rails is a major problem worldwide. Common RCF defects that can be observed in rails are *tounge lipping*, *head checks* and *squats*. However, only the development of head checks will be investigated in this paper. Head checks are typically closely spaced cracks which initially grow almost parallel. The cracks are initiated at the rail surface and are common near the gauge corner in curves. Also the surface friction conditions affect the initiation of head checks. Cracks are more easily initiated under dry conditions than in wet.

To properly simulate the propagation of a crack, we need to model how fast and in what direction it grows. A *generalized crack driving force* (*GCDF*), based on the concept of material forces, is used to model the growth of the crack. Results from simulations using three crack propagation methods are evaluated against experimental results. Based on this evaluation, one propagation method is chosen for subsequent studies.

Next, the propagation of a single head check crack in a piece of rail, under realistic RCF loading conditions, is simulated by the use of a 2D model. Results from the simulations are presented and qualitatively compared to field observations.

2 FATIGUE CRACK PROPAGATION

The GCDF (adopted in this study) can be expressed as[1]

$$\boldsymbol{\mathcal{G}} = \int_{\Omega_X} -\boldsymbol{\Sigma} \cdot (\varphi \boldsymbol{\nabla}_X) \, \mathrm{dV_X} \tag{1}$$

where $\boldsymbol{\Sigma}$ is the Eshelby stress tensor and φ is a suitably chosen weight function of unit value at the crack tip. In this manner, the GCDF is the change of rate of mechanical dissipation due to an advancement of the crack tip.

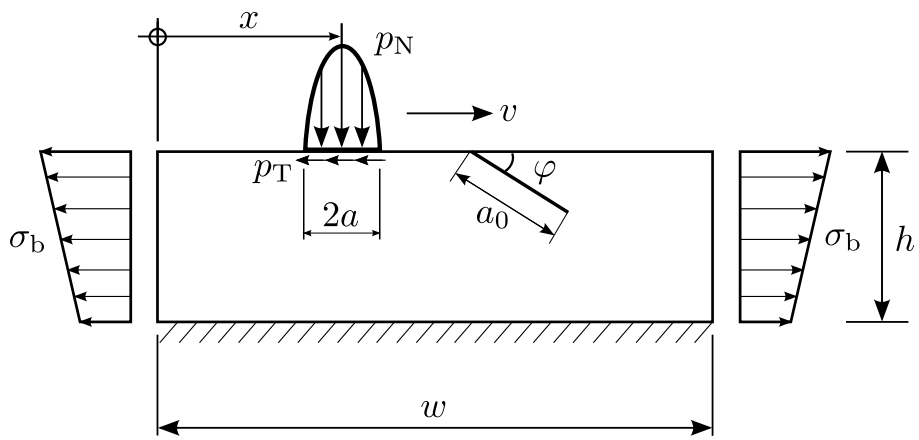

Figure 1: 2D problem setup.

Based on the GCDF for the existing crack, we may formulate a propagation law as

$$\dot{\boldsymbol{a}} = \gamma < \dot{\Phi} > \frac{\partial \Phi}{\partial \boldsymbol{\mathcal{G}}} \tag{2}$$

with the constitutive parameter γ and the crack-driving potential Φ. The expression for the potential Φ is assumed as follows:

$$\Phi = |\boldsymbol{\mathcal{G}}| - \mathcal{G}_{\mathrm{cr}} \tag{3}$$

where $\mathcal{G}_{\mathrm{cr}}$ is a parameter that describes the fracture toughness of the material. By this particular choice of Φ, the crack growth is proportional in direction to the GCDF, which has shown to produce results in good agreement with experiments. It may also be noted that the proposed propagation is of a rate independent type.

The propagation law in eq. (2) is expressed in terms of the crack tip velocity. Therefore, by integrating over one load cycle (N) the crack growth per load cycle can be computed.

$$\frac{\mathrm{d}\boldsymbol{a}}{\mathrm{dN}} = \int_{t_N}^{t_{N+1}} \dot{\boldsymbol{a}} \, \mathrm{dt} \tag{4}$$

From this, the crack growth is then extrapolated a given number of cycles and the mesh is updated accordingly. The procedure is then repeated until the total number of loading cycles has been reached.

3 NUMERICAL EXAMPLE

To get an understanding of the characteristics of the propagation of a single surface crack in a piece of rail material, a simplified 2D-example is investigated, cf. Figure 1. The material is assumed to be linear elastic and in a state of plane strain. The rail is subjected to the loads from a passing bogie (velocity v) with 2 wheelsets. This produces bending stresses in the rail together with normal and traction stresses in the wheel-rail contact. Bending stresses σ_{b} is evaluated from the bending moment developed in the rail as the bogie passes. The normal load $p_{\mathrm{N}}(x,t)$ is assumed to be given by an elastic Hertzian contact pressure distribution[2] (with with

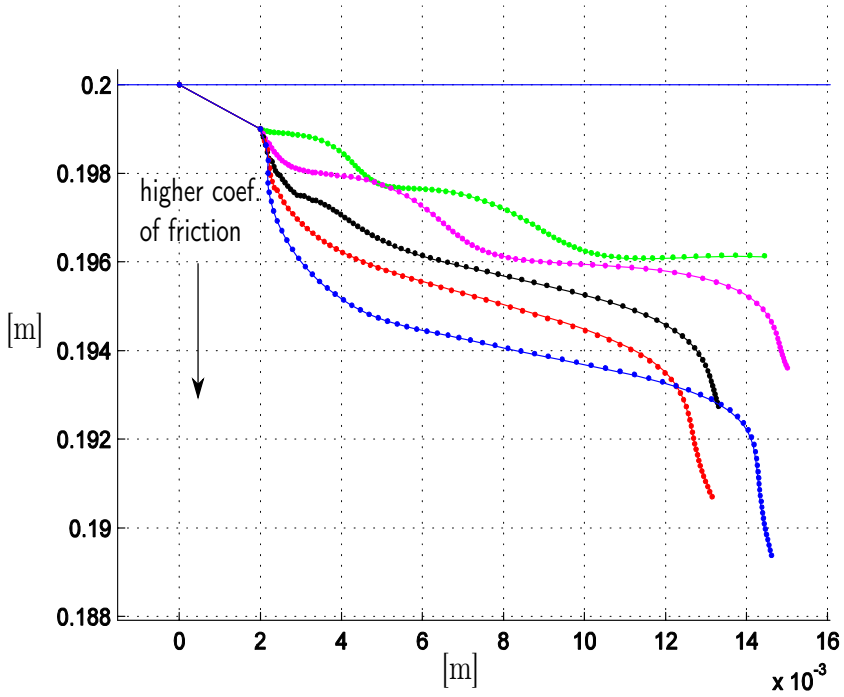

Figure 2: Example of simulated crack paths for varying coefficient of friction ($\mu = 0.2 - 0.6$).

$2a$). Moreover, the traction stress $p_{\mathrm{T}}(x,t)$ is obtained from the normal pressure $p_{\mathrm{N}}(x,t)$ and the coefficient of friction μ by assuming full slip, i.e $p_{\mathrm{T}}(x,t) = \mu p_{\mathrm{N}}(x,t)$. The traction stress p_{T} acts in the direction opposite to the velocity of the wheel. Furthermore, the crack surfaces are assumed smooth (i.e. no friction).

Results from simulations of crack growth for various parameters will be presented and discussed. The studied parameters are initial crack angle φ, initial crack length a_0 and coefficient of friction μ. In Figure 2, an example of simulated crack paths for varying coefficient of friction can be seen.

REFERENCES

[1] G.A. Maugin, Material forces: Concepts and applications, *Appl. Mech. Rev.*, **48(5)**, 213–245, (1995)

[2] K.L. Johnsson, *Contact mechanics*, Cambridge University Press, (1985).

23rd Nordic Seminar on Computational Mechanics
NSCM-23
A. Eriksson and G. Tibert (Eds)

MECHANICAL RESPONSE AND FRACTURE OF ADHESIVELY BONDED JOINTS

HARALD OSNES*, DAG MCGEORGE† AND GEIR O. GUTHU*

*Mechanics Division, Department of Mathematics
University of Oslo
P.O.Box 1053, Blindern, NO-0316 Oslo, Norway
e-mail: osnes@math.uio.no

†Det Norske Veritas
Høvik, Norway
e-mail: dag.mcgeorge@dnv.com

Key words: Adhesively Bonded Joints, Strength Analysis, Fracture.

Summary. The strength of adhesively bonded double-lap shear joints has been studied. Failure loads obtained experimentally have been presented and compared with theoretical predictions. Capacity estimates provided by traditional strength of materials approaches do not agree with experiments. On the other hand, results obtained using a recent inelastic fracture-based analysis represent measured strength values well.

1 INTRODUCTION

High-speed craft and ships have traditionally been made of aluminum or steel. To improve the performance, there is a tendency to seeking lighter weight structures, at least in parts of the structure where weight-saving is particularly beneficial, such as in the superstructure. Light-weight materials can be fibre reinforced composites. When combining metals and composite materials, traditional joining by welding is not an option. Instead, one may apply bolting. However, bolted joints suffer from high stress concentrations. Moreover, such joints are costly to make and maintain. Therefore adhesive bonding becomes an attractive option for joining composite materials to metals.

Another important application area of adhesive bonding, is repair of floating production storage and offloading units (FPSOs) and other kinds of offshore storage units. Experience has shown that FPSOs develop corrosion and cracks during service. Such defects are no serious problem for ordinary tankers - the defects are simply welded and possibly reinforced when the ship calls into the next harbour. Welding is, however, hot work that is not allowed for FPSOs during production. Closing down can be very expensive. Thus, composite patch repair using adhesives is an attractive alternative.

In the present study, the mechanical response and strength of adhesively bonded joints have been investigated experimentally, as well as theoretically using analytical derivations and finite element analysis.

2 EXPERIMENTAL STRENGTH MEASUREMENTS

In several recent research projects, the strength of adhesively bonded joints has been investigated experimentally. Here we will present a set of results obtained within the context of a network of excellence on marine structures (MARSTRUCT), to which one of the authors belongs. A set of double-lap shear joints was analysed. In all cases, the inner adherend was made of 10 mm steel, while the outer adherends consisted of 0/90 woven rowing glass fibre reinforced plastics (GFRP) or 0/90 uni-directional carbon fibre reinforced plastics (CFRP) laminates of various thicknesses. The composite laminates were bonded to the steel plate using an epoxy adhesive of the type Araldite 2015. More details are available from[1].

The measured failure loads for various overlap lengths are shown in Fig. 1. It is seen that for short overlap lengths, the strength is proportional to the overlap length. This behaviour lasts until a plateau level is reached, from which the failure load is almost constant and does not depend on the overlap length. The same kind of strength behaviour of bonded steel-composite joints was obtained in a recent EUCLID project[2].

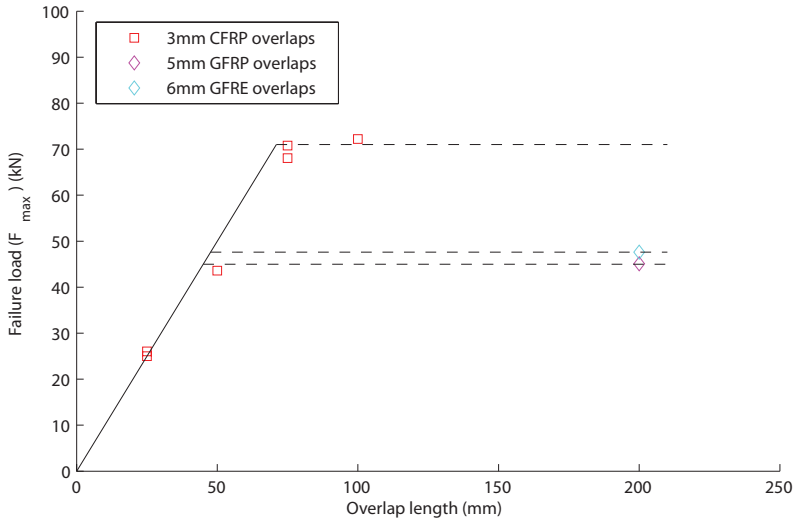

Figure 1: Failure loads of double-lap shear joints made of steel/CFRP and steel/GFRP.

In the experimental studies reported above, the thickness of the adhesive layer was the same for each set of test specimens. Thus, the effect of adhesive layer thickness on joint strength could not be studied. However, in a similar joint industry project on patch repair[3], test specimens with different values of the adhesive thickness were produced. In that study it was shown that the adhesive layer thickness played a negligible role on the joint strength.

3 ANALYSIS USING STRENGTH OF MATERIALS APPROACH

3.1 Critical stress approach

The capacity of adhesive joints has traditionally been analysed using a strength of materials method, of which the critical stress approach is the simplest. This is an elastic stress-based

method for predicting the strength, and it is assumed that fracture of the bondline will occur when the maximum shear stress in the adhesive layer reaches a critical level. The critical stress level is determined through comparison of theoretical stress analysis and the experimentally observed failure load of a selected joint with a specific overlap length. The distribution of the adhesive shear stresses in the joint is modeled using, e.g., the classical theory of Volkersen[4], or the modified version developed by Tsai et al.[5], in which adherend shear deformations are included. Analysing the joint subjected to the measured failure load, the critical stress level is defined as the maximum value of the shear stresses in the adhesive layer. Using this value as the maximum allowed stress level, the critical stress approach offers reasonable strength predictions for joints with overlap lengths close to the one selected, but the overall strength behaviour as illustrated in Fig. 1 is not offered.

3.2 Critical plastic strain approach

A slightly more complex analysis method is provided by the critical plastic strain approach. This method is based on the assumption of elastic-plastic behaviour of the shear stresses in the bondline. Thus, plastic effects of the adhesive layer are included, and it is assumed that the joint fails when a critical plastic strain is reached. The theoretical foundation of the method might be provided by the well-known work of Hart-Smith[6] or the extended theory derived by Osnes and McGeorge[2]. In the critical plastic strain approach, the yield stress and the maximum plastic strain of the adhesive layer must be determined. The former value is determined from the experimentally observed failure load of a joint with a short overlap length, while the latter critical property is obtained from the result of a joint at the plateau level. The method offers strength predictions that agree well with the results presented in Fig. 1. However, the theoretically obtained failure loads depend considerably on the adhesive layer thickness, a feature that is not supported by experimental strength measurements.

4 ANALYSIS USING INELASTIC FRACTURE MECHANICS APPROACH

4.1 Analytical derivations

Recently, McGeorge derived an *energy release rate* formulation accounting for plastic deformations[7]. It models the fracture process that causes failure of bonded joints and accounts for the energy released and consumed in the various parts of the bonded assembly during fracture. It is essential that the nonlinear inelastic behaviour of the adhesive bondline is taken into account. The strength parameters to be determined from experiments is the adhesive yield stress and the fracture resistance. In the work of McGeorge[7], certain closed form equations were derived for the fracture load of some simple joint geometries, and good agreement was demonstrated with experimental results.

4.2 Finite element analysis using cohesive elements

In the present study, the new *energy release rate* formulation[7] has been investigated for more general joint geometries. Finite element analysis (FEA) using cohesive elements of the Abaqus software package has been conducted. The equations derived by McGeorge for simplified geometries have been confirmed. Furthermore, the general applicability of FEA has permitted

comparison of theoretical predictions with experiments for a wider range of geometries. Again, very good agreement with experimental results has been obtained. The strength behaviour from Fig. 1 is excellently represented. In addition, the present fracture-based strength method predicts failure loads that are almost independent of the thickness of the adhesive layer. This contributes to gaining confidence in adhesive bonding technology, and this improved confidence will be important for implementation of adhesive bonding in the industry.

5 CONCLUSIONS

In this study, the strength of adhesively bonded double-lap shear joints has been investigated. Experimentally measured failure loads have been presented and compared with predictions offered by theoretical analysis methods. The strategy is to apply the measured strength values for a few (typically one or two) joints to determine the critical strength parameters required in the theoretical models.

The capacity of adhesive joints has traditionally been modeled using a strength of materials approach. However, the results provided by such methods do not agree with experimental predictions. Thus, a new fracture-based *energy release rate* formulation has been derived. Analytical relations have been developed for simplified geometries and FEA using cohesive elements has been conducted for more general joint geometries. In both cases, the results agree well with failure loads measured experimentally.

REFERENCES

[1] Hashim, S. *et al.* Fabrication, testing and analysis of steel/composite dls adhesive joints. In Soares, G. & Das (eds.) *Analysis and design of marine structures*, 379–385 (London: Taylor & Francis Group, 2009).

[2] Osnes, H. & McGeorge, D. Experimental and analytical strength analysis of double-lap joints for marine applications. *Composites: Part B* **40**, 29–40 (2009).

[3] McGeorge, D. *et al.* Repair of floating offshore units using bonded fibre composite materials. *Composites: Part A* **40**, 1364–1380 (2009).

[4] Volkersen, O. Die niektraftverteilung in zugbeanspruchten mit konstanten laschenquerschritten. *Luftfahrtforschung* **15**, 41–47 (1938).

[5] Tsai, M. Y., Oplinger, D. W. & Matthews, F. L. Improved theoretical solutions for adhesive lap joints. *Int. J. Solids Structures* **35**, 1163–1185 (1998).

[6] Hart-Smith, L. J. Adhesive-bonded double-lap joints. *NASA CR-112235* 1–106 (1973).

[7] McGeorge, D. Inelastic fracture of adhesively bonded overlap joints. *Eng. Fract. Mech.* **77**, 1–21 (2010).

23rd Nordic Seminar on Computational Mechanics
NSCM-23
A. Eriksson and G. Tibert (Eds)

NUMERICAL PREDICTIONS OF LOAD-CARRYING CAPACITY OF PIN-LOADED FRC PLATES

MARIO POLANCO-LORIA*, FRODE GRYTTEN† AND EINAR L. HINRICHSEN†

* SINTEF Materials and Chemistry
Applied Mechanics and Corrosion, NO-7465, Trondheim, Norway
e-mail: mario.polanco@sintef.no, web page: http://www.sintef.no

† SINTEF Materials and Chemistry
Polymers and Composites Materials, NO-0314, Oslo, Norway

Key words: Composite laminates, Constitutive modeling, Damage mechanics.

1 INTRODUCTION

Advanced com posite materials are today incr easingly used in a number of industrial sectors due to a favorable com bination of low weight and good m echanical properties. Composite structures have been shown to be susceptible to impact damage and this is a matter of continued concern. Impact can induce variou s types of dam age in the structure including matrix cracking, fibre-m atrix debonding, fibre breakage, delam ination etc. Unlike ductile metals that can absorb large am ounts of ener gy by plastic yielding, brittle com posites absorb energy by irrevers ible micro-cracking m echanisms. The design of com posite com ponents or structures to resist im pact or crash events re presents a difficult task. In this direction, the Norwegian research council, the com posite industry and the SINTEF-NTNU research community have, recently, established the COMPACT project. The main goal of this research project is the develop m ent of generic com petence, experimental techno logies, and num erical methods for the design of safe, robust and cost -efficient composite stru ctures. A recent state-of-art report [1] was written under the task “Modeling of composite m aterials”; this docum ent served as the main inspiration to generate the results presented here.

2 THE ABAQUS DAMAGE MODEL

Abaqus[2] 6.9 offers a dam age m echanics based m odel to p redict the on set and gro wth of damage f or elas tic-brittle m aterials with an isotropic behavior. The m odel is intended to be used with classical fibre reinforced composites materials. The model requires three important inputs: The elas tic behavior, the dam age initia tion criterion and the dam age evolution law.

Shortly the elastic behavior assumes an orthotropic law in plane stress (e.g. LAMINA). The damage initiation follows the Hashin's criterion formulated in the effective stress space and finally, the damage evolution law uses the fracture energy G_f concept. The elastic damaging response follows the constitutive equation $\boldsymbol{\sigma} = \mathbf{C}(d)\,\boldsymbol{\varepsilon}$, where the "damaged" stiffness matrix, $\mathbf{C}(d)$, is defined as:

$$\mathbf{C} = \frac{1}{D}\begin{bmatrix} (1-d_f)E_1 & (1-d_f)(1-d_m)\nu_{21}E_1 & 0 \\ (1-d_f)(1-d_m)\nu_{12}E_2 & (1-d_m)E_2 & 0 \\ 0 & 0 & D(1-d_s)G_{12} \end{bmatrix} \tag{1}$$

where D is a parameter defined by: $D = 1-(1-d_f)(1-d_m)\nu_{12}\nu_{21} > 0$ and the fibre (d_f) and matrix (d_m) damage variables can have different values in tension (d_{ft}, d_{mt}) and compression (d_{fc}, d_{mc}). The shear damage variable is assumed to be dependent on the fibre and matrix damages according to:

$$d_s = 1-(1-d_{ft})(1-d_{fc})(1-d_{mt})(1-d_{mc}) \tag{2}$$

The Hashin's criterion requires tensile and compressive strengths for fibre and matrix directions; in addition to the longitudinal and transversal shear strengths. Finally, the damage evolution law is based on a linear softening model where four fracture energy values (for each failure mode): $G_{ft}, G_{fc}, G_{mt}, G_{mc}$, need to be introduced.

3 PIN-LOADED PLATE PROBLEM

Chang et al. [3] performed a large experimental program on pin-loaded plates made of T300/1034C graphite/epoxy laminate material with different ply orientations. The test program included different geometries where, in addition to the material properties, the failure strength and failure modes were reported. The thickness of the plate was 3 mm. Three stacking sequences, of Chang's work, are considered in this work: $[(0/90)_6]_S$, $[(\pm)_6]_S$ and $[(0/\pm45/90)_3]_S$. The nominal failure strengths and failure modes reported were: 458-S (MPa), 550-T (MPa) and 641-B (MPa), respectively. The capital letters indicate S for shear, B for bearing and T for tension failure modes.

4 NUMERICAL SIMULATIONS

The pin-loaded finite element plate model (shell SR4) and boundary conditions are shown in Figure 1a. A friction coefficient of 0.30 (metal-composite contact Coulomb type) was used

together with the material data reported. However, no data was available for fracture energy values to describe the damage evolution law (e.g. $G_{ft}, G_{fc}, G_{mt}, G_{mc}$). Cheng's work indicated that matrix damage was the main dominating mechanism for failure, consequently, it is believed that fracture energy values for fibre damage are not crucial for the failure strength assessment (here we assumed $G_{ft} = G_{fc} = 16.2$ N/mm, based on the elastic properties and element size). With respect to the matrix, one finds in the literature[4,5,6] fracture energy values in tension, of about 0.15 to 0.30 N/mm for an epoxy based matrix while for the compressive case, we found values of 0.5 to 1.0 N/mm. Based on this information it was decided to introduce in our calculations values of $G_{mt} = 0.25$ and $G_{mc} = 0.50$ N/mm. These assumptions complete the data required to perform the load carrying capacity assessment.

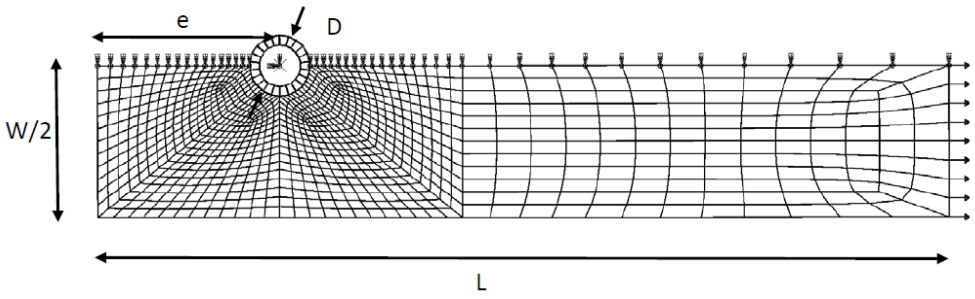

a)

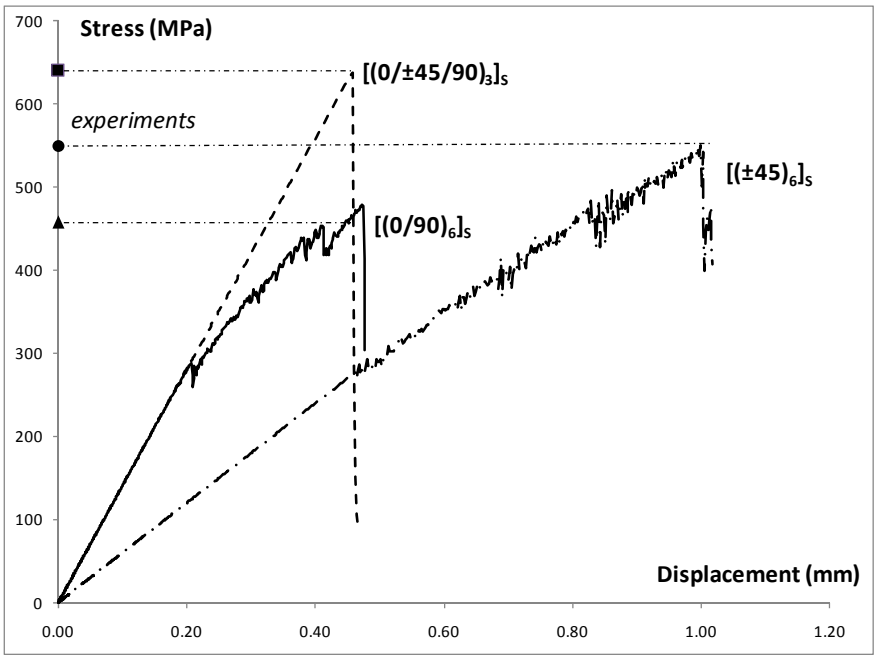

b)

Figure 1: Finite element model and main results

The global response from the experimental tests and numerical simulations is shown as stress-displacement curves in Figure 1b for the three stacking sequences studied. The numerical model provides a fairly good prediction of the load-carrying capacity when compared to the experiments. In addition, the three failure modes were correctly predicted: shear for the $[(0/90)_6]_S$ ply, bearing for the $[(0/\pm45/90)_3]_S$ ply and tensile failure for the $[(\pm45)_6]_S$ ply, see Fig. 2.

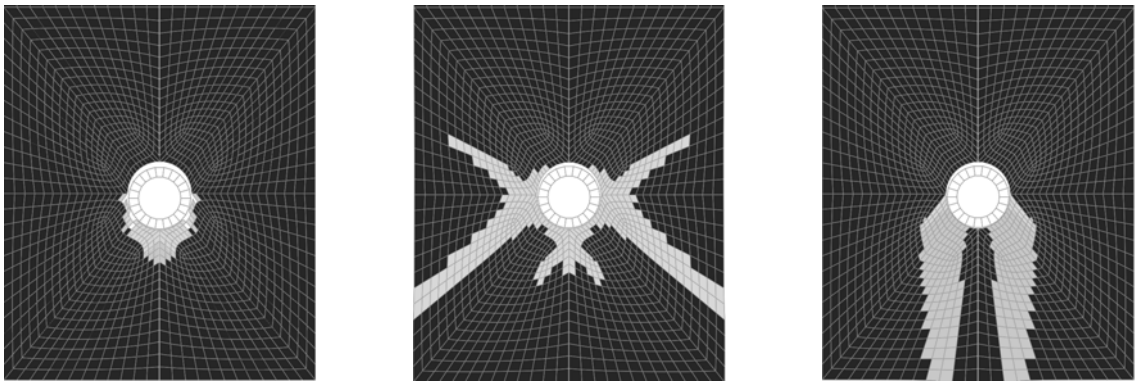

Figure 2: Bearing, "tensile" and shear failure mechanisms predicted (bottom ply)

5 CONCLUSIONS

- Measurements of the fracture energy values: $G_{ft}, G_{fc}, G_{mt}, G_{mc}$ are required for load-carrying capacity failure assessment.
- The shear damage law proposed in the Abaqus model (Eqn. 2) seems to work well for the problems analysed here. However, such a law can not be generalized and should be used with care.

REFERENCES

[1] F. Grytten and M. Polanco-Loria, " *Modeling of fibre reinforced composites subjected to impact loading-State of the Art"* SINTEF report A16579; ISBN: 978-82-1405011-0 (2010).

[2] ABAQUS 6.9 "*User's manual"* Abaqus Inc, Providence, RI, USA (2009).

[3] F.K. Chang, R.A. Scott and G. S. Springer *"Failure of composite laminates containing pin loaded holes-method of solution"* Journal of Composite Materials, 18, 255-278 (1984).

[4] A. J. Brunner *"Experimental aspects of Mode I and Mode II fracture toughness testing of fibre-reinforced polymer-matrix composites"* Comp. Methods Appl. Mech. Eng., 185, 161-172 (2000).

[5] C. S. Lopes, P.P. Camanho, Z. Gurdal, P. Maimi and E.V. Gonzalez *"Low velocity impact damage on dispersed stacking sequence laminates. Part II Numerical simulations" Composites Science and Technology*, 69, 937-947 (2009).

[6] I. Lapczyk and J. Hurtado *"Progressive damage modeling in fiber-reinforced materials"* Composites: Part A Applied Science and Manufacturing, 38, N. 11, 2333-2341 (2007).

23rd Nordic Seminar on Computational Mechanics
NSCM-23
A. Eriksson and G. Tibert (Eds)

ANALYSIS OF THE ACCURACY OF THE CARTESIAN GRID METHOD

M. ASIF FAROOQ* AND B. MÜLLER†

*† Department of Energy and Process Engineering, Fluids Engineering Group
Norwegian University of Science and Technology (NTNU)
Kolbjørn Hejes Vei 2 No-7491 Trondheim, Norway
*e-mail: asif.m.farooq@ntnu.no, web page: http://folk.ntnu.no/asiff/

†e-mail: bernhard.muller@ntnu.no - Web page: http://folk.ntnu.no/bmuller

Key words: Cartesian Grid Method, Node-Centred Finite Volume Approach, Embedded Boundary, Ghost Point Treatment, Shock Wave.

Summary. The accuracy of the Cartesian grid method has been investigated for the 1D Burgers' equation and the 1D and 2D compressible Euler equations. Wall boundary conditions are imposed at ghost points by interpolating the numerical solution at the corresponding mirror points linearly or quadratically. We find that linear interpolation does not affect the accuracy of our node-centred finite volume method. When we employ the MUSCL approach with slope limiters, the convergence rate of the Cartesian grid method is reduced similar to corresponding standard body-fitted methods.

1 INTRODUCTION

The Cartesian grid method[1,2,3] has been becoming popular among researchers due to its simplicity, ease of programming and less computational effort compared to body-fitted grid methods. We have been using the ghost point treatment for embedded boundaries.

In this study we analyze the accuracy of the Cartesian grid method for the 1D inviscid Burgers' equation and the 1D and 2D compressible Euler equations. We impose wall boundary conditions at ghost points by interpolating the numerical solution at the mirror points in the fluid domain and mirroring the interpolated values to ensure reflective wall boundary conditions. First order total variation diminishing (TVD) methods are applied for smooth as well as for shock problems. The order of our method is increased by the MUSCL approach with minmod limiter. The first order explicit Euler and the third order TVD Runge-Kutta methods are used for time integration.

For the scalar problem the Cartesian grid method is applied to a smooth solution. For the 1D compressible Euler equations the Cartesian grid method is applied to a normal shock reflection. For the 2D compressible Euler equations we apply the Cartesian grid method to an oblique shock wave.

2 GOVERNING EQUATIONS

2.1 Inviscid Burgers' Equation

The conservative form of the 1D scalar inviscid Burgers' equation with the initial condition reads

$$u_t + (\frac{1}{2}u^2)_x = 0, \qquad u(x,0) = sin\left(\frac{\pi x}{x_b}\right), \tag{1}$$

where x_b is the location of the wall.

2.2 Compressible Euler Equations

The 2D compressible Euler equations for perfect gas in conservative form are given as

$$U_t + (F)_x + (G)_y = 0, \tag{2}$$

where $U = [\rho, \rho u, \rho v, \rho E]^T$, $F = [\rho u, \rho u^2 + p, \rho uv, (\rho E + p)u]^T$ and $G = [\rho v, \rho uv, \rho v^2 + p, (\rho E + p)v]^T$ are the vector of the conservative variables and the flux vectors in $x-$ and $y-$directions, respectively.

3 NUMERICAL METHODS

3.1 DISCRETIZATION SCHEMES

For the spatial discretization we apply the upwind method for inviscid Burgers' equation. We apply the Lax-Friedrichs (LF) and local Lax-Friedrichs (LLF) method for the 1D compressible Euler equations and local Lax-Friedrichs (LLF) method for the 2D compressible Euler equations. To obtain higher order we apply MUSCL with minmod limiter. For time integration we use the first order explicit Euler and the third order TVD Runge-Kutta methods.

3.2 GHOST POINT TREATMENT

In Fig. 1 we show a simplified ghost point treatment for the 2D case. The mathematical form of the ghost point treatment can be written as follows

$$\begin{aligned} u_{n,G} &= -u_{n,M}, \qquad u_{t,G} = u_{t,M}, \\ \rho_G &= \rho_M, \qquad p_G = p_M, \end{aligned} \tag{3}$$

where u_n, u_t, ρ and p denote normal and tangential velocity with respect to the embedded wall boundary, density and pressure, respectively. In Fig. 1, M and G are the mirror and ghost points, respectively. δ is the distance between the ghost point G and the boundary point on the vertical grid line. The ghost point G in the solid is mirrored to the mirror point M in the fluid with respect to the wall (boldface line) on a grid line. The numerical solution at M is interpolated on that grid line.

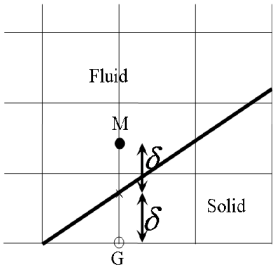

Figure 1: 2D ghost point treatment

4 RESULTS

4.1 INVISCID BURGERS' EQUATION

In this section we present results for the 1D inviscid Burgers' equation. The wall is located at $x_b = 0.5001$ and end time is $tend = 0.02$. In Tables 1 and 2 we show the convergence rates of the first and higher order methods while using linear and quadratic interpolation at the mirror points. It is clear from these tables that linear and quadratic interpolations yield the same error and are not affecting the accuracy of the first and higher order methods.

	Inviscid Burgers' Equation			
	Linear Interpolation		Quadratic Interpolation	
N	Order	L_2-norm	Order	L_2-norm
101	-	0.0018	-	0.0018
201	0.9729	0.009	0.9729	0.009
401	0.9865	0.005	0.9865	0.005
801	0.9932	0.002	0.9932	0.002
1601	0.9965	0.001	0.9965	0.001
3201	0.9980	0.001	0.9980	0.001

Table 1: First order TVD method.

	Inviscid Burgers' Equation			
	Linear Interpolation		Quadratic Interpolation	
N	Order	L_2-norm	Order	L_2-norm
101	-	0.1772×10^{-3}	-	0.1772×10^{-3}
201	1.5906	0.0588×10^{-3}	1.5906	0.0588×10^{-3}
401	1.5940	0.0195×10^{-3}	1.5940	0.0195×10^{-3}
801	1.6000	0.0064×10^{-3}	1.6000	0.0064×10^{-3}
1601	1.6045	0.0021×10^{-3}	1.6045	0.0021×10^{-3}
3201	1.6079	0.0007×10^{-3}	1.6079	0.0007×10^{-3}

Table 2: Higher order TVD method.

4.2 1D COMPRESSIBLE EULER EQUATIONS

In this section we present results for the 1D compressible Euler equations. The wall is located at $x_b = 0.8001$. At the mirror point we apply linear interpolation. For the spatial discretization we apply the higher order LF and LLF TVD methods. In Figs. 2(a) and 2(b) we present results for a moving normal shock wave. In Fig. 2(a) we draw a comparison between the exact and numerical solutions of density. We observe that the density is lower after reflection from the wall. The convergence rate of the higher TVD method is shown in 2(b). The convergence rate is low (~ 0.5 in the L_2-norm) due to the shock wave.

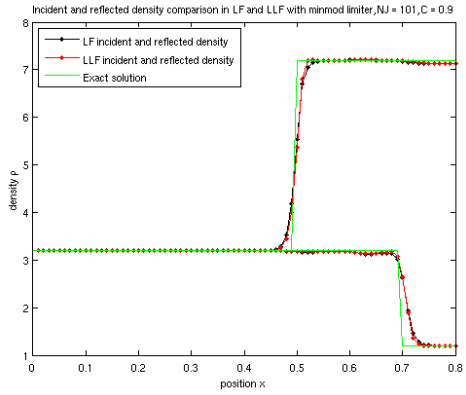

(a) Comparison of incident and reflected shock for density using the higher order TVD method.

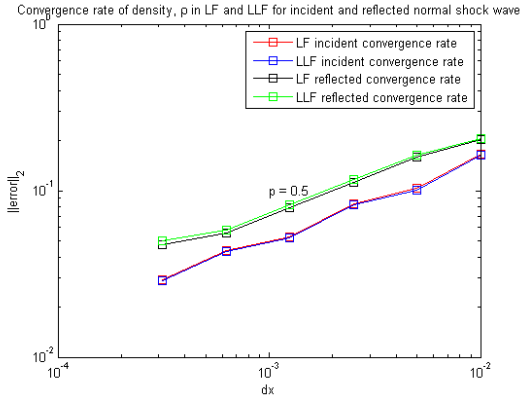

(b) Convergence rate of density for higher order TVD method.

Figure 2: Normal shock wave.

4.3 2D COMPRESSIBLE EULER EQUATIONS

In this section we present results for the 2D compressible Euler equations. We verified our 2D code for an oblique shock wave. We apply the simplified ghost point treatment adjacent to the embedded boundary and use linear interpolation at the mirror points. For spatial discretization we apply the local Lax-Friedrichs (LLF) method. For time integration we employ the explicit Euler method. In Fig. 3(a) we present pressure results for an oblique shock wave at $M_\infty = 2$ and wedge angle of $\Theta = 15$ degrees. In Fig. 3(b) we compare the results for three grids with the exact solution and observe grid convergence for the first order method.

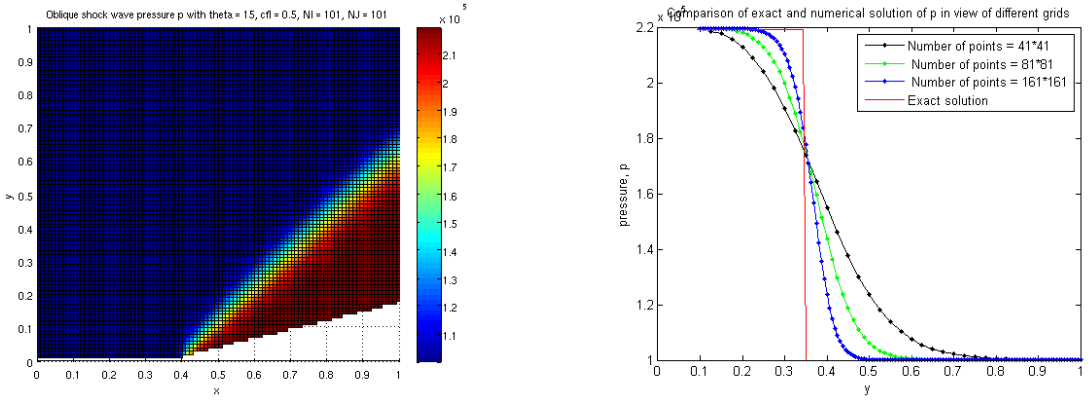

(a) Computed pressure for $M_\infty = 2$ and wedge angle $\Theta = 15$ degrees.

(b) Comparison of exact and numerical solutions for different grids.

Figure 3: Oblique shock wave.

5 CONCLUSIONS

We applied the Cartesian grid method to the scalar 1D inviscid Burgers' equation and the 1D and 2D compressible Euler equations, and both normal and oblique shock waves were computed. Local symmetry boundary conditions were implemented at each ghost point. Accuracy and convergence rate of the Cartesian grid method proved to be similar to standard body fitted methods. We observed the same accuracy for both linear and quadratic interpolation.

REFERENCES

[1] Mittal, R. & Iaccarino, G. Immersed Boundary Methods. *Annual Review of Fluid Mechanics* **37**, 239–261 (2005).

[2] Sjögreen, B. & Petersson, N. A. A Cartesian Embedded Boundary Method for Hyperbolic Conservation Laws. *Commun. Comput. Phys.* **2**, 1199 – 1219 (2007).

[3] Udaykumar, H. S., Krishnann, S. & Marella, S. V. Adaptively Refined Parallelisded Sharp Interface Cartesian Grid Method for Three Dimensional Moving Boundary Problem. *International Journal of Computational Fluid Dynamics* **23**, 1–24 (2009).

23rd Nordic Seminar on Computational Mechanics
NSCM-23
A. Eriksson and G. Tibert (Eds)

BUCKLING OF THE AXISYMMETRIC STRESS-STRAIN STATE AS A POSSIBLE CAUSE OF EDEMA AT THE EDGE OF THE LAMINA CRIBROSA

EVA B. VORONKOVA

St. Petersburg State University
Faculty of Mathematics and Mechanics
28 Universitetskii pr., 198504 St. Petersburg, Russia
e-mail: frumen@yandex.ru, web page: http://www.math.spbu.ru/

Key words: Glaucoma, Lamina Cribrosa, Buckling, Nonaxisymmetric State.

Summary. Nonaxisymmetric loss of stability of a transversely isotropic non-homogeneous plate, modelling the Lamina Cribrosa of a human eye was considered. Numerical results for different type of non-uniformity are presented.

1 INTRODUCTION

Elevated intraocular pressure (IOP) is associated with the development of glaucomatous optic neuropathy. The site of retinal ganglion cell dysfunction in glaucoma is the Lamina Cribrosa (LC), a porous connective tissue spanning the scleral canal[1] (Fig. 1).

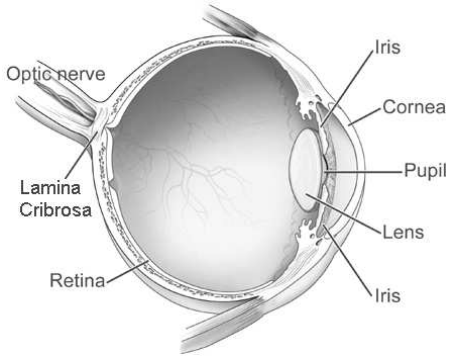

Figure 1: A human eye diagram. Adapted from a diagram by the National Eye Institute.

It was found that under glaucoma the atrophy of the optic nerve axons occurs in the narrow zone at the periphery of LC. In this zone the edema of the optic nerve disc takes place[2]. The purpose of the presented research is to analyze if such edemas could be explained by the bucking of the axisymmetric state of the LC in the nonaxisymmetric state.

2 MATERIALS AND METHODS

Large deformations of homogeneous circular plates under normal pressure produce compressive stresses at the edges, which may cause buckling of the axisymmetric equilibrium state[3].

The LC, as a soft biological tissue, was modelled as a transversely isotropic plate with radial[4]. It was also assumed that the modulus of elasticity in the transverse direction was much smaller than modulus of elasticity in the plane of the plate.

The fundamental equations of a geometrically nonlinear transversely isotropic non-uniform plate can be represented in the form of the system

$$\begin{aligned} \frac{f(r)}{12(1-\nu^2)}\frac{E_0}{E_{av}}\left[\Delta\Delta w - \frac{1}{f}\frac{df}{dr}L_1(w) + \frac{1}{f}\frac{d^2f}{dr^2}L_2(w)\right] &= p + L(w,F), \\ \Delta\Delta F - \frac{1}{f}\frac{df}{dr}L_1(F) + \left(2\left(\frac{1}{f}\frac{df}{dr}\right)^2 - \frac{1}{f}\frac{d^2f}{dr^2}\right)L_3(F) &= -\frac{f(r)}{2}\frac{E_0}{E_{av}}L(w,w), \end{aligned} \tag{1}$$

$$\begin{aligned} L_1(w) &= \frac{\partial^3 w}{\partial r^3} + \frac{2}{r}\frac{\partial^2 w}{\partial r^2} - \frac{1}{r^2}\frac{\partial w}{\partial r} + \frac{2}{r^2}\frac{\partial^3 w}{\partial r \partial\theta^2} - \frac{3}{r^3}\frac{\partial^2 w}{\partial\theta^2} - \frac{\nu}{r}\frac{\partial^2 w}{\partial r^2}, \\ L_2(w) &= \frac{\partial^2 w}{\partial r^2} + \nu\left(\frac{1}{r^2}\frac{\partial^2 w}{\partial\theta^2} + \frac{1}{r}\frac{\partial w}{\partial r}\right), \quad L_3(F) = \frac{\partial^2 F}{\partial r^2} - \nu\left(\frac{1}{r^2}\frac{\partial^2 F}{\partial\theta^2} + \frac{1}{r}\frac{\partial F}{\partial r}\right) \end{aligned}$$

with the boundary conditions at $r = 1$

$$w = \frac{\partial w}{\partial r} = \frac{1}{r}\frac{\partial w}{\partial\theta} = 0, \quad \frac{1}{r}\frac{\partial F}{\partial r} + \frac{1}{r^2}\frac{\partial^2 F}{\partial\theta^2} = -\frac{\partial}{\partial r}\left(\frac{1}{r}\frac{\partial F}{\partial\theta}\right) = 0. \tag{2}$$

All quantities entering into (1) are dimensionless, and are related with those with dimensions by the expressions: $r = r^*/R,\ w = w^*/h,\ p = p^*R^4/E_{av}h^4,\ F = F^*/E_{av}h^3$. Here R is the radius of the plate; w^* — deflection; F^*— stress function; h — thickness of the plate; p^* — normal pressure; r^* — variable radius, θ — circumferential coordinate.

We supposed that in the plane of the plate the modulus of elasticity is defined as $E(r) = E_0 f(r)$. Function $f(r)$ decreases away from the center.

We solved the corresponding problem numerically for different functions $f(r)$ and values E_0 for the constant average value of the modulus of elasticity $E_{av} = \frac{1}{\pi}\int_0^{2\pi}\int_0^1 E(r)rdr$.

System (1) is obtained from the determining relations of the nonlinear theory of anisotropic plates[5].

Following Panov et al.[6], we used Galerkin method to determine the critical value of the load p of nonaxisymmetric buckling. The solution of system (1) was sought in the form

$$\begin{aligned} w(r,\theta) &= A(1-r^2)^\alpha(1+r^2)^\beta + Br^4(1-r^2)^2\cos n\theta \\ F(r,\theta) &= F_0(r) + F_1(r)\cos n\theta + F_2(r)\cos 2n\theta. \end{aligned} \tag{3}$$

To fit the boundary conditions (2) it is necessary $\alpha > 1,\ \beta > 0$. Stress functions F_i $(i = 0, 1, 2)$ were elevated from second equation (1).

Galerkin technique applied to first equation (1) yielded a system of two equations in A, B.

3 RESULTS

The values of critical loads of nonaxisymmetric buckling, p_{nax}, for different parameter of non-uniformity, q, are presented in Fig. 2 in case $f(r) = e^{-qr}$.

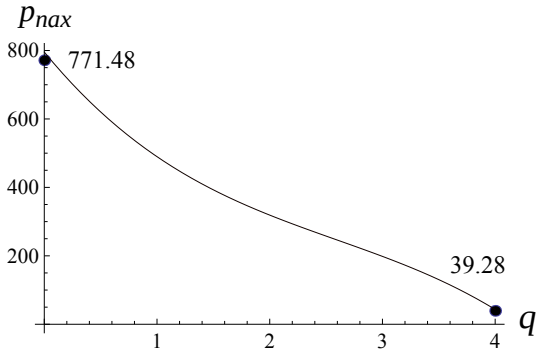

Figure 2: The value of critical loads versus degree of non-uniformity.

It is seen that as the parameter q increases, the values of p_{nax} decrease. For parameters $E_{av} = 1.43\,\text{MPa}$, $R = 1\,\text{mm}$, $h = 1\,\text{mm}$ the non-axisymmetric buckling occurs under pressure equals about 60 mm Hg.

4 ACKNOWLEDGMENTS

The research was supported in part by SI-sponsored Visby program from KTH and by RFBR grant 09-01-00140a.

REFERENCES

[1] D.R. Anderson, W.F. Hoyt. Ultrastructure of intraorbital portion of human and monkey optic nerve. *Arch Ophthalmol*, **82**, 506–3341, (1969).

[2] A.G. Nesterov. Basic principles of open angle glaucoma diagnostic. *Vestnik of ophtalmology*, **2**, 3–6, (1998) (in Russian).

[3] N.F. Morozov. On the existence of a non-symmetric solution in the problem of large deflections of a circular plate with a symmetric load, *Izvestiya Vysshikh Uchebnykh Zavedenii. Matematika*, **2**, 126–129, (1961) (in Russian)

[4] D.B. Yan, J.G. Flanagan, T. Farra, G.E. Trope and C.R. Ethier C.R. Study of regional deformation of the optic nerve head using scanning laser tomography, *Current Eye Research*, **17**, 903-916, (1998).

[5] S.A. Ambartsumian. *Theory of anisotropic plates*, Moscow, (1987) (in Russian).

[6] D.Yu. Panov, V.I. Feodos'ev. On equilibrium and loss of stability of shallow shells under large deflections. Prikladnaya mathematika i mekhanika, **8**, 389–406, (1948). (in Russian).

23rd Nordic Seminar on Computational Mechanics
NSCM-23
A. Eriksson and G. Tibert (Eds)

ON THE STRESS-STRAIN STATE OF THE FIBROUS EYE SHELL AFTER REFRACTIVE SURGERY

SVETLANA M. BAUER, ELENA V. KRAKOVSKAYA

St. Petersburg State University
Faculty of Mathematics and Mechanics
28 Universitetskii pr., 198504 St. Petersburg, Russia
e-mail: s_bauer@mail.ru, web page: http://www.math.spbu.ru

Key words: Ocular Biomechanics, Intraocular Pressure, Fibrous eye shell.

Summary. The change of the cornea strain after the refractive surgeries that involves the varying of the cornea's thickness is examined. The stress state of the joint soft isotropic or transverse-isotropic spherical shells of different radii, the sclera and the cornea, under uniformly distributed Intraocular Pressure (IOP) is analyzed. The numerical solution for the 3D mathematical model is obtained by means of the FEM code ANSYS.

1 INTRODUCTION

Nowadays the surgery LASEK (Laser-Assisted Sub-Epithelial Keratectomy) is widely used refracting operation on myopia and astigmatism of myopia. The surgery is based on reduction of the cornea thickness[1]. The alteration of the cornea stress-strain state after LASEK was estimated[2]. The cornea was considered as a flat shell and the sclera was assumed to be substantially more rigid, than the cornea.

The purpose of the present study is to examine the cornea stress-strain state after the refractive surgeries at various ratio of the sclera and cornea elasticity modulus.

2 MATERIALS AND METHODS

The eye-ball is modeled as two joint shells, the sclera and the cornea (Fig. 1). The sclera is represented by the open-ended uniform spherical shell. The cornea connected with the sclera is considered as shallow uniform shell of the other radius.

To simplify the problem the eye shell is considered as a hemisphere with the free supported edges. In the different cases shells are simulated as isotropic or transverse-isotropic.

3 RESULTS

Table 1 lists the deflection of corneal apex before and after the LASEK surgery under 15 mm Hg of IOP level.

The sclera Young's moduli are supposed to be three[3] or five[4] times larger than the corresponding cornea ones. Then the shells were simulated as transversely isotropic, it was also assumed that the modulus of elasticity in the transverse direction (E') was much smaller than modulus

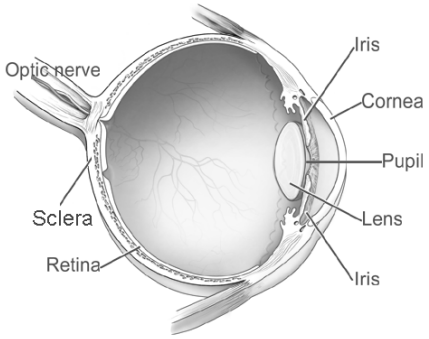

Figure 1: A human eye diagram. Adapted from a diagram by the National Eye Institute.

of elasticity in the plane (E) of the plate[5]. Subscripts s and c denote variables associated with the sclera and the cornea.

The averaged radius of sclera is 12 mm, the cornea radius is 8 mm, the sclera thickness is 0.5 mm, the Poisson coefficient of the cornea and sclera are 0.42 and 0.4 respectively, the elasticity module of the sclera is 14.3 MPa. The deflection is measured in 10^{-3}mm.

	Isotropic Cornea			Anisotropic Cornea		
Thickness, mm	$h = 0.42$	$h = 0.52$	$h = 0.62$	$h = 0.42$	$h = 0.52$	$h = 0.62$
$E_c = E_s/3$	17.2	13.2	10.4	546	480	424
$E_c = E_s/5$	31.1	24.8	21.5	751	652	569

Table 1: Deflections of the cornea apex for isotropic and anisotropic shells ($E' = E/20$) under 15 mm Hg of IOP level.

4 CONCLUSIONS

Comparison of the results for isotropic and transversely isotropic joint shells shows that anisotropy has significant effect on the value and shape of the cornea deflection (Fig. 2): (2a) isotropic shells, (2b) transverse-isotropic shells.

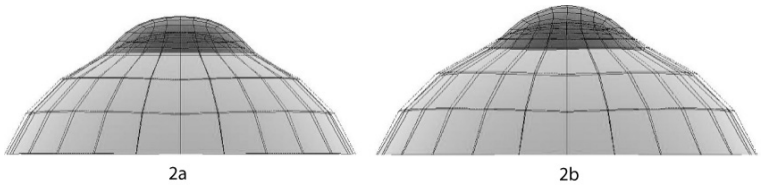

Figure 2: Deflections of the joint isotropic and anisotropic shells.

The deflection of the cornea modelled as a transverse-isotropic spherical shell is larger than for an isotropic shell. The deflection shape of the transverse-isotropic shell well agrees with the shape of the actual the cornea.

5 ACKNOWLEDGMENTS

The research is supported in part by SI-sponsored Visby program from KTH and by RFBR grant 09-01-00140a.

REFERENCES

[1] L.T. Balashevich. *Refractive Surgery*, Textbook for clinicians and hospital physicians, Moscow, (1999) (in Russian).

[2] S.M. Bauer, B.A. Zimin, M.V. Fedorchenko, L.I. Balashevich, A.B. Kachanov. To varying resistance of cornea after laser eximetric surgeries about miopia. *Eye biomechanics*. The Helmholtz Moscow Research Institute of Eye Diseases, **37**, 55–60, (2002) (in Russian).

[3] W. Srodka, M. Asejczyk, H. Kasprzak. Influence of IOP on the geometrical and biomechanicl properties of the linear model of the eye globe effect of the optical selfadjustment. *Proceedings of 13th Conference of the European Society of Biomechanics*, (2002).

[4] E.N. Iomdina. A comparative study of biomechanical properties of the cornea and sclera. *Proceedings of the congress, European Society of Biomechanics*, abstract 394, (2004).

[5] E.N. Iomdina. *Biomechanics of scleral shell of the human eye at miopia and its experimental correction*. Doctoral Thesis in Biology, Moscow, (2000) (in Russian).

23rd Nordic Seminar on Computational Mechanics
NSCM-23
A. Eriksson and G. Tibert (Eds)

ON PRESSURE-VOLUME RELATIONSHIP UNDER EXTERNAL LOADING FOR A HUMAN EYE SHELL

SVETLANA M. BAUER, BORIS N. SEMENOV AND EVA B. VORONKOVA

St. Petersburg State University
Faculty of Mathematics and Mechanics
28 Universitetskii pr., 198504 St. Petersburg, Russia
e-mail: s_bauer@mail.ru, web page: http://www.math.spbu.ru

Key words: Ocular Rigidity, Intraocular Pressure, Eye Shell.

Summary. Three different mechanical models describing the "pressure–volume" relationship for a human eye are considered. The relation "pressure–volume" is obtained for the eyeball shell, which is modeled as ellipsoidal transversal isotropic shell. In the second model the sclera and cornea are simulated as a joint shell consisting of two spherical or ellipsoidal segments with different radii and different mechanical properties at that the sclera and cornea are assumed to be transversal-isotropic shells with small modules of elasticity in the thickness direction. Finally sclera and cornea are considered as 3D elastic solids and in this case the relationship "pressure-volume" is analyzed numerically by means of FEM package ANSYS.

1 INTRODUCTION

As it is noted[1,2] the knowledge of the effect of the intraocular volume (IOV) on the intraocular pressure (IOP) in a human eye is important to draw a physically correct conclusion from the data of standard measurement procedure used in ophthalmology. Clinical tonometry and tonography, recently developed methods to assess the ocular pulse amplitude and pulsatile ocular blood flow and measurements with Ocular Response Analyzer, are based on the concept of ocular rigidity. The ocular rigidity is a parameter, which characterize the "pressure–volume" relationship in the eye[3,4].

The relationship "pressure–volume" for a certain eye can also help to estimate the mechanical parameters of the cornea and sclera for a living eye. Therefore it's important to reveal which mechanical characteristics affect the most significantly on this relationship "pressure-volume" for a human eye.

An outer shell of the eye — fibrous shell — consists of the cornea and sclera. The sclera forms more than 90 % of fibrous eye shell and the sclera is tougher than the cornea. For people with normal sight the sclera has a shape close to spherical one. That is why in all models of the first type the eye shell was represented as "one segment" spherical shell. However, it is known that myopic and hyperopic eyes have out-of-sphericity shapes. As it has been noted[5] the shape of the sclera or cornea under myopia and hyperopia may differ significantly from spherical, and the shape of the sclera differs from spherical most often.

2 MATERIALS AND METHODS

With the first simple model we consider ellipsoidal transversely isotropic shells of revolution of different shapes (modeling the sclera) with equal initial volumes under inner pressure. The results are obtained for different sets of parameters.

In Fig. 1 the increasing of IOV under the pressure 45 mm Hg as a function of the ratio of axial length ($2R_2$) and the equatorial diameter ($2R_1$) is plotted. In Fig. 2 the effect of absolute and relative change of IOV on IOP variation is presented.

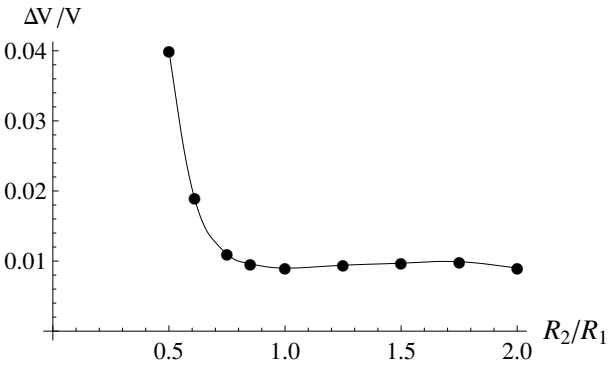

Figure 1: Relative change of IOV versus ratio of axial length ($2R_2$) and the equatorial diameter ($2R_1$).

If the ratio of the axial length (Axl) and the equatorial diameter of the shell (Deq) increases (shell modeling a myopic eye), then factor K ($\Delta P/\Delta V$) decreases up to 5%. If the ratio Axl/Deq decreases (shell modeling a hyperopic eye), then factor K significantly decreases up to 20%.

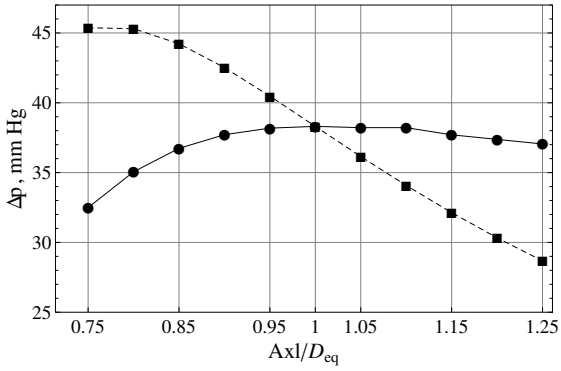

Figure 2: Effect of absolute (dashed line) and relative (solid line) changes of IOV on IOP variation.

In Fig. 3 the relation $IOV - IOP$ is plotted for "one segment" and "two-segment" models, when we take into account the properties of the cornea. Sclera and cornea are assumed to be transversaly isotropic shells with small modules of elasticity in the thickness direction. Modules of elasticity in the tangential directions for cornea are three times smaller than module of elasticity for sclera in the tangential directions. This case is analyzed with the help of the applied

shell theory by Rodionova–Titaev–Chernykh and by means of FEM package ANSYS. Results obtained with both models are well agreed.

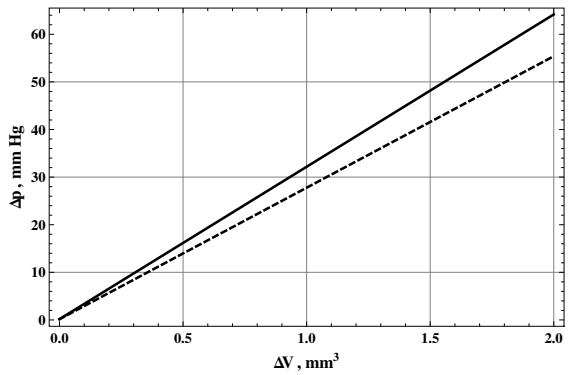

Figure 3: Relative change of IOV for "one-segment" model (solid line) versus "two-segment" model (dashed line).

3 CONCLUSIONS

Both the orthotropic properties of the sclera (the ratio of two tangential modules of elasticity) and the non-uniformity of the sclera affect greatly on the character of the pressure-volume relationship and, thus, on the rigidity of a human eye. Geometric and elastic properties of the cornea also affect the relationship, although to the less extent. It's important, that the initial intraocular pressure also influences on the factor of rigidity K ($\Delta P/\Delta V$), as it is described[1,2]. The less initial IOP leads to the less factor K.

4 ACKNOWLEDGMENTS

The research was supported in part by SI-sponsored Visby program from KTH and by RFBR grant 09-01-00140a.

REFERENCES

[1] A.A. Stein. Pressure–Volume Dependence for Eyeball under External Load. *Fluid Dynamics*, **45**, 177–186, (2010).

[2] G.A. Lyubimov. Opportunities of the Elastometry Method for Investigating for Elastic Properties of the Eyeball Shell. *Fluid Dynamics*, **45**, 169–176, (2010).

[3] O.W. White. Ocular elasticity? *Ophthalmology*, **90**, 1092–1094, (1990).

[4] P. Purslow, W.S. Karwatowsky. Is engineering stiffness a more useful characterization parameter than ocular rigidity. *Ophthalmology*, **105**, 1686–1692, (1996).

[5] G.K. Lang. *Ophthalmology*, Stuttgart–New York, Thieme, (2000).

23rd Nordic Seminar on Computational Mechanics
NSCM-23
A. Eriksson and G. Tibert (Eds)

MATHEMATICAL MODELS FOR APPLANATION TONOMETRY

SVETLANA M. BAUER, ANGELINA A. ROMANOVA AND BORIS N. SEMENOV

St. Petersburg State University
Faculty of Mathematics and Mechanics
28 Universitetskii pr., 198504 St. Petersburg, Russia
e-mail: s_bauer@mail.ru, web page: http://www.math.spbu.ru

Key words: Intraocular Pressure, Tonometry, Eyeball Shells.

Summary. Three mathematical models for measurement of the intraocular pressure by the applanation method are discussed. The eyeball is modeled as two conjugated elliptic shells. The effect of out-of-sphericity of corneal and sclera shape on applanation tonometry readings is estimated.

1 INTRODUCTION

Applanation tonometry estimates intraocular pressure (IOP) by quantifying the force needed to generate the defined deformation of the cornea (flat tonometer tips similar to the Goldmann tips) or by estimating the diameter of the circular contact area between the cornea and flat tonometer under the given load (Maklakoff tonometry). Due to new types of refractive surgery the problem of the IOP measurements standardization and the assessment of the effect of individual variations in geometrical and mechanical parameters of the eyeball on the accuracy of IOP readings acquire special attention. Recently, a number of studies on Goldmann tonometry modeling were published[1,2]. Since the contact zone of the Goldmann tonometer and a cornea is small it is assumed usually[1,2] that the perturbation introduced to fibrous coat by the Goldmann tonometer is localized near the contact area, and on the conjunction of a cornea with a sclera this perturbation is quite small, i.e. it was supposed that cornea deformation depends mainly on the cornea properties. However, as it was reported[2], a sclera may have a essential impact on the deformation process not only under the Maklakoff tonometry, but even under Goldmann's one. It is known that the contact zone of the Maklakoff tonometer and a cornea, especially for 10 g tonometer, is considerably larger than the contact zone under Goldmann tonometry, therefore, an effect of a sclera on corneal deformation could be significant. Thus, developing of a complete model, which takes into account properties of the sclera and the cornea, is highly important problem.

2 MATERIALS AND METHODS

The model, which takes into account properties of the sclera and the cornea, was proposed[3]. The eyeball was modeled as two spherical shells. However, myopic and hyperopic eyes have

out-of-sphericity shapes. As it was noted[4], either curvature of sclera and elongation (Fig. 1a) or shortening (Fig. 1c) of an anterior-posterior axes or curvature of a cornea (Fig. 1b, 1d) could lead to myopia or hyperopia.

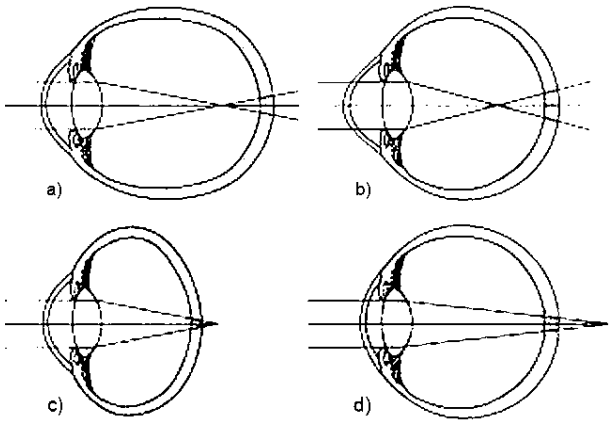

Figure 1: Axial myopia (a) and hyperopia (c), refractive myopia (b) and hyperopia (d). Adapted from a diagram by [4].

Three mathematical models for measurement of the intraocular pressure by the applanation method are discussed. The eyeball is modeled as two conjugated elliptic shells. The two segments shell is filled with uncompressible liquid under the pressure.

The analytical model is based on the theory of momentless (membrane) shells. The nonlinear theory of shell is used to analyze the significant deformations of the shell part, which models the cornea.

The numerical models are analyzed by means of FEM code ANSYS. In the first case the cornea and sclera are modeled as 3D elastic transversal isotropic solids. In the second case cornea is considered as the multilayer shell. The results for different models are compared.

Comparison of the results received with different models reveal good agreement but defer in details.

3 RESULTS

It is assumed that cornea and sclera are the parts of elliptic shells. This assumption permits to study the effect of out-of-sphericity of a corneal and sclera shapes as well as radii of segments on applanation tonometry readings. The results are obtained over a wide range of the parameters of sclera and cornea. The calculations show that the real IOP becomes smaller for more prolate cornea for same contact area. The difference in the corneal and sclera radii of curvature could cause the measurement error of applanation tonometry IOP readings ranged between 3% and 25%. It should be noted that the simulation results are in good agreement with the experimental data[5]. As an example the modeling of the IOP measurement after refractive surgery is presented in Fig. 2.

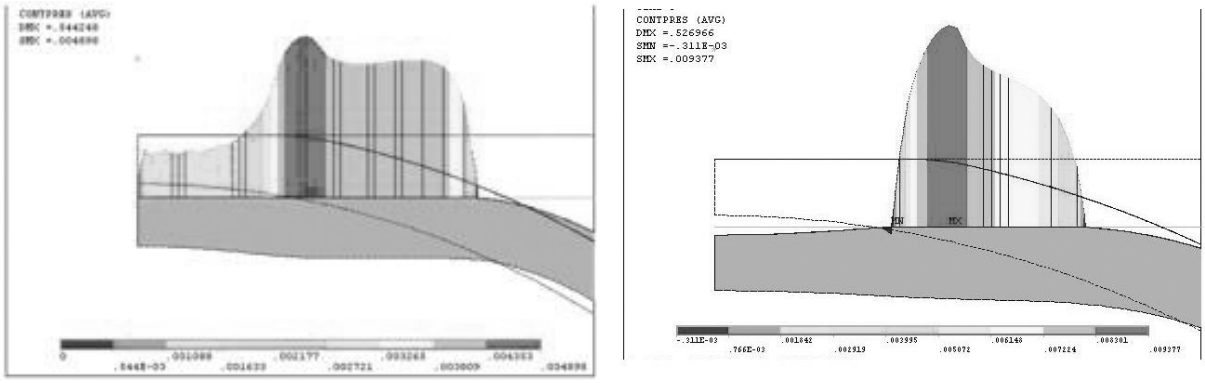

Figure 2: Contact stress distribution after 50 μm and 100 μm central ablation. True IOP level is 15 mm Hg, radius of curvature at the apex R — 7.8 mm, corneal base diameter D — 11 mm, internal radius of the sclera Rs — 12 mm.)

The developed mathematical model could give one of possible biomechanical explanation for the occurrence of false IOP readings during AT measurements. Corneas with flatted profile and/or IOP lower than 15 mm Hg can cause "corneal collapse" — detachment of cornea surface from the tonometer under the applanation tonometry procedure.

4 ACKNOWLEDGMENTS

The research was supported in part by SI-sponsored Visby program from KTH and by RFBR grant 09-01-00140a.

REFERENCES

[1] D. Ljubimova. *Biomechanics of the Human Eye and Intraocular Pressure Measurements.* Doctoral Thesis in Mechanics, Stockholm, Sweden, (2009).

[2] J. Liu, C. Roberts. Influence of corneal biomechanical properties on intraocular pressure measurement. *Journal of Cataract & Refractive surgery*, **31**, 146–155, (2005).

[3] S.M. Bauer, G.A. Lyubimov and P.E. Tovstik. Mathematical Modelling of Maklakoff's Method for Measuring the Intraocular pressure. *Fluid Dynamics*, **40**, 20–33, (2005).

[4] G.K. Lang. *Ophthalmology*, Stuttgart–New York, Thieme, (2000).

[5] E.P. Tarutta, V.P. Erichev and T.Yu. Larina. Controlling intraocular pressure after keratorefractive operations. *Proceedings of Ocular Biomechanics*, Moscow, 120–122, (2004) (in Russian).

23rd Nordic Seminar on Computational Mechanics
NSCM-23
A. Eriksson and G. Tibert (Eds)

A POSTERIORI ERROR COMPUTATION FOR OPTIMAL STEERING OF MECHANICAL SYSTEMS

HÅKAN JOHANSSON* AND KENNETH RUNESSON

Department of Applied Mechanics
Chalmers University of Technology
412 96 Göteborg, Sweden
e-mail: hakan.johansson@chalmers.se

Key words: Optimal control, trajectory control, a posteriori error computation, adaptivity.

Summary. This contribution considers the steering of motion of a mechanical system from an initial state to a target state as an optimal control problem. Suitable FE-approximations for the state and control variables are discussed along with a goal-oriented a posteriori estimate of the discretization errors.

1 INTRODUCTION

A particular class of optimal control problems concerns the steering of motion of a mechanical system from an initial state to a target state (target or trajectory control). The motion of the system depends on forces acting as controls via a set of ordinary differential equations. Upon considering the equations of motion and the relevant kinematic and kinetic limitations, a constrained optimization problem can be formulated where the control forces are sought to minimize a chosen objective function, such as the energy consumption. In this contribution we study the musculoskeletal motion of a human body considered as a discrete mechanical system[2,4].

2 DISCRETIZATION OF THE OPTIMAL CONTROL PROBLEM

In order to solve the optimal control problem numerically, approximations for the state (generalized coordinates and momenta) and control (generalized forces) variables are introduced. The approximations are made in a finite element fashion, such that the state and controls are expressed in terms of (vector-valued) nodal values and basis functions in time. In particular, the control and displacement state variables are discretized separately. For the introduced approximations, the optimality conditions are expressed in weak form, resulting in a nonlinear system of the sought nodal values determining the discrete solution for the state and control. The subject of the present work is to determine the error in the approximate solution compared to the exact solution.

From the optimality conditions on weak form, we may employ previous work on a posteriori error estimates based on the pertinent dual problem to estimate discretization errors in both state and control variables. The sources of errors can be traced to specific regions of the state and control time-meshes, which can be used in an adaptive mesh-refinement procedure. Earlier work on a posteriori error estimation for optimal control problems have been based on the "optimal

control" approach[1,5], whereas the present contribution will use our previous work in error control for parameter identification problems based on a tangent form of the dual problem[3].

3 NUMERICAL EXAMPLE

To illustrate the theoretical strategy, we study an example presented in[4] of a very simple dynamical system (a double pendulum) representing the movement of the upper arm in the sagittal plane. The arm is to be lifted from vertical hanging to a horizontal straight position using minimal energy (or related measure) without violating anthropomorphic constraints (the opening angle of the elbow must be between 0 and 135 degrees) and control constraints (the control variables are restricted by maximum and minimum values). The solution algorithm is based on a nested format with a relaxation of the constraints.

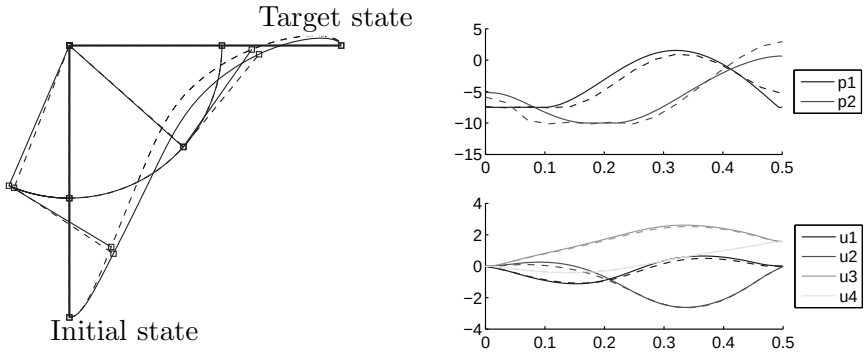

Figure 1: Left: Plot of the arm from vertical hanging to a horizontal straight position. Right: Comparison of the solved state (u_1-u_4) and control (p_1-p_2) variables using fine (dashed line) and coarse discretization (solid line).

The numerical example indicate that a discretization error in the control variable arises in order to "compensate" for discretization errors in the solution of the equations of motion.

REFERENCES

[1] R. Becker. *Adaptive finite elements for optimal control problems*, Habil. thesis, University of Heidelberg, (2004).

[2] A. Eriksson. Optimization in target movement simulations *Comput. Methods Appl. Mech. Engrg.*, **197**, pp 4207-4215 (2008).

[3] H. Johansson, K. Runesson and F. Larsson. Parameter identification with sensitivity assessment and error computation. *GAMM-Mitt.*, **37**, 430-457, (2007).

[4] M. Kaphle. *Simulations of human movements through temporal discretization and optimization.* Lic. thesis, Royal Institute of Technology, (2007).

[5] K. Kraft. *Adaptive finite element methods for optimal control problems.* Lic. thesis, Chalmers University of Technology, (2008).

A PARAMETRIC STUDY OF THE RIGID FOOT-GROUND CONTACT MODEL: EFFECTS ON INDUCED ACCELERATION OF THE BODY DURING WALKING

RUOLI WANG*, ELENA M. GUTIERREZ-FAREWIK*, †

* Department of Mechanics
Royal Institute of Technology
Osquars Backe 18, 100 44 Stockholm, Sweden

† Department of Women's and Children's Health
Karolinska Institutet
Solna, 171 77 Stockholm, Sweden
E-mail: ruoli@mech.kth.se, web page: http://www.mech.kth.se
Email: lanie@mech.kth.se, Web page: http://www.ki.se

Key words: Induced Acceleration Analysis, Foot-Ground Contact Model, Muscle Function.

1 INTRODUCTION

Induced acceleration analysis (IAA) is a method for computing the accelerations produced by an application force or moment to a body or system of bodies[1] and has been used to quantify potential of a muscle force to flex/extend joints, to support and to forward propel the body during walking[2].

The foundation for generating simulations relies on interactive computer-implemented musculoskeletal models which are constructed based on various authors' own assumptions and simplifications. Schwartz *et al*.[3] has modelled the foot-ground contact as rigid contact, a moving revolute joint instantaneously located at the center of pressure (COP). Alternative approaches have included a ball-socket joint at initial contact and toe-off, and rigid contact during foot-flat. In rigid contact modelling, the use of appropriate joint constraints and accurate locations of COP are key factors in validating the investigation of interest.

The aim of the present study was to determine the influence of *Case 1*: location of the COP and *Case 2:* varied constraints of foot-ground joints on potential dynamic function of the ankle muscles during the stance phase.

2 METHOD

2.1 Mathematical model for induced acceleration analysis

The generalized equations-of-motion of a multi-articulated body system[4] can be written as:

$$\vec{I}(\vec{q})\ddot{\vec{q}} = \vec{R}(\vec{q})\vec{f}_M + \vec{G}(\vec{q}) + \vec{C}(\vec{q},\dot{\vec{q}}^2) + \vec{\Gamma}(\vec{q},\dot{\vec{q}}) + \vec{F}_E \quad (1)$$

Where $\vec{q},\dot{\vec{q}},\ddot{\vec{q}}$ are the vectors of generalized coordinates, velocities and accelerations; $\vec{I}(\vec{q})$ the

system mass matrix; $\vec{f}_M$ the vector of muscle forces; $\vec{R}(\vec{q})$ the matrix of muscle moment arms; $\vec{G}(\vec{q})$ the vector of gravitational force; $\vec{C}(\vec{q},\dot{\vec{q}}^2)$ the vector of Centripetal and Coriolis forces; $\vec{\Gamma}(\vec{q},\dot{\vec{q}})$ the vector of ligament torques; $\vec{F}_E$, the vector of external force.

Thus the accelerations $\ddot{\vec{q}}$ are:

$$\ddot{\vec{q}} = \vec{I}(\vec{q})^{-1}\{\vec{C}(\vec{q},\dot{\vec{q}}^2)+\vec{G}(\vec{q})+\vec{\Gamma}(\vec{q},\dot{\vec{q}})+\vec{R}(\vec{q})\vec{f}_M+\vec{F}_E\} \quad (2)$$

Since $\vec{I}(\vec{q})^{-1}$ is non-diagonal, the contribution of an individual muscle force $\vec{f}^i_M$ to the instantaneous accelerations of the segments $\ddot{\vec{q}}$ is presumed to be the summed contribution arising from $\vec{f}^i_M$ at that instant, and the ground-reaction force due to the immediate past trajectory of $\vec{f}^i_M$. Eq (2) can be reformulated as Eq (3) while all other force terms were set to zero.

$$\ddot{\vec{q}} = \vec{I}(\vec{q})^{-1}\{\vec{R}(\vec{q})\vec{f}^i_M+\vec{F}_E{}^{M^i}\} \quad (3)$$

2.2 Musculoskeletal model and configuration data

A generic 3D linkage model was scaled to fit each specific subject, configured by gait data and driven by 1 N muscle force. The model consists of 28 rigid segments and 88 lower extremity muscles. Muscle paths, bone geometry, and segment inertial parameters were based on previous study[5]. Analyse were performed in SIMM and SD/Fast. Captured motion data from five healthy controls (age: 28±3 yrs) examined using a motion capture system (Vicon MX40) was analyzed.

2.3 Foot-ground contact

Foot-ground contact was modelled in four sub-phases: initial-contact to foot-flat ('1st rocker'), foot-flat ('2nd rocker'), heel lift to toe-flat ('3rd rocker') and toe-flat to toe-off ('toe-off'). Three ground-foot joints were added in the model- at the posterior inferior point of the heel ('GFH'), the distal end of the third metatarsal ('GFM'), and the lifting point of foot ('GFT') respectively- which served as the constraint for the estimated COP in gait.

Case 1: The lateral and medial shift of the locations of COP was modelled by moving foot-ground joints laterally or medially by 10% of the subject's foot width.

Case 2 : 'Simple' and 'Multiple' constraints were applied to the foot-ground joints. 'Simple' constraint referred to modelling a ball-socket joint at all sub-phases other than the 2nd rocker, where the foot was completely fixed to the ground. 'Multiple' constraint referred to varying degrees of freedom (DOFs) allowed in the sub-phases. The same constraints as 'Simple' were allowed in the 1st and 2nd rockers. In the 3rd rocker, only a sagittal DOF was allowed at the GFM joint. In toe-off, sagittal and transverse DOFs were allowed at the GFT joint.

3 RESULTS

Case 1

An example of tibialis anterior's IAA is shown in Figure 1A and 1B . No obvious differences can be seen in the fore-aft or vertical potential accelerations of the body COM.

Smaller lateral body COM potential accelerations were found in the 3rd rocker when COP was shifted laterally, and even smaller when the COP was shifted medially.

At the hip joint, abduction, instead of adduction potential acceleration was found in the 1st rocker when COP shifted medially. Otherwise, the general trends were similar at other lower limb joints. Some discrepancies can be found in the 1st rocker.

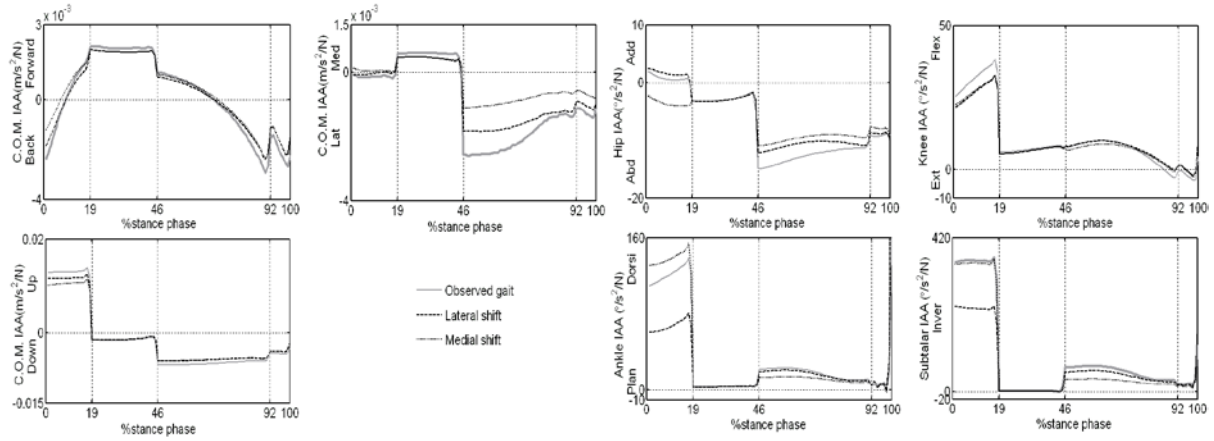

Figure 1: (A) Center of mass potential accelerations induced by tibialis anterior in the stance phase. (B) Induced potential accelerations at the hip, knee, ankle and subtalar joints by tibialis anterior in the stance phase. Lines illustrate the average IAA data in the observed gait, and with COP shifted laterally and medially.

Case 2

The tibialis anterior's potential to accelerate the body COM in the fore-aft and vertical directions was similar with the ' Simple' and 'Multiple' constraints (Figure 2 A). The 'Multiple' constraints, however, had potential to accelerate the body COM medially, and the 'Simple', laterally. General trends of induced accelerations at hip, knee, ankle and subtalar joints were similar (Figure 2B). With the ' Simple' constraints, larger hip abduction and subtalar eversion accelerations were found in the 3rd rocker.

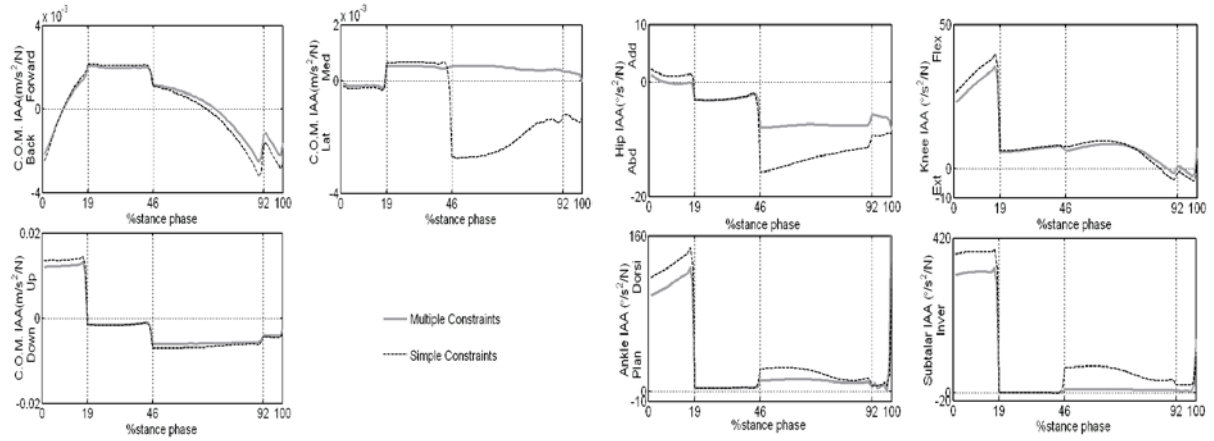

Figure 2: (A) Center of mass potential accelerations induced by tibialis anterior in the stance phase. (B) Induced potential accelerations at the hip, knee, ankle and subtalar joints by tibialis anterior in the stance phase. Lines illustrate the controls' average data with 'Multiple' and 'Simple' foot-ground constraints.

4 DISCUSSIONS

A foot constraint model determines how the interaction of the foot and floor will be defined during stance phase of gait. Particularly in IAA, it plays an important role since only muscle force and corresponding ground reaction force are present in the dynamic equations. As expected, the multiple vs simple constraints did not produce obvious differences in the muscle's sagittal plane potential accelerations, e.g. knee extension-flexion, and fore-aft and vertical COM, but larger deviations were found in the frontal and transverse planes in the 1st and 3rd rockers. Potential accelerations of body COM towards the lateral direction implies that the constraint changes in the frontal and transverse planes are more influential in the medial-lateral induced acceleration.

There are many sources of errors in data generation using IAA, wherein the location of COP can be considered one of them. Kimmel has concluded that moving the COP location had the smallest effect among changing the location of muscle origin, muscle insertion, joint center and COP[6]. In our study, when COP was shifted, we found that deviations mostly occurred in the 1st rocker only few in the 3rd rocker when foot has more freedom to move. Compared to the knee and hip joints, the ankle and subtalar joint induced accelerations were more affected due to their more proximal location and the muscle's anatomical function. It is worth mentioning that the 10% foot width was equivalent to an average of 8.5 mm in our study, and only 1N muscle force was applied, which are both rather trivial magnitudes. Further investigation, e.g. increasing deviations of the COP location, will be valuable to confirm how much IAA results can be affected.

5 CONCLUSION

In the current study, we found that the potential induced accelerations in lateral-medial body COM were more sensitive to the foot-ground constraints as well as the COP locations than in other directions. Although the general trends at the lower extremity joints were similar in both cases, 1st rocker and 3rd rockers are the most affected sub-phases. Care should be taken in applying foot-ground constraints, depending on the specific investigation of interest.

REFERENCES

[1] F.E. Zajac, R.R. Neptune and S.A. Kautz, "Biomechanics and muscle coordination of human walking Part 1: introduction to concepts, power transfer, dynamics and simulations". *Gait Posture*, **16**, 215–232 (2002).
[2] M.Q. May, F.C. Anderson, M.G. Pandy and S.L. Delp, "Muscles that support the body also modulate forward progression during walking", *J Biomech*, **39**, 2623-2630 (2006).
[3] M. Schwartz and G. Lakin, "The effect of tibial torsion on the dynamic function of the soleus during gait". *Gait Posture*, **17**, 113-118 (2003).
[4] F.E. Zajac and M.E. Gordon, "Determining muscle's force and action in multi-articular movement". *Exercise Sport Sci Rev*, 187-230 (1989).
[5] S.L. Delp, J.P.Loan, M.G. Hoy, F.E. Zajac, E.L.Topp and J.M. Rosen, "An interactive graphic-based model of the lower extremity to study orthopaedic surgical procedures". *IEEE Trans Biomed Eng*, **37**, 757-767 (1990).
[6] S.A. Kimmel and M. Schwartz, "A baseline of dynamic muscle function during gait", *Gait Posture*, **23**, 211-221 (2006)

23rd Nordic Seminar on Computational Mechanics
NSCM-23
A. Eriksson and G. Tibert (Eds)

AN INVERSE MODELLING METHODOLOGY FOR PARAMETERS IDENTIFICATION OF THERMOPLASTIC MATERIALS

MARIO POLANCO-LORIA[*§] and ARILD H. CLAUSEN[§†]

[*] SINTEF Materials and Chemistry, NO-7465 Trondheim, Norway
E-mail:mario.polanco@sintef.no

[§]Structural Impact Laboratory (SIMLab), Centre for Research-based Innovation, NO-7491 Trondheim, Norway

[†] Department of Structural Engineering, NTNU, NO-7491 Trondheim, Norway

Key words: Thermoplastics, Computational Plasticity, Material identification, DIC.

1 INTRODUCTION

Development of new material models also involves experimental efforts where well defined material tests are required for calibration of the model parameters. At present, the static uniaxial tension test is the simplest mechanical test used for material characterization. However, for polymeric materials determination of the true tensile stress-strain curve is difficult. Digital image correlation (DIC) is a technique that can overcome this difficulty. Furthermore, interpretation of experimental data and its utilization for material calibration can be cumbersome because of strain rate and temperature dependency. The variables involved in the thermo-mechanical characterization are highly coupled; consequently, material identification by trial and error procedures can be inefficient.

Alternatively, nonlinear inverse computational methods can be applied to identify material parameters in cases where the parameters are not directly measurable or the deformations fields are of heterogeneous nature (e.g. complex boundary conditions, loss of homogeneity during the deformation process). Such methodology is applied here.

2 CONSTITUTIVE MODEL

Polymers are increasingly being used in the transport industry, specially, in structural components related to passengers or pedestrian safety. In this direction, a new hyperelastic-viscoplastic constitutive model for thermoplastics (under isothermal conditions) has been developed by Polanco-Loria et al.[1] (see Fig. 1).

A complete description of the model is given in the corresponding reference[1]. With respect to the plasticity response of Part A (see Fig.1) the model has been enhanced to include isotropic hardening/softening behavior according to Voce's saturation model:

$$R = \left(\sigma^{sat} - \sigma_T\right)\left[1 - \exp^{-H\bar{\varepsilon}^p}\right] \tag{1}$$

where, R is the stress hardening level. The hardening/softening modulus is represented by H, the saturation and yield tensile stress by σ^{sat} and σ_T, respectively. Hence, for the hardening case $\sigma^{sat} > \sigma_T$ while for the softening case $\sigma^{sat} < \sigma_T$:

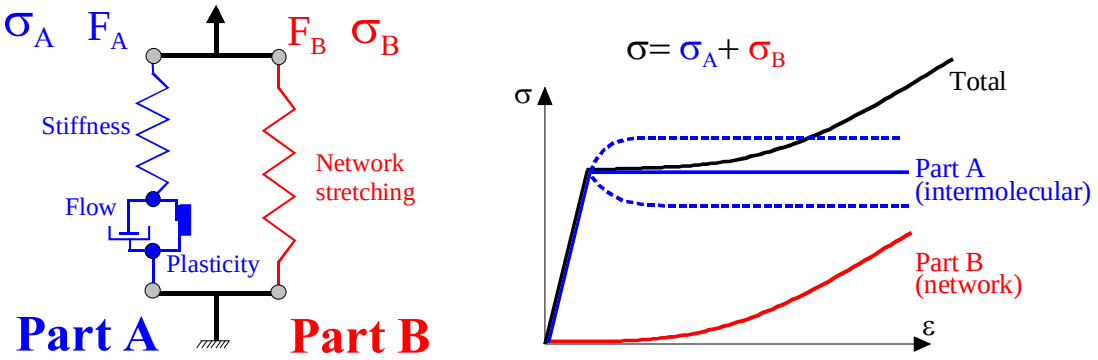

Figure 1: Constitutive model with inter-molecular (A) and network (B) contributions

The constitutive model requires 11 parameters to be identified:

- **Spring A** represents the initial elastic stiffness with a Neo-Hookean formulation. There are two elastic coefficients E (Young's modulus) and ν (Poisson's ratio).
- **Friction element A** models the yielding process with pressure dependency and a non-associative flow rule. Three parameters in this friction element are needed: the uniaxial yield tensile stress σ_T, the pressure sensitive parameter α and the volumetric plastic strain control parameter β. The hardening/softening behaviour necessitates two additional terms (see Eqn. 1): H and σ^{sat}.
- **Dashpot A** is included to represent the rate dependence of the material. The visco-plastic multiplier uses a linear (log scale) strain rate law characterized by two parameters: the reference strain rate $\dot{\varepsilon}_0$ and the strain rate coefficient C.
- **Spring B** represents the elongation of the molecule chains, here modeled with a hyperelastic law. Only the distortional stress-stretch relation is used here where two hardening coefficients C_R and λ_L need to be identified.

The model has been implemented as a user-defined model in the explicit solver LS-DYNA[2] using a semi-implicit algorithm.

3 MATERIAL PARAMETER IDENTIFICATION PROCEDURE

3.1 The parameter identification methodology

The calibration procedure is cumbersome because the nine variables, describing the non-linear behavior, to some degree are coupled to each other. In addition, local strain rates change during the tests. Indeed, because of the necking phenomenon, global and local strain rates can be rather different and homogeneous strain rates fields can be difficult to achieve. For this reason an inverse modeling methodology for thermoplastic materials was proposed by Polanco-Loria et al.[3] where the locally measured strain rate history, associated to the true stress-strain response, was applied to "load" the FE "material point". The identification procedure could be performed by comparing the numerical and the experimental response history by minimizing the least square residual (LSR), see Fig. 2. The methodology was successfully applied to a PP copolymer material[4].

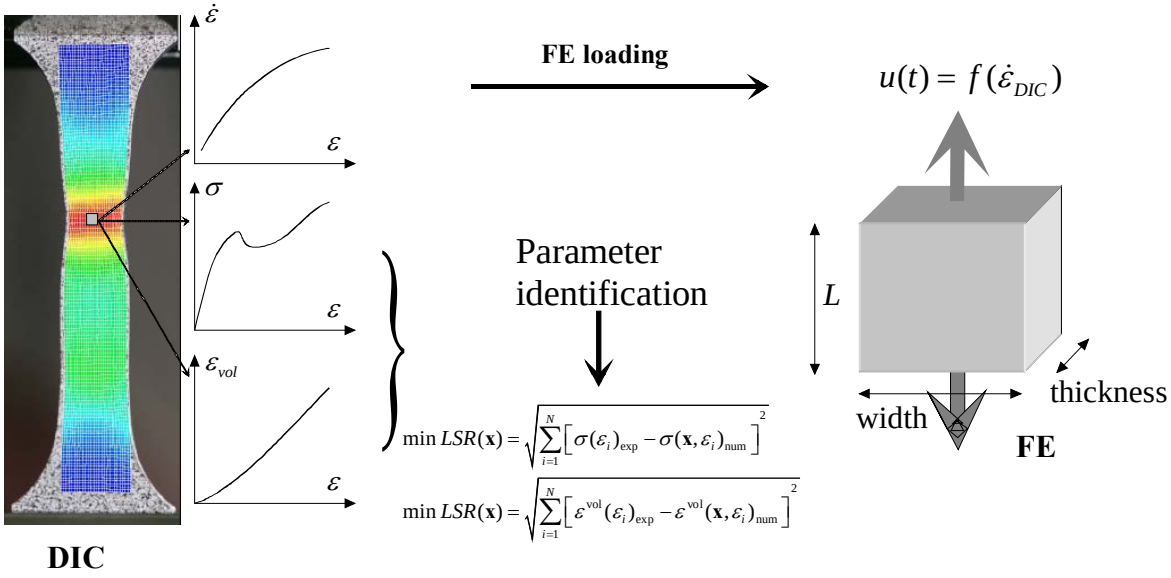

Figure 1: Parameter identification methodology

3.2 Application to HDPE and PVC thermoplastics

An extensive experimental program on HDPE and PVC thermoplastic materials was performed by Hovden[5] using DIC and from that study a semi-analytical identification procedure was proposed. Hovden's results are used as the main input for our procedure. The methodology is restricted to the identification of 5 variables contained in the design vector $\mathbf{x} = \left[C_R \quad \lambda_L \quad H \quad \sigma^{sat} \quad \beta \right]^T$ which characterizes the hardening response together with the volumetric plastic strain. The two elastic parameters, the two strain rate parameters, the pressure sensitivity and the yield tensile stress were kept constants with the values proposed by Hovden as an initial guess for the optimization procedure. In this way a more reasonable comparison could be traced between the semi-analytical and inverse procedures. The

optimization method uses the response surface technique and it was performed using the software LS-OPT[6]. The obtained results are given in Table 1. The two methods provide different sets of material. It is believed that the observed deviations are, mainly, due to a) variations in the local strain rates with respect to the global one (e.g. about 4 times for the HDPE and about 2.5 times for the PVC), and b) the direction of the plastic flow does not remain constant during the deformation process. Nevertheless, the semi-analytical model is very useful because of its practical purpose (e.g. industry) and because it can be used to generate the initial guess data for the inverse modelling procedure.

		σ^{sat} (MPa)	H (MPa)	C_R (MPa)	λ_L	β
HDPE	Semi-analytic.	23.90	39.60	1.74	7.75	1.04
	Inv. Mod.	22.65	49.52	1.96	12.45	1.03
PVC	Semi-analytic.	37.80	15.00	6.07	1.71	1.27
	Inv. Mod.	39.25	11.62	6.11	1.73	1.22

Table 1 : Comparison between inverse modeling and semi-analytical identification procedures

4 CONCLUSIONS

- An inverse modelling approach to identify material parameters, with applications to HDPE and PVC thermoplastics, has been described. An experimental set of $\sigma - \varepsilon - \varepsilon^{vol} - \dot{\varepsilon}$ relations are needed.
- A semi-analytical model is useful for industrial applications as well as an initial guess assessment for the inverse modelling procedure.

REFERENCES

[1] M. Polanco-Loria, A.H. Clausen, T. Berstad, and O.S Hopperstad "Constitutive model for thermoplastics with structural applications" accepted for publication. International Journal of Impact Engineering (2010).

[2] LS-DYNA Keyword User's Manual. Version 971. Livermore Software Technology Corperation (2007).

[3] M. Polanco-Loria, S. Dumoulin and T. Coudert "Constitutive modelling of thermo-plastics: Parameters identification procedure" Computational Plasticity X Fundamentals and Applications. Barcelona, Spain; Eds. E. Oñate, D.R.J. Owen and Suarez (2008).

[4] M. Polanco-Loria, H. Dayan and F. Grytten "Material parameters identification: An inverse modelling procedure applicable for thermoplastic materials" submitted to Polymer Engineering Science (2010).

[5] M. T. Hovden "Tests and numerical simulations of polymer components" Master Thesis, NTNU (2010).

[6] LS-OPT Keyword User's Manual. Version 3.3. LSTC, 2007.

23rd Nordic Seminar on Computational Mechanics
NSCM-23
A. Eriksson and G. Tibert (Eds)

SIMULATION OF TIE-CHAIN CONCENTRATION IN SEMI-CRYSTALLINE POLYETHYLENE

F. NILSSON*

* Royal Institute of Technology (KTH)
Department of Fibre- and Polymer Technology
Polymer Materials Group
Teknikringen 58, 10044, Stockholm, Sweden
e-mail: fritjofn@kth.se

Key words: Polymer Science, Mechanical Modeling, Monte-Carlo Simulation, Semi-Crystalline, Polyethylene, Tie-Chain Concentration.

Summary: Novel Monte-Carlo simulation methods have been developed for examining how the tie-chain concentration of polyethylene and other semi-crystalline polymers affect the mechanical material properties.

1 ESTIMATING TIE-CHAIN CONCENTRATION

When polyethylene and similar semi-crystalline polymers are cooled from melt, typically small crystal nuclei eventually form throughout the material. From these nucleation points stacks of thin crystal lamellae starts growing radially outwards, often forming superstructures like spherulites and axialites. The orientation of each crystal lamellae is depending on both the chemical and physical properties of the material and on the processing conditions. However, they usually become more parallel with increasing crystallinity. Between the layers a portion of amorphous (i.e. non-crystalline) polymer always remains.

A polymer chain leaving a section of a crystal lamellae thus has the following options: (1) immediately return into the same crystal from where it came, (2) enter the amorphous region for a while but eventually return into the initial crystal, (3) enter the amorphous region and end there, and (4) enter the amorphous region and propagate to an adjacent crystal lamellae. The fourth alternative means that a tie-chain is formed. The number of tie-chains leaving a unit area of fold surface largely controls the fracture toghness of semi-crystalline polymers like polyethylene.

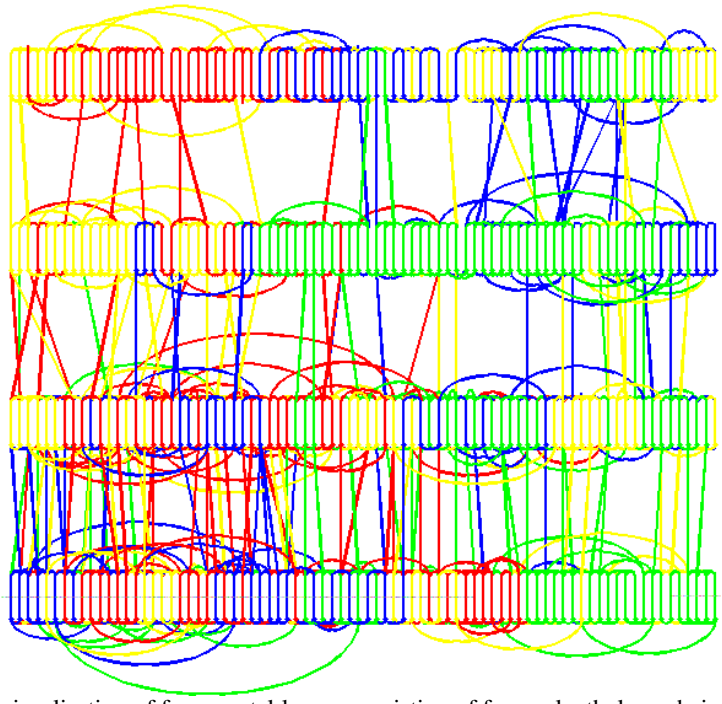

Figure 1: Schematic visualisation of four crystal layers consisting of four polyethylene chains coloured in red, blue, green and yellow. The tie-chains connecting the layers together are for simplicity plotted as straight lines even though the polymer chains in reality are heavily curved in the amorphous regions between the crystals.

Several theoretical models for estimating the tie-chain concentration for linear polyethylenes have previously been suggested. Many molecular dynamics studies have also been focused on the amorphous interlayer of polyethylenes. Anyhow, to our knowledge none of the previous simulations have systematically studied how the tie-chain concentration is affected by polymer-branching density, molecular weight, crystal thickness and temperature. Neither have any other kinds of entanglements than tie-chains been taken into account.

As a part of a larger multi-scale project covering not only mechanics but also diffusion, heat transfer and dielectrics, we have developed a Monte-Carlo model[1] that is able to examine the influence of the properties previously mentioned. Some preliminary results of the model will be presented on the conference.

REFERENCES

[1] F. Nilsson, M. Hedenqvist and U. Gedde, “Small Molecule Diffusion in Semi-Crystalline Polymers as Revealed by Experimental and Simulation Studies”, *accepted for* Poly. Eng. Sci. (2010).

23rd Nordic Seminar on Computational Mechanics
NSCM-23
A. Eriksson and G. Tibert (Eds)

SIZE DEPENDENT BEHAVIOUR OF MICRON-SIZED COMPOSITE POLYMER PARTICLES

J. Y. HE*, Z. L. ZHANG* AND H. KRISTIANSEN†

* NTNU Nanomechanical Lab
Norwegian University of Science and Technology (NTNU)
7049, Trondheim, Norway
email: jianying.he@ntnu.no; zhiliang.zhang@ntnu.no, web page: http://www.ntnu.no

† Conpart AS, 2013, Skjetten, Norway
email: helge@conpart.no, web page: http://www.conpart.no

Key words: Polymer Particles; Size Effect; Stress; Strain; Nanoindentation.

Summary. The mechanical properties of micron-sized composite polymer particles have been investigated by using a nanoindentation-based flat punch technique. The contact load-displacement relationship of particles has been established and the stress-strain relationship has been determined. An interesting size effect on mechanical properties of both polymer particles and metallized polymer particles has been found. The smaller the particle size is, the stiffer the particle is. Finite element analyses indicate that different mechanisms dominate the size effect of two types of particles.

1 INTRODUCTION

Ugelstad monodisperse polymer particles have been widely used in chemical industries and biotechnology [1]. Recently there is a growing interest in polymer particles with potential application in new electronic packaging technologies, such as Anisotropic Conductive Adhesives (ACA) in Flat Panel Displays [2]. The particles are conductive through deposition of nano-scale metal coating on the particle surface. The metallized particles usually consist of a micron sized polymer core for improving contact compliance, a nanoscale Ni inner layer for obtaining electrical conductivity, and a nanoscale Au outer layer for protecting inner layer from oxidation and improving the reliability of electrical performance. The use of metallized polymer particles in ACA technology possesses many advantages in terms of lead-free, reducing package size and achieving high-density interconnections. The electrical characteristics as well as the reliability of the interconnection are mainly determined by the mechanical performance of the conductive polymer particles. Therefore, the mechanical performance of particles is of crucial importance to a reliable connection. This motivates us to study the large deformation behaviours of composite polymer particles. Both experiment study and finite element analysis have been carried out to study the mechanical properties of composite polymer particles.

2 EXPERIMENT

2.1 Materials

Both polymer particles and metallized polymer particles were tested. The chemical composition of polymer particles was 98% polystyrene slightly crosslinked with 2% divinylbenzene (PS-DVB). The PS-DVB particle sizes were varied from 2.6 to 25.1μm. The core of metallized polymer particle was strongly crosslinked by 40wt% acrylic with 60wt% diacrylic (AC-DAC). The core sizes were 3.8μm and 4.8μm in diameter. The Ni and Au were deposited on the polymer core by an electroless plating process. The thickness of Ni inner layer and Au outer layer was about 50nm and 25nm, respectively.

2.2 Experiment

The mechanical test of single acrylic particles was performed by using a nanoindentation-based flat punch methodology. A diamond flat punch of 100μm in diameter was specially designed to compress single particles. During compression the real time force and displacement on particles were monitored and the contact force–displacement curves were obtained. To compare the particle behaviour, the stress–strain relationship was calculated as follows:

$$\sigma_N = \frac{P}{\pi R^2} \tag{1}$$

$$\varepsilon_N = \frac{D}{R} \tag{2}$$

where P was the applied force, D was the half displacement during compression and R was the radius of undeformed particle.

2.3 Finite element Analysis

Large deformation finite element analysis (FEA) with ABAQUS was carried out to study the mechanical behaviour of single polymer particles. The material was assumed to be linear elastic and axisymmetric elements were used to model particles. Axisymmetric analytic rigid surface was used to model the diamond flat punch. Very fine mesh was used in the contact region. The minimum element size in the model was about 0.1% of the initial sphere radius. The mesh and model used in the analysis are shown in Figure 1.

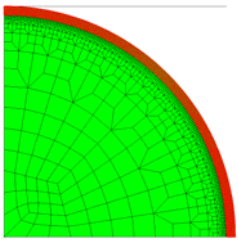

Figure 1: Finite element analysis with non-linear geometry.

3 RESULTS AND DISCUSSION

The normalized compressive stress of PS-DVB particles at 4% deformation level with different strain rates are plotted in Figure 2, in which the compressive stress is normalized to the value of the smallest particle. Particles display distinct size effect on the compressive stress. The size effect also has different trends depending on the strain rate. With the smaller strain rate, the size effect is most evident for the two smaller particles, whereas for the larger strain rate the size effect is more evenly distributed. The size effect of PS-DVB particle is mainly contributed by a "core–shell" structure where there is a higher crosslink density in the surface shell than the core due to different hydrophilicity of DVB and styrene monomers.

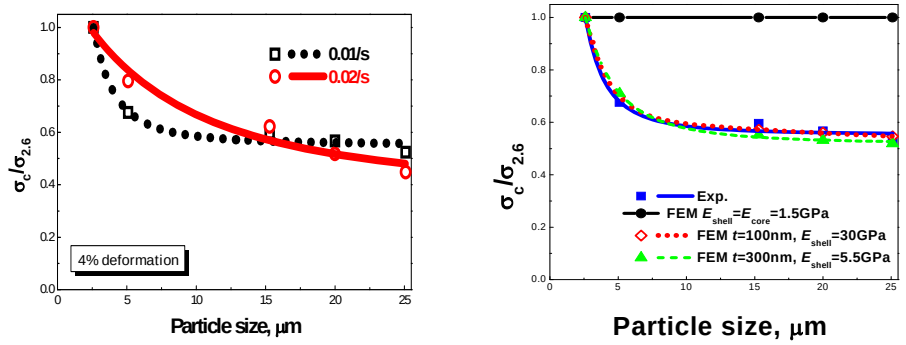

Figure 2: PS-DVB Particle size dependence of the normalized stress (a) experimental results with strain rate 0.01 and 0.02/s at deformation level 4% and (b) finite element solutions.

The compression stress–strain curves of uncoated and metalized AC-DAC particles are shown in Figure 3. The metallized particle sizes are 3.875 and 4.875μm, respectively, while uncoated counterparts are 3.8 and 4.8μm. At the beginning of loading, the metallized particle is significantly stiffer than the uncoated one. The occurrences of a large "pop-in" on the loading segment suggest that a significant change has happened to the metallized particles. With further deformation, one or more additional smaller "pop-ins" occurs, and finally the loading curves of the metallized and uncoated particles overlap each other. At this stage it is evident that the metal coating has no effect on the particle behaviour any more.

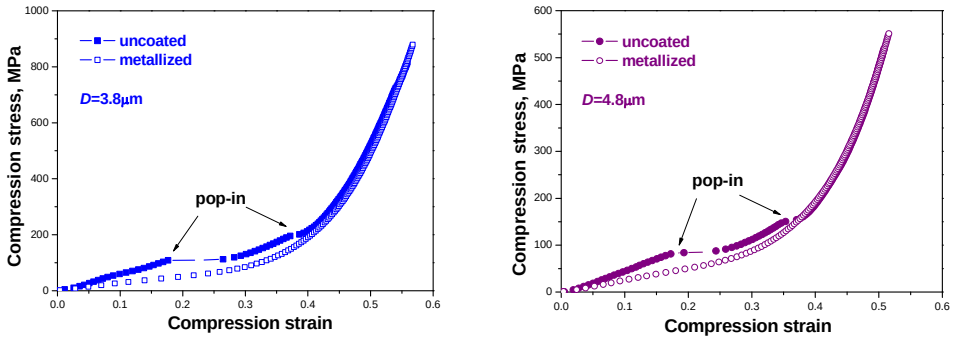

Figure 3: The compression stress–strain curves of uncoated and coated AC-DAC particles: (a) 3.8μm particles and (b) 4.8μm particles.

The stress–strain relationship of two metallized particles is compared in Figure 4 (a). The pop-in on both particles occurs at around 18% deformation. A particle size effect can be clearly observed, which shows that the 3.8μm particle is harder than the larger 4.8μm particle. This is consistent with the PS-DVB particles. Unlike the mechanism of size effect on PS-DVB particles, the presence of the metal coating significantly influences the particle behaviour. Since the metallized particles have different core size but same coating thickness, the volume fraction of the metal coating in two metallized particles are different. This results in the particle size effect. The finite element solutions of metallized AC-DAC particles and uncoated AC-DAC particles are shown in Figure 4 (b). Metallized particles are much stronger than uncoated ones, in agreement with experimental results. Two uncoated particles behave identical while metallized particles display a particle size effect that the smaller particle is harder. This demonstrates that the metal coating plays a dominate role on the particle size effect.

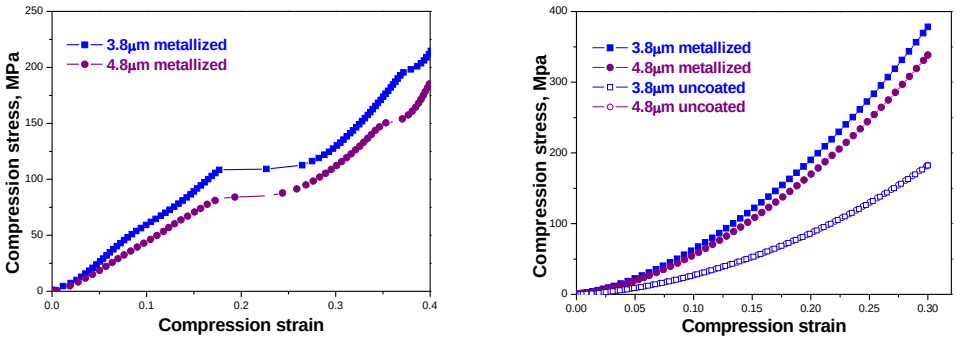

Figure 4 : AC-DAC Particle size dependence of the normalized stress (a) experimental and (b) Finite element solutions.

4 CONCLUSIONS

The mechanical behaviour of PS-DVB polymer particles and metallized AC-DAC particles was studied by using the nanoindentation–based flat punch method. A size effect of both particles was discovered. For the PS-DVB polymer particles, a core-shell structure is possibly a main contributor; while the presence of nanoscale metal coating is the leading factor for the metallized AC-DAC particles. The findings have important implications in the design of the metallized polymer particles for electrical packaging applications.

REFERENCES

[1] J. Ugelstad, A. Berge, T. Ellingsen, R. Schmid, T. N. Nilsen and P. C. Mork, "Preparation and application of new monosized polymer particles", *Prog. Polym. Sci.*, **17**, 87-161 (1992).

[2] J. Liu, A. Tolvgård, J. Malmodin and Z. Lai, "Reliable and environmentally friendly packaging technology—flip-chip joining using anisotropically conductive adhesive", *IEEE T. Compon. Pack. T.*, **22**, 186-190 (1999).

23rd Nordic Seminar on Computational Mechanics
NSCM-23
A. Eriksson and G. Tibert (Eds)

THE EFFECT OF CROSSLINKED AND BRANCHED POLYETHYLENE MOLECULES ON THE THERMO-MECHANICAL PROPERTIES

J.H. ZHAO, S. NAGAO AND Z.L. ZHANG

NTNU Nanomechancial Lab, Department of Structural Engineering, Norwegian University of Science and Technology (NTNU), 7491 Trondheim, Norway
E-mail: junhua.zhao@ntnu.no, shijo.nagao@ntnu.no, zhiliang.zhao@ntnu.no.

Key words: Crosslinked Molecules, Branched Molecules, Mechanical Properties.

Summary. *The effect of crosslinked and branched polyethylene molecules on the thermo-mechanical properties (eg. bulk density, glass transition temperature T_g, Young's modulus E and Poisson's ratio v) has been investigated using united-atom molecular dynamics simulations. We found that all values of v with present branched and crosslinked molecules are almost independent of the molecular shapes and are about a constant 0.4 at 200K. The bulk density and E increase with the increase of crosslink density remarkably, while T_g does not seem to be sensitive to it and is about 290K. For the branched molecules with same molecular weight, the molecular shapes have a weak effect on these parameters and the maximal difference among them is not more than 15%.*

1 INTRODUCTION

The branched and crosslinked polyethylene (PE) molecules are more frequent in the industrial application and synthesis due to the important physical and chemical properties. In recent years, great efforts have been made for decades to clarify these properties in both theoretical and experimental studies. However, all of these work were seldom used to reveal the effect of branched and crosslinked polymer molecules on the thermo-mechanical properties systematically. In this study, we have extensively scrutinized their thermo-mechanical bulk properties (eg. bulk density, glass transition temperature T_g, Young's modulus E and Poisson's ratio v) using extensive united-atom (UA) molecular dynamics (MD) simulations.

2 SIMULATION DETAILS

A united atom approximation is utilized in which the methyl groups are represented by a single "atom" or unit. The effect of the hydrogen atoms on the polymer's configuration is accounted for in the potentials[1, 2]. In present simulation, the two different molecular constraint conditions have been considered (See Fig. 1). The crosslinked molecules are built up with 100 linear molecular chains in which every linear chain includes 142 UA beads. 2). The number of all UA beads in one cell (14200 UA beads) and molecular weight ($C_{142}H_{286}$) are both same. All of the initial configurations for each one of the simulated systems were set up in amorphous cells subjected to periodic boundary conditions in Materials Studio (version 4.2) software package of Accelrys Inc.[3]. These initial structures were transformed to LAMMPS software[4] and all of simulations was executed in *NPT* ensemble and the annealing process are similar with our previous work[5].

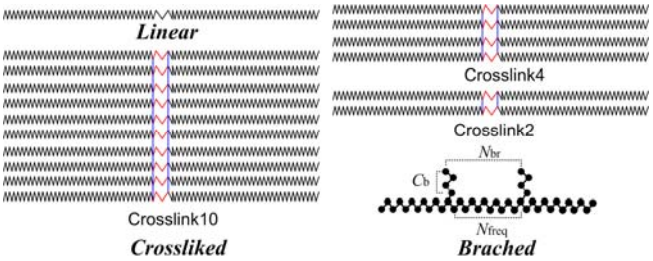

Fig. 1 Schematic plot of the polyethylene molecular architecture. (Branched model represented as $CC_b{*}N_{br}{*}N_{freq}$ here)

3 RESULTS AND DISCUSSIONS

3.1 The effect of crosslinked molecules

To verify the present potential and structure, we compared the bulk density and radial distribution functions g(r) of present results with available experimental data for linear and branched PE molecules. It was found that the present data are in excellent agreement with them. Fig. 2a and b show that the bulk density increases with increasing crosslink density and decreasing temperature, while T_g does not seem to be sensitive to the crosslink density. To reduce the effect of the different direction and facilitate the plot of the curves under both

tension and compression, we calculate the average stress which is under three directions (*x*, *y* and *z*) tension and compression and we define that compressive stress is negative and tensile stress is positive. It is found that the difference of stress-strain curves under tension with crosslink density is not remarkable in Fig. 2c, while it becomes more remarkable under the compression. With increasing compressive strain (after yield strain), the difference becomes larger. The corresponding *E* and Poisson's ratio *v* are fitted by linear function at a tensile and compressive strain of 0.1. It can be found that *E* almost increases with increasing crosslink density, while *v* changes weakly with it in Fig. 2d (The difference is less than 5%).

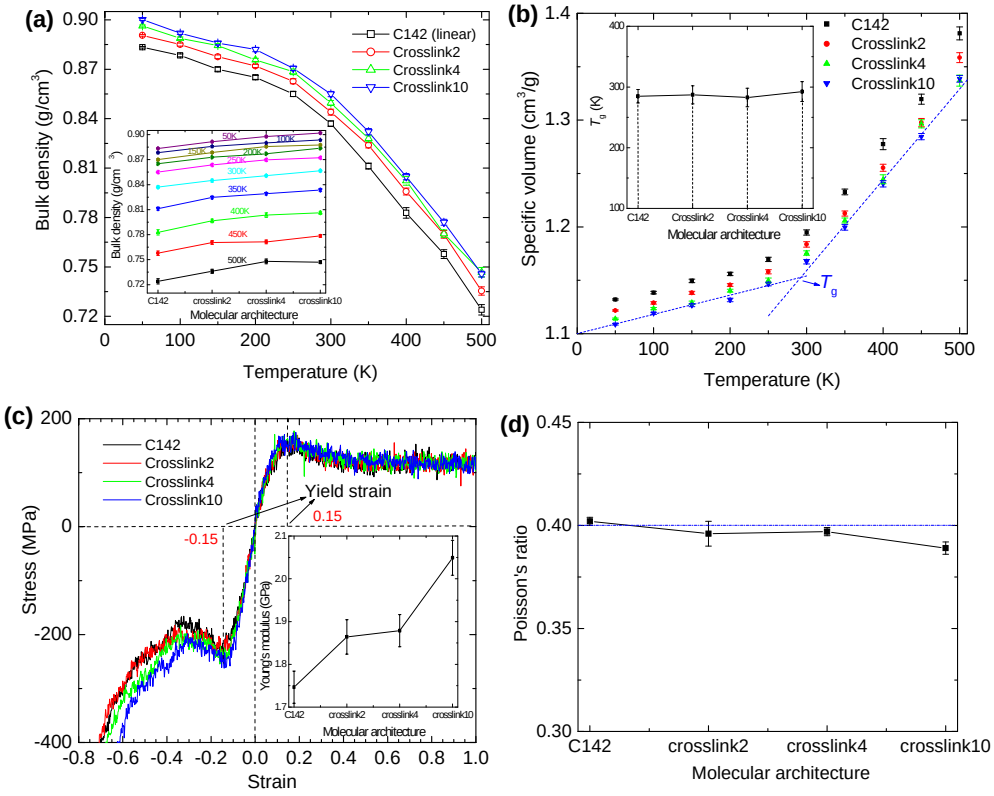

Fig.2. Thermo-mechanical properties of different crosslinked shapes. (a) Bulk density. (b) Specific volume and T_g. (c) The stress-strain curves and Young's modulus. (d) Poisson's ratio.

3.2 The effect of branched shapes with the same molecular weight

Fig. 3a and b show that the bulk density and T_g changes weakly with different molecular architecture. The difference between them is not more than 10%. The stress-strain curves and corresponding *E* with different molecular shapes also change weakly in Fig. 3c. Fig. 3d shows that the molecular shape has a weak effect on Poisson's ratio (The difference is less than 5%) and all the values of *v* with present branched molecules are about a constant 0.4.

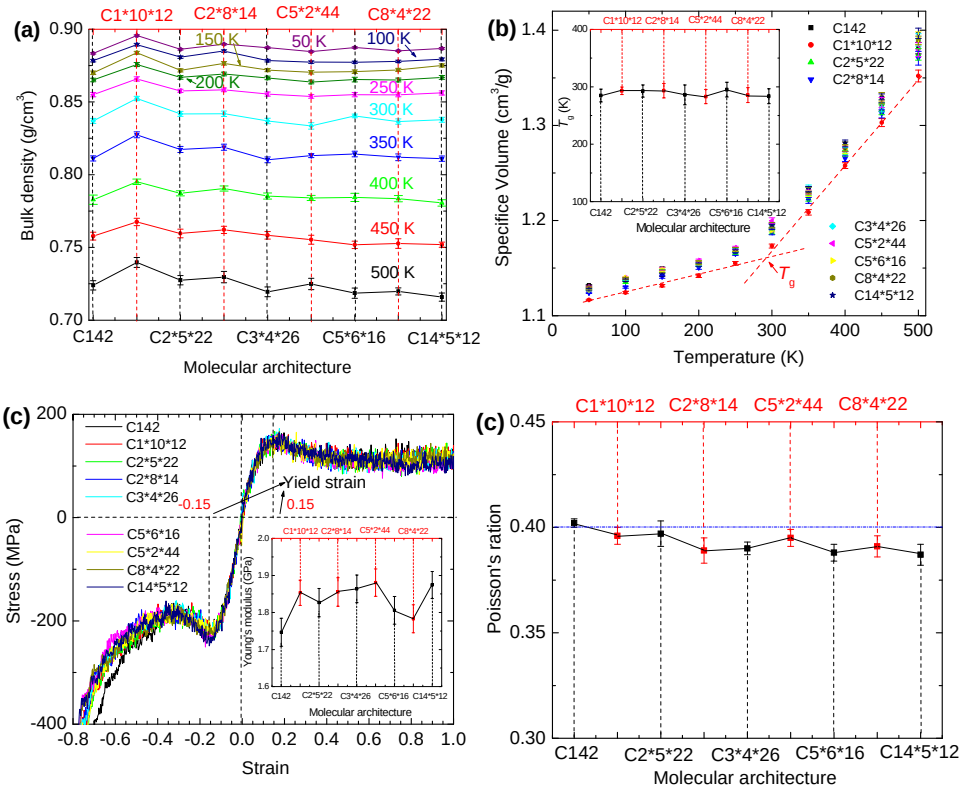

Fig. 3. Thermo-mechanical properties of different branched shapes. (a) Bulk density. (b) Specific volume and T_g. (c) The stress-strain curves and Young's modulus. (d) Poisson's ratio.

4 CONCLUSIONS

The Poisson's ratio is almost independent of present crosslinked and branched architectures and all of the values are about a constant 0.4. The bulk density and E remarkably increase with increasing crosslink density, while T_g does not seem to be sensitive to it. The present branched shapes have a weak effect on the parameters.

REFERENCES

[1] P.V.K. Pant, J. Han, G.D. Smith, R.H. Boyd, "A molecular dynamics simulation of polyethylene". *J. Chem. Phys.* **99**, 597-604 (1993).

[2] M. Laso and E.A. Perpete, Multiscale modelling of polymer properties. Elsevier. p31-45, 333-357 (2006).

[3] Commercial simulation software *Materials Studio* (version 4.2) by Accelrys Inc: www.accelrys.com/mstudio.

[4] S. Plimpton, "Fast Parallel Algorithms for Short-Range Molecular Dynamics". *J. Comp. Phys.* **117**, 1-19 (1995).

[5] J.H. Zhao, S. Nagao, Z.L. Zhang, "Thermo-mechanical properties dependence on chain length in bulk polyethylene: Coarse-grained molecular dynamics simulations", *J. Mater. Res.* **25**, 537-544 (2010).

23rd Nordic Seminar on Computational Mechanics
NSCM-23
A. Eriksson and G. Tibert (Eds)

MECHANICAL BEHAVIOR OF FIVE-FOLD TWINNING FCC IRON NANOROD: A MOLECULAR DYNAMICS STUDY

JIANYANG WU[*], SHIJO NAGAO[*], JUNHUA ZHAO[*], JIANYING HE[*] AND ZHILIANG ZHANG[*]

[*]NTNU Nanomechanical Lab, Department of structural Engineering, Norwegian University of Science and Technology (NTNU), 7491 Trondheim, Norway
Email: zhiliang.zhang@ntnu.no

Key words: Mechanical behavior, five-fold nanorod, embedded-atom method, molecular dynamics

Summary. *The mechanical behaviors of 5-fold twinning FCC iron nanorod under tension have been investigated by a molecular dynamics technique with an embedded-atom method. Tension tests of the rod showed that {111} <112> dislocations pile-up at twin boundaries are formed as nanorods are above a threshold radius of around 2nm, and the yield strength increases with decreasing temperature. However, this strengthening effect becomes less clear as the temperature increases due to the nano-scale size effect.*

1 INTRODUCTION

Metallic nanorods have been synthesized extensively in the past decades due to their great potential application to nanomechanical and nanoelectronic devices. Recently, a new kind of the faceted FCC iron nanorods with a five-fold twinning structure has been fabricated for the first time by Ling et al.[1] These five-fold twinned iron nanorods show that {100} planes on their sides and are capped by {111} planes, growing along the [110] direction, same as other five-fold twinned FCC Ag[2] , Cu[3] and Au[4] metal nanorods. The theoretical angle between two (111) planes is $\alpha \approx 70.53°$, but the $\beta = 72°$ angle is required to get a pentagon by jointing 5 triangles as shown in Fig. 1a, which means the total ~7.5° gap is generated. An example nanorod with a pentagonal cross section is presented in Fig. 1b. Therefore, the nanorod has internal strain with corresponding mechanical stresses and possesses stored elastic energy. Therefore, the mechanical properties of these five-fold FCC twinning iron nanorods subjected to tension are studied by a molecular dynamics technique in the present work. Out of many effects upon the mechanical properties, we focus on the effects of system size and temperature. Comprehensive MD simulations are performed.

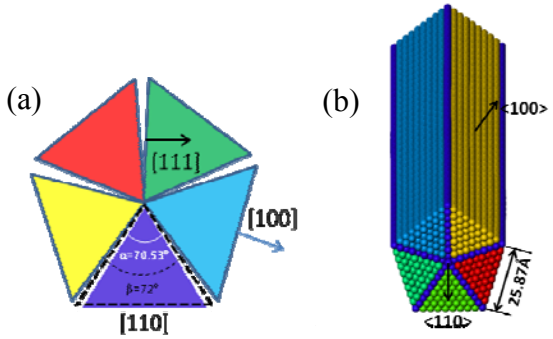

Fig. 1 Schematic illustration of the 5-fold twinning FCC iron nanorod (a) A gap of 1.5° at the twin boundaries (b) An example nanorod with radius r=2.093nm, length L=66nm

2 SIMULATION DETAILS

Molecular dynamics simulations using LAMMPS[5] with an embedded-atom potential of Fe developed by Mendelev et al.[6] confirmed that such nanorods remain stable. In order to explore the size-dependent behavior, the iron nanorods with radius ranging from 1.114nm to 8.706nm were modeled. The radius of the nanorod of pentagon cross section was defined as an average of length of a side and height of the isosceles triangle. In some literatures, the two ends were fixed with free boundary condition in the direction of axial loading which would introduce end-effect to the results. In our case, periodic boundary condition was only applied in the direction of axial loading. The surfaces in other directions were free. Also, the nanorods had same axial length 66nm, which will decrease the effect of periodic boundary condition.

Before loading, the nanorod was fully relaxed at a constant temperature such as T=0.01, 100, 300, 500K and a constant pressure P=0 bar under NPT conditions, the temperatures and pressure were controlled by a Nose-Hoover thermostat and barostat, respectively. Thus the nanorod could change its volume in response to the applied external pressure and the system's internal stress. The volume of the nanorod was re-sized automatically to keep zero pressure along the length direction. After obtaining a free relaxation state, the nanorods were deformed

in tension by homogeneously rescaling the coordinates of all atoms in the length direction with a constant engineering strain rate $R=2\times10^{8}s^{-1}$. Prior to each rescaling step, the atoms virial stress, the atoms von Mises stress, and averaged stress over all of the atoms in the system, were calculated.

3 RESULTS AND DISCUSSION

Fig. 2 shows that the stress-strain curves of 5-fold twinning FCC iron nanorods under tension with different radius at different temperature. The nanorods first show an elastic loading stage, characterized by monotonously increasing stress with increasing applied strain, and then the slope of the curves become less, which implies the nonlinear elasticity of nanorods at larger strain, followed by a sudden stress drop.

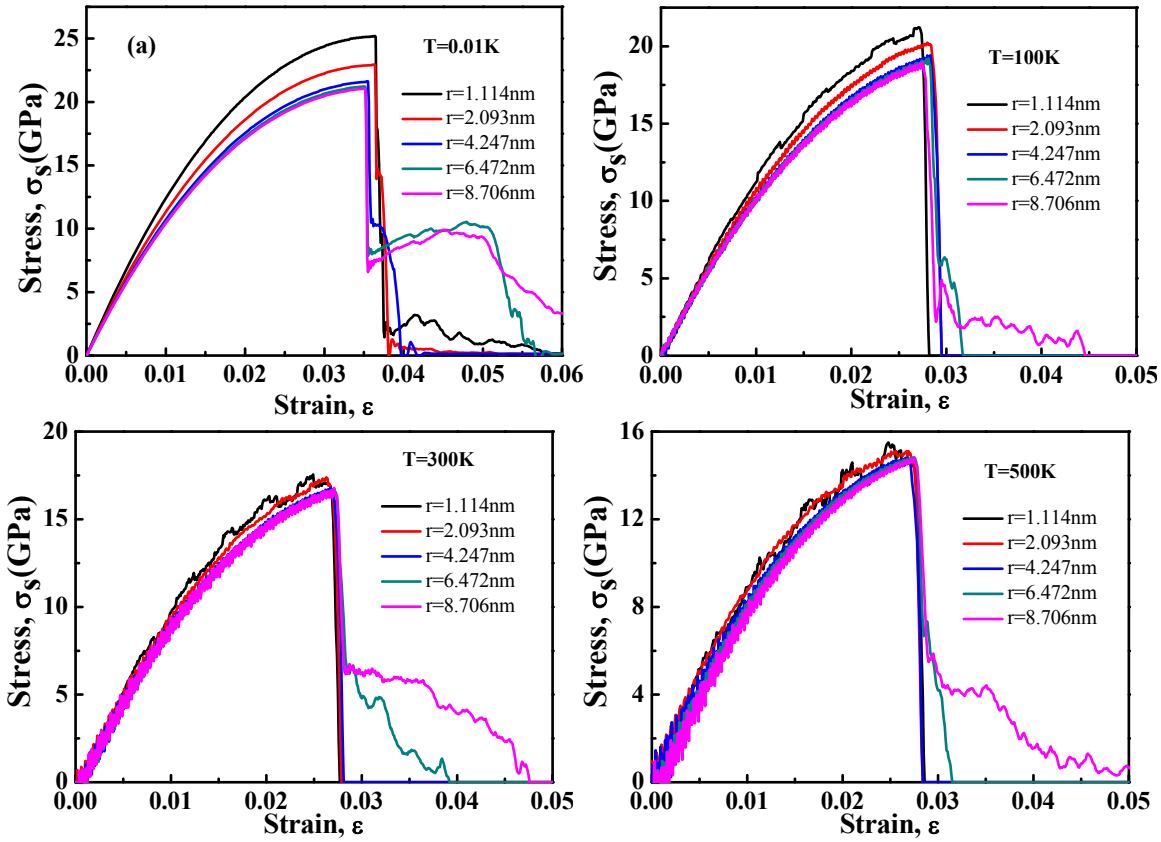

Fig.2 The stress-strain curves of 5-fold twinning FCC iron nanorod under tension with different radius at different temperature

In order to investigate the size effect and temperature effect for the tensile testing, the yield strengths are picked up against the radius of nanorod, which is shown in Fig.3. From this figure, it is found that the yield strength decreases with increasing temperature. However, the trend of the decreasing becomes less clear as the temperature increases. Fig. 4 shows one snapshot of the {111} slip planes of the largest nanorod r=8.706nm at the deformation corresponding to the yield strength. In this snapshot, clarity perfect FCC atoms and surface

atoms of the nanorod are removed to visualize interior defects. Atoms are colored according to the von Mises stress from 0GPa to 400GPa. It is interesting that that {111} <112> dislocations pile-up at twin boundaries are formed as nanorods above a threshold radius of around 2nm during the yielding deformation process.

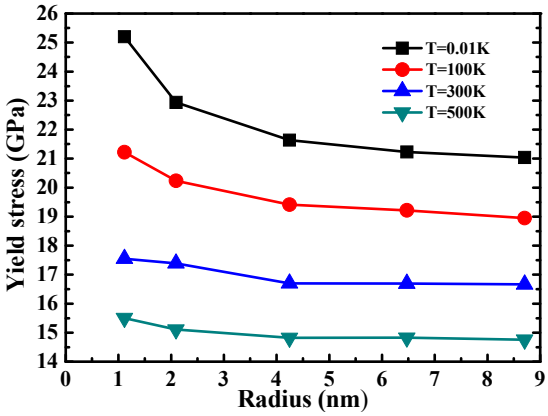

Fig. 3 Yield stress as a function of radius at different T

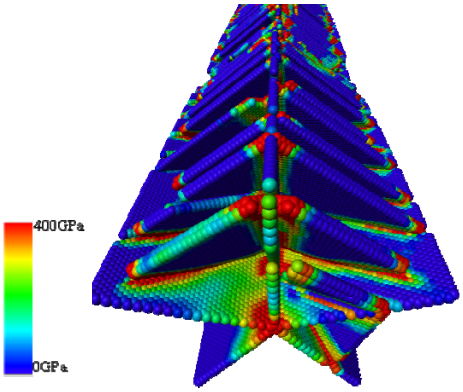

Fig.4 {111} <112> dislocation piles-up at twin boundaries

4 SUMMARY

Molecular dynamics simulation ware performed to investigate the mechanical properties of five-fold twinning FCC iron nanorods. The simulated results have shown that smaller twinned nanorod displays higher strength at the same temperature due to the size effect. This size effect becomes less as the temperature increases. {111} <112> dislocation piles-up at twin boundaries can be found when the radius of nanorod reaches 2nm.

REFERENCES

[1] Ling, T.; Zhu, J.; Yu, H.M.; Xie, L.: *J. Phys. Chem. C*, **113** (22) 9450–9453 (2009).
[2] Sun, Y.G.; Mayers, B.; Herricks, T.; Xia, Y.N.: *Nano. Lett.* **3** (7) 955-960 (2003).
[3] Lisiecki, I.; Filankembo, A.; Sack-Kongehl, H.; Weiss, K.; Pileni, M.P.; Urban, J.: *Phys. Rev. B*., **61**(7) 4968–4974 (2000).
[4] Christopher, J. J.; Erik, D.; Sean, A. D.; Catherine, J. M.; Stephen, M.: *J. Mater. Chem.*, **12**(6)1765-1770 (2002)
[5] Plimpton. S.J.; J. Comput. Phys, **117**(1)1-19 (1995)
[6] Mendelev, M.I.; Han, S.; Srolovitz, D.J.; Ackland, G.J.; Sun, D.Y.; Asta, M.: *Philos. Mag.,* **83** (35) 3977-3994 (2003)

23rd Nordic Seminar on Computational Mechanics
NSCM-23
A. Eriksson and G. Tibert (Eds)

MATHEMATICAL MODELING OF A SEMI-ACTIVE VIBRATION CONTROLLER WITH ELECTROMAGNETIC ELEMENTS

RADOSLAV DARULA*, SERGEY SOROKIN*

* Department of Mechanical and Manufacturing Engineering
Aalborg University
Pontopidanstraede 101, 9000 Aalborg East, Denmark
e-mail: dra@me.aau.dk, svs@me.aau.dk, web page: http://www.me.aau.dk

Key words: Vibration control, electromagnet, stiffness modulation, induced damping

Summary. This paper is concerned with the application of electromagnets in vibration control. A mathematical model of a controller with electromagnetic elements is developed and coupling between a mechanical, an electrical and a magnetic subsystem is modelled. Numerical simulations are done to compare predictions from the model with experimental data.

1 INTRODUCTION

There are two principal approaches to control vibration of machines or structures [1]:

- *Passive* – no change in controller's properties during operation;
- *Active* – controller can change its properties and adjust to different conditions. According to ability to react on changes, there are *fully*- and *semi-active* controllers.

Considering a machine running at constant operation conditions, passive vibration control can be used. However, while starting up or changing its operation cycle, machine passes its resonances and the semi-active controller can be used to modify the natural frequencies and/or reduce amplitude at the resonances. This can be achieved by:

- *Changing equivalent stiffness* – changing a natural frequency of the system;
- *Introduction of damping* – reducing amplitude of vibration at the resonance.

Mizuno [2], Sodano [3] analyzed and verified utilization of electromagnet in vibration control from various view points, and showed that electromagnetic elements behave as:

- *Spring Element* – non-linear force-displacement relationship [Figure 2 (c)] allows to modify (shift) the natural frequency of the system;
- *Damping Element* – induced current in electromagnet due to vibration can be dissipated in a shunt resistance.

This was proved experimentally [4] using clamped-clamped beam setup shown in Figure 1 (a). By turning the electromagnet on, a resonance was shifted to lower frequency region by an amount of Δf [Figure 1 (b)] and additional damping was introduced (reduction of the amplitude at the resonance by ΔA). It proves feasibility of using electromagnetic elements in vibration control.

The paper focuses on multidisciplinary modelling of a vibration control system with electromagnetic element. The coupled system of equation of electro-magneto-mechanical interaction is solved numerically to demonstrate change both in stiffness and damping of the system.

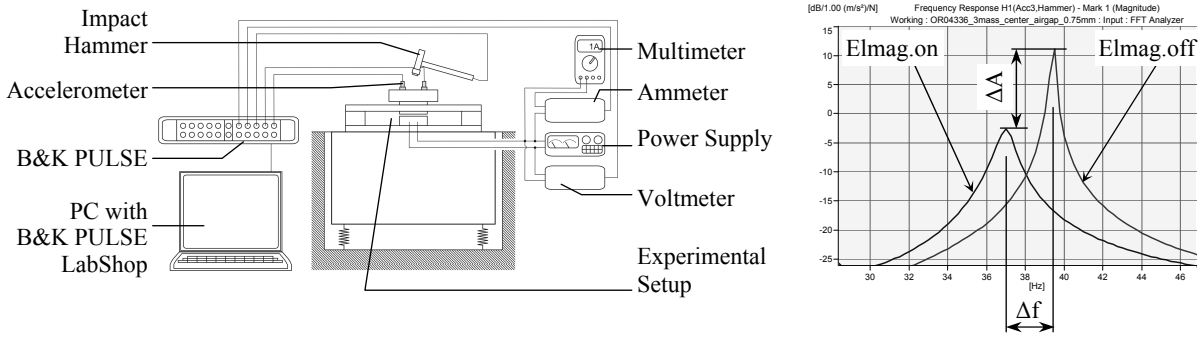

(a) (b)

Figure 1: (a) Experimental set-up used to investigate the vibration controller's operation; (b) results of impact hammer tests [4]

2 MATHEMATICAL MODEL

An electro-magneto-mechanical model is formulated to describe dynamical behaviour of the vibration controller mathematically.

2.1 Electro-Magnetic Model

A model of the electrical subsystem includes the RL circuit, which represents the electromagnet, with iron losses included, as shown in Figure 2 (a). The magnetic subsystem is composed of an electromagnet with a core and yoke [Figure 2 (b)]. Parameters of the model were determined experimentally. A force-displacement relationship of electromagnetic force, a coupling force between electro-magnetic and mechanical system, is shown in Figure 2 (c).

The mathematical formulation of the electro-magnetic model is [4]:

$$\left[1+\frac{1}{R_{iron}}\frac{dL_{mag}(w_{airGap})}{dw_{airGap}}\frac{dw_{\mathrm{var}}(t)}{dt}\right]u_{\mathrm{sup}}=\left[R_{wind}+\left(1+\frac{1}{R_{iron}}\right)\frac{dL_{mag}(w_{airGap})}{dw_{airGap}}\frac{dw_{\mathrm{var}}(t)}{dt}\right]i_{\mathrm{sup}}(t) \quad (1)$$
$$+L_{mag}(w_{airGap})\left(1+\frac{R_{wind}}{R_{iron}}\right)\frac{di_{\mathrm{sup}}(t)}{dt}$$

see [4] for details.

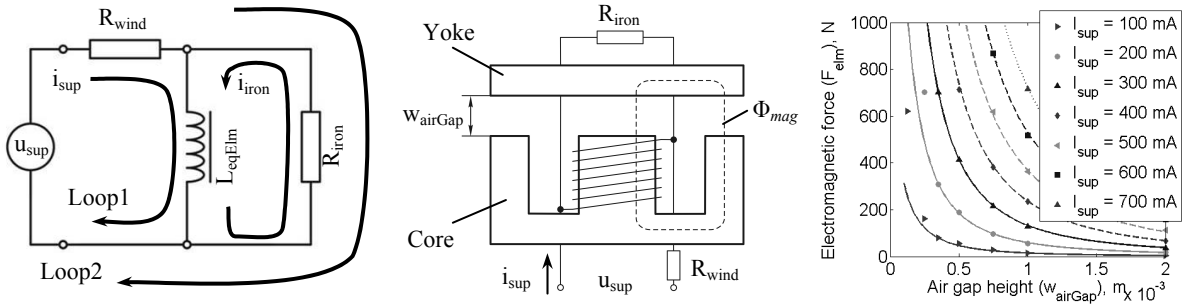

(a) (b) (c)

Figure 2: Mathematical model of (a) electric circuit; (b) magnetic circuit; (c) electromagnetic force – displacement diagram [4]

2.2 Mechanical Model

The mechanical model of the measurement setup [Figure 1 (a)] is derived in two steps:

1. *Model of the beam* [Figure 3 (a)] – Euler-Bernoulli beam theory used. A beam is constrained at both ends by general boundary conditions, modelled by torsion and compression springs. Parameters of the model were found experimentally;
2. *Lumped parameter modelling* [Figure 3 (b)] – to simplify analysis of dynamics of the mechanical model, the stiffness and mass of the beam setup [Figure 3 (a)] were lumped in order to reduce it to a single degree of freedom system.

The mathematical formulation of the lumped parameter model is [4]:

$$m_{eqMass}\frac{d^2 w_{\mathrm{var}}(t)}{dt^2} + k_{eqSpring} w_{\mathrm{var}}(t) = \frac{c_1\left(i_{\mathrm{sup}}(t) + i_{iron}(t)\right)^2}{\left(2\left(w_{airGap} - w_{\mathrm{var}}(t)\right) + c_3\right)^2} + F_{exc}(t) \tag{2}$$

see [4] for details.

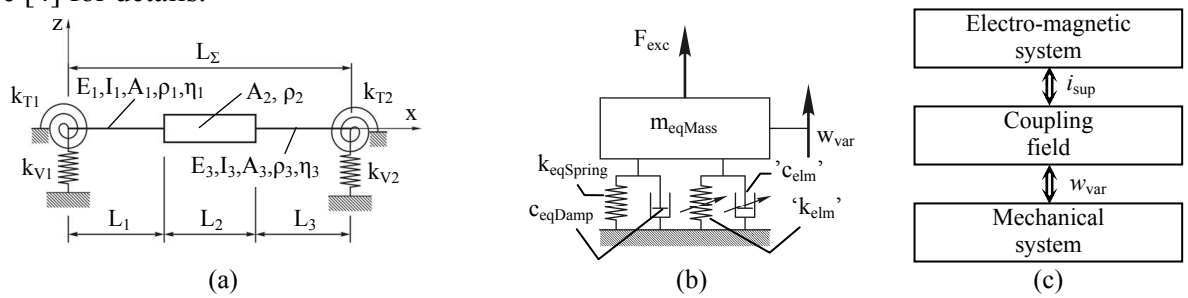

Figure 3: Mechanical model: (a) general model; (b) lumped parameter model; (c) coupling between electro-magneto-mechanical sub-systems [4]

2.3 Coupled Model

Comparing Eq. (1) and (2) it can be concluded, the electro-magnetic and the mechanical systems are mutually coupled by two terms: displacement of the beam w_{var} and coil current of electromagnet i_{sup} [Figure 3 (c)]. Therefore, in order to model the interaction, the system of coupled equations, Eq. (1) and (2), needs to be solved simultaneously.

3 EVALUATION OF VIBRATION CONTROLLER'S OPERATION

The coupled electro-magneto-mechanical model [Eq. (1) and (2)] is solved numerically, using MATLAB software. Three cases are presented in Figure 4:

a. *Free vibration of coupled system* [Figure 4 (a)] – time domain analyzed – increasing current in the coil of electromagnet, the system acquires more damping (larger logarithmic decrement is obtained);
b. *Forced vibration, no inductance assumed* [Figure 4 (b)] – frequency domain analyzed – filtering out the induced current, only change in stiffness is obtained, i.e. resonance curves are shifted to the lower frequency region as coil current increases;
c. *Forced vibration, no stiffness change assumed* [Figure 4 (c)] – frequency domain analyzed – if induced current is large enough, the introduction of damping is dominant. The higher the supply current is, the larger amount of damping is introduced into the system (i.e. the smaller the amplitude at the resonance is);

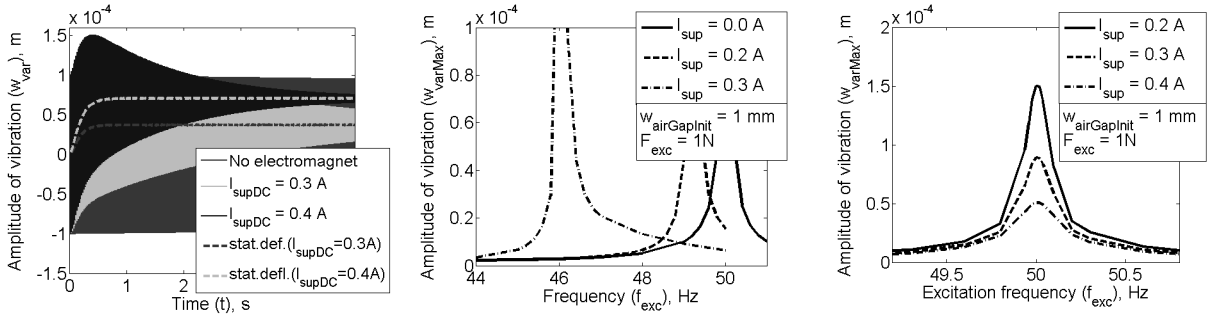

(a) (b) (c)

Figure 4: (a) time capture of free vibration of coupled system; (b) FRF of system with no inductance assumed; (c) FRF of system with no stiffness change assumed [4]

The results from numerical simulations (Figure 4) proved that the coupled model of vibration controller with electromagnetic element is able to mimic qualitatively behaviour of experimental setup [Figure 1 (b)]. The model needs to be tuned further in order to fit experimental data also quantitatively.

4 CONCLUSIONS AND SUGGESTIONS FOR FURTHER WORK

The multidisciplinary model of semi-active vibration controller with the electromagnetic element was formulated as the system of coupled equations [Eq. (1) and (2)], which describe the interaction between the electro-magnetic and the vibration fields.

The model was qualitatively verified by comparison of numerical results with measured data. Experimentally detected effects of the frequency shift and the damping in dynamical behaviour of the system due to the electromagnet were also observed in numerical simulations.

The project will be continued with the quantitative analysis of the behavior of the coupled system. The mechanical model was verified and is found adequate [4]. However, deeper characterization of the electromagnet and analysis of induction process in electromagnetic system due to vibration of a yoke is required. The eddy current losses should be assessed as an additional source of damping to improve dynamic characterization of electromagnet.

ACKNOWLEDGEMENTS

The PhD project is a part of the INTEREG ‘Silent Spaces’ project supported by the European Union.

REFERENCES

[1] C.R. Fuller, S.J. Elliot and P.A. Nelson, *Active Control of Vibration*, Academic Press, (1997).
[2] T. Mizuno, *et al.*, “Vibration isolation system combining zero-power magnetic suspension with springs”, *Control Eng. Practice*, **15**, 187-196 (2007).
[3] H.A. Sodano, J-S Bae and D.J. Inman, “Improved Concept and Model of Eddy Current Damper”, *ASME J. Vib. Acoust.*, **128**, 234-302 (2006).
[4] R. Darula, *Multidisciplinary Analysis and Experimental Verification of Electromagnetic SAVC*, Master Thesis, Aalborg University, (2008).

CALCULATION OF A STEADY STATE RESPONSE OF RIGID ROTORS SUPPORTED BY FLEXIBLE ELEMENTS AND CONTROLLABLE DAMPERS LUBRICATED BY MAGNETORHEOLOGICAL FLUID

JAROSLAV ZAPOMĚL*, PETR FERFECKI*

* Centre of Smart Systems and Structures
Institute of Thermomechanics - Branch at VSB-Technical University of Ostrava
Czech Academy of Sciences
17. listopadu 15, 708 33 Ostrava-Poruba, Czech Republic
e-mail: jaroslav.zapomel@vsb.cz, petr.ferfecki@vsb.cz

Key words: Rotors, Magnetorheological Dampers, Steady State Response, Collocation Method.

Summary. To achieve optimum attenuation of lateral vibration of rotors, the damping effect must be controllable. This is enabled by magnetorheological squeeze film dampers. In this paper, there is presented a computational procedure for calculation of the steady state response of rigid rotors coupled with their casings by flexible elements and short magnetorheological dampers. Application of this approach makes possible to propose the control of the damping effect to achieve optimum performance of the dampers.

1 INTRODUCTION

Lateral vibration of rotors can be significantly reduced by inserting damping elements between the shaft and its casing. To achieve their optimum performance, the damping effect must be controllable. This is enabled by application of magnetorheological squeeze film dampers. Control of the damping effect is carried out by changing intensity of magnetic field in the lubricating layer.

At present time, the magnetorheological dampers are a subject of intensive research. E.g. Forte et al. [1] presented results of the theoretical and experimental investigations of a long magnetorheological damper. In [2], Zapomel and Ferfecki introduced the mathematical model of a short squeeze film damper lubricated with magnetorheological liquid. The equations of motion of rotors attenuated by magnetorheological damping devices are nonlinear. An efficient tool for obtaining their steady state solution is a trigonometric collocation method. It was used e.g. by Zhao et al. [3] to analyze behaviour of a flexible rotor supported by classical squeeze dampers. Zapoměl and Malenovský [4] extended application of this method for investigation of rotors mounted with hydrodynamic bearings and excited by baseplate excitation. In this paper, the emphasis is put on application of the collocation method for determination of the steady state response of rotors damped by magnetorheological dampers.

2 CALCULATION OF THE DAMPING FORCES

The magnetorheological dampers consist of two rings, between which there is a thin film of magnetorheological liquid. The outer ring is coupled with the casing of the rotating machine directly, the inner one by a flexible element. The shaft is supported by a rolling element bearing, whose outer race is coupled with the inner ring of the damper. The damping effect is produced by squeezing the liquid in the lubricating layer due to lateral vibration of the rotor. In the stationary part of the damper, there are the coils, which are the source of magnetic field. Its intensity in the gap of the damper influences resistance of the magnetorheological liquid against its flow and therefore the change of magnitude of the applied electric current can be used to control the damping effect.

In the developed mathematical model, it is assumed that ratio of the length of the damper to the diametre of its rings is small (short damper) and that the lubricant is Bingham liquid.

On these conditions, the distribution of the pressure gradient in the lubricating layer is described by the differential equation

$$h^3 p'^3 \pm 3(h^2 \tau_y \mp 4\eta_B \dot{h} Z) p'^2 \mp 4\tau_y^3 = 0 . \tag{1}$$

p' is the pressure gradient in the axial direction, τ_y, η_B are the yield shear stress and viscosity of the Bingham liquid, Z is the axial coordinate, h is the lubricating film thickness and $\dot{}$ denotes the first derivative with respect to time. The upper signs are valid for negative, the lower signs for the positive pressure gradient.

In the case of the simplest design of the damper, the inner and outer rings form a core of an electromagnet that is divided by two gaps. Then the relation between the yield shear stress and the applied current in the coil can be expressed

$$\tau_y = k_B \left(\frac{NI}{2h} \right)^{n_B} . \tag{2}$$

N is the number of the coil turns, I is the electric current and k_B, n_B are the material constants.

The pressure profile is calculated by integration of the pressure gradient in the axial direction with the boundary condition expressing that the pressure at the edge of the damper is equal to the atmospheric one. At location, where the thickness of the oil film rises, a cavitation takes place. Pressure of the medium in cavitated areas is assumed to be constant and equal to the pressure in the ambient space. Components of the damping force are then obtained by integration of the pressure distribution.

3 THE EQUATIONS OF MOTION OF THE INVESTIGATED ROTOR

The investigated rotor (Fig.1) consists of a shaft and of one disc. The rotor is mounted with rolling element bearings, whose outer races are coupled with the casing by flexible elements. The magnetorheological dampers are inserted between the spring elements and the casing. The system is symmetric relative to the middle plane of the disc. The rotor turns at constant angular speed, is loaded by its weight and is excited by a centrifugal force produced by the disc unbalance. The springs are prestressed in the vertical direction to eliminate their deflection caused by the rotor weight.

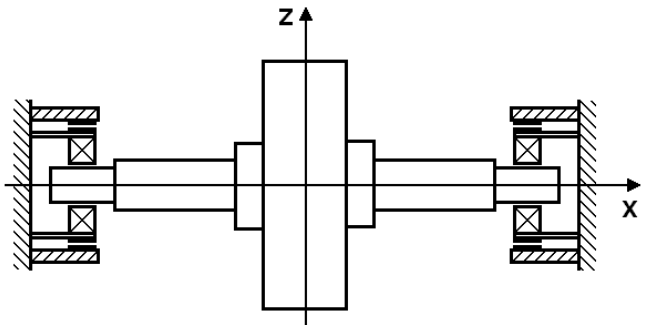

Figure 1: The investigated rotor system

In the computational model, the rotor and the stationary part are considered to be absolutely rigid. The magnetorheological liquid is modelled by Bingham material.

Lateral vibration of the rotor is then described (taking into account the system symmetry)

$$0.5\,m_R\ddot{y} + 0.5\,b_P\dot{y} + k_D y = F_{dy}\left(y, z, \dot{y}, \dot{z}\right) + 0.5\,m_R e_T \omega^2 \cos\left(\omega t + \psi_o\right), \tag{3}$$

$$0.5\,m_R\ddot{z} + 0.5\,b_P\dot{z} + k_D z = F_{dz}\left(y, z, \dot{y}, \dot{z}\right) + F_{PS} + 0.5\,m_R e_T \omega^2 \sin\left(\omega t + \psi_o\right) - 0.5\,m_R g\,. \tag{4}$$

m_R is the mass of the rotor, k_D is the stiffness of the rotor flexible support, b_P is the coefficient of external damping, e_T is eccentricity of the rotor centre of gravity, ω is angular speed of the rotor turning, ψ_o is the phase leg, g is the gravity acceleration, F_{dy}, F_{dz} are components of the damping force, F_{PS} denotes the prestress force, t is time, y, z are displacements of the rotor centre and $(\dot{})$ and $(\ddot{})$ denote the first and second derivatives with respect to time.

Because of the prestress, trajectory of the rotor centre has a circular shape. This enables to assume the steady state solution of the equations of motion (3) and (4) in the form

$$y = r_C \cos\omega t - r_S \sin\omega t\,, \qquad z = r_C \sin\omega t + r_S \cos\omega t\,. \tag{5}$$

The unknown values of coefficients r_C and r_S can be calculated by application of a collocation method. This requires to substitute (5) and their first and second derivatives with respect to time into (3) and (4) and to express the resulting equations at the collocation points of time. As the number of unknown parameters and the number of equations is 2, only one collocation point is needed. After carrying out the mentioned manipulations related to the collocation time equal to 0 s, the resulting set of nonlinear algebraic equations takes the form

$$\left(k_D - 0.5\,m_R\omega^2\right) r_C - 0.5\,\omega\,b_P\, r_S - 0.5\,m_R e_T \omega^2 - F_{dy}\left(r_C, r_S\right) = 0\,, \tag{6}$$

$$0.5\,\omega\,b_P\, r_C + \left(k_D - 0.5\,m_R\omega^2\right) r_S - F_{dz}\left(r_C, r_S\right) = 0\,. \tag{7}$$

4 THE COMPUTATIONAL SIMULATIONS

The task of the computational simulations was to analyze the steady state vibration of the rotor system, whose principal parameters are: mass of the rotor 425.9 kg, stiffness of the supporting springs 2.10^6 N/m, length, diameter and width of the gap of the damper 50 mm, 150 mm, 1.0 mm, number of the coil turns 400, Bingham viscosity 0.003 Pa·s and the yield

stress material coefficients of the magnetorheological liquid 2.5 10^{-8} N/A^2 and 2 (exponent). In Fig.2 and 3, there are drawn orbits of the rotor centre and time history of the force transmitted into the stationary part in the horizontal direction for two magnitudes of the applied current. It is evident that increasing current leads to reduction of the rotor oscillations but on the other hand also to rising magnitude of the force transmitted into the rotor casing.

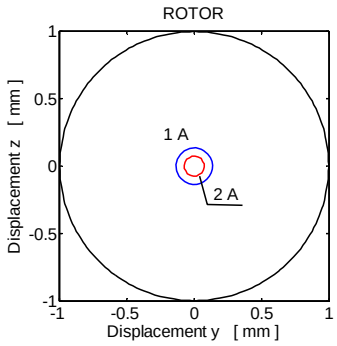

Figure 2: Orbits of the rotor centre

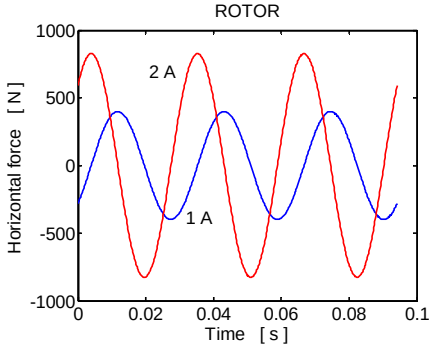

Figure 3: Force transmitted into the casing

5 CONCLUSIONS

The described approach represents a computational procedure for determination of the steady state response of rigid symmetric rotors supported by flexible couplings combined with short magnetorheological squeeze film dampers. It is intended for proposing control of the damping effect to achieve the optimum performance of the dampers.

6 ACKNOWLEDGEMENT

This research work has been supported by the research grant projects P101/10/0209 and AVO Z20760514. The support is gratefully acknowledged.

REFERENCES

[1] P. Forte, M. Paterno and E. Rustighi, "A magnetorheological fluid damper for rotor applications", *International Journal of Rotating Machinery*, **10**(3), 175-182 (2004).

[2] J. Zapoměl and P. Ferfecki, "Mathematical modelling of a short magnetorheological damper", *Transactions of the VŠB – Technical University of Ostrava, Mechanical Series*, **LV**(1), 289-294 (2009).

[3] J. Y. Zhao, I. W. Linnett and L. J. McLean, "Stability and bifurcation of unbalanced response of a squeeze film damped flexible rotor", *Transactions of the ASME, Journal of Tribology,* **116**(2), 361-368 (1994).

[4] J. Zapoměl, E. Malenovský, "Numerical methods for the stability investigation of flexural vibration of rotor systems supported by fluid-film bearings", *Proc. 5th International Conference on Rotor Dynamics*, Darmstadt, Germany, 212-223 (1998).

23rd Nordic Seminar on Computational Mechanics
NSCM-23
A. Eriksson and G. Tibert (Eds)

NUMERICAL MODELING OF ROTATING COMPRESSOR BLADE WITH ARBITRARY STAGGER ANGLE

J. SUN* AND L. KARI*

*The Marcus Wallenberg Laboratory for Sound and Vibration Research
Department of Aeronautical and Vehicle Engineering, KTH
SE-100 44 Stockholm, Sweden
e-mail: jias@kth.se, leifkari@kth.se, web page: http://www.ave.kth.se/

Key words: Numerical Modeling, Dynamics, Rotating Blade.

Summary. This paper presents a task on numerical modeling to investigate the dynamics of rotating compressor blade with different geometrical parameters. Numerical results are also compared with FEM results to show a good agreement.

1 INTRODUCTION

Compressor blade is an important component to supply high pressure gas flow into combustion chamber of turbomachinery. The dynamic behavior of blade under high rotation speed has been studied for a long time[1]. Most of studies are to model blades as a beam structure[2,3,4,5,6], such as Euler beam, Timoshenko beam[7] or thin-walled beam[8]. Beam structure with one dimension is quite widely used for both analytical and numerical calculations. Also to be deep into details, both shell and plate theories are used to give numerical results with two dimensions. Meanwhile, the finite element method (FEM) is utilized for blades with complex geometry. FEM is straightforward to simulate dynamic characteristics of blades. However, the drawback of FEM is that parametric analysis about geometry is time-consuming because in each case, a new CAD model needs to be imported. For numerical model, it is quite easy to change arbitrary parameter once the model is established.

2 METHODOLOGY

In this paper, a plate theory[9,10] is utilized to establish a single rotating blade model with arbitrary stagger angle at various rotation speeds. The governing equation is derived by Hamilton's Principle via integration by parts which extracts dynamic boundary conditions[11,12]. Since this blade model is a cantilever plate, it is difficulty to find an analytical solution. Instead, Extended Galerkin Procedure is used to give approximate solution including eigenfrequency and mode shape. The idea of Extended Galerkin Procedure is to assume trial functions for unknown variables (in this paper, i.e., displacement components). Then, the next step is to use these trial functions as weight functions and integrate the multiple of residue with weight functions. In Galerkin sense, the integration should be suppressed to zero, which results in a classic second order ordinary differential equation (ODE). Finally, it only needs to solve a typical eigen value problem.

3 RESULTS AND CONCLUSION

Finite element (FE) calculations as a reference are implemented by the commercial software COMSOL[13]. Fig.1 shows both numerical and FE results of a straight blade made of stainless steel with rotation speed from 3000 to 15000 RPM and a good agreement is obtained in the whole rotation speed range. The method is applicable for elastodynamics analysis for rotary structure, especially blades of turbomachineries. The system of equations of motion also can be used to perform force response analysis by using finite difference method.

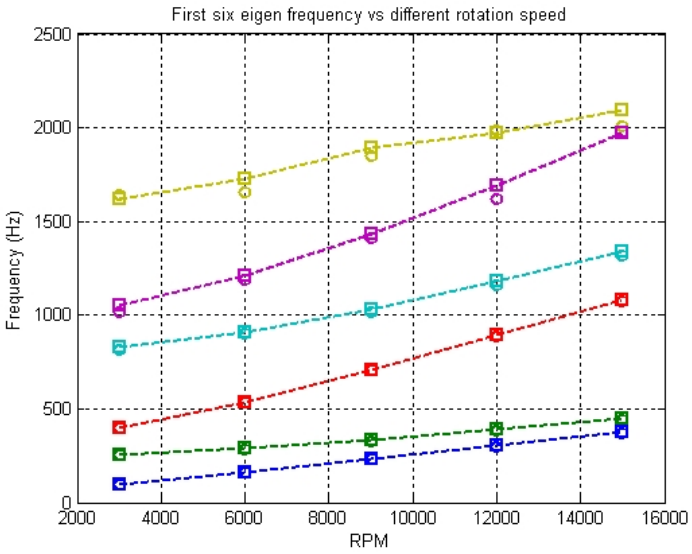

Figure 1: First six eigen frequencies vs RPM (Square: Numerical results; Circle: COMSOL results)

4 ACKNOWLEDGEMENTS

The present study has been promoted by the Swedish Energy Authority through the TURBOPOWER initiative within the TurboVib project. The authors gratefully acknowledge this financial support.

REFERENCES

[1] V. Ramamurti and R. Kielb, Natural Frequencies of Twisted Rotating Plates, *Journal of Sound and Vibration*, **97**(3), 429–449, (1984).

[2] L. Librescu, S. -Y. Oh, O. Song and H. -S. Kang, Dynamics of Advanced Rotating Blades Made of Functionally Graded Materials and Operating in A High-temperature Field, *J Eng Math*, **61**, 1–16, (2008).

[3] S. -Y. Oh, L. Librescu and O. Song, Vibration of Turbomachinery Rotating Blades Made-up of Functionally Graded Materials and Operating in A High Temperature Field, *Acta Mechanica*, **166**, 69–87, (2003).

[4] S. -Y. Oh, O. Song and L. Librescu, Effects of Pretwist and Presetting on Coupled Bending Vibrations of Rotating Thin-walled Composite Beams, *International Journal of Solids and Structures*, **40**, 1203–1224, (2003).

[5] H. H. Yoo, J. Y. Kwak and J. Chung, Vibration Analysis of Rotating Pre-twisted Blades with A Concentrated Mass, *Journal of Sound and Vibration*, **240(5)**, 891–908, (2001).

[6] N. S. Vyas, and J. S. Rao, Equations of Motion of A Blade Rotating with Variable Angular Velocity, *Journal of Sound and Vibration*, **156(2)**, 327–336, (1992).

[7] S. P. Timoshenko and J. N. Goodier, *Theory of Elasticity*, McGraw-Hill, Tokyo, (1970).

[8] L. Librescu and O. Song, *Thin-Walled Composite Beams-Theory and Application*, Springer, Netherland, (2006).

[9] Y. C. Fung and P. Tong, *Classical and Computational Solid Mechanics*, World Scientific, (2001).

[10] Y. C. Fung, *Foundations of Solid Mechanics*, Prentice-Hall, New Jersey, (1977).

[11] J. C. Houbolt and G. W. Brooks, Differential Equations of Motion for Combined Flapwise Bending, Chordwise Bending, and Torsion of Twisted Nonuniform Rotating Blades, *NASA TR 1364*, (1958).

[12] C. Fox, *An Introduction to The Calculus of Variations*, Oxford University Press, Oxford, (1950).

[13] *Structural Mechanics Module Model Library*, COMSOL AB, (2008).

23rd Nordic Seminar on Computational Mechanics
NSCM-23
A. Eriksson and G. Tibert (Eds)

APPLICATION OF MAX-MIN METHOD TO FIND ANALYTICAL SOLUTION FOR OSCILLATORS WITH SMOOTH ODD NONLINEARITIES

ALI MOHAMMADI[*], MOHAMMADHASSAN MOHAMMADI[†] AND AMIN KIMIAEIFAR[+]

[*] Islamic Azad University, Shiraz Branch, Member of Young Researchers Club, Iran
E-mail: Ali.mohammadi68@gmail.com,

[†] KTH (Royal Institute of Technology), Stockholm, Sweden
Email: mohmoh@kth.se

[+]Aalborg University, Aalborg, Denmark.
Email: akf@me.aau.dk

Key words: Oscillator, Max-Min method, Smooth nonlinearity, Duffing-oscillators

Summary

Nonlinear functions are known as vital terms to be processed and solved in most of engineering problems. Most scientific problems in vibration and dynamics are inherently nonlinear. Except a limited number of these problems, most of them do not have analytical solutions. Therefore, these nonlinear equations should be solved using other methods. In this paper, it is tried to present and apply a new analytical technique known as Max-Min method to solve the equations of oscillators with smooth odd nonlinearities. The results obtained in this study are compared with numerical results and released in the literature. Close agreement of the two sets of results indicates the accuracy of the Max-Min method. The method can obtain an expression which is acceptable for all values of effective parameters and also is able to control the convergence of the solution. After validating the results, influence of each parameter on the system response and phase plan are discussed. Finding maximum/minimum threshold of a solution of a nonlinear equation is easy in most of engineering problems. Besides, the angular frequency can be readily calculated in Max-Min method. A promising approach is illustrated step by step which is suggested by the algorithm. It is shown that, this method is not only accurate and convenient to use, but also easy to apply to other nonlinear oscillations extensively.

1 INTRODUCTION

Recently a large number of research have been related to nonlinear systems, because in most of engineering problems we are facing to nonlinear equations which are difficult to solve, especially analytically. Therefore, these nonlinear equations should be solved using methods such as homotopy perturbation method (HPM)[1,2], homotopy analysis method (HAM) [3,4] and He's parameter expanding method (HPEM) [5,6] .A new technique which is introduced recently is Max-min method. In most nonlinear problems, it is easy to find maximum/minimum thresholds of a solution of a nonlinear equation[7].Max-min method is

based on this advantage of nonlinear equations. This approach is based on the relationship between maximum and minimum threshold and the exact value of solution. He presented the method for the first time and this method is based on ancient Chinese mathematics[8].
In this study Max-Min Method is used to investigate the behaviors of nonlinear problems in vibration. To show the accuracy and application of this method, an example is studied and it is compared with numerical values.

2 APPLICATION OF MAX-MIN METHOD

2.1 Example

We consider a special case of a system to show the applicability if the method .It would be the equation of motion of a Duffing-type nonlinear oscillator

$$u'' = -\frac{u^3}{1+u^2}, \quad u(0)=A, u'(0)=0 \tag{1}$$

Note that for small u Eq.(1) becomes $u'' + u^3 \approx 0$
and for large u , it becomes large $u'' + u \approx 0$.
Thus, for small u, the equation of motion is a Duffing-type nonlinear oscillator, while for large u, the equation of motion approximates that of a linear harmonic oscillator; hence, Eq. (1) is called the Duffing-harmonic oscillator. The system will oscillate between symmetric bounds [−A, A], and the frequency and corresponding periodic solution of the nonlinear oscillator are dependent on the amplitude A [9]. According to the initial conditions, we choose a trial-function in the form of following equation, which can satisfies the conditions.

$$u = A\cos\omega t \tag{2}$$

where ω is the frequency to be determined.
After substituting Eq.(2) into Eq.(1) and using some simplification we can observe that Square of ω is greater than zero and never exceeds the $\frac{A^2}{1+A^2}$ so

$$0 < \omega^2 < \frac{A^2}{1+A^2} \tag{3}$$

According to He Chengtian's interpolation, we have

$$\omega^2 = \frac{m(0)+nA^2}{m+n(1+A^2)} = \frac{kA^2}{1+A^2} \tag{4}$$

Where m and n are weighting factors, and $k = \frac{n}{m+n}$
So the frequency can be approximated as

$$\omega = \sqrt{\frac{kA^2}{1+A^2}} \tag{5}$$

And its approximate solution is:

$$u(t) = A\cos\left[\left(kA^2/1+A^2\right)^{1/2} t\right] \tag{6}$$

By substituting the solution into Eq. (1), we have:

$$u'' + (kA^2/1 + A^2)u = -u^3 - u^2u'' + (kA^2/1 + A^2)u \tag{7}$$

If we assume Eq. (6) is the exact solution, the right side of Eq. (7) can be vanished, so we have:

$$I = \int_0^{T/4} \left[-u^3 - u^2u'' + (kA^2/1 + A^2)u \right] \cos \omega t dt = 0 \tag{8}$$

Where $T = 2\pi/\omega$ .By Substituting (6) in (8), we obtain sub-term of I which equals to $I_1 + I_2 + I_3$ To simplify the solution for readers, we divide I as a Singular term located in the integral to some terms and solve them one by one in the manuscript, so we have:

$$I_1 = \int_0^{\pi/2\omega} -A^3 \cos^4 \omega t dt \Rightarrow I_1 = -\frac{3\pi A^3}{16(kA^2/1 + A^2)^{1/2}}$$

$$I_2 = \int_0^{\pi/2\omega} A^3(kA^2/1 + A^2)\cos^4 \omega t dt \Rightarrow I_2 = \frac{3\pi A^3(kA^2/1 + A^2)}{16(kA^2/1 + A^2)^{1/2}}$$

$$I_3 = \int_0^{\pi/2\omega} A(kA^2/1 + A^2)\cos^2 \omega t dt \Rightarrow I_3 = \frac{\pi A(kA^2/1 + A^2)}{4(kA^2/1 + A^2)^{1/2}}$$

$$I_1 + I_2 + I_3 = 0 \tag{9}$$

After some simplification we have:

$$k = \frac{3(1 + A^2)}{3(1 + A^2) + 1} \tag{10}$$

Finally the frequency is obtained:

$$\omega^2 = \frac{3A^2}{4 + 3A^2} \tag{11}$$

Moreover, the approximate period is:

$$T = \frac{2\pi}{\omega} = \frac{2\pi}{A}\sqrt{\frac{4 + 3A^2}{3}} \tag{12}$$

3 RESULTS AND DISCUSSION

To validate the results, Range Kutta method has been employed to obtain numerical solutions. In Fig (1) a comparison has been made between the results of applying Max-min method and the results from numerical solution. The Comparison with the numerical ones represents a remarkable accuracy even for large value of nonlinear terms. Also, it has been shown that by increasing the domain of the problem, obtained results converge. After validating the results, the influence of each parameter on the system response and phase plan can be easily discussed. Max-Min Method can be successfully applied to provide analytical solutions for other vibrations and dynamics problems.

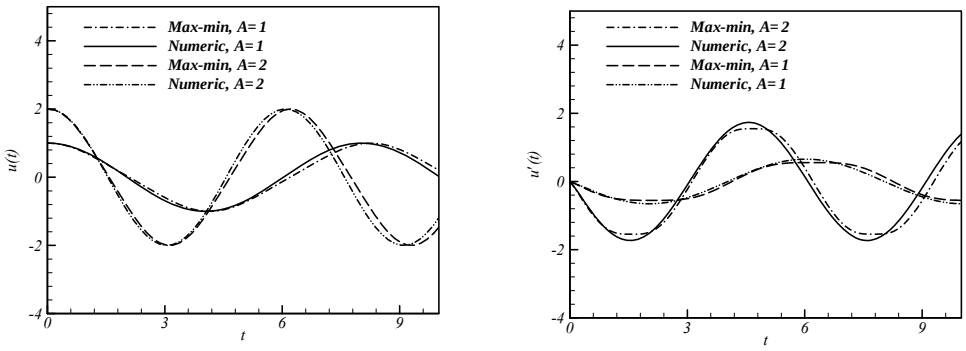

Figure 1: comparison between Max-min and numerical solution. (a) u (t), (b), u'(t).

4 CONCLUSION

Applying He's Max–min method to Duffing-type nonlinear oscillator equation which is a strong nonlinear equation shows that this method could be useful to oscillators and vibrations in several branches of sciences, such as: Dynamical and vibrational systems, civil structures, fluid mechanic, etc. It can be also used for analyzing nonlinear systems.The results indicate that this method has a simple and direct procedure for determining approximations to the periodic solutions. We demonstrated the accuracy , simplicity and efficiency of this method by an example. He's Max–min method have the potential to be extended to any nonlinear equation.

REFERENCES

[1] J. H. He, "Homotopy perturbation method for bifurcation of nonlinear problems", *Int. J. Non-linear Sci. Numer Simul* ,**6**,207–8(2005).
[2] J. H. He, "A coupling method of a homotopy technique and a perturbation technique for non-linear problems", *International Journal of Non-linear Mechanics* ,**35(1)**,37–43(2000).
[3] S.J. Liao, "*Beyond perturbation: introduction to the homotopy analysis method* ". Boca Raton, Chapman & Hall/CRC Press, (2003).
[4] A. Kimiaeifar, et al "Analytical solution for Van der Pol –Duffing oscillators", *Chaos, Solitons and Fractals*; doi:10.1016/2009.03.145 , (2009).
[5] J.H. He ,"Modified Lindstedt–Poincare methods for some strongly non-linear oscillations, Part I: expansion of a constant" *Int. J. Non-Linear Mech*. ,**37**,No.2, 309–314(2002).
[6] M.H.Mohammadi, A.Mohammadi, A. kimiaeifar, H.Tabaei, "Application of HPEM to Investigate the Response and Stability of Nonlinear Problems in Vibration" *Aust. J. Basic & Appl. Sci.*, **4(4)**, 557-563 (2010).
[7] J.H. He,"Max-Min Approach to Nonlinear Oscillators", *International Journal of Nonlinear Sciences and Numerical Simulation*, **9(2)**, 195-198 (2008).
[8] Z. Ji , "*Mathematics in Northern-Southern* " , Sui and Tang Dynasties, Shijiazhuang, hebeiScience and Technology Publishing House , (in Chinese) (1999).
[9] M.T. Darvishi et al., "Application of He's parameter-expansion method for oscillators with smooth odd nonlinearities", *Physics Letters A*, **372**,5381–5384 (2008).

23rd Nordic Seminar on Computational Mechanics
NSCM-23
A. Eriksson and G. Tibert (Eds)

RANDOM VIBRATION STRESS ANALYSIS OF THE BEPICOLOMBO BOOM DEPLOYMENT SYSTEM

SOHEIL KHOSHPARVAR*, LARS BYLANDER†, NICKOLAY IVCHENKO† AND GUNNAR TIBERT*

*KTH, Royal Institute of Technology
School of Engineering Sciences, Department of Mechanics
SE-100 44 Stockholm, Sweden
e-mail: tibert@kth.se, web page: http://www.mech.kth.se

†KTH, Royal Institute of Technology
School of Electrical Engineering, Laboratory of Space and Plasma Physics
SE-100 44 Stockholm, Sweden
e-mail: nickolay@kth.se, web page: http://www.alfvenlab.kth.se/plasma

Key words: Random vibration, Mile's equation, root-mean square von Mises stress, finite element analysis.

Summary. Two methods for the stress analysis of a spacecraft structure under random vibration loading are studied and applied to a wire boom deployment structure for the future BepiColombo mission to Mercury to qualify the structure for launch.

1 INTRODUCTION

A spacecraft is typically subjected to the largest loads during launch and every part on the spacecraft must be able to sustain the random vibration launch loads without permanent deformation or failure. MEFISTO-S is a wire boom deployment system with an electric field measurement unit that will be used in one of the spacecraft of the BepiColombo mission. The qualification of each part is typically done by computing the stress factors of safety against the yield and ultimate strengths. In a structural stress analysis, the von Mises stress criterion plays a major role. In most cases, static or dynamic, when the input forces are deterministic, calculating the von Mises stress is a straightforward process. In cases when the forces are non-deterministic or, in another words, when the structure is under random or stochastic input conditions, the response parameters will also be in a statistical and probabilistic format. In random vibration analysis, the input is often given as a power spectral density (PSD). The linear method which is used to evaluate the root-mean-square (rms) acceleration, displacement and stress components cannot be directly used to derive the rms von Mises stress since it is a non-linear function of the linear stress components. The aim in this study[1] is to compare the current methods available to engineers when dealing with random vibration stress levels with the MEFISTO-S structure as example.

2 MILE'S VERSUS RMS VON MISES STRESS

The most common method when dealing with the stress levels caused by random vibration on a spacecraft structure is to use *Mile's equation*[2]. In that method, one chooses a single eigenfrequency of the structure, typically the dominant one, which relates to the highest modal effective mass within the bandwidth of the imposed input frequencies. With the use of modal damping, the PSD of the input acceleration and Mile's equation, the rms of the response acceleration is computed as

$$\ddot{x}_{\text{rms}} = \sqrt{\frac{f_D\,\pi}{4\xi}\text{APSD}(f_D)} \tag{1}$$

where APSD is the PSD of the acceleration, f_D is the dominant eigenfrequency and ξ is the damping ratio. This rms response acceleration is multiplied by a factor of 3 and applied to the structure as an equivalent static gravity field. Applying a field with a gravity acceleration of $3\ddot{x}_{\text{rms}}$ to the structure results in a von Mises stress that is considered to cover the highest response peaks for 99.73% of the duration of the imposed random vibration disturbance.

Mile's equation is very simple to implement, but it has some limitations that are important to consider. The equation has been derived for a single-degree-of-freedom system, so therefore it cannot consider all the eigenfrequencies within the input bandwidth for a multi-degree-of-freedom system. There is also the assumption that the input PSD is of white noise nature, so more complex inputs with changing octaves PSDs might produce errors.

The major simplification in Mile's equation is that it is not considering the rms von Mises stress, but assumes that the rms static acceleration is causing the stresses in the structure. The most direct method to accurately estimate the rms von Mises stresses is to evaluate all the stress components in each time step and the rms value is then derived from time integration for each location in the model, but this method would computationally be very expensive to process. Segalman *et al.*[3] have developed an efficient method to evaluate the rms von Mises stress for structures subjected to random vibration. In this method, the rms von Mises stress is evaluated as a summation of modal stress eigenvectors and the modal cross-covariance which itself consists of the modal transfer functions and input PSDs. The rms von Mises stress is[3]:

$$\sigma_{\text{rms von Mises}} = \sqrt{\sum_{i,j}\Gamma_{ij}T_{ij}} \tag{2}$$

where T_{ij} presents the modal stress eigenvectors contribution[3]:

$$T_{ij} = \boldsymbol{\psi}_i^{\sigma T}\mathbf{A}\boldsymbol{\psi}_j^{\sigma} \tag{3}$$

and $\mathbf{A}$ is the von Mises stress coefficients matrix. Γ_{ij} in Eq. (2) is the modal cross-covariance[3]:

$$\Gamma_{ij} = \sum_{a}^{N_f}\sum_{b}^{N_f}\phi_{ai}\phi_{bj}\left(\frac{1}{\pi}\int_0^{\infty}\text{Re}(\overline{D_i(\omega)}D_j(\omega)[\mathbf{S}_{ff}(\omega)]_{ab})\text{d}\omega\right) \tag{4}$$

where $\boldsymbol{\psi}$ is the modal stress eigenvector, $\boldsymbol{\phi}$ is the displacement eigenvector, $\mathbf{D}$ is the modal transfer function and $\mathbf{S}_{ff}$ is the cross-spectral density matrix of the input random vibration. N_f represents the number of forces that are imposed on the structure.

When implementing this method, the von Mises stress and $\mathbf{T}$ are to be computed for every integration point. $\mathbf{\Gamma}$ is computed only once, as it depends on the modal properties of the structure. In practice, $\mathbf{\Gamma}$ depends on the number of truncated modes, modal damping ratios and the input PSDs, so the integral in Eq. (4) can be approximated by summation over the bandwidth frequency[3]:

$$\Gamma_{ij} = \sum_{a}^{N_f} \sum_{b}^{N_f} \phi_{ai}\phi_{bj} \left(\sum_{n=1}^{N_\omega} \mathrm{Re}(\overline{D_i(\omega_n)} D_j(\omega_n) [\mathbf{S}_{ff}(\omega_n)]_{ab}) \frac{\Delta\omega}{\pi} \right) \tag{5}$$

In deriving the rms von Mises stress method[3], an assumption is that all the loads are stationary with a zero mean value, which in practice might not be the case. Nevertheless, the values obtains from rms von Mises stress method are found to be conservative and accurate. The advantage of the rms von Mises stress method in comparison with Mile's equation is that the former includes all the truncated modes and mode shapes in the bandwidth of the excitation.

3 QUALIFICATION OF THE MEFISTO-S STRUCTURE

To test the accuracy of Mile's equation in comparison with the rms von Mises method, both methods have been applied to the MEFISTO-S structure. Figure 1 shows the maximum rms von Mises stress, with a probability of 99.73%, as a function of the number of eigenmodes included in Eq. (5). The first seven modes are the eigenfrequencies of the structure which are in the input bandwidth. The rule of thumb in calculating the rms von Mises stress is to truncate the modes of the structure with one and half times of the actual bandwidth upper bound frequency[3]. For each mode, the von Mises stress by Mile's equation has been computed and the value of the von Mises stress achieved with the same probability for each mode has been recorded. As seen in Fig. 1, the Mile's stress value for the dominant mode of the structure (fourth mode) is conservative compared to the maximum rms von Mises stress.

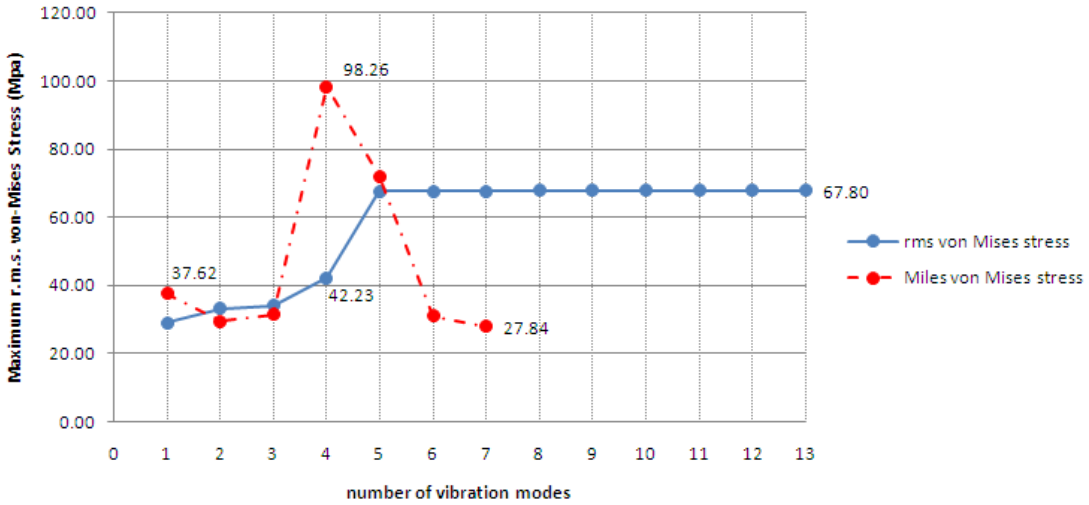

Figure 1: Comparison between Mile's equation and and the rms von Mises stress method.

The comparison also shows that the stress by Mile's method is only close to the rms von Mises method when the deformed shape caused by the gravity field is similar to the dominant mode shape which is used in Eq. (1). In the case of the MEFISTO-S structure, the fifth eigenmode, which is not the dominant mode, would have given a more accurate result by Mile's equation, as the deformed shape in that mode is similar to the fifth mode shape of the structure.

4 CONCLUSIONS

The stress analysis of the MEFISTO-S structure shows that Mile's equation presents higher stresses than the rms von Mises stress method and might therefore be a less good method from a design point of view, due to the strict mass limits in the aerospace industry. Mile's equation is producing good results only if the deformed shape caused by the static gravity field is similar to the dominant mode shape. For other cases, Mile's equation can give either unsafe or too conservative results.

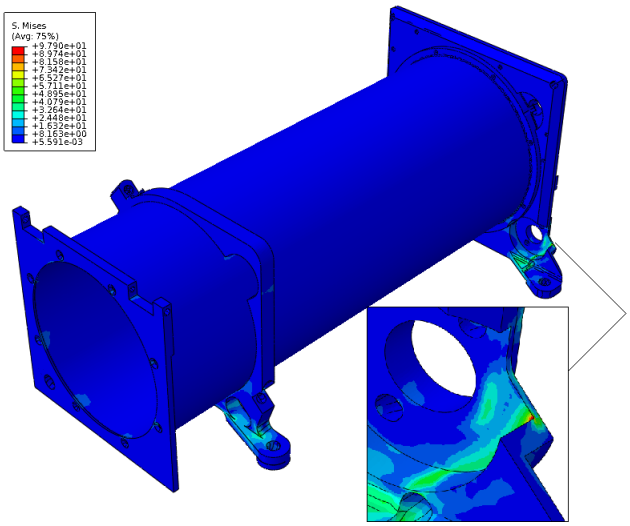

Figure 2: Von Mises stresses (MPa) in the MEFISTO-S structure under static gravity field load (fourth eigenmode).

REFERENCES

[1] Khoshparvar, S. *Random Vibration Stress Analysis of the BepiColombo Wire Boom Deployment System* (MSc thesis, KTH, 2010).

[2] Wijker, J. *Random Vibrations in Spacecraft Structures Design: Theory and Applications* (Springer, 2009).

[3] Segalman, D. J., Fulcher, C. W. G., Resse, G. M. & Field, Jr., R. V. An efficient method for calculating RMS von Mises stress in a random vibration environment. *Journal of Sound and Vibration* **230**, 393–410 (2000).

23rd Nordic Seminar on Computational Mechanics
NSCM-23
A. Eriksson and G. Tibert (Eds)

CONSTITUTIVE MODELING AND VALIDATION OF CGI MACHINING SIMULATIONS

GORAN LJUSTINA*, MARTIN FAGERSTRÖM* AND RAGNAR LARSSON*

*Department of Applied Mechanics
Chalmers University of Technology
Göteborg, Sweden

Key words: Johnson-Cook plasticity, hypoelastic-inelastic consitutive modelling, objective strain rates

1 INTRODUCTION

We note that continuum mechanical modeling in the area of machining simulations traditionally considers ”hypo”-formulations, where incremental stress-strain relations are postulated in terms of various objective stress rates. The idea of the current contribution is to recapture the well known Johnson-Cook (JC) model[1] for machining simulations and compare the model behaviors obtained with respect to the different objective rates. It has been shown in the literature that one of the most frequently considered stress rates, the Zaremba-Jaumann stress rate, leads to unwanted and inaccurate oscillations in the stress response in the case of f nite simple shear deformation. Particularly in the case of kinematic hardening[2] but also in special cases of isotropic hardening[3]. Since f nite shear is a natural deformation mode in machining, it is important to ensure that such oscillations are avoided in the simulations, whereby the effect of the adopted stress rates for the JC-model is investigated in this work. Another interesting issue related to the handling of ”rate formulated” constitutive models concerns thermodynamic consistency. The question is how to repair/formulate new rate models with respect to this issue. We thereby introduce the concept of hyperelastic-inelastic response in the framework of multiplicative decomposition of the deformation gradient, where the JC-model is reformulated. The idea is to identify the proper postulation of the rate response in order to assure that the resulting model is thermodynamically consistent.

2 THE JOHNSON-COOK PLASTICITY MODEL

The present model is to be utilized in simulation of machining operations of Compacted Graphite Iron (CGI). In order to account for the considerable levels of strain, strain rate, temperature and pressure in the work piece material, we adopt the material model by Johnson and Cook[1], frequently used for chip formation simulations and other transient dynamic simulations. Thereby, a fairly good accessibility of material constants exists in the literature. The model basically assumes f ve material constants, cf. Eq. (1), where the coeff cient A is the yield strength, B is the hardening modulus, C is the strain rate sensitivity coeff cient, n is the hardening coeff cient and m is the thermal softening coeff cient. Thus, for this model, the actual f ow stress function take on the following multiplicative structure:

$$\sigma_y(\boldsymbol{\varepsilon}^p, \dot{\varepsilon}^p, \theta) = \left(A + B\left(\varepsilon^p\right)^n\right)\left(1 + ln\left(\frac{\dot{\varepsilon}^p}{\dot{\varepsilon}_0}\right)\right)\left(1 + \hat{\theta}^m\right) \tag{1}$$

where ε^p is the total equivalent plastic strain, $\dot{\varepsilon}^p$ is the equivalent plastic strain rate and where $\dot{\varepsilon}_0$ is a reference strain rate controlling the model rate dependence. The temperature dependence is accounted for via the so-called homologous temperature

$$\hat{\theta} = \frac{\theta - \theta_{trans}}{\theta_{trans} - \theta_{melt}} \tag{2}$$

where θ_{trans} is the transition temperature def ned as the one at or below which there is no temperature dependence (usually taken as room temperature).

3 HYPO AND HYPERELASTIC-INELASTIC MODELS

Hypoelastic-inelastic constitutive relations means constitutive relations postulated on rate-form in terms of an objective stress rate, cf. subsection 3.1 below for a number of alternatives used in the literature. Generically, for the case of isotropic hardening, these constitutive rate-relations are formulated as

$$\mathring{\boldsymbol{\tau}} = \boldsymbol{E}[k] : (\boldsymbol{l} - \boldsymbol{l}_p - \boldsymbol{l}_{th}) + \boldsymbol{h}[\boldsymbol{\tau}, k] = \boldsymbol{E}[k] : \boldsymbol{l}_e + \boldsymbol{h}[\boldsymbol{\tau}, k] \tag{3}$$

where $\mathring{\boldsymbol{\tau}}$ is the considered objective stress rate and where $\boldsymbol{E}$ is a spatial material operator tangent modulus tensor, k is an internal variable associated with the isotropic hardening and $\boldsymbol{l}$, $\boldsymbol{l}_p$ and $\boldsymbol{l}_{th}$ are the total, the plastic and the thermal portion of the spatial velocity gradient def ned as

$$\boldsymbol{l} = \boldsymbol{v} \otimes \boldsymbol{\nabla} = \dot{\boldsymbol{F}} \cdot \boldsymbol{F}^{-1},\ \boldsymbol{l}_p = \lambda \frac{\partial \Phi}{\partial \boldsymbol{\tau}},\ \boldsymbol{l}_{th} = \alpha \dot{\theta} \boldsymbol{1}. \tag{4}$$

In practice, this means that only the rate of deformation is necessary to determine the stress state, in contrast to hyperelastic-inelastic models where the total deformation is required, and the consequent stress rate behavior is merely a consequence of the hyper elastic-inelastic formulation. The drawbacks of the hypo-formulation are that they lack the property of being (unconditionally) thermodynamically consistent and also that no explicit expression for the mechanical dissipation can be derived.

Therefore, it is of signif cant interest to relate the proposed constitutive relations based on hypoelastic-inelastic response to the more thermodynamically consistent hyperelastic-inelastic formulation for which the basic assumption is to assume the presence of the isotropic stored energy function $\psi\left[\bar{\boldsymbol{C}}, k, \theta\right]$ as a function of the reversible part of the deformation, here represented by the reversible right Cauchy-Green deformation $\bar{\boldsymbol{C}}$ tensor, the temperature θ and an internal hardening variables k. Within the hyperelastic-inelastic framework, the structure of the constitutive relations are based on the second law of thermodynamics, which may be specif ed as the dissipation inequality in terms of the second Piola-Kirchhoff stress $\boldsymbol{S}$ as

$$\mathcal{D} = \frac{1}{2}\boldsymbol{S} : \boldsymbol{C} - \frac{\partial \psi}{\partial \bar{\boldsymbol{C}}} : \dot{\bar{\boldsymbol{C}}} - \frac{\partial \psi}{\partial k}\dot{k} - \frac{1}{\theta}\boldsymbol{H} \cdot \nabla_X \theta \geq 0 \tag{5}$$

which directly yields the corresponding state equations for the intermediate second Piola-Kirchhoff stress $\bar{\boldsymbol{S}}$ and the heat f ux $\boldsymbol{H}$ as

$$\bar{\boldsymbol{S}} = 2\frac{\partial \psi}{\partial \bar{\boldsymbol{C}}},\ \boldsymbol{H} = -\boldsymbol{K} \cdot \nabla_X \theta \tag{6}$$

3.1 Objective stress rates for Hypo-formulation of constitutive response

The idea is to scrutinize hypo-formulations based on the spatial Green-Naghdi, Oldroyd and Zaremba-Jaumann stress rates. The two former objective stress rates are obtained based on induced, differently back–rotated stresses - either the material stress tensor $\boldsymbol{T}$ or the second Piola Kirchhoff stress tensor $\boldsymbol{S}$ associated with the Kirchhoff stress $\boldsymbol{\tau}$, respectively. These stresses and their associated objective rates are def ned as

$$\boldsymbol{T} = \boldsymbol{R}^t \cdot \boldsymbol{\tau} \cdot \boldsymbol{R} \Rightarrow \dot{\boldsymbol{T}} = \boldsymbol{R}^t \cdot \hat{\boldsymbol{\tau}} \cdot \boldsymbol{R} \tag{7}$$

$$\boldsymbol{S} = \boldsymbol{F}^{-1} \cdot \boldsymbol{\tau} \cdot \boldsymbol{F}^{-t} \Rightarrow \dot{\boldsymbol{S}} = \boldsymbol{F}^{-1} \cdot \tilde{\boldsymbol{\tau}} \cdot \boldsymbol{F}^{-t} \tag{8}$$

where $\hat{\boldsymbol{\tau}}$ and $\tilde{\boldsymbol{\tau}}$ are the symmetric Green-Naghdi and Oldroyd stress rates, respectively, and where $\boldsymbol{F}$ is the deformation gradient and $\boldsymbol{R}$ is the rotational part of the continuum deformation gradient according to the polar decomposition $\boldsymbol{F} = \boldsymbol{R} \cdot \boldsymbol{U}$ with $\boldsymbol{U}$ being the symmetric right stretch tensor. As a consequence of Eqs. (7) and (8), we f nd that $\hat{\boldsymbol{\tau}}$ and $\tilde{\boldsymbol{\tau}}$ are obtained as

$$\hat{\boldsymbol{\tau}} = \dot{\boldsymbol{\tau}} - \boldsymbol{\omega} \cdot \boldsymbol{\tau} + \boldsymbol{\tau} \cdot \boldsymbol{\omega} \tag{9}$$

$$\tilde{\boldsymbol{\tau}} = \dot{\boldsymbol{\tau}} - \boldsymbol{l} \cdot \boldsymbol{\tau} - \boldsymbol{\tau} \cdot \boldsymbol{l}^t \tag{10}$$

where (again) $\boldsymbol{l}$ is the spatial velocity gradient and $\boldsymbol{\omega}$ is a material spin according to $\boldsymbol{\omega} = \dot{\boldsymbol{R}} \cdot \boldsymbol{R}^t$. For later comparisons, let us introduce also the convective Zaremba-Jaumann stress rate def ned with the subtle difference that $\boldsymbol{\omega} \rightarrow \boldsymbol{w}$ from the Naghdi-Green stress rate so that

$$\vec{\boldsymbol{\tau}} = \dot{\boldsymbol{\tau}} - \boldsymbol{w} \cdot \boldsymbol{\tau} + \boldsymbol{\tau} \cdot \boldsymbol{w} \tag{11}$$

where $\boldsymbol{w}$ is the skew symmetric part of the spatial velocity gradient $\boldsymbol{l}$.

3.2 Hypoelastic-inelastic formulation

Traditionally, for hypoelastic-inelastic consitutive models the stress rate response is postulated for the objective stress rate in terms of the elastic material operator $\boldsymbol{E}^e$ as

$$\acute{\boldsymbol{\tau}} = \boldsymbol{E}^e : \boldsymbol{l}_e \tag{12}$$

where $\boldsymbol{E}^e$ is taken as the constant isotropic spatial material tensor

$$\boldsymbol{E}^e = 2G\boldsymbol{I}_{dev} + K\mathbf{1} \otimes \mathbf{1} \text{ with } \boldsymbol{I}_{dev} = \boldsymbol{I}_{sym} - \frac{1}{3}\mathbf{1} \otimes \mathbf{1} \tag{13}$$

where $\boldsymbol{I}_{sym}$ is the fourth order symmetric unit tensor. Moreover, G and K are the elastic constants pertinent to shear and volumetric response, respectively.

3.3 Hyperelastic-inelastic formulation

To compare the hypo and hyper formulations let us from Eq. (6_1) express the rate of the second Piola-Kirchhoff stress tensor as

$$\dot{\bar{\boldsymbol{S}}} = \frac{1}{2}\boldsymbol{L}_2^e : \bar{\boldsymbol{C}} \text{ with } \boldsymbol{L}_2^e = 4\frac{\partial^2 \psi}{\partial \bar{\boldsymbol{C}} \otimes \partial \bar{\boldsymbol{C}}} \tag{14}$$

where $\boldsymbol{L}_2^e$ is the elastic second Lagrangian material tangent operator. Push-forward transformation of this relation yields (after some elaborations under the assumption of elastic and plastic isotropy) to the Oldroyd stress rate as

$$\tilde{\boldsymbol{\tau}} = \boldsymbol{E}_2^e : \boldsymbol{l}^e - 2\boldsymbol{l}_p \cdot \boldsymbol{\tau} \tag{15}$$

where $\boldsymbol{E}_2^e = \left(\bar{\boldsymbol{F}}\overline{\otimes}\bar{\boldsymbol{F}}\right) : \boldsymbol{L}_2^e : \left(\bar{\boldsymbol{F}}^t\overline{\otimes}\bar{\boldsymbol{F}}^t\right)$ is the elastic second Eulerian material tangent operator induced via $\boldsymbol{L}_2^e$. Please carefully note that it was used that $(\boldsymbol{a}\overline{\otimes}\boldsymbol{b})_{ijkl} = a_{ik}b_{jl}$. Thus, in order to compare with the postulation proposed in Eq. (3), choosing $\boldsymbol{E} = \boldsymbol{E}_2^e$ and $\boldsymbol{h} = 2\boldsymbol{l}_p \cdot \boldsymbol{\tau}$ implies a thermodynamically consistent formulation in the sense that the postulated Oldroyd rate behavior is in line with a hyperelasto-viscoplastic formulation based on multiplicative split of the deformation gradient.

4 NUMERICAL EXAMPLE

Let us consider next the response at simple shear deformation and uniaxial stress compression. We thus emphasize that different responses are generally obtained depending on which stress rate the rate behavior $\boldsymbol{E}^e : \boldsymbol{l}^e$ is postulated with respect to. We thus consider the shear response with respect to the stress rates *Green-Naghdi* (SGN), *Zaremba-Jaumann* (SJM) and two version of the *Oldroyd* stress rate, the first one is the ad–hoc model (SOR) where linear elastic response in the Oldroyd stress rate is specified, whereas for the second one (SORa) the Oldroyd stress rate is consistent with the hyperelastic–inelastic model as outlined in Subsection 3.3. For comparison, we also consider two hyperelastic-inelastic Neo-Hooke models (NH) and (NHL) where the latter is formulated in logarithmic strains. The results for the simple shear test are shown in Figure 1a, where it is observed that all stress rate formulations yields more or less the same response. The same tendency is observed for the uniaxial compressive test, cf. Figure 1b. However, the results differ slightly at large strains between the consistent neo–Hookean NHL–model and the SGN, SJM, and SORa–models.

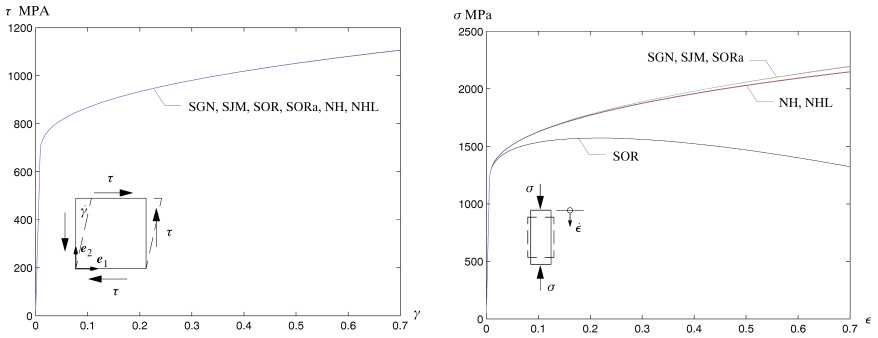

a) b)

Figure 1: Stress response in finite shear deformation a) and uniaxial compression b)

REFERENCES

[1] Johnson, G. R. & Cook, W. H. A constitutive model and data for metals subjected to large strains, high strain rates and high temperatures. *Proc. 7th Int. Symp. On Ballistics* 541–547 (1983).

[2] Nagtegaal, J. C. & Dejong, J. E. Some aspects on non-isotropic work-hardening in finite strain plasticity. *Proc. of the Workhop on Plasticity of Metals at Finite Strain* 65–107 (1981).

[3] Cescotto, S. & Habraken, A.-M. A note on the response to simple shear of elasto-plastic materials with isotropic hardening. *European Journal of Mechanics, A/Solids* **10**, 1–13 (1991).

23rd Nordic Seminar on Computational Mechanics
NSCM-23
A. Eriksson and G. Tibert (Eds)

METAL PLUGS FOR CARTILAGE DEFECTS - A FINITE ELEMENT STUDY

KRISHNAGOUD MANDA

KTH Mechanics, Royal Institute of Technology
Osquars backe 18, SE-100 44 Stockholm, Sweden
e-mail: krishnagoud@mech.kth.se, web page: http://www.mech.kth.se/

Key words: Articular Cartilage Defects, Metal Plug, Finite Element Analysis, Poroelastic, Biphasic, Sheep Knee

Summary. Articular resurfacing metal plugs have recently been tested in animal models to treat full thickness cartilage defects, showing promising results. However, the mechanical behavior of cartilage surrounding the metal plug has not been studied yet. Therefore, we implemented a detailed numerical f nite element model by approximating one of the condyles of the sheep tibiofemoral joint. Using this model, the mechanical behavior of the surrounding of metal plug was studied. We demonstrated that treating cartilage defects with the metal plug was mechanically advantageous. Two types of prof les were investigated for metal plug. A plug with a double-curved prof le, i.e., a prof le fully congruent with the articular surfaces in the knee, has better performance than the plug with unicurved spherical prof le. The plug should be placed at a certain distance into the cartilage to avoid damage to opposing biological surface. Too deep positions, however, lead to high shear stresses in the cartilage edges around the plug. The mechanical sealing was achieved with the wedge shape of the plug which also might be useful for biochemical sealing of cartilage edges at the defect.

1 INTRODUCTION

Full thickness cartilage defects can cause pain and functional limitation, have poor capacity for repair or regeneration and may lead to degenerative arthritis. Currently, the available biological repair techniques are not eff cient and all have drawbacks[1]. Alternatively, a defect-sized biocompatible metallic articular resurfacing plug can be used to treat localized cartilage defects in the joints[2,3,4,5]. The mechanical behavior of the soft tissues surrounding the metal plug have not been predicted. Therefore, we implemented a f nite element (FE) model of one of the condyles of the sheep tibiofemoral joint. The FE model was based on a plug (Episurf Medical AB, Stockholm, Sweden) developed for insertion into small full-thickness chondral defects in the femoral condyle and to articulate against tibial cartilage. The plug (implant) is presently subject to validation studies in a sheep model. The main purpose of the present study was to simulate the cartilage mechanical behavior. The FE simulations considered axial loading situations for two prof les of the plug: a symmetric spherical articulating surface and a double-curved articulating surface modelled from CT scans of a sheep knee. Primary f xation is achieved by interference f t of a pin into the subchondral bone.

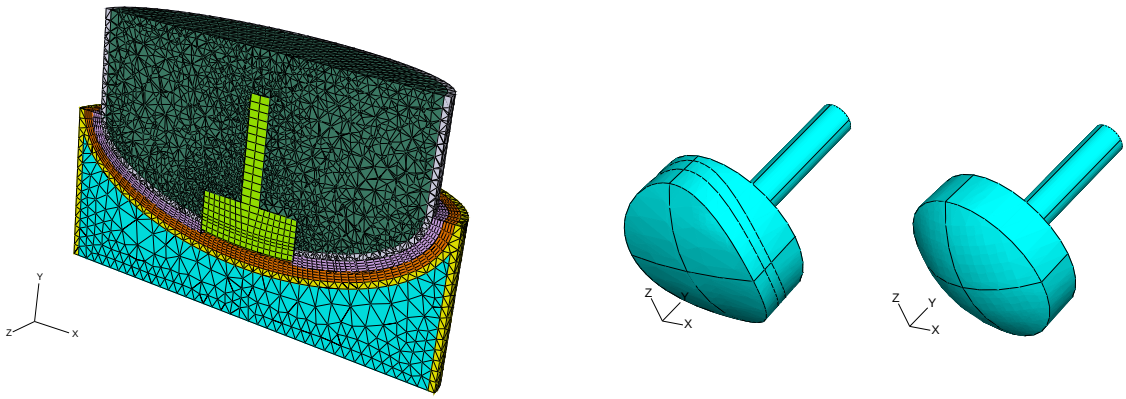

(a) (b)

Figure 1: (a) Simplif ed geometry for one of the condyles of the sheep knee (a sectional view through FE mesh), (b) Double-curved (left) and Spherical (right) plugs

2 FORMULATION AND METHODS

A 3D simplif ed geometrical representation was developed for one of the condyles (approximated as a semi-ellipsoid with two different principal radii, 17.36 and 7.53 mm) of the sheep's knee joint including the cartilages. A hole, representing the defect, was assumed at the center of the femoral condyle and expressed as diameter (6, 8, 10 and 12 mm). Dimensions were measured from a cadaveric sheep knee. The meniscus was mimicked by introducing a full congruency between the articular cartilages. The plugs had a diameter of specif c defect size; cap height of 2.5 mm; the pin of 2 x 10 mm. The radius of curvature of the spherical prof le was 8.5 mm, whereas the double-curved plug exactly matched the femoral cartilage prof le within a circle of defect sized diameter. The sealing of the surrounding cartilage was achieved by wedging the plug's cap.

Extensive parametric simulations were performed by varying the axial position of plug with respect to cartilage surface, wedge shape/angle of the plug's cap, and the size of the defect. These cases were compared to healthy and defected conditions with perfect cartilage and with a circular hole, respectively. The axial positioning of plug was def ned as "at $\pm$ x mm", where the positive sign indicates an plug inserted into the femoral bone. Articular cartilages were always described as a linear isotropic biphasic poro-elastic materials and all other materials were considered as isotropic linearly elastic.

The models were implemented using the commercial FE software ABAQUS V6.7. The nodes on the bottom plane of the tibia were constrained to move equally in vertical (axial) direction. The top plane of the femur was rigidly constrained in all directions. Frictionless small sliding contact was assumed between cartilages and also between plug and femoral cartilage. The free surfaces of the cartilages, which are not in contact, were allowing free f uid f ow. No f uid leakage was allowed from the femoral cartilage surface when in contact with the plug. The knee joint forces were represented by equal vertical displacements on the bottom plane of the tibia in the form of pressure (2 times body weight of the sheep).

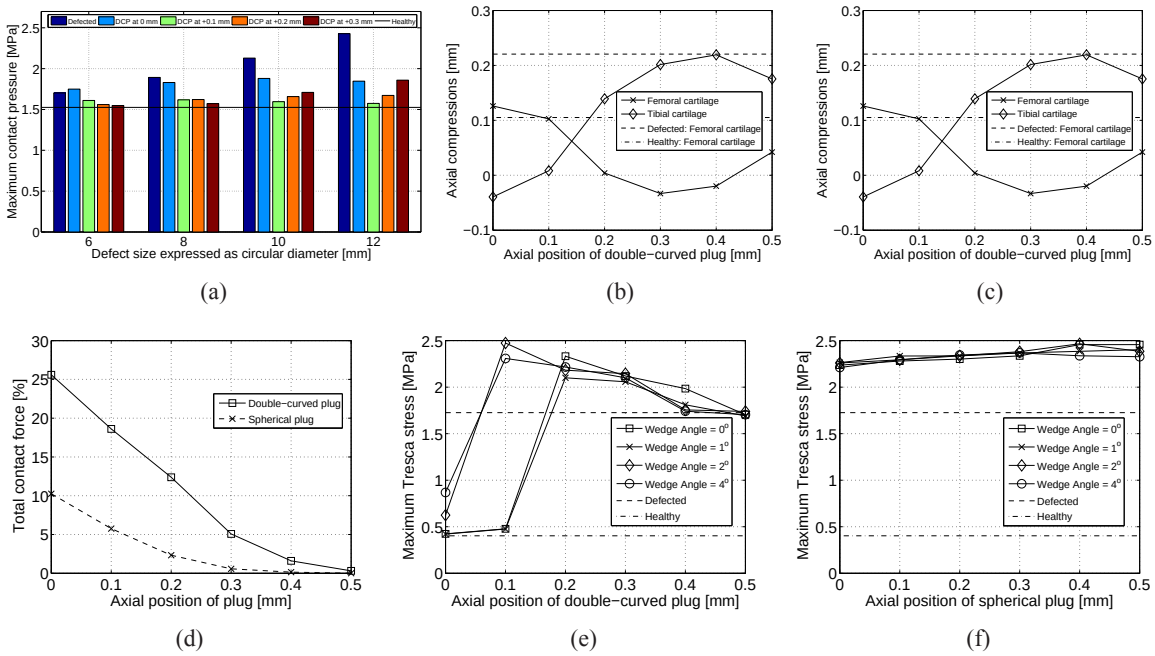

Figure 2: (a) The maximum contact pressures for different defect sizes with defect sized double-curved plug (DCP). In the 10 mm defect model, axial compressions of cartilages immediately surrounding the plug with the (b) double-curved plug, (c) spherical plug, (d) total contact force transmitted through the plug expressed as a percentage of applied load, maximum Tresca (Shear) stress in the femoral cartilage with the (e) double-curved plug, (f) spherical plug

3 RESULTS

For any position of the plug, the maximal contact pressure was either almost equal or lower than that of the defected joint for 6, 8, 10, 12 mm defect sizes. For 6 and 8mm defect sizes, the double-curved plug positioned at +0.3 mm gave the lowest maximum contact pressure, whereas for 10 and 12 mm defect sizes the plug position at +0.1 mm gave the lowest maximum, Fig. 2(a). In the 10 mm defect model, the forces transmitted through the plugs were found around 25% (125 N) and 10% (50 N) of applied load with the double-curved and spherical plugs positioned at 0 mm, respectively, Fig. 2(d). With the plug deeper into femoral bone, the force transmitted through the plug was reduced, approaching the defected situation.

The maximum Tresca stress (indicating shear) in the femoral cartilage was signif cantly affected by the position of the double-curved plug. There were limited changes with the wedge angle. The maximum Tresca stress in the 10mm defect model was 0.4213 and 0.4750 MPa, close to that of healthy joint (0.4026 MPa), with a double-curved plug positioned at 0 and +0.1 mm. As the double-curved plug sits deeper, the Tresca stress in the cartilage edges increases if the edges deform less than the plug's depth, approaching defected condition. The edges of the spherical plug always sink into cortical bone in the A-P (anterior-posterior) plane for any axial position, giving higher Tresca stress: 2.2 to 2.4 MPa, in the cartilage edges. This was always higher than for the corresponding defected joint (1.726 MPa), Fig. 2(f). The maximum

Tresca stress in the femoral cartilage was almost independent of wedge angle for a spherical plug.

The axial compressions of the cartilages, on the implanted side (femoral cartilage) and the opposing side (tibial cartilage), immediately surrounding the plug are shown in Figs. 2(b), 2(c) for various positions of spherical and double-curved plugs of size 10 mm. For a 10 mm defect, the maximum radial inward displacement of the femoral cartilage edges towards the center was 30% and 19% of the defect size in A-P and M-L directions. There were no signif cant differences in the deformations and contact pressures due to wedge angle. Void ratio (f uid volume fraction) in the cartilage edges around the plug was 4 and 3.65 for $0°$ and $4°$ wedge angles with double-curved plug positioned at 0 mm and decreased with the deeper positions.

4 DISCUSSION

This study was initially aimed at developing a conceptual poroelastic FE model of the sheep knee. Using the model, two plug prof les with various positions of the plug with respect to cartilage surface were verif ed. With this model we found qualitatively realistic contact pressure distributions, mechanical stresses and strains in the cartilage edges at the defect with or without plug. The contact pressure was more evenly distributed with the double-curved plug than with the spherical one. Since the spherical plug sunk into the bone in A-P plane, the stresses at the rim of the defect were higher than those of double-curved plug. It is observed the solidif cation of material in the cartilage edges around the plug due to the increasing wedge angle, indicating mechanical sealing of cartilages. All the results show that a double-curved plug is preferable to a spherical plug. Mechanically, it is advantageous to have plug's cap slightly sunk into the cartilage to avoid damage to the opposing biological structures and high local pressures, but too deep positions may lead to high rim stresses at the defect and shear stresses in cartilage. The study supports the idea of using a metal resurfacing plug for the treatment of full thickness cartilage defects. The obtained results will be compared to results from the ongoing animal study, and can be used to improve the plug design and placement.

REFERENCES

[1] Hangody, L. & Füles, P. Autologous osteochondral mosaicplasty for the treatment of full-thickness defects of weight-bearing joints: Ten years of experimental and clinical experience. *Journal of Bone and Joint Surgery - Series A* **85**, 25–32 (2003).

[2] HemiCAP^{TM}. made by arthrosurface, http://www.arthrosurface.com/ (2002).

[3] Kirker-Head, C. A., van Sickle, D. C., Ek, S. W. & McCool, J. C. Safety of, and biological and functional response to, a novel metallic implant for the management of focal full-thickness cartilage defects: Preliminary assessment in an animal model out to 1 year. *Journal of Orthopaedic Research* **24**, 1095–1108 (2006).

[4] Custers, R. J. H. *et al.* Reliability, reproducibility and variability of the traditional histologic/histochemical grading system vs the new OARSI osteoarthritis cartilage histopathology assessment system. *Osteoarthritis and Cartilage* **15**, 1241–1248 (2007).

[5] Custers, R. J. H. *et al.* Articular damage caused by metal plugs in a rabbit model for treatment of localized cartilage defects. *Osteoarthritis and Cartilage* **15**, 937–945 (2007).

23rd Nordic Seminar on Computational Mechanics
NSCM-23
A. Eriksson and G. Tibert (Eds)

FE ANALYSIS OF ORTHOGONAL CUTTING

MATHIAS AGMELL[*], AYLIN AHADI[†] AND JAN-ERIC STÅHL[†]

[*] Department of Production and Materials Engineering
LTH, Lund University, Sweden
e-mail: mathias.agmell@iprod.lth.se

[†] Department of Mechanical Engineering
LTH, Lund University, Sweden
e-mail: aylin.ahadi@mek.lth.se

[†] Department of Production and Materials Engineering
LTH, Lund University, Sweden
e-mail: jan-eric.stahl@iprod.lth.se

Key words: Orthogonal cutting, deformation zones.

Summary. The development of a coupled thermo-mechanical FE analysis of orthogonal cutting is presented. The work piece material is modeled with Johnson-Cook plasticity and damage formulation. The focus of study is on the deformation zones occurring in the work piece in a machining process.

1 INTRODUCTION

One of the most common operations in manufacturing is metal cutting. There is a wide range of cutting operations such as turning, milling, drilling etc. Many studies and experiments has been performed since the beginning of the 20th century. First analytical models of orthogonal cutting were created on the base of experiments and empirically based research such as Merchant's orthogonal force model (1945). The problem of analytically models is to express wide range of materials, their properties and cutting conditions. Development of the Finite Element Method (FEM) in early 1970s first pioneered simulations of orthogonal cutting. FEM simulations of the machining process is a typical dynamic non/linear problem for use of the explicit method. In FEM modeling there are three major formulations: Lagrangian, Eulerian, Arbitary Lagranian Eulerian (ALE). The most common and with the simplest code is the Lagranian one, this method requires a separation criteria or remshing method (Adaptive meshing) to describe the chip formation. The earliest studies used a predefined criterion for chip separation from the work piece along the separation area. The adaptive meshing technique gives better results, but this method is characterized by long computational times. The ALE-formulation and remeshing scheme combined the Lagranian and Eulerian formulation which leads to shorter computational times since you eliminate the element distortion in certain areas of the model. Chip thickness ratio, cutting forces and deformation zones for different theoretical chip thicknesses has been studied. The

deformation zones is of great interest, since this has a big influence on the machining process when cutting in deformation hardening materials since if the tool is cutting in the hardened material on the second revolution it will experience higher stresses than expected which leads to higher wear on the tool and in turn can lead to standstill in the production line.

2 MATERIAL MODEL

The work piece was modeled as AISI 4140 material, and a cemented carbide material is used for the tool. The general thermal and mechanical properties are presented in details in [1].

2.1 Constitutive law

The material model utilized is Johnson Cook plasticity model, see [2]. This constitutive relation is commonly used when modeling orthogonal cutting with FEM, since it takes in account strain rate and temperature which has a strong effect on the strain/stress relationship in the machining process and that its often already implemented in commercial software. The constitutive law is given by

$$\sigma = (A + B(\varepsilon^{\mathrm{p}})^{n})\left[1 + C\ln\left(\frac{\dot{\varepsilon}^{\mathrm{p}}}{\dot{\varepsilon}_0}\right)\right]\left[1 - \left(\frac{\theta - \theta_0}{\theta_{melt} - \theta_0}\right)^{m}\right] \tag{1}$$

where σ is the equivalent stress, $\dot{\varepsilon}^{\mathrm{p}}$ is the equivalent plastic strain rate, ε^{p} is the equivalent plastic strain, $\dot{\varepsilon}_0$ is the reference strain rate, A is the initial yield stress, B is the hardening modulus, C is the strain rate dependency coefficient, n is the strain hardening exponent, m is the thermal softening coefficient, θ is the process temperature, θ_{melt} is the melting temperature and θ_0 is the bulk temperature.

2.2 Chip separation criteria

For this study the Johnson Cook damage law is used to model the chip separation, see [2]. The cumulative damage law is given by

$$D = \sum\left(\frac{\Delta\varepsilon^{\mathrm{p}}}{\varepsilon_f}\right) \tag{2}$$

where D is the damage parameter, $\Delta\varepsilon^{p}$ is the increment of the equivalent plastic strain and ε_f is equivalent strain at failure. According to the Johnson-Cook model, $\Delta\varepsilon^{p}$ is updated at every load step and ε_f is expressed by

$$\varepsilon_f = \left[D_1 + D_2\exp D_3\left(\frac{P}{\sigma}\right)\right]\left[1 + D_4\ln\left(\frac{\dot{\varepsilon}^{\mathrm{p}}}{\dot{\varepsilon}_0}\right)\right]\left[1 + D_5\left(\frac{\theta - \theta_0}{\theta_{melt} - \theta_0}\right)\right] \tag{3}$$

where $\dot{\varepsilon}^{\mathrm{p}}$ is the equivalent plastic strain rate, $\dot{\varepsilon}_0$ is the reference equivalent strain rate, θ is the process temperature, θ_{melt} is the melting temperature, θ_0 is the bulk temperature and ratio of hydrostatic pressure to equivalent stress $\frac{P}{\sigma}$. Failure will occur when the damage parameter D, given by equation (2) reaches 1. When this condition is meet with in an element, the stress component are set to zero and remains zero for the rest of the calculation.

2.3 Modeling of the tool-chip interface contact

The contact interaction in machining has two distinct zones sliding and sticking friction, around the tool tip sticking friction appear due to the high pressures in the region, for the rest of the contact interface sliding friction is active. This has been modeled with Coulomb's friction law with an upper bound on the frictional force, the region where maximum frictional stress is produced models the sticking region, which is defined by

$$\begin{cases} \tau_f = \mu\sigma_n & \text{when } \mu\sigma_n < \tau_{max} \\ \tau_f = \tau_{max} & \text{when } \mu\sigma_n > \tau_{max} \end{cases} \quad (4)$$

where σ_n is the normal stress along the tool-chip interface, μ is the friction coefficient, τ_f is the frictional stress and τ_{max} is the maximal value of the frictional stress.

2.4 Heat generation and heat transfer between the tool and chip

There are two sources for heat generation in machining material plastic deformation and friction. Most of the plastic deformation energy is converted in to heat. In this study the percentage was taken as 90% . The heat generated by friction is assumed to be fully absorbed by the material hence the fraction of heat generated from friction is set to 1.0. To simulate the heat flow between the tool and the work piece a thermal boundary condition was defined. Heat conduction between the tool and the work piece is pressure dependant. The heat conduction coefficient, h is defined as a function of pressure, see [1].

3 FINITE ELEMENT MODEL

The orthogonal cutting process was simulated using a 2D model in ABAQUS/Explicit v6.9 a fully coupled thermo-mechanical analysis was used. The work piece length was taken as 5 mm and its height as 2 mm. The cutting tool had a clearance angle of 5°, rake angle of 0°, edge radius 50μm, height and length of 2 mm, the cutting speed v_c was set to 260 m/min. The tool was considered as a rigid body, to shorten the simulation time.

4 RESULTS

In this section the simulation model is firstly validated by comparing the cutting forces at different theoretical chip thicknesses h_1. Then the model is used to predict the deformation zones.

4.1 Cutting forces

The force has been experimentally determined with a stepwise increased feed test in the interval $0.05 \leq h_1 \leq 0.40$ mm. In figure 1 it can be seen that the cutting force reaches steady state within the simulation time. This justifies the use of a machining length 2.5 mm.. As seen in figure 2 a good agreement is obtained between the simulated and measured cutting forces for all theoretical chip thicknesses.

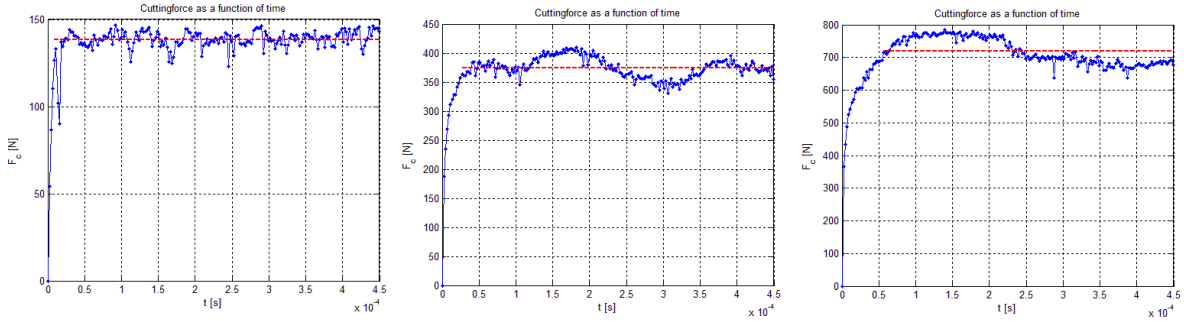

Figure 1: The cutting force as a function of time for the FE simulations with $h_1 = 0.05$ mm to the left, $h_1 = 0.15$ mm in the middle and $h_1 = 0.30$ mm to the right. The dashed red line is the mean value for the cutting force in the steady state interval.

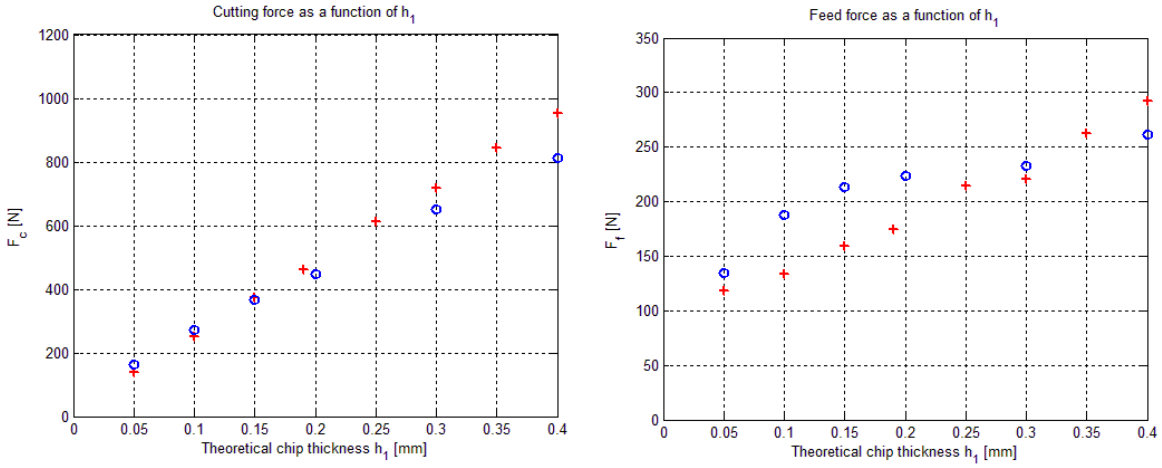

Figure 2: To the left cutting force as a function of h_1 the red dots is predicted and blue is measured values. To the right feed force as a function of h_1 the red dots is predicted values and blue is measured values.

4.2 Deformation zones

The deformation zones will simulated for $0.1 \leq h_1 \leq 0.4$. The deformation zones and deformation widths is of great interest in machining when your are working with strain hardening materials, since if the machining takes place in a predeformed material layer the tool will experience a material with different properties. This can lead to higher forces and tool ware than expected and in the worst case standstill in production due to machine failure. Therefore it is important to study how the deformation zones and deformation width varies with the theoretical chip thickness (h_1) in orthogonal machining. Figure 3 shows the equivalent strain distribution for $h_1 = 0.15$ and 0.30.

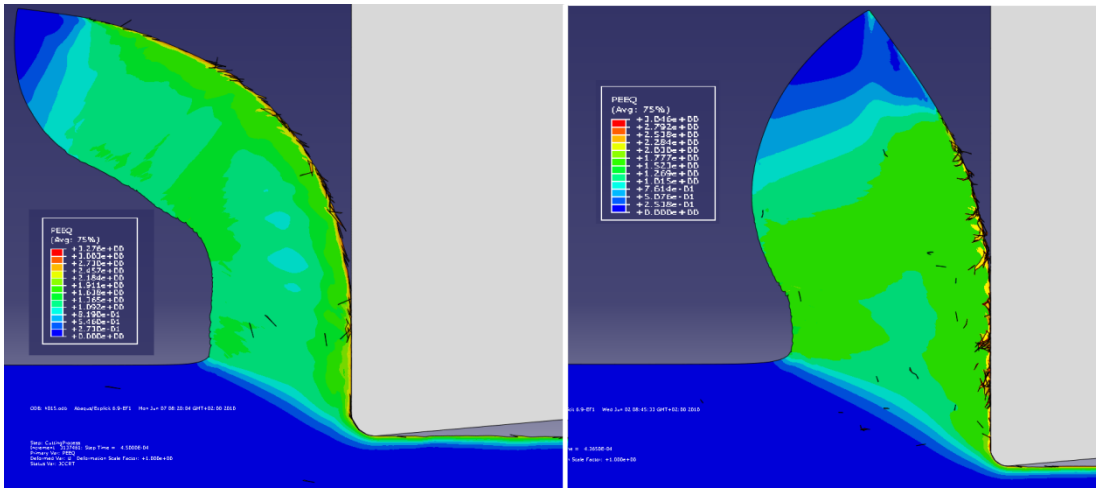

Figure 4: Distribution of the equivalent strain for $h_1 = 0.15$ to the left and 0.30 to the right.

The relative deformation width is only defined for the secondary- and tertiary zone. These are defined in equation 5. If δ_{III} exceeds 1.0 machining will take place in predformed material after the first revolution, since $\varepsilon_{III} > h_1$.

$$\begin{cases} \delta_{II} = \dfrac{\varepsilon_{II}}{h_2} \\ \delta_{III} = \dfrac{\varepsilon_{III}}{h_1} \end{cases} \tag{5}$$

The measured relative deformation widths is taken from [3], where the defromation widths has been determined with a quick-stop method where the tool pushed away from the cutting process with a small gunpowder charge, in this way a freezed sequence of the process is achieved. As seen in figure 5 a there is a very good agreement between measured and predicted values of the deformation widths.

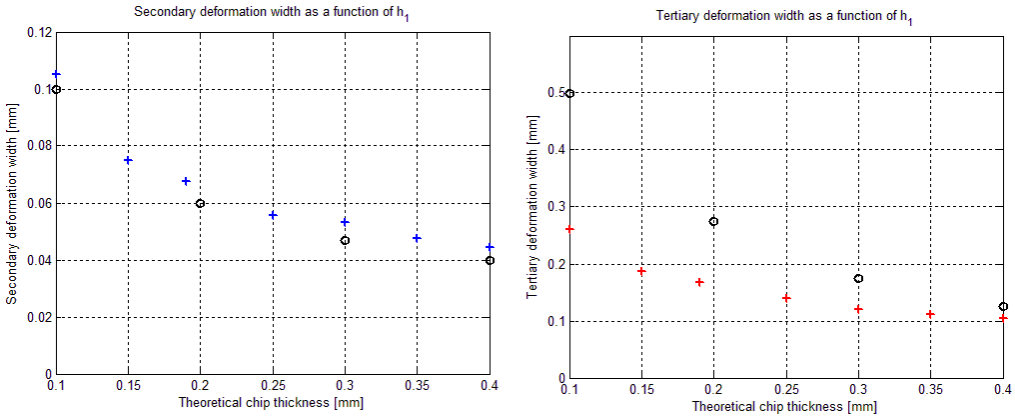

Figure 5: Relative deformation widths, the secondary to the left measured data points are in black and predicted are in blue. The tertiary zone is to the right, measured data points are in black and predicted are in red.

5 CONCLUSIONS

This study presents results of a coupled thermo-mechanical FE analysis with the aim of studying the theoretical chip thickness influence on the shape of deformation zones in orthogonal machining. The predicted cutting forces, chip thickness ratio and deformation widths shows good correlation with experimentally measured data thereby validating the model. The study shows that you can model the deformation zones which enables a high resolution of the strain distribution in the deformation zones, which can be difficult to achieve with good accuracy for conventional quick-stop methods.

REFERENCES

[1]. A coupled thermo-mechanical FE analysis of orthogonal cutting, Department of Mechanical Engineering, LTH, Lund University, Sweden, September 2010 (In preparation).

[2]. Fracture characteristics of three metals subjected to various strains, strain rates, temperatures and pressures, GR Johnson, WH Cook, 1985.

[3]. Skärande Bearbetning - Teori och modeller, J.-E. Ståhl, 2009.

23rd Nordic Seminar on Computational Mechanics
NSCM-23
A. Eriksson and G. Tibert (Eds)

CONTINUUM MODELING OF SIZE-EFFECTS IN SINGLE CRYSTALS

CHRISTIAN F. NIORDSON*, JEFFREY W. KYSAR†

*Department of Mechanical Engineering, Solid Mechanics, Technical University of Denmark, DK-2800 Kgs. Lyngby, Denmark e-mail: cn@mek.dtu.dk, web page: http://www.mek.dtu.dk/

†Department of Mechanical Engineering, Columbia University, New York, NY 10027, USA e-mail: jk2079@columbia.edu - Web page: http://www.engineering.columbia.edu/

Key words: Size-effects, Strain Gradient Crystal Plasticity, Finite Element

Summary. In the present work the strain gradient formulation for isotropic plasticity, proposed by Fleck and Willis, is extended to crystal visco-plasticity. Size-effects are predicted by the theory due to the addition of gradient terms in both the free energy as well as through a dissipation potential. A robust numerical method applicable for crystal plasticity is presented. Some plane deformation problems relevant for certain specific orientations of a face centered cubic crystal under plane loading conditions are studied. The problem of pure shear of a single crystal between rigid platens is studied, and convergence properties of the numerical method proposed are discussed.

1 INTRODUCTION

In metals strain gradient effects lead to significant strengthening on the micron scale. Experimental investigations on size-effects in metals have been carried out for a variety of materials and under different loading conditions such as bending[1,2], torsion[3], indentation and contact compression[4], as well as the characterization of the density of geometrically necessary dislocations[5]. While some experiments suggest that the yield strength increases with decreasing size[3,6], other experiments show that the size-effect mainly affects the material hardening behavior[7]. Some experiments even show size-effects on both yield strength and hardening behavior[2].

Much research has been devoted to modeling observed size-effects. This includes modeling of the above mentioned experiments in addition to studies of size-effects in void growth, fiber reinforced materials and fracture problems.

In this paper variational principles for a strain gradient crystal plasticity theory are laid out along the lines developed for isotropic plasticity by Fleck and Willis[8,9]. Furthermore, the details of a robust finite element formulation of the strain gradient crystal plastic theory is presented. The theory is closely related to that proposed by Gurtin and co-workers[10] even though the numerical method is quite different.

2 MATERIAL MODEL

Within a small strain framework an additive decomposition of the total strain, ϵ_{ij}, into and elastic part, ϵ^e_{ij}, and a plastic part, ϵ^p_{ij}, is used

$$\epsilon_{ij} = \epsilon^e_{ij} + \epsilon^p_{ij} \tag{1}$$

The plastic strain rate is due to crystallographic slip on the slip planes α

$$\dot{\epsilon}^p_{ij} = \sum_{(\alpha)} \dot{\gamma}^{(\alpha)} \mu^{(\alpha)}_{ij} \tag{2}$$

with the Schmid orientation tensor given by

$$\mu^{(\alpha)}_{ij} = \frac{1}{2}(s^{(\alpha)}_i m^{(\alpha)}_j + s^{(\alpha)}_j m^{(\alpha)}_i) \tag{3}$$

where $s^{(\alpha)}_i$ and $m^{(\alpha)}_j$ are the direction of slip and the slip plane normal, respectively.

The material model is based on the following form of the principle of virtual work

$$\int_V \left(\sigma_{ij}\delta\epsilon_{ij} + \sum_\alpha (q^{(\alpha)} - \tau^{(\alpha)})\delta\gamma^{(\alpha)} + \sum_\alpha \xi^{(\alpha)} s^{(\alpha)}_i \delta\gamma^{(\alpha)}_{,i} \right) dV = \int_S \left(T_i \delta u_i + \sum_\alpha r^{(\alpha)} \delta\gamma^{(\alpha)} \right) dS \tag{4}$$

Here, σ_{ij} is the stress tensor, ϵ_{ij} is the strain tensor, $q^{(\alpha)}$ is the micro-stress on slip plane α and $\tau^{(\alpha)} = \sigma_{ij}\mu^{(\alpha)}_{ij}$ is the Schmid stress. The higher order nature of the theory is due to the terms $\xi^{(\alpha)}$, which are the higher order stresses work conjugate to the slip gradients, $\gamma^{(\alpha)}_{,i}$, where $(\,)_{,i}$ signifies the gradient operator. With n_i denoting the outward unit normal, the right hand side of the principle of virtual work includes the conventional traction vector $T_i = \sigma_{ij} n_j$, work conjugate to the displacement vector u_i, and the higher order tractions $r^{(\alpha)} = \xi^{(\alpha)} s^{(\alpha)}_i n^{(\alpha)}_i$, which are work conjugates to the slips, $\gamma^{(\alpha)}$.

Accounting for both dissipative and energetic gradient effects, the higher order stresses are decomposed into a dissipative part, $\bar{\xi}^{(\alpha)}$ and an energetic part, $\tilde{\xi}^{(\alpha)}$

$$\xi^{(\alpha)} = \bar{\xi}^{(\alpha)} + \tilde{\xi}^{(\alpha)} \tag{5}$$

whereas the micro-stresses are assumed to have a dissipative part, $\bar{q}^{(\alpha)}$, only.

2.1 Dissipative contributions

To account for dissipative gradient effects, a visco-plastic potential is used from which the following constitutive equations for the dissipative stress-quantities are derived

$$\bar{q}^{(\alpha)} = \tau^{(\alpha)}_e \frac{\dot{\gamma}^{(\alpha)}}{\dot{\gamma}^{(\alpha)}_e} \quad \text{and} \quad \bar{\xi}^{(\alpha)} = \tau^{(\alpha)}_e \frac{(L^{(\alpha)}_d)^2 \dot{\gamma}^{(\alpha)}_{,i} s^{(\alpha)}_i}{\dot{\gamma}^{(\alpha)}_e} \tag{6}$$

Here, $\tau^{(\alpha)}_e$ is an effective stress, $\dot{\gamma}^{(\alpha)}_e$ is an effective slip rate, and $L^{(\alpha)}_d$ are dissipative length parameters.

2.2 Energetic contributions

Assuming that free energy, Ψ, is stored due to a decoupled quadratic form in the elastic strain and the gradients of slip, the energetic higher order stresses are derived according to

$$\tilde{\xi}^{(\alpha)} = \frac{\partial \Psi}{\partial(\gamma^{(\alpha)}_{,i} s^{(\alpha)}_i)} = G\left(L^{(\alpha)}_e\right)^2 s^{(\alpha)}_i \gamma^{(\alpha)}_{,i} \tag{7}$$

where G is the shear modulus and $L^{(\alpha)}_e$ are energetic length parameters.

2.3 Minimum principles used for generating solutions

To solve for the slip rate fields the following minimum principle is used within a finite element setting:

$$H[\dot{\gamma}^{(\alpha)}] = \int_V \left(\Phi[\dot{\gamma}^{(\alpha)*}]\dot{\gamma}^{(\alpha)*} + \tilde{\xi}^{(\alpha)} s_i \dot{\gamma}^{(\alpha)*}_{,i} - s_{ij}\mu^{(\alpha)}_{ij}\dot{\gamma}^{(\alpha)*}\right) dV - \int_{S_T} r^{(\alpha)}\dot{\gamma}^{(\alpha)*} dS \tag{8}$$

Here, Φ is a visco-plastic potential, and s_{ij} is the stress deviator

When knowing the solution for the slip rate fields, nodal velocities are found from minimizing

$$J[\dot{u}^*_i] = \int_V \frac{1}{2} L_{ijkl}\left(\dot{\epsilon}^*_{ij} - \sum_\alpha \mu^{(\alpha)}_{ij}\dot{\gamma}^{(\alpha)}\right)\left(\dot{\epsilon}^*_{kl} - \sum_\alpha \mu^{(\alpha)}_{kl}\dot{\gamma}^{(\alpha)}\right) dV - \int_{S_T} \dot{T}_i \dot{u}^*_i dS \tag{9}$$

This two step solution method is a suitable modification for crystal plasticity of corresponding minimum principles for isotropic plasticity laid out by Fleck and Willis[8,9].

3 RESULTS AND CONCLUSIONS

Results are obtained using a finite element discretization. An iterative algorithm is used to minimize the functional $H[\dot{\gamma}^{(\alpha)}]$ in order to obtain the slip rate fields. Then solution of a standard elastic-visco plastic finite element system yields the nodal velocities as a result of minimizing $J[\dot{u}^*_i]$.

In Fig. 1a response curves in terms of shear stress versus shear strain are shown for pure shear of a long film of elastic-plastic material of thickness H between rigid platens. It is seen how increasing the dissipative length parameter relative to the thickness of the film increases the yield strength of the material system over that of conventional predictions (conv.). In Fig. 1b the number of iterations used to obtain converged solutions when minimizing $H[\dot{\gamma}^{(\alpha)}]$ are shown. It is seen that a large number of iterations are used in the transition from elastic to plastic behavior, and a small number of iterations are used otherwise.

REFERENCES

[1] Stölken, J. S. & Evans, A. G. A microbend test method for measuring the plasticity length scale. *Acta Materialia* **46**, 5109–5115 (1998).

[2] Haque, M. A. & Saif, M. T. A. Strain gradient effect in nanoscale thin films. *Acta Materialia* **51**, 3053–3061 (2003).

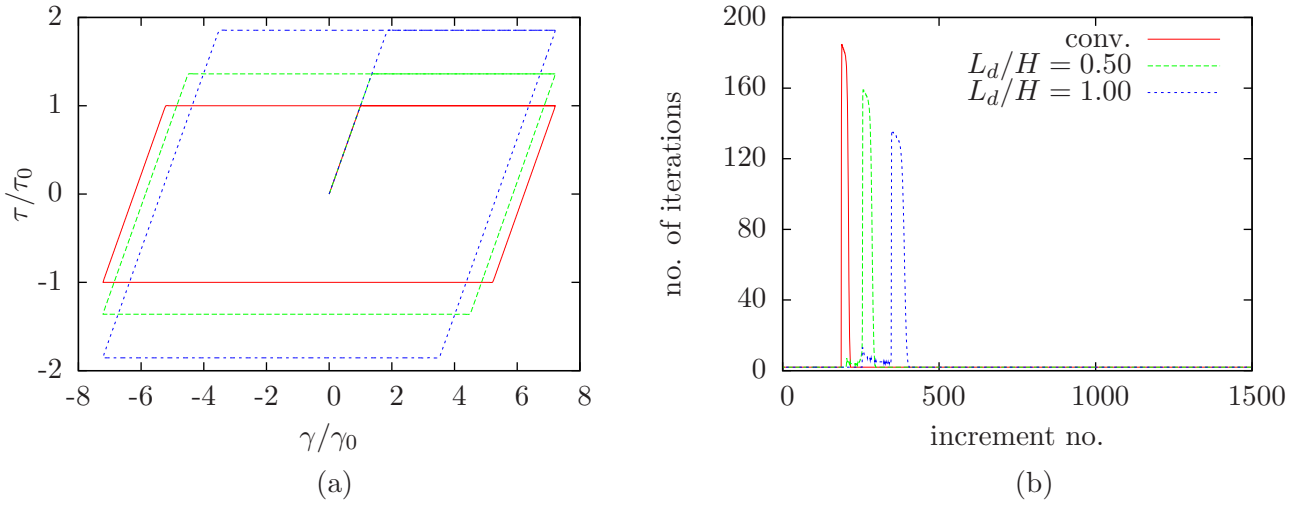

Figure 1: (a) Size-dependent response curves in pure shear for different values of the dissipative length parameter normalized by the film thickness. (b) Number of iterations used to minimize $H^{(\alpha)}$ per load increment.

[3] Fleck, N. A., Muller, G. M., Ashby, M. F. & Hutchinson, J. W. Strain gradient plasticity: Theory and experiment. *Acta Metallurgica et Materialia* **42**, 475–487 (1994).

[4] Ma, Q. & Clarke, D. R. Size dependent hardness of silver single crystals. *Journal of Materials Research* **10**, 853–863 (1995).

[5] Kysar, J. W., Saito, Y., Oztop, M. S., Lee, D. & Huh, W. T. Experimental lower bounds on geometrically necessary dislocation density. *International Journal of Plasticity* **26**, 1097–1123 (2010).

[6] Swadener, J. G., George, E. P. & Pharr, G. M. The correlation of the indentation size effect measured with indenters of various shapes. *Journal of the Mechanics and Physics of Solids* **50**, 681–694 (2002).

[7] Xiang, Y. & Vlassak, J. J. Bauschinger and size effects in thin-film plasticity. *Acta Materialia* **54**, 5449–5460 (2006).

[8] Fleck, N. A. & Willis, J. R. A mathematical basis for strain-gradient plasticity theory - Part I: Scalar plastic multiplier. *Journal of the Mechanics and Physics of Solids* **57**, 161–177 (2009).

[9] Fleck, N. A. & Willis, J. R. A mathematical basis for strain-gradient plasticity theory - Part II: Tensorial plastic multiplier. *Journal of the Mechanics and Physics of Solids* **57**, 1045–1057 (2009).

[10] Gurtin, M. E., Anand, L. & Lele, S. P. Gradient single-crystal plasticity with free energy dependent on dislocation densities. *Journal of the Mechanics and Physics of Solids* **55**, 1853–1878 (2007).

23rd Nordic Seminar on Computational Mechanics
NSCM-23
A. Eriksson and G. Tibert (Eds)

STIFFNESS VISUALIZATION FOR TENSEGRITY STRUCTURES

SEIF DALILSAFAEI, ANDERS ERIKSSON AND GUNNAR TIBERT

KTH, Royal Institute of Technology
School of Engineering Science
Department of Mechanics
SE-100 44 Stockholm, Sweden
e-mail: tibert@kth.se, web page: http://www.mech.kth.se/mech/

Key words: Tensegrity structures; Pre-stress; Flexibility analysis; Non-linear

Summary. This paper presents a tool for stiffness evaluation of tensegrity structures considering large external loads applied at the initial configuration, and small external disturbance loads applied at the loaded structure. The presented method is based on a geometrical non-linear analysis and is a visual evaluation of the flexibility of the self-stressed structure.

1 INTRODUCTION

Structures composed of tension elements (strings, tendons or cables) and compression elements (bars or struts) are often denoted tensegrity structures[1]. The process of finding the initial member forces for a given geometry is known as pre-stress design. In this paper, we assume that the form-finding step has been completed, meaning that the structure is in a stable pre-stressed configuration. The axial stiffness of the elements are also known. In the design process, the form-finding step must be complemented with requirements on the response of the structure to a variety of loading situations. The aim is to determine the pre-stress magnitude which is the only variable to reach certain stiffness. The idea here is to introduce a tool for stiffness evaluation of a given structure when it is exposed to different load combinations. The tool is based on the finite element method to handle the non-linear static analysis.

2 FORMULATION AND METHODS

Figure 1 illustrates the proposed method. A test load is an external load of a certain magnitude which tests the response of the structure in each direction for each unconstrained node. Thus, the test load rotates around each unconstrained node. The aim of the test load analysis is to investigate the response of the structure for different load levels from zero to maximum magnitude of the external load. The load levels are given by the type of application, the geometry of the structure and the maximum design load level. A loaded structure must also be stable when it is exposed to disturbance loads, e.g. wind gusts. Disturbance loads are assumed to be random in magnitude, direction and point of attack. In the simulations, they are not assumed to have an absolute magnitude, but are seen as small loads, acting in addition to the fixed external loads. In the analysis, they can thereby be seen formally as differential quantities, or more practically

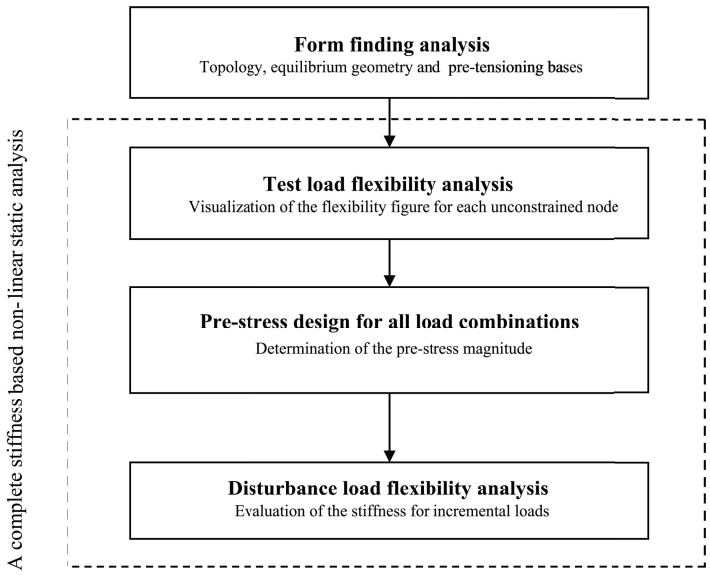

Figure 1: The proposed flexibility-based pre-stress design.

as a percentage of the magnitude of the test load. The random nature of disturbance loads mean that they should be considered for any unconstrained node, and in any unsupported direction. The aim of incremental load analysis is to evaluate the incremental stiffness of a loaded structure in order to find the minimum acceptable pre-stress level.

3 NUMERICAL EXAMPLE

In the non-linear analysis, the tangent stiffness formulation presented by Guest**(author?)**[2] for a simple bar element was used. The cable elements were assumed to be of the no-compression type with zero stiffness when slack. In tension, the tangent stiffness formulation of the bar and the cable element is similar.

The test load is rotated around each unconstrained node separately, and the displacements in all nodes are computed and visualized. The resulting geometric shape of the structure is denoted *flexibility figure*. If all cable elements are in tension, the flexibility figures resembles ellipses implying a strong linear behavior of the structure. Slackening of a cable element causes deformation of the elliptic flexibility figures in the direction of the slack cable element. The flexibility ellipse concept comes from Ströbel[3] who shows that the flexibility ellipse can be obtainable through analysis of the flexibility submatrix for each node. Figure 2 shows flexibility figures for various test loads. In Fig. 2, the structure with chosen pre-stress magnitude shows a linear behavior for a 10 kN test load and non-linear behavior for 20 and 30 kN test loads. Unfortunately Fig. 2 cannot show which cable elements gone slack.

The aim of Fig. 3 is to show the effect of a test load on the structure. The response of each load direction is shown in the load direction. In this way one can see the displacement deduced from each load, and also the directions of the test loads which cause the largest displacements. Figure 4(a) shows a design load case, and Fig. 4(b) shows the flexibility figure of each unconstrained

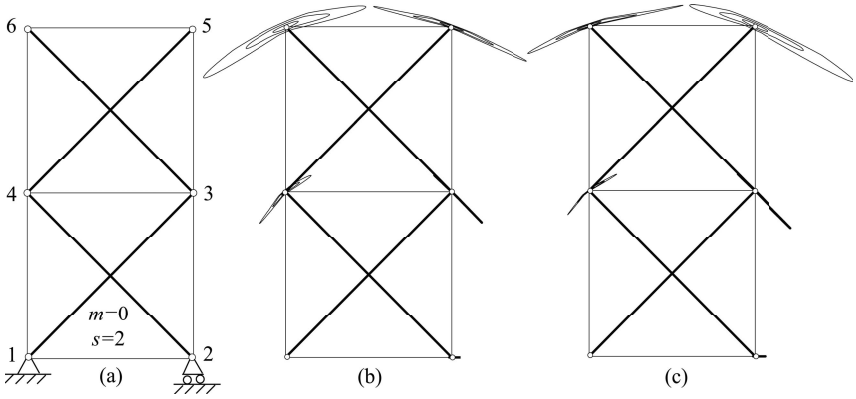

Figure 2: (a) Topology and node numberings of the two module tensegrity beam. (b) and (c) flexibility figures for 10, 20, and 30 kN test loads. Test loads applied at node (b) 6, (c) 5.

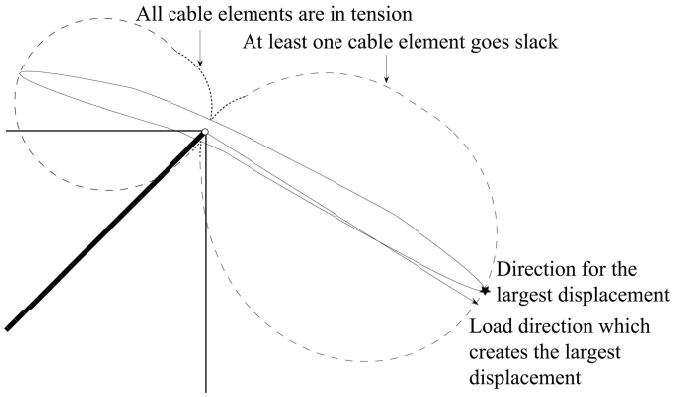

Figure 3: Flexibility figure and displacements in test load directions (dotted line) of node 5.

node for a 2 kN incremental load acting on the loaded structure in Fig. 4(a) for two different magnitudes of the pre-stress. The dotted line displacements show that at least one cable element goes slack, because the flexibility figures are not elliptic. Increasing the pre-stress magnitude, the flexibility figures are more elliptic, indicating a linear behavior.

4 CONCLUDING REMARKS

This study has taken a new look on the pre-stress problem. The pre-stress problem has mostly been seen as finding the bases of the pre-stress considering the unilateral property of the elements and the stability of the structure. The focus has been to find a good level of the pre-stress with the help of flexibility figures. By providing a visual presentation of the flexibility of all unconstrained nodes, we have a tool to determine the pre-stress magnitude considering both slackening effect and breaking load capacity of the cable elements. The advantages of the flexibility figures are:

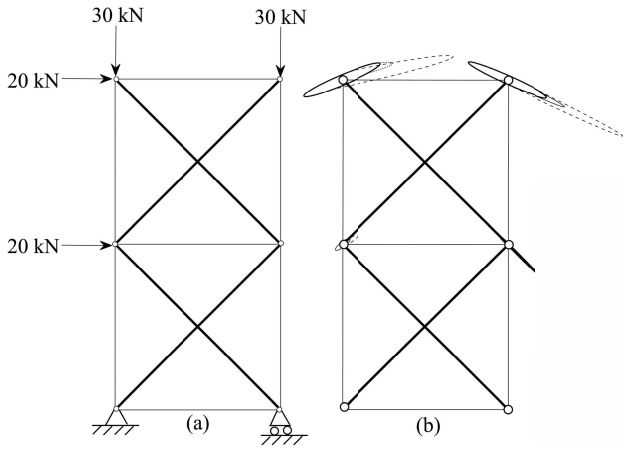

Figure 4: (a) Assumed design load case (b) flexibility ellipses for two different pre-stress magnitude. The dotted line displacements are for the slack case.

- Better knowledge of the influence of various of external loads magnitudes, identification of critical load combinations, and disturbances on the structure. An important consequence is the estimation of maximum displacement of unconstrained nodes for both an unloaded structure exposed to large external loads and a loaded structure exposed to disturbances.

- Easier identification and evaluation of the boundary between linear and non-linear structural behavior.

- Detection of very flexible nodes and directions of external loads which cause slackening or large displacements.

- Detection of cable elements with the highest risk of slackening.

The tool is thought to be useful for both engineers who design a complex truss structure, and researchers who evaluate the result of the form-finding process, placement of sensors and actuators for pre-tensioning.

REFERENCES

[1] Motro, R. & Raducanu, V. Tensegrity systems. *International Journal of Space Structures* **18**, 77–84 (2003).

[2] Guest, S. The stiffness of prestressed frameworks: A unifying approach. *International Journal of Solids and Structures* **43** (2006).

[3] Ströbel.D. Die Anwendung der Ausgleichungsrechnung auf Elastomechanische Systeme. *Universität Stuttgart, PhD thesis* (1995).

23rd Nordic Seminar on Computational Mechanics
NSCM-23
A. Eriksson and G. Tibert (Eds)

PREDICTION OF LONG-TERM MECHANICAL BEHAVIOR OF GLASSY POLYMERS

SAMI HOLOPAINEN* **AND MATHIAS WALLIN†**

*Department of Solid Mechanics
Lund University
P.O.Box 118, 22 100 Lund, Sweden
e-mail: Sami.Holopainen@solid.lth.se, web page: http://www.solid.lth.se/

†Department of Solid Mechanics
Lund University
P.O.Box 118, 22 100 Lund, Sweden
e-mail: Mathias.Wallin@solid.lth.se, web page: http://www.solid.lth.se/

Key words: Polymers, Long-term behavior, Anisotropic hardening, Computational methods.

Summary. Glassy polymers are frequently used in industrial applications and in consumer products and the need for accurate constitutive models is evident. The microstructure of a glassy polymer has a strong influence on the mechanical properties and it is typically described by means of network models where the network of molecular chains is connected at physical entanglements between macromolecules. Several network-based models for glassy polymers are available. The most popular approach is the 8-chain BPA model, cf. Arruda and Boyce [1], [2], where the randomly oriented molecular chains are replaced by eight interconnected polymer chains. The BPA model is capable of capturing the monotonic loading accurately, but for unloading and long-term behavior, the response of the BPA model is found to deviate significantly from the experimental data, cf. Dreistadt et al. [4]. Therefore, we suggest an extension of the BPA model that significantly improves the predictive capability of the BPA model during unloading and dwell.

1 INTRODUCTION

A successful and popular approach to model the nonlinear behavior of glassy polymers including orientation hardening was proposed by Arruda and Boyce [2] (BPA-model). Even though the BPA model depends on a few material parameters, it yields satisfactory results which has made the model popular for industrial applications. Recently Dreistadt et al. [4] showed that the BPA model collapses under unloading as well as long-term dwell, where the stress level is fixed during a time interval. In the present paper we extend the 8-chain BPA model such that the long-term behavior is significantly improved. Our model is based on the use of two separate dashpots in series with a nonlinear Langevin spring. For that, only one new material parameter is introduced, which results that the modified model retains the simplicity of the original BPA model. The new concept is applied to illustrative examples, where the response of original BPA

model and our modification for PC are compared to the experimental results by Dreistadt et al. [4].

2 Description of the BPA model

The present study is concerned with an extension of the BPA model and therefore we will start by briefly recapturing the fundamental ingredients in the BPA model. In the BPA model use is made of the Kröner-Lee decomposition of the deformation gradient, i.e.

$$\boldsymbol{F} = \boldsymbol{F}^e \boldsymbol{F}^p, \tag{1}$$

where $\boldsymbol{F}^p$ represents the deformation from the reference configuration to the intermediate configuration and $\boldsymbol{F}^e$ represents the deformation from the intermediate configuration to the current configuration. The stress-strain relation is given in terms of Cauchy-stress and the logarithmic (true) strain as

$$\boldsymbol{\sigma} = \frac{1}{J}\boldsymbol{\mathcal{L}}^e : ln\boldsymbol{V}^e, \tag{2}$$

where $\boldsymbol{\mathcal{L}}^e$ is a constant fourth order elasticity tensor, and J is the determinant of $\boldsymbol{F}^e$. The incremental relations for the plastic deformation is given from

$$\dot{\boldsymbol{F}}^p = \bar{\boldsymbol{L}}^p \boldsymbol{F}^p, \quad \bar{\boldsymbol{L}}^p = \bar{\boldsymbol{D}}^p + \bar{\boldsymbol{W}}^p, \tag{3}$$

where $\bar{\boldsymbol{D}}^p$ and $\bar{\boldsymbol{W}}^p$ are the symmetric and the skew symmetric parts of $\bar{\boldsymbol{L}}^p$, and they will be discussed subsequently.

In the BPA model the chain segment rotation is described by means of the viscous dashpot, which enables the initial strain softening to be captured in material. The anisotropic hardening due to reorientation of the molecular chain network is in the BPA model captured via a nonlinear Langevin spring, and characterized by the backstress. The backstress, $\bar{\boldsymbol{B}}$ is taken to be coaxial with the plastic stretch tensor, $\boldsymbol{V}^p$ and it is expressed in terms of the principal plastic stretches, λ^p_α, $\alpha = 1, 2, 3$ as

$$\bar{B}_\alpha := \frac{C_R}{3\lambda^p}\sqrt{N}\mathfrak{L}^{-1}\left(\frac{\lambda^p}{\sqrt{N}}\right)\left((\lambda^p_\alpha)^2 - (\lambda^p)^2\right), \quad \lambda^p = \frac{1}{\sqrt{3}}\sqrt{\sum_i (\lambda^p_i)^2}, \tag{4}$$

where C_R is material parameter taking into account temperature and molecular chain density, $\mathfrak{L}^{-1}$ is the inverse Langevin function, and N is a statistical parameter related to the limiting value of the chain stretch. The push-forward of the backstress to the current placement by $\boldsymbol{F}^e$ is

$$\boldsymbol{b}^p := \boldsymbol{F}^e \bar{\boldsymbol{B}} \boldsymbol{F}^{e-1}. \tag{5}$$

The evolution for of the plastic deformation is given by

$$\bar{\boldsymbol{D}}^p = \frac{\dot{\gamma}^p}{\sqrt{2}}\boldsymbol{N}, \tag{6}$$

where direction of the plastic flow, $\boldsymbol{N}$, is assumed to be aligned with the deviatoric reduced stress, $\bar{\boldsymbol{\sigma}}^{dev}$, i.e.

$$\boldsymbol{N} = \frac{\bar{\boldsymbol{\sigma}}^{dev}}{||\bar{\boldsymbol{\sigma}}^{dev}||}, \quad ||\bar{\boldsymbol{\sigma}}^{dev}|| = \sqrt{\frac{1}{2}\bar{\boldsymbol{\sigma}}^{dev} : \bar{\boldsymbol{\sigma}}^{dev}}, \quad \bar{\boldsymbol{\sigma}}^{dev} = \boldsymbol{\sigma}^{dev} - \boldsymbol{b}^p, \tag{7}$$

where the superscript *dev* denotes the deviatoric part. The rate of plastic deformation is taken in accordance with Argon [3] who based on a model for chain segment orientation suggested

$$\dot{\gamma}^p = \dot{\gamma}_0 exp\big(-\frac{As_s}{T}(1-(\frac{\tau}{s_s})^{\frac{5}{6}})\big), \quad s_s = s_1 + \alpha p, \quad \tau := ||\bar{\boldsymbol{\sigma}}^{dev}||, \tag{8}$$

where $\dot{\gamma}_0$ is pre-exponential factor, A is proportional the activation volume/Boltzmann's constant, p is pressure, α is pressure dependence factor and T is the temperature. The strain softening is modeled by taking the athermal shear stress s to evolve to s_{ss}, which is the assumed saturation value of s_1, i.e.

$$\dot{s}_1 = h_1(1-\frac{s_1}{s_{ss}})\dot{\gamma}^p, \quad s_1(0) = s_0, \tag{9}$$

where h_1 and s_0 governs rate of post-yield drop. To complete the plastic evolution laws an evolution law for $\bar{\boldsymbol{W}}^p$ must be provided. In the original BPA model the assumption of $\boldsymbol{R}^e$ being equal to unity was adopted. In turn, this implies that the plastic spin, $\bar{\boldsymbol{W}}^p$ in Eq. (3) generally is nonzero.

3 Extension of the BPA model

Based on the experimental investigations by Dreistadt et al. [4] it can be concluded that the original BPA model predicts a premature Bauchinger effect, and the creep during long-term dwell is highly overpredicted by the BPA model. Motivated by these experimental findings, an extension for the BPA model will be proposed. Contrary to the BPA-model, in our modified model the chain segment rotation is modeled using two separate dashpots. The internal variables corresponding to the dashpots are denoted by s_1 according to Eq. (8), and a new one by s_2, which is determined as

$$\dot{s}_2 = h_2\dot{\gamma}^p \quad s_2(0) = 0, \quad s = s_1 + s_2, \tag{10}$$

where h_2 is an additional constitutive parameter. The purpose of the extra dashpot is to better capture the unloading behaviour while keeping the model as simple as possible.

4 Model results

We calibrate the extended BPA model to uniaxial compression tests performed by Dreistadt et al. [4]. Single and repeated unloading tests are simulated. During the calibration procedure the Runge-Kutta integration scheme is used to integrate the underlying system of differential equations, now given by Eqs. (3), (9), and (10). Further, during dwell the rate of the nominal stress, $\dot{\boldsymbol{\pi}}$ is constant and we therefore have

$$\dot{\boldsymbol{\pi}} := \frac{d}{dt}(J\boldsymbol{\sigma}\boldsymbol{F}^{-*}) = \boldsymbol{0} \quad \text{or} \quad \dot{\pi}_1^1 = 0 = E\frac{d}{dt}\big(\ln(V_1^{e1,})(V_1^1)^{-1}\big),$$

where E is the Young's modulus. The modified model is calibrated to the experimental data in Dreistadt et al. [4]. The athermal strength s, and its components s_1 and s_2 are depicted in Fig. 1(b). As shown, the new internal variable, s_2 grows with the plastic deformation in quasi monotonic manner and induces the isotropic hardening effect in the model. Also, the maximum level of the backstress prior the unloading is reduced using the modified model, see Fig. 1(a). It

can be concluded that excessive evolution of the backstress leads to an overestimated recovery. As shown in Fig. 1(a), the final simulated strain after 400 days is about 0.52 and 0.062 using the extended and original BPA model respectively. The experimental result is 0.62 according to Dreistadt et al. [4].

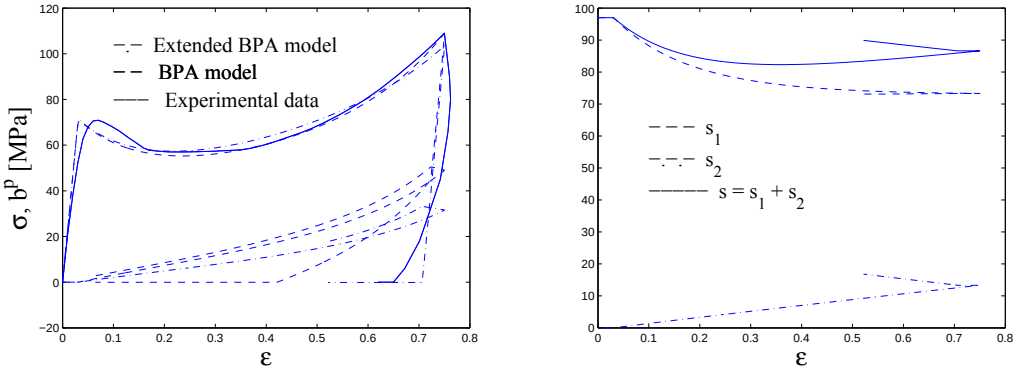

Figure 1: a) True stress and back stress vs. true strain. b) Athermal shear strength s and its components s_1 and s_2 vs. true strain.

Conclusions

The mechanical behavior of polycarbonate (PC) during complex loadings was simulated using the BPA model. It was found that the BPA model could not properly reproduce the long-term behavior. Motivated by that, we have modified the BPA model using an additional viscous dashpot. The purpose of extra dashpot is to better capture the strain softening during unloading and dwell while keeping the model simple; only one new material parameter is required. It was found that our modified model gives a remarkable improvement of the simulated response when compared to the experimental data of long-term dwell and unloadings.

REFERENCES

[1] E.M. Arruda, M.C. Boyce. In Anisotropy and Localization of Deformation (edited by J.-P. Boehler and A.S. Khan), *Elsevier Applied Science, London*, (1991).

[2] E.M. Arruda, M.C. Boyce. Evolution of plastic anisotropy in amorphous polymers during finite straining, *Int. Journal of Plasticity*, **9**:697–720, (1993).

[3] Argon. A.S. Argon, *Phil. Mag.*, **28**:839, (1973).

[4] C. Dreistadt, A-S. Bonnet, P. Chevrier, P. Lipinski. Experimental study of the polycharbonate behaviour during complex loading and comparison with the Boyce, Parks and Argon model predictions, *Materials and Design*, **30**:3126–3140, (2009).

23rd Nordic Seminar on Computational Mechanics
NSCM-23
A. Eriksson and G. Tibert (Eds)

EXACT AND SIMPLIFIED MODELLING OF WAVE PROPAGATION IN CURVED ELASTIC LAYERS

MAZIYAR N. ZADEH[*], SERGEY V. SOROKIN[†]

[*] Research & Development, Product Development
FLSmidth A/S
Vigerslev Allé 77, 2500 Valby, Denmark
e-mail: mnz@flsmidth.com - web page: http://www.flsmidth.com

[†] Department of Mechanical and Manufacturing Engineering
Aalborg University
Pontopiddanstraede 101, 9220 Aalborg East, Denmark
e-mail: svs@me.aau.dk - web page: http://www.me.aau.dk

Key words: Wave guide, Elastodynamics, Asymptotics, Dispersion curves

Summary. This paper is concerned with wave propagation in a curved elastic layer with rectangular cross section. By applying the classical Lamé formulation of displacements, the exact solutions of equations of elastodynamics for such a layer in the plane and antiplane formulations are compared with their counterparts for a straight layer. Simultaneously, the classical Bernoulli-Euler theory for a curved beam is also used in the comparison and the static limit case of the Lamé decomposition is also investigated.

1 INTRODUCTION

In various industrial applications it is necessary to investigate the wave guide properties of circular elastic layer with rectangular cross section. To carry through this task it is reasonable to develop an idealized method where the wave propagation is considered as uncoupled in terms of in-plane and anti-plane[2] motion. This simplification allows for hierarchy of models to be developed and analyzed whilst aiming at a model to describe out-of-plane wave motion.

2 THEORY

The displacement field in an elastic medium can be expressed in terms of longitudinal and transverse motion[1]:

$$\boldsymbol{u} = \boldsymbol{u_l} + \boldsymbol{u_t} \tag{1}$$

Eq. (1) can also be expressed in terms of potentials:

$$\boldsymbol{u} = grad\varphi + curl\boldsymbol{\psi} \tag{2}$$

Wherein φ and $\boldsymbol{\psi}$ are scalar and vector potentials, respectively.

3 THE ANALYSIS

3.1 Exact solution for in-plane wave motion for straight and curved layer

By applying Eq. (2) to derive an expression for the displacement and stress field in cylindrical coordinates[4], it is possible formulate the dispersion equation for the straight and curved elastic layer, See Figure 1, with the application of different boundary conditions.

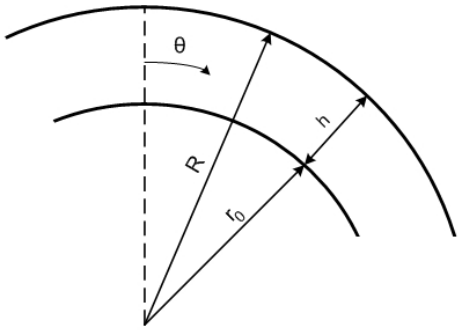

Figure 1: Curved layer

Figure 2 and Figure 3 are showing the dispersion curves for in-plane wave motion for the straight and curved elastic layer, respectively, in plane strain formulation.

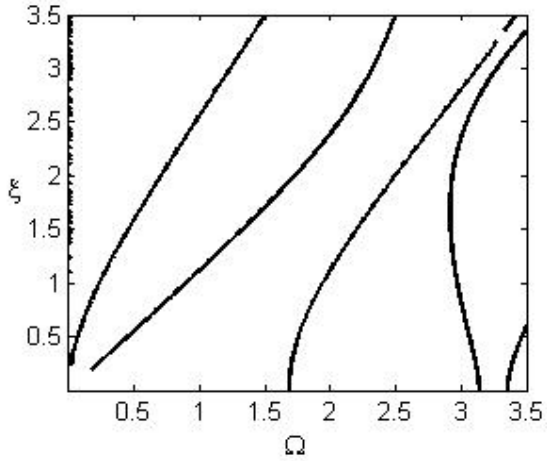

Figure 2: Dispersion curve for a straight elastic layer with free boundaries

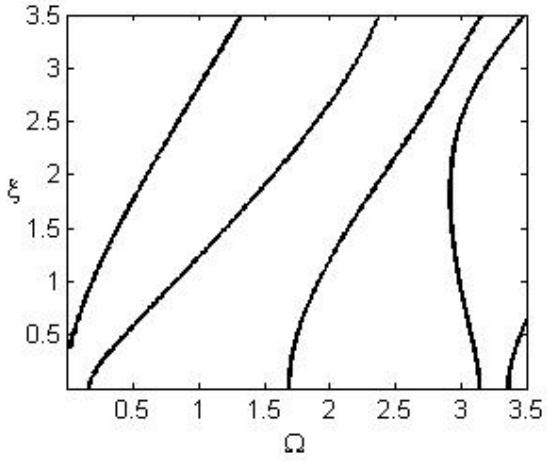

Figure 3: Dispersion curve for a curved elastic layer with free boundaries and a ratio r_0/h=5

As it is observed, there is a good agreement between the dispersion curves for the two different cases even though the ratio r_0/h is small.

3.2 Exact solution for curved layer and curved beam theory

To further analyze the exact solution of the dispersion equation for the curved layer the classical Bernoulli-Euler beam theory is applied[3]. Figure 4 and Figure 5 illustrate the dispersion curves for low and high frequency range, respectively, for r_0/h=5 where Ω is the non-dimensional frequency and ξ is the non-dimensional wave number.

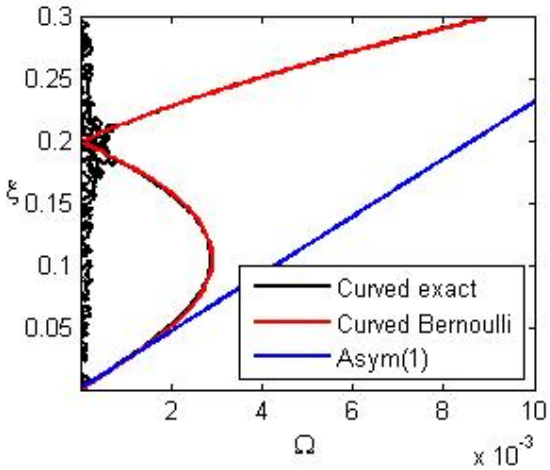

Figure 4: Dispersion curves, low frequency range

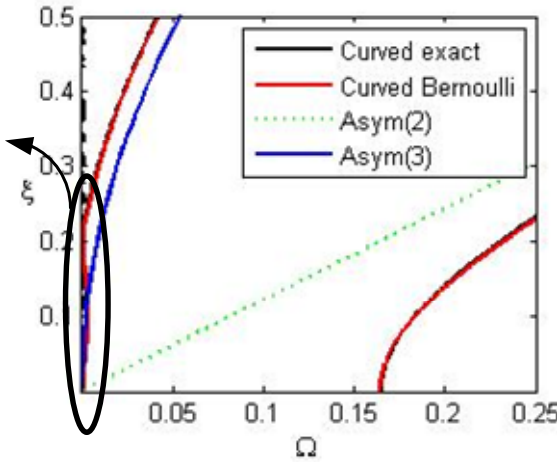

Figure 5: Dispersion curves, low frequency range

Both figures show good agreement between the exact and curved beam solution. The blue line on Figure 4 is the low frequency asymptotic expansion of the form $\xi = 2\sqrt{3}\kappa\Omega$, where $\kappa = \frac{c_l}{c_0}$, c_l is the longitudinal wave speed and $c_0 = \sqrt{\frac{E}{1-\nu^2}}$. On Figure 5 the dottet line represents the high frequency asymptotic for the longitudinal wave which has the form $\xi = \kappa \times \Omega$ and the blue line represents the high frequency asymptotic for the flexural wave in the form $\xi = \sqrt{2\sqrt{3}\kappa\Omega}$. The imperfections on Figure 4 at the low frequencies appear due to numerical instability. It indicates that the Lamé decomposition fails at the static limit.

3.3 Anti-plane

So far in-plane waves have been investigated in plane strain formulation. As the aim of the research project is to formulate the out-of plane waves, the first step is to consider the anti-plane problem formulation. Firstly, the waves are considered as uncoupled, which allows to reduce the expression for the displacement field to only depend upon one scalar potential instead of four as shown in Eq. (1).

The wave motion in the anti-plane problem formulation for the curved layer is a shear wave propagating along the curvature, see Figure 6. Displacements occur in the out-of-plane x-direction, but these are independent on the same coordinate and instead dependent upon the coordinates perpendicular to the x-direction(in-plane coordinates). The latter description is exactly the definition of shear wave motion in anti-plane problem formulation.

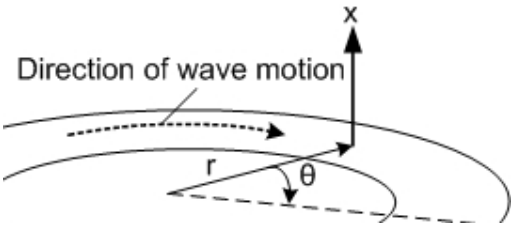

Figure 6: Wave direction

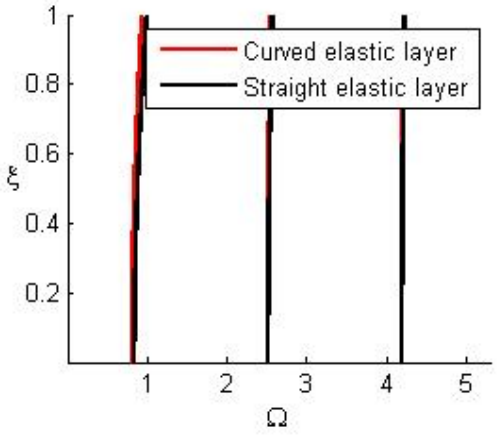

Figure 7: Dispersion curves, anti-plane

Figure 7 illustrates a comparison of the dispersion curves for shear waves in a straight and a curved layer with r_0/h=5, where mixed boundary conditions are introduces. Thereby, it is stated that there is a good agreement between the two cases also with anti-plane problem formulation.

4 CONCLUSION

Based on the comparison of dispersion curves for the straight and curved elastic layer it is concluded the difference is negligible even for relatively large curvatures both in plane and anti-plane formulation. The classical curved beam theory is validated by comparison with the exact solution.

Further work on the low frequency limit for the exact solution should be carried through by applying asymptotic analysis. This is to avoid the numerical instability which occurs when frequency tends to 0.

As an extension to this work, it should be aimed to obtain the dispersion curves with the Wave Finite Element Method(WFE) and compare these with the exact solution. Thereby, a WFE model can be tuned and applied for situations where analytical solutions would not be possible to carry through.

REFERENCES

[1] L.M., Brekhovskikh et. al., *Mechanics of Continua and W ave Dynamics 2nd Ed.* , Springer-Verlag, Berlin Heidelberg New York, 1994.

[2] C. O. Horgan,"Anti-Plane Shear Deformation in Linear and Nonlinear Solid Mechanics, Siam Review, Vol. 37, pp. 53-81, No. 1(Mar., 1995)

[3] A. Soe-Knudsen et. al., "Modelling of linear wave propagation in spatial fluid filled pipe systems consisting of elastic curved and straight elements", JSV 329, 2010

[4] L.I. Slepyan, *Elastic Waves*, Sudostroenie, Leningrad, 374p, 1972, in Russian.

23rd Nordic Seminar on Computational Mechanics
NSCM-23
A. Eriksson and G. Tibert (Eds)

MODELING RESIN FLOW AND PREFORM DEFORMATION IN COMPOSITES MANUFACTURING BASED ON PARTIALLY SATURATED POROUS MEDIA THEORY

MOHAMMAD S. ROUHI*, RAGNAR LARSSON†, MACIEJ WYSOCKI††

*Department of Applied Mechanics, Chalmers University of Technology, SE-412 96 Göteborg,Sweden, e-mail: mohammad.rouhi@chalmers.se

†Department of Applied Mechanics, Chalmers University of Technology, SE-412 96 Göteborg,Sweden, e-mail: ragnar@chalmers.se

††Swerea-Sicomp, P.O. Box 104, 431 22 Mölndal, Sweden, e-mail: maciej.wysocki@swerea.se

Key words: Liquid Resin Infusion (LRI), Resin Transfer Molding (RTM), Free Surface, Porous Medium, Saturation

Summary. In this contribution a generic algorithm to simulate resin infusion in composites manufacturing technologies such as Liquid Resin Infusion (LRI) and Resin Transfer Molding (RTM) is developed. The most important challenge to be addressed is the migration of free surface due to resin infiltration into the highly deformable fibrous preform. To do so, a compressible two-phase porous media formulation is put forward for the problem formulation and a staggered finite element based solution procedure is advocated for the total solution advancement. The approach automatically monitors the free surface, whereby the monitoring of the resin front migration using e.g. level set or front tracking control is completely avoided. The method is exemplified using a hat stringer geometry considering both manufacturing methods.

1 INTRODUCTION

The use of advanced composite materials is now increasing dramatically. Having previously been used predominately in low-volume high-cost products, such as spacecraft and military aircrafts, composite materials are now being introduced on a large scale in commercial aircrafts. This progress requires that new composites manufacturing technologies are developed and industrialized. In particular, Liquid Resin Infusion (LRI) and Resin Transfer Molding (RTM) are the two composites manufacturing methods that have shown great potential for near future. In the process simulation of these technologies the infiltration of resin into a deformable fibrous preform is governed by the theory of porous media. The background theory behind this approach has been developed during almost a century[1]. The main challenge in the present development concerns tracking the flow front in combination with modeling of a deformable fibre bed during the process. There are number of different methods used to trace the flow front, those are moving and fix mesh methods, level-set, control volume (CV) and marker method. The present

development is inspired by the CV method, however the method is improved by defining control volumes by finite elements themselves (CV-FEM) instead of by Voronoi cells[2]. The development by Tucker et al.[2] is further improved accounting for deformable solid and compressible liquid.

The goal of this paper is to combine the theories of porous media and the concept of hyper-elasticity with respect to resin infusion problem together with the CV-FEM. Therefore by focusing on essential properties such as liquid permeability and preform mechanics, the developed biphasic continuum mechanical model accounts for all the relevant physical properties.

2 GOVERNING EQUATIONS AND FEM SOLUTION

To formulate the coupled problem of partially fluid saturated solid, mass balance and momentum balance is used

$$\rho^f \nabla \cdot \boldsymbol{v} + n^f \dot{\rho}^f = -\nabla \cdot \left(\rho^f \boldsymbol{v}^d\right), \tag{1}$$

$$(\boldsymbol{\sigma}^s + \boldsymbol{\sigma}^f) \cdot \nabla + \hat{\rho}\boldsymbol{g} = 0 \quad \forall \boldsymbol{x} \in B. \tag{2}$$

together with the Darcy law,

$$\boldsymbol{v}^d = -(\frac{k}{\mu}\mathbf{1}) \cdot \boldsymbol{\nabla} p, \tag{3}$$

where μ is the liquid viscosity, and k is the permeability modeled using Kozeny-Carman like equation developed in Larsson et al.[3]

The governing equations are now solved by deriving weak form of (1) and (2)

$$\int_{B_0} (\boldsymbol{\tau} - Jp\mathbf{1}) : \boldsymbol{l}[\boldsymbol{w}]\, dV = \int_{\Gamma_0} \boldsymbol{w} \cdot \bar{\boldsymbol{t}_1}\, d\Gamma + \int_{B_0} \hat{\rho}\boldsymbol{w} \cdot \boldsymbol{g}\, dV \quad \forall \boldsymbol{w} \in P, \tag{4}$$

$$\int_{C_0} \boldsymbol{\tau} : \boldsymbol{l}[\boldsymbol{w}]\, dV = \int_{\Gamma_0} \boldsymbol{w} \cdot \bar{\boldsymbol{t}_1}\, d\Gamma + \int_{C_0} \hat{\rho}\boldsymbol{w} \cdot \boldsymbol{g}\, dV \quad \forall \boldsymbol{w} \in P, \tag{5}$$

$$\int_{B_0} \eta\rho^f \dot{J} dV + \int_{B_0} \eta J n^f \dot{\rho}^f dV - \int_{B_0} J\rho^f (\nabla\eta) \cdot \boldsymbol{v}^d dV = -\int_{\Gamma_0} \eta Q d\Gamma \quad \forall \eta \in S, \tag{6}$$

solving them by finite element approximation

$$\left[\delta\hat{\boldsymbol{u}}^t, \delta\hat{\boldsymbol{p}}^t\right] \overset{\text{NEL}}{\underset{e=1}{\mathbb{A}}} \begin{bmatrix} \boldsymbol{b}_e - \boldsymbol{f}_e^{\text{ext}} \\ \boldsymbol{c}_e \end{bmatrix} = 0, \tag{7}$$

and the Newton iteration for balancing of the FE-discretized nodal forces[3].

3 CONSTITUTIVE EQUATIONS

Assuming a hyper-elastic response, the constitutive state equation of the solid reads as

$$S = 2\hat{\rho}_0^s \frac{\partial \psi}{\partial \boldsymbol{C}}, \tag{8}$$

where $\boldsymbol{S} = \bar{\boldsymbol{S}} - J\boldsymbol{C}^{-1}p$ is the consequent effective second Piola Kirchhoff stress in the region due to the Terzahgi effective stress principle, and p is the intrinsic fluid pressure.

Assuming that the same pressure p prevails in the liquid and gas constituent, the fluid pressure may be modeled using the ideal gas law (or the Boyle-Mariotte's law). The linearized response of the gas phase may be represented as

$$\dot{\rho}^f = \frac{\dot{p}}{K^f} \quad \text{with} \quad K^f[p;\xi] = \frac{R\theta}{m^g}\frac{(1-\log[1-\xi]\frac{m^g}{R\theta}\frac{p}{\rho^l})^2}{1-\log[1-\xi]}, \tag{9}$$

where K^f is the compression modulus of the liquid-gas mixture and the parameter $0 \leq \xi \leq 1$ representing the saturation degree.

4 MODELING FLOW FRONT TRACKING

The traction continuity considered across the flow front boundary is used to formulate the coupled problem between two different continua; the fluid saturated one and the non-saturated one-phase continuum. The location of the boundary is determined in a staggered fashion based on the numerical solution to momentum and mass balance relations, providing e.g. $\boldsymbol{v}^f$, with respect to a *given boundary*.

An element based approach is adopted for the motion of the flow front[3], where migration of the boundary is dictated by the temporal saturation increase induced by the fluid front velocity. Hence, no tracking procedure is required in order to determine the location of the flow front boundary. The approach consists of the assessment of the saturation degree ξ, with respect to the liquid saturation of a finite element. The elementwise saturation degree is obtained as $\xi_e = \frac{M^l_{\text{se}}}{M^l_e}$, $e = 1, 2, ..., NEL$ where M^l_{se} is the element stored fluid mass and M^l_e as the total fluid mass. Thus by integration over time and elements we have

$$\xi_e[t] = -\frac{1}{\int_{B_e} n_0\, dV}\int_0^t \int_{B_{0e}} J\left(\nabla\cdot\left(\xi\frac{n_0+J-1}{J}\boldsymbol{v}\right)+\nabla\cdot\boldsymbol{v}^d\right)dV\,dt \tag{10}$$

5 NUMERICAL RESULT

Indeed, the fluid front tracking is an important issue in composite manufacturing simulations, even for injection phenomena without the influence of the preform deformation. Hence, we consider a hat stringer in liquid resin infusion and also in resin transfer molding, which is of relevance in aerospace industry. Stringers, and in particular hat stringer reinforced composites structures, are typically used to prevent skin buckling to increased compression strength and reduced component weight.

Results are shown in figure 1 with the saturation degree and pressure distribution taken when the flow reaches the same location in both processes. It is indicated that the generic algorithm can be applied to both infusion and RTM simulation. The process time for infusion is about 8.3 minutes while for RTM process it takes longer time to complete and it is about 40 minutes. Clearly the advancement of the flow front during the both processes is reflected, while for the infusion the preform deformation is also calculated.

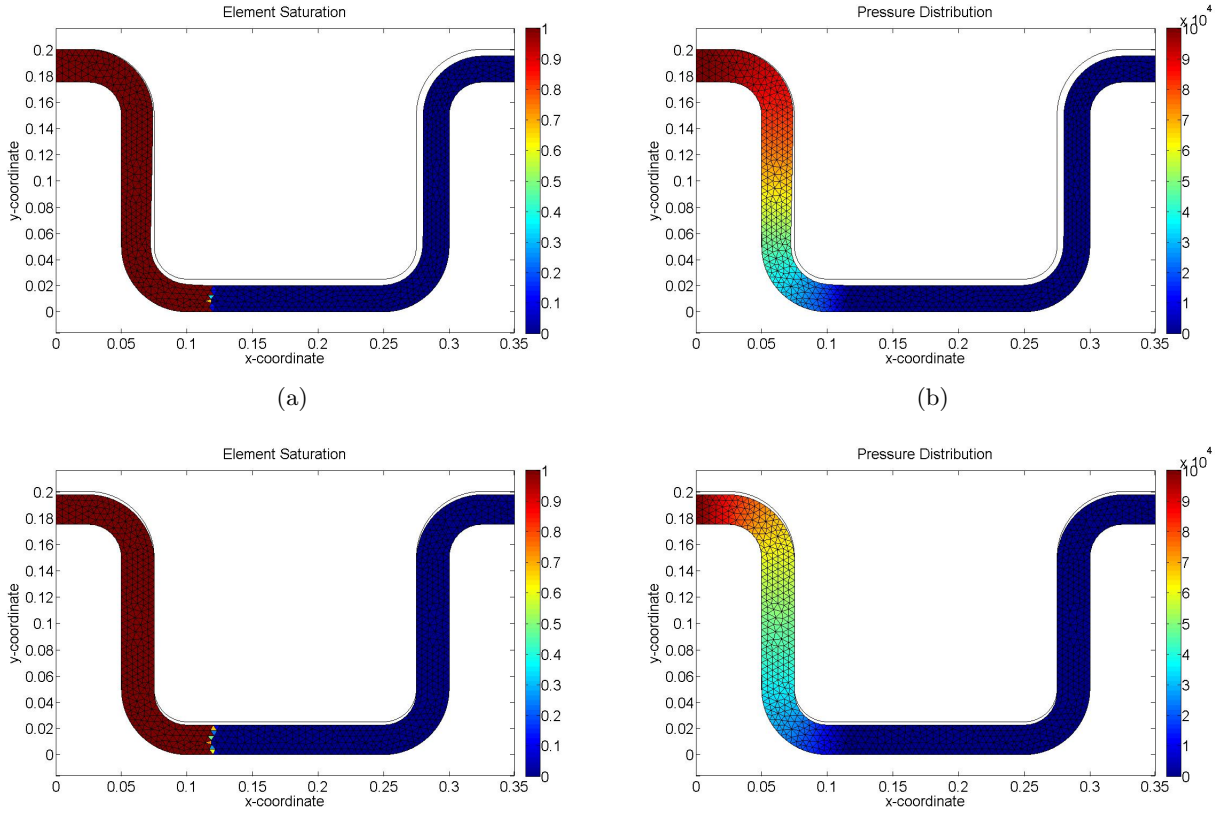

Figure 1: Infusion, saturation (a) and pressure distribution (b) after 0.2 minutes and Resin Transfer Molding, saturation (c) and pressure distribution (d) after 1 minutes from FE-simulation.

REFERENCES

[1] de Boer, R. Highlights in the historical development of the porous mediatheory: Toward a consistent macroscopic theory. *Appl. Mech. Rev* **49**, 201–261 (1996).

[2] Virlouvet, P. & Tucker, C. L. Volume conserving finite elements for molding filling simulations. *Proc. Polymer Processing Society 7th Ann. Meet.* (1991).

[3] Larsson, R., Rouhi, M. & Wysocki, M. Resin flow and preform deformation in composites manufacturing based on a partially saturated porous medium. *European Journal of Mechanics, A/Solids* **Submitted** (2010).

23rd Nordic Seminar on Computational Mechanics
NSCM-23
A. Eriksson and G. Tibert (Eds)

PREDICTION OF THE STIFFNESS OF SHORT FLAX FIBER REINFORCED COMPOSITES BY ORIENTATION AVERAGING

J. MODNIKS AND J. ANDERSONS

Institute of Polymer Mechanics
University of Latvia
23 Aizkraukles iela, LV-1006 Rīga, Latvia
e-mail: janism@pmi.lv, web page: http://www.pmi.lv

Key words: natural fibers; polymer composite; stiffness; orientation averaging.

Summary. Flax fibers, which are being used as reinforcement in polymer matrix composite materials, exhibit highly anisotropic elastic properties due to their complex internal structure. The mechanical properties of fibers can be evaluated by mechanical models reflecting the principal morphological features of fibers. Such a FEM model is applied to estimate the elastic properties of a unit cell of a short-fiber reinforced composite, an elementary flax fiber embedded in a polymer matrix. Orientation averaging approach is used for prediction of the stiffness of short flax fiber reinforced polymer matrix composite. The numerical estimates of Young's modulus are compared to the test results of short fiber flax/poly(ε-caprolactone) composite.

1 INTRODUCTION

Flax, as well as other bast fibers, is increasingly being used as reinforcement of short-fiber/polymer matrix composites manufactured by such production methods as extrusion, resin transfer molding, injection molding etc. The elastic properties of short-fiber composites can be related to fiber and matrix characteristics by models of different complexity. However, an elementary rule-of-mixtures prediction of the Young's modulus is almost exclusively employed for short bast fiber reinforced composites. It is probably related to the scarcity of experimental data of the elastic properties of fibers. However, fiber properties can also be estimated by mechanical models.

In this study, orientation averaging approach is used in prediction of the characteristics of elasticity of short flax fiber reinforced polymer matrix composite. Elastic properties of a unit cell of such composites, an elementary flax fiber embedded in a polymer matrix, are determined numerically, by a FEM model accounting for the principal features of the structure of the fiber. Thus the anisotropy of flax fiber is incorporated in the mechanical response of the unit cell (UC). The model estimates of Young's modulus are compared to the test results of flax/poly(ε-caprolactone) composite.

2 NUMERICAL MODELING OF STIFFNESS

In the subsequent Sections, models of a flax fiber and a unit cell of short fiber reinforced composite are presented, and the orientation averaging procedure for evaluation of composite stiffness described.

2.1 Fiber model

An elementary flax fiber was modeled as a cylindrical body[1]. Its morphological layers were re-grouped for mechanical analysis, resulting in a three-layer cylinder with a lumen. The lumen radius was selected so that the lumen accounted for 1.5 % of the fiber cross-section area. The outer and inner model layer, L1 and L3, thickness was selected at 1 % of the fiber radius. The middle layer (L2) was treated as a unidirectional cellulose fibril composite, with reinforcement direction along a helix at a fixed angle to the fiber axis.

2.2 Unit cell of the composite material

A single fiber embedded in a block of polymer matrix, Fig. 1, was chosen as a UC of short fiber-reinforced composite material. The matrix was assumed to cover the fiber so that the surfaces of the UC were at the same distance, *c*, from fiber surface, see Fig. 1. Then the fiber volume fraction μ is related to fiber length *h* and radius *r* as follows:

$$\mu = \frac{h\pi r^2}{4(h+2c)(r+c)^2} \tag{1}$$

Treating the UC as a transversally isotropic material, its effective technical constants of elasticity are determined via strain energy of the UC under selected loading modes as detailed elsewhere[1].

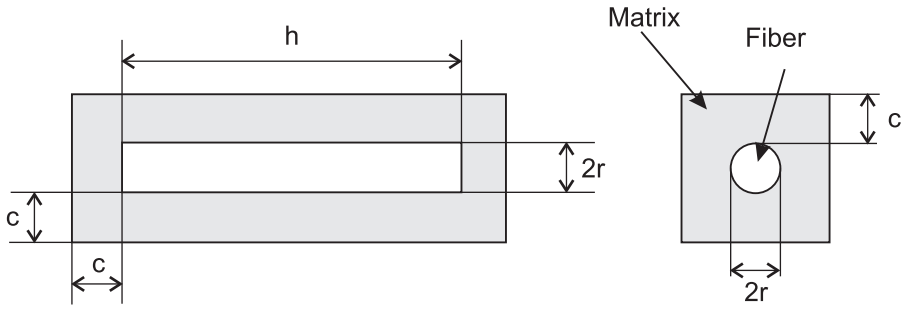

Fig. 1. Unit cell of a short-fiber reinforced composite.

2.3 Orientation averaging of stiffness

Having determined the components of the stiffness tensor C^*_{ijkl} using the technical constants of elasticity, obtained for UC, the stiffness tensor of a fiber-reinforced composite material can be approximately evaluated by orientation averaging of C^*_{ijkl}.

Denoting the distribution density of fiber orientation in the composite by $p(\alpha,\beta)$, where α, β are the elevation and azimuthal angles, composite stiffness C_{ijkl} is expressed as follows (see e.g. [2])

$$C_{ijkl} = \iint C^*_{ijkl}(\alpha,\beta)p(\alpha,\beta)\sin\alpha\, d\alpha\, d\beta \tag{2}$$

where $C^*_{ijkl}(\alpha,\beta)$ designates the stiffness tensor components, in a frame of reference associated to the composite material, of a UC with the principal material axis aligned with the direction given by α, β.

In the case of uniform fiber direction distribution, Eq. (2) takes the form[2]

$$C_{ijkl} = \frac{1}{30}[2(2(C^*_{mmnn} - C^*_{mnmn})\delta_{ij}\delta_{kl} + (3C^*_{mnmn} - C^*_{mmnn})(\delta_{ik}\delta_{jl} + \delta_{i,l}\delta_{jk})] \quad (3)$$

where δ_{ij} is the Kronecker's delta.

3 RESULTS AND DISCUSSION

Finite element modeling of fiber and unit cell was performed using finite element software package ABAQUS. Standart 20-node quadratic brick elements C3D20 were used.

Flax fiber layers L1 and L3 were modeled as an isotropic material with lignin properties. The layer L2 was considered as a unidirectionally reinforced cellulose fibril/lignin matrix composite[1].

To evaluate the longitudinal modulus of the elementary flax fiber, the FEM model of the fiber with length to diameter ratio of 12.5 was loaded by a stress applied in longitudinal direction. Twisting of the fiber was not restricted. The model was calibrated by varying the angle φ of the principal direction of L2 layer with respect to fiber axis until the fiber effective modulus agreed with the average experimental value for ArcticFlax[1] of 69 GPa. This way, it was determined that $\varphi = 7.25°$.

The experimental data of short fiber flax/poly(ε-caprolactone) composite[3] were used to verify the method. The procedure of composite properties prediction was performed in two steps. The first step was calculation of UC properties by the finite element model, using different loading scenarios[1]. The second step was evaluation of Young's modulus and Poisson's ratio of short flax fiber/poly(ε-caprolactone) composite by means of the averaging formula (3) which assumes random orientation fibers.

Young's modulus of poly(ε-caprolactone) matrix was 185 MPa as determined experimentally[3]. Poisson's ratio of the matrix $\nu = 0.3$ was assumed. Since the data concerning average fiber length in flax/poly(ε-caprolactone) composite were not available, this parameter was assessed by varying length of fiber in the unit cell until the predicted Young's modulus of a composite with fiber volume fraction 0.13 was the same as the average experimental stiffness. This way, the fiber length was estimated at 0.72 mm which corresponds to length/diameter ratio 45 (for ArcticFlax fiber diameter of 16 μm). The stiffness calculations were performed for fiber volume fractions 0.2, 0.29, 0.38 and 0.48.

The obtained results (Fig. 2) show good agreement with experimental Young's modulus for fiber volume fractions up to 0.3. For higher fiber volume fractions, calculated modulus becomes considerably higher than the experimentally determined one. This disagreement stems from the choice of unit cell, which should be altered to better reflect the interaction of fibers at relatively high fiber volume fractions. Nevertheless, the proposed model provides accurate estimates of stiffness of short flax fiber reinforced composites at relatively low fiber volume fractions, up to $\mu \sim 0.3$, as suggested by the present results and previous research[1].

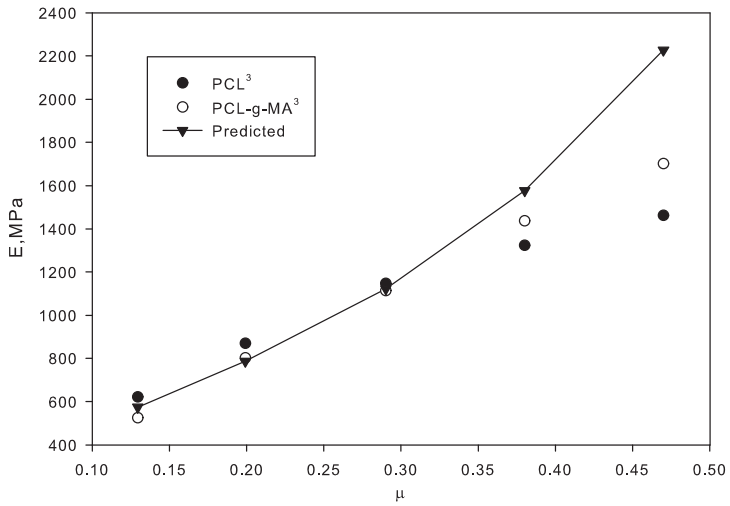

Fig. 2. Young's modulus of short flax fiber reinforced poly(ε-caprolactone) composite as a function of fiber volume fraction.

4 CONCLUSIONS

- A method to estimate the stiffness of short-natural-fiber composites is proposed. It consists of two steps: first, elastic properties of a unit cell with the appropriate fiber volume fraction are determined using FEM; second, the averaging procedure is applied to obtain elastic properties of randomly oriented short fiber composite.
- The predicted stiffness agrees reasonably well with the experimental results up to fiber volume fraction 0.3. For higher volume fractions, the discrepancy of calculated values and experimental data becomes considerable. This disagreement is likely to be related to the choice of the unit cell, which should be altered to better reflect the interaction of fibers in a composite.

ACKNOWLEDGEMENTS

This work has been funded by the ESF via project 2009/0209/1DP/1.1.1.2.0/09/APIA/VIAA/114.

REFERENCES

[1] J. Modniks and J. Andersons, "Modeling elastic properties of short flax fiber reinforced composites by orientation averaging", Submitted to *Comput. Mater. Sci.*

[2] A. Lagzdins and R.D. Maksimov, E. Plume, "Anisotropy of elasticity of a composite with irregularly oriented anisometric filler particles", *Mech. Compos. Mater.*, **45**, 345-358 (2009).

[3] A. Arbelaiz, B. Fernández, A. Valea and I. Mondragon, "Mechanical properties of short flax fibre bundle/poly(ε-caprolactone) composites: Influence of matrix modification and fibre content", *Carbohydr. Polym.*, **64**, 224–232 (2006).

23rd Nordic Seminar on Computational Mechanics
NSCM-23
A. Eriksson and G. Tibert (Eds)

COMPUTATIONAL MODELING OF THE INTERLAMELLAR SPACING IN PEARLITIC STEEL

ERIK LINDFELDT*, MAGNUS EKH AND HÅKAN JOHANSSON

Department of Applied Mechanics
Chalmers University of Technology
Gothenburg, Sweden
e-mail: erik.lindfeldt@chalmers.se, web page: http://www.chalmers.se/am/EN/

Key words: Crystal plasticity, gradient hardening, pearlitic steel, lamella distance

Summary. In this contribution, modeling and numerical aspects of gradient crystal plasticity applied to pearlitic steel will be discussed. The goal is to capture the influence of the cementite lamella spacing on the mechanical response.

1 INTRODUCTION

On the microscopic scale, pearlite is a two-phase material with hard and brittle cementite lamellas that are embedded in a softer ferrite matrix. In each pearlite colony the cementite has a preferred direction, whereas the crystallographic directions for the ferrite are the same within a nodule. An important microstructural property of a pearlitic steel is the distance between the cementite lamellas, i.e. the interlamellar spacing. It is well-known from experiments [1,2] that a decreased interlamellar spacing results in an increased strength of the material.

In this contribution, different modeling assumptions for predicting the dependence of the interlamellar spacing will be discussed. The model adopted for the ferrite is based on crystal plasticity with gradient hardening [3,4] to predict size-dependent response for single-phase polycrystals. Here, an existing model framework [4] will be used but extended to include more advanced modeling of the hardening [5].

In a pearlitic steel, different types of boundaries between the pearlite colonies exist: boundaries between the ferrite and the cementite, boundaries between colonies with the same crystal orientation (i.e. inside a nodule) and boundaries between colonies with different crystal orientation (i.e. between colonies). Clearly, the appropriate choice of boundary conditions for the plastic slip will depend on the type of boundary. The influence of different boundary conditions will be shown in terms of the plastic slip field as well as the homogenized stress-strain response of the grain structure.

Another modeling issue pertains to the particular fashion in which the macroscopic deformation gradient is mapped to displacement boundary conditions on the RVE. Clearly, choosing an entirely unrestricted fluctuation field is beneficial in the sense that fast convergence is expected

for increasing RVE-size, i.e the number grains can be kept small. However, in order to limit the computational effort it is common to employ some sort of Taylor assumption for the displacement field. A possible approach, which is investigated in this paper, is to compute the diplacements along the grain boundaries from the macroscopic deformation gradient in the "Taylor spirit". Whatever the choice, it is always necessary to solve the boundary value problems for the plastic slip fields including the gradient effect. The adopted algorithm employs the so-called dual-mixed FE formulation[4].

Clearly, this type of problem comprises several length scales within which certain mechanisms occur. These length scales are schematically described, for a pearlitic steal, in the figure below.

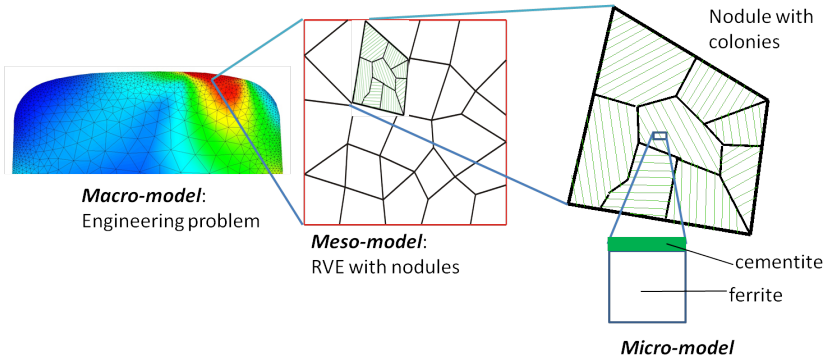

Figure 1: Modelling approach: from macro to micro level

2 Preliminary results

The following results were obtained using a mesomodel consisting of 1 nodule with 7 colonies, all with different lamella orientations. Using the Taylor assumtion (constant strain field) at the meso level means that the constitutive response only needs to be solved once per colony. For the results presented below it is assumed that the meso domain is loaded by simple shear. The figure below shows the shear component, σ_{12}, of the homogenised meso stress for three different sizes of the micro model.

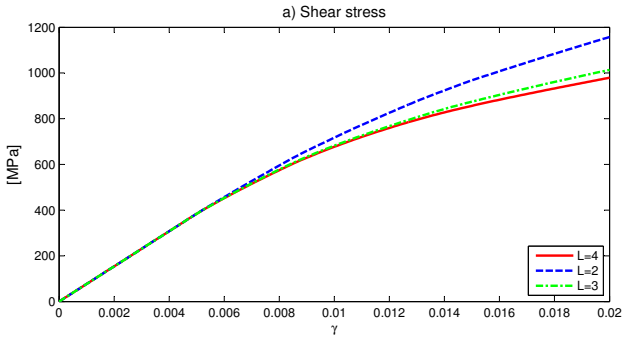

Figure 2: Homogenised meso response, σ_{12}, for different values of L

REFERENCES

[1] Modi, O. *et al.* Effect of interlamellar spacing on the mechanical properties of 0.65% c steel. *Materials Characterization* **46**, 347–352 (2001).

[2] Allain, S. & Bouaziz, O. Microstructure based modeling for the mechanical behavior of ferrite-pearlite steels suitable to capture isotropic and kinematic hardening. *Materials Science and Engineering A* **496**, 329–336 (2008).

[3] Evers, L., Brekelmans, W. & Geers, M. Scale dependent crystal plasticity framework with dislocation density and grain boundary effects. *International Journal of Solids and Structures* **41**, 5209–5230 (2004).

[4] Ekh, M., Grymer, M., Runesson, K. & Svedberg, T. Gradient crystal plasticity as part of the computational modelling of polycrystals. *International Journal for Numerical Methods in Engineering* **72**, 197–220 (2007).

[5] Ekh, M., Lillbacka, R. & Runesson, K. A model framework for anisotropic damage coupled to crystal (visco)plasticity. *International Journal of Plasticity* **20**, 2143–2159 (2004).

23rd Nordic Seminar on Computational Mechanics
NSCM-23
A. Eriksson and G. Tibert (Eds)

ON THE MODELING OF DEFORMATION INDUCED ANISOTROPY OF PEARLITIC STEEL

N. LARIJANI, M. EKH, G. JOHANSSON AND E. LINDFELDT

Department of Applied Mechanics
Chalmers University of Technology, Gothenburg, Sweden
e-mail: nasim.larijani@chalmers.se

Key words: Plasticity, anisotropy, pearlitic steel, homogenization

Summary. A micromechanically based plasticity model for modeling of anisotropy in pearlitic steel is investigated. The model was proposed in Johansson and Ekh [1] and takes into account large strains as well as deformation induced anisotropy. The initially randomly oriented cementite lamellae in the pearlitic steel will tend to align with the deformation which causes a development of anisotropy.

1 INTRODUCTION

Pearlite is a two-phase material where each grain has a preferred direction that is determined by the cementite lamellae. The hard and brittle cementite lamellae are embedded in a softer ferrite matrix. Each grain can be considered to be transversally isotropic. The initial random orientation of the cementite lamellae gives an isotropic pearlitic material. After shear deformation, the orientations of individual grains tend to align with each other which causes a development of anisotropy. In this contribution, the modelled anisotropy on the macroscopic length scale is obtained from homogenization procedures of a micromechanical model of "crystal plasticity"-type, proposed in Johansson and Ekh [1], of the pearlitic microstructure. In this model the plasticity is assumed to be driven by shear stress of the ferrite between the cementite lamellae, and the re-orientation of the cementite lamellae is assumed to be of areal-affine type, cf. Dafalias [2] Through the homogenization procedure all grains in the microstructure are assumed to be subjected to the same deformation gradient and the yield function of the grains have been replaced by a macroscopic yield function motivated from the micromechanical yield function. The macroscopic yield function is calculated by spherical integrations using an integration formula proposed by Bažant and Oh [3]. Finally, results showing the development of the yield surface, the reorientation of cementite lamellae and the macroscopic stress-strain response are given.

2 MICRO-MACROMECHANICAL MODEL

The point of departure is the micromechanical yield function Φ_μ which is formulated as follows:

$$\Phi_\mu = \tau_\mu^2 - Y_\mu^2 \tag{1}$$

where Y_μ is the yield stress (taking into account hardening), and τ_μ is the projected shear stress on the cementite lamella plane (or rather the ferrite in between the cementite lamellae) defined as:

$$\tau_\mu = \boldsymbol{\tau}_\mu : [\boldsymbol{m}_\mu \otimes \boldsymbol{n}_\mu] \,. \tag{2}$$

In this expression we introduced the Kirchhoff stress $\boldsymbol{\tau}_\mu$ and the normal to the cementite lamella $\boldsymbol{n}_\mu$. Further, the direction $\boldsymbol{m}_\mu$ is defined as the closest projection of the traction stress $\boldsymbol{t}_\mu = \boldsymbol{\tau}_{\mu,} \cdot \boldsymbol{n}_\mu$ onto the cementite lamella plane.

The evolution of the cementite lamellae is assumed to be of an areal affine type determined by the deformation gradient, i.e.

$$\boldsymbol{n}_\mu = \frac{\boldsymbol{F}_\mu^{-\mathrm{t}} \cdot \boldsymbol{n}_{\mu,0}}{|\boldsymbol{F}_\mu^{-\mathrm{t}} \cdot \boldsymbol{n}_{\mu,0}|} \tag{3}$$

with $\boldsymbol{n}_{\mu,0}$ being the initial normal to the cementite lamellae. We also propose to adopt an isotropic elastic law of Neo-Hooke type, an associative type of evolution law for the plastic deformation gradient, and a nonlinear hardening of the yield stress Y_μ.

To compute the response of a microstructure of pearlitic steel for a given macroscopic deformation gradient, a finite element analysis using the micromechanical model summarized above with proper boundary conditions can be performed.

We homogenize the micromechanical yield function Φ_μ to motivate a macroscopic yield function Φ as

$$\Phi = \Big[\mathrm{tr}\Big(\boldsymbol{a} \cdot \boldsymbol{\tau}^2\Big) - \boldsymbol{\tau} : \mathbf{B} : \boldsymbol{\tau}\Big] - Y^2, \tag{4}$$

with

$$\boldsymbol{a} = \langle\, \boldsymbol{a}_\mu \,\rangle = \langle\, \boldsymbol{n}_\mu \otimes \boldsymbol{n}_\mu \,\rangle \;, \quad \mathbf{B} = \langle\, \boldsymbol{a}_\mu \otimes \boldsymbol{a}_\mu \,\rangle \,. \tag{5}$$

The current macroscopic yield stress Y takes hardening and lamella distance into account as discussed in Allain and Bouaziz [4]. The computational homogenization procedure to obtain the quantaties $\boldsymbol{a}$ and $\mathbf{B}$ is to carry out an integration over a unit sphere. In order to save the computational time an integration formula proposed in Bažant and Oh [3] was employed. A good example of integration over a unit sphere using the corresponding formula can be found in Miehe et.al. [5].

3 RESULTS

A technical application of pearlitic steel is in heavily drawn cords used for suspension of bridges. The required cold deformation of pearlitic wires is called wire-drawing in the literature. Assume that an initially isotropic material is subjected to a severe uniaxial tension (wire-drawing). In Figure 1 we illustrate the stress response of the model when the pearlitic wire is drawn to a diameter 0.7 of its initial diameter. For this case, where we have assumed no isotropic hardening.

The reorientation of the normals of cementite lamellea for the corresponding loading type is shown in Figure 2.

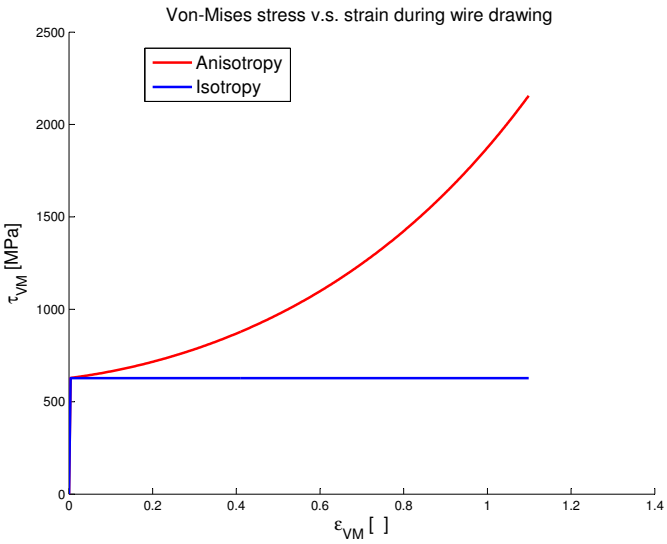

Figure 1: The stress-strain curve of pearlitic steel during wire drawing obtained from the model (comparing the result with evolution of anisotropy and without)

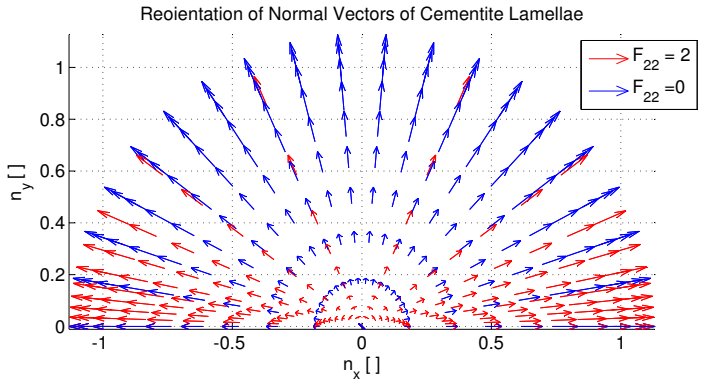

Figure 2: Reorientation of normals of cementite lamellae

REFERENCES

[1] G. Johansson and M. Ekh, On the modeling of evolving anisotropy and large strains in pearlitic steel, *European Journal of Mechanics/A Solids*, 15, 1041-1060, 2006.

[2] Y.F. Dafalias, Orientation distribution function in non-affine rotations, *Journal of Mechanics and Physics of Solids*, 49, 2493-2516, 2001.

[3] Z.P. Bažant and B.H. Oh, Efficient numerical integration on the surface of a sphere, *Zeitschrift für angewandte mathematik und mechanik*, 66, 37-49, 1986.

[4] S. Allain and O. Bouaziz, Microstructure based modeling for the mechanical behavior of ferrite-pearlite steels suitable to capture isotropic and kinematic hardening, *Materials Science and Engineering A*, 496, pp. 329-336, 2008.

[5] C. Miehe, S. Goktepe and F. Lulei, A micro-macro approach to rubber-like materialsPart I: the non-affine micro-sphere model of rubber elasticity, *Journal of the mechanics and physics of solids*, 52, 2617-2660, 2004.

23rd Nordic Seminar on Computational Mechanics
NSCM-23
A. Eriksson and G. Tibert (Eds)

A MICRO-SPHERE APPROACH APPLIED TO THE SIMULATION OF PHASE-TRANSFORMATIONS INTERACTING WITH PLASTICITY

RICHARD OSTWALD*, THORSTEN BARTEL* AND ANDREAS MENZEL*,†

*Institute of Mechanics, TU Dortmund
Leonhard-Euler-Str. 5, D-44227 Dortmund, Germany
e-mail: richard.ostwald@udo.edu, thorsten.bartel@udo.edu, andreas.menzel@udo.edu
web page: http://www.iofm.de/

†Division of Solid Mechanics, Lund University
P.O. Box 118, SE-22100 Lund, Sweden
e-mail: andreas.menzel@solid.lth.se – web page: http://www.solid.lth.se/

Key words: Phase-Transformations, Plasticity, Mixture-Theory.

Summary. We present an efficient model for the simulation of polycrystalline materials undergoing solid to solid phase transformations. As a basis, a thermodynamically consistent, one-dimensional phase-transformation model based on statistical physics is used. The incorporation of plasticity phenomena is established by enhancing the Helmholtz free energy functions of the material phases considered, namely austenite and martensite. For conceptual simplicity, we assume von Mises-type plasticity with linear proportional hardening, where the plastic driving forces acting in each phase are derived from the overall free energy potential of the mixture. The coupled systems of evolution equations are solved in a staggered manner, where the change of plastic strains resulting from propagating phase fronts is considered by introducing a physically motivated exponential-type plasticity inheritance law. The one-dimensional model is embedded into a micro-sphere formulation[1] in order to simulate three-dimensional boundary value problems.

1 A ONE-DIMENSIONAL MODEL FOR THE INTERACTION OF PHASE-TRANSFORMATIONS AND PLASTICITY

The one-dimensional phase-transformation model is based on mixture theory, where we make use of the Voigt assumption, i.e. all material phases are subject to the same strain ε. Each phase is presumed to behave thermo-elasto-plastically, thus a Helmholtz free energy function $\psi^\alpha = \widehat{\psi}^\alpha(\varepsilon, \varepsilon^\alpha_{\rm pl}, \theta)$ of the form

$$\begin{aligned} \rho_0\psi^\alpha &= \frac{1}{2}\mathsf{E}^\alpha[\varepsilon - \varepsilon^\alpha_{\rm tr} - \varepsilon^\alpha_{\rm pl}]^2 - \zeta^\alpha\mathsf{E}^\alpha[\varepsilon - \varepsilon^\alpha_{\rm tr} - \varepsilon^\alpha_{\rm pl}][\theta - \theta_0] \\ &+ \rho_0 c^\alpha_p\theta\left[1 - \log\left(\frac{\theta}{\theta_0}\right)\right] - \rho_0\lambda^\alpha_T\left[1 - \frac{\theta}{\theta_0}\right] \end{aligned} \tag{1}$$

is assigned to each phase α, with E the Young's modulus, $\varepsilon = \nabla_x u$ the total strains, $\varepsilon_{\mathrm{tr}}$ the transformation strains, $\varepsilon_{\mathrm{pl}}$ the plastic strains, ζ the coefficient of thermal expansion, θ the current absolute temperature, θ_0 the reference temperature, c_p the heat capacity, and λ_T the latent heat of the respective material phase. The overall free energy of the mixture $\Psi = \widehat{\Psi}(\varepsilon, \boldsymbol{\varepsilon}_{\mathrm{pl}}^{\mathrm{1d}}, \theta, \boldsymbol{\xi}) = \sum_\alpha \xi^\alpha \psi^\alpha$, with $\boldsymbol{\xi} = [\xi^1, \dots, \xi^\nu]$ and $\boldsymbol{\varepsilon}_{\mathrm{pl}}^{\mathrm{1d}} = [\varepsilon_{\mathrm{pl}}^1, \dots, \varepsilon_{\mathrm{pl}}^\nu]$, can directly be obtained from the free energy contributions of the respective constituents, since the distortional energy of the phase boundaries is neglected here. Based on this, the Gibbs potential $G = \widehat{G}(\partial\Psi/\partial\varepsilon, \boldsymbol{\xi}, \theta)$ is obtained by carrying out a Legendre-transformation, i.e.

$$G = -\sup_{\varepsilon} \left(\left. \frac{\partial \widehat{\Psi}(\varepsilon, \boldsymbol{\varepsilon}_{\mathrm{pl}}^{\mathrm{1d}}, \theta, \boldsymbol{\xi})}{\partial \varepsilon} \right|_{\theta, \boldsymbol{\varepsilon}_{\mathrm{pl}}^{\mathrm{1d}}} \varepsilon - \rho_0 \Psi \right) = -\sup_{\varepsilon} \left(\sum_\alpha \xi^\alpha g^\alpha \right) \quad , \tag{2}$$

where $g^\alpha = \widehat{g}^{\,\alpha}(\sigma, \varepsilon, \varepsilon_{\mathrm{pl}}^\alpha, \theta) \overset{\mathrm{def}}{=} \sigma\varepsilon - \rho_0 \psi^\alpha$ represents the contribution of phase α to the overall Gibbs potential G.

For the evolution of the volume fractions ξ^α we use an approach based on statistical physics. In this regard, a transformation probability matrix $\boldsymbol{Q}_\nu = \widehat{\boldsymbol{Q}}_\nu(\boldsymbol{\xi}) \in \mathbb{R}^{\nu \times \nu}$ is used[2], facilitating to derive the evolution of volume fractions as $\dot{\boldsymbol{\xi}} = \widehat{\boldsymbol{Q}}_\nu(\boldsymbol{\xi}) \cdot \boldsymbol{\xi}$, wherein the notation $\dot{\bullet}$ denotes the material time derivative. In this work, the systems of evolution equations is numerically solved by making use of an efficient A-stable integration algorithm[3].

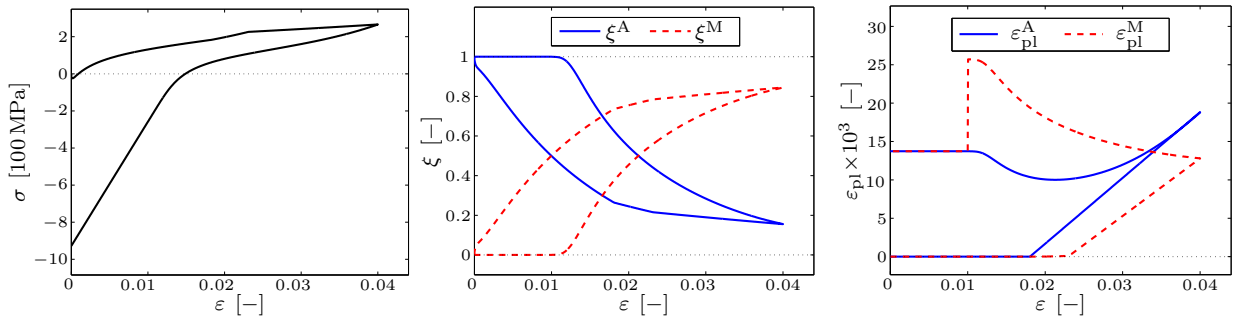

(a) Stress-strain diagramme (b) Evolution of volume fractions (c) Evolution of plastic strains

Figure 1: Phase-transformations in SMA – two-phase model with $\xi^1 = \xi^{\mathrm{A}}$ (austenite) and $\xi^2 = \xi^{\mathrm{M}}$ (martensite): stress-strain diagramme (a), evolution of volume fractions (b) and evolution of plastic strains (c).

1.1 Incorporation of plasticity

To incorporate plasticity, we—for conceptual simplicity—assume von Mises-type plasticity with linear proportional hardening. Based on the overall free energy potential, the plastic driving force $q_{\mathrm{pl},\Psi}^\alpha$ is derived[4] for each phase α. The yield function $\Phi^\alpha = \widehat{\Phi}^\alpha(Y^\alpha, q_{\mathrm{pl},\Psi}^\alpha)$ determining the admissible elastic domain in phase α can then be expressed in terms of the driving force and the current yield stress Y^α, namely

$$\widehat{\Phi}^\alpha(q_{\mathrm{pl},\Psi}^\alpha, Y^\alpha) = |q_{\mathrm{pl},\Psi}^\alpha - \xi^\alpha b^\alpha| - \xi^\alpha Y^\alpha \leq 0 \quad . \tag{3}$$

The current yield stress $Y^\alpha = \widehat{Y}^\alpha(\gamma^\alpha) = Y_0^\alpha + H^\alpha\,\gamma^\alpha$ is given by the initial yield stress Y_0^α being modified by $H^\alpha\,\gamma^\alpha$, facilitating to take into account accumulated plastic strains γ^α of the respective material phase. Here, H^α denotes the constant hardening modulus of phase α. The individual back stress $\xi^\alpha b^\alpha$ is additionally considered in order to prevent plastic flow occurring in the initial equilibrium state.

1.2 Plastic inheritance

When the phase front of a phase α evolves through a crystal, plastic strains present in the decreasing phase β are either inherited by the phase front of the increasing phase or not. Conceptually speaking, a positive volume fraction increment $\Delta\xi^\alpha = {}^{n+1}\xi^\alpha - {}^{n}\xi^\alpha > 0$ of phase α transfers a specific amount of plastic strains from phase β to phase α. In general, the updated plastic strains $\tilde{\varepsilon}^\alpha_{\mathrm{pl}} = \widehat{\tilde{\varepsilon}}^\alpha_{\mathrm{pl}}({}^n\xi^\alpha, \Delta\xi^\alpha, \varepsilon^\alpha_{\mathrm{pl}}, \varepsilon^\beta_{\mathrm{pl}}, \Pi^{\beta\to\alpha})$ in phase α are determined via

$$\tilde{\varepsilon}^\alpha_{\mathrm{pl}} = \frac{1}{{}^{n+1}\xi^\alpha}\left[{}^n\xi^\alpha\,\varepsilon^\alpha_{\mathrm{pl}} + \Pi^{\beta\to\alpha}\,\Delta\xi^\alpha\,\varepsilon^\beta_{\mathrm{pl}}\right] \quad , \tag{4}$$

where $\Pi^{\beta\to\alpha}$ reflects the probability of phase α inheriting the dislocations present in phase β[4].

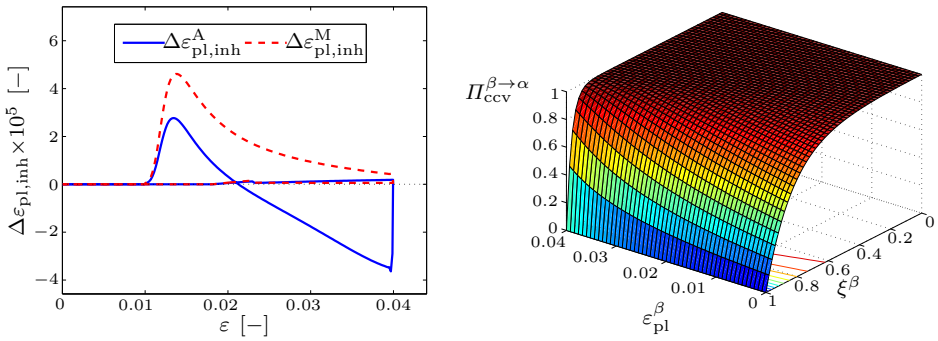

(a) Change of plastic strains due to inheritance (cf. Figure 1(c))

(b) Concave inheritance function

Figure 2: Phase-transformations in SMA: change of plastic strains due to inheritance resulting from the evolution of phases (a) and concave inheritance function (b).

2 MICRO-SPHERE APPLICATION

The one-dimensional phase-transformation model is generalized by embedding it into a kinematically constrained micro-sphere formulation. Here, the one-dimensional micro-strains $\varepsilon^{\mathrm{mic}}$ are obtained using projections of the macro-scale strain tensor $\boldsymbol{\varepsilon}^{\mathrm{mac}}$ with respect to the underlying integration directions $\boldsymbol{r} \in \mathbb{U}^2$. In particular, $\varepsilon^{\mathrm{mic}} = [\boldsymbol{r}\otimes\boldsymbol{r}]:\boldsymbol{\varepsilon}^{\mathrm{mac}}$ represents the strain in radial direction being transferred to the micro level.

Apart from the transfer of macroscopic strains to the micro level, the relevant quantities computed at the micro level, i.e. stresses and volume fractions, have to be transferred back to the macro level. The macroscopic stresses $\widehat{\boldsymbol{\sigma}}^{\mathrm{mac}}(\sigma^{\mathrm{mic}})$ and volume fractions $\boldsymbol{\Xi} = \widehat{\boldsymbol{\Xi}}(\boldsymbol{\xi})$ can be

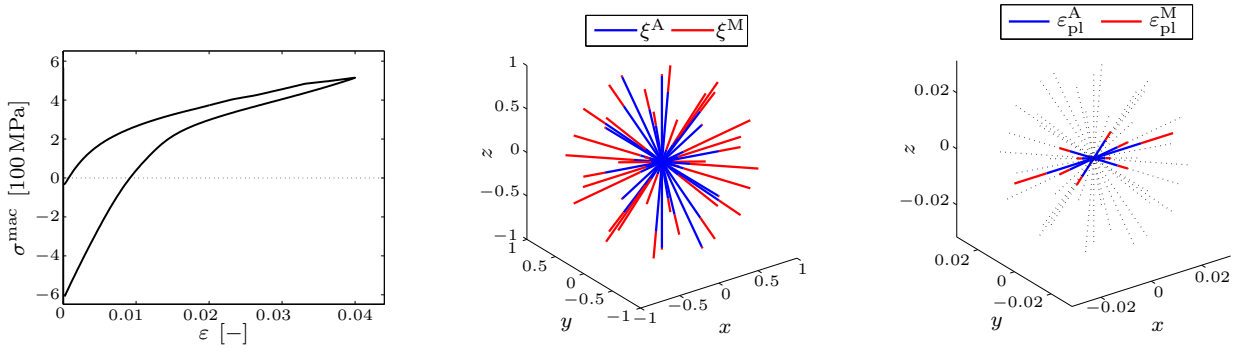

(a) Stress-strain diagramme (b) Volume fractions (c) Plastic strains

Figure 3: Micro-sphere application of the plastic phase-transformation model. The results are obtained by incrementally applying a homogeneous state of deformation $\boldsymbol{\varepsilon}^{\mathrm{mac}}(t) = \widehat{\kappa}(t)\, 0.04\, \boldsymbol{e}_1 \otimes \boldsymbol{e}_1$ with $\widehat{\kappa}(t) \in [0, 1]$. The volume fractions (b) and plastic strains (c) are visualized at the maximum strain state, i.e. at $\boldsymbol{\varepsilon}^{\mathrm{mac}} = 0.04\, \boldsymbol{e}_1 \otimes \boldsymbol{e}_1$.

approximated numerically via

$$\boldsymbol{\sigma}^{\mathrm{mac}} \approx \sum_{i=1}^{n_r} \sigma_i^{\mathrm{mic}}\, \bar{w}_i\, \boldsymbol{r}_i \otimes \boldsymbol{r}_i \quad \text{and} \quad \Xi^{\alpha} = \sum_{i=1}^{n_r} \xi_i^{\alpha}\, \bar{w}_i \quad , \tag{5}$$

with σ_i^{mic} the micro stress acting in i th integration direction $\boldsymbol{r}_i$, ξ_i^{α} the respective volume fraction of phase α situated in this integration direction , and $\bar{w}_i$ the weighting factors depending on the integration scheme used.

Acknowledgements

The support of the Deutsche Forschungsgemeinschaft (DFG), that made possible to develop this research within the research project TRR30 B6, is gratefully acknowledged.

References

[1] E. Kuhl, P. Steinmann and I. Carol, *A thermodynamically consistent approach to microplane theory. Part II. Dissipation and inelastic constitutive modeling*, Int. J. Sol. Struct. 38, 2933–2952 (2001).

[2] S. Govindjee and G.J. Hall, *A computational model for shape memory alloys*, Int. J. Sol. Struct. 37, 735–760 (2000).

[3] R. Ostwald, T. Bartel and A. Menzel, *A computational micro-sphere model applied to the simulation of phase-transformations*, J. Appl. Math. Mech. 90(7-8), 605–622 (2010).

[4] R. Ostwald, T. Bartel and A. Menzel, *A one-dimensional computational model for the interaction of phase-transformations and plasticity*, submitted for publication (2010).

23rd Nordic Seminar on Computational Mechanics
NSCM-23
A. Eriksson and G. Tibert (Eds)

AN IMPLICIT ADAPTIVE FINITE ELEMENT METHOD FOR RATE DEPENDENT STRAIN GRADIENT PLASTICITY

CARL F.O. DAHLBERG* AND JONAS FALESKOG*

*Department of Solid Mechanics
Royal Institute of Technology
Osquarsbacke 1, 100 44 Stockholm, Sweden
e-mail: carl@hallf.kth.se

Key words: Strain Gradient Plasticity, Computational Techniques.

Summary. An implicit FE-method for rate dependent strain gradient plasticity is proposed that takes into account the contributions from internal interfaces. The numerical procedure is stable and the constitutive parameters can be pushed towards the rate independent limit without loss of convergence.

1 INTRODUCTION

Higher order strain gradient plasticity theories[1,2,3] have proven to be difficult to implement into a finite element framework in a consistent way. One of the major hurdles have been the problem of the indeterminacy of the higher order stress tensor before plastic deformation develops. One way around this problem is to make use of a computational pseudo-elastic regime in the rate independent case[4], or some similar penalty method. A constitutive assumption of rate dependent plasticity will alleviate the underlying theoretical problem associated with this indeterminacy. However, such an assumption have been quite restrictive since most implementations of these kind of theories have not, due to numerical difficulties, been able to drive the rate sensitivity exponent to small enough values to closely mimic rate independent plasticity[5,6,7]. Furthermore, the majority of the implementations employ an explicit forward Euler type integration and thus suffer from the need to take a large amount of load steps to accurately capture the material response.

2 STRAIN GRADIENT PLASTICITY

The strain gradient theory of Gudmundson[1] is used as the theoretical starting point for this work. The balance of virtual work is

$$\int_\Omega \left[\sigma_{ij}\delta\varepsilon^{\mathrm{e}}_{ij} + q_{ij}\delta\varepsilon^{\mathrm{p}}_{ij} + m_{ijk}\delta\varepsilon^{\mathrm{p}}_{ij,k}\right] \mathrm{d}V = \int_{\partial\Omega} \left[T_i\delta u_i + M_{ij}\delta\varepsilon^{\mathrm{p}}_{ij}\right] \mathrm{d}S, \tag{1}$$

where $\varepsilon^{\mathrm{e}}_{ij}$, $\varepsilon^{\mathrm{p}}_{ij}$ and $\varepsilon^{\mathrm{p}}_{ij,k}$ denote the elastic and plastic strain and the gradient of plastic strain respectively. The conjugated stress measures are the Cauchy stress σ_{ij}, the micro stress q_{ij} and the moment stress m_{ijk} respectively. The displacements are u_i, and at a boundary force

tractions T_i and higher order tractions M_{ij} appear. The right hand side of (1) shows that both displacements and plastic strains are primary variables of the theory, thus leading to so called higher order boundary conditions that prescribe either $\varepsilon^{\mathrm{p}}_{ij}$ or M_{ij} on the boundary, in addition to the standard displacement/force traction boundary.

The elastic strains are governed by linear elasticity and the constitutive equations for the rate of plastic strains and their gradients are

$$\dot{\varepsilon}^{\mathrm{p}}_{ij} = g(\sigma_f, \Sigma) q_{ij} \quad \text{and} \quad \dot{\varepsilon}^{\mathrm{p}}_{ij,k} = g(\sigma_f, \Sigma) \sum_{I=1}^{3} \frac{m^I_{ijk}}{(\ell^I)^2}, \tag{2}$$

where g is a viscoplastic rate potential that depend on the flow stress σ_f and the effective stress measure Σ. The ℓ^I:s are three microstructural length scales and m^I_{ijk} denotes the orthogonal decomposition of the moment stress, see Gudmundson [1] for details and further references therein.

2.1 INTERFACE CONTRIBUTIONS

Interfaces (here denoted by Γ) within plastically deforming bodies usually affect the plastic strain state since they act to hinder or mediate dislocation motion and/or creation. This will change the energetic state in the vicinity of such an interface and to model this an interface energy, ψ_Γ, dependent on the plastic strain is postulated. There is also a possibility to have a relative displacement across internal boundaries, i.e. a sliding motion. The inclusion of such an internal boundary would give contributions to the balance of virtual work according to

$$\int_\Omega \left[\sigma_{ij}\delta\varepsilon^{\mathrm{e}}_{ij} + q_{ij}\delta\varepsilon^{\mathrm{p}}_{ij} + m_{ijk}\delta\varepsilon^{\mathrm{p}}_{ij,k}\right] \mathrm{d}V + \int_\Gamma \frac{\partial \psi_\Gamma}{\partial \varepsilon^{\mathrm{p}I}_{ij}} \delta\varepsilon^{\mathrm{p}I}_{ij} \mathrm{d}S + \int_\Gamma T_i \delta \lfloor u_i \rceil \mathrm{d}S = \int_{\partial\Omega} \left[T_i \delta u_i + M_{ij}\delta\varepsilon^{\mathrm{p}}_{ij}\right] \mathrm{d}S, \tag{3}$$

where $\lfloor u_i \rceil$ denotes the jump in displacement (sliding displacement) across Γ.

Constitutive formulations at the interface are thus needed to complete the model. The interface energy have been modeled as a function of scalar effective measures of plastic strain at the interface. Several function forms have been investigated and quadratic, linear and exponentially saturating have been deemed the most interesting. For the sliding a modified traction-separation law can be used.

3 FINITE ELEMENT FORMULATION

Here an implicit FE-method for rate dependent plasticity with a consistent tangent modulus and adaptive step size is proposed based on (3). A 3 node 1D element, 8 node plane strain, plane stress and axisymmetric elements and a 20 node 3D brick element have been developed. A quadratic interpolation of the displacements and a linear interpolation of the plastic strains are used so that the total strain field and the plastic strain field have the same degree of interpolation. The nodal degrees of freedom, the stress like quantities and the traction like quantities are collected in vectors

$$\mathbf{d} = \begin{bmatrix} \mathbf{d}_{\mathrm{u}} \\ \mathbf{d}_{\mathrm{p}} \end{bmatrix}, \qquad \mathbf{s} = \begin{bmatrix} \boldsymbol{\sigma} \\ \mathbf{q} \\ \mathbf{m} \end{bmatrix}, \qquad \mathbf{t} = \begin{bmatrix} \mathbf{T} \\ \mathbf{M} \end{bmatrix}. \tag{4}$$

The equilibrium equations can then be expressed as

$$\boldsymbol{\phi} = \int_{\Omega} \mathbf{B}^{\mathrm{T}} \mathbf{s} \mathrm{d}V + \int_{\Gamma} \mathbf{N}^{\mathrm{T}} \mathbf{t} \mathrm{d}S - \int_{\partial\Omega} \mathbf{N}^{\mathrm{T}} \mathbf{t} \mathrm{d}S = 0, \tag{5}$$

where $\mathbf{N}$ is the shape function matrix and $\mathbf{B}$ is the spatial gradient matrix. For the nonlinear problem presented here (5) have to be solved incrementally. The tangent stiffness is

$$\mathbf{K}_{\mathrm{tan}} = \frac{\partial \boldsymbol{\phi}}{\partial \mathbf{d}} = \int_{\Omega} \mathbf{B}^{\mathrm{T}} \mathbf{D}_{\Omega} \mathbf{B} \mathrm{d}V + \int_{\Gamma} \mathbf{N}^{\mathrm{T}} \mathbf{D}_{\Gamma} \mathbf{N} \mathrm{d}S, \tag{6}$$

where $\mathbf{D}_{\Omega}$ is the material point stiffness matrix and $\mathbf{D}_{\Gamma}$ is the stiffness contribution from the interface. The stiffness components are calculated to be consistent with the backward Euler method. For example, the material point stiffness is

$$\mathbf{D}_{\Omega} = \frac{1}{\Delta t} \left(\mathbf{F} + \mathbf{s}^{\mathrm{T}} \frac{\partial \mathbf{F}}{\partial \mathbf{s}} \right)^{-1} \left(\mathbf{I} - \mathbf{s}^{\mathrm{T}} \frac{\partial \mathbf{F}}{\partial \boldsymbol{\epsilon}} \right), \tag{7}$$

where $\mathbf{F}$ is the constitutive matrix that relates the vector of rates of strains and gradient of plastic strains to the stress vector as $\dot{\epsilon} = \mathbf{F}(\mathbf{s}, \boldsymbol{\epsilon})\mathbf{s}$ and $\mathbf{I}$ is the unity matrix of appropriate size.

The stress update procedure for the non-standard stresses relies on the fact that the stress components have to be co-linear with the rates of plastic strains and gradients, which can be inferred from the need to have non-negative plastic dissipation

$$q_{ij} \dot{\varepsilon}^{\mathrm{p}}_{ij} + m_{ijk} \dot{\varepsilon}^{\mathrm{p}}_{ij,k} \geq 0. \tag{8}$$

This puts restrictions on the form of the constitutive laws and the update is performed at the Gauss points by solving a nonlinear scalar equation for the effective stress Σ

$$g(\sigma_f, \Sigma) - \dot{E}^{\mathrm{p}} = 0, \tag{9}$$

where the effective plastic strain rate $\dot{E}^{\mathrm{p}}$ is given from the equilibrium iterations and the flow stress σ_f is updated according to some hardening law. Once the stress state is known a linearization of (5) for increment $k+1$ gives

$$\boldsymbol{\phi}_{k+1} = \boldsymbol{\phi}_k + \frac{\partial \boldsymbol{\phi}_k}{\partial \mathbf{d}} \Delta \mathbf{d}_{k+1} = \boldsymbol{\phi}_k + \mathbf{K}_{\mathrm{tan}} \Delta \mathbf{d}_{k+1} \tag{10}$$

which can be solved for the increments $\Delta \mathbf{d}_{k+1}$ by letting $\boldsymbol{\phi}_{k+1} \to 0$.

4 CONCLUSIONS

The method have been implemented as a Matlab version for debugging and testing as well as a FORTRAN90/95 version for larger problems. The method was benchmarked against a well known case of simple shear of an elastic-plastic strip[8]. The number of load steps to reach an accurate solution is on the order of 10^2 or less, which is much less than for an explicit method. The method was supplemented with an adaptive time step so that smaller steps were taken only in the vicinity of rapid changes to the stress-strain curve, thus further reducing the number of load steps needed. The algorithm was found to very stable and the viscoplastic rate sensitivity

exponent could easily be made very small, 2×10^{-4} was tested without any numerical problems, which is at least two orders of magnitude smaller than other reported cases and should be very close to the rate independent limit.

The interface formulation have been implemented by special interface elements and gives the possibility to prescribe more physically motivated external boundary conditions for the higher order field variables. It also allows the modeling of internal interfaces (with regards to plastic deformation) in an micro mechanically more appealing way.

REFERENCES

[1] *A unified treatment of strain gradient plasticity*, P. Gudmundson, J. Mech. Phys. Solids, 2004.

[2] *A theory of strain-gradient plasticity for isotropic, plastically irrotational material. Part I: Small deformations*, M. E. Gurtin, L. Anand, J. Mech. Phys. Solids, 2005.

[3] *A mathematical basis for strain-gradient plasticity theory. Part II: Tensorial plastic multiplier*, N. A. Fleck, J. R. Willis, J. Mech. Phys. Solids, 2009.

[4] *On higher-order boundary conditions at elastic-plastic boundaries in strain-gradient plasticity*, C. F. Niordson, Phil. Mag., 2008.

[5] *Size-dependent yield strength of thin films*, P. Fredriksson, P. Gudmundson, Int. J. Plast., 2005.

[6] *A one-dimensional theory of strain-gradient plasticity: Formulation, analysis, numerical results*, L. Anand, M. E. Gurtin, S. P. Lele, C. Gething, J. Mech. Phys. Solids, 2005.

[7] *A viscoplastic strain gradient analysis of materials with voids or inclusions*, U. Borg, C. F. Niordson, N. A. Fleck, V. Tvergaard, Int. J. Solid Struct., 2006.

[8] *Energetic interfaces and strain gradient plasticity – An investigation using an adaptive implicit finite element method*, C. F.O. Dahlberg, J. Faleskog, Internal report 477, Dept. Solid Mech. KTH, 2009.

23rd Nordic Seminar on Computational Mechanics
NSCM-23
A. Eriksson and G. Tibert (Eds)

HYBRID STATE-SPACE TIME INTEGRATION OF ROTATING BEAMS

MARTIN B. NIELSEN AND STEEN KRENK

Department of Mechanical Engineering
Technical University of Denmark, Kgs. Lyngby, Denmark
e-mail: mbni@mek.dtu.dk, sk@mek.dtu.dk

Key words: Dynamics in rotating frame, Time integration, Beam elements, Computational Methods.

Summary. Modeling and efficien design of wind turbines require efficien and accurate computational methods for dynamic analysis of the different components. In the present paper an efficien hybrid formulation for beams in a rotating frame of reference is presented for analysis of the rotor system. It is demonstrated that the equations of motion take a particularly simple form when starting from a hybrid state-space in terms of local displacements relative to the rotating frame and absolute velocities using similar interpolation. The equations of motion are formulated for small finit deformation beam elements in terms of translational as well as rotational degrees of freedom and include the effect of geometric stiffness. The dynamic equations are derived from Lagrange's equation and combined with a kinematic relation into a convenient hybrid state-space format.

1 HYBRID STATE-SPACE FORMULATION

It has recently been demonstrated for translation based (solid) elements that the equations of motion take a particularly simple form when starting from a hybrid state-space in terms of local displacements $\mathbf{u}$ relative to the rotating frame and absolute velocities $\mathbf{v}$ [1]. In the present paper this approach is extended to small finit deformation beam elements with rotational degrees of freedom as well by introduction of an additive term to the kinematic relation.

Consider a structure located in a local frame rotating around its origin with local angular velocity vector $\boldsymbol{\Omega}^T = [\Omega_1, \Omega_2, \Omega_3]$. The local position of the structure is described in terms of the N nodes, which are collected in the array $\mathbf{x}^T = [\mathbf{x}_1^T, \mathbf{x}_2^T, \ldots, \mathbf{x}_N^T]$. The position vector $\mathbf{x}$ may be represented as a sum of the initial position $\mathbf{x}_0$ and a displacement vector $\mathbf{u}$

$$\mathbf{x} = \mathbf{x}_0 + \mathbf{u} \tag{1}$$

For 3D beam elements accommodating translational as well as rotational degrees of freedom the displacement vector is conveniently organized in the $2N$ block format $[\mathbf{u}_1^T, \boldsymbol{\varphi}_1^T, \mathbf{u}_2^T, \boldsymbol{\varphi}_2^T, \ldots, \mathbf{u}_N^T, \boldsymbol{\varphi}_N^T]^T$. The absolute velocity of node j can then be formulated as

$$\mathbf{v}_j = \begin{bmatrix} \dot{\mathbf{u}}_j + \tilde{\boldsymbol{\Omega}}\mathbf{x}_j \\ \dot{\boldsymbol{\varphi}}_j + \boldsymbol{\Omega} \end{bmatrix} \quad , \quad j = 1, 2, \ldots, N \tag{2}$$

where $\tilde{\mathbf{\Omega}} = \mathbf{\Omega}\times$. The global velocity components are collected in the array $\mathbf{v}^T = [\mathbf{v}_1^T, \mathbf{v}_1^T, \ldots, \mathbf{v}_N^T]$, thus the system format for the absolute nodal velocities can be obtained from (2) by utilization of the expression (1),

$$\mathbf{v} = \dot{\mathbf{u}} + \tilde{\mathbf{\Omega}}_D \mathbf{u} + \tilde{\mathbf{\Omega}}_D \mathbf{x}_0 + \mathbf{\Omega}_C \tag{3}$$

The matrices $\tilde{\mathbf{\Omega}}_D$ and $\mathbf{\Omega}_C$ are introduced as

$$\tilde{\mathbf{\Omega}}_D = \begin{bmatrix} \tilde{\mathbf{\Omega}} & & \\ & \mathbf{0} & \\ & & \ddots \end{bmatrix} \quad , \quad \mathbf{\Omega}_C = \begin{bmatrix} \mathbf{0} \\ \mathbf{\Omega} \\ \vdots \end{bmatrix} \tag{4}$$

where $\lceil\, \tilde{\mathbf{\Omega}} \;\; \mathbf{0} \,\rfloor$ and $[\,\mathbf{0}^T \;\; \mathbf{\Omega}^T\,]^T$ are repeated for each node of the structure.

A key feature in the present formulation leading to particular simplification of the discretized equations of motion is to use the same shape function representation for the local position $\mathbf{x}_\xi$ as well as the absolute velocity $\mathbf{v}_\xi$ in terms of the nodal components $\mathbf{x}$ and $\mathbf{v}$, respectively. The interpolation for the position $\mathbf{x}_\xi$ can be expressed as

$$\mathbf{x}_\xi = \mathbf{N}(\xi)\mathbf{x} = \mathbf{N}(\xi)[\mathbf{x}_0 + \mathbf{u}] \tag{5}$$

where $\mathbf{N}(\xi)$ denotes a suitable interpolation in terms of the normalized initial coordinate ξ. The interpolation of the absolute velocity is similarly expressed as

$$\mathbf{v}_\xi = \mathbf{N}(\xi)\mathbf{v} = \mathbf{N}(\xi)[(\partial_t + \tilde{\mathbf{\Omega}}_D)\mathbf{x} + \mathbf{\Omega}_C] \tag{6}$$

This particular choice of interpolation leads to a formulation where the angular velocity can be extracted from the integrals definin the inertia effects such as centrifugal and Coriolis forces for the individual elements. It should be noted that if a direct point-wise time differentiation were used, the combined time differentiation and convection term arising from the angular velocity of the rotating frame would appear to the left of the shape function matrix $\mathbf{N}$. As a consequence the matrices related to inertia effects in the discretized formulation need recalculation on element level for changing angular velocity. In the present formulation this change is accounted for by a simple pre- or post-multiplication of the system mass matrix with the angular velocity matrix $\tilde{\mathbf{\Omega}}_D$ and the vector $\mathbf{\Omega}_C$.

Expressing the kinetic energy T in terms of the local mass matrix, $\mathbf{M}$

$$T = \tfrac{1}{2}\mathbf{v}^T\mathbf{M}\mathbf{v} \tag{7}$$

and the internal forces $\mathbf{g}(\mathbf{u})$ from an energy potential $G(\mathbf{u})$

$$\mathbf{g}(\mathbf{u}) = \frac{dG(\mathbf{u})}{d\mathbf{u}^T} \tag{8}$$

the equations of motion follow from Lagrange's equations:

$$\frac{d}{dt}\left(\frac{\partial T}{\partial \dot{\mathbf{u}}^T}\right) - \frac{\partial T}{\partial \mathbf{u}^T} + \frac{\partial G}{\partial \mathbf{u}^T} = \mathbf{f} \tag{9}$$

where $\mathbf{f}$ is the nodal force array.

The equations of motion are conveniently expressed in a hybrid state-space format in terms of the local displacements **u** and absolute velocities **v**. The dynamic equations of motion follow from (9) in the form

$$\left(\partial_t + \tilde{\mathbf{\Omega}}_D\right)\mathbf{M}\mathbf{v} + \mathbf{g}(\mathbf{u}) = \mathbf{f} \tag{10}$$

For the current use the mass matrix is assumed independent of time and the kinematic equation (3) and the dynamic equation (10) are combined into the following state space format:

$$\begin{bmatrix} \mathbf{0} & \mathbf{M} \\ -\mathbf{M} & \mathbf{0} \end{bmatrix}\begin{bmatrix} \dot{\mathbf{u}} \\ \dot{\mathbf{v}} \end{bmatrix} + \begin{bmatrix} \mathbf{g}(\mathbf{u}) + \tilde{\mathbf{\Omega}}_D\mathbf{M}\mathbf{v} \\ \mathbf{M}\tilde{\mathbf{\Omega}}_D^T\mathbf{u} + \mathbf{M}\mathbf{v} \end{bmatrix} = \begin{bmatrix} \mathbf{f} \\ -\mathbf{M}\left(\tilde{\mathbf{\Omega}}_D^T\mathbf{x}_0 - \mathbf{\Omega}_C\right) \end{bmatrix} \tag{11}$$

The state space format is hybrid in the sense that **u** is the local displacements while **v** is the absolute velocity. The discretized equations are separated into a computationally attractive symmetric and anti-symmetric block format. The inertial terms arising from the rotation of the local frame are solely represented by two gyroscopic terms and generalization to accelerated rotation is straight forward leading to a more general and computational attractive format compared to the classic block matrix format in terms of local components, [2].

Using a linearized formulation in terms of the constitutive and an initial stress based geometric stiffness matrix, the equations of motion can be solved using a very efficien two-step integration algorithm without the need for internal iterations. The algorithm is based on an integrated form of the equations of motions as proposed in [3]. The angular velocity is represented by its mean value over the time increment and the internal forces $\mathbf{g}(\mathbf{u})$ are represented in the form of end-point values supplemented by a term involving the increment of the geometric stiffness, [4].

2 EXAMPLE: TRANSIENT ACCELERATION OF PRISMATIC BEAM

The properties and accuracy of the hybrid state space algorithm are illustrated considering a spin-up sequence of a prismatic beam rotating about a fi ed axis. The beam is originally introduced by [5], but parameters corresponding to [6] have been used. These are equivalent to a beam of length $L = 10$ m, with a square cross-section with side-lengths $b = 0.0775$ m. The beam is homogeneous and isotropic elastic with parameters $E = 6.67$ GPa and $G = 2.00$ GPa and mass density $\rho = 200$ kg/m^3. The angular velocity is increased over a period $T_s = 15$ s to it's fina value $\Omega_s = 6$ rad/s according to

$$\Omega_2(t) = \begin{cases} \dfrac{\omega_s}{T_s}\left[t - \dfrac{T_s}{2\pi}\sin\dfrac{2\pi t}{T_s}\right] , & 0 \le t \le T_s \\ \omega_s , & t > T_s \end{cases} \tag{12}$$

Results illustrating the transverse displacement u_1 and the axial displacement u_3 of the tip as function of time are illustrated in Fig. 2 (a) and (b). The transverse displacement shows the characteristic backward bending during the acceleration phase and corresponds closely to the results obtained in [6]. However, due to the applied small displacement beam formulation the results lack in capturing the apparent axial shortening during the acceleration phase, whereas the small elongation due to the centrifugal force in the fina near stationary phase is present. The effect of shortening due to bending may be reproduced by a simple post-processing of the results using the beam column theory from [7] as illustrated by a dashed line in Fig. 2 (b).

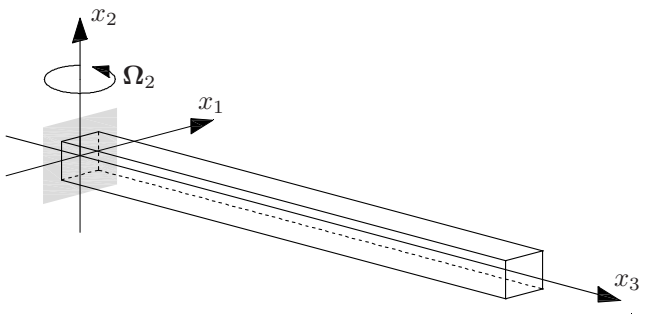

Figure 1: Prismatic beam rotating about a fi ed axis.

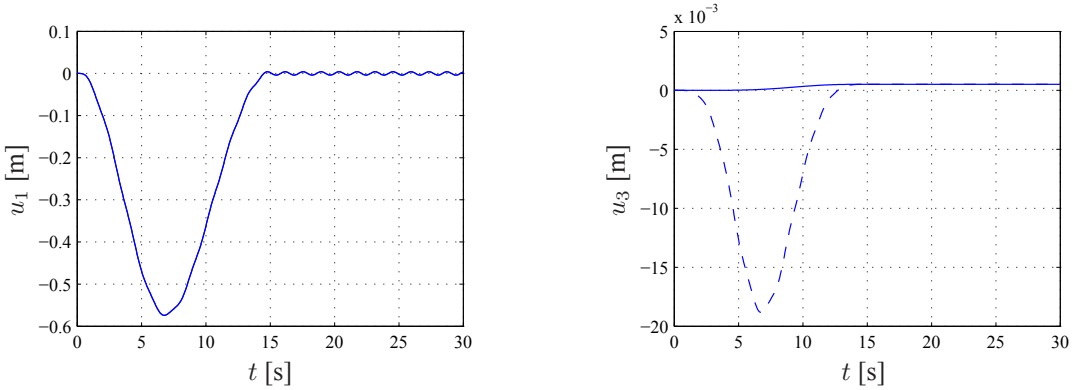

Figure 2: (a) Transverse tip displacement u_1. (b) Axial tip displacement u_3. Small displacement theory (–). Beam-column approximation (- -).

REFERENCES

[1] S. Krenk and M.B. Nielsen, Conservative time integration in a rotating frame using hybrid state-space variables, *To be published*, (2010).

[2] M. Geradin and D. Rixen, *Mechanical Vibrations - Theory and Applications to Structural Dynamics*, 2nd ed., Wiley, Chichester, UK, (1997).

[3] J. C. Simo, N. Tarnow, The discrete energy-momentum method. Conserving algorithms for nonlinear elastodynamics, *Zeitschrift für Angewandte Mathematik und Physik*, **43**, 757-792, (1992).

[4] S. Krenk, The role of geometric stiffness in momentum and energy conserving time integration, *Int. J. Num. Meth. Engng.*, **71**, 631–652, (2007).

[5] T. R. Kane, R. R. Ryan, A. K. Banerjee, Dynamics of a cantilever beam attached to a moving base, *Journal of Guidance*, **10**, 139-151, (1987).

[6] J. C. Simo and L. Vu-Quoc, On the dynamics of fl xible beams under large overall motions - The plane case: part I & II, *Journal of Applied Mechanics*, **53**, 845-863, (1986).

[7] S. Krenk, *Non-linear Modeling and Analysis of Solids and Structures*, Cambridge University Press, Cambridge, (2009).

23rd Nordic Seminar on Computational Mechanics
NSCM-23
A. Eriksson and G. Tibert (Eds)

NEURAL NETWORK MODELING OF FORWARD AND INVERSE BEHAVIOR OF ROTARY MR DAMPER

SUBRATA BHOWMIK[*,†], JAN HØGSBERG[*] AND FELIX WEBER[†]

[*]Section of Coastal, Maritime and Structural Engineering
Department of Mechanical Engineering
Technical University of Denmark
Nils Koppels Allé 403, 2800 Lyngby, Denmark
E-mail: subho@mek.dtu.dk, jhg@mek.dtu.dk

[†]Structural Engineering Laboratory
Swiss Federal Laboratories for Materials Science and Research (EMPA)
Ueberlandstrasse 129, 8600 Duebendorf, Switzerland
Email: felix.weber@empa.ch

Key words: Magneto rheological (MR) damper, neural network.

Summary. This paper describes the modeling of a rotary MR damper applying the feed-forward back propagation neural network method. The forward and inverse MR damper behavior are modeled to estimate the force and to solve the force tracking task in real-time. The training and validation data are generated by dynamic tests of the MR damper mounted on a hydraulic testing machine. The training data for the forward model are velocity and current whereby the force is the target. The inverse modeling training data are absolute velocity and absolute force and the current is the target. This new approach is chosen because current is always positive and thereby leads to a small modeling error independently of the sign of velocity. The validation demonstrates that the proposed neural network approach can reliably represent both the forward and inverse dynamic characteristics of the rotary type MR damper.

1 INTRODUCTION

Magneto-rheological (MR) dampers have received considerable attention within the last decades mainly because of their design simplicity, low power requirements, large force range and robustness. Typically, a rotary type MR damper consists of a rotating disk which is enclosed in a rectangular metallic housing filled with the MR fluid. The MR fluid housed within the rotary type MR damper is operated in shear mode. The dissipative torque produced is transformed into a translational force through the crank shaft mechanism.
The most common models to describe the dynamic behavior of MR dampers are the Bouc–Wen model [1], the LuGre friction model [2] and the Dahl model [3]. These modeling approaches are fairly complicated due to the high degree of nonlinearities in the system under consideration. From a computational point of view the nonparametric neural network technique is very versatile in connection with most types of nonlinear problems [4].

Therefore, this paper applies this method to model the dynamic behavior of the rotary MR damper.

2 EXPERIMENTAL SET-UP

The experimental test set up and its schematic diagram are shown in Fig. 1. The dSPACE is used to output the desired displacement going to the INSTRON controller, to output the desired current going to the current driver KEPCO and to acquire the measured states such as MR damper force, acceleration of the crank-shaft, actual displacement and current. Sinusoidal and triangular displacements with different frequencies from 0.5 Hz to 2.2 Hz are applied. Triangular displacements are used in order to perform tests at constant damper velocity. Constant and half-sinusoidal currents with different frequencies from 0.5 Hz to 2.2 Hz are also applied. The current of the MR damper under consideration is limited to 4 A and the maximum displacement amplitude is constraint to 10 mm due to the crank-shaft mechanism. The measured data is filtered to remove measurement noise and offsets in order to get the training data for the neural networks.

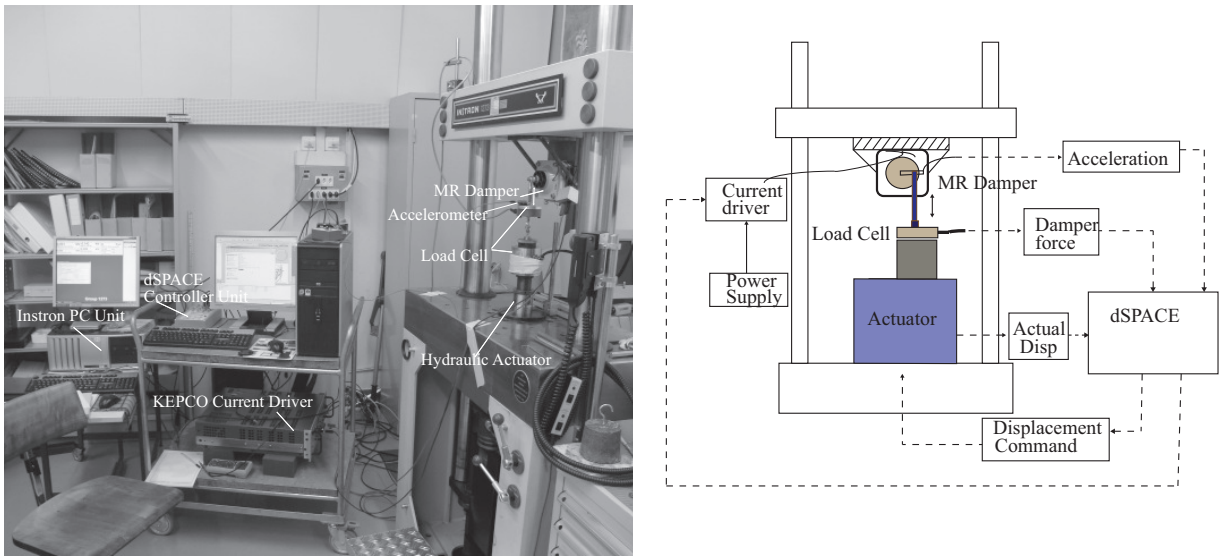

Figure 1. Experimental set-up and its schematic view

3 NEURAL NETWORK MODELING

Feed forward neural network (FFNN) is capable of modeling any nonlinear behaviour with acceptable accuracy. One data set is use as training data and another as validation set.

3.1 Forward MR damper modeling using FFNN

The identification methodology for the modeling of the forward dynamics of MR damper using the FFNN approach is illustrated in Fig. 2. The input states are current and velocity and their associated delay values. The velocity is required due to its significant influence on the hysteretic behavior of the MR damper. It is derived by numerical differentiation of the measured displacement. The noise resulting from the differentiation is removed by additional low pass filtering. The difference between modeled and measured MR damper force, i.e. the

error(k), is used to adjust the weights and the biases of the neural network model until a defined modeling error is reached. The feed forward neural network includes 2 hidden layers with 12 neurons in the first layer and 6 neurons in the second. The output layer includes one neuron and is chosen for input-output comparison. The numbers of layers and neurons have been found by trial and error. The transfer functions of the neurons of the two hidden layers are selected as tangent sigmoid function and the transfer function of the output layer is selected as linear function. The training algorithm is based on the Levenberg-Marquardt algorithm. The detailed mathematics of the neural network method is described well in [5].

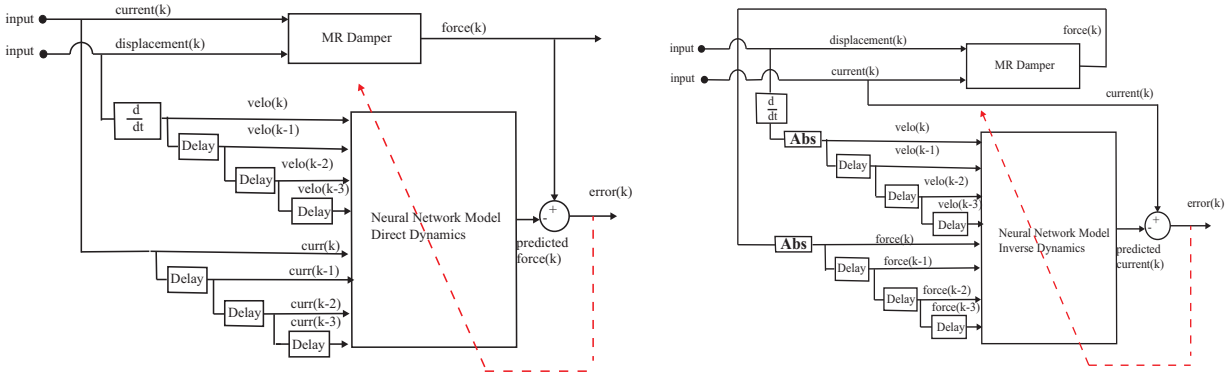

Figure 2. Forward and inverse neural network modeling of MR damper

3.2 Inverse MR damper modeling using FFNN

The architecture of the inverse model using the FFNN method is also shown in Fig. 2. The number of hidden layers and their transfer functions are chosen as before but the number of neurons in both hidden layers is 6. The significant change compared to the forward modeling is that the absolute values of velocity and force are used to train the neural network to get the estimated current because current is always positive. This new approach leads to small modeling error and the modeling error does not depend on the sign of velocity and direction of damper displacement, respectively.

4 MODEL VALIDATION AND DISCUSSION

The validations of both the forward and inverse MR damper models are shown in Fig. 3. The error of the forward model is depicted by comparing the measured and estimated forces resulting from 2 A and sinusoidal displacement (0.5 Hz, 4 mm). The modeling error of the inverse neural network approach is shown for the case of half-sinusoidal current input (0.5 Hz) and sinusoidal displacement (0.5 Hz, 6 mm). The inverse neural network is tested by a half-sinusoidal current because this is quite close to the current time history that is expected when emulating linear viscous damping except that the current spike during the pre-yield region is missing. The validation of the forward model shows an acceptably small error. The current estimated by the inverse MR damper model shows spikes that result from spikes in the measured displacement and force due to bearing plays between crank-shaft and INSTRON piston. Although these spikes have been partially removed by the filters to derive the training data, the estimated current is still spiky. The simple approach of filtering the estimated current cancels the spikes but leads to a still acceptably small time delay of approximately 0.05 s.

5 CONCLUSIONS

This investigation employed the back propagation feed forward neural network method to model the forward and inverse dynamics of an MR damper. The training data was taken on a prototype rotary MR damper that was connected to a hydraulic machine imposing sinusoidal and triangular displacements and constant and half sinusoidal current time histories. The goal of the forward MR damper model was to capture accurately the behavior of the MR damper behavior whereas the inverse MR damper model will later be used for the control force tracking when the MR damper will be connected to a shear frame. The novelty in the proposed neural network when modeling the inverse MR damper behavior is that the absolute values of velocity and force are used to estimate the damper current since current is always positive. The validations of both the forward and inverse MR damper models show that the applied neural network approaches capture the main MR damper dynamics with acceptable accuracy. However, the preliminary results demonstrate that the modeling accuracies can still be improved by further optimization of the filters that are used to process the measurement data to derive the training data for the neural network training.

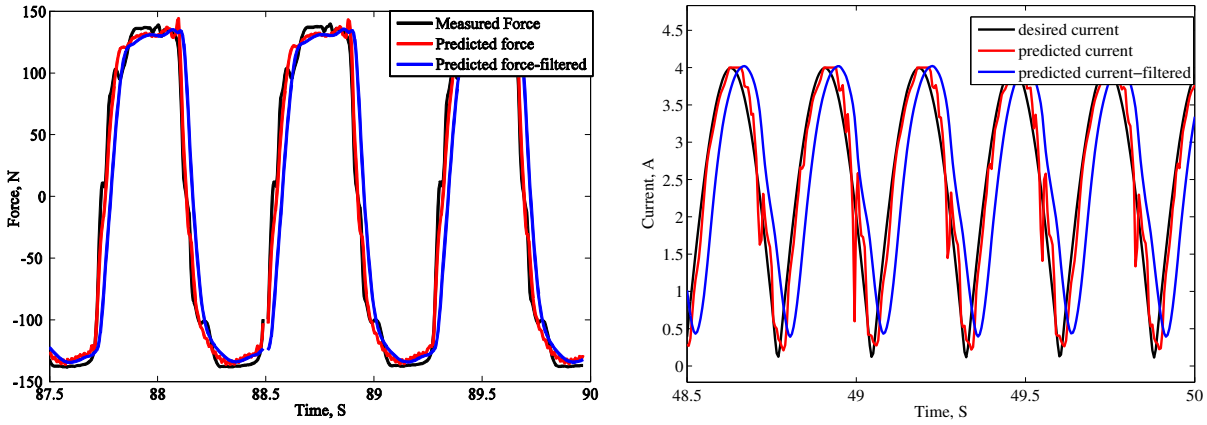

Figure 3. Validation of forward and inverse neural network models

REFERENCES

[1] T. Tse, C. Chang, Shear-Mode Rotary Magnetorheological Damper for Small-Scale Structural Control Experiments, *Journal of Structural Engineering*, 130 (2004) 904-910.

[2] C. Boston, F. Weber, L.Guzzella, Modeling of a disc-type magnetorheological damper, *Smart Mater. and Struct.*, 19 (2010) 045005 (12pp).

[3] F. Ikhouane, S. Dyke, Modeling and identification of a shear mode magneto rheological damper, *Smart Mater. and Struct.*, 16 (2007) 605-616.

[4] H. Metered, P. Bonello, S. Oyadiji, The experimental identification of magnetorheological dampers and evaluation of their controllers, *Mechanical Systems and signal Processing*, 24 (2010) 976-994.

[5] C. Chang, L. Zhou, Neural Network Emulation of Inverse Dynamics for a Magneto rheological Damper, *Journal of Structural Engineering*, 128 (2002) 231-239.

23rd Nordic Seminar on Computational Mechanics
NSCM-23
A. Eriksson and G. Tibert (Eds)

AN ARBITRARY LAGRANGIAN EULERIAN FORMULATION FOR SIMULATION OF WHEEL–RAIL CONTACT

ANDREAS DRAGANIS*, FREDRIK LARSSON AND ANDERS EKBERG

*Dept. of Applied Mechanics, Div. of Material and Computational Mechanics
Chalmers University of Technology
412 96 Gothenburg, Sweden
e-mail: andreas.draganis@chalmers.se, web page: http://www.chalmers.se/am/EN/

Key words: Computational Mechanics, Arbitrary Lagrangian Eulerian, ALE, Finite Elements.

Summary. A novel ALE-formulation of a rolling wheel is presented in the context of finite element simulations. Numerical examples illustrate the proposed strategy for a two-dimensional problem.

1 INTRODUCTION

A proper computational assessment of wheel–rail contact using the finite element method needs to be able to handle evaluation of both contact stresses and heat transfer. Regarding efficiency in these calculations, the standard approach based on a Lagrangian description of motion has a number of significant disadvantages: In a wheel–rail contact setting, this approach necessarily leads to large displacements of wheel material points. Further, it creates a need to model the whole length of rail traversed during a simulation. Even for simulations featuring short rolling distances this is prohibitively computationally expensive [1].

The presented approach suggests an Arbitrary Lagrangian Eulerian (ALE) [2] based formulation of motion. The response of the mechanical system is divided into one part corresponding to the rigid body motion (translation and rotation) and a second part capturing the deformation. The equations of motion are formulated in a reference frame travelling with the wheel. One key advantage of this approach is that the behavior of the system in the chosen intermediate configuration can be properly linearized since the displacements are small whenever strains are small. Furthermore, in the case of stationary dynamics, the solution is time-independent.

2 THEORY

2.1 Proposed ALE Description of Motion

The motion of a continuum can be described by a map, $\boldsymbol{x} = \boldsymbol{\varphi}(\boldsymbol{X}, t)$, relating the undeformed configuration, $\Omega_{\boldsymbol{X}} \ni \boldsymbol{X}$, to the deformed (current) configuration, $\omega_{\boldsymbol{x}} \ni \boldsymbol{x}$. The standard approach to solving a solid mechanics problem is the straight-forward solution of the equations of motion based on Lagrangian kinematics, as illustrated in Figure 1.

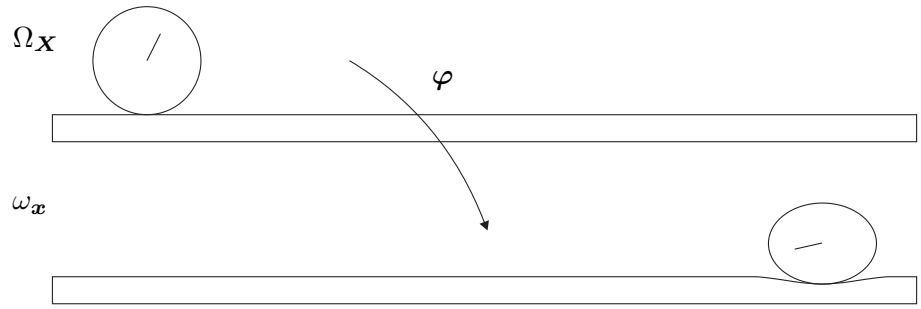

Figure 1: Illustration of the standard straight-forward approach to solving a wheel–rail contact problem.

In a wheel–rail setting however, this approach has a number of disadvantages, including the resulting large displacements of wheel material points and the need to model the whole length of rail traversed during a simulation. The present contribution suggests an Arbitrary Lagrangian Eulerian (ALE) description of motion, constructed so as to avoid these problems. In this description, two intermediate configurations are introduced, the first of which is $\Omega_{\hat{\boldsymbol{X}}} \ni \hat{\boldsymbol{X}}$, where the wheel has been *translated* and *rotated* but where no deformation is included. The second intermediate configuration is $\omega_{\hat{\boldsymbol{x}}} \ni \hat{\boldsymbol{x}}$, which also includes *deformation* of wheel and rail. Both configurations use a reference frame travelling with the wheel. Figure 2 shows a schematic illustration of the four configurations, together with their intermediary maps: $\hat{\boldsymbol{X}} = \hat{\boldsymbol{\phi}}(\boldsymbol{X}, t)$, $\hat{\boldsymbol{x}} = \hat{\boldsymbol{\varphi}}(\hat{\boldsymbol{X}}, t)$, $\boldsymbol{x} = \check{\boldsymbol{\phi}}(\hat{\boldsymbol{x}}, t)$ and $\boldsymbol{x} = \varphi(\boldsymbol{X}, t)$.

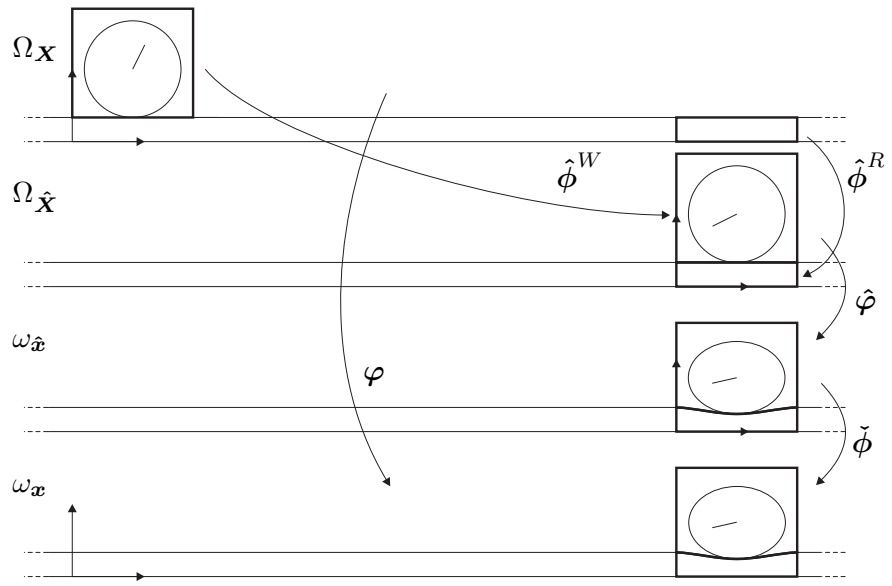

Figure 2: Illustration of configurations and maps relevant to the proposed ALE description of motion.

Recognizing that the maps $\hat{\boldsymbol{X}} = \hat{\boldsymbol{\phi}}(\boldsymbol{X}, t)$ and $\boldsymbol{x} = \check{\boldsymbol{\phi}}(\hat{\boldsymbol{x}}, t)$ can be easily identified from knowledge of the translational and rotational motion of the wheel across the rail, the problem is narrowed down to finding the map $\hat{\boldsymbol{x}} = \hat{\boldsymbol{\varphi}}(\hat{\boldsymbol{X}}, t)$. This transformation will constitute small

displacements in the case of small strains and will be time independent if the dynamical behavior of the system is stationary.

2.2 Equations of Motion

The balance of momentum equation in the standard Lagrangian formulation is

$$\rho_{\boldsymbol{X}} \boldsymbol{a} - \boldsymbol{P} \cdot \nabla_{\boldsymbol{X}} = \boldsymbol{b} \text{ in } \Omega_{\boldsymbol{X}}, \tag{1}$$

where $\rho_{\boldsymbol{X}}$ is the density, $\boldsymbol{a}$ the acceleration, $\boldsymbol{P}$ the second Piola-Kirchhoff stress tensor and $\boldsymbol{b}$ the external volume force field. $\nabla_{\boldsymbol{X}}$ is the Lagrangian gradient operator: $(\cdot)\otimes\nabla_{\boldsymbol{X}} = \partial(\cdot)/\partial\boldsymbol{X}$.

In terms of the ALE description of motion, the momentum equation becomes

$$\rho_{\hat{\boldsymbol{X}}} \left[\ddot{\bar{\boldsymbol{X}}} + d_{tt}\hat{\boldsymbol{x}} + 2\left[(d_t\hat{\boldsymbol{x}}) \otimes \hat{\boldsymbol{\nabla}}\right] \cdot \bar{\boldsymbol{v}} + \hat{\boldsymbol{F}} \cdot (D_t\bar{\boldsymbol{v}}) + \hat{\boldsymbol{G}} : (\bar{\boldsymbol{v}} \otimes \bar{\boldsymbol{v}})\right] - \hat{\boldsymbol{P}} \cdot \hat{\boldsymbol{\nabla}} - \hat{\boldsymbol{b}} = 0 \text{ in } \Omega_{\hat{\boldsymbol{X}}}, \tag{2}$$

where $D_t(\cdot) \equiv \partial(\cdot)/\partial t|_{\boldsymbol{X}}$, $d_t(\cdot) \equiv \partial(\cdot)/\partial t|_{\hat{\boldsymbol{X}}}$, $d_{tt}(\cdot) \equiv \partial^2(\cdot)/\partial t^2|_{\hat{\boldsymbol{X}}}$, $\hat{\boldsymbol{F}} \equiv \hat{\boldsymbol{x}} \otimes \hat{\boldsymbol{\nabla}}$, $\hat{\boldsymbol{G}} \equiv \hat{\boldsymbol{x}} \otimes \hat{\boldsymbol{\nabla}} \otimes \hat{\boldsymbol{\nabla}}$ and $\bar{\boldsymbol{X}}$ is the translation of the wheel center. Furthermore, $\bar{\boldsymbol{v}} = D_t\hat{\boldsymbol{X}}$ is the velocity of material points in the $\Omega_{\hat{\boldsymbol{X}}}$-configuration, implying that many of the terms appearing in the expression for the acceleration arise due to convection of material points through $\hat{\boldsymbol{X}}$-coordinates.

2.3 Contact Formulation

Two types of contact formulation, subsequently described, are employed. The penalty method introduces penalty forces at penetrating nodes that can be seen as having been derived from an additional elastic potential energy term: $\Pi^c(\underline{\boldsymbol{u}}) = \frac{1}{2}\epsilon_N \sum_{i=1}^{n_c} (g_{s_i}(\underline{\boldsymbol{u}}))^2$, where $\underline{\boldsymbol{u}}$ is the finite element displacement vector, ϵ_N is the penalty parameter pertinent to spring stiffnesses, g_{s_i} are gap functions and s_i, $i = 1, 2, \ldots, n_c$ are the node numbers of penetrating wheel nodes. The Lagrange multiplier method uses the additional elastic potential energy term $\Pi^c(\underline{\boldsymbol{u}}, \underline{\boldsymbol{\Lambda}}) = \sum_{i=1}^{n_c} \lambda_{s_i} g_{s_i}(\underline{\boldsymbol{u}})$, thereby introducing a set of Lagrange multipliers, λ_{s_i}, equal in number to the number of penetrating wheel nodes, as additional unknowns of the problem. This method allows no penetration of wheel nodes. Both methods lead to changes in both stiffness terms and external forces in the FE formulation.

3 NUMERICAL EXAMPLES

A few example numerical results are shown below, featuring 2D linear elastic contact and stationary dynamic response. Vertical displacements of the nodes along the inner boundary of the wheel are fixed. Figure 3 shows the mesh dependency regarding evaluated vertical displacement and penetration of the first contact node of the wheel. Figure 4 shows the $\omega_{\hat{\boldsymbol{x}}}$-configuration resulting from a simulation using the penalty method and example geometry, material and motion parameters. The horizontal speed of the wheel is set to 200 km/h.

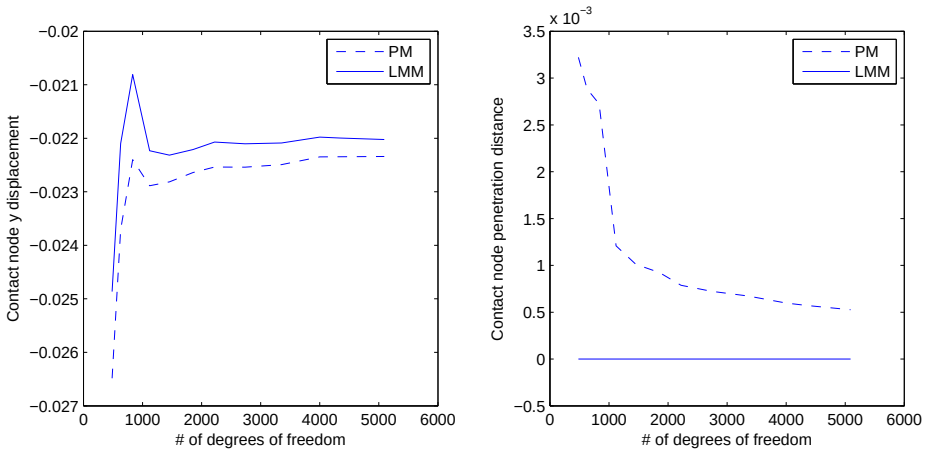

Figure 3: Dependence on mesh size of vertical displacement and penetration of the first contact node of the wheel. Results employing the penalty method and the Lagrange multiplier method are compared.

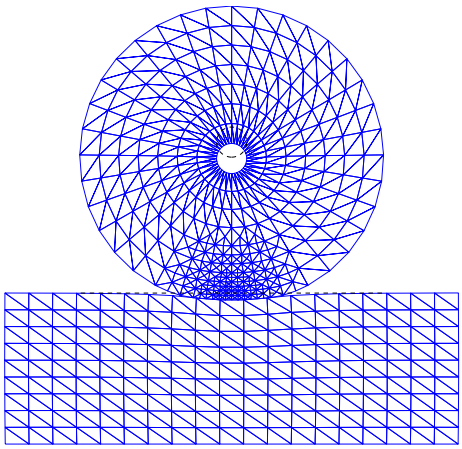

Figure 4: Deformation plot from a simulation featuring the penalty method, fixed vertical displacement of the inner boundary, local mesh refinement of the wheel and example geometry, material and motion parameters.

4 CONCLUSIONS

The proposed ALE description of motion has been described and the pertinent form of the balance of momentum equation derived. One advantage of this approach to solving the wheel–rail contact problem is that small strains leads to small displacements, which means that it provides a natural reference point for linearization of the response in the case of finite strains. Preliminary numerical results have been presented, showing some features of the numerical implementation of the FE formulation derived from the ALE momentum equation.

REFERENCES

[1] E. Kabo, A. Ekberg, P. T. Torstensson and T. Vernersson. Rolling contact fatigue prediction for rails and comparisons with test rig results. *IMechE Journal of Rail and Rapid Transit*, **224**, 303–317, (2010).

[2] J. Donea and A. Huerta, *Finite Element Methods for Flow Problems*, Wiley, (2003).

23rd Nordic Seminar on Computational Mechanics
NSCM-23
A. Eriksson and G. Tibert (Eds)

MULTISCALE MODELING OF POROUS MEDIA

CARL SANDSTRÖM*, FREDRIK LARSSON, HÅKAN JOHANSSON AND KENNETH RUNESSON

*Department of Applied Mechanics
Chalmers University of technology
SE-412 96 Göteborg, Sweden
e-mail: carl.sandstrom@chalmers.se

Key words: Porous Media, FE^2, Computational Homogenization.

Summary. Homogenization of flow in porous media is studied. The continuity equation in conjunction with Darcy's law as a constitutive relation on the macroscale, where the permeability is a function of the pressure gradient, is applied to a macroscopic domain. On the heterogenous mesoscale, a Stokes flow problem is formulated on a Representative Volume Element with a prescribed pressure gradient and suitable boundary condition. The numerical procedure for finite element simulations of the two-scale problem is outlined and illustrated by a few example problems.

1 INTRODUCTION

Porous materials are present in many natural as well as engineered structures. On the mesoscale, the material has a strongly heterogeneous composition consisting of a solid matrix with fluid filled pores, while on the macroscale the material is often modeled as homogeneous using an averaged constitutive relation. Due to the complexity of the mesostructure in this kind of materials, it is difficult to make an accurate model on the macroscopic level, thus exploring the possibilities of a multiscale approach is a natural step.

On the macroscale a Darcy flow is present which is solved using the Finite Element Method. However, instead of using a conventional constitutive relation associating the seepage velocity to the pressure gradient, another Finite Element problem is solved in each Gausspoint in order to produce the velocity given the pressure gradient. The problem solved in each Gausspoint is referred to as the mesoscale problem. This problem consists of a Stokes flow that is solved for on a representative volume element (RVE) which is geometrically a representation of the mesostructure of the porous medium. The solution to the mesoscale problem is homogenized and the result is returned to the macroproblem.

2 THE MACROSCALE PROBLEM

The macroscale problem combines the continuity equation and Darcy's law and is stated in strong form as

$$\boldsymbol{\nabla}\cdot\tilde{\boldsymbol{w}}(\boldsymbol{\nabla}\tilde{p}) = Q \qquad \text{on } \Omega \tag{1}$$

$$\tilde{p} = \tilde{p}_D \qquad \text{on } \Gamma_D \tag{2}$$

$$\tilde{\boldsymbol{w}}\cdot\boldsymbol{n} = -q \qquad \text{on } \Gamma_N \tag{3}$$

where $\tilde{\boldsymbol{w}}$ is the seepage velocity of the fluid, $\tilde{p}$ is the pressure,q is the inflow and Q is the production of fluid. Introducing the shape function $\delta\tilde{p}$, the variational form of the macroscale problem is stated as: For all $\delta\tilde{p} \in \tilde{\mathcal{Q}}$ find $\tilde{p}$ such that

$$\tilde{a}\left(\tilde{p};\delta\tilde{p}\right) = \tilde{L}\left(\delta\tilde{p}\right) \tag{4}$$

The above problem is solved using Newton-Raphson iterations until the residual is sufficiently small. In a multiscale context, the seepage velocity $\tilde{\boldsymbol{w}}$ is evaluated by solving another FE problem on the lower (meso-) scale.

3 THE MESOSCALE PROBLEM

On the mesoscale, a Stokes flow is solved for on a domain that geometrically describes the structure of the porous medium at hand. A Stokes flow can be considered a good approximation of a flow with low Reynolds number. The mesoscale domain consists of two phases, a solid phase that constitutes the matrix in which a fluid phase flows. Here, we consider the special case of rigid solid. We note that the general situation with a deformable solid requires a 3D description. Figure 1 illustrates an example of a RVE $\Omega_\square$ in 2D. On the surface of the obstacles ($\Gamma_\square^{\text{int}}$) a no slip condition is imposed.

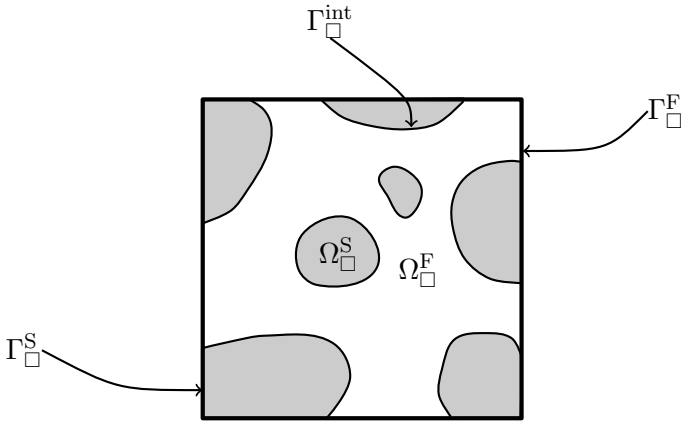

Figure 1: RVE $\Omega_\square$ consisting of a solid and a fluid phase. The solid region is denoted by $\Omega_\square^{\text{S}}$ and the fluid region is denoted $\Omega_\square^{\text{F}}$. The boundary separating the solid and the fluid phases is denoted $\Gamma_\square^{\text{int}}$, while the outer fluid boundary is denoted $\Gamma_\square^{\text{F}}$ and the outer solid boundary $\Gamma_\square^{\text{S}}$.

The strong form of the Stokes flow is stated as:

$$
\begin{aligned}
-\boldsymbol{\nabla}\cdot\boldsymbol{\sigma} &= \boldsymbol{b} && \text{on } \Omega^{\mathrm{F}}_{\square} && (5)\\
\boldsymbol{\nabla}\cdot\boldsymbol{v} &= \mathbf{0} && \text{on } \Omega^{\mathrm{F}}_{\square} && (6)\\
\boldsymbol{v} &= \mathbf{0} && \text{on } \Gamma^{\mathrm{int}}_{\square\ D} && (7)\\
\boldsymbol{v} &= \boldsymbol{v}_D && \text{on } \Gamma^{\mathrm{F}}_{\square D} && (8)\\
\boldsymbol{\sigma}\cdot\boldsymbol{n} &= \boldsymbol{t} && \text{on } \Gamma^{\mathrm{F}}_{\square N} && (9)
\end{aligned}
$$

Since the macroscopic constitutive relation is dependent on the macroscopic pressure gradient $\boldsymbol{\nabla}\tilde{p}$, the mean pressure gradient on the RVE is prescribed to $\boldsymbol{\nabla}\tilde{p}$. This is achieved by introducing an additional equation to the Stokes flow equations. To produce a non-overdetermined system of equations, either the traction or the velocities are set as unknown constants along the edges, thus producing a system with a unique solution. The system of equation takes on different shapes depending on the choice of additional unknowns.

In the case of constant unknown traction along the boundaries of the RVE, the variational form is stated as: Given $\boldsymbol{\nabla}\tilde{p}$, find the velocity $\boldsymbol{v} \in \mathcal{V}$, the pressure $p \in \mathcal{Q}$ and the unknown, constant traction $\boldsymbol{t}_\Gamma$ such that for all test functions $\delta\boldsymbol{v} \in \mathcal{V}$, $\delta p \in \mathcal{Q}$ and $\delta\overline{\boldsymbol{w}} \in \mathbf{R}^n$

$$
\begin{cases}
a_\square(\boldsymbol{v},\delta\boldsymbol{v}) + b_\square(p,\delta\boldsymbol{v}) - c_\square(\boldsymbol{t}_\Gamma,\delta\boldsymbol{v}) &= l_\square(\delta\boldsymbol{v})\\
b_\square(\delta p,\boldsymbol{v}) &= 0\\
\langle\boldsymbol{\nabla}p\rangle_{\Omega^{\mathrm{F}}_{\square}} &= \boldsymbol{\nabla}\tilde{p}
\end{cases}
\tag{10}
$$

where $\boldsymbol{t}_\Gamma$ is the constant unknown traction satisfying the prescribed pressure gradient. Here, we introduce the notation $\langle\bullet\rangle_{\Omega^{\mathrm{F}}_{\square}}$ for the volume average over the fluid domain. The constant traction can vary in different ways along the boundary, e.g in a linear fashion.

In the case of constant velocity along the boundaries, the problem is stated as: Given $\boldsymbol{\nabla}\tilde{p}$ and $\hat{\varphi}$, find the velocity $\boldsymbol{v} \in \mathcal{V}$, the pressure $p \in \mathcal{Q}$ and the unknown, constant velocity $\boldsymbol{v}_\Gamma$ such that for all test functions $\delta\boldsymbol{v} \in \mathcal{V}$, $\delta p \in \mathcal{Q}$ and $\delta\overline{\boldsymbol{w}} \in \mathbf{R}^n$

$$
\begin{cases}
a_\square(\boldsymbol{v}+\hat{\varphi}\boldsymbol{v}_\Gamma,\delta\boldsymbol{v}) + b_\square(p,\delta\boldsymbol{v}) &= l_\square(\delta\boldsymbol{v})\\
b_\square(\delta p,\boldsymbol{v}) &= 0\\
\langle\boldsymbol{\nabla}p\rangle_{\Omega^{\mathrm{F}}_{\square}} &= \boldsymbol{\nabla}\tilde{p}
\end{cases}
\tag{11}
$$

where $\boldsymbol{v}_\Gamma$ is the unknown constant velocity along the boundary of $\Omega_\square$. The scalar $\hat{\varphi}$ is a weight that scales the constant velocity such that it appears to have the shape of fully developed laminar flow in a pipe to prevent large velocity gradients. $\hat{\varphi}$ is computed in such a fashion that the continuity equation is fulfilled.

4 NUMERICAL RESULTS

Special attention is paid to how convergence of the solution depends on the choice of boundary conditions and the size of the RVE. Results show that choosing unknown constant velocity results in much faster convergence than in the case of unknown constant traction. Figure 2 shows the two scales where the magnification is the mesoscale solution at a specific Gauss point. On the

left side boundary of the macroscale domain, a flux q is prescribed while on the right side the pressure p is prescribed.

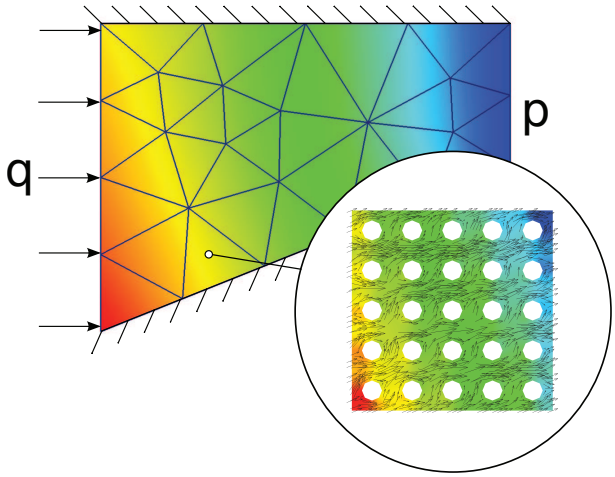

Figure 2: Illustration of the two scales.

5 CONCLUSIONS AND OUTLOOK

A novel two-scale formulation of porous media has been presented. The algorithm has been implemented in 2D using two-scale finite element analysis, so-called FE^2. Future work includes the extension to a deformable solid matrix.

23rd Nordic Seminar on Computational Mechanics
NSCM-23
A. Eriksson and G. Tibert (Eds)

ERROR ANALYSIS OF THE INVERSE POISSON PROBLEM WITH SMOOTHNESS PRIOR

ANTTI H. HUHTALA, SVEN BOSSUYT AND ANTTI J. HANNUKAINEN

Aalto University, Department of Mathematics and Systems Analysis
P.O. Box 11100, FI-00076 AALTO, Finland

Key words: Inverse problem, Poisson problem, Finite element method

1 INTRODUCTION

The inverse Poisson problem is an important prototype of an indirect measurement problem, when the underlying physics can be modeled as a diffusion process. Important examples of this type include inverse heat transfer problems, electrocardiography problems as well as inverse problems of elasticity.

The model describing how the measured quantity depends on the quantity of interest is called the forward problem. The inverse problem can be described as the inverse of the forward problem. The inverse Poisson problem is ill-conditioned in the sense that a small perturbation in the measured quantity can cause an arbitrarily large change in the quantity of interest. Because of this nature, prior knowledge regarding the behavior of the quantity of interest is needed. Often the quantity of interest is assumed to be a smooth function. The solution is then obtained as a regularized inverse of the forward problem.

Since in general not even the forward Poisson problem can be solved exactly, only an approximation to the inverse solution is obtainable. It is due to discretizing the quantity of interest and using a FE-approximation of the forward problem. Both the discretization and the use of an approximate forward problem cause a certain amount of error. The effects of both error sources are investigated.

2 STATEMENT OF THE PROBLEM

2.1 The forward problem

Using the terminology of heat transfer problems, the problem we consider is the problem of reconstructing the heat sources based on a number of temperature measurements.

The model for the transfer of heat is the Poisson equation

$$\begin{aligned} \nabla \cdot (\sigma \nabla u) &= f \quad \text{in } \Omega \\ u &= u_D \quad \text{on } \partial\Omega \end{aligned} \tag{1}$$

where u is the temperature of the material, f describes the heat sources in the domain Ω, u_D is a fixed temperature on the boundary and σ is the heat conductivity of the material.

With suitable additional assumptions, there exists a unique solution to this problem for each $f \in L^2(\Omega)$. Let K be the solution operator to the problem, such that $u = K^{-1}f$. Let K_h^{-1} be the finite element solution operator with mesh density parameter h, and the corresponding FE solution $u_h = K_h^{-1}f$.

The temperature measurements are modeled as linear functionals on the temperature field. That is, the measurement is a vector m such that

$$m = [(h_1, u), (h_2, u), \ldots, (h_N, u)]^T = Hu = HK^{-1}f. \tag{2}$$

For technical reasons, the measurement functionals are assumed to be square integrable, i.e. $h_1, \ldots, h_N \in L^2(\Omega)$.

2.2 Inverse problem

In the inverse problem, the heat sources f are reconstructed from a measurement m. Unfortunately, the relation in equation (2) is not generally uniquely invertible. By injecting additional information to the problem, for instance by using the method of statistical inversion or generalized Tikhonov regularization, a reconstruction can be obtained as the following minimization problem[1]

$$f^r = \underset{f \in F}{\operatorname{argmin}} \left\{ \|HK^{-1}f - m\|^2 + b(f - \bar{f}, f - \bar{f}) \right\}. \tag{3}$$

As we are interested in enforcing the smoothness of the reconstruction, the space F is chosen to be the Sobolev space $H^1(\Omega)$. The bilinear form $b(\cdot, \cdot)$ acts as a cost function, enforcing the reconstruction f^r to have suitable properties. We assume the bilinear form $b(f, g)$ to be (i) continuous and (ii) coercive in F, i.e.

$$\text{(i)} \quad |b(f, g)| \leq C\|f\|_1\|g\|_1 \quad \forall f, g \in F, \tag{4}$$

$$\text{(ii)} \quad b(f, f) \geq c\|f\|_1^2 \qquad \forall f \in F. \tag{5}$$

The term $b(f - \bar{f}, f - \bar{f})$ in the minimization thus enforces that f is close to $\bar{f}$ and that the difference $f - \bar{f}$ is smooth.

This minimization problem can be written in variational form as: find $f^r \in F$ such that

$$a(f^r, g) = l(g) \quad \forall g \in F, \tag{6}$$

where

$$a(f, g) = (HK^{-1}f)^T(HK^{-1}g) + b(f, g) \text{ and } l(g) = m^T(HK^{-1}g) + b(\bar{f}, g). \tag{7}$$

The bilinear form $a(\cdot, \cdot)$ is continuous and coercive in F, so the problem does have a unique solution. However, because both $a(\cdot, \cdot)$ and $l(\cdot)$ contain the solution operator K^{-1} of the forward problem, they cannot be directly evaluated, and thus the problem cannot be directly discretized. To remedy this, we modify the problem to use the FE solution operator K_h^{-1} instead.

The modified problem is then: find $\hat{f}^r \in F$ such that

$$\hat{a}(\hat{f}^r, g) = \hat{l}(g) \quad \forall g \in F, \tag{8}$$

where

$$a(f, g) = (HK_h^{-1}f)^T(HK_h^{-1}g) + b(f, g) \text{ and } l(g) = m^T(HK_h^{-1}g) + b(\bar{f}, g). \tag{9}$$

Since the bilinear form $\hat{a}(\cdot,\cdot)$ is continuous and coercive in the space F, the variational problem (8) has a unique solution. The problem can then be discretized by choosing a suitable finite subspace $F_h \subset F$ and solving the variational equation in that space: find $\hat{f}_h^r \in F_h$ such that

$$\hat{a}(\hat{f}_h^r, g) = \hat{l}(g) \quad \forall g \in F_h. \tag{10}$$

3 ERROR ANALYSIS

The error of the approximate solution $\hat{f}_h^r$ can be broken down into two components

$$\|f^r - \hat{f}_h^r\| = \|f^r - \hat{f}^r + \hat{f}^r - \hat{f}_h^r\| \leq \|f^r - \hat{f}^r\| + \|\hat{f}^r - \hat{f}_h^r\|. \tag{11}$$

The first part, the term $\|f^r - \hat{f}^r\|$, is due to using the FE-approximation of the forward problem instead of the exact solution. We refer to this error source as the consistency error. The second part, $\|\hat{f}^r - \hat{f}_h^r\|$, is the discretization error of limiting the solution to a finite subspace.

To estimate the consistency error, we define two operators

$$E_a(f,g) = a(f,g) - \hat{a}(f,g) \quad \forall f,g \in F \text{ and } E_l(g) = l(g) - \hat{l}(g) \quad \forall g \in F. \tag{12}$$

The operator $E_l(\cdot)$ can be estimated as

$$\begin{aligned} |E_l(g)| = |l(g) - \hat{l}(g)| &= |m^T(H(K^{-1} - K_h^{-1})g)| \leq \|m\|\|H(K^{-1} - K_h^{-1})g\| \\ &\leq \|m\|\|H\|_{L^2(\Omega)\to\mathbb{R}^N}\|K^{-1}g - K_h^{-1}g\|_{L^2(\Omega)} \leq Ch^2\|m\|\|g\|_{L^2(\Omega)}, \end{aligned} \tag{13}$$

where the last inequality is due to the Aubin-Nitsche L^2-error estimate of the finite element solution[2,3]. The operator $E_a(\cdot,\cdot)$ can be estimated similarly to give

$$|E_a(f,g)| \leq Ch^2\|f\|_{L^2(\Omega)}\|g\|_{L^2(\Omega)}. \tag{14}$$

Due to the coerciveness of $a(\cdot,\cdot)$ we can estimate the consistency error as

$$\begin{aligned} \frac{1}{c}\|f^r - \hat{f}^r\|_1^2 \leq |a(f^r - \hat{f}^r, f^r - \hat{f}^r)| &= |E_l(f^r - \hat{f}^r) - E_a(\hat{f}^r, f^r - \hat{f}^r)| \\ &\leq |E_l(f^r - \hat{f}^r)| + |E_a(\hat{f}^r, f^r - \hat{f}^r)| \leq Ch^2(\|m\| + \|f^r\|_{L^2(\Omega)})\|f^r - \hat{f}^r\|_1. \end{aligned} \tag{15}$$

To estimate the discretization error, we note that since $\hat{a}(\cdot,\cdot)$ is continuous and coercive in the space F, then Cea's lemma holds true. It states that the discrete solution $\hat{f}_h^r$ is the best approximation of $\hat{f}^r$ up to a constant C, i.e. for any $f \in F_h$

$$\|\hat{f}^r - \hat{f}_h^r\|_1 \leq C\|\hat{f}^r - f\|_1 \leq C(\|f^r - \hat{f}^r\|_1 + \|f^r - f\|_1). \tag{16}$$

Plugging in the previous estimate for the consistency error and using known interpolation results as well as the Aubin-Nitsche lemma[2,3], the errors in H^1-norm and L^2-norm can be estimated as

$$\|\hat{f}^r - \hat{f}_h^r\|_1 \leq Ch\|f^r\|_2 + Ch^2(\|m\| + \|f^r\|_{L^2(\Omega)}) \leq Ch\|f^r\|_2 \tag{17}$$

$$\text{and } \|\hat{f}^r - \hat{f}_h^r\|_0 \leq Ch\|\hat{f}^r - \hat{f}_h^r\|_1 \leq Ch^2\|f^r\|_2. \tag{18}$$

Combining the consistency error and the discretization error, the following estimates hold

$$\|f^r - \hat{f}_h^r\|_1 \leq Ch^2(\|m\| + \|f^r\|_{L^2(\Omega)}) + Ch\|f^r\|_2 \leq Ch\|f^r\|_2 \tag{19}$$

$$\text{and } \|f^r - \hat{f}_h^r\|_0 \leq Ch^2(\|m\| + \|f^r\|_2). \tag{20}$$

4 NUMERICAL EXPERIMENTS

Numerical tests were run in the rectangular domain $\Omega = (0, 4) \times (0, 1)$. The measurements were average temperatures over discs of radius 0.1, which were scattered in a uniform grid over the domain. The bilinear form $b(\cdot, \cdot)$ was chosen to be $b(f, f) = 10^{-3}\|f\|_1^2$. A highly refined numerical solution acted as the exact solution against which the error was computed.

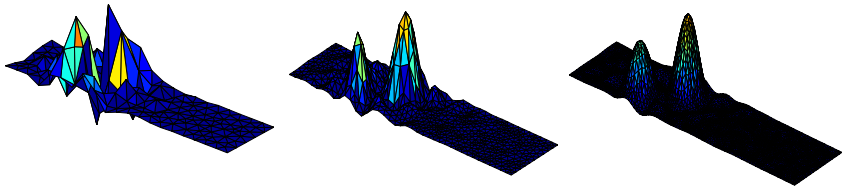

Figure 1: Approximate solutions of the inverse problem with an increasing number of DOFs

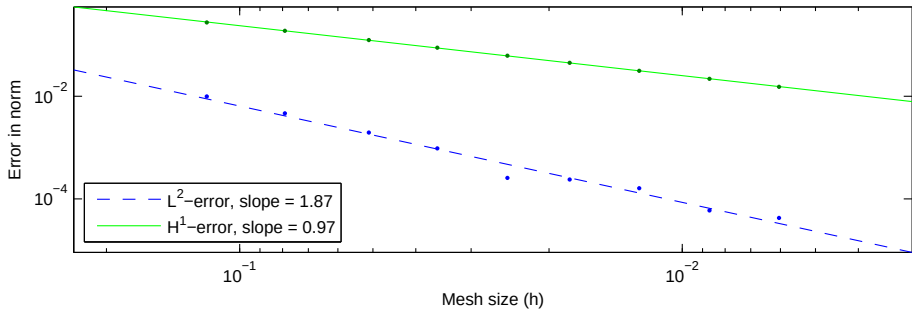

Figure 2: L^2 and H^1 errors of the approximate solution with different values of h. The convergence rates correspond well with the rates estimated a priori in equations (19) and (20)

5 CONCLUSIONS

Surprisingly, the smoothness regularized inverse Poisson problem is very similar to the standard Poisson problem in what comes to analysis. Also, it turns out that the error due to replacing the exact forward problem with a finite element approximation is at most the same order of magnitude as the discretization error.

6 ACKNOWLEDGEMENTS

This research is a part of the ISMO project of the Multidisciplinary Institute for Digitalisation and Energy (MIDE) of Aalto University.

REFERENCES

[1] Somersalo, E. & Kaipio, J. *Statistical and Computational Inverse Problems* (Springer, 2004).

[2] Braess, D. *Finite elements: Theory, Fast Solvers and Applications in Solid Mechanics* (Cambridge University Press, 2007).

[3] Johnson, C. *Numerical Solution of Partial Differential Equations by the Finite Element Method* (Dover Publications, 2009).

23rd Nordic Seminar on Computational Mechanics
NSCM-23
A. Eriksson and G. Tibert (Eds)

FREE VIBRATIONS OF BEAMS WITH NON-UNIFORM CROSS-SECTIONS AND ELASTIC END CONSTRAINTS USING HAAR WAVELET METHOD

HELLE HEIN AND LJUBOV FEKLISTOVA

Institute of Computer Science
University of Tartu
Liivi 2, 50409 Tartu, Estonia
e-mail: helle.hein@ut.ee

Key words: Free Vibrations, Variable Cross-Section, Haar Wavelets, Tapered Beams.

Summary. Free vibrations of beams with non-uniform cross-sections and elastic end constraints are studied in the present paper. The Chen-Chiao Haar wavelet method is applied to different types of cross-sections and end constraints. Euler-Bernoulli theory of bending is used to describe motion of the beam. The computations carried out with the aid of the proposed method are compared with the cases described in literature.

1 INTRODUCTION

Non-uniform beams provide a better distribution of strength and mass along the structure in comparison to uniform beams. Moreover, non-uniform beams satisfy special architectural and functional requirements. The transverse vibrations of non-uniform Euler-Bernoulli beams have been extensively studied by several authors. The governing equation for the free vibrations of non-uniform Euler-Bernoulli beam is a fourth-order linear differential equation with variable coefficients. The analytical solutions have been found only for some special cases including tapered beams. These solutions involve Bessel functions[1], orthogonal polynomials or hypergeometric functions[2], and Frobenius method[3]. Hsu, Lai and Chen[4] applied the Adomian modified decomposition method to the vibrating beams with linearly varying breadth and depth. The Rayleigh-Ritz method has been applied by Zhou and Cheung[5] to the vibrating beams with breadth and depth varying proportionally to the arbitrary power of space coordinate. A special case of exponentially varying cross-section has been considered by Ece, Aydogdu, Taskin[6]. In the present paper, the Haar wavelet method[7,8,9] is adjusted to the free vibration of beams with arbitrary varying cross-sections. The paper is divided into four parts. In section 2, the formulas for calculating the integrals of the Haar wavelets are provided. In section 3, the solution to the problem is described. In section 4, a numerical example is presented.

2 INTEGRATION OF HAAR WAVELETS

The Haar wavelets belong to the special class of discrete orthonormal wavelets. The latter wavelets generated from the same mother wavelet form a basis whose elements are orthonormal

to each other and are normalized to unit length. This property allows each wavelet coefficient to be computed independently of other wavelets. The Haar wavelet family is a group of square waves:

$$h_i(x) = \begin{cases} 1 & \text{for } x \in [\frac{k}{m}, \frac{2k+1}{2m}], \\ -1 & \text{for } x \in [\frac{2k+1}{2m}, \frac{k+1}{m}], \\ 0 & \text{elsewhere.} \end{cases} \tag{1}$$

Integer $m = 2^j (j = 0, 1, \dots J)$ is a factor of scale; $k = 0, 1, \dots m-1$ is the factor delay. Integer J determines the maximal level of resolution. Index i in (1) is calculated as $i = m + k + 1$; the minimal value for i is two (if $j = 0$, then $m = 1, k = 0$); the maximal value of i is $2M$, which is 2^{J+1}. If index i is equal to one, the corresponding scaling function is $h_1(x) = 1$ if $x \in [0, 1]$, and $h_1(x) = 0$ elsewhere.

For further studies, the integrals of the wavelets

$$p_{\alpha,i}(x) = \int_0^x p_{\alpha_{i-1,i}(x)} dx \tag{2}$$

are required. In (2) $p_{0,i}(x) = h_i(x)$. These integrals are calculated analytically[9]. In case $i = 1$, the integral of wavelet is $p_{\alpha,1}(x) = x^\alpha/\alpha!$, and in case $i > 1$

$$p_{\alpha,i}(x) = \begin{cases} 0 \text{ for } x < \frac{k}{m}, \\ \frac{1}{\alpha!}(x - \frac{k}{m})^\alpha \text{ for } x \in [\frac{k}{m}, \frac{2k+1}{2m}], \\ \frac{1}{\alpha!}[(x - \frac{k}{m})^\alpha - 2(x - \frac{2k+1}{2m})^\alpha)] \text{ for } x \in [\frac{2k+1}{2m}, \frac{k+1}{m}], \\ \frac{1}{\alpha!}[(x - \frac{k}{m})^\alpha - 2(x - \frac{2k+1}{2m})^\alpha) + (x - \frac{k+1}{m})^\alpha] \text{ for } x > \frac{k+1}{m}. \end{cases} \tag{3}$$

The values $p_{\alpha,i}(0)$ and $p_{\alpha,i}(1)$ should be calculated in order to satisfy boundary conditions.

3 TRANSVERSE VIBRATIONS OF NON-UNIFORM EULER-BERNOULLI BEAMS

Let us consider an isotropic beam with a variable cross-section of length L. Introducing the quantities:

$$\xi = \frac{x}{L}, k^4 = \frac{\rho A_0 \omega^2 L^4}{E I_0}, \tag{4}$$

the equation of motion for transverse vibrations is given by:

$$\frac{d^2}{d\xi^2}[I(\xi)\frac{d^2 w(\xi)}{d\xi^2}] - k^4 A(\xi) w(\xi) = 0, \xi \in [0, 1], \tag{5}$$

where $w(\xi)$ is the transverse deflection, $A(\xi)$ is the cross-sectional area at position ξ, $I(\xi)$ is the moment of inertia of $A(\xi)$. In (4), ρ is the mass density of the beam material, E is the Young's modulus, k is the dimensionless natural frequency, A_0 and I_0 are the reference cross-section area and the moment of inertia at $\xi = 0$, respectively. The boundary conditions in the presence of translational and rotational spring constraints at $\xi = 0$ are presented as[4]:

$$\frac{d}{d\xi}[I(\xi)\frac{d^2w(\xi)}{d\xi^2}] + k_t w(\xi) = 0, \tag{6}$$

$$I(\xi)\frac{d^2w(\xi)}{d\xi^2} - k_r\frac{dw(\xi)}{d\xi} = 0. \tag{7}$$

In (6) and (7), the non-dimensional translational and rotational spring coefficients k_t and k_r are

$$k_t = \frac{K_T L^3}{EI_0}, k_r = \frac{K_R L}{EI_0}. \tag{8}$$

The boundary conditions at $\xi = 1$ are formulated analogically. The fourth derivative of the solution (5)-(7) is sought in the form:

$$w'''' = \sum_{i=1}^{2M} a_i h_i(\xi), \tag{9}$$

where a_i are the unknown wavelet coefficients. Integration of (9) four times, results in

$$\begin{aligned} w''' &= \textstyle\sum_{i=1}^{2M} a_i p_{1,i}(\xi) + C_1, \\ w'' &= \textstyle\sum_{i=1}^{2M} a_i p_{2,i}(\xi) + C_1\xi + C_2, \\ w' &= \textstyle\sum_{i=1}^{2M} a_i p_{3,i}(\xi) + 0.5C_1\xi^2 + C_2\xi + C_3, \\ w &= \textstyle\sum_{i=1}^{2M} a_i p_{4,i}(\xi) + (\frac{1}{6})C_1\xi^3 + 0.5C_2\xi^2 + C_3\xi + C_4. \end{aligned} \tag{10}$$

Substituting (10) into (5) - (7) and evaluating $I(\xi)$ and $A(\xi)$ at the collocation points, the linear homogeneous system of equations for determination of natural frequencies and mode shapes is obtained.

4 NUMERICAL EXAMPLE

Consider a truncated at α tapered beam[5] with parabolic-taper width $b(\xi) = b_0\sqrt{\xi}$ and linear-taper height $h(\xi) = h_0\xi$. The first three eigenfrequency parameters for boundary conditions (on the left end $k_r = k_t = 0$ and on the right end $k_r \to \infty, k_t \to \infty$) with $J = 5$ are presented in Table 1. The calculated results correspond well to the previous works.

5 CONCLUSIONS

The main advantages of the Haar wavelet method are its simplicity and small computational costs: high accuracy is obtained by a small number of grid points. The method is convenient to solve boundary value problems since the boundary conditions are taken into account automatically.

α	Ω_1 Present	Ω_1 Ref [5]	Ω_2 Present	Ω_2 Ref [5]	Ω_3 Present	Ω_3 Ref [5]
0.1	5.8383	5.8382	16.6901	16.696	34.8190	34.854
0.3	4.7574	4.7577	17.5988	17.600	41.6669	41.660
0.5	4.2101	4.2100	18.9250	18.922	47.9306	47.907
0.8	3.7303	3.7301	20.8437	20.838	56.4426	56.453

Table 1: The first three eigenfrequency parameters $\Omega_i = k^2$ for a beam with parabolic-taper width and linear-taper height

REFERENCES

[1] M. A. De Rosa and N. M. Auciello. Free vibrations of tapered beams with flexible ends. *Comput. Struct.*, **60**, 197–202, (1996).

[2] D. I. Caruntu. Dynamic modal characteristics of transverse vibrations of cantilevers of parabolic thickness. *Mech. Res. Commun.*, **36**, 391–404, (2009).

[3] S. Naguleswaran. Vibration in the two principal planes of a non-uniform beam of rectangular cross-section, one side of which varies as the square root of the axial co-ordinate. *J. Sound. Vib.*, **172**, 305–319, (1994).

[4] J. C. Hsu, H. Y. Lai, C.K. Chen. Free vibration of non-uniform EulerBernoulli beams with general elastically end constraints using Adomian modified decomposition method. *J. Sound. Vib.*, **318**, 965–981, (2008).

[5] D. Zhou and Y.K. Cheung. The free vibration of a type of tapered beams. *Comput. Methods Appl. Mech. Engrg.*, **188**, 203–216, (2000).

[6] M. C. Ece, M. Aydogdu and V. Taskin. Vibration of a variable cross-section beam. *Mech. Res. Commun.*, **34**, 78–84, (2007).

[7] C.F. Chen and C.H. Hsiao. Haar wavelet method for solving lumped and distributed-parameter systems. *IEE. P. Contr. Theor. App.*, **144**, 87–94, (1997).

[8] C.F. Chen and C.H. Hsiao. Wavelet approach to optimising dynamic systems. *IEE. P. Contr. Theor. App.*, **146**, 213–219, (1997).

[9] Ü. Lepik. Buckling of Elastic Beams by the Haar Wavelet Method. *Int. J. Solids Struct.* (to be appear).

23rd Nordic Seminar on Computational Mechanics
NSCM-23
A. Eriksson and G. Tibert (Eds)

ADJOINT SIMULATION OF GUIDED PROJECTILE TERMINAL PHASE

TIMO SAILARANTA AND ARI SILTAVUORI

Aalto University School of Science and Technology, Finland
e–mail: timo.sailaranta@tkk.fi, ari.siltavuori@tkk.fi

Key words: Flight Mechanics, Adjoint, Guided Projectile.

Summary. *Guided projectile terminal phase against target at ground level is investigated using a simplified Adjoint simulation. A pseudo-optimal projectile navigation gain is looked for against a target disturbing the projectile guidance. The use of counter-measures is modeled as a sudden target position shift and velocity change when the true target is finally detected. The miss distances obtained are studied and the "optimal" navigation gain is chosen based on the maximum tolerated miss distance.*

1 INTRODUCTION

Beside the time-forward direct simulations the Adjoint technique is often utilized in guided weapon end-game analysis. The method has particularly merit to quickly give performance projections of linear time-variant systems. So far the method has not been used as widely as one would expect based on its flexibility and application potential[1]. The objective of this paper is to study the capability of the method to predict the end-game miss distance.

2 ADJOINT SIMULATION MODEL

The baseline projectile guidance loop at the background of the Adjoint model is depicted in Fig 1. In this study the guided projectile systems model consists simply of five first order lags in series. The first two are the seeker-head lags (τ_{SH} for seeker-head and τ_N for noise filter) and the third one is for the autopilot. The two remaining are modeling the projectile inertia (τ_{AF}). The time constants are 0.1 s for each component modeled giving the total time constant $\tau_{tot} = 0.5$ s.

Projectile maneuvering capability was not limited to maintain the system linearity. The standard proportional navigation algorithm was used in this study. The closing speed V_c was chosen to be 300 m/s. No aerodynamic data was explicitly present in the computations.

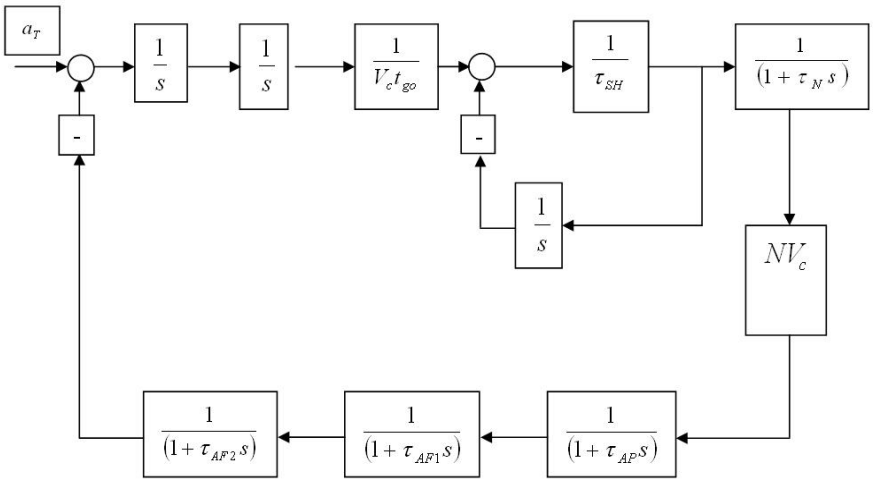

Figure 1: The time-forward missile guidance loop used in this study. The Adjoint model is based on this original system.

In the traditional presentation with the inverted block-diagram signal flow the original system output of interest (the miss distance) is seen to become an impulsive input to the Adjoint system. Correspondingly the original system input turns into an Adjoint output[1]. However, the traditional Adjoint construction is not performed in this study. Instead of that, the presentation follows the text of reference[2] with the Adjoint method derived in the general setting of state-space models.

The block diagram of Fig 1system can be written in state space form

$$\begin{aligned} \dot{\mathbf{x}} &= A\mathbf{x}(t) + B\mathbf{u}(t) \\ \mathbf{y} &= C\mathbf{x}(t) \end{aligned} \tag{1}$$

and we obtain by inspection

$$\frac{d}{dt}\begin{bmatrix} \dot{\xi} \\ \xi \\ \lambda_{SH} \\ \dot{\lambda}_N \\ a_{AP} \\ a_{AF1} \\ a_{AF2} \end{bmatrix} = \begin{bmatrix} 0 & 0 & 0 & 0 & 0 & 0 & -1 \\ 1 & 0 & 0 & 0 & 0 & 0 & 0 \\ 0 & 1/(\tau_{SH} V_c t_{go}) & -1/\tau_{SH} & 0 & 0 & 0 & 0 \\ 0 & 1/(\tau_{SH}\tau_N V_c t_{go}) & -1/(\tau_{SH}\tau_N) & -1/\tau_N & 0 & 0 & 0 \\ 0 & 0 & 0 & NV_c/\tau_{AP} & -1/\tau_{AP} & 0 & 0 \\ 0 & 0 & 0 & 0 & 1/\tau_{AF1} & -1/\tau_{AF1} & 0 \\ 0 & 0 & 0 & 0 & 0 & 1/\tau_{AF2} & -1/\tau_{AF2} \end{bmatrix} \begin{bmatrix} \dot{\xi} \\ \xi \\ \lambda_{SH} \\ \dot{\lambda}_N \\ a_{AP} \\ a_{AF1} \\ a_{AF2} \end{bmatrix} + \begin{bmatrix} 1 \\ 0 \\ 0 \\ 0 \\ 0 \\ 0 \\ 0 \end{bmatrix} n_T \tag{2}$$

The input to system is the target maneuvering $n_T(t)$ which is taken to be 0 in this study. Variable $t_{go} = t_F$, where t_{go} is the time-to-go from the impulse initiation (= resolution of the target location and speed) to the interception and t_F is the final time or the time of flight. The

seeker-head turning angle is denoted as λ.

The initial state vector $\mathbf{x_o}$ is

$$x_0 = \begin{bmatrix} w & \Delta & 0 & 0 & 0 & 0 & 0 \end{bmatrix}^T \tag{3}$$

where the terms w and Δ are the target lateral velocity change and position shift. The miss distance is wished as the result and the output is chosen to be

$$y = \begin{bmatrix} 0 & 1 & 0 & 0 & 0 & 0 & 0 \end{bmatrix} \begin{bmatrix} \dot{\xi} \\ \xi \\ \lambda_{SH} \\ \dot{\lambda}_N \\ a_{AP} \\ a_{AF1} \\ a_{AF2} \end{bmatrix} \tag{4}$$

where the matrix C is

$$C = \begin{bmatrix} 0 & 1 & 0 & 0 & 0 & 0 & 0 \end{bmatrix} \tag{5}$$

The Adjoint of the time-forward state-space model is

$$\frac{\mathrm{d}}{\mathrm{d}t_{go}} \mathbf{x}^{adj} = A^T \mathbf{x}^{adj} \tag{6}$$
$$\mathbf{x}^{adj}(0) = C^T$$

The miss distance ξ due to the target step-like shift is obtained from

$$\xi(t_F) = \Delta {x_2}^{adj}(t_F - t_o) \tag{7}$$

and the miss distance due to the target initial lateral velocity w is

$$\xi(t_F) = w {x_1}^{adj}(t_F - t_o) \tag{8}$$

Since the original system is now reversed the term ${x_1}^{adj}$ is obtained as an integral of ${x_2}^{adj}$

END-GAME GEOMETRY

The target is at ground and is disturbing the terminal phase of the projectile flight. The projectile resolves the true target at some point and this is seen as the sudden target lateral shift (10 m) and/or velocity (±10 m/s). The discontinuously appearing changes are defined to

be positive to East (right, see Fig 2). The projectile is approaching about from above and only the three final seconds are investigated. The projectile pitch and yaw guidance loops are identical and can be studied separately if wished.

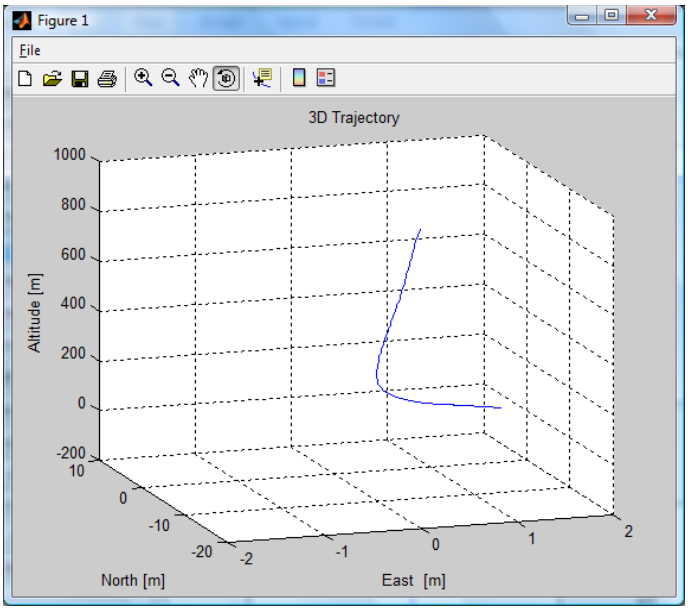

Figure 2: The end game geometry studied. The projectile is flying towards North from about 900 m altitude and the apparent target is located at the Origin at ground level 0 m. The true target at right is detected at some point of the terminal phase. In the Adjoint simulations the sudden lateral shift 10 m and velocity change (±10 m/s) will take place at all t_{go} -values in one run.

RESULTS

The obtained miss distances are depicted in Fig 3 as a function of time-to-go t_{go}. It indicates the true target location/velocity observation time before the interception. The benefit of the Adjoint model is capability to give all the results as a function of t_{go} in a single run. Only four runs were needed to get the results depicted in Fig 3. The combined results were obtained by summing the contributions of the lateral shift and velocity. The miss distance is defined to be positive here when the true target position is to right (east) from the projectile impact point.

The hit-criterion in this paper is defined to be 2 meters or less. The t_{go} –windows to hit for different navigation gains N (0, 1, 2 and 3) are compared. Based on this very limited study it seems that the case with N=2 gives most hit opportunities if the true target is detected at the end of the projectile trajectory.

It is worth of noting that the projectile accelerations obtained at small t_{go}-values are fairly high (up to 25 g) and may exceed some true maneuvering capability available. However it is also interesting to note that a projectile with saturated acceleration may sometimes have a smaller miss distance than a projectile with “unlimited” maneuvering capacity[1]. Particularly

the small t_{go} -miss distances with high gain N might be overestimated in this study.

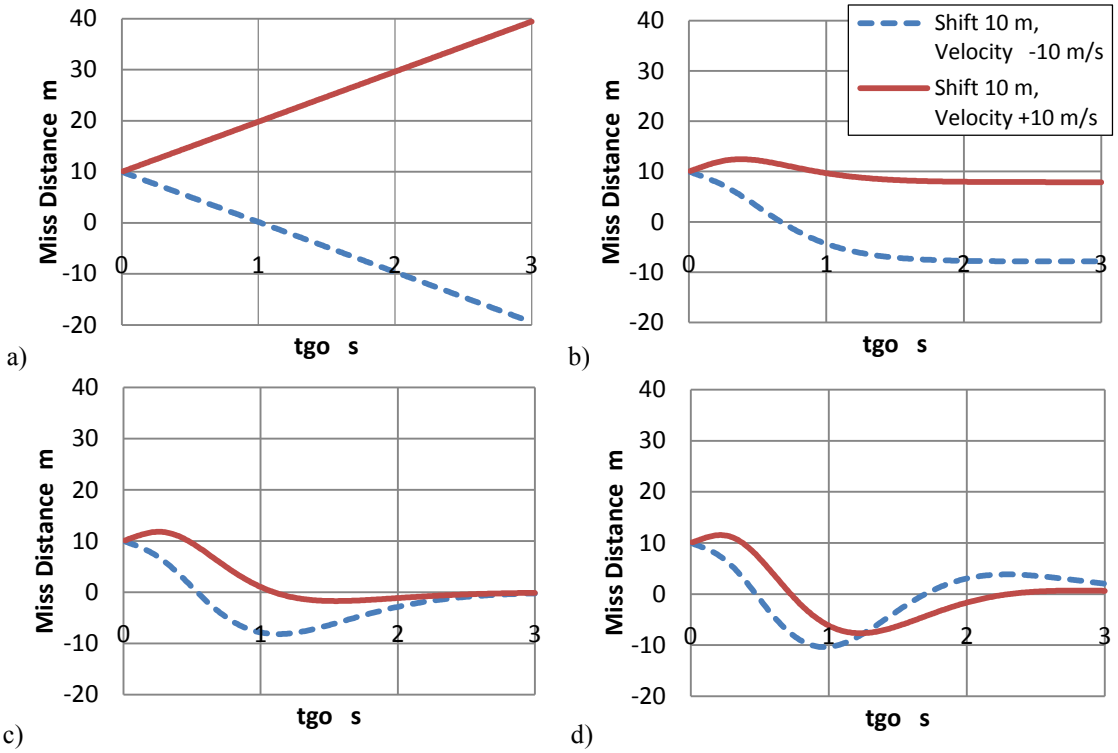

Figure 3: The miss distances obtained for the cases. a) N=0: The projectile is now ballistic and will only hit the target if the target moves towards the impact point. b) N=1: The gain is too small to make the projectile maneuver enough to hit the target. c) N=2. d) N=3.

CONCLUDING REMARKS

The Adjoint method was used to obtain the miss distances against a target located at ground. The navigation gain N was varied and the "optimal" value was found to be 2 for the weapon systems and end-game case studied. With some simplifications and assumptions on mind the method proves to be capable to produce the projectile performance projections quickly. The case studied was very limited and the method flexibility allows investigating far more complex systems.

REFERENCES

[1] Paul Zarchan, *Tactical and Strategic Missile Guidance*, AIAA Progress in Astronautics and Aeronautics, Vol 176, VA USA, Third edition, (1997).

[2] Martin Weiss, Adjoint Method for Missile Performance Analysis on State-Space Models, AIAA Journal of Guidance, Control and Dynamics, Vol. 28, No. 2, March-April 2005.

23rd Nordic Seminar on Computational Mechanics
NSCM-23
A. Eriksson and G. Tibert (Eds)

SIMULATION OF KINKBAND FORMATION IN FIBER COMPOSITES

BADRINATH VELURI AND HENRIK M JENSEN

Department of Mechanical Engineering, Aarhus School of Engineering
Aarhus University
Dalgas Avenue 4, Aarhus C 8000 Denmark
E-mail: vb@agse.dk and hmj@agse.dk , Web page: http://www.au.dk

Key words: Kinkband, microbuckling, Finite Element Analysis, Carbon Fibers, Fiber Composites, Constitutive Model, Implicit Integration, Convergence, ABAQUS/Standard, UMAT.

Summary: Failure of composite materials by the formation of kinkbands is a non-linear phenomenon involving interacting non-linear effects of material behavior of the matrix materials and fiber buckling. A constitutive model for unidirectional layered materials is implemented as User Material (UMAT) user subroutine in ABAQUS/Standard for analyzing the kinkband formation in the fiber composites under compressive loading within the framework of large deformation kinematics. This computational model analyses the effects of misalignment on elastic plastic deformation under plane strain conditions based on the smeared-out, plane constitutive numerical model. The model is successful in simulating the transition of the failure mode by buckling of long, slender beams to material instability by the kink band mechanism for short plate panels.

1 INTRODUCTION

Despite of high tensile strength of continuous fiber composite materials, their failures under compression is a design-limiting feature. The carbon fibers in an epoxy matrix possess excellent tensile strength and often fail in compression by plastic microbuckling at stresses of about 60% of their tensile strength[1]. It has also been found that the compressive strength is governed by plastic yielding in the matrix[2], and furthermore, that small misalignments of the fibers have a large influence on the compressive strength[3]. In these investigations the post-buckling response is also studied, and it is shown that the localized deformation into a well-defined band of bent fibers which is called as kinkband. Kinkband formation in fiber reinforced materials was investigated[4,5], where a plane constitutive model for perfectly bonded layered materials was introduced.

2 CONSTITUTIVE MODEL

The constitutive model was framed on the following assumptions:

1. The fibers and the material lines which are parallel to each other are subjected to a common stretching/compression and rotation
2. Transmission of identical tractions in the planes parallel to the fibers
3. The constituents materials are elastic or elastic-plastic

The general relation between the Cauchy stress and the strain rate in the three dimensions is given by

$$\dot{\sigma}_{ij} = L_{ijkl}\varepsilon_{kl} \tag{1}$$

where L_{ijkl} are the plastic elastic-plastic tangent moduli. The strain rates are given by

$$\varepsilon_{ij} = \frac{1}{2}\left(v_{i,j} + v_{j,i}\right) \tag{2}$$

where $v_{i,j}$ is the velocity gradient of v_i .

The two dimensional constituent equations implemented in ABAQUS/Standard in the form of

$$\dot{s}_{ij} = C_{ijkl} v_{l,k} \tag{3}$$

where $\dot{s}_{ij}$ are the nominal stress rate components, C_{ijkl} nominal moduli tensor components which can be used to determine and is detailed in[4]

$$C_{ijkl} = L_{ijkl} - \frac{1}{2}\delta_{il}\sigma_{kj} - \frac{1}{2}\delta_{ik}\sigma_{lj} - \frac{1}{2}\sigma_{il}\delta_{kj} + \frac{1}{2}\sigma_{ik}\delta_{lj} \tag{4}$$

The nominal moduli tensor components are calculated by combined material properties of constituent's fiber and matrix in the composite structure. Ramberg-Osgood relation for the constituents as yielding condition that defines natural logarithmic strain considering the hardening index n is given by

$$\varepsilon = \frac{\sigma}{E} + \frac{3\sigma^y}{7E}\left(\frac{\sigma}{\sigma^y}\right)^n \tag{5}$$

3 IMPLEMENTATION IN ABAQUS/Standard

The material law is implemented computationally in UMAT as a user subroutine in a commercially available FEA code ABAQUS/Standard to simulate the kinkband formation in the unidirectional fiber composites under compressive loading. Figure (1-a) demonstrates in detail the implementation and the functionality of the UMAT subroutine.

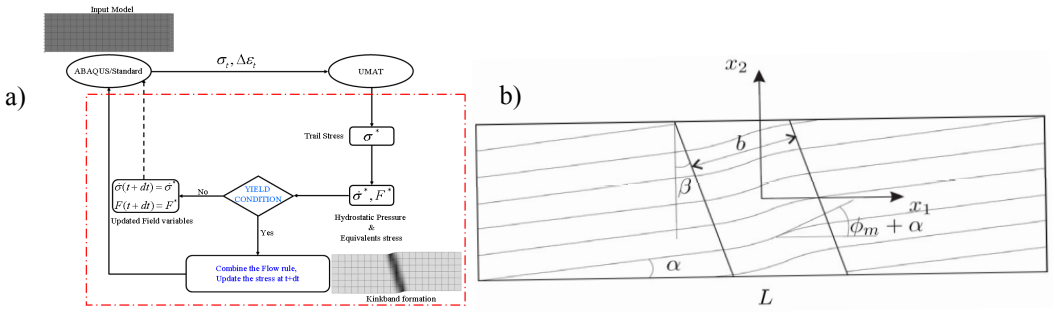

Figure 1: a) Implementation of UMAT subroutine in ABAQUS/Standard UMAT. b) Description of Kinkband geometry in normal structure without any voids.

The model is defined with 9 material properties, Young's moduli of fiber and matrix E^f and E^m, Poisson's ratio of the fiber and matrix ν^f and ν^m, initial yield stresses σ_y^f and σ_y^m, hardening parameters of the fiber and matrix n^f and n^m, the volume fraction c^f. In the current investigation the volume fraction remains constant throughout the deformation process. The kinkband geometry is defined in Figure (1-b).The direction of the fibers outside the band is given by the angle α and in the kinkband region the angle is considered as ϕ, which can be estimated from the following

$$\phi(x_1, x_2) = \frac{1}{2}\phi_m\left[\cos\left(\frac{2\pi\cos\beta}{b}(x_1 + x_2\tan\beta)\right) + 1\right] + \alpha \tag{6}$$

To satisfy the following boundary conditions an initial value ϕ_m of to the imperfection is added to fiber angle α

$$u_1 = 0 \text{ at } x_1 = -\frac{L}{2} \tag{7}$$

$$u_2 = 0 \text{ at } (x_1, x_2) = (-\frac{L}{2}, -\frac{H}{2}) \tag{8}$$

4 RESULTS AND DISCUSSION

Considering the following material properties to simulate the kinkband formation, fiber volume fraction $c^f = 0.6$, hardening parameters for fiber $n^f = 2.5$ and the matrix $n^m = 4.5$ with the ratios of the Young's moduli of the fiber to matrix as $E^f/E^m = 35$ and 100. The study has been done with varying matrix hardening parameter n^m. From Figure (6) the peak stress and the post critical response of the composite structure is observed to be very sensitive to the hardening component n^m.

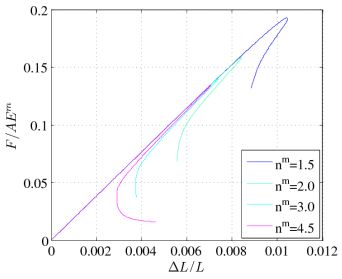

Figure 3: Post-kink Load-Deflection response for various values of matrix hardening parameter n^m.

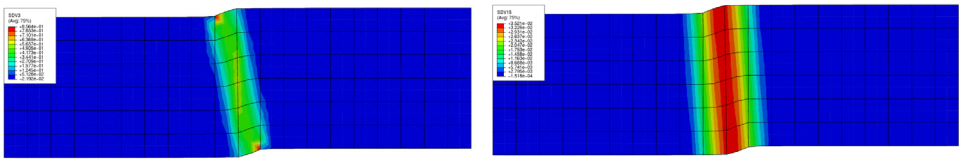

Figure 4: Contour plot of effective plastic strain of the matrix and the fiber misalignment imperfection contour plot for $E^f/E^m = 35$

Figure (4) demonstrates the formation of the kinband and the contour of effective plastic strain in the matrix material and imperfection for moduli ratios of $E^f/E^m = 35$ with a fiber misalignment $\phi_m = 2^o$. Figure (6) shows the kinkband formation is simulated for two different values of moduli ratio E^f/E^m. The calculations have been performed to observe the sensitivity of the peak load by varying the misalignment angle of the fibers which is shown in Figure (7).

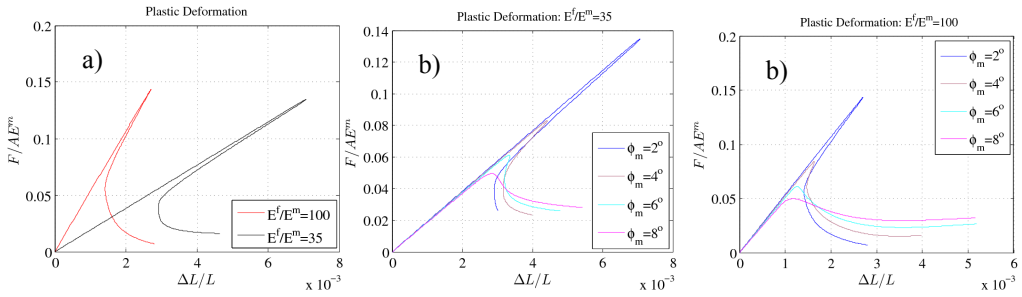

Figure 6: a) Post-Kink Load-Deflection response for various values of varying fiber to matrix ratio E^f/E^m. b) Post-Kink Load-Deflection response for varying fiber misalignment angle ϕ_m for matrix ratios $E^f/E^m = 35$ and 100.

Calculations have been performed on the structural components made from long fiber composites typically having the uncontrollable manufacturing defects like voids, containing fastener holes and sometimes to lighten the structure that may suffer in-service damage. The kinkband formation in the complex structure having a varying size of void or cutout in circular shape is discussed for a ratio of $E^f/E^m = 35$. Figure (8) shows the contour plot of the effective plastic strain of the matrix and fiber misalignment imperfection plot for a structure

with a void/cutout of circular hole with a radius of 0.5. Figure (9) shows the load-deflection response and variation of the maximum failure loads for different values of the ratio r/w. Depending upon the degree of orthotropy the compressive composite structure with the large cylindrical hole will be reduced 20% [6].

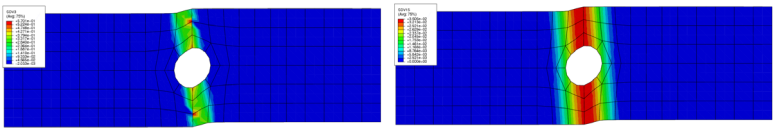

Figure 8: Contour plot of effective plastic strain of the matrix and the fiber misalignment imperfection contour plot for $E^f/E^m = 35$ for a composite structure with a circular void/cutout of 0.5mm radius.

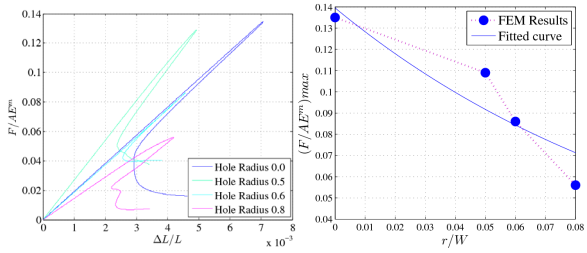

Figure 9: post-kink Load-Deflection response and Variation in the strength of the composite structure during the kinkband formation with a circular void/cutout

5 CONCLUSIONS

The constitutive model was verified numerically for the consistency, convergence and stability in order to simulate the kinkband formation in the unidirectional fiber composites. The model shows a good consistency in simulating the kinkband formation numerically which demands the experimental validation. The imperfection of the composite material applied in the present study is an assumed band of material of a specified width in which the fiber orientation gradually changes from the orientation outside the band to a maximum deviation from this and back to the original orientation again. The band may be arbitrarily oriented relative to the fiber direction. No variation of fiber rotations has been assumed in the direction of the band although this is not a general restriction in the model.

REFERENCES

[1] Awerbuch J and Madhukar M S. "Notched Strength in Composite Laminates: Predictions and Experiments- a review". *Journal of Reinforced Plastic Composites*, **4**, 3-12 (1985).
[2] Budiansky B. Micromechanics. Computers and Structures, **16**, 3-12 (1983).
[3] Kyriakides S, Arseculerante R, Perry E J and Liechti K M. "On the compressive failure of fiber reinforced composites". *International Journal of Solids and Structures*, **32**, 67-189 (1995).
[4] Ivindra Pane and Jensen H M. "Plane strain bifurcation and its relation to kinkband formation in layered materials". *European Journal of Mechanics A/Solids*, **23,** 359–371 (2004)
[5] Jensen H M and Christoffersen J. "Kinkband formation in fiber reinforced materials". *Journal of the Mechanics and Physics of Solids*, **45**, 1121-1136 (1996).
[6] Fleck N A. Compressive Failures of Fiber Composites. *Advances in Applied Mechanics*, **33**, 43-117 (1997).

23rd Nordic Seminar on Computational Mechanics
NSCM-23
A. Eriksson and G. Tibert (Eds)

INFLUENCE OF PISTON DISPLACEMENT ON THE SCAVENGING AND SWIRLING FLOW IN TWO-STROKE DIESEL ENGINES

A. OBEIDAT[†], S. HAIDER,[†] K. M. INGVORSEN [†], K. E. MEYER[†], AND J. H. WALTHER [†]

[†]Department of Mechanical Engineering
Technical University of Denmark
DK-2800 Kgs. Lyngby, Denmark
Tel.: +45-4525 4327
Fax: +45-4588 4325

Key words: diesel engine, swirl, scavenging, LES simulation.

Summary. We study the effect of piston motion on the in-cylinder swirling flow in a low speed, large two-stroke marine diesel engine. The work involves experimental, and numerical simulation using OpenFOAM platform, Large Eddy Simulation was used with three different models, One equation Eddy, Dynamic One equation Eddy, and Ta Phouc Loc model, to study the transient phenomena of the flow. The results are conducted at six cross sectional planes along the axis of the cylinder and with the piston displaced at four fixed piston positions covering the air intake ports by 0%,25%, 50%, and 75% respectively, for the fully opened case LES model with 8/12 million mesh points were used. We find that the flow inside the cylinder changes as the ports are closing, from a Rankine/Burger vortex profile to a solid body rotation while the axial velocity profiles change from a wake-like to a jet-like profile.

1 Introduction

In two stroke engines, compared to 4-stroke engines, the removal of exhaust gases and supply of fresh air for the next cycle is carried out simultaneously using the scavenging process. Scavenging is carried out using air entering the cylinder from intake ports at the cylinder liner walls near the bottom dead centre and scavenging the exhaust gases from cylinder through the exhaust port. The scavenging process removes the exhaust gases, provides fresh air to the engine , and provides the necessary swirl to the flow in which the diesel fuel is to be injected. This makes the scavenging process very important for engine performance and efficiency both in terms of fuel consumption and emissions. Swirling flows are widely used in industrial applications e.g. cyclone separators, swirl combustors etc. Previous studies [1 2 3] involve swirl generators using guide vanes that divert the radially incoming flow and impart the tangential component. In the present study we focus on the swirling flow in the presence of an obstructing piston and the resulting in-cylinder confined swirling flow.

2 Numerical Methods

2.1 Large Eddy Simulation

We study the swirling flow numerically using large eddy simulations. The governing equation are the spatially filtered Navier-Stokes equations:

$$\frac{\partial \bar{u}_j}{\partial x_j} = 0 \tag{1}$$

$$\frac{\partial \bar{u}_i}{\partial t} + \frac{\partial \bar{u}_i \bar{u}_j}{\partial x_j} = -\frac{1}{\rho}\frac{\partial \bar{p}}{\partial x_i} + \nu \frac{\partial^2 \bar{u}_i}{\partial x_j^2} - \frac{\partial \tau^{SGS_{ij}}}{\partial x_j} \tag{2}$$

$$\tau_{ij} = \bar{\rho}\widetilde{u_i u_j} - \bar{\rho}\tilde{u}_i\tilde{u}_j \tag{3}$$

where t denotes the time, u_i is the velocity component in Cartesian coordinates, ρ is the density, p is the pressure, and ν is the kinematic viscosity. As a result of the spatial filtering the subgrid-scale-stresses (SGS) stress tensor $\tau^{SGS_{ij}}$ is introduced into the momentum eq. (2), where $\tau_i^{SGS_{ij}}{}_j = \overline{u_i u_j} - \bar{u}_i\bar{u}_j$.[5 6 7 8 9 10 11]

We apply three different models. The one equation eddy model where the kinetic energy k is solved while another scale is estimated, so if the k is solved then the turbulent velocity u is estimated by $u^* \sim \sqrt{k}$[5]. Eddy viscosity $\mu_i = C_\mu \bar{\rho} k^{\frac{1}{2}} l^*$, where C_μ is a constant, l^* is the turbulent length scale.
The dynamic k-equation eddy-viscosity model, where the model constants are recalculated during the simulation rather than to be pre-calculated, the model stress tensor eq. (3)[12] which can be modeled as

$$\tau_{ij} - \frac{1}{3}\delta_{ij}\tau_{kk} = C\alpha_{ij} \quad C = \frac{L_{ij}M_{ij}}{M_{kl}M_{kl}} \tag{4}$$

where C is the model parameter, M_{ij} is the minimum error, L_{ij} is a stress resolved tensor. α_{ij} is the term needed to be modeled.[5 12]

$$\alpha_{ij} = -2\bar{\rho}\Delta^2(2\tilde{S_{kl}}\tilde{S_{kl}})^{\frac{1}{2}}\tilde{S_{ij}} \tag{5}$$

where $\tilde{S_{ij}}$ is the filtered strain tensor.

The Ta Phouc Loc model, which is based on the velocity-vorticity (v-ω) formulation of the Navier-Stokes equations. Two spatial filters are used, the first filter denoted by $(^-)$ is used on the fine mesh, and the second 'test filter' denoted by $(\tilde{})$ which is used on the coarse mesh. From eq. (2) we find that

$$\tau_{ij} = \bar{U}_i\bar{U}_j = \overline{U_iU_j} = (\bar{U}_i\bar{U}_j - \overline{\bar{U}_i\bar{U}_j}) - (\overline{\bar{U}_iU_j{}' + U_i{}'\bar{U}_j}) - \overline{U_i{}'U_j{}'} \tag{6}$$

where the fluctuations are defined as $U_i{}' = U_i - \bar{U}_i$.

The turbulent stresses are modeled as

$$\tau_{ij} = v_t\left(\frac{\partial \bar{U}_i}{\partial x_j} + \frac{\partial \bar{U}_j}{\partial x_i}\right) - \frac{2}{3}k\delta_{ij} \tag{7}$$

The eddy viscosity v_t is determined by the mixed-scale turbulence model introduced by L.Ta Phouc[13]

$$v_t = C|\bar{\omega}|^\alpha k^{(1-\alpha)/2}\Delta^{(1+\alpha)} \tag{8}$$

where ω is the vorticity, $\Delta = (\Delta_x\Delta_y\Delta_z)^{\frac{1}{3}}$ is an average grid size, k is the turbulent kinetic energy, α is a parameter which takes a value between 0 and 1. From a previous study[14] it was found that the model performs best when $\alpha = 0.5$.

The turbulent kinetic energy is estimated from the test filter $(\tilde{})$ as

$$k = \frac{1}{2}\sum_{j=1}^{3}(U_j - \bar{U}_j)^2 \approx \frac{1}{2}\sum_{j=1}^{3}\left(\bar{U}_j - \tilde{\bar{U}}_j\right)^2 \tag{9}$$

where U_j is the unfiltered velocity field and $\tilde{\bar{U}}_j$ is the doubled filtered velocity field obtained by applying the second filter on the resolved velocity $\bar{U}_j$.[13 14 15]

2.2 Computational domain and results

The computational domain is shown in Fig. 1 and consists of an inlet section (swirl generator), a cylinder and an outlet section. At the inlet of the computational domain a uniform radial and tangential velocity is defined and at the outlet a zero-gradient boundary condition is applied.

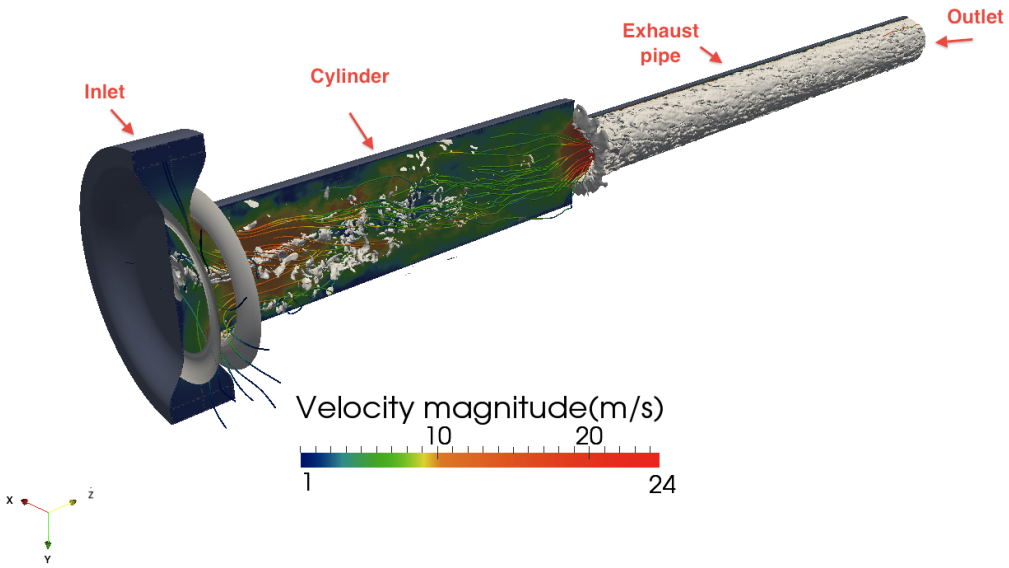

(a)

Figure 1: 3D cross sectional view showing the velocity magnitude, vorticity contours (in white) and streamlines.

The results shown in Fig. 2 show that generally there is a good agreement between computational and experimental particle image velocimetry (PIV) results that have been measured previously[4]. The models capture the wake and jet like profiles of the axial velocity but both are not as pronounced as in the experimental results.

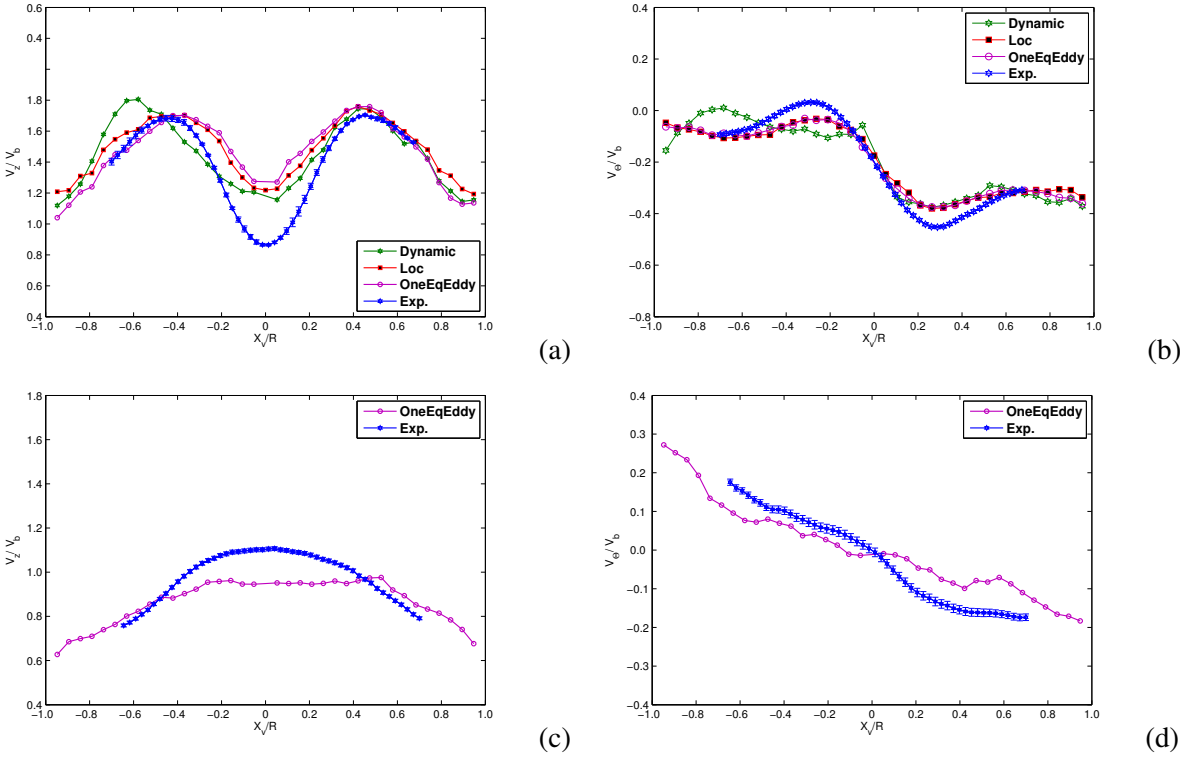

Figure 2: (a) (c) Time averaged axial velocity profiles for the 100%,50% open ports, (b) (d) Time averaged tangential velocity profiles for the 100%,50% open ports, at the axial position $z/D = 2.016$

REFERENCES

[1] Kitoh, S. Experimental Study of turbulent swirling flow in a straight pipe. *J. Fluid Mech.* **225**, 445–479 (1991).

[2] Algifri, A. H., Bhadwaj, R. K. & Rao, Y. V. N. Turbulence Measurements in Decaying Swirl Flow in a Pipe. *Applied Scientific Research* **45**, 233–250 (1988).

[3] Escudier, M. P., Bornstein, J. & Maxworthy, T. The dynamics of confined vortices. *Mathematical and Physical Sciences* **382**, 335–360 (1982).

[4] Haider, S. *Experimental and Numerical Study of Swirling Flow in Scavenging Process for 2-Stroke Marine Diesel Engines*. Ph.D. thesis, Technical University of Denmark (2010).

[5] Wang, P. *Large Eddy simulation of Turbulent Swirling Flows and Turbulent Premixed Combustion*. Ph.D. thesis, Lund Institute of Technology (2005).

[6] Dejoan, A., Jang, Y. J. & Leschziner, M. A. Comparative LES and Unsteady RANS Computation for a Periodically-Perturbed Separated Flow over a Backward-Facing Step. *Fluids Eng.* **127**, 872–879x (2005).

[7] Narasimhamurthy, V. *Unsteady RANS simulation of Turbulent Trailing-Edge Flow*. Ph.D. thesis, Chalmers University of Technology (2004).

[8] Wegner, B., Schneider, C., Dreizler & Janicka, J. Assessment of unsteady RANS in predicting swirl flow instability based on LES and experiments. *Int. J. Heat Fluid Flow* **25**, 528–536 (2004).

[9] Wang, P. & Bai, X. S. Large eddy simulation and experimental studies of a confined turbulent swirling flow. *Phys. Fluids* (2004).

[10] Lesieur, M., Metais, O. & Comte, P. *Large Eddy Simulations of Turbulence* (Cambridge University Press, 2005).

[11] Moene, A. F. *Swirling pipe flow with axial strain Experiment and Large Eddy Simulation*. Ph.D. thesis, Technische Universiteit Eindhoven (2003).

[12] Germano, M., Piomelli, U., Moin, P. & Cabot, W. H. A dynamic subgrid-scale eddy viscosity model. *Phys. Fluids* **3**, 1760–1765 (1991).

[13] Tenaud, C., Pellerin, S., Dulieu, A. & Phouc, L. T. Large Eddy simulations of spatially developing incompressible 3D mixing layer using the $v - \omega$ formulation. *Computers & Fluids* **34**, 67–96 (2005).

[14] Shen, W. Z., Zhu, W. & Sorensen, J. N. Aeroacoustic computations for turbulent airfoil flows. *AIAA* **47** (2009).

[15] Sagaut, P. *Large Eddy Simulation for Incompressible Flows* (Springer), 3 edn.

23rd Nordic Seminar on Computational Mechanics
NSCM-23
A. Eriksson and G. Tibert (Eds)

CURVATURE COMPUTATION FOR A SHARP INTERFACE METHOD USING THE CONSERVATIVE LEVEL SET METHOD

CLAUDIO WALKER*

*Norwegian University of Science and Technology (NTNU)
Department of Energy and Process Engineering
N-7491 Trondheim, Norway
e-mail: claudio.walker@ntnu.no

Key words: Conservative level set, Sharp interface, Curvature

Summary. We compare different approaches for the computation of the curvature at the interface. The first method computes the curvature at the grid points by approximating the derivatives of the conservative level set function. Then the curvature is interpolated to the interface position. The second method uses a distance function which is computed from the conservative level set function by a fast marching method to approximate the derivatives at the grid points. The third method computes the curvature directly at the interface position by fitting a local polynomial through neighboring grid intersections. In our test the method which computes the curvature from approximated derivatives and then interpolates it to the intersections is the most accurate.

1 INTRODUCTION

Computations of two phase flows often use the continuum surface tension approach to handle the surface tension. In order to obtain a smooth solution the jump in the density and viscosity is smeared over multiple grid points around the interface and the singular force resulting from the surface tension is applied as a volume force around the interface. As a result the jump in the pressure is smeared as well. A more accurate description of the jumps at the interface can be obtained using the Ghost Fluid Method (GFM)[1]. It applies the surface tension force directly at the interface and the finite difference stencils are corrected to accommodate the jumps at the interface.

The conventional level set method using a distance function does not conserve the mass of the fluids. To address this problem we use the conservative level set method (CLSM)[2]. The signed distance function is replaced by a hyperbolic tangent function. This allows to write the reinitialization as a conservation law.

The combination of the GFM and the CLSM leads to challenges in the computation of the curvature. Since the surface tension force is applied directly at the interface by the introduction of a jump in the pressure, the curvature has to be computed at the intersections of the interface and the grid lines. These intersection points are obtained by a linear interpolation of the level set function and are therefore second order accurate. To judge whether a method to compute

the curvature is applicable to the GFM, the accuracy of the curvature computation has to be assessed at the intersection points.

2 Curvature computation

2.1 Computation using finite difference approximations

The simplest approach to get the curvature at the intersection points is to approximate the derivatives of the conservative level set function at the grid points. That can be done by using e.g. central finite differences. Then the curvature at the grid points is given as

$$\kappa = \frac{\phi_x^2\phi_{yy} - 2\phi_x\phi_y\phi_{xy} + \phi_y^2\phi_{xx}}{(\phi_x^2 + \phi_y^2)^{3/2}} \ . \tag{1}$$

This is the standard method to compute the curvature in level set applications. Finally the curvature has to be interpolated to the intersection points which can be done by the same linear interpolation method used to find the intersection points.

2.2 Least squares approximation from distance function

If the conservative level set function is advected using certain discretisation schemes, it will develop spurious oscillations, which will lead to problems for the approximation of the interface normals and curvature. To avoid these problems Desjardins et al.[3] propose to first recompute a signed distance function ψ from the conservative level set function ϕ using a fast marching method (FMM). Then the derivatives in equation (1) are approximated from ψ. Because the FMM is at most second order accurate, the curvature will not converge if the derivatives are computed with finite differences. By using the least squares approach[4] first order convergence is observed.

2.3 Curve fitting through the intersection points

Since all intersection points of the interface with the grid lines are known we can use those to compute the curvature directly. Suppose there is a parameterised curve $\vec{x}(s) = (x(s), y(s))$ trough the intersection points. The curvature at a intersection point is then given by

$$\kappa = \frac{\dot{x}\ddot{y} - \ddot{x}\dot{y}}{(\dot{x}^2 + \dot{y}^2)^{3/2}} \ , \tag{2}$$

where $\dot{x}$ and $\ddot{x}$ first and second derivatives, respectively, with respect to the parameter s. To approximate the derivatives at an intersection point $\vec{x}_0 = (x_0, y_0)$ we use two additional intersection points $\vec{x}_m$ and $\vec{x}_p$ which are located before and after $\vec{x}_0$ on the interface, respectively. Assuming that the difference of the parameter s is the same on both sides we can use simple finite difference stencils to compute the derivatives, e.g. $\dot{x}_0 = (x_p - x_m)/2$.

It was only possible to obtain converging curvature estimates if the linear interpolation of the intersection points was replaced by a more accurate cubic interpolation. We got the best results by setting $\vec{x}_m$ and $\vec{x}_p$ to the neighbouring points where the interface intersects a parallel grid line to the one in $\vec{x}_0$. At certain points where two intersection points are located extremely close to a grid point this approach will lead to large errors and the curvature will not converge

as the grid is refined. To find a remedy the symmetry factor q of each curvature approximation stencil is computed as

$$q = \frac{\delta_m + \delta_p - 2\sqrt{\delta_m \delta_p}}{2\sqrt{\delta_m \delta_p}} \ , \tag{3}$$

where $\delta_m = |\vec{x}_m - \vec{x}_0|$ and $\delta_p = |\vec{x}_p - \vec{x}_0|$ respectively. q will be zero if the stencil is perfectly symmetric. If the symmetry factor of the approximation in a certain intersection point is 10 times higher than the average of his two neighbours, the curvature at this point will be linearly interpolated from the adjacent points which have a more symmetric stencil.

3 Numerical test

To test the presented methods for the curvature, we place a circle with radius $r = 1/3$ into the center of a square domain of size $[-1, 1] \times [-1, 1]$ with n grid points in each direction. We initialise the conservative level set function with

$$\phi = \left(1 + e^{d/\epsilon}\right)^{-1} \ , \tag{4}$$

where $\epsilon = 0.2\sqrt{2/n}$ is the parameter for the slope of ϕ at the interface, and d is the analytical distance form the interface. Then the reinitialisation equation is solved to steady state to ensure that we test the curvature comptation on a level set function which can be expected in a two phase solver. This reinitialized conservative level set function is then used to compute the curvature κ at each intersection point. To test the least squares approximations from the distance function (section 2.2) we used the FMM from the LSMLIB[5] with second order upwinding to obtain ψ from d. The error of the curvature is then calculated by

$$e = \left(\frac{1}{m}\sum_{i=1}^{m}(\kappa_i - 3)^2\right)^{1/2} \tag{5}$$

where m is the number of intersection points.

The results are presented in Figure 1. If the finite difference method (section 2.1) is used the error in the curvature reduces with second order, which is consistent with both the finite difference and the interpolation schemes. The curve fitting at the intersection points (section 2.3) leads to a convergence which is between first and second order. At a low resolution 2nd order can be observed. The lower convergence rate at higher resolution stems from the high frequency oscillations which are illustrated on the right of Figure 1. Those oscillations originate from the variance in the stencil quality for each intersection point. The error could be further reduced by low pass filtering the curvature along the interface. The curvature which is computed from ψ using a least squares approximation of the derivatives (section 2.2) is the most accurate one at the lowest resolution, but it does not converge as the grid is refined. The reason for this behavior is that ψ which is computed with the FMM is only second order accurate at the lowest resolution. As the grid is refined the accuracy of the FMM deteriorates to first order.

4 Conclusions

We tested alternative methods to compute the curvature from a conservative level set function. If the curvature is computed by fitting a curve through the intersection points of the

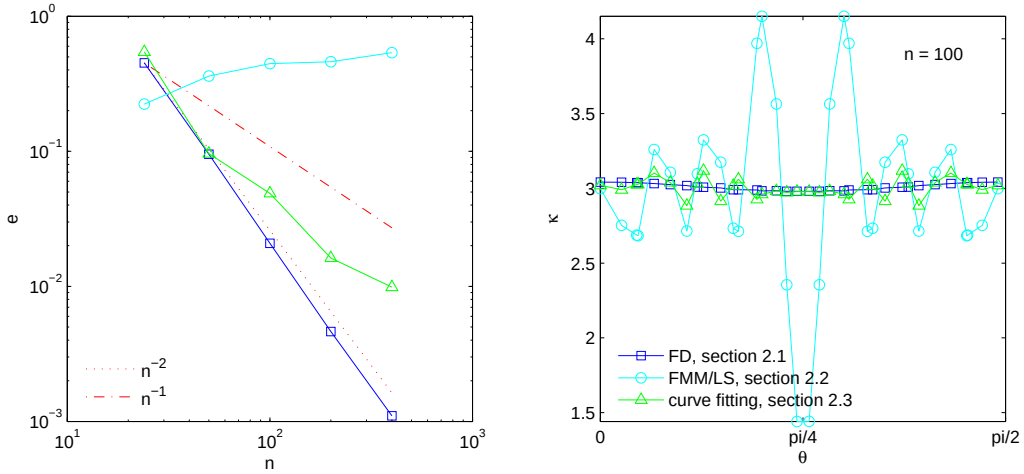

Figure 1: Error of the curvature computation on the left, curvature for $n = 100$ on the right

interface with the gird lines, the intersection points have to be interpolated with at least cubic interpolation to obtain convergent results. The method which fits a curve through the intersection points is less accurate than the method using finite differences, but it converges faster than the least square approximation of the derivatives of a distance function computed by the FMM. In our tests the least squares approximation is not consistent with grid refinement. If an accurate curvature is important, one should try to keep the conservative level set function free from oscillations, e.g. by using WENO schemes for the advection and frequent reinitialisation, such that the curvature can be computed by finite difference from the conservative level set function.

REFERENCES

[1] Kang, M., Fedkiw, R. P. & Liu, X.-D. A boundary condition capturing method for multiphase incompressible flow. *Journal of Scientific Computing* **15**, 323–360 (2000).

[2] Olsson, E., Kreiss, G. & Zahedi, S. A conservative level set method for two phase flow II. *Journal of Computational Physics* **225**, 785–807 (2007).

[3] Desjardins, O., Moureau, V. & Pitsch, H. An accurate conservative level set/ghost fluid method for simulating turbulent atomization. *Journal of Computational Physics* **227**, 8395–8416 (2008).

[4] Marchandise, E., Geuzaine, P., Chevaugeon, N. & Remacle, J.-F. A stabilized finite element method using a discontinuous level set approach for the computation of bubble dynamics. *Journal of Computational Physics* **225**, 949 – 974 (2007).

[5] Chu, K. T. Lsmlib. Website (2009). URL `http://ktchu.serendipityresearch.org/software/lsmlib/index.html`.

23rd Nordic Seminar on Computational Mechanics
NSCM-23
A. Eriksson and G. Tibert (Eds)

STATISTICS OF POLYMER EXTENSIONS IN TURBULENT CHANNEL FLOW

FARANGGIS BAGHERI*, DHRUBADITYA MITRA†, PRASAD PERLEKAR+, LUCA BRANDT*

*Linné Flow Centre, KTH Mechanics, SE-100 44 Stockholm, Sweden e-mail: farangis@kth.se,

†NORDITA, Roslagstullsbacken 23, 106 91 Stockholm, Sweden e-mail: dhruba.mitra@gmail.com

+Department of Mathematics and Computer Science, Eindhoven University of Technology, P.O. Box 513, 5600 MB Eindhoven, The Netherlands

Key words: Drag reduction, Turbulence, Polymers

Summary. We present direct numerical simulations (DNSs) of turbulent channel flow with passive polymer additives tracked in the flow. We study the statistics of polymer elongation for both the Oldroyd-B model (for Weissenberg number Wi < 1) and the FENE model. For the Oldroyd-B model we find that the PDF of polymer extensions shows power-law behaviour irrespective of the wall-normal coordinate of the polymer molecule, but the range of scaling does depend on the wall-normal coordinate.

1 INTRODUCTION

Turbulent flows with polymer additives have been an active field of interest since the early experiments of Toms[1] which showed the phenomenon of drag reduction on the addition of small amounts (few parts per million) of long-chained polymers to turbulent wall-bounded flows. At a very basic level the mechanism of polymeric drag reduction is that in flows with strong shear the polymers can go through coil-stretch transition; the stretched polymers can then make significant contribution to the Reynolds stresses and this can result in drag-reduction[2,3]. Hence a basic ingredient of drag-reduction mechanism is the coil-stretch transition. The polymers make important contribution to the Reynolds stresses only when they are significantly stretched, hence it is important to find out the statistics of polymer extensions in a turbulent flow. This problem in its full generality is not an easy task due to several reasons which we list below. Firstly in experiments it is quite difficult, if not impossible, to accurately measure the extensions of the polymer molecules. Analytical theories have no way of dealing with realistic turbulent flows. Direct numerical simulations (DNSs) are limited by two important constraint, small Reynolds number and small Weissenberg number (ratio of characteristic time scale of polymer relaxation to the characteristic strain rate). In this paper we describe our attempts to make an inroad to this problem. We perform DNS of channel flow at moderate Reynolds number but relatively high

Weissenberg number by the virtue of using Lagrangian model of the polymer molecules instead of the more widely used Eulerian model. The downside of this approach is that the present method ignores the back-reaction of the polymers to the flow, in other words our polymers are considered passive. Below we first describe in brief the equations we solve and the numerical methods we use to solve them. Next we present preliminary results about the PDF of polymer extensions.

2 Model

The fluid is assumed to be described by the Navier–Stokes equations,

$$\partial_t \boldsymbol{u} + \boldsymbol{u}\cdot\boldsymbol{\nabla}\boldsymbol{u} = \nu\nabla^2\boldsymbol{u} + \boldsymbol{\nabla}p \tag{1}$$

with the incompressibility constraint, $\boldsymbol{\nabla}\cdot\boldsymbol{u} = 0$. Here $\boldsymbol{u}$ is the fluid velocity, ν the kinematic viscosity and p the pressure. We use no-slip boundary condition at the walls and periodic boundary condition at all other boundaries. The x axis of our coordinate system is taken along the stream-wise direction, the y axis along the wall-normal direction and z axis along the span-wise direction. The turbulent Reynolds number $Re_\tau = U_* L/\nu = 180$ is defined by the friction velocity $U_* = \sqrt{\sigma_{\rm w}}$ and $L \equiv L_y/2$, the half-channel width, where $\sigma_{\rm w} \equiv \nu\frac{\partial U}{\partial y}|_{\rm wall}$ is the shear stress at the wall[4]. We non-dimensionalise velocity and distance by $U^+ \equiv U/U_*$ and $y^+ \equiv y/y_*$ respectively, using the friction length $y_* = \nu/U_*$. We solve Eqs. (1) by using the SIMSON[5] code which uses a pseudo-spectral method in space (Chebychev-Fourier). For time integration a third-order Runge-Kutta method is used for advection and uniform pressure gradient forcing term. The viscous term is discretized using a Crank-Nicolson method. In addition to the fluid velocity, we track $N_{\rm p} = 2\times10^5$ Lagrangian passive tracers. The Lagrangian velocity of a particle, which is generally at an off-grid point, is obtained by tri-linear interpolating[5] from Eulerian velocity at the neighbouring grid points and time-stepping is done by a third order Runge-Kutta scheme. To model the polymers we assume each of the $N_{\rm p}$ Lagrangian tracers to carry a vector $\boldsymbol{R}^{\rm j}$ which represents the end-to-end distance of a polymer molecule. The evolution equation for $\boldsymbol{R}^{\rm j}$ is modelled by an over-damped Brownian oscillator with a external driving force coming from the velocity stress tensor[7], i.e.,

$$\partial_t R^{\rm j}_\alpha(t) = \sigma^{\rm j}_{\alpha\beta}R^{\rm j}_\beta + f(R^{\rm j}) + \sqrt{\frac{2R_0^2}{3\tau_{\rm P}}}B^{\rm j}_\alpha. \tag{2}$$

Here $\sigma^{\rm j}_{\alpha\beta} = \partial_\beta \boldsymbol{v}^{\rm j}(t|t_0,\boldsymbol{r}_0^j)_\alpha$, $f(R^{\rm j})$ is the restoring force of the polymer, $\tau_{\rm P}$ is the characteristic decay time of the polymer and $\boldsymbol{B}^{\rm j}$ is a Gaussian random noise with $\langle B_\alpha\rangle = 0$ and $\langle B_\alpha(t)B_\beta(t')\rangle = \delta_{\alpha\beta}\delta(t-t')$. The prefactor of the random noise is chosen such that in absence of external flow, i.e., $\sigma^{\rm j}_{\alpha\beta} = 0$, the polymer attains thermal equilibrium. $\langle R^{\rm j}_\alpha R^{\rm j}_\beta\rangle = R_0^2\delta_{\alpha\beta}$. For the Oldroyd-B model $f(R) = -R/\tau_{\rm P}$. For the FENE model $f(R) = -R/\tau_{\rm P}\{1-(R/R_{\rm max})^2\}$. Eq. (2) is also solved by a third order Runge-Kutta scheme except for the noise which is integrated by an Euler-Marayuma method[8]. More details about the code validation can be found in Ref[6]. To the best of our knowledge such Lagrangian simulations of polymer where first performed in Ref.[9]. An equivalent Eulerian description of the equation for the polymers can be obtained. The numerical solution of such an equation has certain disadvantages[10,11,12,13]. Lagrangian methods[14,15] are able to

avoid such numerical pitfalls and can attain higher Weissenberg number but have difficulties when the back-reaction of the polymer to the flow needs to be incorporated [14,15].

3 Results

Here we summarise preliminary results from our simulations. We calculate the cumulative probability distribution function (PDF) of the polymer extensions for different wall-normal coordinates. For Weissenberg number less than unity we use the Oldroyd-B model. The cumulative PDF s for different Wi are shown in Fig 1(a). The cumulative PDF shows a power-law tail with an exponent that depends on Wi. But this exponent does not depend on the wall-normal coordinate, see Fig 1(b) . We next compare this model with the FENE model. If the maximum extension of the polymers allowed in the FENE model is large enough a small power-law range emerges here too. But for polymers used in experiments this range will be too small to detect. The exponent of the power law matches with the theoretical study in Ref. [16]. Details of this comparison which requires calculation of the finite-time Lyapunov exponent of the flow will be presented elsewhere. For Wi > 0 no stationary state can be obtained for the Oldroyd-B model. The FENE model shows coil-stretch transition.

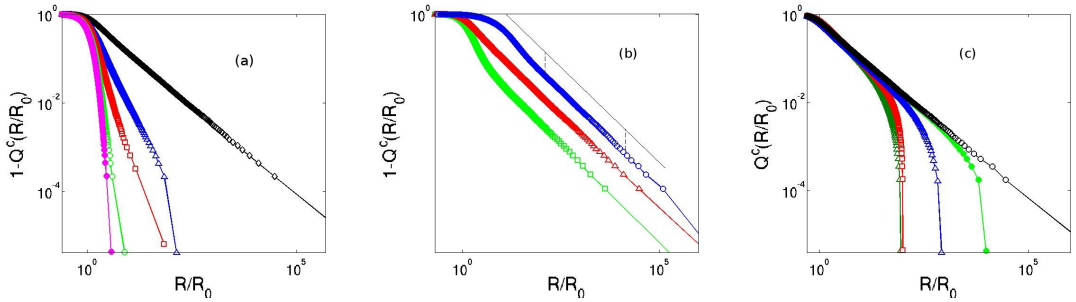

Figure 1: (Color online) (a) The cumulative PDF $Q^c(R)$ of the polymer extensions R as a function of R for different values of Wi, v.i.z, Wi $= 0.05(\bullet), 0.1(\circ), 0.2(\square), 0.3(\triangle)$, and $0.5(\Diamond)$. (b) The cumulative PDF $Q^c(R)$ of the polymer extensions R as a function of R for different y^+, v.i.z, $y^+ = 8(\circ), 74(\triangle)$, and $180(\square)$. (c) The cumulative PDF $Q^c(R)$ of the polymer extensions R as a function of R for the Oldroyd-B model $(\circ)$, Oldroyd-B model with all polymers with $R/R_{\max} > R_{\text{cutoff}}$ removed with $R_{\text{cutoff}} = 10^4(\bullet)$ and $R_{\text{cutoff}} = 100(\square)$, FENE model with $R_{\max}/R_0 = 10^3(\triangle)$ and with $R_{\max}/R_0 = 10^2(\blacktriangle)$.

REFERENCES

[1] Toms, B. In *Proceedings of First International Congress on Rheology*, Section II, 135 (North-Holland, Amsterdam, 1949).

[2] Lumley, J. Drag reduction in turbulent flow by polymer additives. *J. Polymer Sci* **7**, 263–290 (1973).

[3] Hinch, E. Mechanical models of dilue polymer solution in strong flows. *Phys. Fluids.* **20**, S22 (1977).

[4] Monin, A. & Yaglom, A. *STATISTICAL FLUID MECHANICS: Mechanics of Turbulence, volume 1* (Dover Publications, Inc, Mineola, New York, 2007).

[5] Chevalier, M., Schlatter, P., Lundbladh, A. & Henningson, D. *SIMSON: A pseudospectral solver for incompressible boundary layer flows.* Mekanik, Kungliga Tekniska högskolan (2007).

[6] Bagheri, F. *Numerical Study of Polymers in Turbulent Channel Flow.* Master's thesis, KTH, School of Engineering Sciences (SCI), Mechanics (2010).

[7] Bird, R., Curtiss, C., Armstrong, R. & Hassager, O. *Dynamics of Polymeric Liquids* (Wiley, New York, 1987).

[8] Higham, D. An algorithmic introduction to numerical simulations of stochastic differential equations. *SIAM Review* **43**, 525–546 (2001).

[9] Terrapon, V. *Lagrangian simulations of turbulent drag reduction by a dilute solution of polymers in a channel flow.* Ph.D. thesis, Department of Mechanical Engineering, Stanford University. (2005).

[10] Vaithianathan, T. & Collins, L. Numerical approach to simulating turbulent flow of a viscoelastic polymer solution. *Journal of Computational Physics* **187**, 1–21 (2003).

[11] Vaithianathann, T., Robert, A., Brasseur, J. & Collins, L. An improved algorithm for simulating three-dimensional viscoelastic turbulence. *J. Non-newtonian Fluid Mech.* **140**, 3 (2006).

[12] Perlekar, P., Mitra, D. & Pandit, R. Manifestations of drag reduction by polymer additives in decaying, homogeneous, isotropic turbulence. *Phys. Rev. Lett.* **97**, 264501 (2006).

[13] Perlekar, P. *Numerical Stuides of three dimensional turbulence with polymer additives and two dimensional turbulence in this films.* Ph.D. thesis, Indian Institute of Science, Bangalore, India (2009).

[14] Dubief, Y. *et al. J. Fluid. Mech* **514**, 271 (2004).

[15] Peters, T. & Schumacher, J. Two-way coupling of fene dumbbells with a turbulent shear flow. *Phys. Fluids* **19**, 065109 (2007).

[16] Balkovsky, E., Fuxon, A. & Lebedev, V. Turbulent dynamics of polymer solutions. *Phys. Rev. Lett.* **84**, 4765 (2000).

23rd Nordic Seminar on Computational Mechanics
NSCM-23
A. Eriksson and G. Tibert (Eds)

MODEL AND RESULTS FOR THE MOTION IN THE PLANETARY RINGS OF SATURN, AT THE MOON DAPHNIS, IN KEELER GAP

L STRÖMBERG

previously Department of Solid Mechanics
Royal Institute of Technology (KTH), Stockholm
e-mail: lena_str@hotmail.com

Key words: Planetary Ring, Fluid mechanics, Constitutive Diffusion, Gravity, (Relative) harmonic oscillator
Summary. The wave-like patterns in planetary rings close to a moon are analysed. It is found that an expansion of the Newtonian gravitational potential give transient solution. To obtain a harmonic oscillating solution, a diffusion type condition relating the relative motion and the density gradient, is applied.

1 INTRODUCTION

In planetary rings, there are small gaps, in which a moon rotates with the ring system. One such planetary system is Saturn, with the moon Daphnis, in the Keeler Gap. The paper adresses the wave-like pattern in the rings close to the moon in the gap.

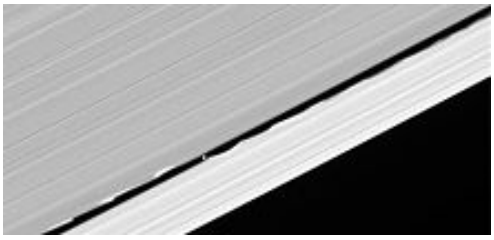

Figure 1: 'The Keeler Gap is a 42-kilometre-wide gap in the A Ring, approximately 250 kilometres from the ring's outer edge. The small moon Daphnis, discovered 1 May 2005, orbits within it, keeping it clear. The moon induces waves in the edges of the gap. Because the orbit of Daphnis is slightly inclined to the ring plane, the waves have also a component that is perpendicular to the ring plane, (from wikipedia).

Models are proposed and the in-plane-wavelength in the pattern, is related to the parameters that describe the geometry and masses of the planetary system. The objective is to describe the nature of the motion, qualitatively, and quantitatively. Transients, derived from considering only Newtonian gravitational potentials, give a solution where relaxation length in the orbit are longer than those observed in the wave pattern. Therefore, additional assumptions are considered in a description with continuum mechanics. Mass of orbiting bodies are modeled with density fields, and an interaction between parts in the planetary system appears as a momentum supply, derived from continuum mixture theory[1].

From the data for Daphnis in wikipedia, the mean density is in the interval [500,5000] kg/m^3. The moon is dense in 3-dim. and the thin planetary ring has a smaller density, and therefore a magnified density gradient is present at the location of Daphnis. The oscillations appear in the model as a harmonic oscillator, when assuming a diffusion-type law. The diffusion constant can be related to the universal G, and with some assumptions, the wave-length in the orbit depends on the masses and radius, but not on gravity G. Also, solutions with long wave-length will be discussed.

2 PROPERTIES OF MATERIAL PARAMETERS

Approximate magnitudes of mass, density and lengths give that mass of Saturn is M_s=5.7*10^{26} kg , the radius R=136504 km, the ratio of mass to Daphnis M_s/M_D=ca10^{12}-10^{13}, Half gap=20 km, radius of Daphnis r_D=4 km, mass M_D=5-50*10^{13}kg, thickness of planetary ring t=20m. The moon is located closer to the outer ring. The distance to the inner ring; a=25 km. From the figure, the wave length in orbit denoted s, measurement for the inner ring gives s=(7-8)a. The system in another view [wiki.se Daphnis] provides somewhat different data.
Angular velocity Daphnis, from 0.59d is 1.2*10^{-4} rad/s, The ratio R/a=0.5*10^4, quotient $Q=(M_s/M_D)(a/R)^3$=8-80 and universal G=6.7*10^{-11}Nm^2/kg^2.

2 MODEL

To determine an eigen-frequency, and expose other characteristics, two approaches are considered, both within the framework of (generalized) continuum mixture theory[1].
The forces acting on the planetary ring; constituent 2, are a momentum supply, partly derived from continuum mixture theory, which include the main gravitational force, and other forces from neighbor systems. The momentum supply is due to

- a relative velocity between the mixture and the particles in wave pattern
- a particle redistribution (absent particles) in the centerline of the orbit in the planetary ring, at the wave pattern
- a density gradient because of the more dense moon.

The equation of motion for constituent 2 reads
Balance of mass $\rho_{2,t}+\mathrm{div}(\rho_2\,\mathbf{v}_2)=c_2$
Balance of momentum $\rho_2\,\mathbf{a}_2=\mathbf{p}_2+\mathbf{f}_D$

For constituent 1, it is assumed that $\mathbf{p}_1=0$, $c_1=0$. Hereby $\mathbf{p}_2=-\,c_2\mathbf{u}_2$, where $\mathbf{u}_2$ is the relative velocity for constituent 2.
Constitutive assumption. A diffusion law relating the relative velocity to the density gradient, is established as $\mathbf{u}_2=E\,\mathrm{grad}\,\rho_2$

The equations will be applied to
1. a mixture of a general orbiting ring of planets and primary, to calibrate
2. a mixture of the planetary ring with magnified density gradient, and Saturn
3. a mixture of the planetary ring and Daphnis, with the constitutive assumption

4. a mixture planetary ring and Daphnis, in a kinematic approach with $\mathbf{p}_1=0$ and the exact expression $\mathbf{p}_2 = - c_2(\mathbf{v}_2 - \mathbf{v}_1)$;

w

Kinematics. Velocity and acceleration at the ring are $\mathbf{v}_2=w_p(R+r)$, $\mathbf{a}=\mathbf{a}_0+w_p^2 r+r_{,tt}$, where $_p$ is the angular velocity of the ring, r is a small deviation from the central orbit, with radius R, and $r_{,tt}$ is the relative acceleration from point 0, at the ring.

2.1 Calibration

To calibrate, the parameter E is determined from a derivation to achieve the Newtonian gravitational potential for a planet orbiting a star with mass M_s, when assuming $\text{grad}\rho_2=\rho_2/R$. Hereby, identification gives $w_pE=(R^2/\rho_2)GM_s/R^3$.

2.2 Planetary ring, specified density field

At the ring, the density gradient is scaled with the volume fraction, to achieve a consistent format comparing an orbiting dense planet with a thin planetary ring.
Hereby, grad $\rho_2=(r_D/t)e\ \rho_2/R$, where t/r_D is the volume fraction and e is the ratio between the absolute densities of ring and Daphnis (approximately 20). The material constant E can either be invoked in the format wE, where w is the angular velocity, or as E. The choice defines the material behavior. Here, the first will be denoted a wE-material ring.

2.3 Planetary ring, mixture with Daphnis

Consider a constitutive assumption as in 1, with G replaced by G_1, since not a steady state rotation around Daphnis. Further, the density gradient, and the angular velocity around Daphnis, needs to be specified.
The density gradient is estimated with an increased participating mass q, $\text{grad}\rho_2=q\rho_2/a$. The angular velocity, from that the ring is about to switch to an orbit around Daphnis, is denoted w_3. Note that for an wE-material ring, this need not be specified.

2.4 Kin. approach

Additional assumptions needs to be invoked to obtain the small wave length solution.

2.5 'Tidal wave'-type-solution

Equation of motion about Saturn, without refined assumptions for density and density gradient, gives solutions with long wave length, where centripetal acceleration is of the same magnitude as the forces.

3 RESULTS

3.1 Results for planetary ring, model 2

$\mathbf{f}_D$ and w^2r are neglected since small. Then r satisfies the equation of an harmonic oscillator with $(\text{eigenfrequency})^2=wE(r_D/t)^2e^2\rho_2/R^2$. Remaining constant term is large compared with

Newtonian gravity, and acts locally in vicinity of Daphnis. It is assumed that a small part of the constant give the angular velocity of the ring, as a centrifugal force, and the remaining part give transients for the time-dependent density field $\rho_2(t,r)$ in the central line of the orbit, (and out-of-plane-components of density and velocity). Thus, the angular velocity of the ring, may differ to that of Daphnis, as indicated in Figure-caption. When they are almost equal (and a wE-mtrl ring), the wave-length in orbit is, $s = 2\pi R/(er_D/t)$, approximately 8a. When not wE-mtrl ring, the wave-length in orbit reads $w^{-1/2}(GM_S/R^3)^{1/4}2\pi R/(er_D/t)$, and may depend on G.

3.2 Comparison of the solutions to 2, and 3

To investigate if G_1 is smaller or larger than G, and if there is a threshold, model 2 and 3 are compared. When the eigen-frequencies are equal, a relation between G_1 and G is given by $G_1/G=Q(w_D/w_3)(r_D/t)^2e^2(1/q)^2$
This is a functional expression for G_1 at non-orbiting state. Assuming w_3 and q are bounded by $w_3<w_D$ and $q<(R/a)$ gives $G_1>G$. If valid, the larger G_1 when not steady state rotation, results in a modified Roche-limit, and magnified tidal force. To further evaluate, additional assumption could be added.

12 CONCLUSIONS

- A continuum model with increased density gave accurate bounds for the wave length. A constitutive assumption for the relative velocity $\mathbf{u}_2$ was assumed in the format $\mathbf{u}_2= \mathbf{u}_2(\mathbf{F}_2, \text{grad}\mathbf{F}_2, \text{skew}(\mathbf{L}_2))$, where $\mathbf{F}_2$ is the deformation gradient and $\mathbf{L}_2$ is the velocity gradient. Dependency on $\mathbf{F}_2$ is through density $\rho_2=\det\mathbf{F}_2$. The format with volume fraction was adopted from an example in Comsol, describing droplet break up in a T-junction.
- Comparison with data for angular velocity of ring and moon, and other systems, would reveal if there are bifurcations, and validity of the present model. Then, from measured wavelength, bounds for masses and other data may be refined. The formula for wavelength is in agreement with pattern in the Encke-gap due to shepherd Pan, when thickness of ring is assumed 30 m.
- Other issues are to compare with results from a generalization of the Roche limit[2], particular solutions to orbit equations[2] and relate to potentials with anisotropy and density fields[3].

REFERENCES

[1] Bowen, R.M., *Theory of Mixtures.* Continuum Physics (1976) ed. by A.C. Eringen, Vol III, Academic Press.
[2] Straumann N, *General relativity and relativistic astrophysics*, Springer Verlag, (1984), pp 375, pp 176.
[3] Chandrasekhar, "The virial theorem in hydromagnetics, *J. of Math. An. and Appl*, Vol 1, Issue 2, pp. 240-252 (1960).

23rd Nordic Seminar on Computational Mechanics
NSCM-23
A. Eriksson and G. Tibert (Eds)

BIOFLUID MECHANICS – FSI AND LES

MATTS KARLSSON

Divisions of Applied Thermodynamics and Fluid Mechanics & Biomedical Modelling and Simulation
Department of Management and Engineering, Linköping University
SE-58183 Linköping, SWEDEN
Email: matts.karlsson@liu.se

Key words: Biofluids, Fluid-Structutre Interaction, Large-Eddy Simulation, High-Performance Computing

Summary. We seek to create patient specific models of the human cardiovascular system, in particular arteries, in order to understand age related changes in structure and function as well as early detection of cardiovascular diseases such as atherosclerosis and dilatation. We utilize the basic principles of applied mechanics as well as the modelling and simulation capabilities from computational engineering and high performance computing in combination with modern imaging modalities and image processing.

1 INTRODUCTION

From a basic physiological point of view we are interested in why, how and where atherosclerosis occurs whereas in the clinical setting we may ask the same questions for diagnosis, intervention planning and follow-up. The combined approach of patient specific geometry with individual blood flow and pressure wave forms, individual viscosity and, individually estimated parameters of arterial wall mechanics enables even an analysis of flow-induced gene expression on an individual basis in the near future. The proportion of older persons in the communities of the western world is rapidly increasing, and cardiovascular disease (CVD) is the number one cause of death and the most serious health threat (National Center of Health Statistics and National Heart Lung and Blood Institute, USA). The forces created by flow and pressure dictate a continuous remodelling to create the most optimal form and function of the cardiovascular system. It is probable that they are of vital importance in the pathophysiology of both occlusive (atherosclerotic) and dilating (aneurysmal) disease, and they determine the structural and functional consequences of wall repair in response to injury[1]. Few reliable and consistent means of measuring these forces, as well as their effects on the arterial wall have been available so far. Interaction of fluids (e.g. blood) with their surrounding vessels (e.g. arteries or the heart wall) is crucial for determining normal physiology and patho-physiology as well as how well artificial devices (eg stents) may perform when used as implants. These new and exciting techniques may in the future be used for *patient specific* diagnostics, intervention planning and follow-up.

2 BACKGROUND

Wall Shear Stress (WSS), the frictional load from the blood on the vessel wall, and its role

in the genesis and progression of atherosclerosis have been subject for numerous studies since the late 1960's[2,3]. It is believed to influence the function of the endothelial cells[4]; a functional endothelium is of crucial importance to maintain hemodynamic stability, and dysfunctional endothelial cells may for example enhance uptake of lipoproteins and leukocyte adhesion[5], thus promoting initiation of an atherosclerotic plaque. *Several studies have found regions with low and/or oscillating WSS to be more prone to the development of disease*. Recent findings also suggest different properties of atherosclerotic lesions depending on whether WSS is low or oscillating. Furthermore, if an atherosclerotic plaque ruptures or erosion injures the covering endothelial cell layer, a coagulation process initiates to heal the damaged wall. *High shear stress now stimulates thrombosis* at the site of the injury[6], and the growing thrombus may eventually occlude the entire vessel causing severe ischemic disease or infarction. Hence, WSS may play different roles during atherogenesis, plaque formation, and thrombosis. Recent findings by us suggest, however, a complex interplay between the blood flow and the endothelium. Therefore, alongside FSI, new tools for high-fidelity simulations of the flow, such as Large Eddy simulations (LES), have been utlilized. These tools offer a new window for the investigation of complex flow patterns and wall shear stress, see Figure 1.

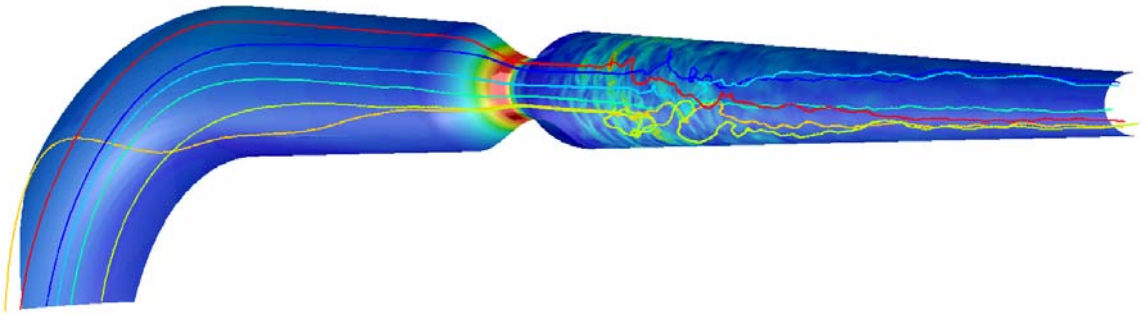

Figure 1: Flow field of a simplified aorta in the vicinity of an arterial stenosis, color coded streamlines depict the complexity of the flow and WSS magnitude on the arterial wall. Note the size of the disturbed flow region

3 METHOD

Patient specific models are created using MRI for geometrical models as well as blood flow velocity information (Phase-Contrast MRI). Using computational fluid dynamics (CFD) the wall shear stress can be calculated on the vessel wall. The segmentation is done using semi-automatic procedures. This has been shown as proof-of-concept in Renner[9]. WSS is (simply) the shape of the velocity profile at the wall (the wall shear rate) multiplied by the viscosity. However, no practical and robust method exists today. The Hagen-Poiseuille equation describes steady flow of a Newtonian fluid in a long straight tube which is very far from the situation encountered in the aorta. Despite this, WSS-HP has unfortunately been used extensively in the literature due to its simplicity.

We utilize MRI to obtain patient specific geometries (static as well as dynamic) and wall thickness. The segmentation process has been automated. The boundary conditions are measured using 3D cine phase-contrast MRI. Both time-dependent geometry and time-dependent wave propagation must also be taken into account. Modelling time-dependent wave propagation in a patient specific model of the aorta requires also a coupling of the three-dimensional model of the aorta to a one-dimensional and/or lumped model of the heart and the systemic circulation. We have pioneered the development of three-dimensional time-resolved phase-contrast MRI for quantification of blood flow and cardiac kinematics[7,8] and recently extended it to non-invasive WSS estimation using computational fluid dynamics and high performance computing[9]. The most recent development utilizing MRI includes the measurement of turbulence[10]. We have also developed a way of looking at WSS by introducing a decomposition of the WSS into a *mean* part and an *oscillatory* part in analogy with a Reynolds-like decomposition[11].

MRI data are used to construct a patient specific geometry and to set the flow velocity at the inlet boundary. Geometric information is extracted and segmented from MRI images with 3D level set algorithm. Hexahedral computational meshes were constructed and used for both the fluid and the solid geometries. In the solid domain a linear-elastic wall model is used, with a Young's modulus of 1 MPa and a Poisson's ratio of 0.49. The fluid was modeled as a Newtonian fluid with blood-like material properties, and was assumed to be laminar.

As boundary conditions at the inlet as well as the three upper outlets, specified mass flow rates was prescribed, based on MRI measurements. To get a physiologically realistic pressure in the fluid domain, the pressure at the lower outlet was computed with a Windkessel model, which describes a relationship between the aortic outflow and pressure. We have developed models for the mechanical behaviour of arteries and other biological tissues[12].

Figure 2 shows the coupling between the global, local and micro mechanics. Figure 3, right, shows the wall shear stress gradient (WSSG) for different locations along the pipe; time is on the vertical axis. It is clearly seen that WSSG have very different behaviour: at Z= 4D there is a significant back flow and the WSSG is mostly stretching/compressing the endothelium whereas at Z=5D (in the middle of the complex flow) WSSG is mostly shearing the endothelium. The size of the square boxes are 10 x 10 endothelial cells.

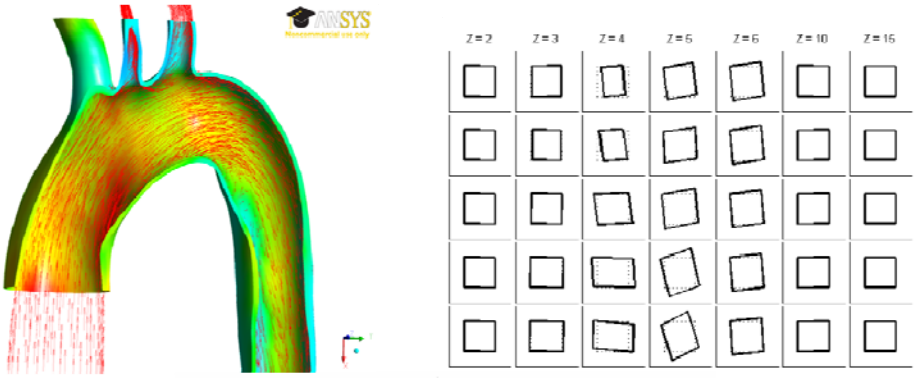

Figure 2: The upper left color panel shows pathlines in a deformable model of the aorta during peak systole whereas the upper right panel shows the Wall Shear Stress Gradient (WSSG)

REFERENCES

[1] Cheng C, Tempel D, van Haperen R, van der Baan A, Grosveld F, Daemen M, Krams R, de Crom R. Atherosclerotic lesion size and vulnerability are determined by patterns of fluid shear stress. *Circulation* 113;2744-2753 (2006)

[2] Fry DL: Acute vascular endothelial changes associated with increased blood velocity gradients. *Circ Res* 22:165–197 (1968)

[3] Caro CG, Fitz-Gerald JM, Schroter RC: Atheroma and arterial wall shear. Observation, correlation and proposal of a shear dependent mass transfer mechanism for atherogenesis. *Proc R Soc Lond B Biol Sci*, 177:109–159 (1971)

[4] Gimbrone MAJ, Resnick N, Nagel T, Khachigian TC, Topper JN: Hemodynamics, Endothelial Gene Expression, and Atherogenesis. Ann N Y Acad Sci, 15:1–10 (1997)

[5] Traub O, Berk BC: Laminar Shear stress: Mechanisms by Which Endothelial cells Transduce an Atheroprotective Force. *Arter Thromb Vasc Biol*, 5:677–685. (1998)

[6] Mohler III ER, Schafer AI: Atherothrombosis: Disease Initiation, Progression, and Treatment. In *Williams Hematology*, 7th edition. Edited by Lichtman MA, E B, Kipps TJ, Seligsohn U, Kaushansky K, Prchal JT, Lewin RA, USA: McGraw-Hill (2006)

[7] L Wigström, T Ebbers, A Fyrenius, M Karlsson, J Engvall, B Wranne and AF Bolger: Particle Trace Visualization of Intracardiac Flow Using Time-Resolved 3D Phase Contrast MRI, *Magnetic Resonance in Medicine*, Vol 41:793-799, (1999)

[8] T Ebbers, L Wigström, AF Bolger, B Wranne and M Karlsson: Non-invasive Measurement of Time-varying Three-Dimensional Flow and Relative Pressure Fields within the Human Heart. *J Biomech Eng*. Jun;124(3):288-93, (2002)

[9] J Svensson, R Gårdhagen, E Heiberg, T Ebbers, D Loyd, T Länne and M Karlsson; Feasibility of Patient Specific Aortic Blood Flow CFD Simulation, *MICCAI* 2006, 2-4 Oct, Copenhagen, (2006)

[10] P Dyverfeldt: Extending MRI to the Quantification of Turbulence Intensity, Linköping Studies in Science and Technology, *Dissertation* No 1297, Linköping University 2010, ISBN: 978-91-7393-453-4 (2010)

[11] R Gårdhagen, J Lantz, F Carlsson and M Karlsson: Quantifying Turbulent Wall Shear Stress in a Stenosed Pipe using Large Eddy Simulation, *ASME J Biomech Eng*, In Press (2010)

[12] Stålhand J, Klarbring A, Karlsson M. Towards in vivo aorta material identification and stress estimation. *Biomechan Model Mechanobiol*, Vol 2, pp. 169-186 (2004)

23rd Nordic Seminar on Computational Mechanics
NSCM-23
A. Eriksson and G. Tibert (Eds)

NUMERICAL SIMULATIONS OF GRAVITY INDUCED SEDIMENTATION OF SLENDER FIBERS

KATARINA GUSTAVSSON * AND ANNA-KARIN TORNBERG *

*School of Computer Science and Communication
Numerical Analysis/Linné Flow Centre
Royal Institute of Technology (KTH), S-100 44 Stockholm, Sweden
e-mail: katarina@nada.kth.se, web page: http://www.nada.kth.se/~katarina
e-mail: annak@nada.kth.se, web page: http://www.nada.kth.se/~annak

Key words: Fiber Suspension, Sedimentation, Numerical Simulations, Stokes Flow, Boundary Integrals.

Summary. Gravity induced sedimentation of slender fibers in a viscous fluid is investigated by large scale numerical simulations. The fiber suspension is considered at a *microscopic* fiber-level and the flow is described by the Stokes equations in a three dimensional periodic domain. Numerical simulations are performed to study in great detail the time evolution of the micro-structure in the suspension during sedimentation, and how the micro-structure affects macroscopic properties like the sedimentation velocity.

1 INTRODUCTION

In this work we are concerned with numerical simulations of a slowly sedimenting fiber suspension made up of identical slender and rigid fibers in a Newtonian fluid. The velocity is small, so inertial effects can be neglected and the dynamics of the fluid phase can accurately be modeled by the Stokes equations.

Despite the simplicity of the Stokes equations, the dynamical problem with many moving and interacting fibers is not an easy problem to model and solve numerically. Many of the characteristic quantities of the sedimentation process such as mean sedimentation velocity and velocity fluctuations depend strongly on the micro-structure (i.e. the relative position and orientation of the fibers) of the suspension. The strong coupling between long-range hydrodynamic interactions and the micro-structure induces a complex dynamical behavior of the fibers which needs to be accurately captured in the modelling and the simulations in order to predict a correct behavior of the sedimentation process.

With this in mind, we have designed an accurate mathematical model and numerical method based on a boundary integral formulation and slender body asymptotics. It is a particle-based method that computes the dynamics of all individual fibers in the suspension and their interaction with the surrounding fluid.

Using numerical simulations, we are able to successfully reproduce many of the characteristic features of a sedimenting fiber suspension such as e.g. creation of flocs and fibers aligning with the direction of gravity. Furthermore, we have also conducted a detailed study of how the

micro-structure in the suspension evolves during the sedimentation process and how it influences macroscopic properties of the suspension.

2 MATHEMATICAL MODEL AND NUMERICAL TREATMENT

We consider a suspension of M immersed slender, rigid fibers in a three dimensional periodic domain. We model the flow using the Stokes equations for which boundary integral equations and a class of numerical techniques, boundary integral methods, can be used to solve the problem. Their great advantage over grid-based numerical methods is the reduction of dimensionality. Instead of solving a three-dimensional PDE in the whole computational domain for the motion of the fibers and the velocity of the fluid, a two-dimensional boundary integral equation is solved over the surfaces of the fibers for a distribution of unknown densities (or strengths) of Stokes singularities.

For slender particles like fibers, a *non-local slender body approximation*,[1], can be used to reduce the dimensionality of the problem even further. The main idea is that for a slender fiber, the dynamics of the problem can accurately be approximated by a line distribution of Stokes singularities placed along the centerline of the fiber. The slender body approximation yields a system of one-dimensional integral equations relating the force on the fibers to the velocity of the fiber centerline and include the nonlocal interaction of the fiber with itself as mediated by the fluid. The accuracy of the final equation for the center-line velocities of several interacting fibers is of order $O(\varepsilon)$, where $\varepsilon = a/2L << 1$, is the slenderness parameter, a is the fiber radius, and $2L$ is its length. The slender body approximation, but to a lower order of accuracy, has also been used by e.g. Saintillan *et al.*[2] modelling sedimenting fiber suspensions and by Fan *et al.*[3] for fibers in a shear flow.

To compute the force distribution on the fibers for a given configuration of fibers (position and orientation), the system of integral equations is discretized using a combination of a high order Gauss quadrature formula together with analytical integration for certain parts of the integrals. A linear system of equations is assembled and solved using GMRES. Once the forces are obtained, the position and orientation of the fibers can be updated by numerically solving two ordinary differential equations relating the forces on the fibers to their translational and rotational velocities.

To assemble the linear system of equations, like in any multi-body problem, all fiber-to-fiber interactions need to be accounted for. This is extremely time consuming for a large number of fibers and in order to speed up the computations, this part of the numerical algorithm is parallelized using MPI.

For a detailed description of the model and the numerical treatment, see Tornberg and Gustavsson[4].

3 NUMERICAL RESULTS

A large number of simulated data has been analyzed and compared to other studies, both experimental and numerical, see Gustavsson and Tornberg[5] and references therein. In Fig. 1, we present results from a simulation with 800 sedimenting fibers in a periodic domain. Here, we display only one third of the total box height. At the initial time, $t = 0$, Fig. 1(a), the fibers are randomly distributed in the periodic box. At the later time, $t = 500$, the results show, in

agreement with experimental data, that the suspension has formed large scale inhomogeneities in the fiber distribution. At this point, the suspension consists of one elongate fiber-dense streamer surrounded by channels of clear fluid. The large streamer and the clear fluid channels spans the whole height of the box, which can be seen in the lower figure in Fig. 1(b), where we display a top view of the full-height box.

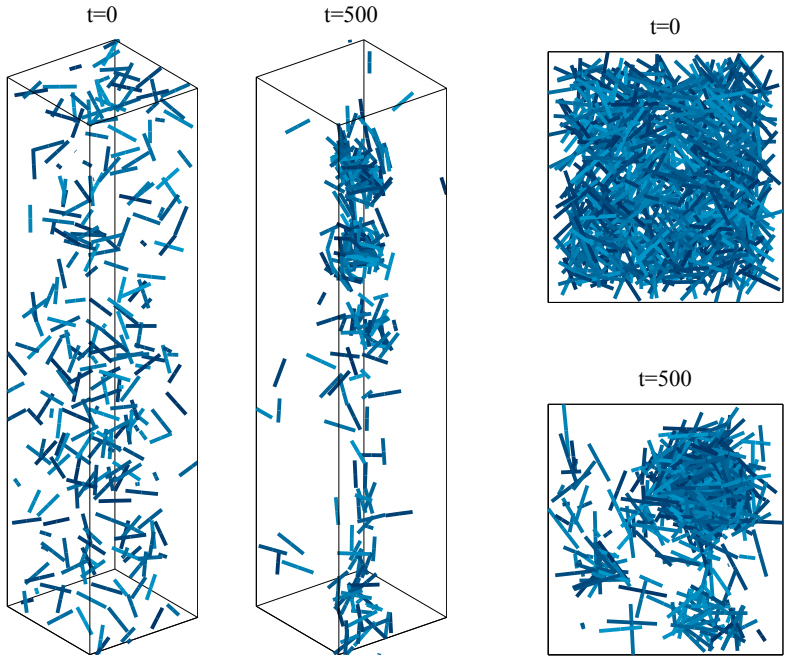

(a) Side view (b) Top view

Figure 1: 800 fibers sedimenting in a periodic box. The fiber configuration is displayed at the initial time and at a later time.

As can be seen in Fig 1. (a), the streamer consists of a number of small distinct clusters of high concentration of fibers. The clusters sediment faster than surrounding single fibers and the fast downward flow of the clusters create a strong backflow in the fluid channels. Occasionally, some of the fibers in the outer region of the streamer are even carried upward by the fluid. This has also been observed in experiments,[6].

The clusters within the streamer are created and dispersed in a repetitive fashion during sedimentation. We have observed a strong correlation between this repetitive cycle and the velocity fluctuations in the sedimentation velocity of the suspension. Another effect of the clustering is an increase of the sedimentation velocity above the maximum settling speed of one isolated fiber.

Another interesting observation is that two simulations with the same macroscopic properties (fiber concentration and periodic box geometry) but with different random initial distribution of fibers can produce mean sedimentation velocities that differ remarkably, with up to 50 %,

during the sedimentation. A detailed study of two cases revealed that the dynamical behavior of the fibers were indeed very different; in both cases a streamer with distinct clusters were formed and the mean sedimentation velocity of the suspension increased. In one of the cases the streamer and clusters persisted during the whole sedimentation process whereas in the other case, the streamer dissolved into smaller clusters randomly distributed in the box and a large drop of the sedimentation velocity was observed.

4 CONCLUSIONS AND FUTURE WORK

One of the great advantages with our model and numerical method is its ability to produce accurate data on a very detailed level. We have exploited this fact by conducting a careful study of the evolution of the micro-structure in the suspension during the sedimentation process. We have found that the micro-structure indeed has a large effect on certain quantities often used to characterize a suspension, such as mean sedimentation velocity and velocity fluctuations.

So far, we have considered the fiber suspension confined to a periodic 3D computational domain with no boundaries and our findings agree to a large extent with reported experimental results. However, the situation in a physical experiment can be quite different. The suspension is confined to a container with bounding walls and some of the interesting features are affected by the presence of walls. E.g. it has been observed in sedimentation experiments, where the fibers eventually settles at the bottom of the container, that the velocity fluctuations decay over time. This is something that is not captured in our simulations.

Motivated by this we are currently investigating different ways of including wall boundary conditions in our simulated system. Using boundary integral methods, this is not as straightforward as in the case with ordinary grid based methods.

REFERENCES

[1] Johnson, R. An improved slender-body theory for Stokes flow. *J. Fluid Mech.* **99**, 411–431 (1980).

[2] Saintillan, D., Shaqfeh, E. S. G. & Darve, E. The growth of concentration fluctuations in dilute dispersion of orientable and deformable particles under sedimentation. *J. Fluid Mech.* **553**, 347–388 (2006).

[3] Fan, X., Phan-Thien, N. & Zheng, R. A direct simulation of fibre suspensions. *J. Non-Newtonian Fluid Mech.* **74**, 113–135 (1998).

[4] Tornberg, A.-K. & Gustavsson, K. A numerical method for simulations of rigid fiber suspensions. *J. of Comput. Phys* **215**, 172–196 (2006).

[5] Gustavsson, K. & Tornberg, A.-K. Gravity induced sedimentation of slender fibers. *Phys. Fluids* **21**, 123301–1 (2009).

[6] Metzger, B., Guazzelli, E. & Butler, J. E. Large-scale streamers in the sedimentation of a dilute fiber suspension. *Phys. Rev. Lett.* **95**, 164504 (2005).

23rd Nordic Seminar on Computational Mechanics
NSCM-23
A. Eriksson and G. Tibert (Eds)

A WALL TREATMENT FOR CONFINED STOKES FLOW

OANA MARIN, KATARINA GUSTAVSSON AND ANNA-KARIN TORNBERG

Linné FLOW Centre, Numerical Analysis
KTH, SE-100 44 Stockholm, Sweden
email: oanam@kth.se, web page: http://www.csc.kth.se/na/

Key words: Stokes Flow, Boundary Integral, Wall Effects, Periodic Boundary Conditions

Summary. The development and validation of a wall treatment based on a boundary integral formulation for Stokes flow is described. The confinement is discretized using high-order quadratures for the resulting singular integrals. This approach offers an alternative to the classical method of images. In order to assess the properties of the model we have used the classical problem of the sedimentation of a sphere for which an analytical expression is available.

1 INTRODUCTION

The study of bodies immersed in Stokes flow arises in various microfluidic applications. An efficient numerical method is to recast the equations as boundary integrals thus reducing three-dimensional problems to two-dimensional integral equations to be discretized over the surface of the submerged objects. The presence of a wall is in this setting most commonly modeled by the method of images. Although efficient and robust, a main drawback is the lack of generality. The method of images was originally developed for one *infinite* flat wall. There are analytical expressions available also for two parallel walls, however they include cumbersome infinite series with slow convergence which are not well suited for numerical computations.

The present work focuses on the development and validation of a wall treatment where the wall is discretized in the same fashion as the immersed bodies.

2 PROBLEM DESCRIPTION

Consider a computational domain where periodic boundary conditions are imposed in the x and y directions, with periods Lx and Ly respectively, where a flat plate, Γ, is placed in the xy plane at $z = z_0$. Above this plate a sphere S is moving downward towards the plate due to gravity.

Using a boundary integral formulation for Stokes flow we have that the flow velocity at any point $\mathbf{x}_0$ is given by

$$\mathbf{u}(\mathbf{x}_0) = \frac{1}{8\pi\mu}\int_S \mathbf{G}(\mathbf{x}-\mathbf{x}_0)\mathbf{f}_s(\mathbf{x})\mathrm{d}S_{\mathbf{x}} + \frac{1}{8\pi\mu}\int_\Gamma \mathbf{G}(\mathbf{x}-\mathbf{x}_0)\mathbf{f}_w(\mathbf{x})\mathrm{d}\Gamma_{\mathbf{x}}\ , \tag{1}$$

where $\mathbf{f}_s$ and $\mathbf{f}_w$ are the force densities on the sphere and wall, respectively. Here μ is the fluid viscosity and the fundamental solution $\mathbf{G}$ is composed of the free-space component $\mathbf{G}_0$ and the

periodic remainder $\mathbf{G}_p$ derived as in[1], together yielding

$$\mathbf{G}(\mathbf{x}-\mathbf{x_0}) = \mathbf{G}_0(\mathbf{x}-\mathbf{x_0}) + \mathbf{G}_p(\mathbf{x}-\mathbf{x_0}) \ , \quad \mathbf{G}_0(\mathbf{x}-\mathbf{x_0}) = \frac{\mathbf{I}}{|\hat{\mathbf{x}}|} + \frac{\hat{\mathbf{x}}\otimes\hat{\mathbf{x}}}{|\hat{\mathbf{x}}|^3} \ . \tag{2}$$

where $\hat{\mathbf{x}} = \mathbf{x} - \mathbf{x_0}$ and $\mathbf{I}_{ij} = \delta_{ij}$ the identity matrix $i, j = 1, .., 3$. In order to determine the unknown force distributions $\mathbf{f}_s$ and $\mathbf{f}_w$ we need to impose4 boundary conditions on the two interacting objects. Thus we distinguish two cases according to whether the pole $\mathbf{x}_0$ is located at the wall or at the sphere. At the wall, $\mathbf{x}_0 \in \Gamma$, a no slip condition is imposed and we obtain the first equation of the system by setting in (1): $\mathbf{u}(\mathbf{x}_0) = 0$. The second equation is obtained by using the requirement that the sphere performs a rigid body motion, i.e. by setting $\mathbf{u}(\mathbf{x_0}) = \mathbf{V} + \mathbf{\Omega} \times (\mathbf{x_0} - \mathbf{x_c})$ for $\mathbf{x}_0 \in S$ in equation (1). Here $\mathbf{x}_c$ is the center of mass of the sphere, $\mathbf{V}$ and $\mathbf{\Omega}$ represent the translational and rotational velocity.

Additional constraints are required to close this system. The integrated force $\mathbf{F}$ over the sphere must balance the buoyancy force given by the product of the density difference $\Delta\rho$, volume of the object V and gravity force $g\mathbf{e_g}$. At the same time the integrated torque $\mathbf{L}$ must vanish since no external torques are applied. Thus yields

$$\mathbf{F} = \int_S \mathbf{f}_s(\mathbf{x}) \mathrm{d}S_{\mathbf{x}} = \Delta\rho V g \mathbf{e_g} \ , \quad \mathbf{L} = \int_S (\mathbf{x} - \mathbf{x}_c) \times \mathbf{f}_s(\mathbf{x}) \mathrm{d}S_{\mathbf{x}} = 0 \ . \tag{3}$$

As a consequence of periodicity the integrated forces over the wall are undetermined and we therefore require

$$\int_\Gamma (f_w)_i(\mathbf{x}) \mathrm{d}\Gamma_{\mathbf{x}} = 0 \ , \quad i = 1, .., 3 \ . \tag{4}$$

This constraint on the forces is included as a Lagrangian multiplier. The complete system to solve is (1) with $\mathbf{u}(\mathbf{x}_0) = 0$ when $\mathbf{x}_0 \in \Gamma$ and $\mathbf{u}(\mathbf{x}_0)$ replaced by $\mathbf{u}(\mathbf{x_0}) = \mathbf{V} + \mathbf{\Omega} \times (\mathbf{x_0} - \mathbf{x_c})$, when $\mathbf{x}_0 \in S$, together with the constraints (3), (4). For legibility we shall denote the terms arising from the discretization of the integrals in equations (1) by I followed by a subscript denoting the pole and a second subscript that designates the domain of integration, therefore we have I_{ss}, I_{sw} for $\mathbf{x}_0$ on the sphere and I_{ws}, I_{ww} for $\mathbf{x}_0$ on the wall.

3 NUMERICAL TREATMENT

The periodic Stokeslet of (2) has a smooth component $\mathbf{G}_p$ whose numerical integration poses no numerical problems while the free-space component $\mathbf{G}_0$ is singular for poles $\mathbf{x}_0$ that belong to the integration domain. Thus a special treatment of the singularity must be considered when evaluating I_{ss} and I_{ww}.

The wall is discretized on a uniform grid in $x \in [-Lx/2, Lx/2)$ and $y \in [-Ly/2, Ly/2)$ with grid resolution h. A special quadrature has been developed in order to accurately perform the integral over the wall despite the singular nature of the integrand. This rule Q_h^p is based on the 'punctured' trapezoidal rule where the singular point is skipped, T_h^0, and a correction operator A_h^p which incorporates the singularity into the weights in a small vicinity of the singularity as given below

$$Q_h^p \mathbf{G}_0(\mathbf{x}) \mathbf{f}_w(\mathbf{x}) = T_h^0 \mathbf{G}_0(\mathbf{x}) \mathbf{f}_w(\mathbf{x}) + A_h^p(\tilde{\mathbf{G}}_0 \mathbf{f}_w), \quad \tilde{\mathbf{G}}_0 = |\hat{\mathbf{x}}| \mathbf{G}_0 \ , \tag{5}$$

with

$$A_h^p(\mathbf{f}_w) = h \sum_{q=0}^{p} \sum_{m=0}^{[q/2]} \omega_q^m \sum_{|\boldsymbol{\beta}|=q} \mathbf{f}_w(\boldsymbol{\beta} h) \ , \quad \boldsymbol{\beta} \in \mathbb{Z}^2 \ .$$

Details about the values of the weights ω_q^m and discretization points $\boldsymbol{\beta}$ are given in[2]. The parameter p determines the accuracy of the method and we choose $p = 4$. This provides a method of $\mathcal{O}(h^{11})$ accuracy.

The integration of I_{ss} on the sphere is based on the singularity subtraction method decomposing the free-space Stokeslet $\mathbf{G}_0$ as

$$\int_S \mathbf{G}_0(\mathbf{x}-\mathbf{x}_0)\mathbf{f}_s(\mathbf{x})\mathrm{d}S_{\mathbf{x}} = \int_S \mathbf{G}_0(\mathbf{x}-\mathbf{x}_0)(\mathbf{f}_s(\mathbf{x})-\mathbf{f}_s(\mathbf{x}_0))\mathrm{d}S_{\mathbf{x}} + \mathbf{f}_s(\mathbf{x}_0)\int_S \mathbf{G}_0(\mathbf{x}-\mathbf{x}_0)\mathrm{d}S_{\mathbf{x}} \ . \quad (6)$$

where the latter integral can be evaluated analytically to be $16/3\pi r\mathbf{I}$, with $\mathbf{I}$ being the identity matrix. By isolating the singular part of the integral (6) the middle term can be evaluated numerically in spherical coordinates with $\theta \in [0, 2\pi)$, $\phi \in [0, \pi]$ by means of the trapezoidal rule yielding a second order error.

The coupling terms I_{sw}, I_{ws} are non-singular. The term I_{sw}, which integrates the wall for poles $\mathbf{x}_0$ on the sphere, can be evaluated with spectral accuracy due to the periodic boundary conditions at the boundaries of the wall. The corresponding integral, I_{ws}, for poles $\mathbf{x}_0$ on the wall is evaluated in spherical coordinates. The accuracy in the non-periodic direction can be improved by using boundary corrections as in[3] and we have used a rule that is $\mathcal{O}(h_\phi^8)$ accurate.

The algebraic solution of the system is computed by using the Schur complement method where the matrix block arising from the term I_{ww} is inverted at the first time-step and stored throughout the computation. This is possible since the wall is immobile and the block I_{ww} does not change its values over time thus rendering the computations more efficient.

4 METHOD VALIDATION AND EFFECTS OF PERIODICITY

Although the wall model developed here is meant to be used in conjunction with any kind of bodies immersed in Stokes flow we have chosen a sphere for validation. The sedimentation of a sphere is a classical test case for which an analytical expression is provided by the Stokes law correction as described in[4]. The classical theory offers a relationship between the drag force, $\mathbf{F}$, and the sedimentation velocity $\mathbf{U}$ of the sphere, as given by

$$\mathbf{F} = 6\pi\mu r\lambda(H/r)\mathbf{U} \ ,$$

where the function $\lambda(H/r)$ includes the wall effect, assuming an infinite wall. Here, H/r is the distance to the wall from the center of the sphere scaled by the radius of the sphere. Since the drag force $\mathbf{F}$ is known (needs to balance the gravitational force) we can compute $\mathbf{U} = \mathbf{F}/(6\pi\mu r\lambda(h/r))$ using the expression for λ from[4].

In our set-up, the domain is periodic in the wall-parallel directions, with periodic length $L_x = L_y = L$. To study the effect of periodicity, and to validate that our results approach the results for an infinite domain as the periodic box size is increased, we perform a sequence of runs with L/r ranging from 10 to 25, see Fig. 1. The radius of the sphere is kept fixed at $r = 0.2$, while L is varied. The grid sizes used were $h = 0.1$ and $h_\theta = 0.314$, $h_\phi = 0.157$.

It is clear that far away from the wall the periodicity has a stronger influence on the drag on the sphere leading to a slower velocity as compared to the unbounded case, while closer to the wall the effect that dominates is the wall influence and the numerical results closely approach the analytical one, also for a small periodic box.

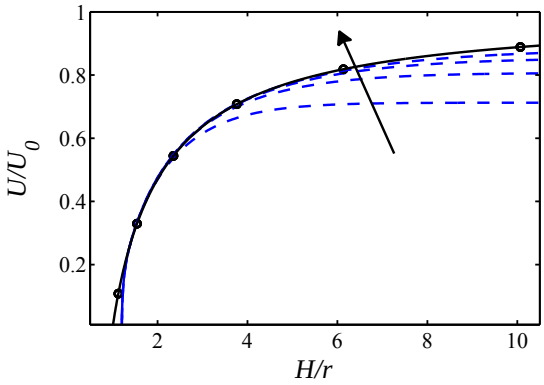

Figure 1: Sedimentation velocity $U = |\mathbf{U}|$ versus wall distance H, normalized by the free-space velocity $U_0 = |\mathbf{U}_0|$ and sphere radius r: (solid) analytic solution[4], (dashed) simulations. In direction of arrow increasing periodic box size from $L/r = 10$ to $L/r = 25$.

5 DISCUSSION AND CONCLUSIONS

In this note, we have introduced a wall treatment which is based on an actual discretization of the wall. We have developed high order quadrature rules to handle the integration of the singular Stokeslet kernel over the wall, and the solution of the coupled system has been expedited by the use of a Schur complement algebraic treatment. We have used this method to study the effect of periodicity on the classical problem on a sphere sedimenting down towards a wall, and we have shown that we closely reproduce the analytical results for an infinite wall as the periodic domain is increased.

Straight-forward extensions of this work include multiple bodies of different shapes interacting with one or two parallel walls in this doubly periodic three-dimensional setting. Future extensions of this type of approach to wall discretization involve more complicated geometries.

REFERENCES

[1] Pozrikidis, C. Computation of periodic Green's functions of Stokes flow. *J. Eng. Math.* **30**, 79–96 (1996).

[2] Marin, O. *A Wall Treatment for Confined Stokes Flow.* Licentiate thesis, KTH Stockholm, Sweden (2010). In preparation.

[3] Alpert, B. K. High-order quadratures for integral operators with singular kernels. *J. Comput. Appl. Math.* **60**, 367–378 (1995).

[4] Happel, J. & Brenner, H. *Low Reynolds Number Hydrodynamics* (Kluwer, Dordrecht, The Netherlands, 1983).

23rd Nordic Seminar on Computational Mechanics
NSCM-23
A. Eriksson and G. Tibert (Eds)

NUMERICAL SIMULATIONS OF A FREE SQUIRMER IN A VISCOELASTIC FLUID

LAILAI ZHU*, ERIC LAUGA† AND LUCA BRANDT*

*Linné Flow Centre, KTH Mechanics, S-100 44 Stockholm, Sweden

† Department of Mechanical and Aerospace Engineering, University of California San Diego, 9500 Gilman Drive, La Jolla CA 92093-0411, USA.

Key words: Fluid mechanics, locomotion, microorganisms.

Summary. In several biologically relevant situations, cell locomotion occurs in polymeric fluids with Weissenberg larger than one. Here we present results of three-dimensional numerical simulations for the steady locomotion of a self-propelled body in a model polymeric (Giesekus) fluid at low Reynolds number. Locomotion is driven by steady tangential deformation at the surface of the body (so-called squirming motion). In the case of a spherical squirmer, we show that the swimming velocity is systematically less than that in a Newtonian fluid, with a minimum occurring for Weissenberg numbers of order one. The rate of work done by the swimmer always goes up compared to that occurring in the Newtonian solvent alone, but is always lower than the power necessary to swim in a Newtonian fluid with the same viscosity. The swimming efficiency, defined as the ratio between the rate of work necessary to pull the body at the swimming speed in the same fluid and the rate of work done by swimming, is found to always be increased in a polymeric fluid. Our computational results are also extended to prolate spheroidal swimmers and smaller polymer stretching are obtained for slender shapes compared to bluff swimmers. The swimmer with an aspect ratio of two is found to be the most hydrodynamically efficient.

1 Introduction

Small organisms displaying the ability to move usually do so in the presence of a viscous fluid [1]. This is the case, in particular, for swimming cells such as bacteria, protozoa, or spermatozoa, which exploit the viscous forces induced by the movement of appendages such as flagella or cilia in order to propel themselves in a fluid environment [2]. One topic of renewed interest concerns the locomotion of biological cells in complex (non-Newtonian) fluids. In many instances eukaryotic or prokaryotic cells move in fluids displaying time-dependent and nonlinear rheological properties. Examples include the progression of spermatozoa through the cervical mucus of mammals and along the mucus-covered fallopian tubes, or the locomotion of bacteria through host mucus and tissues. Bacteria in biofilms are also embedded in a viscoelastic matrix.

In this paper we present results of numerical simulations for a steady spherical squirmer free-swimming in a model (Giesekus) polymeric fluid. Locomotion is achieved by steady tangential surface deformation of the cell, which displays no shape change. It is thus a model for locomotion by cells which swim using the propulsion generated by large arrays of short cilia, and is akin to

the spherical envelope approach first proposed by Blake[3]. In this approximation, an effective non-homogenous boundary condition is imposed at a fixed outer surface, which is impermeable to the fluid. For the simulations presented in this paper, the surface velocity is assumed to be axisymmetric and time independent. The surface velocity on our squirmer is $u_\theta(\theta) = B_1 \sin\theta$, and has its maximum surface velocity located at the equator. For the simulations of the prolate organisms we assume the same boundary condition for the velocity component tangential to the surface of the ellipsoid. To the best of our knowledge, the results we present below are the first three-dimensional simulations for self-propelled motion in a complex fluid.

2 Polymeric fluid dynamics

For incompressible low-Reynolds number flow in a viscoelastic fluid, the momentum and continuity equation are written as

$$-\nabla p + \nabla \cdot \boldsymbol{\tau} = 0, \tag{1}$$

$$\nabla \cdot \mathbf{u} = 0, \tag{2}$$

upon nondimensionalizing velocity with B_1, length with the diameter of the squirmer D, time with D/B_1, and pressure and stresses with $\eta B_1/D$, where η is the solution viscosity. The deviatoric stress $\boldsymbol{\tau}$ can be splited into two components, the viscous solvent stress ($\boldsymbol{\tau}^s$) and the polymeric stress ($\boldsymbol{\tau}^p$); $\boldsymbol{\tau}^s$ is thus given by

$$\boldsymbol{\tau}^s = \beta(\nabla \mathbf{u} + \nabla \mathbf{u}^T), \tag{3}$$

where $\beta < 1$ represents the ratio of the solvent viscosity, η_s, to the total zero shear rate viscosity, η. To complete the model, a transport equation for the polymeric stress $\boldsymbol{\tau}^p$ is required. Here we adopt the nonlinear Giesekus model[4], which, in addition to shear-thinning material properties, provides two important features, namely saturation of polymer elongation, and a non-negative entropy production during the time evolution of the polymers. The nondimensionalized constitutive equation can be written as

$$\frac{\boldsymbol{\tau}^p}{We} + \overset{\triangledown}{\boldsymbol{\tau}}^p + \frac{\alpha}{1-\beta}(\boldsymbol{\tau}^p \cdot \boldsymbol{\tau}^p) = \frac{1-\beta}{We}(\nabla \mathbf{u} + \nabla \mathbf{u}^T), \tag{4}$$

where upper-convected derivative, $\overset{\triangledown}{\mathbf{A}}$, defined for a tensor $\mathbf{A}$, is given by

$$\overset{\triangledown}{\mathbf{A}} = \frac{\partial \mathbf{A}}{\partial t} + \mathbf{u} \cdot \nabla \mathbf{A} - \nabla \mathbf{u}^T \cdot \mathbf{A} - \mathbf{A} \cdot \nabla \mathbf{u}. \tag{5}$$

In the expression above, We is the Weissenberg number, defined as $We = \lambda B_1/D$ where λ is the polymer relaxation time. The so-called mobility factor α is introduced in the nonlinear stress term representing an anisotropic hydrodynamic drag on the polymer molecules, and it limits the extensional viscosity of the fluid. We fix it to be 0.2 in all our simulations. The finite-element code Femlego, developed at KTH[5] is used in our simulations.

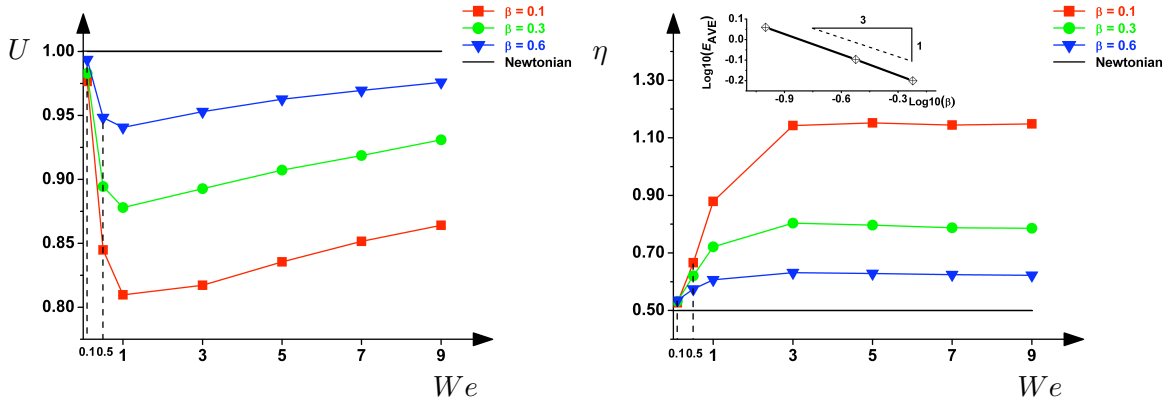

Figure 1: Left: Swimming speed U in the polymeric fluid divided by that of the Newtonian swimmer, versus Weissenberg number, We, for three values of the viscosity ratio, β: 0.1 (red squares), 0.3 (green circles), 0.6 (blue triangles). Right: Swimming efficiency, η, in a polymeric fluid: ratio between the power needed to pull the spherical body at the velocity equal to its swimming speed and the power required to swim in the same fluid. Efficiency is displayed as a function of We for three values of β. Inset: Value of the efficiency at large We as a function of β (log-log plot); the line is a guide for the eye showing a 1/3 power law.

3 Results

Simulations are performed with different values of the Weissenberg number, We, and for three values of the viscosity ratio, β (0.1, 0.3, and 0.6). The swimming speed in the polymeric fluid divided by that of the Newtonian swimmer is displayed in Fig. 1 as a function of We. We see that the swimming speed of the squirmer decreases for low Weissenberg numbers, reaches its minimum value near $We = 1$, and then slowly recovers with increasing polymeric elasticity (or We). The largest decrease in swimming speed is observed for the lowest value of β considered, i.e. for the largest polymer viscosity under investigation. It is interesting to note that the minimum speed is always obtained when the polymer relaxation time is approximately equal to the time it takes for the swimmer to swim its own length. The swimming efficiency, η, is also shown in Fig. 1 as a function of We. The efficiency is defined here as the ratio between the power needed to pull the spherical body at the swimming velocity of the squirmer and the power required to swim in the same fluid. The efficiency is seen to always be larger in the viscoelastic fluid than in a Newtonian fluid, which is one of the main results of our work. This is in agreement with the findings of Teran et al.[6] who simulated a two-dimensional swimming sheet finite length in an Oldroyd B-fluid, as well as the results by Leshansky[7] who considered the locomotion of a squirmer in a suspension of rigid spheres. The efficiency is seen to remain essentially constant beyond $We \gtrsim 3$. By considering the averaged values of the efficiency in the large-We limit, the relation between the viscosity ratio and the asymptotic efficiency is examined. As shown by the inset in the figure, there seems to be a power-law relationship with exponent close to 1/3, $\eta \sim \beta^{-1/3}$.

After considering spherical bodies, we extend our results to the case of prolate swimmers of different aspect ratios. We assume the body to be an axisymmetric prolate spheroid with an aspect ratio, $\mathcal{AR} > 1$, defined as the ratio between its major (symmetry) axis, and its minor axis.

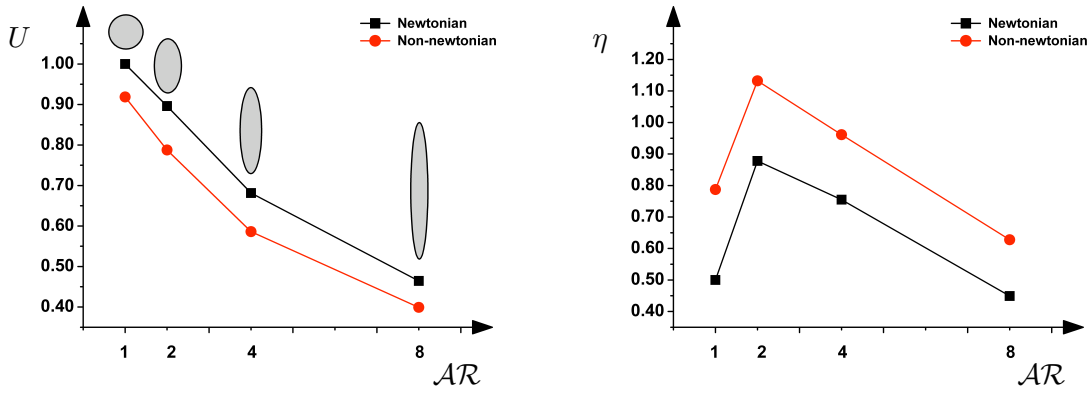

Figure 2: Left: Swimming speed in the polymeric fluid with $We = 7$ and $\beta = 0.3$ divided by that of the spherical Newtonian swimmer for the prolate microorganism sharing the same volume but with different aspect ratio $\mathcal{AR}$. Right: Swimming efficiency of the prolate squirmer in a polymeric fluid as a function of aspect ratio $\mathcal{AR}$, with $We = 7$ and $\beta = 0.3$.Squirmers of different aspect ratio have the same volume.

In order to present a proper comparison between organisms of different shapes, we keep their volume fixed. In Fig. 2 we show the variation of the swimming speed with the prolate aspect ratio. We plot the results in the Newtonian case (black squares) as well as the polymeric case with $We = 7$ and $\beta = 0.3$ (red circles). The swimming speed is normalized with the swimming velocity of the spherical Newtonian squirmer, and is seen to decrease with the aspect ratio. The swimming efficiency is also displayed in Fig. 2. We find that the swimmer of aspect ratio $\mathcal{AR} \approx 2$ is the most efficient, a result which is valid both in the Newtonian and non-Newtonian limit. In addition, a robust increase in efficiency in the viscoelastic fluid is also evident.

REFERENCES

[1] Vogel, S. *Life in Moving Fluids* (Princeton University Press, Princeton, NJ, 1996).

[2] Bray, D. *Cell Movements* (Garland Publishing, New York, NY, 2000).

[3] Blake, J. R. A spherical envelope approach to ciliary propulsion. *J. Fluid Mech.* **46**, 199–208 (1971).

[4] Giesekus, H. A simple consititutive equation for polymer fluids based on the concept of the deformation-dependent tensorial mobility. *J. Non-Newtonian Fluid Mech.* **11**, 69–10+ (1982).

[5] Amberg, G., Tonhardt, R. & Winkler, C. Finite element simulations using symbolic computing. *Math. Comput. Simul.* **49**, 257–274 (1999).

[6] Teran, J., Fauci, L. & Shelley, M. J. Viscoelastic fluid response can increase the speed and efficiency of a free swimmer. *Phys. Rev. Lett.* **104**, 038101 (2010).

[7] Leshansky, A. M. Enhanced low-Reynolds-number propulsion in heterogeneous viscous environments. *Phys. Rev. E* **80**, 051911 (2009).

23rd Nordic Seminar on Computational Mechanics
NSCM-23
A. Eriksson and G. Tibert (Eds)

MULTIPHASE FLOW IN PAPERMAKING: STATE-OF-THE-ART AND FUTURE CHALLENGES

F. LUNDELL*, C. AHLBERG*, M.C. FÄLLMAN*, K. HÅKANSSON† AND M. KVICK†

*Linné FLOW Centre, KTH Mechanics
Royal Institute of Technology
S-100 44 Stockholm, Sweden
e-mail: fredrik@mech.kth.se

†Wallenberg Wood Science Center, KTH Mechanics
Royal Institute of Technology
S-100 44 Stockholm, Sweden

Key words: Papermaking, Fibre suspension, Turbulence.

Summary. Three experimental studies that demonstrate different aspects of fibre suspension flows are presented. The flow cases are fibres in a confined shear flow, turbulent mixing of a fibre suspension and fibres near a wall under a turbulent flow. The experiments provide quantitative data on fiber suspension flow that can pose as validation data for modelling work.

1 INTRODUCTION

Paper is made by spraying a fairly dilute (typical mass concentrations are 1% or less) suspension of water and cellulose fibres onto permeable bands. As the water is drained through the band (various methods can be used in order to drain the water as efficient as possible), the fibres remain on the band and a fibre network, or paper, is obtained. The general process is similar for various end applications, such as printing paper, tissue paper or packaging board.

During papermaking, it is desirable to control aspects such as fibre orientation and concentration, and their variations. Chemical additives are mixed into the suspension in order to either improve the quality of the final paper product or increase the runnability of the process. Furthermore, the fibres are modified by chemical or mechanical treatment prior to the papermaking as such.

In this contribution, three experiments that are generalisations of flow situations occuring during papermaking or suspension preparation are presented. The results provide either quantitative data on the behaviour of fibres as such, or measurements of how the fibres alter the flow, compared to pure water flow. The data from these experiments show drastic effects of fibre and flow variations and provide flow cases that can be used as benchmark cases for simulations.

2 METHODS

Three experiments will be reviewed:

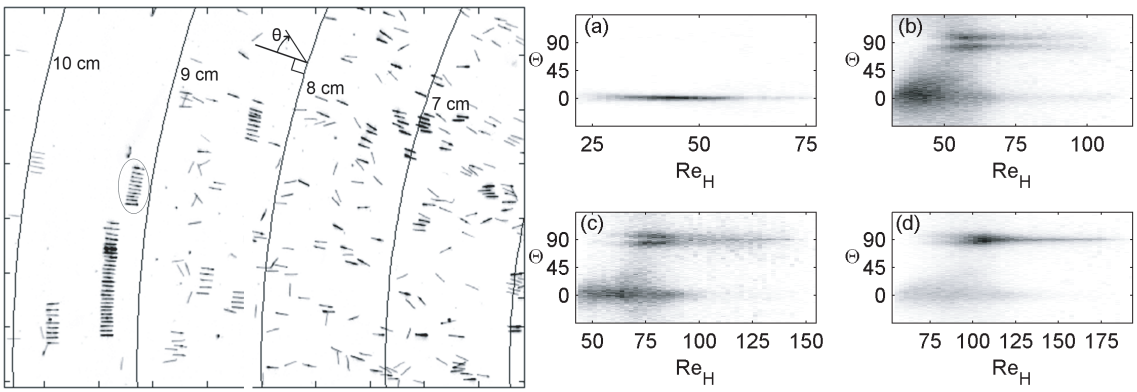

Figure 1: Left: image of fibres in between two parallell disks rotating with rotating velocities having the same amplitude but opposite signs. Right: Probability density distributions of the fibre occurences as function of orientation and $Re_H = 2\Omega RH/\nu$ where Ω is the absolute rotational velocity of one disk, R the radial position, H the distance between the disks and ν is the kinematical viscosity of the fluid. The distance between the disks is 0.2, 0.3, 0.4 and 0.5 fibre lengths from (a) to (d).

1. fibres in the flow between counter rotating disks[1],
2. turbulence in a mixing flow with and without cellulose fibers[2] and
3. fibres on a wall under a turbulent wall shear layer[3].

In all experiments, water is used as liquid. The fibres are synthetic cellulose acetate fibres in case (i),(iii) and pulp fibres in case (ii). The measurements are performed by taking images of the fibres and use image analysis to detect fibre positions and orientations in case (i) and (iii). In case (ii), one of the streams is doped with salt and the difference in conductivity is used together with a micro-conductivity probe to make time resolved measurements of the mixing in the opaque and particulate flow. Further details on the experiments are found in the references[1,2,3].

3 RESULTS

3.1 Fibres in between counter-rotating disks

Figure 1 shows fibres in between two parallel, counter rotating disks. The visualization to the left shows several features. At some radii, the fibres tend to organize themselves in well defined structures, which we have denoted as fibre trains. Furthermore, the fibres seem to prefer different orientations depending on radial position. The orientation-position distribution is also a function of the distance between the disks, as shown to the right where it is seen that for small gaps in (a), the fibres tend to be oriented in the radial direction ($\theta = 0$, as in the trains) whereas more and more fibres are found to be oriented in the tangential direction ($\theta = 90°$) as the gap is increased from (a) to (d). The distributions in (a) to (d) show several quantitative features that are still to be captured in simulations. This flow case has been studied on detail in a recent licentiate thesis from KTH Mechanics[1]

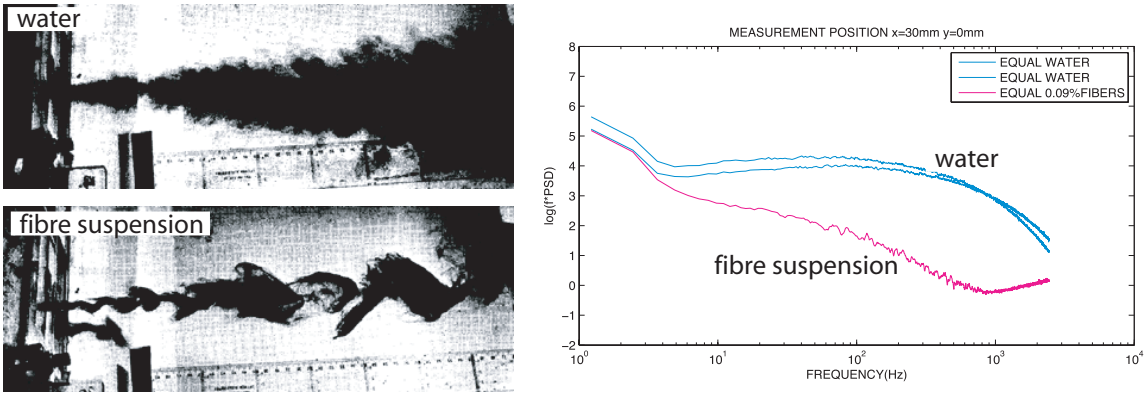

Figure 2: Left: visualization of a dyed water (top) and fibre suspension (bottom) jet issuing into still water (Bark *et al.*[4]). Right: spectra from turbulent mixing flow of two water and fibre suspension streams, respectively. The spectra are measured on the centreline 30 mm downstream of a round pipe (diameter 10 mm) issuing into a surrounding flow with the same velocity as the mean velocity of the jet.

3.2 Turbulent mixing

The addition of fibres have drastic effects on turbulent mixing. An example of this is seen to the left in figure 2 where visualizations[4] are illustrating this phenomenon. A quantitative measurement, obtained with a micro conductivity probe in the mixing of two coflowing fibre suspension streams, is shown to the right. The spectra show the frequency content of conductivity variations that occur since one of the streams is doped with salt. The spectra clearly shows that the high frequency content decreases as fibres are added to the flow already at concentrations as low as 0.09%. This effect on the spectra is in agreement with the visualization to the left; as fibres are added, the visualization shows a considerable lack of generation (and possibly survival) of the smallest scales. Further details can be found in a licentiate thesis[2].

3.3 Fibres on a wall under a turbulent shear layer

Another challenging aspect is the interaction of fibres with a wall. Figure 3 (left) shows fibres that have sedimented down to a wall under a turbulent wall layer[3]. Note that the fibres tend to organise themselves in streaks and orient themselves in different directions. As an example of a quantified measurement that can serve as validation data for simulations, orientation distributions for different aspect ratios r_p of the fibres (at similar crowding factors nl^3 where n is the number density and l the fiber length) are shown to the right. Note that the long ($r_p = 28$) fibres tend to orient themselves in the streamwise ($\beta = 0$) direction whereas the shorter ones ($r_p = 7$) have wider distributions that are centred around $\beta = 0$, *i.e.* normal to the flow direction.

4 CONCLUSIONS

Proper modelling of fibre suspension flows is necessary for optimization and development in many applications where non-spherical particles are present. In addition to papermaking, ketchup production, natural gas processing, wear in nuclear power plants and particle motion

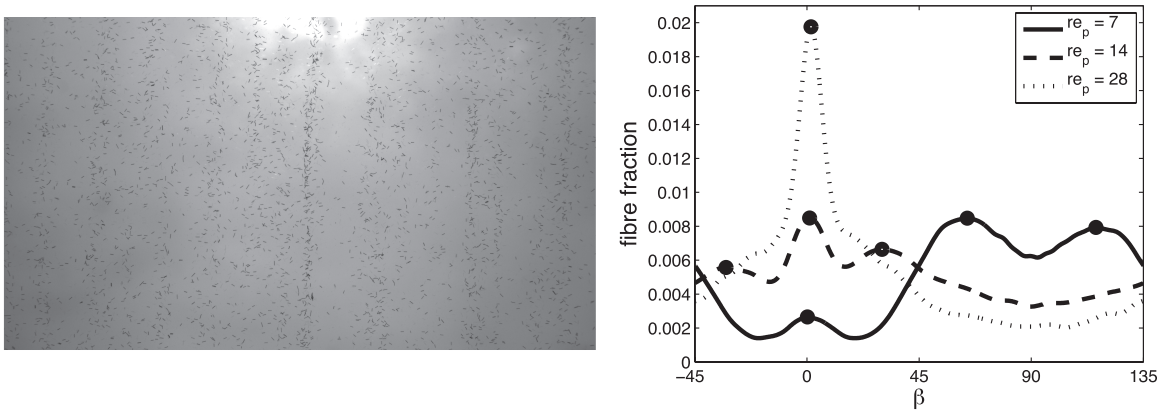

Figure 3: Left: visualization of fibres on a flat plate under a turbulent wall layer. Right: orientation distributions for different fibre aspect ratios r_p of the fibres on the wall.

in the respiratory system are examples that illustrate the width of applicability.

Three examples of fundamental fibre suspension flows have been shown: fibres in confined shear flow, turbulent mixing of fibre suspensions and fibres on a wall under a turbulent wall layer. Considerable effects of running conditions, fibres as such and fibre aspect ratio have been observed and quantified in a manner that makes comparisons with numerical simulations possible.

REFERENCES

[1] C. Ahlberg, *An experimental study of fiber suspensions between counter-rotating discs* Licentiate Thesis, KTH Mechanics (2009)

[2] M. C. Fällman, *Turbulence measurements in fiber suspension flows: experimental methods and results* Licentiate Thesis, KTH Mechanics (2009)

[3] M. Kvick, K. Håkansson, F. Lundell, D. Söderberg and L. Prahl-Wittberg. Fibre streaks in wall bounded turbulent flow. *7th Int. Conf. Multiphase Flow*, Tampa, FL, May 30–June 4, (2010)

[4] L. Filipsson, T. Lagersted and F. Bark. A note on the analogous behaviour of turbulent jets of dilute polymer solutions and fibre suspensions. *J. Non-Newtonian Fluid Mech.*, **3**, 97103 (1977)

ANALYSIS OF DYNAMIC SOIL-STRUCTURE INTERACTION AT HIGH-TECH FACILITY

PETER PERSSON*, KENT PERSSON*

* Division of Structural Mechanics
Lund University
Box 118, 221 00 Lund, Sweden
e-mail: peter.persson@construction.lth.se
web page: http://www.byggmek.lth.se

Key words: Soil-Structure Interaction, Dynamic analysis, Finite Element Method.

1 INTRODUCTION

MAX-lab is a national laboratory operated jointly by the Swedish Research Council and Lund University. The Max project consist of three facilities (three storage rings): Max I, Max II, Max III and one electron pre-accelerator called Max Injector. A new storage ring is needed to improve material science, such as nanotechnology. MAX-IV will be 100 times more efficient than already existing synchrotron radiation facilities, i.e. it is planned to be the next generation Swedish synchrotron radiation facility. The second source will be the Linac injector that will provide short pulses. The Linac will be built as an underground tunnel next to the main ring[1]. The floor of the MAX IV building will mainly be constituted of a concrete structure that is built on soil consisting of mostly clay till. The inner and the outer radius of the main building are approximately 70 m and 110 m respectively, see Figure 1. The structure is exposed to both to harmonic and transient excitations. The harmonic excitation is typically working machines and transient excitations are typically traffic from the nearby roads and other human activities in the building such as walking, closing doors and dropping objects. A very strict vibration requirement is put on the structure of 26 nm RMS during 1s.

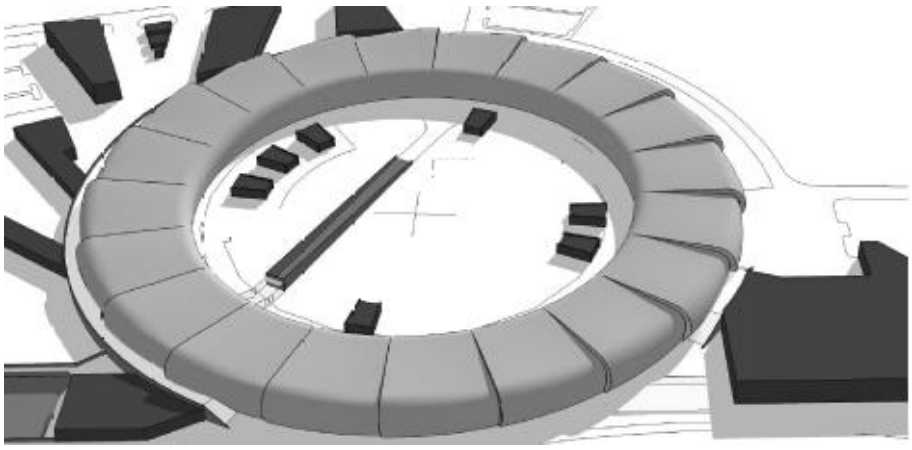

Figure 1: Main building – MAX IV.

2 OBJECTIVE AND METHOD

The MAX IV was analysed by the finite element method[2]. In that report it was concluded from the analyses that the material parameters of the soil have a significant influence on the vibration levels of the magnet foundations and more reliable material parameters are needed to get more reliable results from the finite element analyses.

The main objective of this study is to study vibrations is the soil. The aim is to establish realistic finite element models that predict vibrations with high accuracy.

Vibration measurements were performed at site. A comparison between finite element analysis and the measurements was performed. The model contains the bedrock, the soil and the road were the excitation point was located. The vibrations are analysed by the finite element method with dynamic analysis.

3 MEASUREMENTS

The measurements were performed at the location of MAX IV. To simulate the load from heavy traffic from nearby roads a Falling Weight Deflectometer (FWD) from KUAB was generating a pulse on a nearby road. The FWD applies a known pulse load with a peak force of 72 kN and a duration of 0.07 s, see Figure 2. The measurements were performed with accelerometers placed 20, 40, 60 and 80 m from the excitation point. Measured data is then integrated twice to obtain the displacements, see Figure 3.

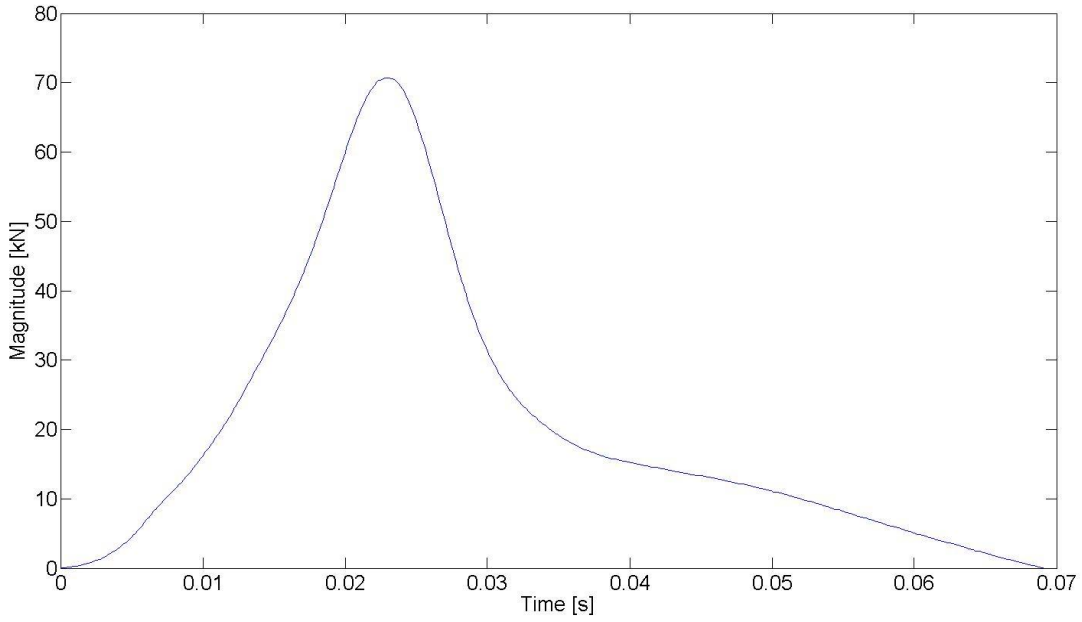

Figure 2: Pulse load from FWD

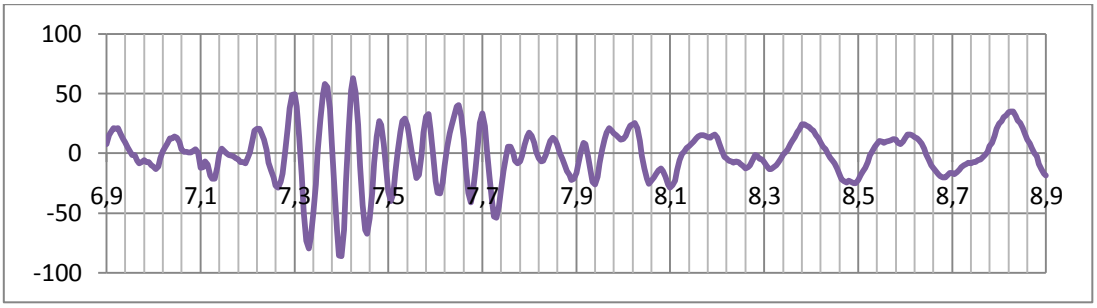

Figure 3: Example of measured displacement in nm 80 meters from the FWD, from Brian Jensen.

3 MATERIALS

The model consists of a road, divided into asphalt and UGM, two soil layers and a bedrock layer. The soil consists of two different layers with different tills. The upper layer consists of 4 m Low Baltic till clay and the lower layer consists of 10 m Northeast till. The soil rests on the bedrock consisting of shale and mudstone. The first estimate of the material properties of the layers are given in Table 1. The damping ratio and the Poisson's ratio of the upper clay till are the most uncertain parameters and were therefore varied to investigate its influence.

Table 1: Properties of the materials.

	Depth [m]	MOE [MPa]	Poisson's ratio	Density [kg/m^3]	Damping ratio
Asphalt	0.15	5000	0.25	2600	2%
UGM	0.5	315	0.2	2300	5%
Upper clay	4	250	0.2-0.45	2100	2-6%
Lower clay	10	1400	0.2	2300	2%
Bedrock	50	8300	0.2	2400	2%

4 FE-MODEL

An axisymmetric model was made to investigate if the estimation of the soil properties was valid, Figure 4. The excitation was applied as a distributed load at the 150 mm closest to the symmetry axis. The force-time history shown in Figure 2 was enforced. The model reached to a radius of 150 m. Symmetry boundary conditions was applied at the symmetry axis and fixed boundary conditions was applied at the bedrock base.

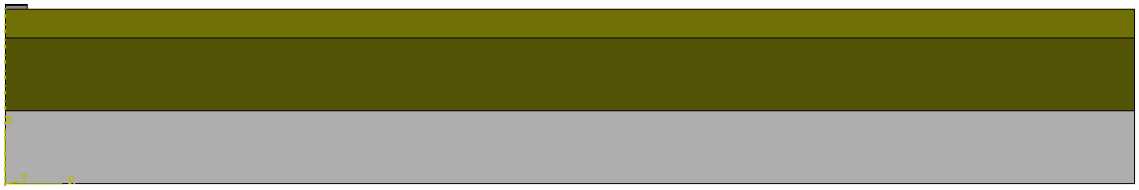

Figure 4: FE-model (not showing the full extension of the bedrock layer).

5 RESULTS

Several analyses were made to investigate the influence of damping and Poisson's ratio. Figure 5 and 6 show examples of resulting displacements 80 m from the pulse load. The displacement amplitudes and the frequency content correlates fairly well to the experimental data shown in Figure 2. The influence of various depth of the bedrock was also investigated. The analyses show that the depth of the bedrock must be at least 50 m to not influence the displacements amplitudes.

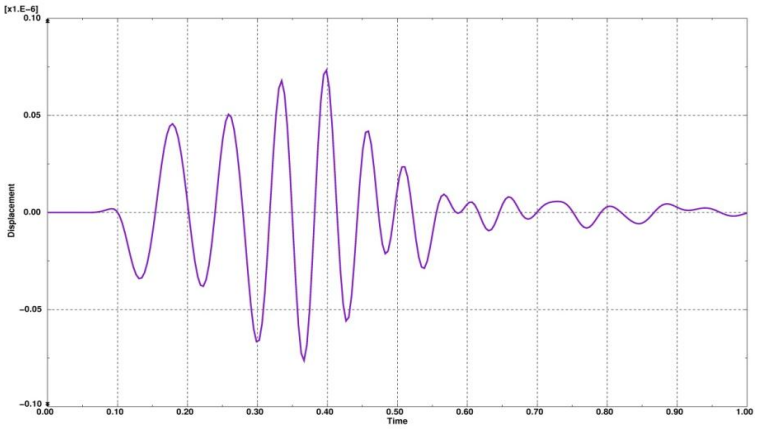

Figure 5: Vertical displacements 80m from the pulse.

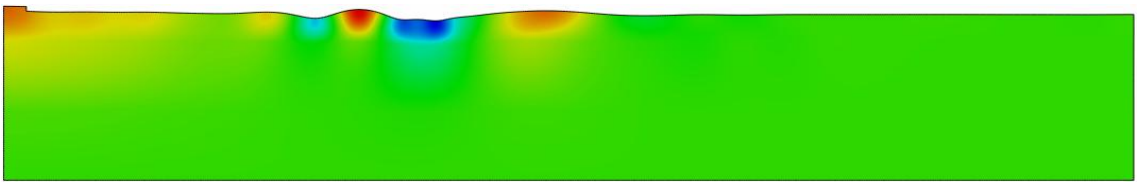

Figure 6: Vertical displacements at 0.40 s after the pulse

6 CONCLUSIONS

More calculations are needed to ensure that the material properties of the FE-model are consistent with the measurements data. The goal is then to investigate the influence of changes of the structure or stabilizations of the soil that can be investigated with high accuracy by the FE-model.

REFERENCES

[1] Lund University and SWECO AB, *MAX IV – Framtidens synkrotron inom Brunnshögsområdet i Lund, Förutsättningar 2009-07-08*, Sweden, (2009).

[2] P. Persson. *Analysis of Vibrations in High-Tech Facility.* Division of Structural Mechanics, Lund University, Report TVSM-5164, Sweden, (2010).

23rd Nordic Seminar on Computational Mechanics
NSCM-23
A. Eriksson and G. Tibert (Eds)

VIBRATION ANALYSIS OF UNDERGROUND TUNNEL AT HIGH-TECH FACILITY

J. NEGREIRA MONTERO[*], K. PERSSON[†], D. BARD[*], P-E AUSTRELL[†], AND G. SANDBERG[†]

[*] Division of Engineering Acoustics
Lunds Tekniska Högskola
BOX 118, 221 00 Lund, Sweden
E-mail: Juan.Negreira_Montero@construction.lth.se - web page: http://www.akustik.lth.se

[†] Division of Structural Mechanics
Lunds Tekniska Högskola
BOX 118, 221 00 Lund, Sweden
Web page: http://www.byggmek.lth.se

Key words: MAX IV, Tunnel, Vibration Analysis, Finite Element Method.

Summary. The investigation presented in this paper deals with the vibration analysis inside the Linac tunnel at the future synchrotron facility MAX IV in Lund. It was done by means of the Finite Element Method considering both steady-state and transient analysis.

1 INTRODUCTION

MAX-lab is a national laboratory operated jointly by the Swedish Research Council and Lund University. Nowadays it consists of three storage rings and one electron pre-accelerator. Due to the improvement of nanotechnology, a new storage ring is needed. Hence, MAX IV will be 100 times more efficient than already existing synchrotron radiation facilities, becoming a leading facility for studies of particles at a nano-level[4].

As shown in Figure 1, MAX IV consists basically in one circular-storage-ring and one linear underground tunnel (Linac) next to it. Both the ring and the Linac converge at one point, where the electrons have already almost reached the speed of light after being accelerated along the tunnel and are then shot into the ring so they can begin to spin around. The beam line is then bent with magnets in order to produce the so-called synchrotron light.

2 OBJECTIVE AND METHOD

In this investigation, the vibration levels at the Linac were analyzed. Since this construction will be used for high precision measurements, it will be asked to have a very strict vibration requirement where only very low vibration levels will be allowed. Thus, the technical condition states that only an RMS value of 100 nm during 1 second will be permitted in the vertical direction under the foundations supporting the beam line.

Real finite element models of the Linac were established in order to analyze the influence of the surrounding vibration sources on the tunnel . To achieve this purpose both steady-state and transient analysis were performed. In the first case, a parameter study was made by varying material properties and checking their influence on the model. Likewise and since a bridge for bus traffic was supposed to be built over the Linac, a simulation of the dynamic component of a bus load was performed as well. For the transient loading, a realistic irregularity on the road was assumed

Figure 1: MAX IV

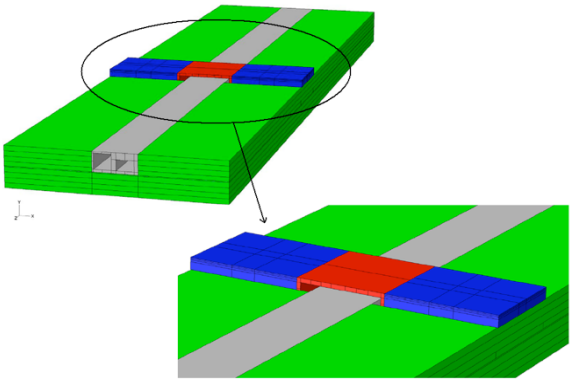

Figure 2 : Finite Element Model

3 FINITE ELEMENT MODEL

The Linac was modeled as a unique section made of concrete extruded along its way, not distinguishing between the different shapes of the cross-sections due to their negligible influence on the results. The cavity on the left (Figure 2) is intended for installations and pedestrian traffic while the right cavity is where the beam line will be accelerated. It is indeed under the foundations of the right cavity supporting the beam line where the technical requirement must be fulfilled.

A concrete bridge for bus traffic was planned to be built over the Linac, being the major external source of vibrations due to the road traffic. At its both sides, a road was modeled too as its continuation.

The soil is manly boulder clay and it was divided vertically in 8 different equal thick layers since its modulus of elasticity varies with the depth[3].

4 MODELLING RESULTS

The technical requirement is meant to be fulfilled at the magnets where the beam will be mounted. Therefore, all the displacement amplitudes were evaluated under the beam line along the Linac, at the bottom of the foundations supporting it since they are really stiff and the vibration levels on top of them will be the same as at their bottom.

4.1 Parameter Study

Several analyses were done in order to investigate the influence of several parameters in the model. A harmonic concentrated force with amplitude of 1 kN was applied in the middle point of the walking path carrying out a frequency sweep from 0 to 50 Hz in 1 Hz steps. This load is very high and may not be realistic but since the response is linear the vibration levels obtained may be scaled to the load applied.

Several parameters such as the modulus of elasticity of the concrete and the thickness of the concrete floor were varied between reasonable values, not having them a large influence in the response of the structure. However, when varying the damping ratio of the soil due to the uncertainness of its properties, it turned out that it does have a great influence on the displacement amplitudes. Therefore, it can be concluded that the soil is the main influence on the structure.

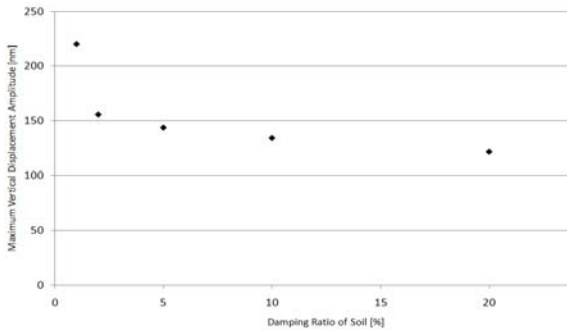

Figure 3 : Vibration levels in the tunnel for different damping ratios of the soil.

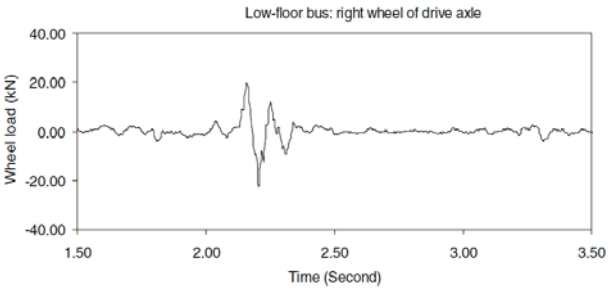

Figure 4 : Time record of dynamic load component of a bus passing over a Word plank

4.2 Dynamic Component of a Bus Load

The purpose of this investigation was to simulate the behavior of the structure when a bus crosses through an even road (no irregularities). To achieve that, a sinusoidal harmonic concentrated force of 0.7 kN was placed on four points representing each wheel and then the frequency sweep was carried out. The loads were taken from measurements of a bus[2]. Various analyses were made trying to find the worst scenario. The maximum displacement amplitude was for this case 301 nm, at a frequency of around 2 Hz, and 100 nm at 10-15 Hz.

4.3 Road irregularity. Bus Load

It is well known that most severe traffic vibrations are created by heavy vehicles moving rapidly along roads. And even more if the road has any kind of irregularity. Therefore and in order to take into account all the cases, a calculation with a road irregularity was performed.

Due to the lack of traffic measurements in the future location of the Linac, data from [2] was taken. The load resulting from a bus or truck hitting a road surface irregularity is composed of an initial impact force and a oscillating force from the subsequent “axle hop” of the vehicle.

The “pulse load” was modeled only taking into account the first initial impact of the recorded wheel-load versus time diagram[2], Figure 4.

Three dynamic/transient forces were placed in different locations trying to find the worst scenario, having for this case an RMS value in the vertical direction of 365 nm, a much higher value than the one allowed (100 nm).

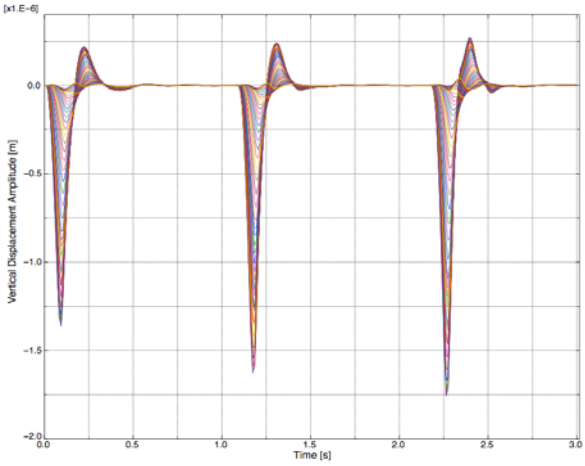

Figure 5 : Displacement amplitudes on the beam floor

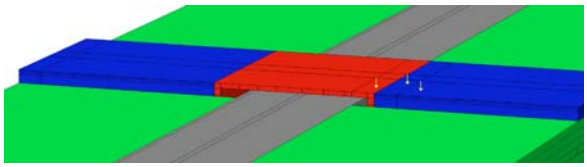

Figure 6 : Location of the road irregularities

5 CONCLUSIONS

- As proved in the parameter study, the properties regarding the soil have a great influence of the vibration levels of the floor, specially the damping ratio. As it is the key on the model, it is of vital importance their determination through on site tests.
- Regarding a bus passing a road that is constituted of smooth asphalt, it was proved that the requirement may be reached in that case.
- However, small irregularities on the road at the bridge will result in pulse loads that will always occur if the road is not in perfect conditions or if, for instance, ice, snow, potholes or objects like branches, soil or small rocks exist on the road. They will create vibration levels that are too high and the quality of the measurements at the MAX IV will be affected.
- Since the probability of not always having a smooth road is rather high, especially during the winters, it was recommended that the bridge is avoided and finally as result of this study the road will be relocated to not crossing the Linac.

REFERENCES

[1] J. Negreira Montero, *Vibration Analysis of Under ground Tunnel at High -Tech Facility*, Lund University, TVSM-5170, (2010).

[2] O. Hunaidi, W. Guan and J. Nicks, *Building vibrations and dynamic pavement loads induced by transit buses,* National Research Council Canada, (2000).

[3] SWECO A.B. *MAX IV Drawings,* (2009).

[4] MAX-lab, Lunds University, *http://www.maxlab.lu.se*

23rd Nordic Seminar on Computational Mechanics
NSCM-23
A. Eriksson and G. Tibert (Eds)

UNSTABLE NON-LINEAR DYNAMIC RESPONSE INVESTIGATION OF SUBMERGED TUNNEL TAUT MOORING ELEMENTS DUE TO PARAMETRIC EXCITATION.

ANDERS RÖNNQUIST *, SVEIN REMSETH AND GEIR UDAHL

Norwegian University of Science and Technology, NTNU
Department of Structural Engineering
Richard Birkelandsvei 1a, 7491 Trondheim, Norway
* anders.ronnquist@ntnu.no

Key words: Dynamic instability, Parametric excitation, taut mooring system, submerged floating tunnel

Summary. A submerged floating tunnel moored at a limited number of mooring locations is studied. The mooring system consists of sets of inclined taut mooring elements. Possible unacceptable response of a mooring element is studied by analytical and numerical modeling. Loading from swell sea states will introduce parametric excitation to the mooring system. Results from the analytical solution coincide well with corresponding results from the numerical model for a range of different swell waves where possible conditions of very large increase in mooring element response level may be identified.

1. INTRODUCTION

Submerged floating tunnels represent an attractive strait crossing concept, particularly for long spans. The present study considers a fjord crossing of 1500 m and a maximum water depth of 550 m. A submerged floating tunnel moored at a limited number of mooring locations is investigated.

The purpose of the study is to identify possible swell sea states that may cause very large increase in lateral dynamic motion of mooring lines during parametric excitation. The excitation is imposed as end displacements at the tunnel mooring connection as well as wave loading on the mooring line itself. Possible unacceptable response of a mooring element is studied by analytical and numerical modeling considering a range of swell waves, possible conditions of very large increase in mooring element response level may be identified.

2. SOLUTION OF THE PARAMETRIC EXCITATION EQUATION BY GENERALIZED COORDINATES [1, 2, 3]

To solve the parametric excitation the differential equation of motion is established in Eq. (1) for the cable motion with distributed loading, q, in the lateral direction on the cable.

$$-(N+\Delta N(t))\frac{\partial^2 y}{\partial x^2}-\Delta N(t)\frac{\partial^2 y_0}{\partial x^2}+m\frac{d^2 y}{dt^2}+c\frac{dy}{dt}=q(x,t) \tag{1}$$

Here N is the initial axial force, ΔN is the variation of the axial force due to variation in the end displacement at the tunnel, m is the mass per unit length of the cable and c is the damping. We assume a displacement function of the form

$$y(x,t) = Y(t)\phi(x) \tag{2}$$

where $\phi(x) = \sin(\frac{\pi x}{L_0})$ is chosen with a harmonic time variation $Y(t) = Y_1 \sin(\omega t) + Y_2 \cos(\omega t)$. Equation (1) with Eq. (2) inserted, multiplication with $\phi(x)$ and integrated over the length of the cable gives

$$\frac{mL_0}{2}\ddot{Y}(t) + \frac{cL_0}{2}\dot{Y}(t) + \frac{\pi^2}{2L_0}\left[N + \Delta N(t)\right]Y(t) + \frac{16a_0}{\pi L_0}\Delta N(t) = \int_0^{L_0} q(x,t)\sin\left(\frac{\pi x}{L_0}\right) \tag{3}$$

In Eq. (3) L_o is the initial length of the cable, and a_o is the maximum value of the initial lateral displacement. For a selected ratio between the excitation frequency, Ω (frequency of harmonic change in axial force, ΔN), and the fundamental mooring line frequency, ω, we can now find a solution. A special case is found when $\Omega = 2\omega_o$. When the frequency ratio and the phase conditions are satisfied, the conditions for extreme response amplification exist. If the equations are made non-dimensional by introducing the quantities

$$\tilde{\omega} = \frac{\omega}{\omega_0}, \omega_0 = \frac{\pi}{L_0}\sqrt{\frac{N}{m}}, \varsigma_0 = \frac{c}{2m\omega_0}, \quad n = \frac{N}{EA}, \quad \gamma = \frac{a_0}{L_0}, \quad \delta_x = \frac{\Delta x}{L_0}, \quad \delta_y = \frac{\Delta y}{L_0}, \quad \tilde{Y}_1 = \frac{Y_1}{L_0}, \quad \tilde{Y}_2 = \frac{Y_2}{L_0}$$

where EA is the axial stiffness of the cable, we find the equation system

$$\begin{bmatrix} (1-\tilde{\omega}^2)n + 2\left(\frac{4}{\pi}\right)^4\gamma^2 - \frac{\delta_x}{2} + \frac{\delta_y^2}{4} & -2\varsigma_0\tilde{\omega}n \\ 2\varsigma_0\tilde{\omega}n & (1-\tilde{\omega}^2)n + 2\left(\frac{4}{\pi}\right)^4\gamma^2 + \frac{\delta_x}{2} + \frac{\delta_y^2}{4} \end{bmatrix} \begin{bmatrix} \tilde{Y}_1 \\ \tilde{Y}_2 \end{bmatrix} = \begin{bmatrix} 0 \\ 0 \end{bmatrix} \tag{4}$$

Other relationships between Ω and ω_o may give a right hand side with cable end excitation terms and thus definite response solution. For the special case shown given in Eq. (4) above will a possible unstable solution exist when the determinant of the coefficient matrix equals zero. This solution will then be of the form

$$\delta = \sqrt{\frac{-A - 2\pi^2\sqrt{B}}{\pi^2\cos(\alpha)}} \tag{5}$$

Here A and B are products from the coefficient matrix and α is the angle between the cable and the horizontal at bottom level.

The above solution is plotted for a number of parameter sets in Fig. 1 shown below. Solutions for a_o = 0 with ζ = 1 % and 10 % respectively are plotted as broken lines with minimum values as expected at $\tilde{\omega} = 2$. The thin solid line in Fig. 1 corresponds to a_o = 5 m, with ζ = 4.5 %. The minimum value now occurs for Ω/ω_o approximately equal to 3.2. This is associated with a fundamental frequency being lower than ω_o for this maximum value of a_o.

The case plotted with bold solid represents actual damping, $\zeta = 4.5$ % and the sag $a_o = 0.5$m from the longest cable set in the FE-analyses. The natural frequency is only slightly lower than for a straight cable and thus the minimum value occurs for $\tilde{\omega}$ being slightly larger than 2.

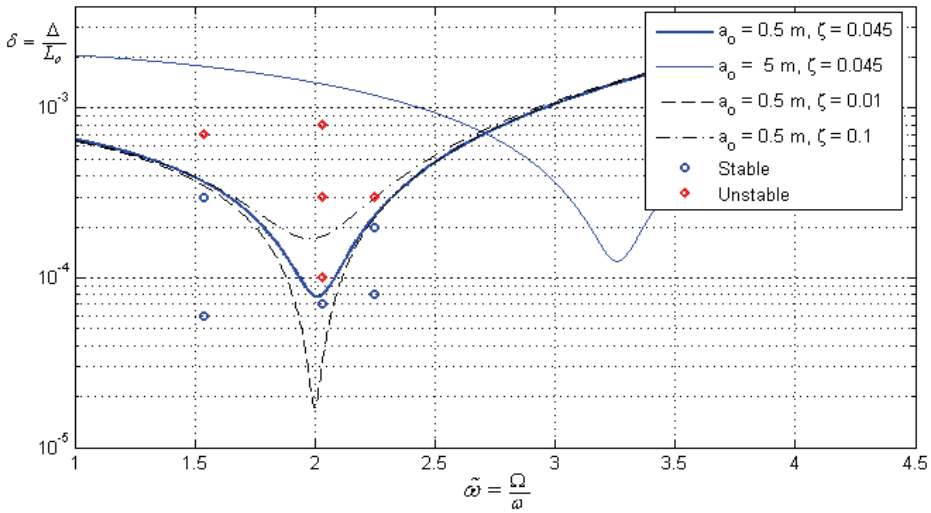

Figure 1: Theoretical results from parametric excitation given as lines and numerical results given as point values.

3. NUMERICAL VERIFICATION OF POSSIBLE INSTABILITY AS INDICATED BY PARAMETRIC EXCITATION

To investigate possible unstable response of the structure a 3D FE-model has been implemented in Abaqus [4]. The model includes both axial bending- and geometrical stiffness contributions. Mooring lines are connected to the midpoint of the tunnel wall thickness by stiff connecters to the centerline of the tunnel cross section. Furthermore, structural damping is assumed low, in the order of 0.5 %. Thus most of the damping is hydrodynamic.

The numerical investigation uses the Abaqus/aqua module where the structure is exposed to gravity forces as well as buoyancy forces in addition to wave loads. The waves are defined by the use of Stokes 5th order wave theory, as optional to linear Airy wave theory.

It is chosen to run numerical simulation for a number of swell sea states with three different values of the excitation frequency, Ω. The selected values correspond to ratios Ω/ω_o of 1.54, 2.02 and 2.25. At each of the selected excitation frequencies, various sea states are chosen to give displacement values on both sides of the bold solid line presented in Fig. 1. The sea states are neither chosen as design sea states nor to represent any one single bridge location, rather as options to capture possible sea states from swell waves selected to investigate possible unstable response.

Time domain results from the numerical investigations are presented below. In Fig. 2 is a stable solution from the present mooring line shown. The response shows frequency peaks at 0.045 Hz, which is in the vicinity of its first natural frequency, as well as the sea state wave frequency of 0.071 Hz (wave period of 14s) corresponding also to the tunnel section response.

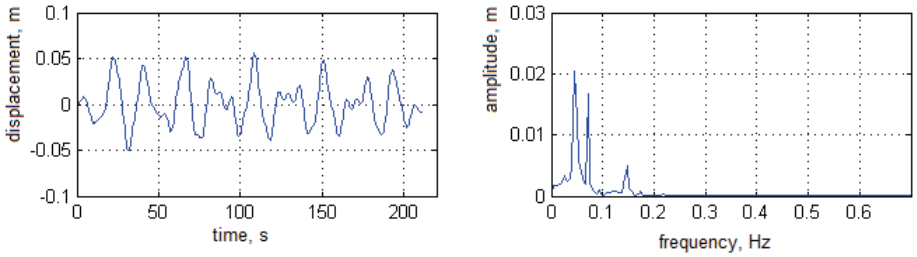

Figure 2: Numerical results for a stable solution at midpoint on present mooring line. Two first peaks at 0.045 Hz and 0.071 Hz representing the natural frequency and the wave load respectively.

A mooring line response with dramatic increase in amplitude is shown in Fig. 3 below, corresponding to the numerical simulation case indicated by the point in Fig.1 above the bold stability curve for Ω / ω_o = 2.25. The direction of this amplified response will be in the inclined plain with axes in the bridge direction and along the cable.

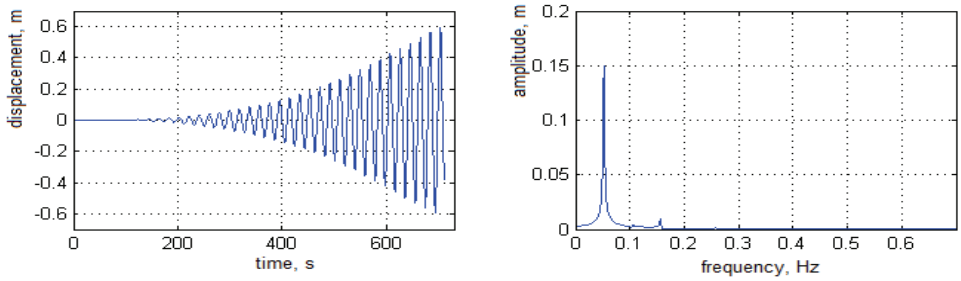

Figure 3: Numerical results for transverse unstable solution at midpoint on present mooring line. The peak frequency at 0.051 Hz corresponds with the expected one half of the excitation frequency.

4. CONCLUSIONS

Possible dynamic instability of mooring lines of a submerged floating tunnel has been investigated by analytical methods and verified by a full three dimensional finite element numerical analysis. The solutions to the parametric excitation equations of motion give indications of boundaries between stable and unstable domains. The numerical solutions confirm these bounds. The analytical method will then represent a convenient mean of preliminary check of instability conditions. It should be noted that other sea states than the selected ones could also cause dynamic instability for other sets of mooring lines along the bridge.

REFERENCES

[1] Hayashi, Chihiro. *Nonlinear Oscillations in Physical Systems.* Princeton University Press; (1985)
[2] Nayfeh, A H and Mook D T. *Nonlinear Oscillations.* John Wiley & Sons, Inc.; (1979)
[3] Xie, Wei-Chau. *Dynamic Stability of Structures.* Cambridge University Press, New York (2006)
[4] Dassault Systèmes Simulia Corp. *Abaqus v.6.9-2*. www.Simula.com

23rd Nordic Seminar on Computational Mechanics
NSCM-23
A. Eriksson and G. Tibert (Eds)

NUMERICAL MODELLING OF BIT-ROCK INTERACTION IN PERCUSSIVE DRILLING BY MANIFOLD APPROACH

TIMO J. SAKSALA*, JARI M. MÄKINEN†

Department of Mechanics and Design
Tampere University of Technology
P.O. Box 589, FI-33101 Tampere, Finland
*Email: timo.saksala@tut.fi
† Email: jari.m.makinen@tut.fi

Key words: Bit-rock interaction, Constitutive modelling, Damage and fracture, Manifold.

Summary. This paper considers numerical simulation of rock fracture in percussive drilling. An explicit dynamics based FE procedure is presented, including a constitutive model for rock and a method for bit-rock interaction based on parametrization of the constraint manifold. The performance of the constitutive model is demonstrated at a material point level and the bit-rock interaction is simulated in axisymmetric case.

1 INTRODUCTION

Rock drilling is widely used, e.g. in open pit mines, quarries and construction sites. A thorough understanding of the bit-rock fracture mechanisms is of considerable importance in developing rock drilling machines, especially in drill bit design. During the past few decades numerical modelling has become an increasingly popular method due to the computational power now available.

In this paper a method for dynamic bit-rock interaction simulation is presented. The method includes a constitutive model presented in [1,2] and a method for simulating the bit-rock interaction. The contact constraints are eliminated through parametrization of the contact manifold. The constitutive model is implemented in explicit dynamics FEM. The rock heterogeneity, as it has a substantial influence on the rock fracture processes, is taken into account at the mesoscopic level by a statistical approach based on the Weibull distribution. The performance of the constitutive model is demonstrated in confined compression test simulation at the material point level. The developed method is applied to a simulation of dynamic bit-rock interaction under axisymmetric conditions.

2 THEORY OF THE MODEL

2.1 Constitutive model for rock under dynamic loading

The constitutive model is presented in detail in [1,2]. It is based on a combination of the viscoplastic consistency model, an isotropic tensile damage model and rate-independent

compression cap plasticity model. The viscoplastic yield surface consists of Drucker-Prager yield function, Modified Rankine criterion (tension cut-off) and a parabolic compression cap illustrated in Fig. 1a. Viscoplasticity provides a localization limiter under dynamic loading and thus retains the initial/boundary value problem involving strain softening well-posed. It naturally accommodates strain rate effects, such as strain rate hardening, being thereby ideal method for the present application.

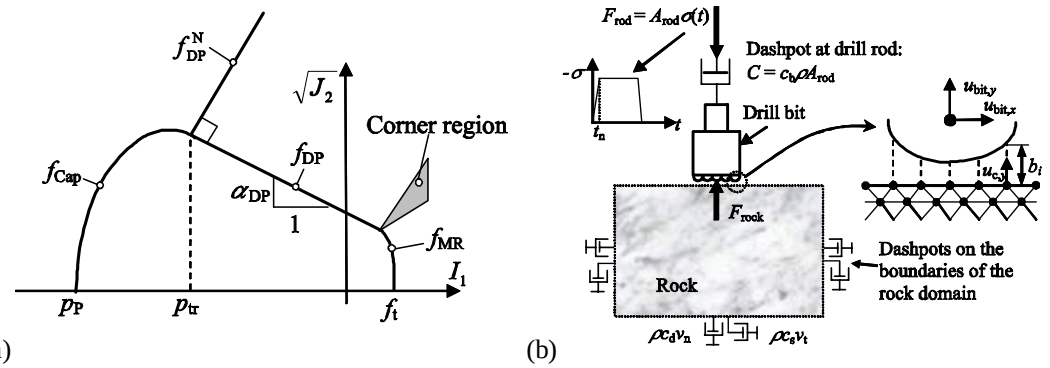

Figure 1: The combined yield surface (a) and the principle of the bit-rock interaction method (b).

In low-confined compression region a viscoplastic strain softening law calibrated using the degradation index concept by Fang & Harrison [3] governs the material behavior while in tension the softening is due to an isotropic damage model driven by viscoplastic strain. Upon reaching the brittle-to-ductile transition pressure in compression the parabolic cap hardening plasticity is activated. The stress integration method is based on the generalized cutting plane algorithm.

The microstructural heterogeneity of rock has a major influence on its failure processes. Here, a statistical method based on the Weibull distribution is selected for characterising the rock strength heterogeneity at the mesoscopic level.

2.2 Bit-Rock interaction method

The principle for modelling the bit-rock interaction is illustrated in Fig. 1b. The drill bit is considered as a rigid body by idealizing its buttons as nodes. Thence, the button geometry can be defined by kinematic contact constraints specifying the distances b_i between the virtual button surface and the nodes on the rock surface (see Fig. 1b).

Contact constraints, i.e. the displacement inequalities, generate a contact manifold with a boundary. When a contact constraint is active the solution lies on the boundary of the contact manifold. The contact problem can be solved with the elimination of additional degrees of freedom. This elimination technique can be viewed as a parameterization of the contact manifold. The solution procedure begins with the detection of the contact: $\mathbf{Gu} - \mathbf{b} = \mathbf{0}$.

If any contact constraint is active, say *i*, then this nodal displacement u_i is eliminated by solving the active constraint equation with respect to u_i, yielding $u_i = u_{bit,y} - b_i$. Moreover, the velocity and acceleration for *i* are equalled, i.e. $v_i = v_{bit,y}$ and $a_i = a_{bit,y}$. Thus, the degrees of

freedom of the problem reduce in one for every active constraint. Finally, the detection of separation of the active contact constraint can be examined via the nodal internal forces. The separation occurs when the nodal internal force is a tractive force. The tractive force converts the active constraint inactive.

The impact-induced compressive wave travelling in the rod and forcing the bit penetration into the rock is simulated as an external stress pulse applied to the button node. Viscous dashpots are applied on the boundaries of the rock domain and at the button node in order to prevent the stress wave reflections. The Modified Euler explicit time integrator is chosen for solving the spatially discretized equations of motion.

3 NUMERICAL SIMULATIONS

First, the performance of the constitutive model is demonstrated at a material point level using a single 8-node hexahedral element. The results in the confined compression test for Carrara marble are shown in Fig. 2c. Below the brittle-to-ductile transition level (68.5 MPa) the model response is linear elastic up to peak strength and linearly softening until the residual strength. Therefore, the nonlinear response of the laboratory size specimen cannot be captured at the material point level. The peak and residual strengths are, however, matched with a good accuracy. In contrast, at level 165 MPa of confinement, when the non-linear cap hardening plasticity is active, the experimental curve for Carrara marble is very accurately matched.

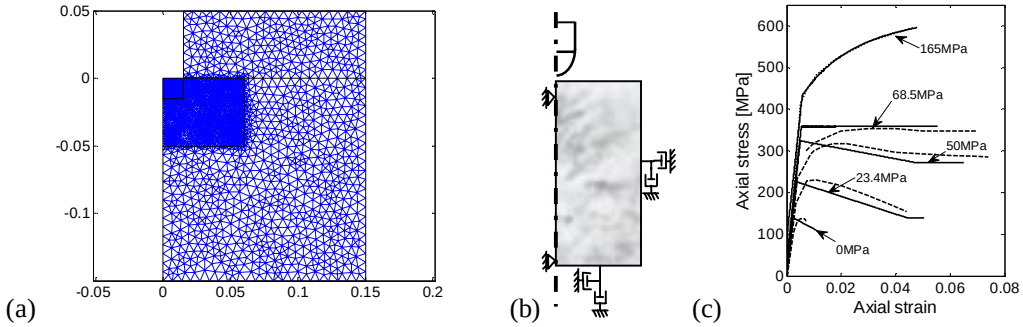

Figure 2: CST-mesh for the initial hole simulation (a), axisymmetric model (b), and the prediction of the constitutive model at the material point level in confined compression for Carrara marble (dashed line).

Next, the bit-rock interaction is simulated with and without the initial hole shown in Fig. 2a. The stress pulse parameters are chosen as σ_A = 200 MPa, $t_{\text{rise}} = 1\times10^{-5}$ s and $t_{\text{dur}} = 1\times10^{-4}$ s. This corresponds to an impact of 300 mm long piston with the velocity of 10 m/s. A hemispherical bit-button with a radius of 10 mm is used. The results, shown in Fig. 3, are plotted at the end of unloading in the form of tensile damage, ω_t, and minor (in-plane) viscoplastic strain, ε_{vp2}, distributions and force-penetration curve for the half space case. With the initial hole (50 mm deep) a button radius 100 mm is used. Moreover, the surface nodes are displaced by magnitude of 0.2 mm to model the surface asperities in a real *in-situ* bore hole.

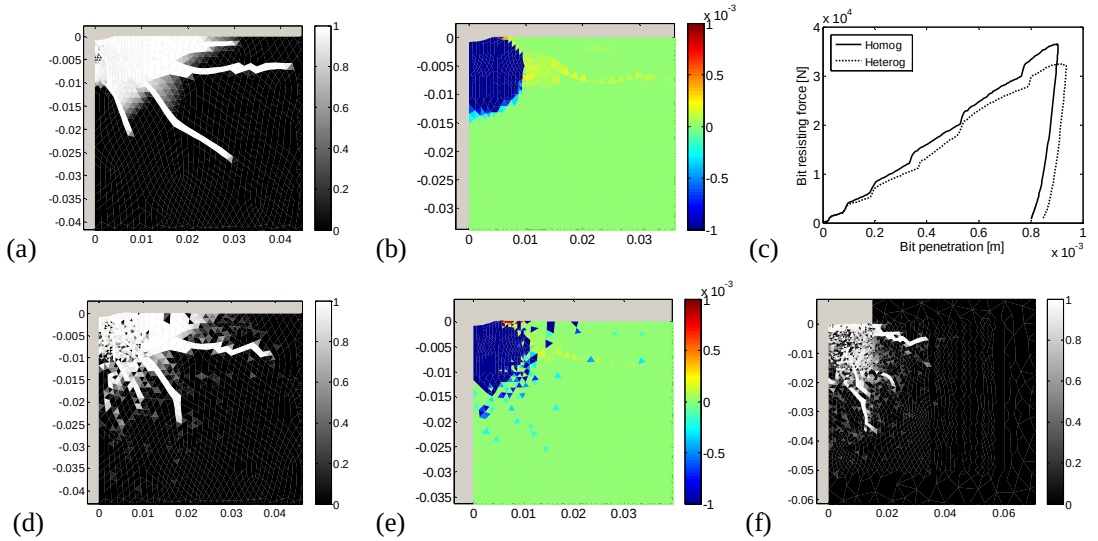

Figure 3: Simulation results : ω_t (a), ε_{vp2} (b) with homogeneous material, force-penetration curves (c), ω_t (a), ε_{vp2} (b) with heterogeneous material, ω_t for the initial hole case (f) (heterogeneous material).

The main features of the results are similar for both the heterogeneous and homogeneous case, i.e. both display clear side and median cracks (see Fig. 3a,d) and spherical crushed zones (see Fig. 3b,c). The edge of the bottom in the initial bore hole cause long side cracks to propagate horizontally. In addition, the elements at the bore hole bottom surface have failed in tensile mode simulating the crushing of surface asperities.

4 CONCLUSIONS

- An explicit dynamics FE based method to simulate the bit-rock interaction during percussive drilling was presented in this paper.
- The simulations predicted the typical features of fracture patterns occurring in the laboratory experiments. Moreover, the results were quantitatively realistic as the bit penetration-force curves are close to those reported in the experiments.
- The statistical method to account for the rock strength heterogeneity adds to the reality of the simulation results. Indeed, the presence of weaker elements results in isolated failure events which simulate the micro-cracking of real rocks.

REFERENCES

[1] T. Saksala, “Damage-viscoplastic consistency model with a parabolic cap for rocks with brittle and ductile behaviour under low-velocity impact loading”, *Int J Numer Anal Meth Geomech*, **34**, 1362–1386 (2010).

[2] T. Saksala, “Numerical modelling of bit-rock fracture mechanisms in percussive drilling with a continuum approach”, *Int J Numer Anal Meth Geomech*, (In press).

[3] Z. Fang Z and J.P. Harrison, “A mechanical degradation index for rock”, *Int J Rock Mech Min Sci*, **38**, 1193-1199 (2001).

23rd Nordic Seminar on Computational Mechanics
NSCM-23
A. Eriksson and G. Tibert (Eds)

FREE VIBRATIONS OF STEPPED CYLINDRICAL SHELLS CONTAINING FLAWS

JAAN LELLEP, LARISSA ROOTS
Institute of Mathematics, University of Tartu
2 Liivi str. Tartu, Estonia
e-mail: jaan.lellep@ut.ee, a42119@ut.ee, web page: http://www.math.ut.ee/mm

Key words: non-axisymmetric vibration, cylindrical shells, flaws.

Summary. Assuming that the deformations are non-axisymmetric vibrations of stepped cylindrical shells are studied. A simple tool for the vibration analysis of shells accounting for the influence of cracks is presented. The changes of flexibility of the shell near cracks are prescribed by means of the compliance coupled with the stress intensity factor defined in the linear elastic fracture mechanics. The shell wall has an arbitrary number of steps and circular cracks of constant depth.

1 BASIC EQUATIONS

Let us consider a cylindrical shell of length l,as shown in Fig.1, where x and θ are surface coordinates and z is the inward normal to the reference surface. The origin of the coordinate system is located on the middle surface of the shell, and the radius of the middle surface is denoted by R.

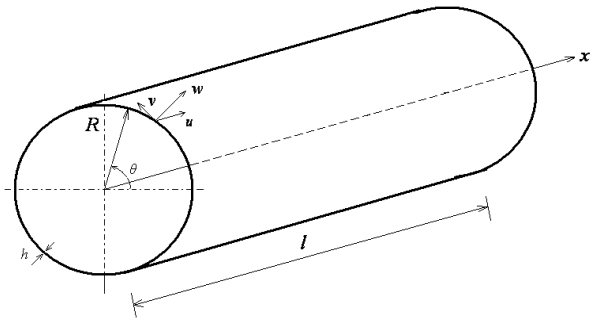

Fig.1: Circular cylindrical shell: coordinate system and dimensions.

A cylindrical coordinate system (x, θ, z) is used in order to take advantage from the axial symmetry of the structure, the origin of the reference system is located at the centre of left end of the shell.The shell thickness is $h(x)=h_j$ for $x\in(a_j,a_{j+1})$, where $j=0,...,n$. Here the quantities h_j ($j=0,...,n$) stand for fixed constants. Similarly, a_j ($j=0,...,n+1$) are given constants whereas it is reasonable to use notations $a_o=0$, $a_{n+1}=l$ .In Fig.1 three displacement fields are represented: axial $u(x, \theta, t)$, circumferential $v(x, \theta, t)$, and radial $w(x, \theta, t)$, where t is time.

Assume that the ends of the shell are simply supported.

A system of displacement equilibrium equations, based on Donnell's approximations, is used to investigate the vibrational characteristics of a cylindrical shell [1], in which $u_j(x,\theta,t)$, $v_j(x,\theta,t)$ and $w_j(x,\theta,t)$ are the displacements of the jth ring segment in the x, θ, and radial directions, ρ is the mass density of the shell, E is the Young's modulus and v is the Poisson's

ratio. Donnell has obtained from the system of equilibrium equations by using special function φ a following equation for w_j [1]

$$D_j \nabla^8 w_j + \frac{Eh_j}{R^2}\frac{\partial^4 w_j}{\partial x^4} = \nabla^4 p_j, \tag{1}$$

where

$$D_j = \frac{Eh_j^3}{12(1-\nu^2)},\ p_j = -\rho h_j \frac{\partial^2 w_j}{\partial t^2}\ ,\ \nabla^8 = (\nabla^2)^4,\ \nabla^4 = (\nabla^2)^2, \text{ where } \nabla^2 = \frac{\partial^2}{\partial x^2} + \frac{1}{R^2}\frac{\partial^2}{\partial \theta^2}.$$

Substituting

$$w_j(x,\theta,t) = e^{r_j x}\cos n\theta \sin \omega t, \tag{2}$$

where n – number of waves in a circumferential direction;

ω – the circular natural frequency.

One obtains the characteristic equation

$$\frac{Eh_j^3}{12(1-\nu^2)}(r_j^2 - \frac{n^2}{R^2})^4 + \frac{Eh_j}{R^2}r_j^4 - \rho h_j \omega^2 (r_j^2 - \frac{n^2}{R^2})^2 = 0. \tag{3}$$

The equation (3) has following roots:

$$r_{1j} = \pm i\frac{1}{R}\sqrt{\frac{a_j R}{h_j} - n^2}, \qquad r_{2j} = \frac{1}{R}\sqrt{\frac{a_j R}{h_j} + n^2}, \tag{4}$$

where $a_j = k_j R$, $i^2 = -1$.

The value of k_j can be a real or a complex number $\alpha + i\beta$.

We can write general solution in the form

$$w_j(x,\theta,t) = (A_{1j}\sin r_{1j}x + A_{2j}\cos r_{1j}x + A_{3j}\sinh r_{2j}x + A_{4j}\cosh r_{2j}x)\sin n\theta \sin \omega t, \tag{5}$$

where A_{1j}, A_{2j}, A_{3j}, A_{4j} - unknown constants;

The solution (5) has to meet appropriate boundary conditions at both ends with the four continuity and jump conditions. The determinant of the resulting 4×4 matrix will give the roots $\lambda_m = a_m/\beta$, where $\beta = h/R$.

It follows from equation (3)

$$\omega_{mn} = \sqrt{\frac{E}{\rho 12(1-\nu^2)}}\frac{\beta}{R}\sqrt{\lambda_m^2 + 12(1-\nu^2)\beta^{-2}\frac{(\lambda_m - n^2)^2}{\lambda_m^2}}. \tag{6}$$

Let the vibration frequency ω be expressed in terms of a non-dimensionalized frequency parameter

$$\Omega = \omega R\sqrt{\frac{\rho(1-\nu^2)}{E}}.$$

This results in

$$\Omega_{mn} = \frac{\beta}{\sqrt{12}}\sqrt{\lambda_m^2 + 12(1-\nu^2)\beta^{-2}\frac{(\lambda_m - n^2)^2}{\lambda_m^2}}. \tag{7}$$

2 JUMP AND BOUNDARY CONDITIONS

Let us study a cylindrical shell with a step at the section $x=a$. Assume that there exists a circumferential surface crack with uniform depth c in the cylindrical shell at $x=a$. Let the segments adjacent to the crack have thicknesses h_0 and h_1, respectively (Fig.2).

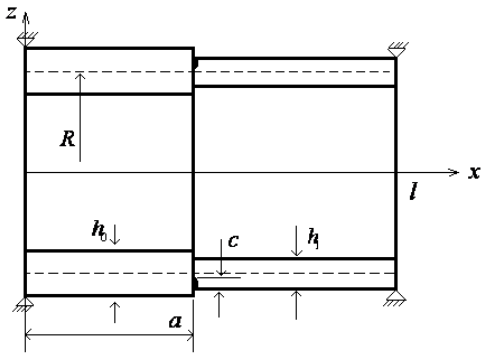

Fig. 2: Circular cylindrical shell with crack and a unique step.

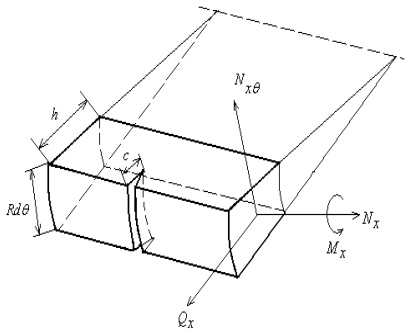

Fig. 3: Geometry of an element of cracked shell.

For the simplicity sake we assume that these flaws are stable circular surface cracks. To avoid confusion, it is assumed that the surface crack is always open. A longitudinal element of unit width of the shell is shown in Fig. 3.

The surface crack in the shell can be modeled as a distributed line spring [2]. The presence of the crack in the shell will cause the local flexibility, which is taken into account by means of the compliance at the current section coupled with the stress intensity factor know in the fracture mechanics.

The continuity and jump conditions at $x=a$ are [2]

$$w_1(a,\theta,t)=w_0(a,\theta,t),$$

$$\frac{\partial w_1}{\partial x}(a,\theta,t)=\frac{\partial w_0}{\partial x}(a,\theta,t)-\frac{72\pi}{E'h_1^2}f(s_1)D_0\left(\frac{\partial^2 w_0(a,\theta,t)}{\partial x^2}+\frac{\nu}{R^2}\frac{\partial^2 w_0(a,\theta,t)}{\partial\theta^2}\right),$$

$$D_1\left(\frac{\partial^2 w_1(a,\theta,t)}{\partial x^2}+\frac{\nu}{R^2}\frac{\partial^2 w_1(a,\theta,t)}{\partial\theta^2}\right)=D_0\left(\frac{\partial^2 w_0(a,\theta,t)}{\partial x^2}+\frac{\nu}{R^2}\frac{\partial^2 w_0(a,\theta,t)}{\partial\theta^2}\right),$$

$$D_1\frac{\partial}{\partial x}\left(\frac{\partial^2 w_1(a,\theta,t)}{\partial x^2}+\frac{\nu}{R^2}\frac{\partial^2 w_1(a,\theta,t)}{\partial\theta^2}\right)=D_0\frac{\partial}{\partial x}\left(\frac{\partial^2 w_0(a,\theta,t)}{\partial x^2}+\frac{\nu}{R^2}\frac{\partial^2 w_0(a,\theta,t)}{\partial\theta^2}\right),$$

where w_0, D_0 and w_1, D_1 stand for the quantities w and D in the segments with thickness h_0 and h_1, respectively, and

$$f(s)=1{,}862s^2-3{,}95s^3+16{,}375s^4-37{,}226s^5+76{,}81s^6-$$
$$-126{,}9s^7+172{,}5s^8-143{,}97s^9+66{,}56s^{10}.$$

The boundary conditions for a cylindrical shell simply supported at the ends are

$$w=0, \qquad M_x=0.$$

3 NUMERICAL RESULTS

Numerical analyses for simply supported shells with one-step thickness variation and a crack are carried out in the case when: h_1=0,009m; l=1,2m; R=0,12m; a/l=0,5; $\gamma=h_1/h_0$; ν=0,3. The influence of the crack length c/h on the fundamental frequency parameters of simply supported circular cylindrical shells with one step of the thickness variation is depicted in Figs. 4 and 5.

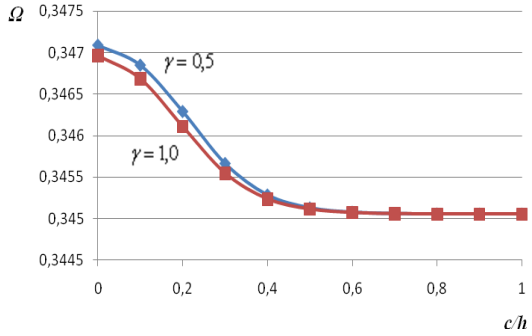

Fig.4: Frequency parameters Ω for simply supported shells, the case n=4; m=1.

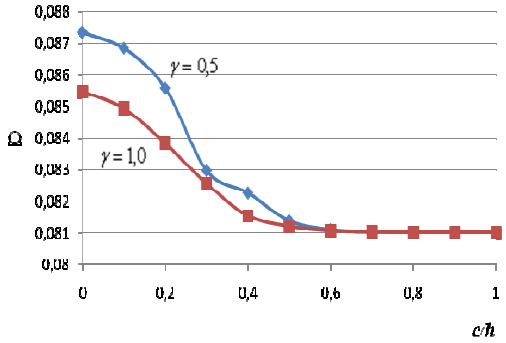

Fig.5: Frequency parameters Ω for simply supported shells, the case n=2; m=1.

4 CONCLUDING REMARKS

Calculations carried out showed that the eigenfrequency of the free vibrations of the shell decreases when the crack depth increases as might be expected.

Acknowledgement. The partial support through the grant # 7461 of the Estonia Science Foundation and through the target financed project "Models of Applied Mathematics and Mechanics" SF 0180081s08 is acknowledged.

REFERENCES

[1] L. H. Donnell. , *Beams, Plates and Shells* , McGraw Hill, 1976.

[2] J. Lellep, L. Roots, Vibration of stepped cylindrical shells with cracks, *3rd WSEAS International Conference on Engineering Mechanics, Structures, Engineering Geology (WORLDGEO'10),* WSEAS Press, 116-121 (2010).

23rd Nordic Seminar on Computational Mechanics
NSCM-23
A. Eriksson and G. Tibert (Eds)

DISPERSION ANALYSIS OF B-SPLINE BASED FINITE ELEMENT METHOD FOR ONE-DIMENSIONAL ELASTIC WAVE PROPAGATION

RADEK KOLMAN, JÁN KOPAČKA, JIŘÍ PLEŠEK, MILOSLAV OKROUHLÍK AND DUŠAN GABRIEL

Institute of Thermomechanics
Department of Impact and Waves in Solids
Academy of Sciences of the Czech Republic
Dolejškova 5, 182 00 Prague, Czech Republic
e-mail: kolman@it.cas.cz, web page: http://www.it.cas.cz/en/kolmanr

Key words: B-spline based finite element method, Dispersion analysis, Wave propagation.

Summary. The spatial discretization of elastic continuum by finite element method introduces the dispersion error to numerical solutions of stress wave propagation. For higher order Lagrangian finite elements there are the optical modes in the spectrum resulting in spurious oscillations of stress and velocity distributions near the sharp wavefront. Furthermore, the high mode behaviour of classical finite elements is divergent with the order of approximation of a field of displacements. B-spline based finite element method has a potencial of this disadvantage of classical finite element method to eliminate. Moreover, the high mode behaviour of B-spline based finite elements is convergent with the order of approximation.

1 INTRODUCTION

The numerical solution of a fast transient elastodynamics problem by the classical Lagrangian type of the finite element method[1] (FEM) is influenced by the dispersion errors caused by both spatial and temporal discretizations[2]. These parasitic effects do not exist in 'ideal' continuum. Furthermore, the FE mesh behaves as a frequency filter. In seismology the spectral finite elements[3] appeared recently. Spectral finite elements are of h-type finite elements, where nodes have special positions along the elements corresponding to the numerical quadrature schemes, but the displacements along element are approximated by the Lagrangian interpolation polynomials.

A modern approach in the finite element analysis is the isogeometric analysis[4], where the shape functions are based on varied types of splines. For examples, Bézier curve, B-spline, NURBS, PB-spline, T-spline, LR-spline, PHT-spline and other are used for spatial discretization. This approach has an advantage that the geometry and approximation of the field of the solution is prescribed by the same technique. Another benefit is that the aproximation is smooth.

Dispersion of B-spline based finite elements was established for the same recurrent B-spline functions. It was shown, that the optical modes did not exist[5]. Next, dispersion errors were reported to decrease with increasing order of B-spline shape functions. This is very a good

results for the explicit dynamics, where critical time step is bounded by the highest eigen-frequency of the whole system. In this paper, the dispersion of B-spline based finite element will be determimed for a one-dimensional elastic wave propagation problem.

2 PROPAGATION OF ELASTIC WAVES IN ONE-DIMENSIONAL CASE

The classical equation governing elastic wave propagation in one-dimensional case[6] without the loading source is given by

$$c_0^2 \frac{\partial^2 u}{\partial x^2} - \frac{\partial^2 u}{\partial t^2} = 0, \tag{1}$$

where c_0 denotes the wave propagation speed, $u(x,t)$ is the displacement field, x is position and t is time. For a elastic bar, the speed is given by $c_0 = \sqrt{E/\rho}$, where E denotes the Young's modulus and ρ is the mass density.

3 B-SPLINE BASED FINITE ELEMENT METHOD

For a given knot vector, the B-spline basis functions are defined recursively starting with piecewise constants (p = 0)

$$N_{i,0}(\xi) = \begin{cases} 1 & \text{if} \quad \xi_i \le \xi \le \xi_{i+1}, \\ 0 & \text{otherwise.} \end{cases} \tag{2}$$

For p = 1, 2, 3, . . . , they are defined by

$$N_{i,p}(\xi) = \frac{\xi - \xi_i}{\xi_{i+p} - \xi_i} N_{i,p-1}(\xi) + \frac{\xi_{i+p+1} - \xi}{\xi_{i+p+1} - \xi_{i+1}} N_{i+1,p-1}(\xi). \tag{3}$$

This is referred to as the Cox-de Boor recursion formula[7]. A knot vector in one dimension is a non-decreasing set of coordinates in the parameter space, written $\Xi = \{\xi_1, \xi_2, ..., \xi_{n+p+1}\}$, where $\xi_i \in R$ is the i-th knot, i is the knot index, $i = 1, 2, \ldots, n+p+1$, p is the polynomial order, and n is the number of basis functions used to construct the B-spline curve.

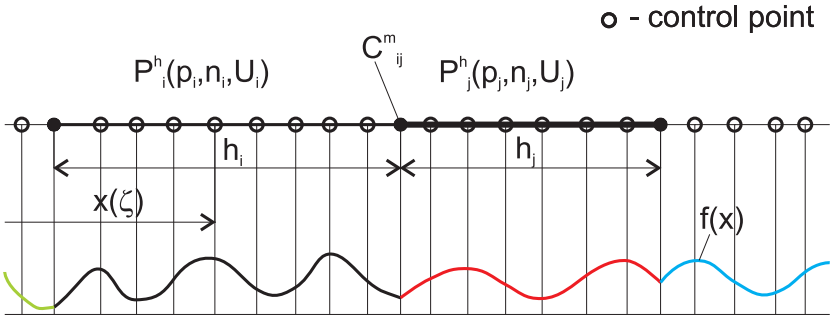

Figure 1: Scheme for spatial discretization of one-dimensional space by B-spline based FE

The approximation of the displacement field u^h by the B-spline approach is given by

$$u^h(\xi) = \sum_{i=1}^{n} N_{i,p}(\xi)\, u_i^B, \tag{4}$$

where u_i^B is the component of the vector of control variables–displacements corresponding to the control points. A scheme of a admissible progress of a one dimensional displacement field based on B-splines is presented in Figure 1.

In the following text, the Galerkin method[1] for the solution of partial differencial equations is used and the stiffness and consistent mass matrices[1] are computed numerically by the Gauss-Legendre quadrature formula[1].

4 DISPERSION ANALYSIS

The complex wavenumber dispersion analysis was performed for a one-dimensional FE[8], where the nodal displacement u_i^h corresponds to given spatial discretization is prescribed in the form of wave solution

$$u_i^h = A_i e^{\mathrm{i}(\omega t - k^h x_i)}, \tag{5}$$

where A_i is displacement amplitude, ω is angular velocity, imaginary unit $\mathrm{i} = \sqrt{-1}$, the discrete (numerical) wavenumber equals to the real part $\mathrm{Re}\, k^h$ and imaginary part $\mathrm{Im}\, k^h$ has the meaning the attenuation intensity and x_i is the nodal or control point position. The assumed solution (5) is inserted to the equation (1) and the dispersion relation $\omega = f(k^h)$ is obtained. The dispersion errors can be measured by numerical phase velocity defined as $c^h = \omega / \mathrm{Re}\,(k^h)$.

It can be derived, that the dispersion error is also influenced by the basic functions $N_{i,p}$ defined near to the patch domain boundary, where the shape function are not homogeneous. From this reason, the band gaps[9] exist also for the B-spline based element method.

Generally, the dispersion for the discretization by B-splines can be controlled by a) length of element patch (*h-refinement*), b) order of spline (*p-refinement*), c) the number of control points (*k-refinement*), d) positions of control points e) multiplicity of knot in the knot vector Ξ, f) C^m continuity between patches, $m < p - 1$ order of continuity.

5 RESULTS OF DISPERSION ANALYSIS FOR B-SPLINE BASED FEM

In this paper, the influence of the number of control points and order p of splines is tested for C^0 continuity between B-spline identical patchs with an uniform knot vector and a linear parametrization. For example, dispersion errors c^h/c_0 of the quadratic ($p = 2$) and cubic ($p = 3$) B-spline based FE with different number of control points are depicted in Figure 2, where h denotes the patch length (see Figue 1). The vertical jump corresponds to the decay solution with non-zero attenuation. These parts of the dispersion dependences detect the passing and band gaps in the frequency range[9].

6 CONCLUSIONS

It was shown that the dispersion errors of B-spline based FE for increasing number of control points converge to the continuum solution. The solution with high number of control points is almost the same as to the solution with homogeneous B-spline shape functions[5]. On the other hand, its progress is shaked from the reason of existing of passing and band gaps. Moreover, the spurious modes are reduced by the B-spline based spatial discretization with high number of the control points. B-splines as the shape functions have a potencial for using in high performance finite element analysis of elastic wave propagation by the explicit direct time integration.

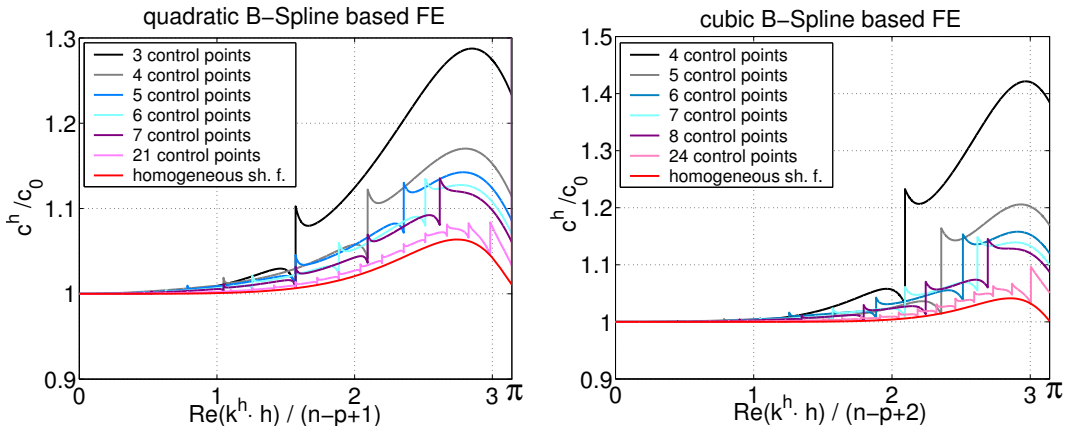

Figure 2: Normalized dispersion errors for quadratic (on the left) and cubic (on the right) B-spline based FE with different number of control points. The red line corresponds to homogeneous shape functions[5].

Acknowledgment

This work was supported by the grant projects GA ČR P101/10/P376, 101/09/1630 and 101/07/1471 under AV0Z20760514.

REFERENCES

[1] T.J.R. Hughes. *The Finite Element Method: Linear and Dynamic Finite Element Analysis*, New York: Prentice-Hall, Englewood Cliffs, (1983).

[2] T. Belytschko and R. Mullen. On dispersive properties of finite element solutions. In *Modern Problems in Elastic Wave Propagation.* J. Miklowitz, (Eds.), John Wiley, 67–82, (1978).

[3] G. Seriani and S.P. Oliveira. Dispersion analysis of spectral element methods for elastic wave propagation. *Wave Motion*, **45**(6), 729–744, (2008).

[4] J.A. Cottrell, T.J.R. Hughes and Y. Bazilevs. *Isogeometric Analysis: Toward Integration of CAD and FEA*, John Wiley & Sons, New York, (2009).

[5] T.J.R. Hughes, A. Reali and G. Sangalli. Duality and Unified Analysis of Discrete Approximations in Structural Dynamics and Wave Propagation: Comparison of p-method Finite Elements with k-method NURBS. *Comput. Methods Appl. Mech. Engrg.*, **197**, 4104–4124, (2008).

[6] H. Kolsky. *Stress Wave in Solids*, New York: Dover Publications, (1963).

[7] L. Piegl and W. Tiller. *The NURBS Book*, Springer-Verlag, (1997).

[8] L.L. Thompson and P.M. Pinky. Complex wave-number Fourier-analysis of the p-version finite element method. *Computational Mechanics*, **13**(4), 255–275, (1995).

[9] L. Brillouin. *Wave propagation in Periodic Structures: Electric Filters and Crystal Lattices*, New York: Dover Publications, (1953).

23rd Nordic Seminar on Computational Mechanics
NSCM-23
A. Eriksson and G. Tibert (Eds)

RESPONSE PROPAGATION ANALYSIS OF IMPERFECT STIFFENED PLATES WITH A FREE OR FLEXIBLE EDGE USING A SEMI-ANALYTICAL METHOD

LARS BRUBAK[*,†] **AND JOSTEIN HELLESLAND**[*]

[*]Mechanics Division, Department of Mathematics, University of Oslo, NO-0316 Oslo, Norway

[†]Section for Advanced Structural Analyses, DNV Technical Advisory
Ships and Offshore, Det Norske Veritas AS, Norway

Key words: Snap-through and snap-back response, Postbuckling, Rayleigh-Ritz method.

Summary. A large deflection, semi-analytical method for response propagation analysis of stiffened plates with a free edge is presented. The formulations derived are implemented into a FORTRAN computer program, and numerical results are compared with fully nonlinear finite element analyses. Good agreement is obtained.

1 INTRODUCTION

A semi-analytical method [1] for pre- and postbuckling analysis of stiffened elastic plates is presented, and its ability to analyse complex plate responses, such as snap-through and snap-back problems, is demonstrated. Geometric nonlinear finite element analysis (FEA) can also be used for such predictions, but for some applications, these are often too time consuming to prepare, run and post-process.

2 THEORY

The method is capable of studying rectangular plates such as those in Fig. 1. The plates may have one edge that is free or provided with an edge stiffener, and supported in the out-of-plane direction at the three other edges. Two opposite supported edges, perpendicular to the free edge, are subjected to an external in-plane stress S_x. The assumed displacement fields are defined by

$$w = w^a + w^b, \quad u = u^a + u^b + u^c, \quad v = v^a + v^b + v^c \tag{1}$$

Here, u, v and w are in the x-, y- and z-direction (parallel and perpendicual to the free edge, and out-of-plane), respectively, and

$$w^a(x,y) = \sum_{i=1}^{M_{wa}} w_i^a \frac{y}{b}\sin(\frac{\pi i x}{L});\ w^b(x,y) = \sum_{i=1}^{M_{wb}}\sum_{j=1}^{N_{wb}} w_{ij}^b \sin(\frac{\pi i x}{L})\sin(\frac{\pi j y}{b}) \tag{2}$$

$$u^a(x,y) = \sum_{i=1}^{M_{ua}} u_i^a \frac{y}{b}\sin(\frac{\pi i x}{L});\ u^b(x,y) = \sum_{i=1}^{M_{ub}}\sum_{j=1}^{N_{ub}} u_{ij}^b \sin(\frac{\pi i x}{L})\sin(\frac{\pi j y}{b});\ u^c(x,y) = u^c\frac{x}{L} \tag{3}$$

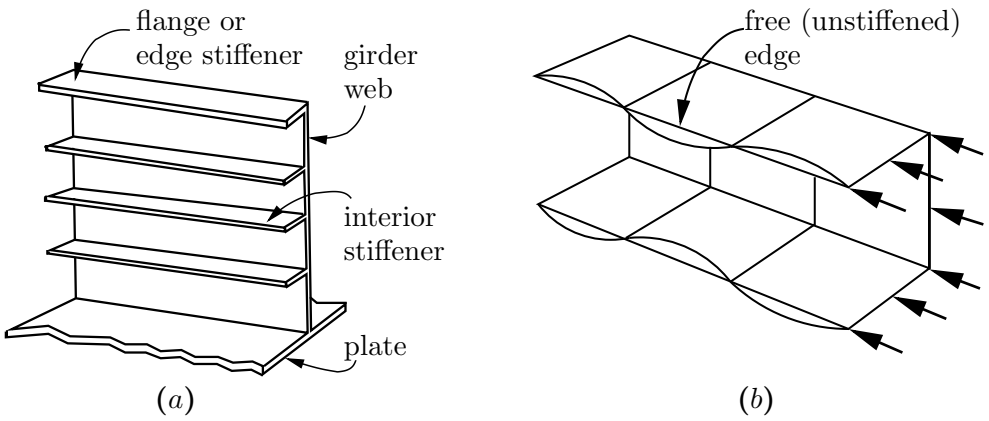

Figure 1: (a) Section of a typical stiffened girder with an edge provided with an stiffener, and (b) a free edge example of a flange outstand of a channel beam.

$$v^a(x,y) = \sum_{i=1}^{M_{va}} v_i^a \frac{y}{b}\cos(\frac{\pi i x}{L});\ v^b(x,y) = \sum_{i=1}^{M_{vb}}\sum_{j=1}^{N_{vb}} v_{ij}^b \sin(\frac{\pi i x}{L})\sin(\frac{\pi j y}{b});\ v^c(x,y) = v^c\frac{y}{b} \qquad (4)$$

Here w_i^a, w_{ij}^b, u_i^a, u_{ij}^b, u^c, v_i^a, v_{ij}^b, v^c are amplitudes, L is the plate length and b the plate width.

By using a solution procedure discussed in detail elsewhere (Steen[2], Brubak and Hellesland[3], Steen, Byklum and Hellesland[4]), the model is able to trace the pre- and postbuckling response, and consequently, it may be used in studies of reserve strengths (beyond the elastic buckling load) typical for slender plates. The Rayleight-Ritz method is used to establish equilibrium equations on the rate form. These equations are solved incrementally using an arc length parameter η. In the common matrix notation, the final set of equations can be given by

$$\mathbf{K}\dot{\mathbf{d}} + \mathbf{G}\dot{\Lambda} = 0 \quad \text{and} \quad \dot{\Lambda}^2 + \frac{1}{t^2}\dot{\mathbf{d}}^T\dot{\mathbf{d}} = 1 \qquad (5)$$

where, $\mathbf{K}$ is a generalised, incremental (tangential) stiffness matrix, $-\mathbf{G}\dot{\Lambda}$ is a generalised, incremental load vector, $\mathbf{d}$ is the displacement amplitudes and Λ is the load factor. A dot above a symbol means differentiation w.r.t. η. The incremental stiffness matrix, load vector and displacement vector can be divided into submatrices and subvectors and given by

$$\mathbf{K} = \begin{bmatrix} \mathbf{K}_{uu} & \mathbf{K}_{uv} & \mathbf{K}_{uw} \\ \mathbf{K}_{vu} & \mathbf{K}_{vv} & \mathbf{K}_{vw} \\ \mathbf{K}_{wu} & \mathbf{K}_{wv} & \mathbf{K}_{ww} \end{bmatrix}, \quad \mathbf{G} = \begin{bmatrix} \mathbf{G}_u \\ \mathbf{G}_v \\ \mathbf{G}_w \end{bmatrix}, \quad \mathbf{d} = \begin{bmatrix} \mathbf{u} \\ \mathbf{v} \\ \mathbf{w} \end{bmatrix} \qquad (6)$$

where the displacement amplitude vector $\mathbf{d}$ is an assembly of all the displacement amplitudes.

At each increment (step) there are two possible solutions. They have the same numerical value, but opposite signs. One solution is in the direction of an increasing arc length and the other in the opposite direction. The correct solution corresponds to that giving a continuous increase of the arc length. This is assumed to be the solution which results in the smoothest equilibrium curve. In the same manner as in Steen [2], this is expressed by the requirement that

the absolute value of the angle between the tangents of two consecutive states ("$k-1$" and "k") in the load-displacement ($\Lambda - d_j/t$) space is smaller than 90 degrees. Thus, for the correct sign of the load rate $\dot{\Lambda}^k$ at state "k", the following criterion must be satisfied:

$$\dot{\Lambda}^k(\frac{(\mathbf{Q}^k)^T\dot{\mathbf{d}}^{k-1}}{t^2} + \dot{\Lambda}^{k-1}) > 0 \quad \text{where } \mathbf{Q} = -\mathbf{K}^{-1}\mathbf{G} \tag{7}$$

When the solution of Eq. (5) at a stage "k" is computed, the displacement amplitudes and load parameter at the next stage "$k+1$" are then obtained from a linear Taylor series expansion as

$$\mathbf{d}^{k+1} = \mathbf{d}^k + \dot{\mathbf{d}}^k\Delta\eta; \qquad \Lambda^{k+1} = \Lambda^k + \dot{\Lambda}^k\Delta\eta \tag{8}$$

In this manner, the solution propagation is continued until a specified limit, or a given strength criterion, is reached. The present solution procedure is capable of passing limit points, including tracing of snap-through and snap-back equilibrium curves. A more detailed presentation of the method is given by Brubak [1].

3 SNAP-BACK RESPONSE EXAMPLE

The present semi-analytical method has been applied to a number of different plate cases [1, 5, 6]. To demonstrate its capability of tracing complex response curves, a snap-back problem [6] is considered for an unstiffened, initially imperfect plate. The plate has a length $L = 3000$ mm, width $b = 1000$ mm, thickness $t = 14$ mm, an imperfection shape taken equal to the first eigenmode of the plate, and a maximum imperfection (at the midlength of the free edge) equal to 5 mm. The eigenmode has one half-wave in the x-direction (parallel to the free edge).

The load-shortening response computed by the present model (using a very small arc length increment of $\Delta\eta = 0.005$) and by the FEA (by ABAQUS) is presented in Fig. 2(a). The agreement between the curves is very good. It can been seen that the response is very unstable, and at a certain load level, both the load and the plate shortening decrease. This is characteristic for a snap-back equilibrium curve.

Initially, the deflection shape will be similar to the imperfection shape (one half wave in the x-direction). At some load stage, the deflection shape changes into several half waves, thereby causing a snap-back. The deflection shapes before and after the snap-back are shown in Fig. 2(b) and (c), respectively.

It should be noted that a snap-back response occurs very late in the post-buckling region, and it is therefore of more academic than practical interest. The intention was to demonstrate that such complex responses are well captured by the present solution procedure. Usually, if material yielding is accounted for, the ultimate strength is reached before snapping occurs. Typically, ultimate strength is reached when the plate shortening Δ_x is about $\epsilon_Y L$ (or $\Delta_x/\epsilon_Y L \approx 1$). In comparison, for this case, snapping occurs at a plate shortening Δ_x of about $2.5\,\epsilon_Y L$.

4 CONCLUDING REMARKS

An efficient computational model is presented for large deflection analysis of rectangular, stiffened elastic plates with an edge being free or provided with an edge stiffener. The applicability of the method has been documented by comparison with finite element analysis results.

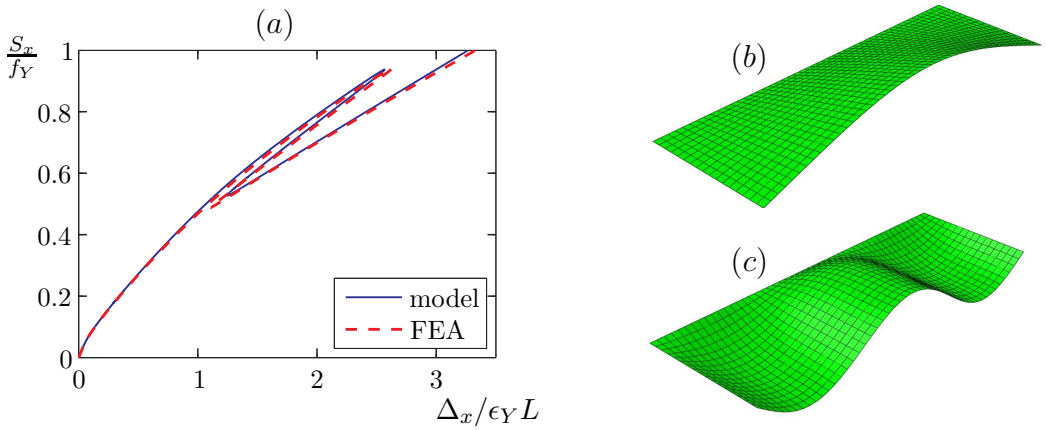

Figure 2: (a) A snap-back load-shortening response computed by the semi-analytical model and FEA, and the deflection shape (b) before and (c) after snap-back of an unstiffened plate with a free edge.

ACKNOWLEDGEMENTS

The authors would like to thank dr. scient. Eivind Steen at Det Norske Veritas (DNV) for his interest, suggestions and valuable discussions during the study.

REFERENCES

[1] L. Brubak, Semi-analytical postbuckling analysis of stiffened plates with a free edge, Research Rep. in Mechanics, No. 08-3, Dept. of Mathematics, Univ. of Oslo, Norway, 2008, 98 pp.

[2] E. Steen. Application of the perturbation method to plate buckling problems, Research Rep. in Mechanics, No. 98-1, Dept. of Mathematics, Univ. of Oslo, Norway, 1998, 60 pp.

[3] L. Brubak and J. Hellesland. Semi-analytical postbuckling and strength analysis of arbitrarily stiffened plates in local and global bending, Thin-Walled Structures, 2007; 45(6), 620–633

[4] E. Steen, E. Byklum and J. Hellesland. Elastic postbuckling stiffness of biaxially compressed rectangular plates, Engineering Structures, 2008; 30(10): 2631–2643

[5] L. Brubak and J. Hellesland. Approximate postbuckling analysis of imperfect stiffened plates with a free edge, In: T. Kvamsdal, B. Pettersen, P. Bergan, E. Oñate, J. García (Eds), Computational Methods in Marine Engineering III, CIMNE 2009: 335-338. (MARINE 2009, Third International Conference on Computational Methods in Marine Engineering, NTNU, Trondheim, Norway, June 2009).

[6] H. S. Andersen. Semi-analytical buckling code development of stiffened and unstiffened plates with a free edge, M.Sc. thesis, Mechanics Division, Dept. of Mathematics, Univ. of Oslo, Norway, 2010, 102 pp.

23rd Nordic Seminar on Computational Mechanics
NSCM-23
A. Eriksson and G. Tibert (Eds)

STRENGTH CRITERION FOR STIFFENED PLATES WITH A FREE OR STIFFENED EDGE

H. S. ANDERSEN [+], J. HELLESLAND[*] AND L. BRUBAK[*,†]

[*]Mechanics Division, Dept. of Mathematics, University of Oslo, Oslo, Norway

[†]Section for Advanced Structural Analyses, DNV Technical Advisory Ships and Offshore, Det Norske Veritas AS, Norway

[+]Dr.techn.Olav Olsen a.s, Oslo, Norwary

Key words: Stiffened plates; Free edge; Postbuckling analysis; Semi-analytical method; Strength criterion.

Summary. Ultimate strengths of stiffened plates with a free or stiffened edge is considered. A large deflection, semi-analytical model for pre- and postbuckling calculations is used in combination with a proposed strength criterion. Strength estimates are compared with finite element analyses (FEA) results, and good agreement is found.

1 INTRODUCTION

Ultimate strengths of rectangular elasto-plastic, stiffened plates with a free or stiffened edge are considered. Such strengths may be computed using fully non-linear FEA (finite element analyses). These FEA may become very time consuming, both w.r.t. modelling and execution, when a large range of cases are considered. A significantly more efficient approach for such cases, is adopted here. It is based on an elastic, semi-analytical pre- and postbuckling model [1], in combination with a proposed strength criterion [2] presented here.

2 SUMMARY OF ELASTIC THEORY

The rectangular plates studied are defined in Fig. 1 (a) and (b). Only one stiffener is shown in each direction, but the number of stiffeners and stiffener spacings can be arbitrary.

The semi-analytical approach is based on a Rayleigh-Ritz discretisation of the displacements, and the equilibrium equations are solved using an incremental procedure with arc length control, as presented in Steen, Byklum and Hellesland [3]. Similar formulations were used in the semi-analytical model for simply supported stiffened plates developed by Brubak and Hellesland [4, 5]. All the displacement components (u, v, w) are included in the current formulation. The displacement fields consist of three parts, one representing an unstiffened plate with a free edge (a), one representing a simply supported stiffened plate (b), and one representing uniform elongation (compression) (c). Mathematically, the assumed displacement fields are defined as follows:

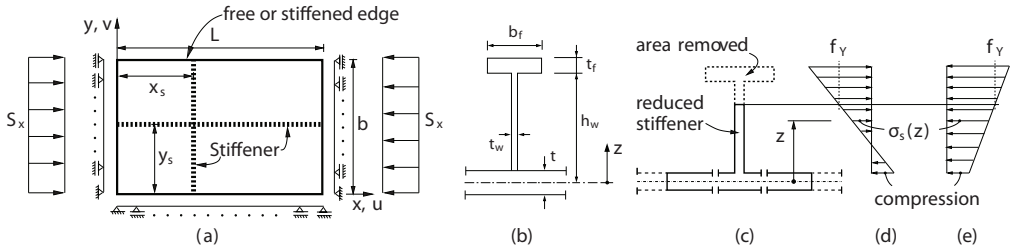

Figure 1: (a) Uniaxially loaded stiffened plate with a free or stiffened edge, (b) cross section of an eccentric stiffener, (c) reduction of stiffener area due to yielding, (d) stiffener stress distribution due to bending in the positive z-direction and (e) in the negative z-direction.

$$w = w^a + w^b, \quad u = u^a + u^b + u^c, \quad v = v^a + v^b + v^c \tag{1}$$

where u, v and w are the displacements in x-, y- and z-direction, respectively, as defined elsewhere [1, 2]. The resulting incremental stiffness relationship can, on matrix form, be given by:

$$\mathbf{K}\dot{\mathbf{d}} + \mathbf{G}\dot{\Lambda} = 0 \tag{2}$$

where $\mathbf{K}$ is a generalised incremental stiffness matrix, $-\mathbf{G}\dot{\Lambda}$ is a generalised incremental load vector, $\mathbf{d}$ denotes a vector consisting of displacement amplitudes and Λ is the load factor. The incremental solution propagation is described elsewhere [1, 2, 4].

3 SELECTED STRENGTH CRITERION

The ultimate strength criterion selected for stiffened plates is defined by:

$$(\sigma_e^{pm})_{max} + \beta_{mod} \cdot \bar{\sigma}_e^{pb} = f_Y \tag{3}$$

where $(\sigma_e^{pm})_{max}$ is the maximum von Mises *membrane* stress, $\bar{\sigma}_e^{pb}$ is the average von Mises *bending* stress along the line in the y-direction on which the maximum von Mises membrane stress is located, and f_Y is the yield stress of the material. The factor β_{mod} is given by:

$$\beta_{mod} = \beta_{mod}(\bar{\sigma}_e) = \begin{cases} B_{mod} \cdot \left(\frac{\bar{\sigma_e} - f_Y}{f_Y}\right), & \bar{\sigma_e} > f_Y \\ 0, & \bar{\sigma_e} \leq f_Y \end{cases} \tag{4}$$

where $\bar{\sigma}_e$ denotes the average of the *total* von Mises stress (at the outer fibres) along the same line that $\bar{\sigma}_e^{pb}$ was calculated, and B_{mod} is defined as follows:

$$B_{mod} = \left[1 + \tanh\left(4\pi \frac{w_{t,edge}}{w_{t,max}} - 2\pi\right)\right] \tag{5}$$

where $w_t = w(x, y) + w_0(x, y)$ is to be taken as the absolute values of the deflections.

The criterion shall be checked on the line, perpendicular to the free edge, that is most critical (i.e., that gives the largest left hand side in Eq. (3)). For cases with symmetrical bending shapes in the x-direction, this "critical line" is defined by $x = L/2$. For more details, see ref. [2].

A stiffener height reduction criterion [5] is applied to the stiffeners in order to account for yielding in the stiffeners. This criterion removes the parts of the stiffener where yielding has occurred. The cross section is reduced over the entire stiffener length with respect to the cross section with the most yielding. This scheme for reducing the stiffener height is illustrated in Fig. 1 (c) - (e).

4 ULTIMATE STRENGTH ESTIMATES

Ultimate strength limit (USL) estimates by the proposed model are presented here and compared with FEA results, obtained using the ABAQUS software program. The first elastic buckling mode, with a maximum amplitude of 5 mm, is used as imperfection shape. Steel properties with Young's modulus $E = 208000$ MPa, Poisson's ratio $\nu = 0.3$ and yield strength $f_Y = 235$ MPa, are used.

Stiffened plates with three equally spaced flatbar stiffeners ($h_f = t_f = 0$) are considered. Dimensions are defined in Table 1, and the general plate geometry in Fig. 4 (d).

Table 1: Plate and stiffener dimension

Plate	**L (mm)**	**b (mm)**	**t (mm)**	t_w **(mm)**	h_w **(mm)**
1000X1000	1000	1000	12	10	16-116
2000X1000	2000	1000	30	10	25-165
2400X2523	2400	2523	11	12	45.5-205.5

Results for varying stiffener heights are presented in Fig. 4 (a) - (c). The ultimate strength limit (USL) estimates are generally seen to be in good agreement with the FEA results. Some conservative deviations are encountered for large ratios of stiffener heights to web thickness (Figs. 4 (a), (c)). Elastic buckling limits (ESL) are also included in the figures.

Similar results were also found for cases with one and two stiffeners [2]. Furthermore, USL results for "combined" imperfections shapes, obtained by combining both a local and a global mode, has also been considered and found to be in good agreement with FEA results [2].

A transition from a global (approximately unstiffened) to a local deflection shape is observed for the plate cases studied, as the stiffener heights become large and thus increasingly resist the out-of-plane deflections under stiffeners. As this happens, a simple support condition will, as expected, be approached at the stiffened edge.

5 CONCLUDING REMARKS

A semi-analytical model for estimating the ultimate strength limit (USL) of stiffened plates with a free or partially stiffened edge is developed and presented. It provides USL estimates that compare very well with FEA (ABAQUS) results.

In practical cases, it may be preferable to incorporate combined local and global imperfections into the analyses, in particular when local and global elastic buckling loads are close. Such imperfections are used by DNV in their PULS design code.

ACKNOWLEDGEMENT

The authors would like to thank dr. scient Eivind Steen for his interest and valuable discussions.

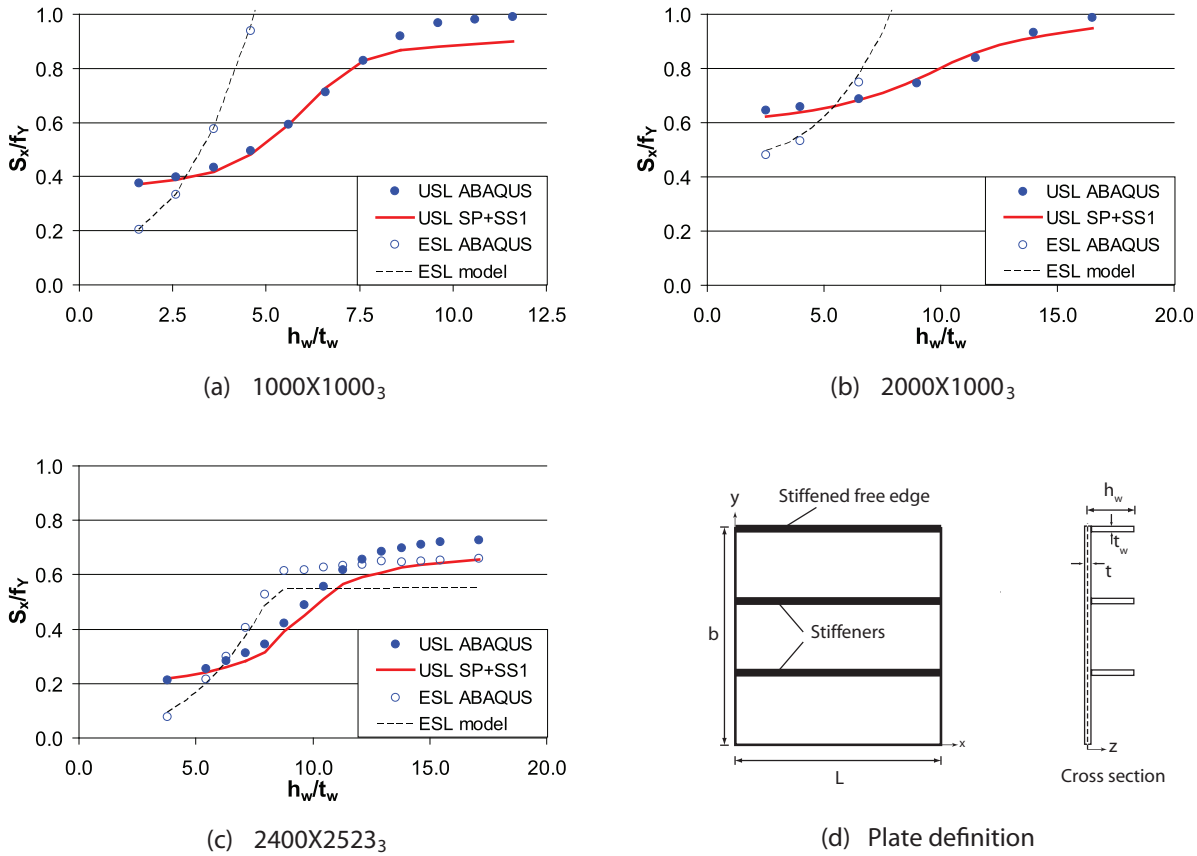

Figure 2: Ultimate strength limit (USL) and elastic buckling strength limit (ESL) vs. stiffener hight for (a) 1000X1000 plate, (b) 2000X1000 plate and (c) 2400X2523 plate; (d) plate geometry and plate cross section.

REFERENCES

[1] L. Brubak, Semi-analytical postbuckling analysis of stiffened plates with a free edge, Research Report in Mechanics, No. 08-3, Dept. of Math., Univ. of Oslo, Norway, 2008, 98 pp.

[2] H. S. Andersen. Semi-analytical buckling code development of stiffened and unstiffened plates with a free edge, M.Sc. thesis, Mechanics Division, Dept. of Math., Univ. of Oslo, Norway, 2010, 102 pp.

[3] E. Steen, E. Byklum and J. Hellesland. Elastic postbuckling stiffness of biaxially compressed rectangular plates, Engineering Structures, 2008; 30(10): 2631–2643

[4] L. Brubak and J. Hellesland. Semi-analytical postbuckling and strength analysis of arbitrarily stiffened plates in local and global bending, Thin-Walled Structures, 2007; 45(6), 620–633

[5] L. Brubak and J. Hellesland. Strength criteria in semi-analytical, large deflection analysis of stiffened plates in local and global bending, Thin-Walled Structures, 2008; 46(12), 1382–1390

23rd Nordic Seminar on Computational Mechanics
NSCM-23
A. Eriksson and G. Tibert (Eds)

STEEL-ELASTOMER SANDWICH PANELS UNDER COMBINED LOADINGS

BRIAN HAYMAN[*] AND JOSTEIN FLADBY[†]

[*] Mechanics Division, Department of Mathematics, University of Oslo, NO-0316 Oslo, Norway
E-mail: brianha@math.uio.no, web page: http://www.uio.no

[†] Flapres Limited, Gamleveien 36, NO-1482 Nittedal, Norway. E-mail: josteifl@gmail.com

Key words: Sandwich Plate System, Combined loadings, Ultimate load.

1 INTRODUCTION

The Sandwich Plate System (SPS), developed by Intelligent Engineering, has steel faces and elastomer core. The ultimate strength of SPS panels has been studied for in-plane shear loading combined with other loading types, and interaction curves and formulae have been developed for clamped and simply-supported, rectangular panels. The sandwich lay-ups and dimensions considered are shown in Table 1, in which a and b are the panel length and width and t_f and t_c are the face and core thicknesses. Only cases with equal faces are considered. The geometries include the extreme cases from a study by Kennedy *et al.*[1] that considered combined lateral pressure and in-plane compression (uni-axial and bi-axial).

Table 1: Layups and dimensions of SPS panels analysed

Panel no.	SPS layup t_f-t_c-t_f (mm)	b x a (mm)	Comment
1	SPS 10-35-10	2000 x 2000	
2	SPS 10-15-10	3200 x 6400	
3	SPS 10-15-10	2000 x 2000	
4	SPS 7-35-7	3200 x 6400	
5	SPS 5-32-5	1200 x 1800	Tested by Little[2]
6	SPS 3-35-3	3200 x 6400	
7	SPS 3-35-3	2000 x 2000	
8	SPS 3-15-3	3200 x 6400	

2 NON-LINEAR FINITE ELEMENT MODELLING

Non-linear finite element (FE) modelling was performed with ABAQUS Version 6.9 [3]. In all cases the panel edges were allowed to "pull in", but were constrained to remain straight. The steel faces are assumed to be ideally elastic-plastic with Young's modulus 206 GPa and yield stress σ_{Yf} = 355 MPa. The elastomer core is assumed linear-elastic, with modulus 750 MPa, up to a stress of 0.75 MPa; beyond this non-linear elastic-plastic behaviour is assumed, with ultimate tensile strength and strain of approximately 39 MPa and 30%.

A study of modelling strategies, including comparison with laboratory test results reported by Little[2], showed that use of thick shell elements S4R with reduced integration and a mesh with 100x100 elements gave consistently good results for the relevant responses.

3 LATERAL PRESSURE LOADING

Jones[4] presents both upper and lower bound plasticity solutions for collapse of rectangular plates under uniform lateral pressure loading. These are summarised in Table 2, in which M_p is the plastic moment per unit length, which for a sandwich plate is given by

$$M_p = \sigma_{Yf} t_f \left(t_f + t_c\right) \tag{1}$$

The contribution of the core to M_p is neglected. For simply supported panels, the upper and lower bound solutions are identical for square panels and differ by only 1% for b/a = 0.5.

Non-linear FE analysis for lateral pressure loading showed that:

- Relatively thick or small panels (e.g. panels 1, 3 and 7) display a "knee" in the response that is reasonably well bounded by the upper and lower bound solutions (as Figure 1 left).
- Slender panels (e.g. panels 2 and 8) do not display a clear failure load or "knee" but continue to deform with increasing membrane stiffening effects (as Figure 1 right).

Table 2: Upper and lower bound collapse loads cited by Jones[4]

Boundary conditions	Upper bound		Lower bound	
	P_{YU}	k_{aU}	P_{YL}	k_{aL}
Simply supported	$\frac{8M_p k_{aU}}{b^2}$	$\frac{3}{\left(\sqrt{3+(b/a)^2} - b/a\right)^2}$	$\frac{8M_p k_{aL}}{b^2}$	$1+(b/a)+(b/a)^2$
Clamped	$\frac{16M_p k_{aU}}{b^2}$		$\frac{16M_p k_{aL}}{b^2}$	$1+(b/a)^2$

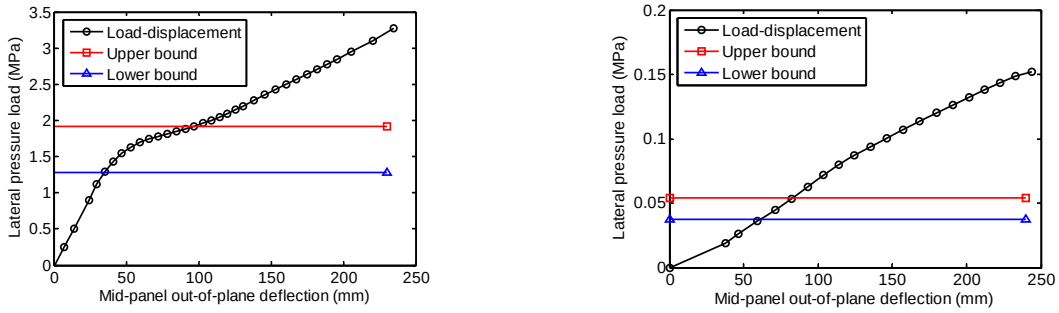

Figure 1: Load-deflection curves for Panel 1 (left) and Panel 8 (right) with clamped edges, under uniform lateral pressure loading, obtained by nonlinear FEA. Upper and lower bound plasticity solutions are also shown.

4 IN-PLANE SHEAR LOADING

For pure in-plane shear loading of an idealised panel with perfect geometry and homogeneous, isotropic materials, yielding will occur throughout the face sheets and core when the applied shear load reaches the value:

$$Q_Y = 2\tau_{Yf} t_f + \tau_{Yc} t_c = \frac{1}{\sqrt{3}}\left(2\sigma_{Yf} t_f + \sigma_{Yc} t_c\right) \tag{2}$$

where τ_{Yf} is the yield stresses of the face sheets in shear and σ_{Yc} and τ_{Yc} are the yield stresses of the core in tension and shear, respectively. Critical values of applied shear force per unit

length, Q_{crit}, for elastic buckling were obtained by FE eigenvalue analysis. For simply supported, slender SPS panels (Panels 2 and 8) $Q_{crit} < Q_Y$. For the very slender Panel 8 this also applies with clamped edges. For all other cases considered, $Q_Y < Q_{crit}$.

Non-linear FEA has been applied with a small initial imperfection in the shape of the first buckling mode. For the cases where $Q_Y < Q_{crit}$ the yield load Q_Y is found to be a good estimate of the ultimate load. For cases where $Q_{crit} < Q_Y$ collapse occurs close to, or slightly above, Q_{crit}, the induced buckles leading to extensive yielding with little further increase of loading.

5 COMBINED LATERAL PRESSURE AND IN-PLANE SHEAR LOADINGS

Ultimate loads for cases with two loading components in combination can be presented in terms of interaction curves or formulae. An interaction curve consists of a graph in which the two axes represent the two load magnitudes, and each combined failure condition is represented by a single point. The interaction curve should meet the axes at the ultimate strengths for the separate loading cases, and these points are important for defining the curve. As indicated in Section 3, for the SPS panels the ultimate strength for lateral pressure is in many cases not well defined. Thus the interaction curve is also difficult to define in the region where lateral pressure dominates. This has been confirmed with both proportionally increasing load and when the lateral pressure is applied first and the shear load after. In order to define a curve, the use of the bound solutions for ultimate pressure load has been investigated.

An interaction curve that gives a conservative estimate for the combination of in-plane shear Q and uniform lateral pressure p for those cases where $Q_Y < Q_{crit}$ (as Figure 2, left) is

$$\left(\frac{Q}{Q_Y}\right)^2 + \left(\frac{p}{p_{YU}}\right)^{1.2} = 1 \tag{3}$$

For cases with $Q_Y > Q_{crit}$ the interaction curve has a different form as in Figure 2 (right).

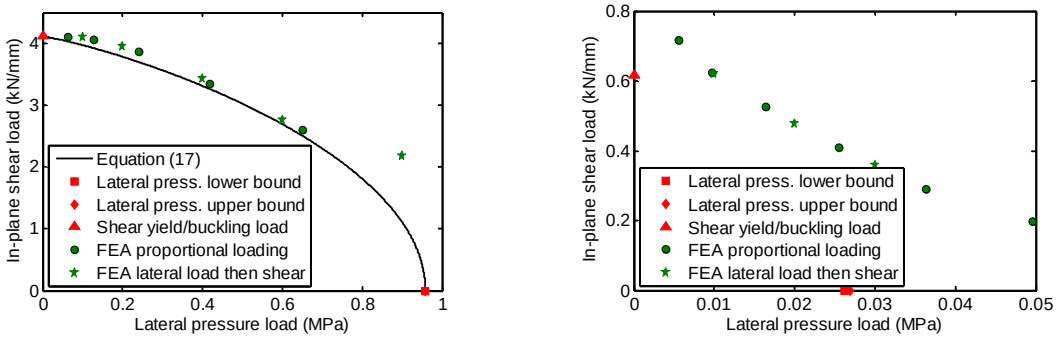

Figure 2: Interaction curves for Panel 1 (left) and Panel 8 (right) for combined lateral pressure loading and in-plane shear loading, with simply supported edges, obtained by nonlinear FEA.

6 LATERAL PRESSURE WITH IN-PLANE COMPRESSION AND SHEAR

For panel no. 5 (for which elastic critical load for in-plane compression is much higher than the yield load), a three-way interaction surface has been obtained for combined lateral pressure, in-plane uni-axial compression (N) and in-plane shear loadings:

$$\left(\frac{N}{N_Y}\right)^2+\left(\frac{Q}{Q_Y}\right)^2\left[1-\left(\frac{p}{p_{YU}}\right)^{1.2}\right]^{1/3}=\left[1-\left(\frac{p}{p_{YU}}\right)^{1.2}\right]^{4/3} \quad (4)$$

7 LIMITATIONS IMPOSED BY OTHER CONSIDERATIONS

7.1 Shear strength of core and face-core bond

Teixeira de Freitas *et al.*[5] have shown that the bond between the elastomer core and the steel faces can only withstand a shear stress of about 6 MPa (though this may depend on the surface preparation). This presents a more severe limitation than failure of the core itself. The bond shear stress is mainly determined by the lateral loading so the effect on the interaction curves will be a panel-dependent cut-off at a specific value of pressure p.

7.2 Acceptable deflections

For the relatively slender panels the lateral pressure loading does not give a clearly defined collapse load. If such panels are used in practice it is likely that a limit will be applied to the maximum deflection; typically limits of 1-3% of the panel width b are specified in design codes. Unless Q is close to Q_{crit}, this is mainly determined by the lateral pressure p and the influence on the interaction curves is similar to that described in Section 7.1.

7.3 Reduction of face sheet yield strength

In many practical applications a lower strength steel is used, e.g. σ_{Yf} = 235 MPa. Then:

- A clearer "knee" is seen in the load-displacement curve for lateral pressure loading.
- The deformation is smaller when the ultimate capacity is reached so membrane effects are less significant.
- The deformation, core shear and debonding limits are less likely to be determining factors.

ACKNOWLEDGEMENTS

The analyses were performed by the second author as part of a Master's thesis project at the University of Oslo, in collaboration with Det Norske Veritas and Intelligent Engineering. The authors wish to thank Simulia Europe for providing free use of the ABAQUS software.

REFERENCES

[1] S. Kennedy, A.E. Martino & J. Kong, "Development of Rules for Designing Steel-Elastomer Sandwich Plates for Ship Structures", 9th Int. Conf. on Sandwich Structures, Pasadena, USA, 2010.
[2] J. Little, *Sandwich Plate System Panels under In-plane and Uniform Lateral Pressure*, Master's Thesis, Civil and Environmental Engineering, Univ. of Alberta, Canada, 2007.
[3] Simulia, ABAQUS Documentation Manual 6.9-1, 2009.
[4] N. Jones. *Structural Impact*. Cambridge University Press, 1989.
[5] S. Teixeira de Freitas, H. Kolstein & F. Bijlaard, "Sandwich systems for renovation of orthotropic steel bridge decks", 9th Int. Conf. on Sandwich Structures, Pasadena, USA, 2010.

23rd Nordic Seminar on Computational Mechanics
NSCM-23
A. Eriksson and G. Tibert (Eds)

ON COMPUTING CRITICAL EQUILIBRIUM POINTS BY A DIRECT METHOD

JARI MÄKINEN*, REIJO KOUHIA† AND ANTTI YLINEN*

*Department of Mechanics and Design
Tampere University of Technology
P.O. Box 589, FI-33101 Tampere, Finland
e-mail: jari.m.makinen@tut.fi,antti.ylinen@tut.fi, web page: http://www.tut.fi/

†Department of Structural Engineering and Building Technology
Aalto University School of Science and Technology
P.O. Box 12100, FI-00076 Aalto, Finland
e-mail: reijo.kouhia@tkk.fi, web page: http://www.tkk.fi/

Key words: Non-linear eigenvalue problem, Critical point, Geometrically exact theory, Finite rotation

Summary. Computation of critical points on an equilibrium path requires solution of a non-linear eigenvalue problem, for which solution several techniques exist. Their algorithmic treatment is usually focused for direct linear solvers and thus use the block elimination strategy. Due to the non-uniqueness of the critical eigenmode a normalizing condition is required. In addition, for bifurcation points, the Jacobian matrix of the augmented system is singular at the critical point and additional stabilization is required in order to quarantee the quadratic convergence of the Newton's method. Depending on the normalizing condition, convergence to a critical point with negative load parameter value can happen. The form of the normalizing equation is critically discussed and an alternative form is proposed.

1 INTRODUCTION

Determination of a critical point is the primary problem in structural stability analysis. Mathematically it means solution of an eigenvalue problem, which in general is non-linear, together with the equilibrium equations. However, if the pre-buckling displacements are negligible, it is usually sufficient to solve the linearized eigenvalue problem, where the linearization is performed with respect to the undeformed configuration.

The non-linear stability eigenvalue problem constitutes of solving the equilibrium equations simultaneously with the criticality condition. First appearance of this idea seems to be from 1973 by Keener and Keller[1]. In their approach the criticality condition is augmented as an eigenvalue equation, such approach has been used also in Refs.[2,3,4,5]. Another approach uses a scalar equation indicating the criticality[6,7] or expansion to a higher order polynomial eigenvalue problem[8,9].

In computational structural analysis, direct solution of the critical points along the equilibrium path requires complete kinematical description of the underlying kinematical model. In

particular, for dimensionally reduced models, like beam- and shell models, the description has to be capable to handle large rotations. Development of a geometrically exact model with large rotations is not a trivial task[10,11,12].

2 STABILITY EIGENVALUE PROBLEM

The problem of finding a critical point along an equilibrium path can be stated as: find the critical values of $\mathbf{q}, \lambda$ and the corresponding eigenvector $\boldsymbol{\phi}$ such that

$$\left\{ \begin{array}{rcl} \mathbf{f}(\mathbf{q},\lambda) & = & \mathbf{0} \\ \mathbf{f}'(\mathbf{q},\lambda)\boldsymbol{\phi} & = & \mathbf{0} \end{array} \right. \tag{1}$$

where $\mathbf{f}$ is a vector defining the equilibrium equations and $\mathbf{f}'$ denotes the Gateaux derivative (Jacobian matrix) with respect to the state variables $\mathbf{q}$, i.e. the stiffness matrix. At the critical point the equilibrium equations $(1)_1$ has to be satisfied at the same time with the criticality condition $(1)_2$, which states the zero stiffness in the direction of the critical eigenmode ϕ. Such a system is considered in Refs.[3,13,5].

The equilibrium equation $(1)_1$ constitutes the balance of internal forces $\mathbf{r}$ and external loads $\mathbf{p}$, which is usually parametrized by a single variable λ, the load parameter, defining the intensity of the load vector:

$$\mathbf{f}(\mathbf{q},\lambda) \equiv \mathbf{r}(\mathbf{q}) - \lambda \mathbf{p}_{\mathrm{r}}(\mathbf{q}). \tag{2}$$

If the loads does not dependent on deformations, like in dead-weight loading, the reference load vector $\mathbf{p}_{\mathrm{r}}$ is independent of the displacement field $\mathbf{q}$.

The system (1) consists of $2n+1$ unknowns, the displacement vector $\mathbf{q}$, the eigenmode $\boldsymbol{\phi}$ and the load parameter value λ at the critical state. Since the eigenvector $\boldsymbol{\phi}$ is defined uniquely up to a constant, the normalizing condition can be added to the system (1). In addition some stabilizing conditions might also be needed. In general, the full augmented system can be written as

$$\mathbf{g}(\mathbf{q},\boldsymbol{\phi},\boldsymbol{\lambda}) = \left\{ \begin{array}{l} \hat{\mathbf{f}}(\mathbf{q},\boldsymbol{\lambda}) \equiv \mathbf{f}(\mathbf{q},\lambda) + \mathbf{f}_0(\mathbf{q},\boldsymbol{\lambda}) = \mathbf{0} \\ \mathbf{h}(\mathbf{q},\boldsymbol{\phi},\boldsymbol{\lambda}) \equiv \mathbf{f}'(\mathbf{q},\boldsymbol{\lambda})\boldsymbol{\phi} + \mathbf{h}_0(\boldsymbol{\phi},\boldsymbol{\lambda}) = \mathbf{0} \\ \mathbf{c}(\mathbf{q},\boldsymbol{\phi},\boldsymbol{\lambda}) = \mathbf{0}, \end{array} \right. \tag{3}$$

where $\boldsymbol{\lambda}$ is a vector of control and auxiliary parameters and $\mathbf{c}$ is a vector of constraint or stabilizing equations, dimension of these vectors is $p \geq 1$. The additional functions $\mathbf{f}_0$ and $\mathbf{h}_0$ are chosen such that $\mathbf{f}_0 = \mathbf{h}_0 = \mathbf{0}$ at the solution point. The Newton step can be written as

$$\left[\begin{array}{ccc} \mathbf{K}_f & \mathbf{0} & \mathbf{P} \\ \mathbf{Z} & \mathbf{K}_h & \mathbf{N} \\ \mathbf{C}_q & \mathbf{C}_\phi & \mathbf{C}_\lambda \end{array} \right] \left\{ \begin{array}{c} \delta\mathbf{q} \\ \delta\boldsymbol{\phi} \\ \delta\boldsymbol{\lambda} \end{array} \right\} = - \left\{ \begin{array}{c} \hat{\mathbf{f}} \\ \mathbf{h} \\ \mathbf{c} \end{array} \right\}, \tag{4}$$

where

$$\mathbf{Z} = \left[\mathbf{f}'\boldsymbol{\phi}\right]', \quad \mathbf{C}_q = \mathbf{c}' = \frac{\partial \mathbf{c}}{\partial \mathbf{q}}, \quad \mathbf{C}_\phi = \frac{\partial \mathbf{c}}{\partial \boldsymbol{\phi}}, \quad \mathbf{C}_\lambda = \frac{\partial \mathbf{c}}{\partial \boldsymbol{\lambda}}. \tag{5}$$

$$\mathbf{K}_f = \mathbf{K} + \mathbf{f}_0', \quad \mathbf{K}_h = \mathbf{K} + \frac{\partial \mathbf{h}_0}{\partial \boldsymbol{\phi}}, \quad \mathbf{P} = \frac{\partial \mathbf{f}}{\partial \boldsymbol{\lambda}} \quad \text{and} \quad \mathbf{N} = \frac{\partial \mathbf{h}}{\partial \boldsymbol{\lambda}} \tag{6}$$

Computation of the matrix $\mathbf{Z}$ requires second order derivatives of the residual. In the literature these are usually obtained by numerical differentiation. For the geometrically exact Reissner's beam model analytical derivation of the $\mathbf{Z}$-matrix is given in[14].

If the system (4) is solved by using a direct solver, the block elimination scheme is a feasible choice. Partitioning the iterative steps $\delta\mathbf{q}$ and $\delta\boldsymbol{\phi}$ as

$$\delta\mathbf{q} = \mathbf{q}_f + \mathbf{Q}_p\delta\boldsymbol{\lambda}, \quad \delta\boldsymbol{\phi} = \boldsymbol{\phi}_h + \boldsymbol{\Phi}_n\delta\boldsymbol{\lambda}, \tag{7}$$

where the vectors $\mathbf{q}_f, \boldsymbol{\phi}_h$ and the $n \times p$ matrices $\mathbf{Q}_p, \boldsymbol{\Phi}_n$ can be solved from equations

$$\mathbf{K}_f\mathbf{q}_f = -\hat{\mathbf{f}}, \qquad \mathbf{K}_f\mathbf{Q}_p = -\mathbf{P}, \tag{8}$$

$$\mathbf{K}_h\boldsymbol{\phi}_h = -\mathbf{h} - \mathbf{Z}\mathbf{q}_\mathrm{f}, \qquad \mathbf{K}_h\boldsymbol{\Phi}_n = -\mathbf{N} - \mathbf{Z}\mathbf{Q}_p. \tag{9}$$

The iterative change of the control parameters can be solved from the constraint conditions resulting in

$$\delta\boldsymbol{\lambda} = -(\mathbf{C}_\lambda + \mathbf{C}_q\mathbf{Q}_p + \mathbf{C}_\phi\boldsymbol{\Phi}_n)^{-1}(\mathbf{c} + \mathbf{C}_q\mathbf{q}_f + \mathbf{C}_\phi\boldsymbol{\phi}_h). \tag{10}$$

The specific choice by Wriggers and Simo[5] yields $\mathbf{K}_h = \mathbf{K}_f$, which is computationally very attractive. Solution of the augmented system (4) by the block elimination method requires factorization of one matrix of order n, reductions and backsubstitutions of $2(1+p)$ r.h.s.-vectors. An alternative procedure suitable for the use of preconditioned iterative linear solvers is presented in[15].

For the eigenvector normalization the following constraints can be used:

$$\|\boldsymbol{\phi}\|^2 - 1 = 0, \tag{11}$$

$$\lambda\|\boldsymbol{\phi}\|^2 - 1 = 0, \tag{12}$$

$$\mathbf{e}_i^\mathrm{T}\boldsymbol{\phi} - 1 = 0, \tag{13}$$

$$\lambda(\mathbf{e}_i^\mathrm{T}\boldsymbol{\phi})^2 - 1 = 0, \tag{14}$$

where $\mathbf{e}_i$ is a unit vector having the element 1 at i:th component. The constraint (13) is used by Wriggers and Simo[5]. Constraints (12) and (14) guarantees that the iteration will converge to a solution with a positive critical value of the load parameter λ. A proper scaling of the constraint equation is also important. For the constraint equation (12) the best numerical performance is obtained when the initial scaling of the eigenvector approximation is of order $\|\boldsymbol{\phi}\| \sim \lambda_\mathrm{cr}^{-1}$. Numerical experiments indidate that the constraint (12) results in slightly more efficient scheme than (11).

REFERENCES

[1] Keener, J. & Keller, H. Perturbed bifurcation theory. *Archive for Rational Mechanics and Analysis* **50**, 159–175 (1973).

[2] Keener, J. Perturbed bifurcation theory at multiple eigenvalues. *Archive for Rational Mechanics and Analysis* **56**, 348–366 (1974).

[3] Seydel, R. Numerical computation of branch points in nonlinear equations. *Numerische Mathematik* **33**, 339–352 (1979).

[4] Wriggers, P., Wagner, W. & Miehe, C. A quadratically convergent procedure for the calculation of stability points in finite element analysis. *Computer Methods in Applied Mechanics and Engineering* **70**, 329–347 (1988).

[5] Wriggers, P. & Simo, J. A general procedure for the direct computation of turning and bifurcation problems. *International Journal for Numerical Methods in Engineering* **30**, 155–176 (1990).

[6] Abbot, J. An efficient algorithm for the determination of certain bifurcation points. *Journal Computational and Applied Mathematics* **4**, 19–27 (1987).

[7] Battini, J.-M., Pacoste, C. & Eriksson, A. Improved minimal augmentation procedure for the direct computation of critical points. *Computer Methods in Applied Mechanics and Engineering* **192**, 2169–2185 (2003).

[8] Huitfeldt, J. & Ruhe, A. A new algorithm for numerical path following applied to an example from hydrodynamic flow. *SIAM Journal on Scientific and Statistical Computing* **11**, 1181–1192 (1990).

[9] Huitfeldt, J. Nonlinear eigenvalue problems - prediction of bifurcation points and branch switching. Tech. Rep. 17, Department of Computer Sciences, Chalmers University of technology (1991).

[10] Cardona, A. & Huespe, A. Evaluation of simple bifurcation points and post-critical path in large finite rotation problems. *Computer Methods in Applied Mechanics and Engineering* **175**, 137–156 (1999).

[11] Ibrahimbegović, A. & Mikdad, M. A. Quadratically convergent direct calculation of critical points for 3d structures undergoing finite rotations. *Computer Methods in Applied Mechanics and Engineering* **189**, 107–120 (2000).

[12] Mäkinen, J. Total Lagrangian Reissner's geometrically exact beam element without singularities. *International Journal for Numerical Methods in Engineering* **70**, 1009–1048 (2007).

[13] Werner, B. & Spence, A. The computation of symmetry-breaking bifurcation points. *SIAM Journal on Numerical Analysis* **21**, 388–399 (1984).

[14] Mäkinen, J., Kouhia, R., Fedoroff, A. & Marjamäki, H. Direct computation of critical equilibrium states for spatial beams and frames. In preparation.

[15] Mäkinen, J., Kouhia, R., Fedoroff, A. & Marjamäki, H. Implementation of a direct procedure for critical point computations (2010). Paper presented at the Tenth International Conference on Computational Structures Technology, Valencia, Spain, 14-17 September, 2010.

23rd Nordic Seminar on Computational Mechanics
NSCM-23
A. Eriksson and G. Tibert (Eds)

ON LATERAL BUCKLING OF ARMOUR WIRES IN FLEXIBLE PIPES

NIELS H. ØSTERGAARD*, ANDERS LYCKEGAARD AND JENS H. ANDREASEN

*Department of Mechanical Engineering / NKT-Flexibles
Aalborg University, Aalborg, Denmark
e-mail: Niels.HojenOstergaard@nktflexibles.com

Key words: mechanics of flexible pipes, buckling of armour wires

Summary. This paper introduces the concept of lateral buckling of the armour tendons of flexible pipes. A model for prediction of the equilibrium state of a single tensile armour wire embedded in a surface subjected to bending and axial loadings is presented as basis for a global pipe analysis.

1 INTRODUCTION

Flexible riser pipes are widely used in the offshore industry for extraction of oil or gas from subsea reservoirs at large water depths. In order to obtain a structural design capable of resisting external and internal pressure, axial loads and large deflections, flexible pipes are constructed as composite structures comprised by a number of different layers, usually of steel and polymer materials. Due to the extreme loadings, which flexible pipes may be exposed to at large water depths, numerous failure modes are identified and can be predicted by engineering analysis. A number of failure modes are, however, still subject of academic and industrial research, since computational models for prediction have not yet been developed. Among those are buckling of the tensile armour layers, which are comprised by two layers of helically wound steel wires. This specific failure mode has been observed during installation of flexible pipes in ultra deep waters. In the installation scenario, flexible pipes are exposed to axial compression due to hydrostatic pressure, since the pipe is empty, and repeated bending cycles due to vessel movements, waves and current. The failure mode is characterized by very large lateral deflections of the armour wires, see figure 1. Though the failure mechanism cannot be predicted, it is possible to reproduce by laboratory experiments, see [1]. In order to obtain a model capable of predicting the lateral buckling failure mode, the mechanics of a single tensile armour wire must be analyzed, before a global model can be formulated. The single wire model will be based on equilibrium of curved beams, see [2] and [3] and differential geometry of curves on surfaces, see [4] and [5].

2 METHODS

The analysis of a single tensile armour wire will be carried out considering a helically wound rod on a cylindrical surface, which is deformed into a torus. This corresponds to that the flexible pipe is bent to a constant radius of curvature, $R = \frac{1}{\kappa}$, see figure 2. The underlying surface will

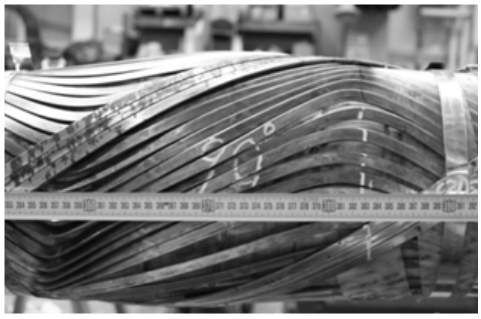

Figure 1: Lateral buckling of armour wires

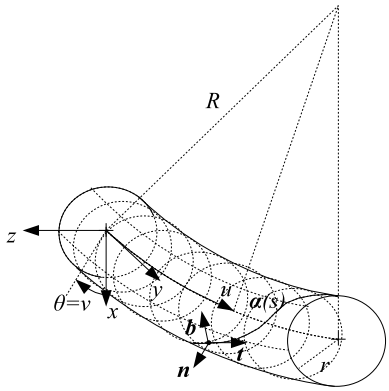

Figure 2: Tensile armour wire on torus surface

be considered frictionless since the analysis aims to determine the wire equilibrium limit state corresponding to an infinite number of bending cycles having been applied to the pipe. While the curvature components of a single tensile armour wire in the analysis are allowed to be large, the axial strain of the wire is assumed sufficiently small to determine using Cauchy's definition of strain. It will furthermore be assumed that the curvature components can be determined on basis of the geometry of an inextensible curve due to small axial strains. A torus surface can be defined as

$$\mathbf{x}(u,v) = \begin{bmatrix} \left(\frac{1}{\kappa} + r \cdot cosv\right) cos(\kappa u) - \frac{1}{\kappa} \\ \left(\frac{1}{\kappa} + r \cdot cosv\right) sin(\kappa u) \\ r \cdot sinv \end{bmatrix} \tag{1}$$

on which a curve is constructed by defining a relation between the u, v-coordinates. Assuming that a curve $\boldsymbol{\alpha}(s)$ is defined and parametrized by arclength s, a curvilinear coordinate triad of unit length can be attached to the curve, see figure 2. The triad vectors are given by

$$\mathbf{t} = \frac{d\boldsymbol{\alpha}}{ds} \qquad \mathbf{n} = \frac{\mathbf{x}_u \times \mathbf{x}_v}{\|\mathbf{x}_u \times \mathbf{x}_v\|} \qquad \mathbf{b} = \mathbf{t} \times \mathbf{n} \tag{2}$$

in which $\mathbf{x_u} = \frac{\partial \mathbf{x}}{\partial u}$ and $\mathbf{x_v} = \frac{\partial \mathbf{x}}{\partial v}$. The triad vectors and their first order derivatives in arclength can now be related by the normal curvature κ_n, geodesic curvature κ_g and torsion τ of the wire

$$\frac{d}{ds}\begin{bmatrix} \mathbf{t} \\ \mathbf{n} \\ \mathbf{b} \end{bmatrix} = \begin{bmatrix} 0 & \kappa_n & -\kappa_g \\ -\kappa_n & 0 & \tau \\ \kappa_g & -\tau & 0 \end{bmatrix} \begin{bmatrix} \mathbf{t} \\ \mathbf{n} \\ \mathbf{b} \end{bmatrix} \tag{3}$$

A tangent to the wire can alternatively be defined as a linear combination of the normed surface derivatives with respect to the torus coordinates. In order for this to be consistent with the definition given in equation 2, the following equations governing the tangent geometry must hold

$$\frac{du}{ds} = (1+\epsilon)\frac{cos\phi}{\|\mathbf{x}_u\|} \qquad \frac{dv}{ds} = (1+\epsilon)\frac{cos\phi}{\|\mathbf{x}_v\|} \tag{4}$$

in which the tangent vector can be observed to be subject of a small deformation due to axial strains. The curvature components can now, on basis of definitions given in [4] and [5] be defined

as

$$\kappa_n = -\frac{\kappa cosv}{1 + r\kappa cosv} cos^2\phi - \frac{1}{r} sin^2\phi \tag{5}$$

$$\kappa_g = \left(\frac{\kappa sinv}{1 + r\kappa cosv} cos\phi + \frac{d\phi}{ds} \right) \tag{6}$$

$$\tau = \left(\frac{\kappa cosv}{1 + r\kappa cosv} - \frac{1}{r} \right) cos\phi sin\phi \tag{7}$$

in which ϕ denotes the angle between $\mathbf{x}_u$ and $\boldsymbol{\alpha}'(s)$. The derived expressions can be shown to be consistent with the definition given in equation 3. Vectorial equations of equilibrium for a curved rod can be derived by considering a curved beam segment of infinitesimal length, see [2] and [3]. Applying equation 3, the vector equlibrium equations can be written on component form

$$\frac{dP_t}{ds} - \kappa_n P_n + \kappa_g P_b + p_t = 0 \qquad \frac{dP_n}{ds} + \kappa_n P_t - \tau P_b + p_n = 0 \tag{8}$$

$$\frac{dP_b}{ds} - \kappa_g P_t + \tau P_n + p_b = 0 \qquad \frac{dM_t}{ds} - \kappa_n M_n + \kappa_g M_b + m_t = 0 \tag{9}$$

$$\frac{dM_n}{ds} + \kappa_n M_t - \tau M_b - P_b + m_n = 0 \qquad \frac{dM_b}{ds} - \kappa_g M_t + \tau M_n + P_N + m_b = 0 \tag{10}$$

The constitutive relations, linking sectional moments to changes of curvature and sectional axial force to axial strain, will be assumed linear. This is reasonable since the wire dimensions are small compared to both major and minor radius of the torus. A system of field equations can now be derived. Since the torus surface is considered frictionless, the distributed loads on a wire in the tangent plane and the distributed moments in the normal and binormal directions are neglected, hence, $p_t = p_b = 0$ and $m_n = m_b = 0$. Now considering the tangent geometry in equation 4, the definition of the geodesic curvature in equation 6, the tangential and binormal force equilibrium and the normal moment equilibrium in equation 8, a consistent sixth order system of differential equations in u, v, ϕ, P_t, P_b and M_n is obtained in which P_n can be determined by analytical means.

3 RESULTS

Applying boundary conditions corresponding to prescribed displacements and rotations in accordance with the physical system being modeled, the system of equations can be solved using a commercially available solver. Initially, by redefining the angular torus coordinate v as an arclength-coordinate $w = vr$, and setting $r = R = \infty$, a straight simply supported beam can be modeled in the plane. In order to construct a test case for the algorithm, it will be examined if the Euler-load can be predicted. Adding an imperfection representing the first mode of buckling directly to the geodesic curvature and applying compression in steps, the system can be solved.

$$\kappa_g = \frac{M_n}{EI_n} + \gamma_{amp} \cdot sin\left(\frac{\pi x}{L}\right) \tag{11}$$

Setting $\gamma_{amp} = 0.001m^{-1}$, the displacement of the beam midpoint and the applied force can in figure 3 be observed to exhibit the expected physical behavior corresponding to softening approaching the buckling load $P_E = \frac{\pi^2 EI}{L^2}$. Now a pipe with bending radius $R = 10m$ and a

pipe strain $\frac{\Delta L}{L} = -0.001$ applied in steps to a $3 \times 10mm$ steel wire with 5 pitches of length $L_{pitch} = 1.263m$, and with pipe radius $r = 0.1006m$ is considered. The axial force in the loaded end of the pipe is given by

$$P_u = P_t cos\phi + P_b sin\phi \tag{12}$$

With no applied imperfection the relation between axial loads and pipe strain presented in figure 4 obtained by solving the equations exhibit significant softening behavior.

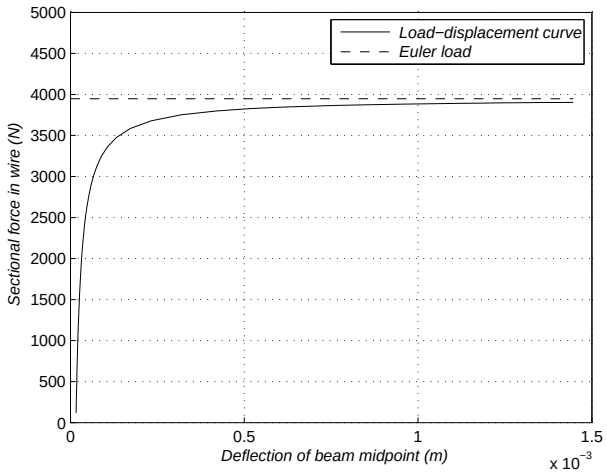

Figure 3: $(\frac{\Delta L}{L}, P_u)$-curve for simply supported beam

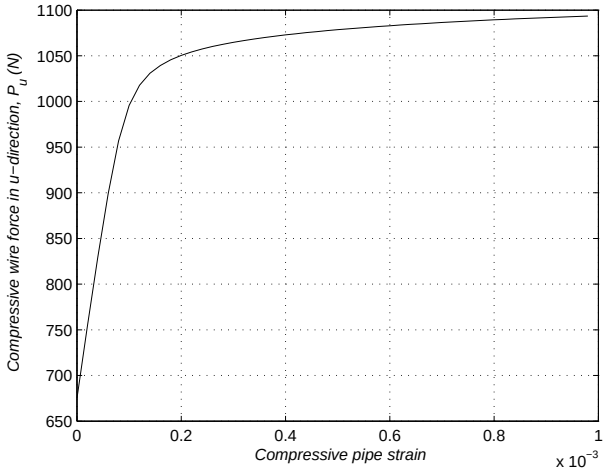

Figure 4: $(\frac{\Delta L}{L}, P_u)$-curve for wire

4 CONCLUSIONS

A computational model capable of predicting the equilibrium state of a helically wound wire on a cylindrical surface subjected to bending and axial loads has been presented. The model may serve as basis for further studies leading to an algorithm which can predict the limit load of an entire flexible pipe structure. A global model can be validated against lateral buckling laboratory experiments and may serve as an engineering tool for flexible pipe design.

REFERENCES

[1] M.P. Braga, P. Kaleff. Flexible pipe sensitivity to birdcaging and armor wire lateral buckling. *Proceedings of OMAE*, 2004.

[2] A.E.H. Love. A treatise on the Mathematical Theory of Elasticity. *Dover Publications, Inc., N.Y,* 1944.

[3] E. Reissner. On finite deformations of space-curved beams. *Journal of Applied Mathematics and Physics (ZAMP)*, Vol. 32, 1981.

[4] M P. do Carmo. Differential Geometry of Curves and Surfaces Prentice Hall, 2008.

[5] J. Oprea. Differential Geometry and its Applications Prentice Hall, 1997.

23rd Nordic Seminar on Computational Mechanics
NSCM-23
A. Eriksson and G. Tibert (Eds)

STRESS INTENSITY FACTORS FOR BOLT FIXED LAMINATED GLASS

MARIA FRÖLING AND KENT PERSSON

Dept. of Construction Sciences
Lund University
P.O. Box 118, SE-221 00 Lund, Sweden
e-mail: maria.froling@construction.lth.se
e-mail: kent.persson@construction.lth.se
Web page: http://www.byggvetenskaper.lth.se

Key words: Stress Intensity Factor, Laminated Glass, Bolt Fixing.

Summary. A method for determining stress intensity factors for bolt fixed laminated glass balustrades is suggested. With the aid of a graphical representation of the stress intensity factors, the maximum principal stresses of the structure could be determined.

1 INTRODUCTION

It is becoming increasingly common to use glass as a structural material. When constructing with bolt fixed laminated glass, there are few methods and guidelines on how to perform stress predictions. Current methods on stress predictions mainly involve guidelines for finite element analyses, which requires decent knowledge of the finite element method. In this work, a method for determining stress intensity factors for stress prediction of laminated glass balustrades with 2 + 2 bolt fixings with non-fixed positions is developed. When developing the method, finite element simulations are made. The simulations are based on previous work by the authors [2,3].

2 PRINCIPAL STRESSES FOR A LAMINATED GLASS BALUSTRADE WITHOUT HOLES

In this work, a method for determining the stress intensity factors, α, for bolt fixed laminated glass balustrades is developed. α relates the nominal stress value, σ_{Nom}, to the maximum (positive) principal stress value, σ, as $\sigma = \alpha\sigma_{Nom}$. σ_{Nom} is defined as the maximum (positive) principal stress for the case of a laminated glass structure of the same dimensions as the balustrade, but without holes. The boundary conditions as well as the load are symmetric, which means that the balustrade without holes can be modelled as a simply supported beam that is subjected to a bending moment. The maximum principal stresses could thus be determined analytically [1]. Figure 1 shows the geometry of the beam model applied to the balustrade consisting of two layers of glass with a PVB interlayer.

The load is a uniformly distributed line load, P, applied at the top of the balustrade in the direction normal to the glass pane. Multiplying the line load with the width, w, of the glass pane gives the total load, P_{Tot}.

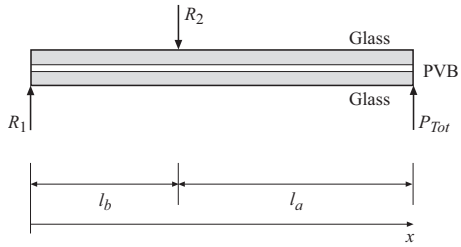

Figure 1: Geometry of beam model

In the work of Carrick and Vasur[1], a differential equation that governs the behavior of the laminated beam problem is derived

$$\frac{d^2}{dx^2}N(x) - c_2 N(x) = c_1 M_{Ext}(x), \tag{1}$$

where $N(x)$ is the normal force in the upper glass ply and $M_{Ext}(x)$ is the external moment .

$$c_1 = k_{PVB}\frac{h_t}{E_g I_1 + E_g I_2}, c_2 = k_{PVB}(\frac{1}{E_g A_1} + \frac{1}{E_g A_2} + \frac{h_t^2}{E_g I_1 + E_g I_2}), \tag{2}$$

where

$$k_{PVB} = \frac{G_{PVB} w}{t_{PVB}}, h_t = t_g/2 + t_g/2. \tag{3}$$

E_g is the elastic modulus of glass, (I_1, I_2) are the moments of inertia of cross sections of the upper and lower glass panes respectively, (A_1, A_2) are the cross section areas of the upper and lower glass panes, G_{PVB} is the shear modulus of PVB, t_{PVB} is the thickness of the PVB layer and t_g is the glass pane thickness. The glass panes have equal cross section geometries, and thus $I_1 = I_2 = I$ and $A_1 = A_2 = A$ are used in the following. The total solution to (1), invoking the appropriate boundary conditions[1], is given by

$$N(x) = \frac{c_1 R_2 l_a}{c_2\sqrt{c_2}(l_a + l_b)\cosh(\sqrt{c_2}l_b)}\sinh(\sqrt{c_2}x) - \frac{c_1 R_2 l_a x}{c_2(l_a + l_b)}. \tag{4}$$

In Carrick and Vasur[1], it is shown that the following relations holds for this case

$$M(x) \equiv M_1(x) = M_2(x) = \frac{1}{2}(M_{Ext}(x) + h_t N(x)). \tag{5}$$

From Navier's formula, the normal stresses in the x-direction of one glass pane can be computed. The maximum tensile stress occurs at the lower edge of the laminate. The tensile stresses at the lower edge of the laminate are equal to the maximum (positive) principal stresses, and thus equal to σ_{Nom} (evaluated at the location $x = l_b$). Thus,

$$\sigma_{Nom} = \frac{M(l_b)}{\frac{w t_g^2}{6}} - \frac{N(l_b)}{w t_g}. \tag{6}$$

Note that equation (6) is valid for glass panes with rectangular cross sections only and the equation is only valid on the interval $0 \leq x \leq l_b$.

3 STRESS INTENSITY FACTORS FOR A BOLT FIXED BALUSTRADE

When σ_{Nom} has been determined, the case of a balustrade with bolt fixings can be considered. It remains to find the stress intensity factor, α. Finite element simulations are used in order to determine σ and thus α may be determined. α is represented graphically in design charts for all relevant combinations of the geometry parameters. The in-plane geometry of the balustrade is displayed in Figure 2. The bore hole has the diameter d_h and the bolt head has the diameter d_b. The height of the balustrade, l_a, and the vertical position of the bolts, l_c, are set to fixed values. A standard value is used for t_{PVB}. In the finite element model, only the EPDM bush between the bolt head and the glass pane is included and its thickness is denoted t_{EPDM}. Table 1 summarizes the relevant geometry parameters and states whether the parameters are fixed or variable.

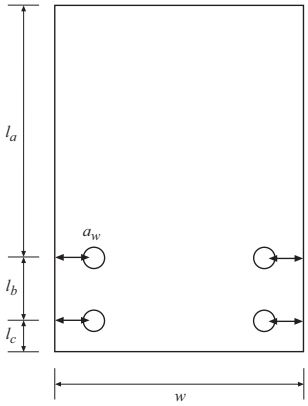

Figure 2: Geometry of balustrade

Fixed parameters	Variable parameters
$l_a = 1.25$ m	$l_b = [0.2, 0.4, 0.8]$ m
$l_c = 0.24$ m	$a_w = [0.1 : 0.025 : w/2 - 0.1]$ m
$t_{PVB} = 0.76$ mm	$w = [0.9 : 0.3 : 2.7]$ m
$t_{EPDM} = 3$ mm	$d_h = [15 : 5 : 40]$ mm
	$t_g = [6, 8, 10, 12]$ mm
	$d_b = 60$ mm

Table 1: List of geometry parameters

The material parameters used are $E_g = 78$ GPa, $\nu_g = 0.3$, $E_{PVB} = 6$ MPa, $\nu_{PVB} = 0.43$, $E_{EPDM} = 20$ MPa, and $\nu_{EPDM} = 0.45$.

4 DESIGN CHARTS FOR DETERMINATION OF STRESS INTENSITY FACTORS

One design chart is made for each possible combination of [t_g, w, d_b, d_h]. As an example, the design chart for the parameter combination [$t_g = 6$ mm, $w = 0.9$ m, $d_b = 60$ mm, $d_h = 15$ mm] is shown in Figure 3.

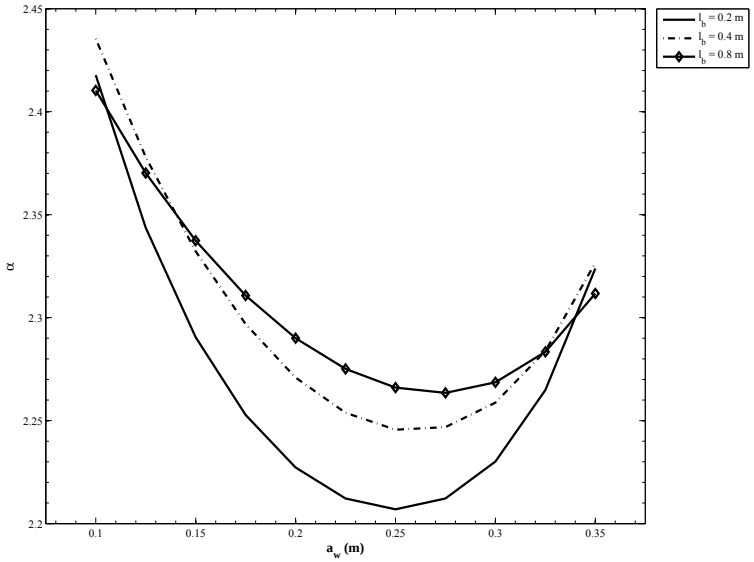

Figure 3: Example of design chart for $t_g = 6$ mm, $w = 0.9$ m, $d_b = 60$ mm and $d_h = 15$ mm

Given that the corresponding value of σ_{Nom} has been determined, σ can be computed and used in the design process.

5 CONCLUSIONS

A method for determining stress intensity factors for two ply laminated glass balustrades with $2 + 2$ bolt fixings has been developed. With the use of the stress intensity factors, maximum principal stresses of the balustrade can be determined without using advanced mathematics or finite element analysis.

REFERENCES

[1] Carrick, C. and Vasur, J. Styvhet och Hållfasthet hos Laminerat Glas. Masters thesis, Royal Institute of Technology, 2002.

[2] Fröling, M. and Persson, K. Application of Solid-shell Elements to Laminated Glass. Proceedings of the 22nd Nordic Seminar on Computational Mechanics, Aalborg, Denmark, 2009.

[3] Fröling, M. and Persson, K. Application of Solid-shell Elements to Laminated Glass Structures. Proceedings of the XXIV A.T.I.V. Conference/59th NGF Annual Meeting, Parma, Italy, 2009.

23rd Nordic Seminar on Computational Mechanics
NSCM-23
A. Eriksson and G. Tibert (Eds)

COMPUTATION OF PARTICLE-LADEN TURBULENT FLOWS

HELGE I. ANDERSSON[*] AND LIHAO ZHAO[*]

[*] Division of Fluids Engineering
Department of Energy and Process Engineering
The Norwegian University of Science and Technology (NTNU)
N-7491 Trondheim, Norway
e-mail: helge.i.andersson@ntnu.no; lihao.zhao@ntnu.no

Key w ords: Particle Dynamics, Turbulence Modulation, Multiphase Flow, Chemical Engineering.

Summary. This paper aims to outline the mixed Eulerian-Lagrangian approach to simulations of dilute suspensions of spherical particles in turbulent fluid flows. An extension to non-spherical particles will also be discussed. Both one-way coupled and two-way coupling schemes will be addressed. Examples from ongoing research work at NTNU will be given.

1 INTRODUCTION

Dilute suspensions of solid particles in a turbulent gas or liquid flow offer problems of greater complexity than mono-phase turbulence, but are nevertheless of immense practical concern both in natural flows and in industry. The vast majority of investigations have naturally focused on the behaviour of *spherical* particles in a fluid flow and occasionally also on how the flow field is affected by the presence of the particles. The recent review article by Balachandar and Eaton[1] provides a useful introduction to the state-of-the-art in this vast area of research.

The particle-laden flows considered are either homogenous in space or of the shear-flow type like in boundary layers, channels and pipes. In the majority of applications, the fluid flow is turbulent and therefore inherently unsteady and three-dimensional. If the suspension is sufficiently dilute, the carrier fluid is unaffected by the presence of the particles and the focus is on the translational motion of the particles. It is known beyond any doubt[1] that spherical particles tend to concentrate in the near-wall region of a wall-bounded shear flow and furthermore that the particles are not evenly distributed but rather accumulate in preferred areas. For somewhat larger particle concentrations, the fluid flow is influenced by the solid particles embedded in the flow field. The current understanding of such particle-fluid interactions was summarized by Soldati[2].

Suspensions of *non-spherical* particles are also encountered in practice, for instance in the fields of aerosol science, phytoplankton dynamics, dispersion of carbon nano-tubes (CNTs), and transport of cellulose fibers in the pulp and paper industry. As far as the dynamics of non-spherical particles is of concern, not only their translational motion is of importance, but their rotational motion and their orientation become essential.

2 COMPUTATIONAL MODELLING APPROACH

A variety of different approaches have been taken to numerically simulate suspensions of solid particles in a fluid flow. Each approach has its own advantages and limitations. Here, we follow the mixed Eulerian-Lagrangian approach. Both the particle dynamics and the fluid motion are governed by the fundamental laws of mechanics and the modeling is therefore in accordance with so-called '*first principles*'.

2.1 Eulerian representation of the flow field

Since we are concerned with turbulent flow fields, the fluid motion is governed by the full Navier-Stokes equation. As long as the Reynolds number is not too high, the discretized Navier-Stokes equation is integrated on a three-dimensional mesh and in time. It is essential that the mesh sizes do not exceed the size of the smallest turbulent eddies, i.e. the Kolmogorov scales, since no turbulence models are to be used. Such direct numerical simulations (DNSs) are considered as true realizations of turbulent flow fields and serve as reliable computer experiments.

2.2 Lagrangian particle dynamics

The motion of the particles is governed by the Lagrangian equation of motion:

$$m d\boldsymbol{v}/dt = \mu K(\boldsymbol{u}-\boldsymbol{v}). \tag{1}$$

Here, $\boldsymbol{v}$ and $\boldsymbol{u}$ denote the velocity vector of the particle and the fluid, respectively. The physical quantities involved are the particle mass m, the fluid viscosity μ and the resistance parameter K. Assuming that the particle Reynolds number based on the particle diameter $2a$ and the slip velocity $|\boldsymbol{u} - \boldsymbol{v}|$ is smaller than unity only Stokes drag is taken into account. For spherical particles these three quantities combine into the particle response time:

$$\tau = m/\mu K = 2\rho D a^2/9\mu \tag{2}$$

where D is the ratio between particle and fluid densities.

3 COUPLING BETWEEN PARTICLES AND FLUID

The presence of solid particles in a turbulent flow is known to affect the flow field. A point force from each and every particle in accordance with Newton's third law is added to the Navier-Stokes equation which governs the fluid flow. In such *two-way coupled* simulations the amount of feedback from the particles on the carrier fluid depends on the particle size, shape and concentration. Recent two-way coupled simulations of spherical particles in turbulent channel flow by Zhao et al.[3] showed pronounced turbulence modulations accompanied by a significant drag reduction. Figure 1 shows the uneven distribution of spherical particles in a turbulent channel flow obtained in a two-way coupled simulation.

4 NON-SPHERICAL PARTICLES

If non-spherical rather than spherical particles are considered, the Lagrangian equation of translational motion is still valid but the resistance parameter K in eq. (1) is then a tensor rather than a scalar. The particle response time τ in eq. (2) is no longer dependent only on the

particle radius a but also on the particle aspect ratio λ.

Even more important is the fact that the rotational motion becomes of major concern and determines, for instance, the instantaneous orientation of a given particle relative to the primary flow direction. The rotational motion of a solid particle is given, for instance, by

$$I_{xx}\, d\omega_x/dt - \omega_y\omega_z\,(I_{yy} - I_{zz}) = N_x. \tag{3}$$

Here, ω_x is the x-component of the angular velocity of a particle with principle moments of inertia I_{xx}, I_{yy}, and I_{zz}. N_x is the x-component of the torque on the particle and involves the spin of the particle relative to the fluid vorticity. The equations of translational and rotational particle motion (1) and (3) are integrated forward in time in a reference frame attached to the particle whereas the Navier-Stokes equation for the fluid flow is solved in a fixed frame of reference; see Zhang et al.[4] Three independent Euler angles specify the transformation between these two coordinate systems. In practice, however, we adopted the four Euler parameters (*quaternions*) instead of the Euler angles. We first used this approach to study the spin of spherical particles and observed that the particle spin deviated from the fluid vorticity (Mortensen et al.[5])

As a protype model of a non-spherical particle we consider a *spheroid* which is characterized not only by the equatorial radius a but also by its aspect ratio λ. Results from one-way coupled turbulent channel flow simulations of prolate spheroids with some different aspect ratios and particle response times were presented by Mortensen et al.[6, 7] Figure 2 gives a first impression of the different orientations of prolate spheroids in a turbulent flow field.

5 CLOSING REMARKS

Our current investigations are proceeding along two different paths. We are continuing our investigations of two-way coupled simulations of spherical particles with the view to explore how the turbulence modulation is affected by the particle response time and the particle loading. In this context the energy exchange between the fluid and the particles is investigated by means of conditional averages. In parallel two-way coupled simulations of non-spherical particles are underway. For that purpose a novel method to account for torque-coupling between the fluid and the particles is explored.

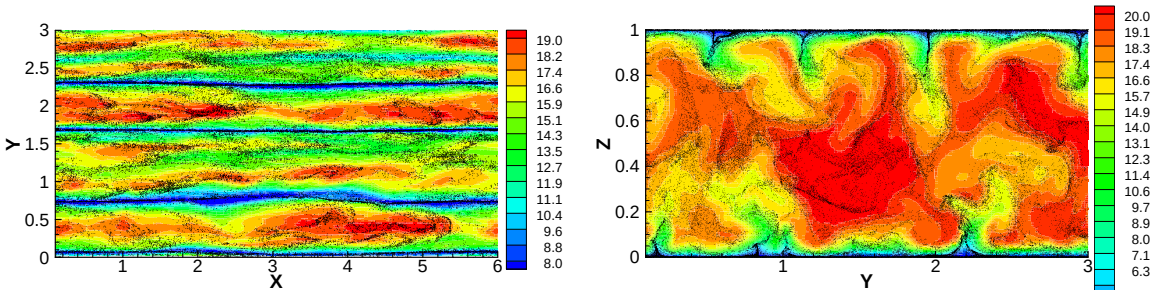

Figure 1: Contours of the streamwise velocity component in a wall-parallel X-Y plane (left) and a cross-sectional Y-Z plane (right). The black dots represent the instantaneous particle positions.

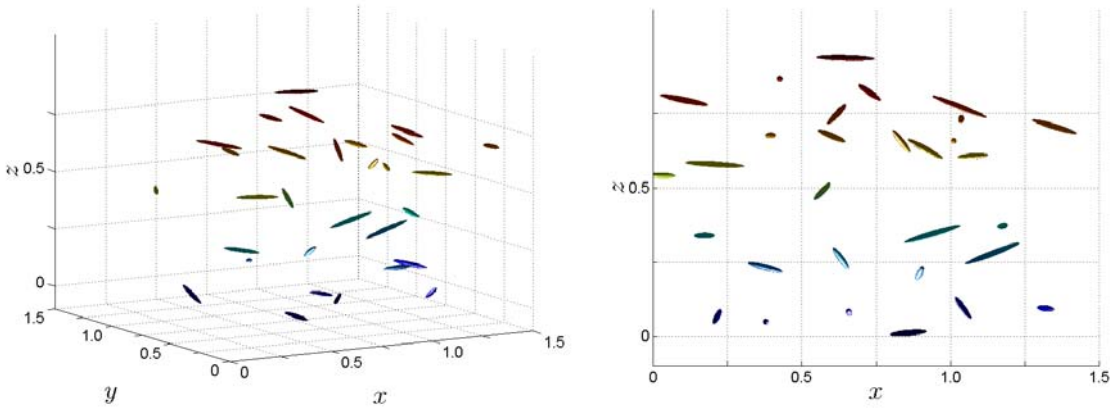

Figure 2: Instantaneous orientation of non-spherical particles in a turbulent channel flow. The orientation of the prolate spheroids varies in time and with position. A perspective view is shown to the left and a planar view to the right. Statistics of the particle orientations are deduced from the instantaneous orientations.

ACKNOWLEDGEMENTS

This work is currently funded by The Research Council of Norway (NFR) and A/S Norske Shell. Computing time on the 'Stallo' compute cluster HP BL 460c in Tromsø is granted by NFR (Programme for Supercomputing). The collaboration with Prof. B.J. Boersma and Dr. J.J.J. Gillissen (TU Delft) is greatly appreciated.

REFERENCES

[1] S. Balachandar and J.K. Eaton, "Turbulent dispersed multiphase flow", *Annu. Rev. Fluid Mech.*, **42**, 111-133 (2010).

[2] A. Soldati, "Particles turbulence interactions in boundary layers", *Z. Angew. Math. Mech.,* **85**, 683-699 (2005).

[3] L.H. Zhao, H.I. Andersson and J.J.J. Gillissen, "Turbulence modulation and drag reduction by spherical particles", *Phys. Fluids*, **22**, 081702 (2010).

[4] H. Zhang, G. Ahmadi, F.G. Fan and J.B. McLaughlin, "Ellipsoidal particle transport and deposition in turbulent channel flows", *Int. J. Multiphase Flow*, **27**, 971-1009 (2001).

[5] P.H. Mortensen, H.I. Andersson, J.J.J. Gillissen and B.J. Boersma, "Particle spin in a turbulent shear flow", *Phys. Fluids*, **19**, 078109 (2007).

[6] P.H. Mortensen, H.I. Andersson, J.J.J. Gillissen and B.J. Boersma, "Dynamics of prolate ellipsoidal particles in a turbulent channel flow", *Phys. Fluids*, **20**, 093302 (2008).

[7] P.H. Mortensen, H.I. Andersson, J.J.J. Gillissen and B.J. Boersma, "On the orientation of ellipsoidal particles in a turbulent shear flow", *Int. J. Multiphase Flow*, **34**, 678-683 (2008).

23rd Nordic Seminar on Computational Mechanics
NSCM-23
A. Eriksson and G. Tibert (Eds)

LARGE-EDDY SIMULATION OF CERTAIN DROPLET SIZE EFFECTS IN FUEL SPRAYS

V.VUORINEN*, H.HILLAMO*, O.KAARIO*, M.LARMI*, AND L.FUCHS†

*Department of Energy Technology
Aalto University School of Science and Technology
P.O.BOX 14300, FIN-00076, Aalto, Finland
e-mail: ville.vuorinen@tkk.fi, web page: http://www.tkk.fi/

†KTH, CICERO
Department of Mechanics,
SE-10044, Stockholm, Sweden
e-mail: lf@mech.kth.se - Web page: http://www.kth.se

Key words: Large-Eddy Simulation, Fuel Sprays, Mixing, OpenFOAM

Summary. Views on the role of spray as a multiphase flows is given using the implicit Large-Eddy Simulation approach and the Lagrangian Particle Tracking approaches. Effect of droplet size, or the Stokes number, on mixing is quantified.

1 INTRODUCTION

The fuel spray has a key role in the formation of emissions in diesel engines. The strength of the coupling between the turbulent scales and a spectrum of droplet sizes determines the quality of mixture. The mixture homogeneity determines the level of emissions and engine efficiency. In modern engine concepts, such as low temperature combustion, this picture becomes even more enhanced. From the literature it is known that small droplets mix remarkably better than the larger droplets. This paper focuses on numerically investigating the physics of droplet dispersion better.

The state-of-the-art computational diesel engine research relies still much on the Reynolds-Averaged Navier-Stokes (RANS) approach. However, as RANS is a time averaged approach, Large-Eddy Simulation (LES) or Direct Numerical Simulation (DNS) are needed in order to gain detailed information on the local spray mixture quality. In fact, to date, only very few research papers have been published on the LES and DNS of diesel sprays. Hence, basic research is required which discuss the potential of LES in engine spray simulations. The present research paper summarizes some of our recent work published elsewhere[1,2,3,4].

2 COMPUTATIONS

2.1 The Governing Equations

In the present work LES is applied to solve the full, compressible Navier-Stokes equations in the low Mach number regime using a standard pressure correction approach[2]. A spray momentum source term is used in order to account for the spray-turbulence coupling. The energy source term is neglected as the effect of the droplets on the enthalpy fluctuations is assumed to be small. Droplets are modeled as point particles that obey a standard equation of motion[1].

2.2 The Numerical Tool - OpenFOAM

OpenFOAM is one of the most rapidly growing opensource CFD softwares. Importantly, OpenFOAM provides a compact notation to express the governing equations of fluid dynamics within the finite volume framework on unstructured grids. Parallelization is automatically adopted as a field property and hence the user does not oftenmost need to consider this complicated aspect at all. An example of the OpenFOAM syntax is given of the continuity equation which may be discretized and solved as follows:

```
solve(fvm::ddt(rho) + fvc::div(phi, rho) == 0),
```

where 'rho' is the fluid density and 'phi' is the flux of velocity interpolated linearly to the cell face. OpenFOAM is in key role when carrying out computations in unstructured grids since the field operations are very conveniently imbedded into the package.

3 RESULTS

3.1 Spray Shape

It is well known that droplets of small diameter (d) mix better with turbulence than the large droplets due to their smaller timescale $\tau_p = \frac{\rho_p d^2}{18\rho_g \nu_g}$ with respect to the flow timescale τ_f. Hence they have a small Stokes number $St_p = \tau_p/\tau_f$. What has currently not been very clear to the automotive engineering community is how to actually simulate the dispersion effect in a physically realistic way. Usually a stochastic random walk dispersion model is applied in order to achieve this objective in the RANS computations. Using LES, we have carefully demonstrated the dispersion effect as a function of droplet size and created a post-processing algorithm for spray visualization. As a result, the simulated sprays can not be visually distinguished from their experimental counterparts as can be seen from Fig. 1.

3.2 The Fuel Spray Structure

As a result of droplet-turbulence coupling the fuel spray structure may be highly heterogenous. Fig. 2 shows how the smaller droplets mix better than the larger droplets. The effect can be from the spray shape, internal structure and droplet group mixing. We have studied the heterogenous mixing in detail and we have shown that the small droplets mix remarkably better than the large droplets[3]. As in real sprays droplets break, the role of droplet breakup influences

droplet size and thereby the Stokes numbers. We have demonstrated certain a priori aspects of droplet breakup by developing a novel stochastic breakup model[4].

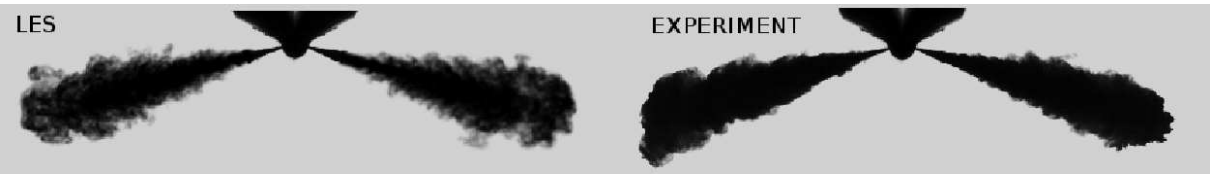

Figure 1: Qualitative comparison on the spray shapes as obtained with LES (left) and shadowgraphy (right). In the LES the initial part of the spray is not simulated. Adopted from[2].

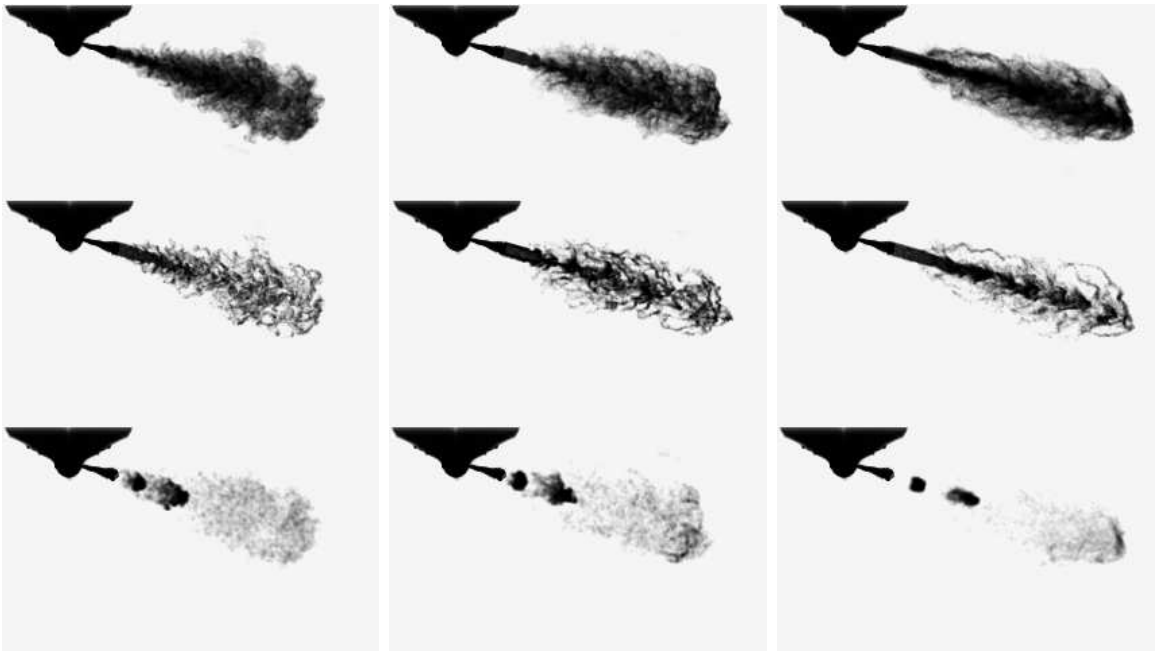

Figure 2: Droplet size increases from from left to right having values $2, 5$ and 10μ . **Row 1:** Spray cloud visualization. **Row 2:** Internal spray structure. **Row 3:** Visualization of only certain droplet groups[3].

3.3 The Fundamental Mixing Indicator

Our findings indicate that conventional means of studying mixing in a spray using e.g. average droplet concentration or a passive scalar might not give good enough picture on the level of mixing. Hence, we adopted a straighforward approach to study mixing by labeling all the droplets and studying how the configuration of the droplets changes: the larger/smaller the change, the larger/smaller the standard deviation of droplet index number $\sigma_\tau = \sigma_\tau(St_p, x, y, z, t)$ (both, locally averaged over a small length scale and globally averaged over the whole spray), and the better/worse the mixing. In fact, this can be considered to be a basic definition of mixing and applies to all turbulent flows. The PDF of σ_τ is shown in Fig. 3. It is seen how the effect of

droplet size (Stokes number) on mixing is clearly distinguished and a thorough discussion has been given in[3]. The average of σ_τ quantifies clearly how small droplets mix better than the larger droplets. In fact, this might be one of the first attempts to rigorously quantify mixing in a spray. In general, we have noted that as it would be very difficult to take the anisotropy and transient nature of the spray problem into account, the mentioned statistics and averages are simply calculated over the whole spray.

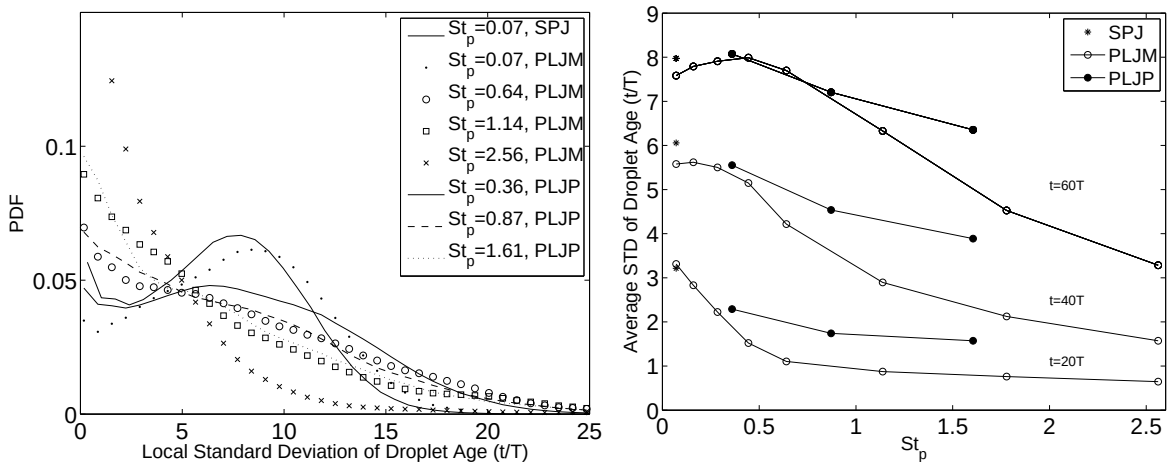

Figure 3: **Left:** PDF of local standard deviation of droplet age. **Right:** Average standard deviation of droplet age i.e. the droplet index number. Adopted from[1,2,3].

4 CONCLUSIONS AND OUTLOOK

An extensive LES study on fuel spray development has been carried out and quantitative measures for mixture quality have been developed. Our current studies are focusing on improving the OpenFOAM environment to the simulation of fully explicit, density based Runge-Kutta solvers with complex chemistry.

REFERENCES

[1] V.Vuorinen, LES of Certain Droplet Size Effects in Fuel Sprays. Doctoral Thesis, Aalto University School of Science and Technology, (2010).

[2] V.Vuorinen, H.Hillamo, O.Kaario, M.Larmi and L.Fuchs, Large-Eddy Simulation of Droplet Stokes Number Effects on Spray Shape, Atomization and Sprays, **20**, 93-114, (2010).

[3] V.Vuorinen, H.Hillamo, M.Nuutinen, O.Kaario, M.Larmi and L.Fuchs, Large-Eddy Simulation of Droplet Stokes Number Effects on Mixture Quality in Fuel Sprays, Atomization and Sprays, **20**, 435-451, (2010).

[4] V.Vuorinen, H.Hillamo, O.Kaario, M.Larmi and L.Fuchs, Effect of Droplet Size and Atomization on Spray Shape: A Priori Study Using Large-Eddy Simulation, Flow, Turbulence and Combustion, (online 2010).

23rd Nordic Seminar on Computational Mechanics
NSCM-23
A. Eriksson and G. Tibert (Eds)

DROPLET IMPACT AND PENETRATION ON A POROUS SUBSTRATE: A PHASE FIELD MODEL

MINH DO-QUANG*, FREDRIK LUNDELL*, ASAF OKO†, AGNE SWERIN†, GUSTAV AMBERG*

*Linné Flow Centre, Department of Mechanics, Royal Institute of Technology,
SE-100 44 Stockholm, SWEDEN
e-mail: minh@mech.kth.se - Web page: http://www.mech.kth.se

†YKI, Ytkemiska Institutet AB/Institute for Surface Chemistry,
Box 5607, SE-114 86 Stockholm, Sweden
Web page: http://www.yki.se

Key words: Fluid Mechanics; Porous medium; Liquid droplets; Impact;

Summary. In this paper we present a numerical model, based on a free energy formulation, to simulate the dynamics of the impact, spreading and absorption of a liquid droplet impinging on a porous material. This model consists of the Navier-Stokes equations with the Cahn-Hilliard equation. This system allows us to simulate the motion of a free surface in the presence of surface tension of droplets upon the surface and inside the porous medium. The porous substrate is modeled using the solid boundary of fiber-like obstacles. Numerical results with different chemical surface of the porous material and its structure are presented. We demonstrate the influence on the droplet penetration and spreading characteristics by varying these parameters.

1 INTRODUCTION

The behaviour of droplets impacting onto porous media finds its importance in a myriad of applications and processes, varying from environmental applications to inkjet printing technology. Due to the complexity of such phenomena, involving droplet impact and absorption onto the porous medium, it is still not completely understood although it have been subject for intensive investigation.

When a liquid droplet is impinged onto a paper coated with a porous layer it experiences evaporation, expansion of the droplet base diameter and imbibition into the porous matrix, as illustrated in Figure 1. The drying time of liquid droplets on a permeable substrate is set by the liquid evaporation rate and the imbibition rate, and that the relative importance of these processes strongly depends on the substrate characters such as porosity and surface energy as well as on the degree of liquid volatility.

In this work, a numerical model is used to study the dynamics of the impact/absorption of a liquid droplet on a porous medium. This problem addresses a more complicated set of physical phenomena than impingement of liquid droplets on non-permeable surfaces, as presented in our previous work[1]. Here, not only the axial momentum of the droplet transformed to radial

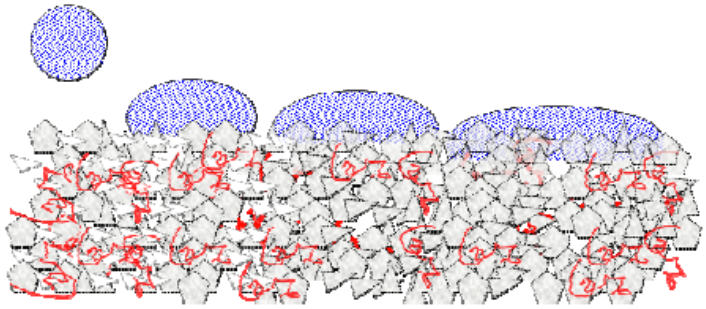

Figure 1: Illustration (not to scale) of spreading and imbibition of a liquid droplet impinged on a paper coated with a porous layer consisting of pigment particles of different shapes and a binder (red lines).

momentum, but also the pressure at the impact point also forced the liquid to move through the permeable surface and into the substrate. Furthermore, the capillary effects and wettability tended to draw the liquid into the porous substrate.

2 RESULTS

The modelled used for the numerical analysis demonstrate how local structural variations reflect on wetting behaviour and imbibition dynamics on e.g. coated inkjet papers as shown in Figure 2. For more information, please refer to [2].

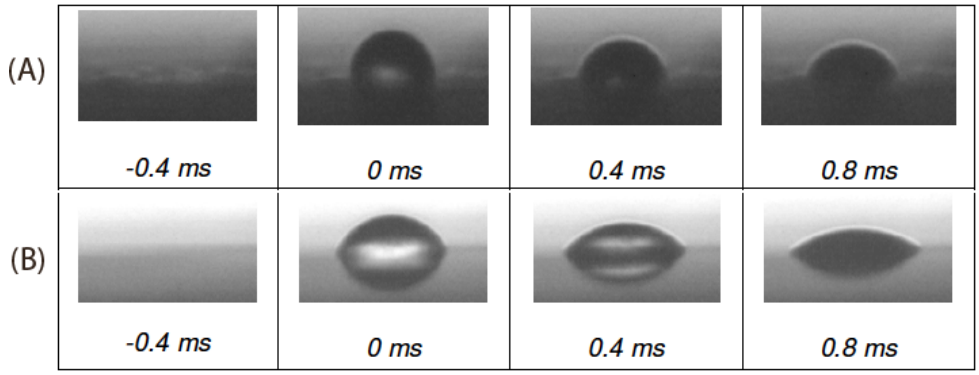

Figure 2: A sequence of images showing a droplet impinged on a matte coated paper: $230g/m^2$, photo supreme double-sided matte, staples (A); and on a gloss coated paper: $240g/m2$, photo plus gloss, staples (B).

The numerical simulations were carried out using femLego [3], a symbolic tool to solve partial differential equations with adaptive finite element methods. The partial differential equations, boundary condition, initial conditions, and the method of solving each equation are all specified in a Maple worksheet. The Cahn-Hilliard equation is treated as a coupled system for the chemical potential and the composition. Both the chemical potential and the composition equations are discretised in space using piecewise linear functions. The coupled nonlinear algebraic system of the chemical potential and the composition is solved by an exact Newton's method. Within

each Newton iteration, the sparse linear system is solved by GMRES method.

Fig.(3) shows the droplet shapes of a liquid ink impact into three different paper substrate. The chemical energy of those porous medium is 10° for case (A); 90° for case (B) and 150° for case (C). In this figure, we observed the volume of liquid ink that penetrates into the porous medium depend on its chemical energy.

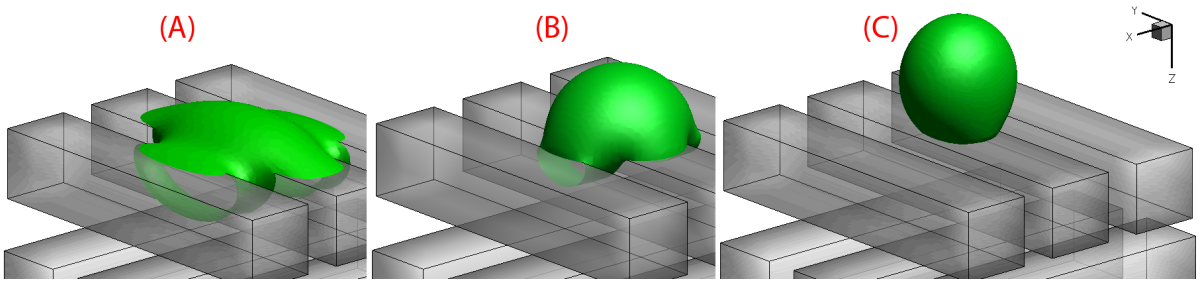

Figure 3: Numerical simulation of a droplet impact and spreading on the different wettable porous medium: (A) the wetting contact angle $\theta = 10°$; (B) $\theta = 90°$ and (C) $\theta = 150°$.

3 CONCLUSIONS

We adopt the Phase Field method to numerically investigate the impact of an ink-droplet onto the porous medium. The case studied here consists of a multiphase flow of air-liquid along with the interaction between a solid structure and an interface. By only changing the wettability of the porous material, droplets were either deposited on the surface or could bounce off. Several porous medium structures are used to investigate the absorption behavior of liquid droplets into the porous medium. This identifies the wettability to be key parameter to control the absorption process.

REFERENCES

[1] Carlson, A., Do-Quang, M. & Amberg., G. Modeling of dynamic wetting far from equilibrium. *Physics of Fluids* **21**, 121701–4 (2009).

[2] Oko, A., Swerin, A. & Claesson., P. *Journal of Imaging Science and Technology* Accepted 2010 and presented at NIP26 – Non impact printing conference, Austin, TX, September 20-23, 2010.

[3] Do-Quang, M., Villanueva, W., Singer-Loginova, I. & Amberg, G. Parallel adaptive computation of some time-dependent materials-related microstructural problems. *Bull Pol Acad Sci-Te* **55**, 229–237 (2007).

23rd Nordic Seminar on Computational Mechanics
NSCM-23
A. Eriksson and G. Tibert (Eds)

ACCOUNTING FOR AERODYNAMIC INTERACTION IN PARTICLE-LADEN TURBULENT JET FLOWS

ASIM JADOON AND JOHAN REVSTEDT

Energy Sciences/Fluid Mechanics, LTH
Lund University
P.O. Box 118, 221 00, Lund, Sweden
e-mail: johan.revstedt@energy.lth.se, web page: http://www.fm.energy.lth.se/

Key words: Fluid Dynamics, Two-phase Flow, Particle Interactions.

Summary.

1 INTRODUCTION

The introduction of particles (solid phase) to a gas phase may result in a change of properties of the motion of either or both phases. From a modelling perspective this can be separated into different levels of approximation. If the particle-fluid volume ratio is low and the ratio between average inter-particle distance and particle diameter is large (typically greater than 10) then one can assume that only the the dispersion effects of the gas phase turbulence on the particles is of importance, i.e. one-way coupling. However, when the number of particles is sufficiently large the particle influence on the gas phase can no longer be neglected (two-way coupling). Furthermore, one may also account for inter-particle collisions, which can, even for fairly low volume fractions have an effect on the motion. The present study is focused on investigating the effects of accounting for aerodynamic interaction on the modelling of two-way coupling, i.e. the effects arising from that a particle will locally affect the flow field which in turn may influence the force loading on particles in close proximity.

2 MATHEMATICAL AND NUMERICAL FORMULATION

2.1 Modelling of the continuous phase

In LES, the large scales which are containing most of energy in turbulent flows are resolved, whereas the small scales, more universal in nature, are modelled using a suitable sub-grid scale (SGS) model. Here we use the concept of implicit SGS modelling, which means that the effects of the unresolved turbulent scales are accounted for by the dissipative nature of the third order upwind scheme used to discretise the convective terms of the momentum equations.

2.2 Particle equation of motion

Lagrangian particle tracing (LPT) is based on solving the equation of motion for each particle, i.e.

$$m\frac{d\vec{U}_p}{dt} = \vec{F} \tag{1}$$

where m is the particle mass and $\vec{F}$ is the force acting on the particle. The force can be decomposed into contributions originating from different physical effects (cf. Maxey and Riley[1]). However, if the density of the particles is much larger than the density of the fluid (in our case tha ration is 2000) one may neglect all contributions except drag and gravity. Reformulating the equation of motion on non-dimensional form one may write the drag contribution as

$$\vec{F}_D^* = -\frac{3}{4}\frac{\rho_c}{\rho_p}\frac{1}{d_p^*}C_D f_d \mid U_r^* \mid U_r^* \tag{2}$$

Here C_D is is the drag coefficient, which is calculated using the correlations given by Shiller and Naumann[2]. The coefficient f_d is used to account for aerodynamic interaction (three-way modelling). Also, the particle interaction will result in a lift force which is accounted for using the following expression:

$$\vec{F}_L^* = \frac{3}{4}\frac{\rho_c}{\rho_p}\frac{1}{d_p^*}\vec{C}_L \mid \vec{U}_r^* \mid \vec{U}_r^* \tag{3}$$

The corrections (f_D and $\vec{C}_L$) are computed based on the relative position of the particles[3,4,5]. The data from these studies is tabulated for a wide range of particle Reynolds numbers, particle separation distances and angles. As the drag and the lift corrections are calculated for a fixed particle pair, the direction of motion of two particles must be close to parallel for the corrections to be applied.

The governing equations of the continous phase are discretised on a Cartesian staggered grid using the third order upwind scheme by Rai and Moin[6] for the convective terms and a fourth order central scheme for other terms. The equations are solved using a split solver, the momentum equations are solved using a Runge-Kutta type scheme while the the pressure correction equation solver uses a multi-grid accelerated Gauss-Seidel scheme. The disperse phase solver is based on the same Runge-Kutta type scheme as for the continous phase.

3 PROBLEM SET-UP

A rectangular computational domain of $[8, 24, 8]D_N$ (D_N is the diameter of the nozzle) corresponding to $[X, Y, Z]$ direction is used. The jet enters at the center of the $X - Z$ plane and flows in the Y (stream-wise) direction. The jet Reynolds number is 13000. At the inflow, fluctuations in the radial velocities are introduced as $\pm 10\%$ of the axial velocity and no slip boundary conditions at walls. At outflow Neumann boundary conditions are applied. The investigation is carried out using several Stokes numbers and particle mass loadings. However, here we only show results for a Stokes number of 10 since that is where we observe the largest effects of three-way coupling.

4 RESULTS

Fig. 1a shows a comparison of the particle mean axial velocity along the centerline for a mass loading $\zeta = 0.12$. In case of three-way coupling (considering only drag), there is a slight tendency for the centre line particle mean axial velocity to be higher beyond $Y = 9D_N$, whilst including also the lift will not result in any change compared to the two-way coupled case. However, considering the axial velocity fluctuations (shown in Fig. 1b) the three-way coupled

case has lower values than the two-way case, which might be caused by the lower drag for three-way which in turn results in a lower momentum transfer from the continous phase. The experimental results of Hardalupas et al.[7] show high levels of fluctuations already at the nozzle, which we are not able to capture. However beyond the jet core region ($D_N > 7$), the results are in good agreement.

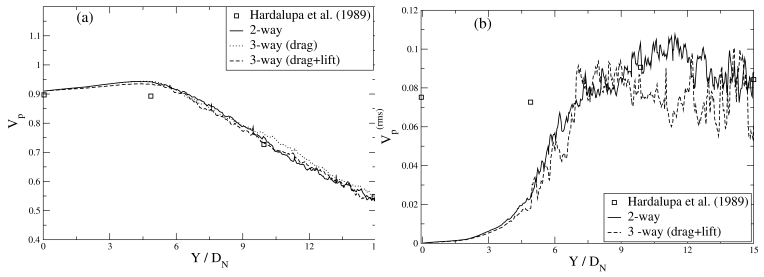

Figure 1: Particle mean axial velocity (a) and rms of its fluctuations (b) along the centreline of the jet for $\zeta = 0.12$.

Increasing the mass loading by a factor of about 6 to 0.86, gives an overall increase in mean particle centre line velocity. Also, the difference in particle mean axial velocity along centre line between two-way and three-way coupling s larger and at $Y = 15D_N$ it is approximately 7% (Fig. 2a). The particles gain higher mean axial velocities since the drag on particles generally decreases when corrections are applied. The particle velocity fluctuations follows the same trend as for the lower mass loading (Fig. 2b). Althouth the experimental data has too few points to draw any conclusions, a rough comparison with the results of Hardalupas et al.[7] shows that simulations for all cases over estimates the the rms. of the fluctuations.

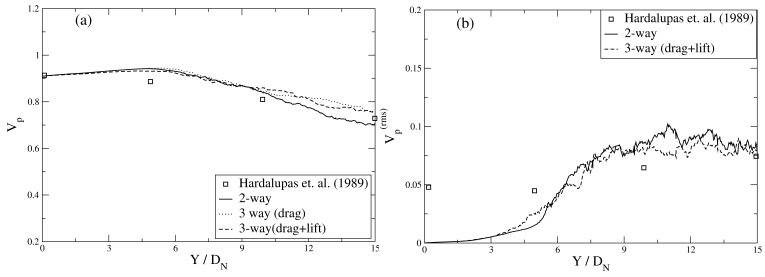

Figure 2: Particle mean axial velocity (a) and rms of its fluctuations (b) along the centreline of the jet for $\zeta = 0.86$.

The difference in the continuous phase velocities along the centre line between two-way and three-way cases is as can be senn in Fig 3a negligible. As the particles are accelerated by the gas, the gas looses momentum to the particles. This implies that in three-way coupling case, one might expect the continuous phase velocity to be higher compared to the two-way case. However, this is not the case. A propable explanation for this is that in the three-way coupling case the jet have a somewhat larger spreading rate which causes the axial velocity along the centre line to decay faster.

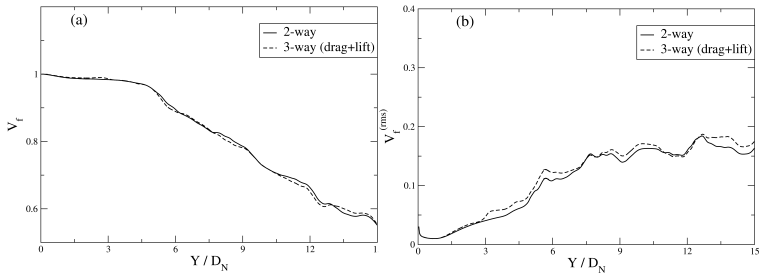

Figure 3: Gas phase mean axial velocity (a) and rms of its fluctuations (b) along the centre line of the jet for $\zeta = 0.86$.

5 CONCLUSIONS

The maximum effect of the three-way aerodynamic modelling is observed at relatively lower Stokes number of 10 and mass loading of 0.86. An increase of approximately 7% in the particle mean axial velocity compared to two-way coupling is observed when three-way coupling considering only drag and both drag and lift is applied. The continuous phase velocity fluctuations are observed to be higher in three-way coupling along the axis of the jet resulting in higher radial velcoity. The spread of the jet is larger in three-way coupling compared to the two-way case. The aerodynamic three-way coupling is strongly dependent on Stokes number and particle number density.

REFERENCES

[1] Maxey, M. & Riley, J. Equation of motion for a small rigid sphere in a nonuniform flow. *Phys. Fluids* **26**, 883–889 (1983).

[2] Schiller & Nauman, A. Z. A drag coefficient correlation. *Ver. Deut. Ing* **77**, 318–320 (1933).

[3] Jadoon, A., Prahl, L. & Revstedt, J. Dynamic interaction of fixed dual spheres for several configurations and inflow conditions. *European J. Mech. B/Fluids* **29**, 43–52 (2010).

[4] Prahl, L. *et al.* A study of the interaction between two fixed spherical particles. *Int. J. Multiphase Flow* **33**, 707–725 (2007).

[5] Prahl, L., Jadoon, A. & Revstedt, J. Interaction between two spheres placed in tandem arrangement in steady and plusating flow. *Int. J. Multiphase Flow* **35**, 963–969 (2009).

[6] Rai, M. M. & Moin, P. Direct simulations of turbulent flow using finite-difference schemes. *J. Comput. Phys.* **96**, 15–53 (1991).

[7] Hardalupas, Y., Taylor, A. & Whitelaw, J. Velocity and particle-flux characteristics of turbulent particle-laden jets. *Proceeding of Royal society of London* **426**, 31–78 (1989).

23rd Nordic Seminar on Computational Mechanics
NSCM-23
A. Eriksson and G. Tibert (Eds)

LARGE-SCALE ACCUMULATION OF INTERTIAL PARTICLES IN TURBULENT CHANNEL FLOW

GAETANO SARDINA*, FRANCESCO PICANO*, PHILIPP SCHLATTER†, LUCA BRANDT† AND CARLO M. CASCIOLA*

*Department of Mechanics and Aerospace Engineering
University of Rome "La Sapienza"
Via Eudossiana 18, IT-00184 Roma, ITALY
e-mail: gaetano.sardina@uniroma1.it, web page: http://dma.dma.uniroma1.it/dima/

†Linné FLOW Centre, KTH Mechanics
Osquars Backe 18, SE-100 44 Stockholm, SWEDEN
e-mail: pschlatt@mech.kth.se - Web page: http://www.mech.kth.se

Key words: Lagrangian Particles in Turbulence, Direct Numerical Simulation, Turbulent Channel Flow.

Summary. Spatially inhomogeneous turbulent flows induce peculiar phenomena on the transport of a dispersed phase of intertial particles. In channel flows the most striking effect is the spatial segregation of particles that may achieve a concentration at the wall largely exceeding that in the bulk. Here, we approach the issue by considering direct numerical simulations in a channel seeded with different populations of diluted, tiny particles. The structures found in the fully developed turbulent stage of the process show strong spanwise correlations more intense than those found in the corresponding eloganted structures of low and high speed fluid. For a standard domain size, the spanwise organisation is extremely regular, corresponding to a mean spacing of about 120 plus units. The simulations with an increased box size highlight some significant differences in the correlation of particle concentrations. We note the these DNS at $Re_\tau = 180$ have been performed using the largest domain size so far. A possible explanation of this feature can be related to large-scale structures of the velocity field, which might carry a considerable amount of energy. Correlations between turbulent events such as sweep and ejections, and the particle motions towards and from the wall will be discussed.

1 INTRODUCTION AND METHODS

The dynamics of small intertial particles transported by a turbulent flow is crucial in many engineering applications, for instance internal combustion engines or pollutant transport in pipes. Small, diluted particles, much heavier than the carrier fluid, are essentially forced only by the viscous drag. Hence their velocity v is determined by $\dot{v} = (u - v)/\tau_p$, where $\tau_p = d_p^2 \rho_p/(18\rho\nu)$ is the Stokes response time (d_p, ρ_p are the particle diameter and density respectively; ρ and ν are the fluid density and viscosity). In this model Lagrangian fluid particles are recovered in the limit of vanishing Stokes time. The opposite limit of ballistic particles is achieved for τ_p tending to infinity. The difference between particle velocity v and fluid velocity u produces

various widely discussed anomalous phenomena such as small-scale clustering or preferential accumulation at the wall (turbophoresis) even for incompressible flows, see among others[1,2].

The latter phenomenon (see Fig. 1 below) is represented by the non-uniform instantaneous particle configurations at the wall. Particles at the wall seem to accumulate in preferential structures which are extremely long and aligned along the mean velocity direction. The specific nature and dynamics of these structures is still not completely understood, so the aim of our work is to investigate the origin of these phenomena and in particular their link with turbulent large-scale motions[2].

The simulations in the channel-flow geometry were performed using an adapted version of the general spectral Navier-Stokes solver SIMSON[3]. The code is parallelized using MPI over the spanwise direction, and can therefore be used efficiently on computer clusters. We are considering two different simulation domains. The smaller domain is of size $4\pi \times 2 \times 4\pi/3$, see Ref.[4], with a total of $128 \times 129 \times 128$ modes. In order to study the effect of limiting box size, we have also studied a substantially larger domain with effective size $12\pi \times 2 \times 4\pi$. The number of grid points is increased accordingly by a factor of 3 in both the streamwise and spanwise directions. For both domain sizes, the same Reynolds number $Re_\tau = 180$ is considered, maintained by a fixed mass flux $Re_b = 2800$. A total of five populations of inertial particles ($St^+ = 0.2, 1, 5, 10, 50$) and one of tracers ($St^+ = 0$) are considered, every run evolves $200,000$ and $1,800,000$ particles per population respectively, in order to keep equal the mean concentration inside the box domain. We remark that the second simulation is performed in the largest domain among those we have found in literature for multiphase flow.

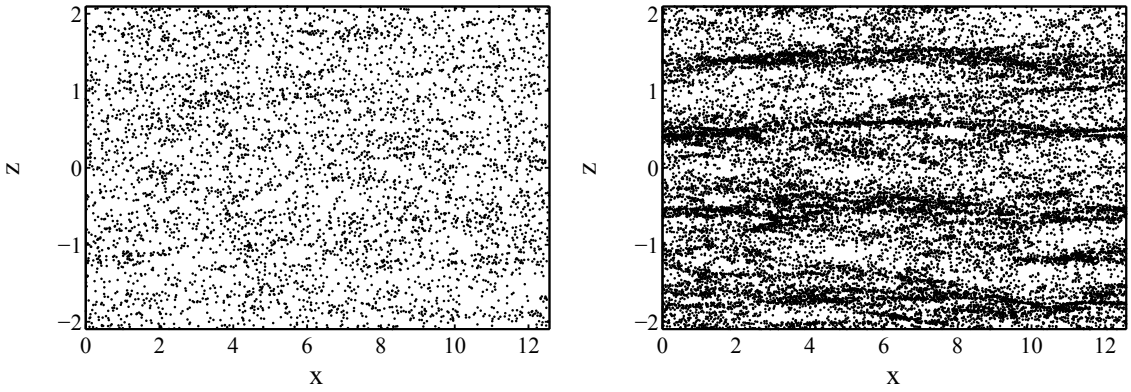

Figure 1: *Instantaneous particle visualization ($St^+ = 10$) of particles near the wall. Left and right panels represent times $t^+ = 450$ and $t^+ = 17000$ respectively.*

2 RESULTS AND DISCUSSION

The transient phases of the particle evolution in turbulent channel flow are shown in Fig. 1. Initially seeded randomly in a developed turbulent flow, particles begin to move towards the wall without having preferential localization or correlation to certain fluid events. However, after reaching statistical stationarity for later times, particles tend to persist in preferential zones organized in long streaky patterns, and the homogeneous wall distribution is lost during this

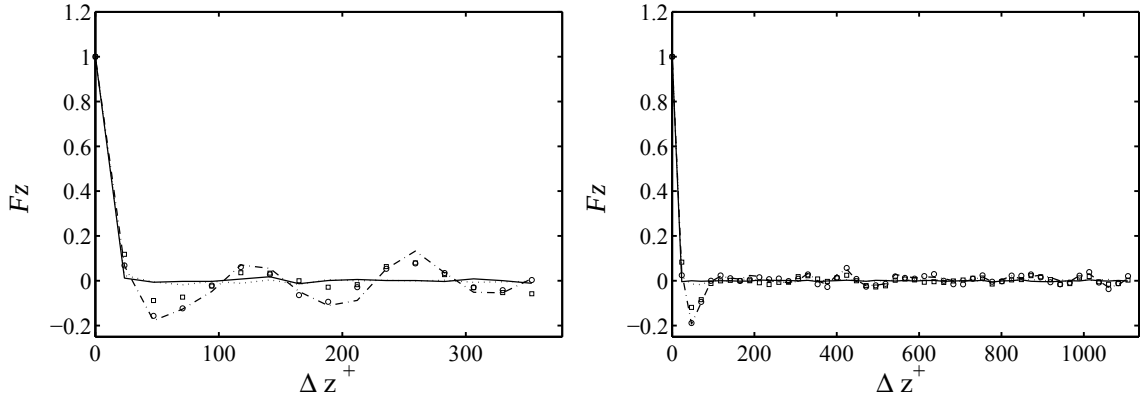

Figure 2: Spanwise two-point correlation coefficients of particle concentration fluctuations at $y^+ = 1$. The two panels are for the small (left) and large (right) simulation domains, respectively. The symbols correspond to different Stokes numbers.

phase. The localization of particles in these patterns is associated with slow fluid departing motions. This feature, enhancing the particle migration from the wall, may balance the turbophoretic drift and may lead to equilibrium conditions, i.e. zero particle wall normal flux. This behavior suggests a strong connection between the asymptotic particle accumulation level and the large scale structures of the flow. It is noteworthy that in the channel the asymptotic state is reached only after long times depending on the Stokes number (up to 10000 viscous time units for $St^+ = 10$.

To investigate more quantitatively the accumulation structures at the wall we use the spanwise two-point correlation coefficient of the Eulerian concentration c. By defining a binning size, one may evaluate the number of particles found in a certain binning volume centered around a given wall-normal position y, exploiting the wall-parallel homogeneity of the flow. Naturally, the Eulerian concentration is dependent on the binning size[2]. Figure 2 reports the spanwise correlation coefficient $Fz(y, \Delta z) = F(y, \Delta z\, \hat{\mathbf{e}}_z)$ in the near wall region, $(y^+ = 1)$, for the both the large and the small channel simulations. In both boxes, particles with a small Stokes number do not show appreciable correlation neither in the streamwise nor in the spanwise direction. Heavier particles are instead much more correlated as shown by the oscillatory correlation coefficient in the spanwise direction. The characteristic length of these oscillations is $\Delta z^+ \approx 120$, featuring a similar spacing as the turbulent velocity streaks measured by spanwise two-point correlation of the streamwise velocity. However, unlike velocity correlations, the oscillations in the particle concentration correlation persist at larger separations, e.g. at twice the basic separation $\Delta z^+ \approx 2 \cdot 120$. This clearly indicates that the particle patterns are much more regular and straight than the corresponding velocity streaks. Clear multiple maxima and minima imply that particle streaks are moving in a much more collaborative manner than velocity.

Like the smaller one, the simulation in the larger domain shows a negative peak in the spanwise correlation. However the oscillatory trend for large separations is clearly attenuated. We infer that the very regular and temporally invariant accumulation pattern found for the smaller box is essentially due to a restricting effect of the boundary conditions.

It is interesting to note that the position of the first minimum is nevertheless unchanged

between the small and the large simulation domain. This suggests that the local structure of single streaks is unaffected by the boundary conditions, while their collective behavior is instead strongly influenced.

As far as the streamwise correlations of the particle phase is concerned (not shown here), the lighest particles show again no significant correlation irrespective of the domain size. For $St^+ > 5$ the long structures visible in Fig. 1 above give rise to positive correlations even for large streamwise displacements (*i.e.* order or 1000 plus units), certainly not reaching zero (streamwise independence) in the case of the smaller domain size. In the longer box, values close to zero are obtained for the largest separations[2].

As mentioned above, the present use of a binning procedure to compute the correlation coefficients gives a natural dependence on the exact choice of the binning parameters. This can be avoided by considering more complex observables which allow the investigation of the particle structure without referring to Eulerian binning.

3 CONCLUSIONS

Particles transported in fully turbulent wall-bounded flow predominantly form narrow, but very long streamwise patterns, located preferably along low-speed streaks of the velocity field[1], characterized by an outward wall-normal motion. However, a closer analysis of the streamwise two-point correlations of the particle concentration in the near-wall region clearly shows that the length of these particle streaks is significantly larger than the corresponding velocity structures in a turbulent channel flow. In particular, it is documented that for the smaller channel box (a box similar to what has been commonly used in all other studies) the spanwise organization of the particle streaks is extremely regular even for larger separations and corresponds to a mean spacing of about 120 plus units. In addition, the streamwise two-point correlation of the particle concentration does not reach zero at the ends of the domain. This clearly indicates that such a domain is not large enough for the particles to freely move about. To what extent the limiting box sizes considered so far have an influence on physical conclusions drawn from simulations is part of current work.

REFERENCES

[1] Picciotto, M., Marchioli, C. & Soldati, A. Characterization of near-wall accumulation regions for inertial particles in turbulent boundary layers. *Phys. Fluids* **17** (2005).

[2] Sardina, G., Picano, F., Schlatter, P., Brandt, L. & Casciola, C. M. Large-scale accumulation patterns of inertial particles in wall-bounded turbulent flows. *Flow Turbulence Combust.* (2009). Submitted.

[3] Chevalier, M., Schlatter, P., Lundbladh, A. & Henningson, D. S. SIMSON - A Pseudo-Spectral Solver for Incompressible Boundary Layer Flows. Tech. Rep. TRITA-MEK 2007:07, KTH Mechanics, Stockholm, Sweden (2007).

[4] Moser, R. D., Kim, J. & Mansour, N. N. Direct numerical simulation of turbulent channel flow up to $Re_\tau = 590$. *Phys. Fluids* **11**, 943–945 (1999).

23rd Nordic Seminar on Computational Mechanics
NSCM-23
A. Eriksson and G. Tibert (Eds)

STRESS CONCENTRATION AND DESIGN OF SPLINE SHAFT

NIELS L. PEDERSEN

Dept. of Mechanical Engineering, Solid Mechanics
Technical University of Denmark
Nils Koppels Allé, Building 404, DK-2800 Kgs. Lyngby, Denmark
e-mail: nlp@mek.dtu.dk

Key words: Straight-sided spline, Torsion, Stress concentration, Optimization, Laplace equation, FE.

Summary. Spline connection of shaft and hub is commonly applied when large torque capacity is needed together with the possibility of disassembly. The designs of these splines are generally controlled by different standards. In view of the common use of splines, it seems that few papers deal with splines and the subject of improving the design. The present paper concentrates on the optimization of splines and the predictions of stress concentrations, which are determined by finite element analysis (FEA).

Using different design modifications, that do not change the spline load carrying capacity, it is shown that large reductions in the maximum stress are possible. Fatigue life of a spline can be greatly improved with up to a 25% reduction in the maximum stress level. Design modifications are given as simple analytical functions (modified super elliptical shape) with only two active design parameters and therefore the designs are practical realizable.

1 STRESS CONCENTRATION OF SPLINED SHAFTS (ISO14/DIN 5462)

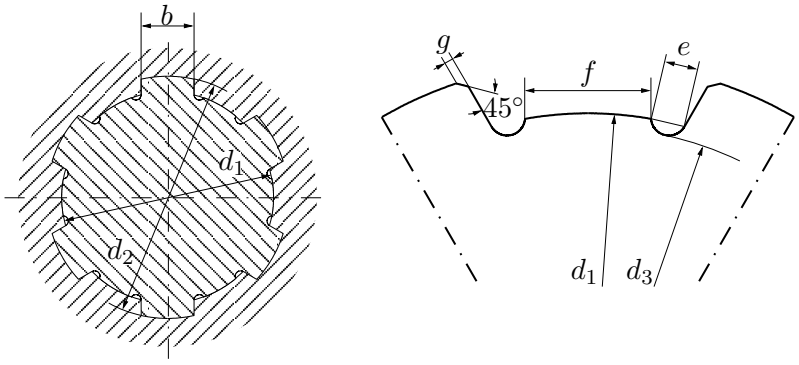

Figure 1: An example of a spline connection, the dimensions correspond to DIN ISO 14 ($7 \times 28 \times 32$ light series), i.e. $b = 7\text{mm}$, $d_1 = 28\text{mm}$, $d_2 = 32\text{mm}$ and the number of teeth $N = 6$. The specific design of, e.g. the tooth root shown to the right is taken from the outdated DIN 5462.

In Figure 1 a standard spline that follows ISO 14 light series is shown. The loading of the spline is restricted to pure torsion, and the relative dimensions are controlled by the standard. In the present work

the maximum allowable value of e according to the standard has been selected. Due to symmetry we need only consider half a tooth as seen in Figure 2. The full mathematical formulation of the torsional

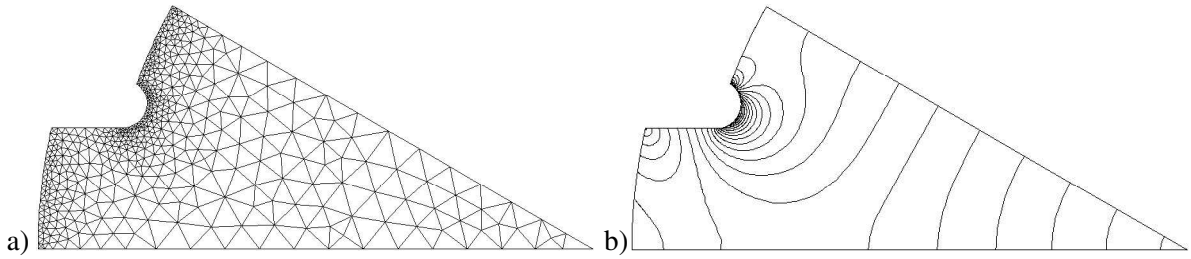

Figure 2: The figures are for one twelfth of the shaft given in Figure 1. a) Example of a finite element mesh, the shown mesh is with 953 elements. b) Iso lines of resulting stress level, indicating the stress concentration at the corner, the result is obtained with a higher number of elements 8529 (400 elements along the circular part with the highest stress concentration) to achieve convergence of maximum stress.

problem can be found in [1]. The torsional moment is given by

$$M_t = GJ\frac{\phi}{l} \tag{1}$$

where G is the shear modulus of elasticity, J is the cross sectional torsional stiffness factor, ϕ angular rotation of torsional cross section and l it the shaft length. It is assumed that a prismatic shaft is aligned with a Cartesian coordinate system with the x-, y- and z-directions such that the shaft axis is aligned with the z-direction. Saint-Venant have introduced the warping function $\Psi(x, y)$ by which the shaft displacement under torsion is given by

$$v_x = -yz\frac{\phi}{l} \qquad v_y = xz\frac{\phi}{l} \qquad v_z = \Psi(x, y)\frac{\phi}{l} \tag{2}$$

With zero volume force the force equilibrium gives the Laplace differential equation that the warping function must fulfill

$$\Delta\Psi = 0 \tag{3}$$

By formulating the torsional problem as (3) with suitable boundary conditions it is possible to use a standard PDE solver. In the present work the program COMSOL [2] is used. In Figure 3 the stress concentration is given along the splined shaft outer boundary shown in Figure 2. From an optimization point of view it is clear that this is not optimal because the stress should be constant along major boundary parts in order for the design to be optimal, see e.g. [3]. The nominal stress used in the definition of the stress concentration is defined relative to the inner diameter d_2. Using the geometry as specified by ISO14 the stress concentration with the nominal stress defined relative to the outer diameter d_1 is shown in Figure 4. The presented factors correspond nicely to the reported values in [4], except for a shift down in the overall size, this is probably due to the selected radii values. From Figure 4 it is noticed that the values are relative constant facilitating a simple linear curve fit.

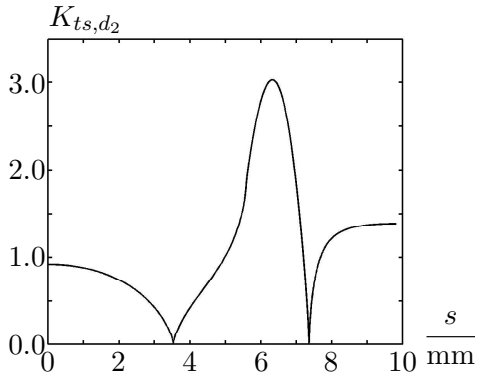

Figure 3: The figure is for the cross sectional part of the shaft shown in Figure 2. It shows the stress concentration as a function of the arc length around the outer boundary starting from the lowest point until the top point. Maximum value for this specific case, where the radius at the stress concentration is selected to $r = 0.7\text{mm}$, is $K_{ts,d_2} = 3.03$.

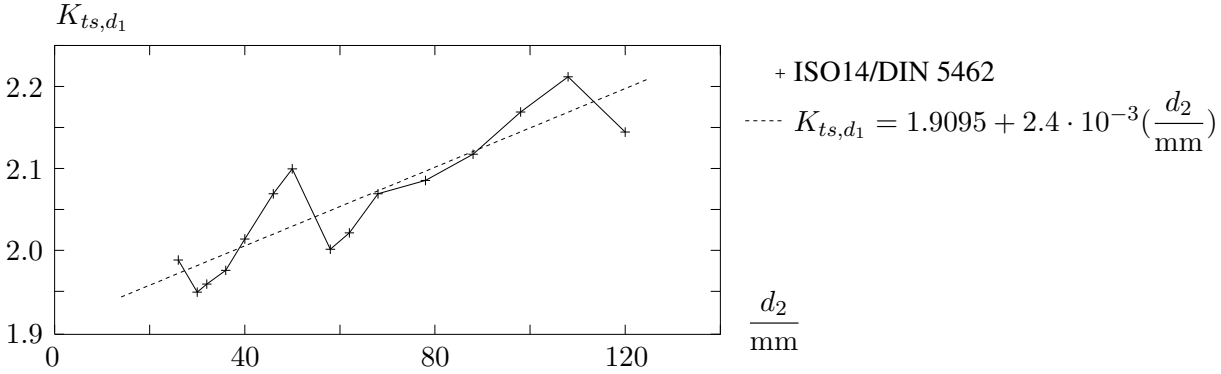

Figure 4: The stress concentration factor of a splined shaft as a function of the outer diameter d_2. The nominal stress is defined relative to the inner diameter, i.e. $\tau_{\text{nom}} = \frac{16M_t}{\pi d_1^3}$. Also shown are the linear curve fit to the result.

2 SPLINE OPTIMIZATION

A simple design modification to ISO14 is given in Figure 5. Teeth height is unchanged and at the root a quarter of a super ellipse is used instead of a circle. The super ellipse continues in a straight shoulder (length L_3) that finally ends at the inner diameter. The super ellipse (with super elliptical power η) is in parametric form given by

$$X = -L_1 + A\cos(\theta)^{(2/\eta)}, \qquad \theta \in [0:\frac{\pi}{2}], \qquad A \leqq A_{\max} = L_1 - \frac{d_1}{2}\cos(\frac{\pi}{N}) \tag{4}$$

$$Y = \quad L_2 - B\sin(\theta)^{(2/\eta)}, \qquad \theta \in [0:\frac{\pi}{2}], \qquad B \leqq B_{\max} = \frac{d_1}{2}\sin(\frac{\pi}{N}) - \frac{b}{2} \tag{5}$$

There are in principle three design parameters for this revision, the two half axis A and B and the super elliptical power η. For this parameterization it is found that $A = A_{\max}$ is optimal so there is only two active design parameters. Using this design revision we find the optimized stress concentration factors seen in Figure 6. The average stress reduction is 24.3%.

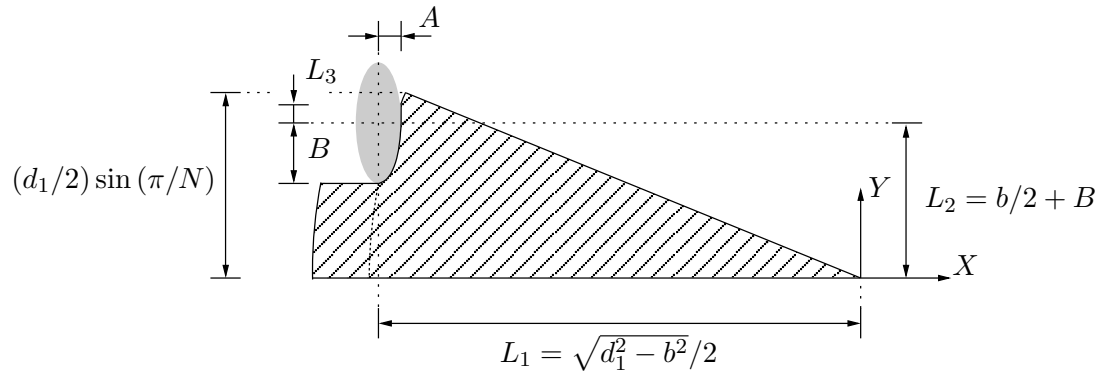

Figure 5: Design parameterization of design revision I. Design parameters are half axis A and B and the super elliptical power η, here shown for the specific case $\eta = 2$.

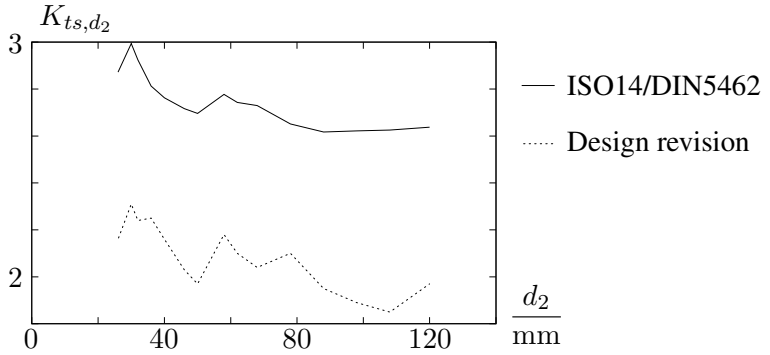

Figure 6: Stress concentration factors of splined shafts for the ISO14/DIN5462 standard and for the optimized values given in Table 1.

d_1/mm	23	26	28	32	36	42	46	52	56	62	72	82	92	102	112
B/mm	1.74	2.18	2.18	1.44	1.58	1.96	2.13	2.27	2.70	2.80	1.93	2.64	2.93	3.23	3.27
η	1.55	1.55	1.55	1.58	1.56	1.56	1.56	1.55	1.55	1.55	1.58	1.58	1.58	1.58	1.58

Table 1: Optimized values of design parameters, it should be noted that $A = A_{\max}$ for all designs.

REFERENCES

[1] N. L. Pedersen. Stress concentrations in keyways and optimization of keyway design (accepted). *Journal of Strain Analysis for Engineering Design*, 2010.

[2] COMSOL AB. Stockholm, www.comsol.se, 1998-2009.

[3] N. L. Pedersen and P. Pedersen. Design of notches and grooves by means of elliptical shapes. *Journal of Strain Analysis for Engineering Design*, 43(1):1–14, 2008.

[4] F. G. Kollmann. *Welle-Nabe-Verbindungen: Gestaltung, Auslegung, Auswahl*. Springer-Verlag, Berlin Heidelberg New York, 1984.

23rd Nordic Seminar on Computational Mechanics
NSCM-23
A. Eriksson and G. Tibert (Eds)

CELL BASED FINITE VOLUME DISCRETIZATION OF CONTROL IN THE COEFFICIENTS PROBLEMS

ANTON EVGRAFOV*, MISHA M. GREGERSEN* AND MADS P. SØRENSEN*

*Department of Mathematics
Technical University of Denmark
DK–2800 Kongens Lyngby, Denmark
e-mail: a.evgrafov@mat.dtu.dk, web page: http://www.mat.dtu.dk/

Key words: Topology optimization, control in the coefficients, optimal design.

Summary. Problems of control in the coefficients of partial differential equations (PDEs) arise as a popular approach for solving optimal design problems, and is often known under the names of topology optimization through homogenization or material distribution. With a long term goal of solving topology optimization problems within application domains where finite volumes methods (FVMs) constitute a standard approach to discretizing PDEs, most notably computational fluid dynamics, we rigorously investigate a convergence of a cell based FVM applied to a model problem of control in the coefficients. We illustrate our approach with numerical examples.

1 INTRODUCTION

Utilizing control in the coefficients of PDEs for the purpose of optimal design, or topology optimization, is a well established technique in both academia and industry[1]. Advantages of using control in the coefficients for optimal design purposes include the flexibility of the induced parametrization of the design space that allows optimization algorithms to efficiently explore it, the ease of integration with existing computational codes in a variety of application areas, and the simplicity and efficiency of sensitivity analyses.

Finite volume methods (FVMs) constitute a very mature and versatile technique for discretizing partial differential equations in the form of conservation laws of varying types[2]. Advantages of FVMs include the simplicity of implementation, their local conservation properties, and the ease of coupling various PDEs in a multi-physics setting. Among various flavours of FVMs, cell based approaches, where all variables are associated only with cell centers, are particularly attractive, as all involved PDEs on a given domain are discretized using the same and the lowest possible number of degrees of freedom. In spite of their numerous favourable advantages, FVMs have seen very little adoption within the topology optimization community, where the absolute majority of numerical computations is done using finite element methods (FEMs). Despite some limited recent efforts[3,4], we have not even scratched the surface as far as our understanding of the interplay between the control in the coefficients and FVMs is concerned.

To illustrate the issues arising when FVM is applied to control in the coefficients problems, let us informally consider the following example steady-state conservation law:

$$\operatorname{div}(F(u, \nabla u; \alpha_F)) + s(u; \alpha_s) = 0, \qquad \text{in } \Omega, \tag{1}$$

where Ω is a polygonal domain in $\mathbb{R}^d$, $d \in \mathbb{N}$, $u : \Omega \to \mathbb{R}$ is a sought solution of the conservation law (1), $F : \mathbb{R} \times \mathbb{R}^d \times \mathbb{R} \to \mathbb{R}^d$ and $s : \mathbb{R} \times \mathbb{R} \to \mathbb{R}$ defines the flux and the source terms of the law, and finally $\alpha_F : \Omega \to \mathbb{R}$, $\alpha_s : \Omega \to \mathbb{R}$ are controllable coefficients entering the flux and the source terms. Let us now apply an FVM discretization to (1). We decompose Ω into polygonal control volumes $K \in \mathcal{T}$, integrate over each control volume while applying Gauss–Ostrogradsky theorem to the flux term; we finally arrive at the following formulation:

$$\int_{\partial K} F(u, \nabla u; \alpha_F) \cdot \mathbf{n} \, \mathrm{d}x + \int_K s(u; \alpha_s) \, \mathrm{d}x = 0, \qquad \forall K \in \mathcal{T}, \tag{2}$$

where $\mathbf{n}$ is an outwards directed normal for the control volume K. Suddenly we see the distinct rôles which α_F and α_s play in the FVM discretization: α_F is involved in the boundary integrals with respect to $d-1$-dimensional Lebesgue measure, whereas α_s only enters volume integrals w.r.t. d-dimensional Lebesgue measure. Of course, small w.r.t. d-dimensional Lebesgue measure perturbations to α_F may introduce very large changes to the flux integrals involved in (2), see Figure 1. Therefore, a study of the interplay between the FVM discretization and the control in the coefficients approach, where the control coefficient enters the flux integral, is warranted.

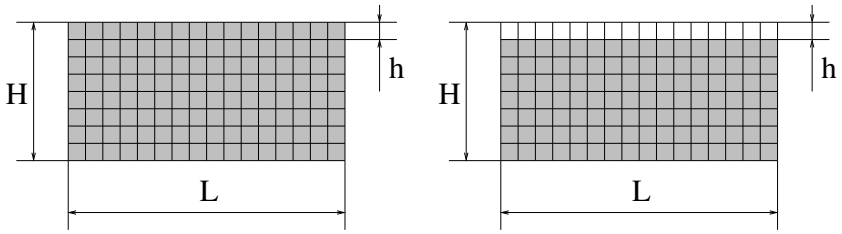

Figure 1: Modifying a control coefficient α_F or α_s on a small set of d-dimensional Lebesgue measure hL ($h \to 0$) introduces a small perturbation of the order $O(hL\Delta\alpha)$ to the volume integrals involved in conforming FEM discretizations of (1). However, the same change to α_F introduces a finite perturbation of the order $O(L\Delta\alpha)$ to the boundary integrals involved in the FVM discretization (2).

2 MODEL PROBLEM

A typical setup found in the engineering optimization problems is as follows. Let Ω be polygonal domain in $\mathbb{R}^d$, $d \in \mathbb{N}$ with a boundary $\partial\Omega = \Gamma$. Further, let $G \subset \mathcal{M}(\Omega)$ be a given subset of measurable functions $\gamma : \Omega \to [0, 1]$ closed with respect to a.e. convergence on Ω. We will be interested in numerically approximating solutions to the following minimization problem:

$$\begin{aligned} &\text{minimize} \quad c(\gamma) := \int_\Omega \mathcal{C}(x, \gamma(x), u_\gamma(x), \nabla u_\gamma(x)), \\ &\text{subject to} \quad \gamma \in G, \end{aligned} \tag{3}$$

where $u_\gamma \in H_0^1(\Omega)$ is the unique solution of the BVP

$$-\operatorname{div}[\alpha(\gamma)\nabla u_\gamma] = f, \tag{4}$$

$f \in L^2(\Omega)$, $\alpha : [0,1] \to [\underline{\alpha}, \overline{\alpha}]$ is a continuous mapping of the "design space" G to the space of the diffusion coefficients, $0 < \underline{\alpha} \leq \overline{\alpha} < +\infty$.

Additionally, assuming that G is convex and $\alpha \in C^1([0,1])$, and C is independent from ∇u, we can write the stationarity conditions for (3) as

$$Dc(\gamma^*; \gamma - \gamma^*) = \int_\Omega \frac{\partial \mathcal{C}}{\partial \gamma}(x, \gamma^*, u_{\gamma^*})(\gamma - \gamma^*)\,\mathrm{d}x + \int_\Omega \alpha'(\gamma^*)(\gamma - \gamma^*)\nabla u_{\gamma^*} \cdot \nabla \lambda_{\gamma^*}\,\mathrm{d}x, \geq 0, \tag{5}$$

$\forall \gamma \in G$, where $Dc(\gamma^*; \gamma - \gamma^*)$ is the Fréchet derivatie of c at γ^* in the direction $\gamma - \gamma^*$ and $\lambda_\gamma \in H_0^1(\Omega)$ is the unique solution to the adjoint problem

$$-\operatorname{div}[\alpha(\gamma)\nabla \lambda_\gamma] = -\frac{\partial \mathcal{C}}{\partial u}(x, \gamma, u_\gamma). \tag{6}$$

3 MAIN THEORETICAL RESULTS

We consider a sequence of admissible[2] FVM discretizations $\mathcal{T}_n$ of Ω such that the mesh size h_n goes to zero. and a sequence of finite-dimensional optimization problems P_n obtained by applying cell-based FVM-discretization to (3), (4). We establish that every limit point (with respect to a.e. convergence in Ω) of globally optimal solutions to P_n must be a globally optimal solution of the original continuous problem (3) under the assumption that discrete approximations of the admissible set G are "good enough." Under similar assumptions, limit points of sequences of first-order stationary points to P_n must satisfy the stationarity conditions (3).

Finally, we consider a different approach to stationarity. Namely, we apply a cell-based FVM discretization to (5), (6), in line with "continuous adjoint" approach[3] to topology optimization. Under the same assumptions as above, we show that limit points of the sequence of FVM-discretized stationarity conditions must be solutions to (5), that is stationary in (3).

4 NUMERICAL EXAMPLE

We consider a benchmark problem of distributing a limited amount of a material with high heat conductivity in a uniformly heated domain, which is insulated everywhere on the boundary apart from a small heat sink at the bottom where a fixed temperature is prescribed; see Figure 2. Using the developed cell based FVM discretization approach we obtain results that qualitatively match those obtained using a FEM discretization approach.

5 CONCLUSIONS AND FUTURE WORK

We have rigorously analyzed the use of cell based FVMs for discretization of control in the coefficients problems. In addition to the difficulties illustrated in Sections 1 we have to deal with the fact that finite difference approximations of fluxes are evaluated across the boundaries of the control volumes where the diffusion coefficients have jumps. Surprisingly, in spite of these difficulties we have been able to obtain certain convergence results regarding limits of global optimal solutions and stationary points, see Section 3.

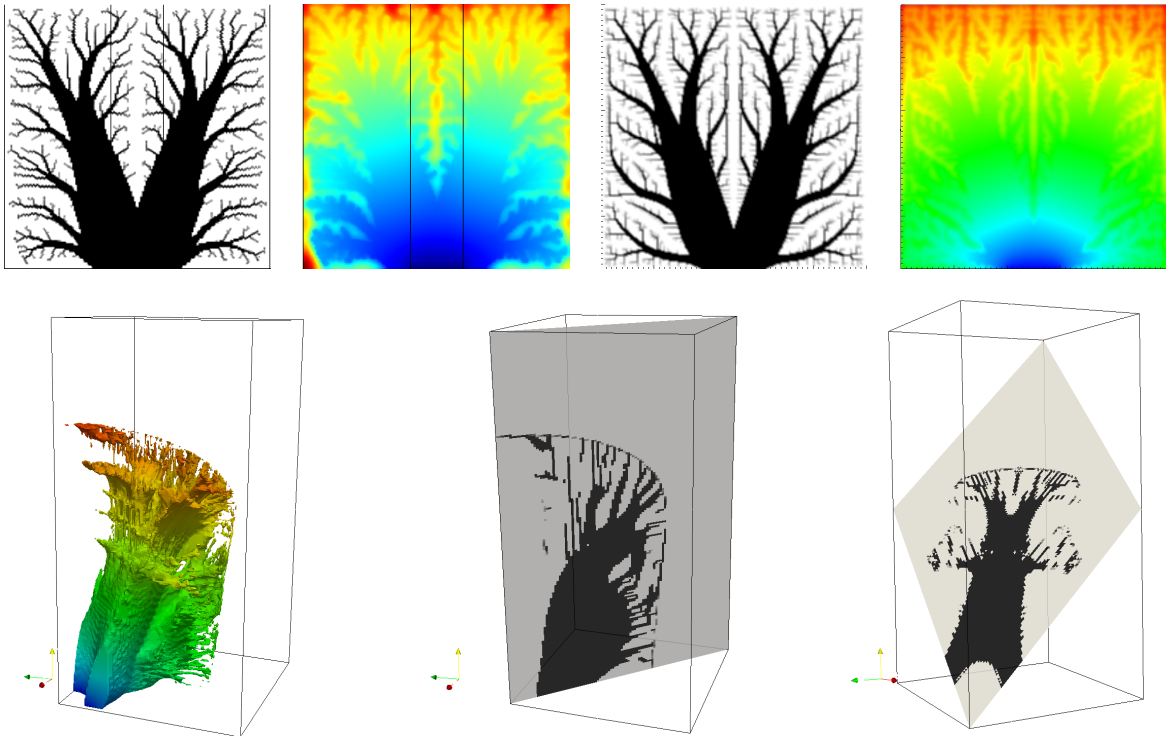

Figure 2: Top: A comparison of FEM and FVM discretizations of a benchmark problem. From left to right: optimized material layout of highly conductive material (black) within a low conductor (white) and a corresponding temperature distribution obtained using a FEM discretization; same for the FVM discretization. Bottom: a 3D equivalent of the benchmark problem discretized using a cell-based FVM. From left to right: iso-surface corresponding to interface between two conductors, coloured with the corresponding temperature values; two cutting planes throught the material distribution.

ACKNOWLEDGMENT

The authors acknowledge the support of the European Commission in the project "FLOW-HEAD: Fluid Optimisation Workflows for Highly Effective Automotive Development Processes" under theme SST.2007-RTD-1: Competitive product development.

REFERENCES

[1] Bendsøe, M. P. & Sigmund, O. *Topology Optimization: Theory, Methods, and Applications* (Springer-Verlag, Berlin, 2003).

[2] Eymard, R., Gallouët, T. & Herbin, R. Finite volume methods. In Ciarlet, P. G. & Lions, J. L. (eds.) *Handbook of Numerical Analysis*, vol. 7, 713–1020 (North Holland, 2000).

[3] Othmer, C. A continuous adjoint formulation for the computation of topological and surface sensitivities of ducted flows. *Internat. J. Numer. Methods Fluids* **58** (2008).

[4] Gersborg-Hansen, A., Bendsøe, M. & Sigmund, O. Topology optimization of heat conduction problems using the finite volume method. *Struct. Multidiscip. Optim.* **31**, 251–259 (2006).

23rd Nordic Seminar on Computational Mechanics
NSCM-23
A. Eriksson and G. Tibert (Eds)

NONLINEAR BUCKLING OPTIMIZATION INCLUDING "WORST" SHAPE IMPERFECTIONS

E. LUND AND E. LINDGAARD

Department of Mechanical and Manufacturing Engineering,
Aalborg University, Denmark
e-mail: {el,elo}@me.aau.dk, web page: http://www.me.aau.dk

Key words: Composite Structures, Nonlinear Buckling Optimization, Imperfections.

Summary. This paper focuses on nonlinear buckling optimization of multi-material laminated composite structures, where sensitivity to geometric imperfections is taken into account. The optimization method proposed performs gradient based buckling load optimization on a "worst" case shape imperfect geometry where the "worst" shape imperfections are also determined using gradient based optimization techniques. The approach is demonstrated on several examples.

1 INTRODUCTION

The design problem of maximizing the load capacity of compressively loaded laminated composite structures is challenging due to the complex structural performance of general purpose engineering structures. The laminated composites are typically thin-walled shell-like structures that are sensitive to geometric imperfections when loaded in compression. In this work focus is put on this design problem using a gradient based optimization approach, and the formulation includes the determination of the "worst" shape imperfection, see Section 3. The laminate design problem is solved using the Discrete Material Optimization (DMO) approach, see [1, 2], where the discrete problem of optimal distribution of different materials in multi-layered composite shell structures is converted to a continuous problem by introducing interpolation functions with penalization. In this way material properties can be computed as weighted sums of candidate materials, and the topology design problem can be solved using standard gradient based optimization techniques.

2 NONLINEAR BUCKLING ANALYSIS AND DESIGN SENSITIVITY ANALYSIS

The analysis and optimization procedure for nonlinear buckling load optimization described in [3] is applied, i.e. optimization w.r.t. stability is accomplished by including the nonlinear response by a path tracing analysis, after the arc-length method, using the Total Lagrangian formulation.

Structural stability/buckling is estimated in terms of geometrically nonlinear analyses and restricted to limit point instability, despite that the presented formulas also work well for bifurcation points. In addition, bifurcation instability is in many cases transformed into limit point instability with the introduction of small disturbances/imperfections to the system. The

proposed procedure for nonlinear buckling analysis, considering limit points, is schematically shown in Fig. 1 and consists of the steps stated in Algorithm 1.

Algorithm 1 Pseudo code for the nonlinear buckling analysis

1: Geometrically nonlinear (GNL) analysis by arc-length method
2: Monitor and detect limit point during GNL analysis
3: Re-set all state variables to configuration at load step just before limit point
4: Perform eigenbuckling analysis on deformed configuration at load step before limit point

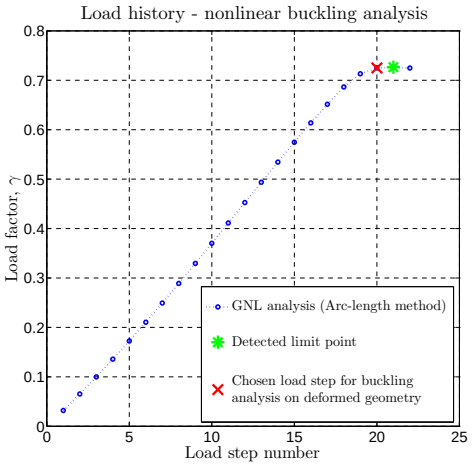

Figure 1: Detection of limit load in step 2 and chosen equilibrium point for the nonlinear buckling problem.

The nonlinear path tracing analysis is stopped when a limit point is encountered and the critical load is approximated at a precritical load step by performing an eigenbuckling analysis on the deformed configuration by extrapolating the nonlinear tangent stiffness to the critical point.

Design sensitivities of the critical load factor are obtained semi-analytically by either the direct differentiation approach or the adjoint approach on the approximate eigenvalue problem described by discretized finite element equations.

3 OPTIMIZATION FORMULATION

The determination of the "worst" imperfection for a given structure is formulated as an optimization problem whereby imperfections are directly introduced in the analysis model, see also [4] where the approach is applied in connection with fiber angle optimization of composite structures. By including geometric imperfections, unstable bifurcation points, if present, are in general avoided and converted into limit points. The "worst" imperfection is in this study defined as the "worst" case imperfection shape for a structure, i.e. an imperfection shape which yields the lowest limit load. The imperfections are represented by a linear combination of base shapes $\boldsymbol{\Psi}_l$ where the base shapes in this study are constructed from a number of buckling modes. The geometry of the imperfect structures is thus described by finite element nodal point coordinates

$\mathbf{X}$ as

$$\mathbf{X} = \mathbf{X}_p + \overline{\mathbf{X}} \qquad \text{where} \qquad \overline{\mathbf{X}} = \sum_{l=1}^{N} \alpha_l \mathbf{\Psi}_l \tag{1}$$

$\mathbf{X}_p$ is the initial perfect geometry, α_l are the unknown shape parameters, $\mathbf{\Psi}_l$ are the base shapes, and $\overline{\mathbf{X}}$ the total imperfection vector. The unknown shape parameters α_l are obtained as a solution to following the optimization problem.

The mathematical programming problem for minimizing the lowest critical load and determining the "worst" imperfection shape is a min-min problem which is solved directly using the following optimization formulation:

$$\begin{aligned} &\text{Objective :} && \min_{\boldsymbol{\alpha}} \min \ \ \gamma_j^c, \quad j = 1, 2, \ldots \\ &\text{Subject to :} && \text{state equations} \\ & && \left|\overline{\mathbf{X}}^m\right| \leq e_0^m \quad ...m \in [n_1, n_2, ..., n_{cp}] \\ & && \underline{\alpha_l} \leq \alpha_l \leq \overline{\alpha_l}, \quad l = 1, \ldots, N \end{aligned}$$

where $\alpha_l,\ l = 1, \ldots, N$ are the shape design variables and the lowest of the critical load factors, $\gamma_j^c,\ j = 1, 2, \ldots$, is minimized. The maximum amplitudes of the total imperfections are limited by e_0^m, where m refers to the m^{th} constraint, typically obtained from manufacturing experience. The mathematical programming problem is solved by the Method of Moving Asymptotes (MMA) by Svanberg [5].

In the optimization approach the "worst" imperfection problem is solved first, and then a max-min problem of maximizing the load factor is solved for the laminate design variables x_i, while the "worst" imperfect geometry is fixed. This problem is formulated using the bound formulation [6] where the artificial variable and objective function β is introduced:

$$\begin{aligned} &\text{Objective :} && \max_{\boldsymbol{x}, \beta} \ \ \beta \\ &\text{Subject to :} && \gamma_j^c \geq \beta, \quad j = 1, \ldots, N_\lambda \\ & && \text{state equations} \\ & && \underline{x_i} \leq x_i \leq \overline{x_i}, \quad i = 1, \ldots, I \end{aligned}$$

By introducing the bound parameter β the lowest N_λ eigenvalues are considered when solving the max-min problem of maximizing the lowest eigenvalue, and the possibility of crossing eigenvalues (mode switching) and creation of multiple eigenvalues is taken into account during the optimization process. The min-min problem seems to have less problems with crossing eigenvalues during the design optimization process and thus no precautions are taken.

4 EXAMPLE

The optimization approach has been demonstrated for several engineering examples including nonlinear buckling load optimization of parts of wind turbine blades. One example considered is a main spar as illustrated on Fig. 2.

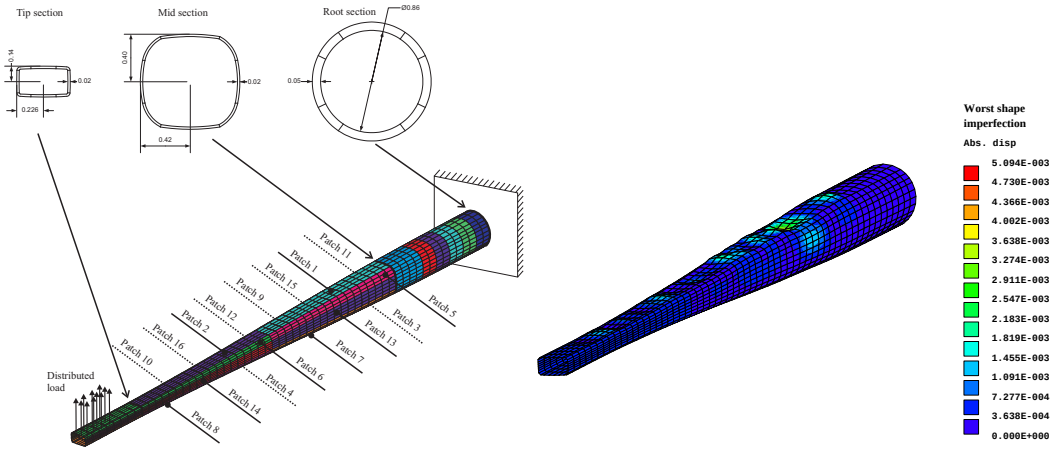

Figure 2: Left: the definition of the main spar design problem and the patches used for the laminate parameterization. Right: "worst" shape imperfections (scaled with a factor of 25) for the initial design.

It is interesting to note for this example that the scaling factor α_1 on buckling mode 1 is nearly zero when solving for the "worst" imperfection shape. Thus, the common approach of considering the "worst" imperfection shape as a scaling of the lowest bifurcation mode would not give the most critical shape in this case. For this example the DMO optimization approach is used for the laminate optimization problem. In the first iteration, the limit load factor γ_1^c is reduced from 1.91 to 1.60 by "worst" shape imperfection for fixed DMO variables. Next the limit load factor γ_1^c is increased from 1.60 to 3.16 by DMO optimization while fulfilling mass and compliance constraints for the problem. This optimization process of switching between the two subproblems can be continued, and in general convergence is reached within 3-4 global iterations, see examples in [4]. This procedure leads to robust designs, i.e. optimal laminate designs that are least sensitive to geometric imperfections.

REFERENCES

[1] J. Stegmann and E. Lund, Discrete material optimization of general composite shell structures. *Internation Journal for Numerical Methods in Engineering*, 62(14):2009–2027, 2005.

[2] E. Lund, Buckling topology optimization of laminated multi-material composite shell structures. *Composite Structures*, 91:158–167, 2009.

[3] E. Lindgaard and E. Lund, Nonlinear buckling optimization of composite structures. *Computer Methods in Applied Mechanics and Engineering*, 199(37-40): 2319–2330, 2010.

[4] E. Lindgaard, E. Lund and K. Rasmussen, Nonlinear buckling optimization of composite structures considering "worst" shape imperfections. *International Journal of Solids and Structures*, 47:3186–3202, 2010.

[5] K. Svanberg, Method of moving asymptotes - a new method for structural optimization. *Internation Journal for Numerical Methods in Engineering*, 24:359–373, 1987.

[6] M. P. Bendsøe, N. Olhoff and J. Taylor, A variational formulation for multicriteria structural optimization. *Journal of Structural Mechanics*, 11:523–544, 1983.

23rd Nordic Seminar on Computational Mechanics
NSCM-23
A. Eriksson and G. Tibert (Eds)

A PHASE FIELD BASED TOPOLOGY OPTIMIZATION SCHEME

M. WALLIN*, M. RISTINMAA† AND H. ASKFELT†

* † Department of Solid Mechanics
Lund University
SE-21100 Lund
e-mail: Mathias.Wallin@solid.lth.se, web page: http://www.solid.lth.se/

Key words: Topology optimization, Phase-field, Cahn-Hilliard.

Summary. A topology optimization method allowing for perimeter control is presented. The procedure is based on a functional in terms of the material density distribution and the displacement field. The optimum of the functional is found by using the Cahn-Hilliard phase-field model. To solve the problem use is made of the finite element method.

1 Introduction

The SIMP (Simple Isotropic Material Penalization) formulation used for topology optimization is known to have the major deficiency of lacking the existence of a solution for the continuum problem. In a numerical implementation using the finite element method this deficiency appears as a severe mesh-dependence, i.e. the optimized structure will tend to be finer as the finite element mesh is refined. The remedy to this problem is to introduce a length scale into the formulation.

In the current paper we will present a topology optimization procedure that is based on minimizing a functional that in addition to the strain energy also includes the cost for creation of new surfaces as well as the cost for having a diffuse material distribution. Moreover, the constraints of preserving the total amount of material as well as satisfying the equilibrium is introduced in the functional via two Lagrangian multipliers. This minimization problem is solved using the Cahn-Hilliard framework in conjuction with an adaptive finite element method.

2 Formulating a new method

In this paper the stiffness of a structure within the domain Ω is taken as the objective of the optimization. The maximum stiffness approach can be reformulated as a minimization of the (macroscopic) structural compliance C defined as

$$C = \int_{\partial\Omega_t} t_i u_i dS + \int_{\Omega} b_i u_i dV \tag{1}$$

where t_i is the traction vector and b_i the body force vector. The displacement vector is denoted u_i and $\partial\Omega_t$ being the part of the boundary where the traction is applied. The minimization

of the compliance can upon using Cauchy's formula and Gauss's theorem be expressed as a minimization of the strain energy since

$$C = \int_\Omega w(\rho, \epsilon_{ij}) dV \quad \text{where} \quad w(\rho, \epsilon_{ij}) = \epsilon_{ij} D_{ijkl} \epsilon_{kl} \tag{2}$$

where ρ represents the density. To avoid singularities in the mechanical problem the stiffness tensor D_{ijkl} is defined as

$$D_{ijkl} = g(\rho) D^0_{ijkl} \tag{3}$$

where $g(\rho)$ captures a linear dependence for $\rho > 0$ while leaving a residual stiffness for small and negative $\rho < 0$, $g(\rho)$ is illustrated in Fig 1.a.

In order to avoid diffuse designs intermediate values of ρ are penalized. The penalization is here performed by introducing a "cost" for designs where ρ is not equal to 0 or 1. The cost function F is taken as a double well function and is illustrated in Fig 1.b.

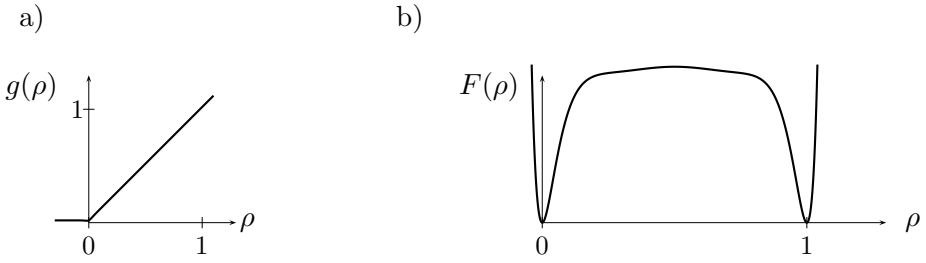

Figure 1: Illustration of the residual stiffness function g and cost function F

A consequence of introducing the cost function F is that the method becomes mesh dependant. To resolve this issue we introduce another penalization which aims to penalize all gradients $\rho_{,i}$, i.e.

$$\int_\Omega \rho_{,i} \rho_{,i} d\Omega \tag{4}$$

Combining the objective function with the penalizations we end up with the new objective functional E

$$E(\rho, u_i) = \int_\Omega \left(F(\rho) + \frac{\gamma}{2} \rho_{,i} \rho_{,i} \right) dV + \eta \int_\Omega w(\rho, \epsilon_{ij}) dV \tag{5}$$

Here the parameter γ introduces a length-scale into the formulation and thereby allowing control over the total perimeter of the design. For $\gamma = 0$ a problem similar to the SIMP problem is recovered. The parameter η defines the influence of the strain energy on the objective functional. When minimizing E the following constraints are imposed

- The total amount of material that is available for the design is given by V_0, i.e. the material density function is subject to the constraint

$$\int_\Omega \rho(\boldsymbol{x}) dV - V_0 = 0 \tag{6}$$

- The local form of the static equilibrium equations should be fulfilled i.e.

$$\sigma_{ij,j} + b_i = 0, \quad \forall \boldsymbol{x} \in \Omega \tag{7}$$

  where σ_{ij} is the Cauchy stress tensor and b_i is the body force vector.

Combining the objective functional E (cf. (5)) with the constraints (6) and (7) allow us to construct a functional Ψ for which we will seek a stationarity point

$$\Psi(\rho, u_i, \lambda_k^e, \lambda^c) = E(\rho, u_i) + \int_V \lambda_i^e \left(\sigma_{ij,j} + b_i\right) dV + \lambda^\rho \left(\int_V \rho dV - V_0\right) \tag{8}$$

where the vector field λ_i^e is a Lagrangian multiplier field that enforces equilibrium and λ^ρ is a Lagrangian multiplier that enforces the total volume of the body being equal V_0.

3 Solution procedure

An extremum to (8) can be found by using the Cahn-Hilliard phase-field model which describes the diffusion of material over time. The Cahn-Hilliard model is defined by:

$$\dot{\rho} + J_{j,j} = 0 \tag{9}$$

$$\rho_{,j} n_j = \mu_{,j} n_j = 0 \quad \text{along} \quad \partial\Omega \tag{10}$$

where the flux vector J_j here is defined as $J_j = -\mu_{,j}$ and $\mu = \frac{\delta \psi}{\delta c}$

Application of the Cahn-Hilliard model to the current problem results in that the rate of the functional Ψ becomes

$$\dot{\Psi} = -\int_\Omega \mu_{,i} \mu_{,i} dV \leq 0 \tag{11}$$

With (11) we conclude that the Cahn-Hilliard model will guide us to a state that minimizes the functional (5). It should be noted that the present approach only provides a local minimum and not a global minimum to the structural optimization problem. This feature is, however, shared between most structural optimization formulations.

Numerically we solve this problem by a mixed finite element formulation using the field variables ρ, μ and the displacements u_i. The time discretization is based on a backward-Euler scheme and the residual equations are solved using the Newton-Raphson scheme.

4 Results

To demonstrate the presented scheme we apply the procedure to a well-known problem. The structure considered consists of a cantilever beam loaded with a point load F, cf. Fig. 2a. The initial material distribution is shown in Fig. 2b.

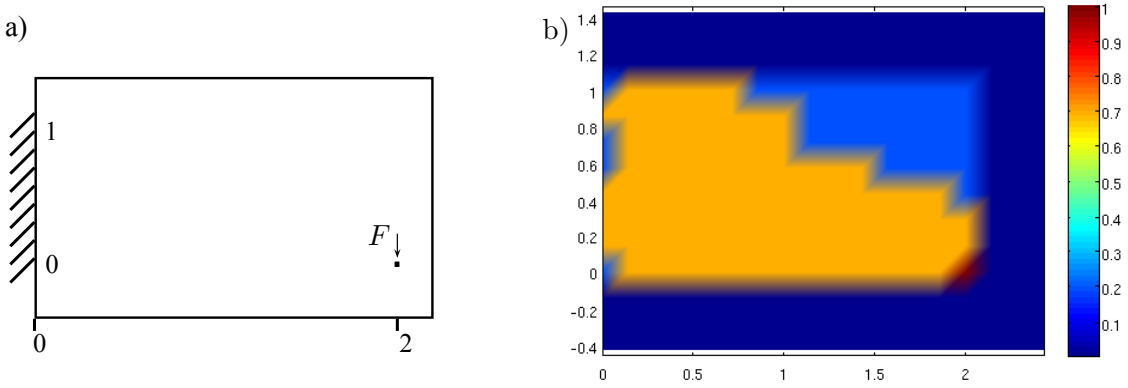

Figure 2: a) Illustration of the design space, b) Initial material distribution

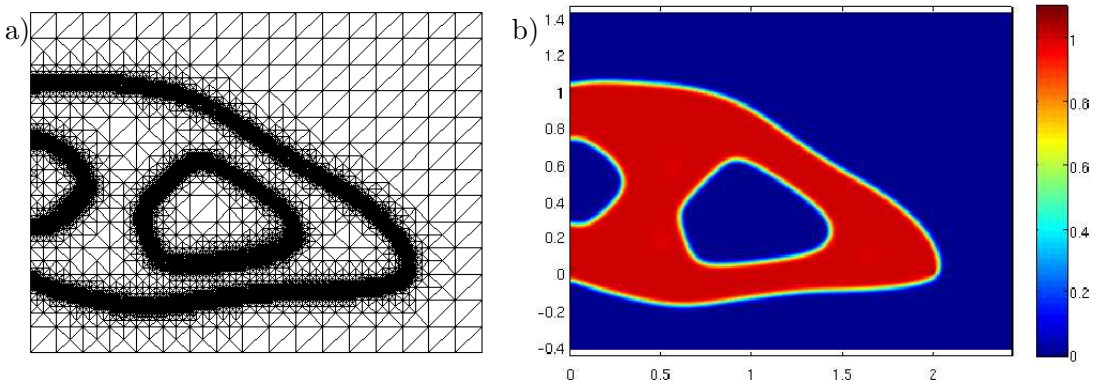

Figure 3: a) Finite element mesh after optimization b) Material distribution after optimization

As can be seen in Fig. 3b the optimized density distribution is close to $\rho \in \{0, 1\}$ with exception in the thin interface between regions of $\rho = 1$ and $\rho = 0$. Moreover from Fig. 3a it can be seen that the interface is resolved using approximately 10 elements. At the point where the load is applied a density slightly above 1 can be observed. In Fig. 3b the optimal structure is shown where the underlying finite element mesh consists of approximately 30000 elements and the mesh is adaptively chosen to follow the interface.

23rd Nordic Seminar on Computational Mechanics
NSCM-23
A. Eriksson and G. Tibert (Eds)

A MASS-CONSERVING FINITE ELEMENT METHOD FOR THE BRINKMAN PROBLEM

JUHO KÖNNÖ* AND ROLF STENBERG*

*Department of Mathematics and Systems Analysis
Aalto University
00076 AALTO, Espoo, Finland
e-mail: juho.konno@tkk.fi, rolf.stenberg@tkk.fi

Key words: Finite element method, porous flow, Brinkman problem, postprocessing, a posteriori.

Summary. In this paper, we analyze a non-standard finite element method for the Brinkman equation for viscous porous flow. We present complete a priori and a posteriori results along with some numerical examples.

1 Introduction

In soil mechanics, the Brinkman equations describe the flow of a viscous fluid in a porous matrix. Typical applications lie in the modelling of oil reservoirs, groundwater flow and in filtration technology. Mathematically, the Brinkman model is a parameter-dependent combination of the Darcy and Stokes flow models. Inclusion of viscosity plays a paramount role in the presence of large vugs or cracks, both of which are typical in oil reservoirs, in particular. We study the application of $\boldsymbol{H}(\mathrm{div})$-conforming finite elements designed for the Darcy problem to the more complicated Brinkman problem. This constitutes a non-standard approximation of the Brinkman problem. To obtain a stable method, the so-called Nitsche's method first introduced in[1] is used.

In addition, we use a postprocessing scheme to increase the accuracy of the pressure approximation to match that of the velocity approximation. This allows us to introduce a residual-based a posteriori estimator, which is both reliable and effective. We will verify the results numerically. Proofs for all the theoretical results can be found in[2] and the references therein.

2 The Brinkman model

For a derivation of the Brinkman equations, see e.g.[3]. The main difference to the simpler Darcy model is the introduction of viscosity to the equations. Let $\boldsymbol{u}$ be the velocity field of the fluid, p the pore pressure, and $\Omega \in \mathbb{R}^n$, with $n = 2, 3$. Denoting by the parameter t the effective viscosity of the fluid, the Brinkman equations are

$$-t^2 \Delta \boldsymbol{u} + \boldsymbol{u} + \nabla p = \boldsymbol{f}, \quad \text{in } \Omega, \tag{1}$$

$$\mathrm{div}\ \boldsymbol{u} = g, \quad \text{in } \Omega. \tag{2}$$

3 The mixed method and the norms

Mixed finite element discretization of the problem is based on finite element spaces $\boldsymbol{V}_h \times Q_h \subset \boldsymbol{H}(\mathrm{div}, \Omega) \times L^2_0(\Omega)$ of piecewise polynomial functions with respect to $\mathcal{K}_h$. We will focus here on the Brezzi-Douglas-Marini (BDM) family of elements[4].

To assure the stability and conformity of the approximation, we use Nitsche's method[5,1] with a suitably chosen stabilization parameter α. We define the following mesh-dependent bilinear form

$$\mathcal{B}_h(\boldsymbol{u}, p; \boldsymbol{v}, q) = a_h(\boldsymbol{u}, \boldsymbol{v}) - (\mathrm{div}\ \boldsymbol{v}, p) - (\mathrm{div}\ \boldsymbol{u}, q), \tag{3}$$

in which

$$\begin{aligned} a_h(\boldsymbol{u}, \boldsymbol{v}) = (\boldsymbol{u}, \boldsymbol{v}) + t^2 \sum_{K \in \mathcal{K}_h} (\nabla \boldsymbol{u}, \nabla \boldsymbol{v})_K \\ + t^2 \sum_{E \in \mathcal{E}_h} \{ \frac{\alpha}{h_E} \langle [\![\boldsymbol{u} \cdot \boldsymbol{\tau}]\!], [\![\boldsymbol{v} \cdot \boldsymbol{\tau}]\!] \rangle_E - \langle \{ \frac{\partial \boldsymbol{u}}{\partial n} \}, [\![\boldsymbol{v} \cdot \boldsymbol{\tau}]\!] \rangle_E - \langle \{ \frac{\partial \boldsymbol{v}}{\partial n} \}, [\![\boldsymbol{u} \cdot \boldsymbol{\tau}]\!] \rangle_E \}. \end{aligned} \tag{4}$$

Then the discrete problem is to find $\boldsymbol{u}_h \in \boldsymbol{V}_h$ and $p_h \in Q_h$ such that

$$\mathcal{B}_h(\boldsymbol{u}_h, p_h; \boldsymbol{v}, q) = (\boldsymbol{f}, \boldsymbol{v}) + (g, q), \quad \forall (\boldsymbol{v}, q) \in \boldsymbol{V}_h \times Q_h. \tag{5}$$

We introduce the following mesh-dependent norms for the problem. For the velocity we use

$$\|\boldsymbol{u}\|^2_{t,h} = \|\boldsymbol{u}\|^2 + t^2 \left(\sum_{K \in \mathcal{K}_h} \|\nabla \boldsymbol{u}\|^2_{0,K} + \sum_{E \in \mathcal{E}_h} \frac{1}{h_E} \|[\![\boldsymbol{u} \cdot \boldsymbol{\tau}]\!]\|^2_{0,E} \right), \tag{6}$$

and for the pressure

$$|\!|\!| p |\!|\!|^2_{t,h} = \sum_{K \in \mathcal{K}_h} \frac{h_K^2}{h_K^2 + t^2} \|\nabla p\|^2_{0,K} + \sum_{E \in \mathcal{E}_h} \frac{h_E}{h_E^2 + t^2} \|[\![p]\!]\|^2_{0,E}. \tag{7}$$

Note that both of the norms are both mesh- and parameter-dependent.

4 Postprocessing method

In this section we present a postprocessing method for the pressure in the spirit of[6]. We seek the postprocessed pressure in an augmented space $Q_h^* \supset Q_h$, defined as

$$Q_h^* = \{ q \in L^2(\Omega) \mid q|_K \in P_{k+1}(K)\ \forall K \in \mathcal{K}_h \}. \tag{8}$$

The postprosessing method reads: Find $p_h^* \in Q_h^*$ such that

$$P_h p_h^* = p_h \tag{9}$$

$$(\nabla p_h^*, \nabla q)_K = (t^2 \Delta \boldsymbol{u}_h - \boldsymbol{u}_h + \boldsymbol{f}, \nabla q)_K, \quad \forall q \in (I - P_h) Q_h^*|_K. \tag{10}$$

For the postprocessed solution, we have the following a priori estimate. Note, that at the Darcy limit we get one extra order of convergence.

$$\|\boldsymbol{u} - \boldsymbol{u}_h\|_{t,h} + |\!|\!| p - p_h |\!|\!|_{t,h} \leq C h^{k+1} (\|\boldsymbol{u}\|_{k+1} + t \|\boldsymbol{u}\|_{k+2}). \tag{11}$$

5 A posteriori estimates

In this section we present a residual-based a posteriori estimator for the postprocessed solution. It should be noted that the postprocessing procedure is vital for a properly functioning estimator. We divide the estimator into two distinct parts, one defined over the elements and one over the edges of the mesh. The elementwise and edgewise estimators are defined as

$$\eta_K^2 = \frac{h_K^2}{h_K^2+t^2}\| - t^2\Delta \boldsymbol{u}_h + \boldsymbol{u}_h + \nabla p_h^* - \boldsymbol{f}\|_{0,K}^2 + (t^2+h_K^2)\|g - P_h g\|_{0,K}^2, \tag{12}$$

$$\eta_E^2 = \frac{t^2}{h_E}\|[\![\boldsymbol{u}_h\cdot\boldsymbol{\tau}]\!]\|_{0,E}^2 + \frac{h_E}{h_E^2+t^2}\|[\![p_h^*]\!]\|_{0,E}^2 + \frac{h_E}{h_E^2+t^2}\|[\![t^2\frac{\partial \boldsymbol{u}_h}{\partial \boldsymbol{n}}]\!]\|_{0,E}^2. \tag{13}$$

The global estimator is

$$\eta = \left(\sum_{K\in\mathcal{K}_h}\eta_K^2 + \sum_{E\in\mathcal{E}_h}\eta_E^2\right)^{1/2}. \tag{14}$$

Note, that setting $t=0$ gives the estimator for the Darcy problem[6]. In[2] it is show, that the estimator is both an upper and a lower bound for the error in the displacement $\boldsymbol{u}_h$ and in the postprocessed pressure p_h^*, uniformly in the parameter t.

6 Numerical results

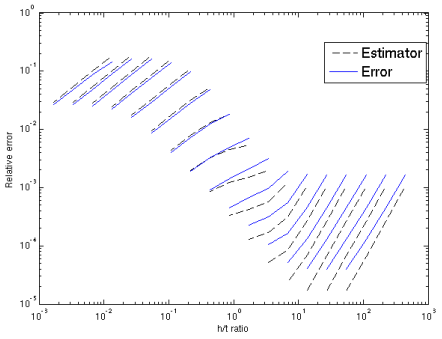

Figure 1: Relative error in the mesh dependent norm for $\beta = 3.1$

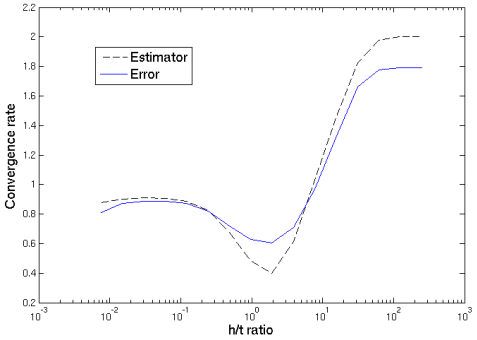

Figure 2: Converge rate for different values of t for $\beta = 3.1$

In polar coordinates (r,Θ) the pressure is chosen as

$$p(r,\Theta) = r^\beta \sin(\beta\Theta) + C, \tag{15}$$

where the constant C is chosen to give a zero-mean pressure. Now we have $p \in H^{1+\beta}(\Omega)$, and hence $\boldsymbol{u} \in [H^\beta(\Omega)]^n$. In the following, we have tested the convergence with a wide range of different parameter values, and the results are plotted with respect to the ratio of the viscosity parameter t to the mesh size h. Our aim is to demonstrate numerically, that the change in the nature of the problem indeed occurs at $t=h$, and that the convergence rates are optimal in both

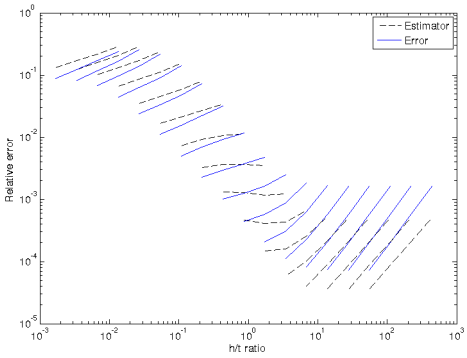

Figure 3: Relative error in the mesh dependent norm for $\beta = 1.52$

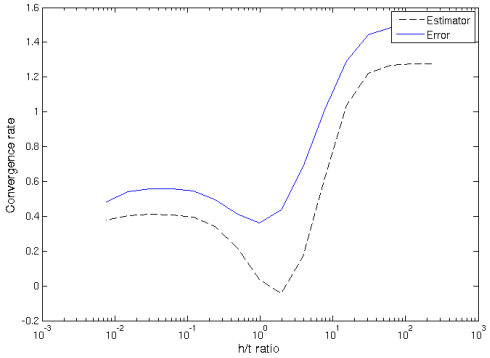

Figure 4: Converge rate for different values of t for $\beta = 1.52$

of the limiting cases. We choose $\beta = 3.1$ (Figures 1 and 2) and $\beta = 1.52$ (Figures 3 and 4)to test the convergence rates. Evidently, we have the convergence rates predicted by the theory for both cases, and in particular the problem type changes when the parameter equals the mesh size.

7 Conclusions

We derived both a priori and a posteriori bounds that are both optimal and robust in t by using a simple elementwise post-processing technique. In additions, our numerical results verify the performance of the method for all parameter values.

REFERENCES

[1] Nitsche, J. Über ein Variationsprinzip zur Lösung von Dirichlet-Problemen bei Verwendung von Teilräumen, die keinen Randbedingungen unterworfen sind. *Abh. Math. Sem. Univ. Hamburg* **36**, 9–15 (1971). Collection of articles dedicated to Lothar Collatz on his sixtieth birthday.

[2] Könnö, J. & Stenberg, R. Analysis of H(div)-conforming finite elements for the Brinkman problem. *Helsinki University of Technology Institute of Mathematics Research Report A 582 (2010)* **Submitted for publication**.

[3] Arbogast, T. & Lehr, H. L. Homogenization of a Darcy-Stokes system modeling vuggy porous media. *Comput. Geosci.* **10**, 291–302 (2006).

[4] Brezzi, F. & Fortin, M. *Mixed and Hybrid Finite Element Methods* (Springer-Verlag, 1991).

[5] Juntunen, M. & Stenberg, R. Analysis of finite element methods for the Brinkman problem. *Calcolo* (2009). DOI:10.1007/s10092-009-0017-6.

[6] Lovadina, C. & Stenberg, R. Energy norm a posteriori error estimates for mixed finite element methods. *Math. Comp.* **75**, 1659–1674 (electronic) (2006).

23rd Nordic Seminar on Computational Mechanics
NSCM-23
A. Eriksson and G. Tibert (Eds)

MODELING OF MASS TRANSFER IN THE MICRO-STRUCTURE OF CONCRETE

TOWARDS COMPUTATIONAL HOMOGENIZATION WITHIN A FE^2- STRATEGY

F. NILENIUS[†‡*], F. LARSSON[†], K. LUNDGREN[‡] AND K. RUNESSON[†]

[†]Chalmers University of Technology
Department of Applied Mechanics
Hörsalsvägen 7B, 412 96 Göteborg, Sweden

[‡]Chalmers University of Technology
Department of Civil and Environmental Engineering
Sven Hultins gata 8A, 412 96 Göteborg, Sweden

[*]e-mail: filip.nilenius@chalmers.se

Key words: Concrete, Diffusion, Transient, Micro-structure

Summary. Mass transfer in the heterogenous micro-structure of concrete is modeled, as a key feature in establishing a multiscale model. The macro-scale properties are then obtained by suitable homogenization of the micro-scale response. Numerical results are presented for the micro-scale setup.

1 INTRODUCTION

Chloride ion ingress in concrete is of great concern for concrete structures as the ions can initiate corrosion of embedded reinforcement bars. The micro-scale constituents of concrete are the cement paste and gravel, and the porosity of the cement paste allows for transport of the chloride ions. Furthermore, the transport of chloride ions within the cement paste is nonlinearly coupled to the transport of moisture. Due to the inherent coupling, and the strongly heterogenous micro-structure of concrete, it is of interest to find a suitable homogenization tool in order to simulate mass transfer on the macro-scale level.

2 PROBLEM FORMULATION

The principle of mass balance requires that the change of any conserved quantity in an arbitrary domain, $\Omega_\square$, must equal the flux of that same quantity across the boundaries of $\Omega_\square$. This leads to the initial boundary value problem, stated on the micro-scale as

$$\mathrm{d}_t \Phi_v + \boldsymbol{q_v} \cdot \boldsymbol{\nabla} = 0 \quad \text{in}\, \Omega_\square \times [0,T] \tag{1}$$

$$\mathrm{d}_t \Phi_C + \boldsymbol{q_C} \cdot \boldsymbol{\nabla} = 0 \quad \text{in}\, \Omega_\square \times [0,T] \tag{2}$$

where $\Phi_v(v)$ is the moisture content, $\Phi_C(C)$ is the chloride content, $\boldsymbol{q_v}(\boldsymbol{\nabla} v, \boldsymbol{\nabla} C; v, C)$ is the flux of moisture and $\boldsymbol{q_C}(\boldsymbol{\nabla} v, \boldsymbol{\nabla} C; v, C)$ is the flux of chloride ions. Eqs. (1) and (2) are complemented

Figure 1: Image showing the strongly heterogenous micro-structure of concrete. The visible pores of the cement paste matrix allow for mass transfer.

with appropriate boundary values and initial conditions. It thus follows from the formulation that the vapor content, $v = v(\boldsymbol{x}, t)$, and the chloride concentration, $C = C(\boldsymbol{x}, t)$, are the two primary unknown scalar fields of interest.

The explicit choice of constitutive relations for the flux vectors is taken as[1]

$$\boldsymbol{q}_v = -(\varepsilon_C D_C \boldsymbol{\nabla} C + D_v \boldsymbol{\nabla} v) \tag{3}$$

$$\boldsymbol{q}_C = -(D_C \boldsymbol{\nabla} C + \varepsilon_v D_v \boldsymbol{\nabla} v) \tag{4}$$

where $D_v(v)$ and $D_C(v, C)$ are diffusion coefficients and ε_v and ε_C are coupling parameters. Hence, the choice of constitutive relations cross-couples eqs. (1) and (2). Constitutive relations for the moisture content, $\Phi_v(v)$, and chloride content, $\Phi_C(C)$, have been taken from the literature[2,3].

2.1 Variational formulation

By employing the cG(1)dG(0) method for solving eq. (1) and (2), the variational problems read: Find $v(\boldsymbol{x}, t), C(\boldsymbol{x}, t) \in \Omega$ such that

$$R_v({}^n v, {}^n C) \overset{\text{def}}{=} \big({}^n\Phi_v, \delta v\big) - \big({}^{n-1}\Phi, \delta v\big) - \Delta t\big({}^n\boldsymbol{q}_v, \boldsymbol{\nabla}\delta v\big) + \Delta t \int_\Gamma {}^n q_n \delta v \mathrm{d}\Gamma = 0 \tag{5}$$

$$R_C({}^n v, {}^n C) \overset{\text{def}}{=} \big({}^n\Phi_C, \delta C\big) - \big({}^{n-1}\Phi, \delta C\big) - \Delta t\big({}^n\boldsymbol{q}_C, \boldsymbol{\nabla}\delta C\big) + \Delta t \int_\Gamma {}^n q_n \delta C \mathrm{d}\Gamma = 0 \tag{6}$$

where $(\bullet, \bullet)$ denotes the inner product and $R_\bullet$ is the residual, for each time step, in terms of the conserved quantities v and C. Additionally, δv and δC denote a variation of vapor and chloride

concentration, respectively. Eqs. (5) and (6) are linearized and solved using Newton's method, where Newton iterations are performed until pre-defined tolerance levels of the residuals, R_v and R_C, are reached.

2.2 FE- discretization

Eqs. (5) and (6) are FE- discretizised in standard fashion with proper account of the heterogenous micro-structure of concrete. In this model, the cement paste matrix and the ballast are separated between in terms of conservation properties and diffusion coefficients. In practice, the storing capacity and diffusion in the ballast are ignored. Thus, the transport of moisture and chloride ions only take place in the cement paste matrix.

Additionally, the interface between cement paste and ballast, in the literature called ITZ, is accounted for in the model. The interface is of importance as it consists of cement paste with locally much greater porosity, allowing for higher diffusion rate. In the model, the interface is represented as 1D elements having a numerically higher diffusion coefficient than the remaining cement paste matrix.

2.3 Numerical results

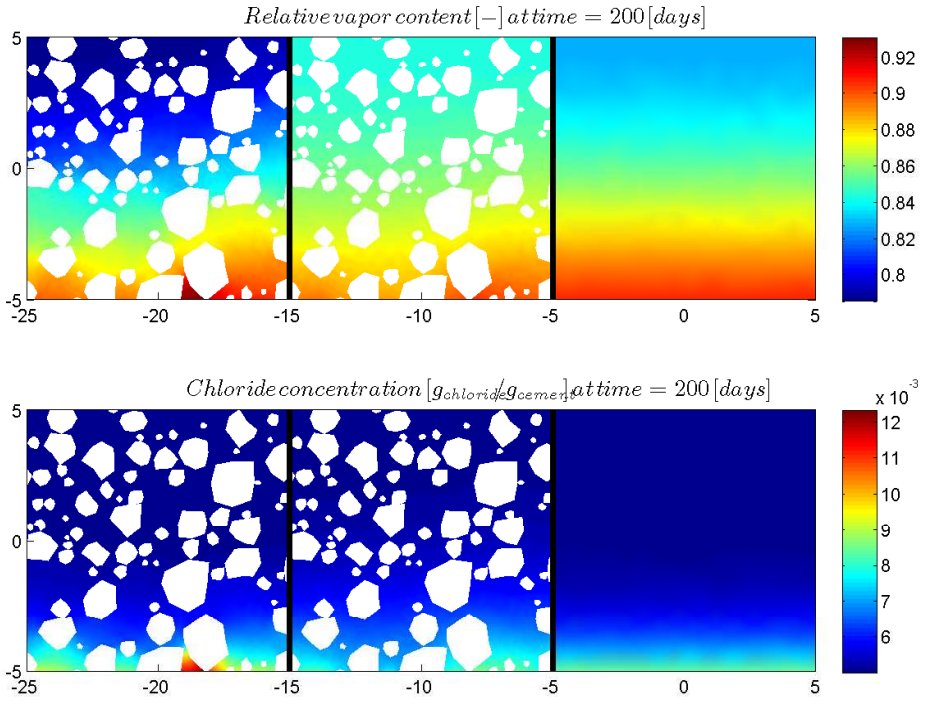

Figure 2: Numerical results for vapor content and chloride concentration. Convective boundary conditions are applied to the lower boundary. All other boundaries are insulated.

In Figure 2, numerical results are presented for different setups of micro-structures. The left domain shows a micro-structure including cement paste and ballast, the middle one includes the ITZ, while the fare right micro-structure contains cement paste only. The initial values and boundary conditions were the same for all domains. It is notable how the micro-structure influences the diffusion process, and how the ITZ can increase the rate of diffusion. It follows that having a physically realistic setup of the micro-structure is crucial in order to execute proper diffusion simulations.

3 CONCLUSIONS

1. By employing the cG(1)dG(0) method, modeling of diffusion processes in the micro-structure is enabled. The method allows to separate between the micro-scale constituents both geometrically and in terms of material properties in the constitutive relations. In this way, studying how the micro-structure's composition effects the diffusion process is possible. Compositional effects of interest can be ballast- content, distribution and shape.

2. The numerical results show the importance in having a realistically modeled micro-structure. The next step is to employ the micro-structural analysis on a Representative Volume Element (RVE) as part of computational homogenization within a FE^2- strategy.

REFERENCES

[1] A. Ababneh, F. Benboudjema and Y. Xi, *Chloride Penetration in Nonsaturated Concrete*, Journal of Materials in Civil Engineering, Vol. 15, No 2, pp 183-191, (2003).

[2] Z.P.. Bažant and L.J. Najjar, *Nonlinear Water Diffusion in Nonsaturated Concrete*, Materials and Structures, Vol. 5, No 1, pp 3-20, (1971).

[3] L. Tang and L.O. Nilsson, *Chloride Binding Capacity and Binding Isotherms of OPC Pastes and Mortars*, Cement and Concrete Research, Vol. 23, Issue 2, pp 247-253, (1993).

23rd Nordic Seminar on Computational Mechanics
NSCM-23
A. Eriksson and G. Tibert (Eds)

ATOMISTIC SIMULATIONS OF BUCKLING PROPERTIES OF GOLD NANOWIRES

PÄR A. T. OLSSON* AND HAROLD S. PARK†

*Division of Mechanics
Lund University
P.O. Box 118, SE-221 00 Lund, Sweden
e-mail: Par.Olsson@mek.lth.se - Web page: http://www.mek.lth.se/

†Department of Mechanical Engineering
Boston University
730 Commonwealth Avenue, ENA 212, Boston, MA 02215
e-mail: parkhs@bu.edu - Web page: http://people.bu.edu/parkhs/

Key words: Nanowires, Molecular Statics, Buckling

Summary. The purpose of this work is to present results from an ongoing study on how the presence of surfaces influences the buckling properties of nanowires. This study is performed using molecular statics simulations where the interatomic interaction is modelled using an embedded atom potential (EAM) fitted to gold properties. The considered nanowires have rectangular cross sections with cross sectional dimensions spanning from 2-6 nm and aspect ratios between 20-50. Three different crystallographic orientations have been considered; [100]/{100}, [100]/{110} and [110]/{110}{100}. The simulations show that depending on how the crystal is oriented the critical load may increase or decrease in comparison with the bulk counterpart. The [100] systems display decreases in the critical forces in comparison with the bulk, whereas for the [110] system the relative critical force increases.

1 INTRODUCTION

Nanowires are one dimensional structures characterized by their small dimensions spanning from hundreds down to only a few nanometers. Due to the large surface to volume ratios, they tend to display many deviant physical properties from those of macroscopic structures, which makes them suitable as building blocks for the development of next generation electronics, optoelectronics, and sensor systems. This has triggered a great deal of interest from the research community to explain and to model the nanoscale properties accurately[1].

Elastic properties of nanowires are experimentally obtained, mainly, through two different methods; either through beam bending experiments or through dynamic resonant experiments[2,3]. However, one more method has recently emerged for determining the elastic properties experimentally, and that is by studying at which amount of force the buckling instability of nanowires occurs in compression and then to relate the critical force to existing continuum relations from which the elastic properties are extracted[4].

Molecular dynamics (MD) and molecular statics (MS) has been a popular simulation tool for simulating the elastic properties and mechanical response of nanowires, and has revealed that the surface stress induces relaxation strains for small structures. In fact, it has been found that the surface stresses have been sufficiently large to induce phase transformations and to cause the core to contract which induces nonlinear elastic effects. These contractions may cause Young's modulus either to decrease or increase depending on the crystallographic orientation[5,6]. MD simulations have also been employed for studying buckling behaviour of nanowires and nanotubes and has revealed many interesting features such as significantly large buckling strain and increment dependent critical strains[7,8]. The purpose of this work is to study how the presence of surfaces influences the buckling properties of nanowires.

2 MS SIMULATIONS

MS simulations are performed for the numerical part of this work. The simulations are displacement controlled and in order to trigger the instability, a perturbation was employed to break the symmetry. This was done by adding small additional external forces acting on the free atoms, so that the resulting force on the free atoms is written as

$$\mathbf{F}_i = -\frac{\partial \Phi}{\partial \mathbf{r}_i} + \delta \mathbf{F} \tag{1}$$

where Φ denotes the total potential energy and the vector $\delta\mathbf{F} = (0, \delta F, \delta F)$ is a perturbation which is employed to disturb the symmetry of the system. In the simulations the perturbations were chosen to be of the order $10^{-9} < \delta F < 10^{-11}$ eV/Å which was found to be sufficiently large to get the nanowires to buckle and small enough not to influence the response notably. The interaction between the atoms is modelled using an EAM potential for gold. All the considered nanowires are biclamped and have rectangular cross sections. Three different crystallographic orientations have been considered; [100]/{100}, [100]/{110} and [110]/{110}{100}.

3 RESULTS AND DISCUSSION

In traditional Bernoulli-Euler beam theory the critical force for a biclamped beam is written

$$P_{cr} = \frac{4\pi^2 EI}{L^2} \tag{2}$$

where EI and L denote the flexural rigidity and length of the nanowire, respectively. In Figs. 1 and 2 we have compared the ratios between the obtained critical forces from the MS simulations and those of the ideal bulk for nanowires with the respective aspect ratios 20 and 40. It is seen that the critical force increases with decreasing size for the [110]/{110}{100} orientation whereas it decreases with decreasing size for the [100]/{100} and [100]/{110} orientations. These findings do agree with results from previous researchers who have observed that Young's modulus increases with decreasing size for [110]/{110}{100} and decreases for the other considered orientations[9].

There are, however, some indications implying that Eq. (2) fails to describe the buckling behavior accurately. In Fig. 3 we have compared the ratio between the scaled critical forces of

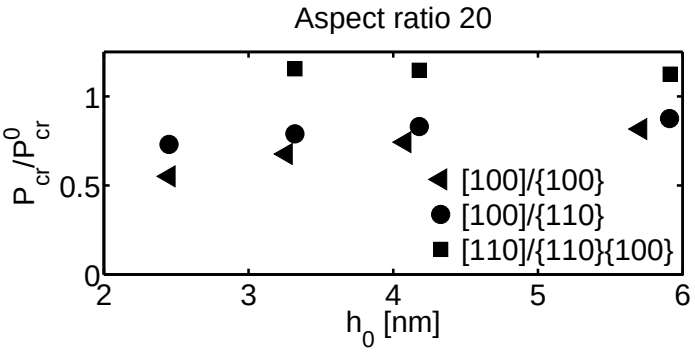

Figure 1: Ratio between the measured critical force from the MS simulations and the corresponding bulk value for nanowires with the aspect ratio 20.

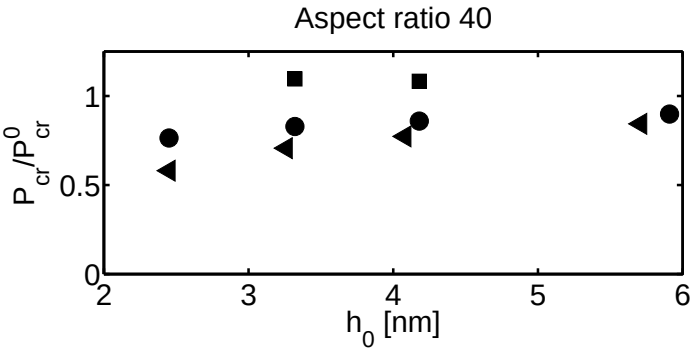

Figure 2: Ratio between the measured critical force from the MS simulations and the corresponding bulk value for nanowires with the aspect ratio 40.

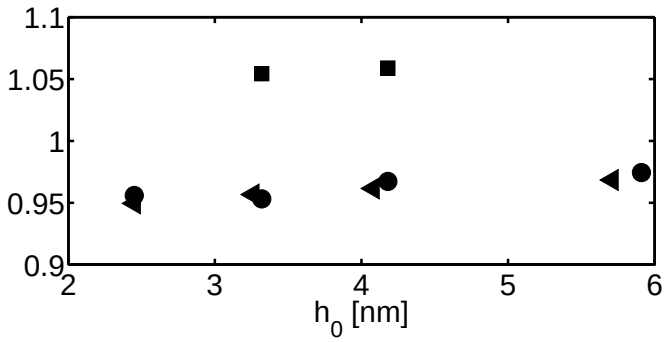

Figure 3: The ratio of scaled critical forces for nanowires with aspect ratios 20 and 40.

nanowires with the same cross section but with different lengths, i.e.,

$$\frac{(P_{cr}L^2)_i}{(P_{cr}L^2)_j} = \frac{(EI)_i}{(EI)_j} \tag{3}$$

which should be equal to 1 for nanowires with identical cross sections. However, close inspection of Fig. 3 reveals that the ratios differ from 1. The deviations are up to about 5% when nanowires with aspect ratios 20 and 40 are considered. These are, of course, different when other aspect ratios are compared, but they do deviate from 1, which does suggest that Eq. (2) loses validity at small dimensions.

4 CONCLUSIONS

In this abstract we have presented results from an ongoing study on buckling properties of nanowires. So far we have found that the critical force can both increase or decrease with decreasing cross sectional size. Moreover, we have found that there are implications suggesting that the traditional Bernoulli-Euler buckling expressions loses validity at small dimensions.

REFERENCES

[1] H. S. Park, W. Cai, H. D. Espinosa and H. Huang, Mechanics of Crystalline Nanowires, *MRS Bull.*, **34**, 178–183, (2009).

[2] B. Wu, A. Heidelberg and J. J. Boland, Mechanical properties of ultrahigh-strength gold nanowires, *Nature Mater.*, **4**, 525–529, (2005).

[3] A. Husain, J. Hone, H. W. Ch. Postma, X. M. H. Huang, T. Drake, M. Barbic, A. Scherer and M. L. Roukes, Nanowire-based very-high-frequency electromechanical resonator, *Appl. Phys. Lett.*, **83**, 1240–1242, (2003).

[4] M. Riaz, O. Nur, M. Willander and P. Klason, Buckling of ZnO nanowires under uniaxial compression, *Appl. Phys. Lett.*, **92**, 103118, (2008).

[5] J. Diao, K. Gall and M. L. Dunn, Surface-stress-induced phase transformation in metal nanowires, *Nature Mater.*, **2**, 656–660, (2003).

[6] H. Y. Liang, M. Upmanyu and H. C. Huang, Size-dependent elasticity of nanowires: Nonlinear effects, *Phys. Rev. B*, **71**, 241403, (2005).

[7] G. Cao and X. Chen, The effect of the displacement increment on the axial compressive buckling behaviours of single-walled carbon nanotubes, *Nanotechnology*, **17**, 3844–3855, (2006).

[8] W. Jiang and R. C. Batra, Molecular statics simulations of buckling and yielding of gold nanowires deformed in axial compression, *Acta Mater.*, **57**, 4921–4932, (2009).

[9] R. Dingreville, A. J. Kulkarni, M. Zhou and J. Qu, A semi-analytical method for quantifying the size-dependent elasticity of nanostructures, *Modell. Simul. Mater. Sci Eng.*, **16**, 025002, (2008).

23rd Nordic Seminar on Computational Mechanics
NSCM-23
A. Eriksson and G. Tibert (Eds)

INFLUENCE OF SPONTANEOUS CONVECTION ON AMPEROMETRIC BIOSENSOR RESPONSE

EVELINA GAIDAMAUSKAITĖ AND ROMAS BARONAS

The Faculty of Mathematics and Informatics
Vilnius University
Naugarduko 24, LT-03225 Vilnius, Lithuania
e-mail: evelina.gaidamauskaite@mif.vu.lt, web page: http://mif.vu.lt/en/

Key words: Apparent diffusion coefficient, Biosensor, Spontaneous convection, Simulation.

Summary. A one-dimensional-in-space mathematical model of an amperometric biosensor is presented in this paper. The modelling biosensor comprises two compartments, an enzyme layer and an outer diffusion layer. In order to integrate microscopic chaotic motions we consider an apparent diffusion coefficient function. In this paper, the effect of an apparent diffusion coefficient on the response of biosensor is studied and compared to the constant diffusion coefficient. The stated problem is solved numerically using the finite difference method.

1 INTRODUCTION

The biosensors are small analytical devices used in various fields, including clinical, industrial and agricultural analyses [1]. A biosensor is composed of biologically responsive material, mostly enzymes, and the electrode. An enzyme interacts with a target substance yielding a product. This process is usually described by Michaelis - Menten kinetics of the enzymatic reactions [2]. Amperometric enzyme electrodes are based on the measurement of the Faraday current when a constant potential is kept. The current on the electrode appears due to the direct oxidation or reduction of an electroactive spieces. The solution cannot be regarded still either because of macroscopic motions (RDE, polarography, wall jet, density gradients, etc.) or because of ubiquitous convection [3, 4]. In order to integrate microscopic chaotic motions we consider an apparent diffusion coefficient function. In this paper, the effect of an apparent diffusion coefficient on the response of biosensor is studied and compared to the constant diffusion coefficient.

2 MATHEMATICAL MODEL

We consider the simplified model of enzyme-catalysed reaction, where the enzyme (E) binds to the substrate (S) producing the product (P) [1],

$$\mathrm{S} \xrightarrow{\mathrm{E}} \mathrm{P}. \tag{1}$$

We assume the symmetrical geometry of the electrode and homogeneous distribution of the immobilized enzyme in the enzyme membrane. The dynamics in the enzyme membrane is

described coupling the enzyme-catalyzed reaction with the one-dimensional-in-space diffusion, described by Fick's second law [5]. Transport by diffusion takes place in the diffusion layer,

$$\frac{\partial S_e}{\partial t} = D_{Se}\frac{\partial^2 S_e}{\partial x^2} - \frac{V_{max}S_e}{K_M + S_e}, \quad 0 < x < d, \tag{2}$$

$$\frac{\partial P_e}{\partial t} = D_{Pe}\frac{\partial^2 P_e}{\partial x^2} + \frac{V_{max}S_e}{K_M + S_e}, \quad 0 < x < d, \tag{3}$$

$$\frac{\partial S_b}{\partial t} = \frac{\partial}{\partial x}\left(D^*_{Sb}\frac{\partial S_b}{\partial x}\right), \quad d < x < d + \delta, \tag{4}$$

$$\frac{\partial P_b}{\partial t} = \frac{\partial}{\partial x}\left(D^*_{Pb}\frac{\partial P_b}{\partial x}\right), \quad d < x < d + \delta, \tag{5}$$

where $S_e(x,t)$ and $S_b(x,t)$ ($P_e(x,t), P_b(x,t)$) are the concentrations of the substrate (product) in the enzyme membrane and the diffusion layer, respectively, t stands for time and x - for space, K_M is the Michaelis-Menten constant, V_{max} is the maximal enzymatic rate attainable when the enzyme is fully saturated with substrate, d is the thickness of the enzyme membrane, δ stands for the thickness of the diffusion layer. The diffusion coefficients D_{Se} and D_{Pe} of the substrate and the product in the enzyme membrane are assumed to be constant. In the diffusion layer we apply the corresponding diffusion coefficients (D^*_{Sb} and D^*_{Pb}) as functions of the distance x from the electrode,

$$D^*_{Ab} = D_{Ab}(1 + 1.522((x-d)/\delta_{conv})^4, \quad A \in (S,P), \tag{6}$$

where δ_{conv} stands for the thickness of the convection-free layer [3, 4]. A solution cannot be regarded as being immobile at the microscopic level, except in the very near vicinity of cell walls and electrode surfaces. Therefore we assume that enzyme layer is convection-free and this immobile layer extends to 0.05-0.1 μm above the enzyme layer. Let $x = 0$ represent the electrode surface, while $x = d$ is the boundary between the enzyme membrane and the diffusion layer. The biosensor operation starts when some substrate appears on the boundary of the diffusion layer,

$$\begin{aligned} &S_e(x,0) = P_e(x,0) = 0, \quad 0 \le x \le d, \\ &S_b(x,0) = 0, \quad d \le x < d + \delta, \quad S_b(d+\delta,0) = S_0, \\ &P_b(x,0) = 0, \quad d \le x \le d + \delta, \end{aligned} \tag{7}$$

where S_0 stands for the concentration of substrate in the bulk solution. In the bulk solution the concentrations of the substrate and the product remain constant ($t > 0$),

$$S_b(d+\delta,t) = S_0, \quad P_b(d+\delta,t) = 0. \tag{8}$$

In the case of amperometric enzyme electrodes, due to the electrode polarization, the concentration of the reaction product at the electrode surface is being permanently reduced to zero. The substrate does not react at the electrode surface,

$$\left.\frac{\partial S_e}{\partial x}\right|_{x=0} = 0, \quad P_e(0,t) = 0. \tag{9}$$

On the boundary between two regions having different diffusivities, we define the matching conditions ($t > 0$),

$$D_{Ae}\frac{\partial A_e}{\partial x}\Big|_{x=d} = D_{Ab}\frac{\partial A_b}{\partial x}\Big|_{x=d}, \quad A_e(d,t) = A_b(d,t), \quad A \in (S,P). \tag{10}$$

The measured current is accepted as a response of the amperometric enzyme electrode in a physical experiment. The current depends upon the flux of the reaction product at the electrode surface, i.e. at the border $x = 0$. Consequently, the density $I(t)$ of the current at a time t can be obtained by

$$I(t) = n_e F D_{Pe}\frac{\partial P_e}{\partial x}\Big|_{x=0}, \tag{11}$$

where n_e is a number of electrons, involved in charge transfer at the electrode surface, and F is the Faraday constant [1]. We assume that the system (2)-(10) approaches a steady state as $t \to \infty$,

$$I_\infty = \lim_{t\to\infty} I(t), \tag{12}$$

where I_∞ is the equilibrium current density.

3 RESULTS AND DISCUSSION

The mathematical model of the enzyme electrode can be solved numerically using explicit finite difference method [6]. The program was implemented in Java programming language [2, 7]. We assume the biosensor response I_P calculated at the moment T_P as the steady state response,

$$I_P = I(T_P) \approx I_\infty, \quad T_P = \min_{j>0,\, I_j>0}\left\{\tau_j : \frac{I_j - I_{j-1}}{I_j} < \varepsilon\right\}, \quad \tau_j = \tau j, \tag{13}$$

where τ stands for the size of time step. We used $\varepsilon = 10^{-5}$ for the calculations.

The following values of the model parameters were employed for the simulation,

$$\begin{aligned} &S_0 = K_M = 100\mu\text{M}, \quad V_{max} = 100\mu\text{M/s}, \quad n_e = 2, \quad d = 0.1\mu\text{m}, \quad \delta = 1\mu\text{m}, \\ &D_{Se} = D_{Pe} = 3\times10^{-10}\text{m}^2\text{/s}, \quad D_{Sb} = D_{Pb} = 6\times10^{-10}\text{m}^2\text{/s}. \end{aligned} \tag{14}$$

Fig. 1 shows the dependance of the biosensor response on the normalised substrate concentration (S_0/K_M). It is apparent that the current saturation level is reached at the smaller substrate amounts when spontaneous convection occurring in the diffusion layer is introduced in the modelling. This could be explained by the substrate flux towards and from the electrode which establishes the saturation current at smaller concentrations of S_0 and reduces the final current level.

4 CONCLUSIONS

The mathematical model (2)-(11) can be used to simulate the biosensor with spontaneous convection occurring in the diffusion layer. It was observed that the response of the bioelectrode changes drastically when spontaneous convection is taken into account. This highlights the necessity to consider the spontaneous convection in the modelling of biosensors even in the macroscopically still solutions.

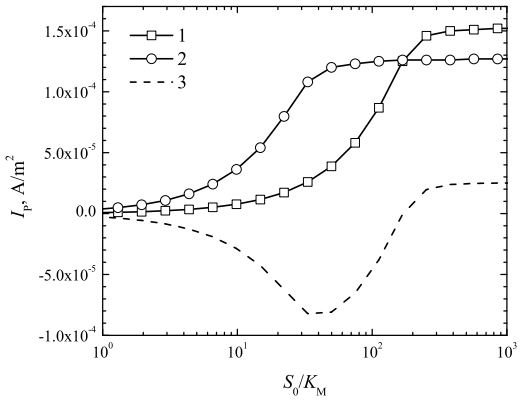

Figure 1: The dependence of the biosensor response I_P on the dimensionless substrate concentration (S_0/K_M) at constant diffusion coefficients D_{Sb}, D_{Pb} (1) and at apparent diffusion coefficient D^*_{Sb}, D^*_{Pb} (2). The curve 3 shows the difference of the responses.

ACKNOWLEDGEMENT

This work was supported by the Global Grant Measure (The Research Council of Lithuania) financed from the European Social Fund and co-financed by the Republic of Lithuania.

REFERENCES

[1] F. Scheller and F. Schubert. *Biosensors*. Elsevier, Amsterdam, (1992).

[2] R. Baronas, F. Ivanauskas and J. Kulys. *Mathematical Modeling of Biosensors*. Springer-Verlag, (2010).

[3] C. Amatore, S. Szunerits, L. Thouin and J. Warkocz. The real meaning of Nernsts steady diffusion layer concept under non-forced hydrodynamic conditions. A simple model based on Levichs seminal view of convection. *Journal of Electroanalytical Chemistry*, **500**, 62-70, (2001).

[4] C. Amatore, C. Pebay, L. Thouin and A. Wang. Cyclic voltammetry at microelectrodes. Influence of natural convection on diffusion layers as characterized by in situ mapping of concentration profiles. *Electrochemistry Communications*, **11**, 1269-1272, (2009).

[5] T. Schulmeister. Mathematical modelling of the dynamic behaviour of amperometric enzyme electrodes. *Selective Electrode Reviews*, **12**, 203–260, (1990).

[6] D. Britz. *Digital Simulation in Electrochemistry*. Springer-Verlag, Berlin, Third edition, (2005).

[7] D. Britz, R. Baronas, E. Gaidamauskaitė and F. Ivanauskas. Futher Comparisons of Finite Difference Schemes for Computational Modelling of Biosensors. *Nonlinear Analysis: Modelling and Control*, **14(4)**, 419–433, (2009).

23rd Nordic Seminar on Computational Mechanics
NSCM-23
A. Eriksson and G. Tibert (Eds)

MULTISCALE MODELING OF SINTERING OF HARD METAL

MIKAEL ÖHMAN*, KENNETH RUNESSON AND FREDRIK LARSSON

Department of Applied Mechanics
Chalmers University of Technology
Gothenburg, Sweden
e-mail: mikael.ohman@chalmers.se, web page: http://www.chalmers.se/am/EN/

Key words: Sintering, Sintering stress, Surface tension, Homogenization, FE^2

Summary. In this contribution, we discuss the multiscale modeling of sintering of hard metal, which is composed of hard particles (WC) with a melted binder (Co). Numerical results are shown for a coupled FE^2 analysis involving homogenization of the consolidating compact.

1 INTRODUCTION

The sintering phenomenon on the mesoscale is driven by surface tension on the melted binder, and the homogenized effect of the surface tension is the so-called sintering stress. From the macroscopic perspective, the specimen (green body) shrinks due to this volumetric sintering stress. In the case of inhomogeneous initial density in the green body, the sintering can result in unwanted final deformations.

2 THEORY

Finite elements and computational homogenization have been applied to a Representative Volume Element (RVE) of the mesoscale. The melted binder is modeled as a Stokes flow, with surface tension potential energy on the free surface. Hard inclusions are modeled by applying a high viscosity. Different choices of boundary conditions are available on the RVE for the prolongation. The advantage of the multiscale approach is that it can capture the complex behavior of sintering with simple material models with measurable parameters.

The surface tension load can be expressed by a traction $\boldsymbol{t}$ on the free surface as

$$\boldsymbol{t} = 2\kappa\gamma\boldsymbol{n} \tag{1}$$

where κ is the Gaussian curvature of the surface, γ is the surface tension coefficient and $\boldsymbol{n}$ is the surface normal. Since the traction is geometry dependent, a tangent with respect to the displacement also appears in the equations. Using the divergence theorem one can avoid the second derivative in the FE-formulation, but the incompressible Stokes flow requires higher order basis functions.

For the homogenization, extra care has to be placed on the formulation to fulfill the Hill-Mandel condition. Since the internal boundary potential on the mesoscale gives rise to a discontinuous stress, the common derivations for stress/strain homogenization do not apply directly.

3 PRELIMINARY RESULTS

Numerical examples are evaluated for a 2D, fully coupled, FE^2 problem as a proof of concept. Taylor-Hood elements for the linear Stokes flow, and quadratic edge elements for the surface tension, are employed for the mesoscale analysis. Linear triangular elements with one integration point are used on the macroscopic scale. Dirichlet boundary conditions are used for the prolongation of the macroscopic strain rate. The geometry is deformed at the end of each time step in the framework of an updated Lagrangian formulation. The model contains only two material parameters, the viscosity ν and the surface tension γ, both set to unit value as they will only scale the linear response.

The finite elements for both meso- and macroscale have been implemented in the open source finite element code OOFEM[1], and extensions will be available in future releases. The multiscale step is carried out by implementing a special constitutive driver for the macroscopic scale. This driver calls and solves a subscale finite element problem for the given macroscale strain, whereafter the homogenized stress is calculated. This approach fits cleanly into the OOFEM framework, and could be used to recursively perform any number of multiscale computations.

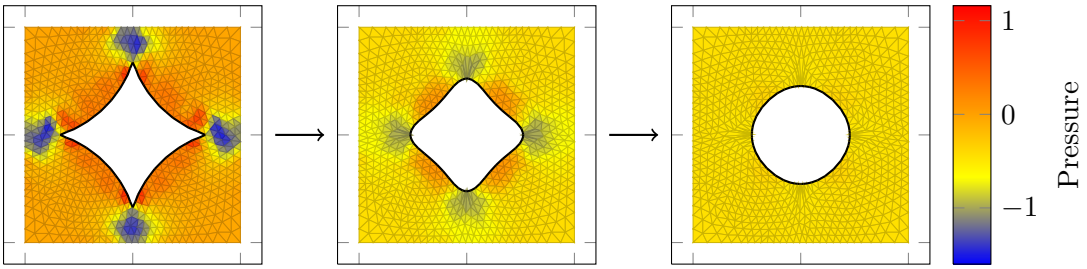

Figure 1: Evolution of the free surface within an RVE and the corresponding pressure field

The first example, shown in Figure 1, concerns an RVE at a single macroscale integration point. The outer boundary is fully prescribed and the liquid/binder-pore surface can be seen to evolve. The negative pressure is represented as the sintering stress on the macroscale.

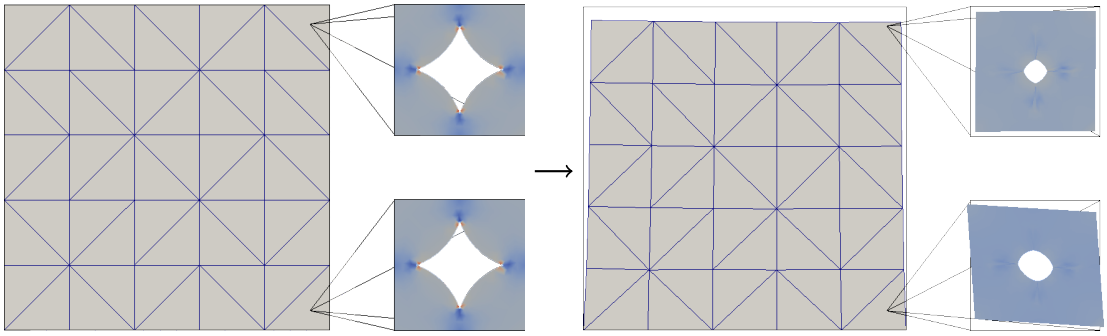

Figure 2: FE^2 analysis of the constrained sintering of a specimen; "snapshots" of two RVE's at the start and end of the process.

The second example concerns a coupled FE^2-analysis, shown in Figure 2, where the lower

boundary has been fully prescribed. Since the initial density can never go lower than around 0.84 in a 2D representation of this microstructure, the possible macroscale volume change is quite limited.

4 DISCUSSION

A major obstacle is the representation of the evolving geometry. Remeshing is required to keep a nice representation despite topological changes. To keep track of the multiple boundaries, level sets are commonly used in free surface flows.

REFERENCES

[1] Patzák, B. OOFEM project home page (2000). URL `http://www.oofem.org`.

23rd Nordic Seminar on Computational Mechanics
NSCM-23
A. Eriksson and G. Tibert (Eds)

HIGH-VELOCITY COMPACTION SIMULATION USING THE DISCRETE ELEMENT METHOD

MUHAMMAD SHOAIB AND LEIF KARI

The Marcus Wallenberg Laboratory for Sound and Vibration Research (MWL),
Department of Aeronautical and Vehicle Engineering,
Royal Institute of Technology (KTH), 100 44 Stockholm, Sweden
e-mail: shoaibm@kth.se,leifkari@kth.se

Key words: High-velocity compaction, Discrete element method, Powder processing, Dynamic loading, Relaxation assists.

Summary. The aim of the present work is to investigate different aspects of high-velocity compaction (HVC) process using the discrete element method (DEM). The focus is on the elasto-plastic shock wave propagation, its influence on the compaction process and to investigate numerically the advantages of relaxation assists which are projectile supports.

1 INTRODUCTION

The discrete element method (DEM) is used to investigate different aspects of high-velocity compaction (HVC) process. High-velocity compaction is a rapid production technique with improved compact properties. In HVC powder is compacted by shock waves in less than 0.01 s compared to a conventional compaction which is about 1 s. In the present work, the dynamic response of the particles is modeled by extending the well-established quasi-static compaction models. The compaction model is a one-dimensional assembly of spherical metal particles and contact between particles is modeled using elastic and plastic loading, elastic unloading. Of particular interest is to study the elasto-plastic shock wave; its development, transmission and reflection through chain of particles. First a homogenous chain of spherical aluminum particles is considered and then heterogeneity is introduced by changing the size and material of the particles and considering voids between them. The compaction process is simulated by considering the typical loading parameters i.e., impact velocity and mass of the hammer.
Although the compaction model is one-dimensional, simulation results yield the information on contact between particles, particle velocity and deformation during compaction process. Particle velocity, duration of its motion and its deformation are mainly dependent on shock propagation. It is shown that disturbance caused by changing the size or material of the particles produces a reflected shock in the material. Propagation of both main and reflected shocks and their combined effects on compaction process are also simulated. Effects of changing loading parameters on the compaction process are also discussed. The DEM is also used to investigate HVC process with relaxation assists. Relaxation assists are the parts of the piston and act as a projectile supports. The simulation results yield the information that relaxation assists better lock the compact during compaction process.

2 Basic contact equations

This section describes the equations for the contact between particles and between particles and die ends during loading, unloading and reloading stages. Here the particles are assumed to be perfectly plastic and having no strain hardening. For two particles in contact labeled 1 and 2; effective radius R_0, equivalent elastic modulus E^* and yield stress at contact σ_y are given by

$$\frac{1}{R_0} = \frac{1}{R_1} + \frac{1}{R_2}, \tag{1}$$

$$E^* = \left(\frac{1-\nu_1^2}{E_1} + \frac{1-\nu_2^2}{E_2} \right)^{-1}, \tag{2}$$

$$\sigma_y = \min\,(\sigma_1, \sigma_2). \tag{3}$$

In the beginning of the compaction process, normal force follows the Hertzian law[1] for small values of overlap

$$F_e = \frac{4}{3} E^* \sqrt{R_0} h^{\frac{3}{2}}, \tag{4}$$

where h is the overlap or indentation between the particles. Normal contact force F_p in the plastic regime is given by[2,3]

$$F_p = 6\pi c^2 \sigma_y R_0 h, \tag{5}$$

with the material invariant $c^2 = 1.43$ for ideally plastic material behavior. The contact radius a is defined as

$$a^2 = 2c^2 R_0 h. \tag{6}$$

At the end of plastic loading stage; contact force, contact radius and overlap are denoted by F_0, a_0 and h_0, respectively. The uniform pressure at the contact is $p_0 = 3\sigma_y$.

The overlap recovered h_u during unloading stage, is given by[4,1]

$$h_u = \frac{2p_0 a_0}{E^*} \sqrt{1 - \left(\frac{a}{a_0}\right)^2}. \tag{7}$$

During unloading stage, Eq. (7) can be used to find contact radius a while normal contct force F_u is given by[4,5]

$$F_u = 2p_0 a_0^2 \left[\arcsin\left(\frac{a}{a_0}\right) - \frac{a}{a_0} \sqrt{1 - \left(\frac{a}{a_0}\right)^2} \;\right]. \tag{8}$$

3 Model

The discrete element method is used to simulate high-velocity compaction process. The contact forces are determined by the contact laws as described in the previous section. The time step used is 2.5 ns which is sufficient to ensure numerical stability during calculations. The compaction models are one-dimensional assemblies of homogeneous and heterogeneous spherical particles. For simulation, one hundred aluminum particles of diameter 100 micron are used. Heterogeneity is introduced by changing the size and material of particles and considering voids between them.The impact velocity used for hammer is 10 m/s which along with different choices of hammer mass result in compaction energy of 1 J/g to 6.5 J/g.

3.1 Results

During compaction process as hammer moves forward to compact the material, particles overlap each other and thus contact forces are developed. The difference between contact forces results in a net force on the particle. This disturbance or shock travels from first particle to the last particle, reflected from the dead end and moves back from last particle to the first one. When shock moves from hammer end to dead end, particles start moving and finally gain hammer velocity. Similarly when shock moves back from dead end to hammer end, particles velocity decreases and eventually become zero resulting in particles deformation. The movement of the shock also effects the kinetic enemy of the hammer. First a homogenous chain of aluminum

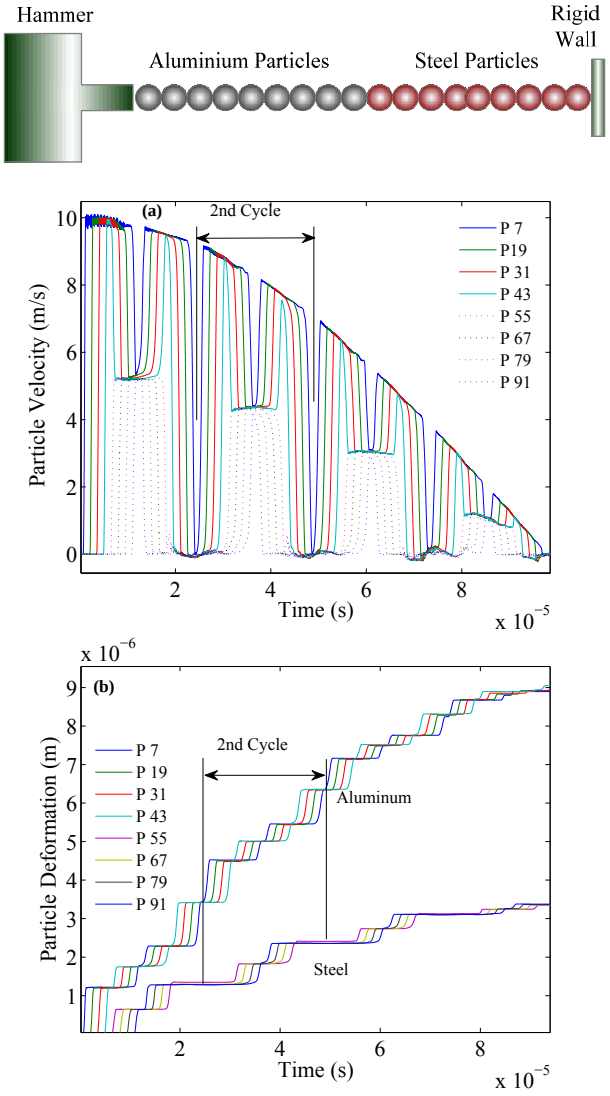

Figure 1: The dynamic loading of a symmetric chain of aluminum and steel particles. (a) Particle velocity. (b) Particle deformation.

particles is studied and simulations show the effects of shock wave on compaction process, especially on contact between particles, their velocity and deformation.
The effects of non homogeneity due to size and material of the particles and voids between the particles are also investigated. Figure 1 shows a symmetric case of aluminum and steel particles during dynamic loading. When shock passes through aluminum particles, they are compacted and start moving with hammer velocity. However, when shock hits the steel particles and since they have large contact stiffness and more mass, therefore they are less compacted and gain less velocity. It reduces the velocity of aluminum particles and creates a reflected shock in aluminum particles. Both particle velocity and its deformation are dependent on main and reflected shocks. Even a single steel particle effects the shock and hence the particles compaction. Disturbance caused by large size particles is of similar nature as that of different material particles. Gap or void between particles also effects the shock propagation. Sudden increase or decrease in the velocity creates shock fluctuations which also propagates like a normal shock. Discrete element method is also used to investigate HVC process with relaxation assists. Relaxation assists are parts of the hammer with same material and diameter as that of the hammer. Simulations show that use of these relaxation assists better lock the material during compaction process and thus supporting the experimental work.

4 CONCLUSIONS

1. The discrete element method is an efficient tool to study the high-velocity compaction process.

2. Simulation results show the propagation and reflection of elasto-plastic shock wave and its influence on compaction process, e.g., contact between particles, their velocity and deformation.

3. Disturbance caused by heterogeneity due to size and material of particles can be simulated.

4. It is also shown that by using relaxation assists, particles can be better locked which improves the compact properties.

REFERENCES

[1] K.L. Johnson, Contact Mechanics, Cambridge University press (1985).

[2] O. Skrinjar and P.-L. Larsson, On discrete element modelling of compaction of powders with size ratio, Comput. Mater. Sci. 31 (2004) 131-146.

[3] C.L. Martin, Elasticity, fracture and yielding of cold compacted metal powders, J. Mech. Phy. Solids, 52(2004), 1691-1717.

[4] C.L. Martin, D. Bouvard, Study of the cold compaction of composite powders by the discrete element method, Acta Mater. 51 (2003) 373-386.

[5] S.D. Mesarovic, K.L. Johnson, Adhesive contact of elastic-plastic sheres, J. Mech. Phy. Solids 48 (2000) 2009-2033.

23rd Nordic Seminar on Computational Mechanics
NSCM-23
A. Eriksson and G. Tibert (Eds)

ISOGEOMETRIC ANALYSIS - GEOMETRY MODELLING OF A WIND TURBINE BLADE

SIV BENTE RAKNES*, KJETIL ANDRE JOHANNESSEN†, TROND KVAMSDAL* AND KNUT MORTEN OKSTAD*

*SINTEF ICT - Department of Applied Mathematics
NO-7491 Trondheim, Norway
E-mails: sivbenr@stud.ntnu.no, trond.kvamsdal@sintef.no,
knut.morten.okstad@sintef.no - Web page: http://www.sintef.no

†Department of Mathematical Sciences
Norwegian University of Science and Technology
NTNU, NO-7491 Trondheim, Norway
E-mail: kjetijo@math.ntnu.no - Web page: http://www.ntnu.no

Key words: Isogeometric analysis, NURBS, CAD, FEM, geometry modeling, wind turbine blade.

Summary. This paper describes the main steps on how to model the geometry of a wind turbine blade by using NURBS as basis functions in both design and analysis.

1 INTRODUCTION

In the article[1] T.J.R. Hughes et. al presented how to construct an exact geometric model with a coarse discretization by employing non-uniform rational B-spline, also known as NURBS. In the article they claim that one may do a seamless transfer of models between design and analysis by using NURBS as basis functions in both design and finite element analysis. As a part of the ICADA (Integrated Computer Aided Design and Analysis) project, we have tested this hypothesis by modelling the geometry of an offshore 5MW baseline wind turbine developed by NREL (the National Renewable Energy Laboratory)[2]. In this paper we will explain how to model a wind turbine blade step by step before discussing results from an eigenvalue analysis performed on the blade.

2 MAIN STEPS TO MODEL THE GEOMETRY

2.1 Proceeding input data and making the spline curves

Our input data consists of seven different airfoils given in xy-coordinates as well as a table describing the geometry of the blade. An example of input data is shown in Table 1. To convert the xyz-coordinates of the wing profiles into splines we used C++ and a CAD drawing program called Rhinoceros. First we wrote a program which reads and proceeds the input data. The program locates, scales and rotates the profiles according to the table describing the geometry. As output we get a file containing all xyz-coordinates of all wing profiles. The file is written in

RNodes(m)	AeroTwst(deg)	Chord(m)	AeroCent(-)	AeroOrig(-)	Airfoil
8.3333	13.308	4.1676	0.1883	0.38	Cylinder
11.7500	13.308	4.557	0.1465	0.30	DU40
15.8500	11.480	4.652	0.1250	0.25	DU35

Table 1: Example on input data. The blade we modelled was described by 19 such wing profiles.

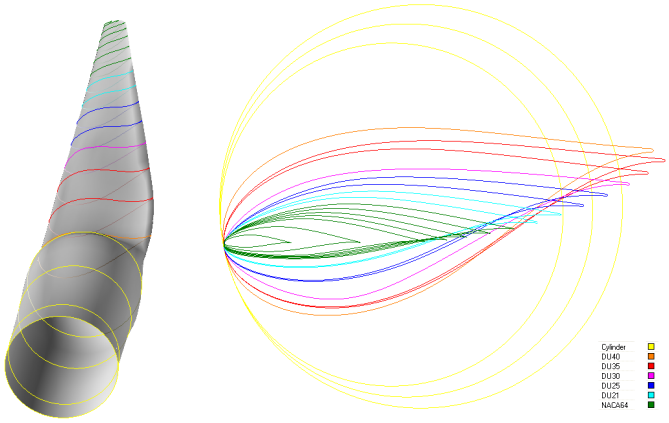

Figure 1: The profiles the blade consists of.

a way that makes Rhinoceros able to read it. In Rhinoceros we can easily make spline curves by interpolating the given points. To later be able to create a topological consistent volume we have divided each profile into two spline curves. Figure 1 shows the input data after processing.

2.2 Creating the spline surfaces

We also use Rhinoceros to create the spline surfaces. The surface model is made by lofting the wing profile curves. As each profile consists of two curves, we perform the lofting such that the blade consists of two separate surfaces, as shown in Figure 2. In Rhinoceros we may choose different options for lofting, making us able to decide the accuracy and the number of control points. Notice that the knot vectors of the surfaces must coincide at the interfacing edges.

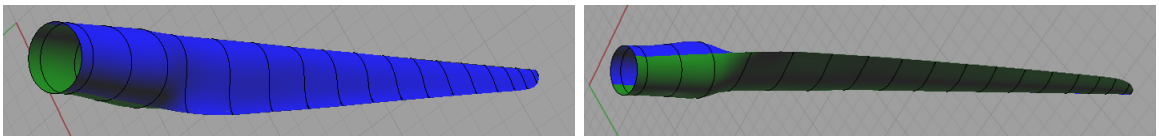

Figure 2: After lofting in Rhinoceros we have two surfaces, here shown in blue and green.

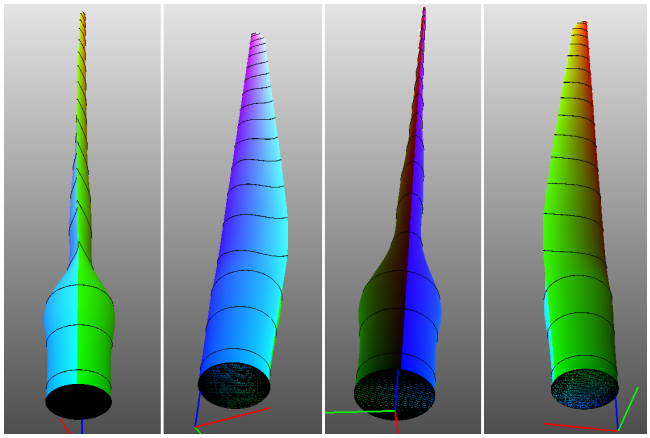

Figure 3: Final volume ready for analysis

2.3 Creating the spline volume

A shortage in todays CAD drawing programs is the possibility to make full 3D volumes. As we are not able to make the final volume in Rhinoceros, we once more need to make use of C++. More exactly, we use a program called GoTools[3]. GoTools is a C++ program developed by SINTEF ICT which consists of routines to handle spline objects. Before we can process the surfaces in GoTools, we must convert the file made in Rhinoceros to a file that GoTools actually can read. We do that by applying a converting program written by K.A. Johannessen. In GoTools we now create the final volume by exploiting an linear interpolation between the two surfaces, all done by one command line. Visualization of the final volume is done in SplineGUI, a program also written by K.A. Johannessen. The final volume is shown in Figure 3.

2.4 Performing analysis

Before we can do a finite element analysis on the blade, we have to assign physical properties (material characteristics and boundary conditions) to it. For this purpose, we have created another C++ application that lets the user select topological entities on the model and assign various properties to them. In addition, this application processes the topology of the model, identifying where we will have coalescing control points due to degeneration and periodicity, etc. Such points should share the same nodal degrees of freedom to maintain continuity in the finite element solution.

We now have all the model data needed to perform the analysis with NURBS as basis functions. Herein, we have done an eigenvalue analysis of the blade only, so no load specification is needed.

3 RESULTS

We first perform a free vibration analysis of the blade model without any boundary conditions, in order to verify that the model is topological consistent and numerically sound. The results in Table 2 show that we do get the six rigid body modes with associated eigenvalues close to zero, and then the deformation modes from Mode 7 and upwards.

Mode	1-6	7	8	9	10
Eigenfrequency [Hz]	$O(10^{-5})$	1.06432	2.95142	4.14656	5.99797

Table 2: Free vibration analysis: The 10 first eigenvalues.

Mode	1	2	3	4	5	6
Eigenfrequency [Hz]	0.63275	1.71422	2.00121	4.13529	5.57076	7.3828

Table 3: Vibration analysis with fixed ends: The 6 first eigenvalues.

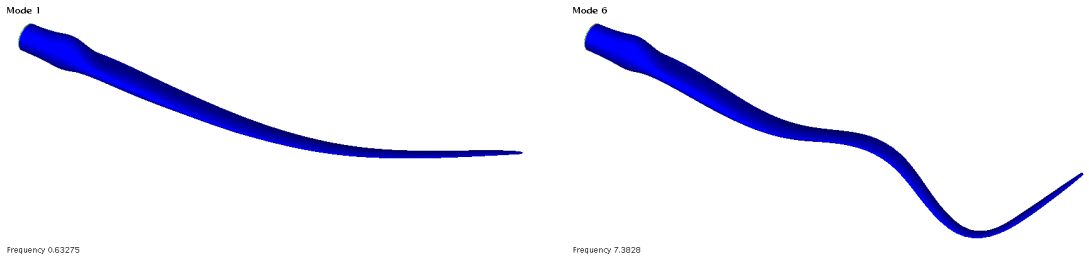

Figure 4: Vibration analysis with fixed ends: Deformed shapes for eigenmodes 1 and 6.

Next, we do a similar analysis but with the end face at the blade root fixed. The results from this analysis is presented in Table 3 and some of the mode shapes are depicted in Figure 4. In lack of more realistic material properties for this wind turbine blade, we have assumed standard steel properties in these analyses ($E = 2.05 \times 10^{11}$, $\nu = 0.3$ and $\rho = 7850.0$).

4 CONCLUDING REMARKS

By using NURBS we were able to represent the geometry exact by few data points. What amazed us the most was how quickly the analysis was executed and how easy the whole process of geometry modeling became. When the input data is set, the whole process from reading the input files to obtaining the results from the analysis only took a few minutes. Based on this work we therefore conclude that using the same geometry in design as well as in analysis reduces the man-hours spent on the preanalysis phase severely, gives more accurate results and executes the analysis much faster. When working with topological consistent geometric models it is consequently adequate to use NURBS as basis functions in finite element analysis.

REFERENCES

[1] Hughes, T., Cottrell, J. & Bazilevs, Y. Isogeometric Analysis: CAD, finite elements, NURBS, exact geometry and mesh refinement. *Computational methods in applied mechanics and engineering* **194**, 4135–4195 (2005).

[2] Jonkman, J., Butterfield, S., Musial, W. & Scott, G. Definition of a 5-MW Reference Wind Turbine for Offshore System Development. Tech. Rep., National Renewable Energy Laboratory (2009).

[3] GoTools. URL `http://sintef.org/Projectweb/Geometry-Toolkits/GoTools/`.

23rd Nordic Seminar on Computational Mechanics
NSCM-23
A. Eriksson and G. Tibert (Eds)

THE SPLITTING FINITE-DIFFERENCE SCHEMES FOR TWO-DIMENSIONAL PARABOLIC EQUATION WITH NONLOCAL CONDITIONS

SVAJŪNAS SAJAVIČIUS

Department of Computer Science II, Faculty of Mathematics and Informatics
Vilnius University
Naugarduko str. 24, LT-03225, Vilnius, Lithuania
e-mail: svajunas.sajavicius@mif.vu.lt, web page: http://mif.vu.lt/en/

Key words: Parabolic Equation, Nonlocal Integral Conditions, Splitting Finite-Difference Schemes, Stability.

Summary. We construct and analyse the splitting finite-difference schemes for a two-dimensional parabolic equation with nonlocal integral conditions. The main attention is paid to the stability of the methods. We apply the stability analysis technique which is based on the investigation of the spectral structure of the transition matrix of a finite-difference scheme. Depending on the parameters of nonlocal conditions the proposed schemes can be stable or unstable.

1 INTRODUCTION

We consider the two-dimensional parabolic equation

$$\frac{\partial u}{\partial t} = \frac{\partial^2 u}{\partial x^2} + \frac{\partial^2 u}{\partial y^2} + f(x,y,t), \quad 0 < x < 1, \quad 0 < y < 1, \quad 0 < t \leqslant T, \tag{1}$$

subject to nonlocal integral conditions

$$u(0,y,t) = \gamma_1 \int_0^1 u(x,y,t)\mathrm{d}x + \mu_1(y,t), \tag{2}$$

$$u(1,y,t) = \gamma_2 \int_0^1 u(x,y,t)\mathrm{d}x + \mu_2(y,t), \quad 0 < y < 1, \quad 0 < t \leqslant T, \tag{3}$$

boundary conditions

$$u(x,0,t) = \mu_3(x,t), \quad u(x,1,t) = \mu_4(x,t), \quad 0 < x < 1, \quad 0 < t \leqslant T, \tag{4}$$

and initial condition

$$u(x,y,0) = \varphi(x,y), \quad 0 \leqslant x \leqslant 1, \quad 0 \leqslant y \leqslant 1, \tag{5}$$

where $f(x,y,t)$, $\mu_1(y,t)$, $\mu_2(y,t)$, $\mu_3(x,t)$, $\mu_4(x,t)$, $\varphi(x,y)$ are given functions, γ_1, γ_2 are given parameters, and function $u(x,y,t)$ is unknown.

The stability of implicit and explicit finite-difference schemes for a corresponding one-dimensional parabolic problem with more general nonlocal integral conditions is investigated in the

paper of M. Sapagovas[1]. The alternating direction implicit (ADI) and locally one-dimensional (LOD) finite-difference schemes for the two-dimensional differential problem (1)–(5) has been proposed in the previous papers of the author[2,3,4]. The present work is devoted to the splitting finite-difference schemes for the two-dimensional differential problem (1)–(5).

2 THE SPLITTING FINITE-DIFFERENCE SCHEMES

To solve the two-dimensional differential problem (1)–(5) numerically, we apply the finite-difference technique. Let us define discrete grids with uniform steps,

$$\omega_{h_1} = \{x_i = ih_1, i = 1, 2, \dots, N_1 - 1, N_1 h_1 = 1\}, \quad \overline{\omega}_{h_1} = \omega_{h_1} \cup \{x_0 = 0, x_{N_1} = 1\},$$
$$\omega_{h_2} = \{y_j = jh_2, j = 1, 2, \dots, N_2 - 1, N_2 h_2 = 1\}, \quad \overline{\omega}_{h_2} = \omega_{h_2} \cup \{y_0 = 0, y_{N_2} = 1\},$$
$$\omega = \omega_{h_1} \times \omega_{h_2}, \quad \overline{\omega} = \overline{\omega}_{h_1} \times \overline{\omega}_{h_2},$$
$$\omega^\tau = \{t^k = k\tau, k = 1, 2, \dots, M, M\tau = T\}, \quad \overline{\omega}^\tau = \omega^\tau \cup \{t^0 = 0\}.$$

We use the notation $U_{ij}^k = U(x_i, y_j, t^k)$ for functions defined on the grid $\overline{\omega} \times \overline{\omega}^\tau$ or its parts, and the notation $U_{ij}^{k+1/2} = U(x_i, y_j, t^k + 0.5\tau)$ (some of the indices can be omitted).

Now we explain the main steps of the splitting finite-difference schemes for the numerical solution of problem (1)–(5). First of all, we replace the initial condition (5) by equations

$$U_{ij}^0 = \varphi_{ij}, \quad (x_i, y_j) \in \overline{\omega}. \tag{6}$$

Then, for any k, $0 \leqslant k < M - 1$, the transition from the kth layer of time to the $(k+1)$th layer can be carried out by splitting it into two stages and solving one-dimensional finite-difference subproblems in each of them:

(1) For each $x_i \in \omega_{h_1}$, solve system

$$\begin{cases} \dfrac{U_{ij}^{k+1/2} - U_{ij}^k}{\tau} = (1-\sigma)\Lambda_1 U_{ij}^k + \sigma\Lambda_2 U_{ij}^{k+1/2} + \sigma f_{ij}^{k+1/2}, \quad y_j \in \omega_{h_2}, \\ U_{i0}^{k+1/2} = (\overline{\mu}_3)_i, \\ U_{iN_2}^{k+1/2} = (\overline{\mu}_4)_i; \end{cases} \tag{7}$$

(2) For each $y_j \in \omega_{h_2}$, solve system

$$\begin{cases} \dfrac{U_{ij}^{k+1} - U_{ij}^{k+1/2}}{\tau} = \sigma\Lambda_1 U_{ij}^{k+1} + (1-\sigma)\Lambda_2 U_{ij}^{k+1/2} + (1-\sigma) f_{ij}^{k+1}, \quad x_i \in \omega_{h_1}, \\ U_{0j}^{k+1} = \gamma_1\big(1, U\big)_j^{k+1} + (\mu_1)_j^{k+1}, \\ U_{N_1 j}^{k+1} = \gamma_2\big(1, U\big)_j^{k+1} + (\mu_2)_j^{k+1}; \end{cases} \tag{8}$$

where

$$\Lambda_1 U_{ij} = \frac{U_{i-1,j} - 2U_{ij} + U_{i+1,j}}{h_1^2}, \quad \Lambda_2 U_{ij} = \frac{U_{i,j-1} - 2U_{ij} + U_{i,j+1}}{h_2^2},$$
$$\overline{\mu}_3 = \sigma\big((\mu_3)^{k+1} - \tau\sigma\Lambda_1(\mu_3)^{k+1}\big) + (1-\sigma)\big((\mu_3)^k + \tau(1-\sigma)\Lambda_1(\mu_3)^k\big),$$
$$\overline{\mu}_4 = \sigma\big((\mu_4)^{k+1} - \tau\sigma\Lambda_1(\mu_4)^{k+1}\big) + (1-\sigma)\big((\mu_4)^k + \tau(1-\sigma)\Lambda_1(\mu_4)^k\big),$$

$$(1,U) = h_1\Big(\frac{U_0+U_{N_1}}{2} + \sum_{i=1}^{N_1-1} U_i\Big).$$

Every transition is finished by calculating

$$U_{i0}^{k+1} = (\mu_3)_i^{k+1}, \quad U_{iN_2}^{k+1} = (\mu_4)_i^{k+1}, \quad x_i \in \overline{\omega}_{h_1}. \tag{9}$$

If $\sigma = 1$ or $\sigma = 1/2$, we have LOD or ADI methods, respectively. The finite-difference scheme is fully-explicit for $\sigma = 0$.

The finite-difference schemes (6)–(9) can be written in the form

$$U^{k+1} = SU^k + \overline{F}^k, \tag{10}$$

where $S = \big(E+\sigma\tau A_1\big)^{-1}\big(E-(1-\sigma)\tau A_2\big)\big(E+\sigma\tau A_2\big)^{-1}\big(E-(1-\sigma)\tau A_1\big)$, $\overline{F}^k$ is the vector of dimension $(N_1-1)\cdot(N_2-1)$, E is the identity matrix of order $(N_1-1)\cdot(N_2-1)$, $A_1 = -E_{N_2-1}\otimes\widetilde{\Lambda}_1$, $A_2 = -\widetilde{\Lambda}_2\otimes E_{N_1-1}$, E_N is the identity matrix of order N, $A\otimes B$ denotes the Kronecker (tensor) product of matrices A and B,

$$\widetilde{\Lambda}_l = h_l^{-2}\begin{pmatrix} -2+\overline{\alpha}_l & 1+\overline{\alpha}_l & \overline{\alpha}_l & \cdots & \overline{\alpha}_l & \overline{\alpha}_l & \overline{\alpha}_l \\ 1 & -2 & 1 & \cdots & 0 & 0 & 0 \\ 0 & 1 & -2 & \ddots & 0 & 0 & 0 \\ \vdots & \vdots & \ddots & \ddots & \ddots & \vdots & \vdots \\ 0 & 0 & 0 & \ddots & -2 & 1 & 0 \\ 0 & 0 & 0 & \cdots & 1 & -2 & 1 \\ \overline{\beta}_l & \overline{\beta}_l & \overline{\beta}_l & \cdots & \overline{\beta}_l & 1+\overline{\beta}_l & -2+\overline{\beta}_l \end{pmatrix}$$

are $(N_l-1)\times(N_l-1)$ matrices, $l = 1,2$, $\overline{\alpha}_1 = \gamma_1 h_1/D$, $\overline{\beta}_1 = \gamma_2 h_1/D$, $\overline{\alpha}_2 = \overline{\beta}_2 = 0$, $D = 1-h_1(\gamma_1+\gamma_2)/2$. We assume that the existence of the matrices $\big(E+\sigma\tau A_1\big)^{-1}$ and $\big(E+\sigma\tau A_2\big)^{-1}$ is ensured by the formulation of the considered two-dimensional differential problem and the proposed finite-difference schemes. We also assume that h_1 is chosen so that $D > 0$.

3 ANALYSIS OF THE STABILITY

In order to analyse the stability of the finite-difference schemes (10), we use the sufficient stability condition $\rho(S) = \max_{\lambda(S)}|\lambda(S)| < 1$, where $\lambda(S)$ are the eigenvalues of the transition matrices S. To be precise, one can prove that if $(-\widetilde{\Lambda}_1)$ is a simple-structured matrix and $\lambda_i(-\widetilde{\Lambda}_1) \geqslant 0$ or $\mathrm{Re}\lambda_i(-\widetilde{\Lambda}_1) \geqslant 0$, where $\lambda_i(-\widetilde{\Lambda}_1)$, $i = 1,2,\ldots,N_1-1$, are real or complex eigenvalues of the matrix $(-\widetilde{\Lambda}_1)$, then:

- LOD and ADI finite-difference schemes are unconditionally stable;
- fully-explicit finite difference scheme is stable under condition $\tau < 2\min\big\{1/\rho(A_1), 1/\Delta_2\big\}$, $\Delta_2 = \max_{\lambda(A_2)}\lambda(A_2) = \max_{1\leqslant j\leqslant N_2-1}\lambda_j(-\widetilde{\Lambda}_2) = \lambda_{N_2-1}(-\widetilde{\Lambda}_2) = 4h_2^{-2}\cos^2(\pi h_2/2)$.

The eigenvalue problem for the matrix $(-\widetilde{\Lambda}_1)$ has been investigated by M. Sapagovas[5]. When $\gamma_1+\gamma_2 \leqslant 2$, then all the eigenvalues of the matrix $(-\widetilde{\Lambda}_1)$ are non-negative and algebraically simple real numbers: $\lambda_i(-\widetilde{\Lambda}_1) \geqslant 0$, $i = 1,2,\ldots,N_1-1$. If $\gamma_1+\gamma_2 > 2$, then there exists one and only one negative eigenvalue of the matrix $(-\widetilde{\Lambda}_1)$.

4 NUMERICAL RESULTS

In order to demonstrate the efficiency of the considered finite-difference schemes and practically justify the stability analysis technique, a particular test problem was solved. In our test problem, functions $f(x,y,t)$, $\mu_1(y,t)$, $\mu_2(y,t)$, $\mu_3(x,t)$, $\mu_4(x,t)$ and $\varphi(x,y)$ were chosen so that the function $u(x,y,t) = x^3 + y^3 + t^3$ would be the solution to the differential problem (1)–(5). The finite-difference schemes where implemented in a stand-alone C application. All numerical experiments were performed using the technologies of grid computing.

Numerical experiments and calculations of the maximum norm of computational errors allow us to estimate the accuracy of the numerical solution. We identify the ranges of the values of parameters γ_1 and γ_2 such that the proposed schemes are stable. The stability domains are rather wider than the ranges of such the values of γ_1 and γ_2 that all real eigenvalues of the matrix $\left(-\widetilde{\Lambda}_1\right)$ are non-negative or real parts of all complex eigenvalues are non-negative.

5 CONCLUSIONS

We developed the splitting finite-difference schemes for the two-dimensional parabolic equation with nonlocal integral conditions. Applying quite a simple technique allow us to investigate the stability of these schemes. The technique is based on the analysis of the spectrum of the transition matrix of a finite-difference scheme. The results of numerical experiments with a particular test problem justify theoretical results. We demonstrate that the proposed schemes can be stable or unstable depending on the parameters of nonlocal conditions.

The results can be generalized for the corresponding two-dimensional differential problem with more general integral or other type nonlocal conditions.

REFERENCES

[1] Sapagovas, M. On the stability of a finite-difference scheme for nonlocal parabolic boundary-value problems. *Lith. Math. J.* **48(3)**, 339–356 (2008).

[2] Sajavičius, S. The stability of finite-difference scheme for two-dimensional parabolic equation with nonlocal integral conditions. In L. Damkilde et al. (ed.) *Proceedings of the Twenty Second Nordic Seminar on Computational Mechanics / DCE Technical Memorandum No. 11*, 87–90 (Aalborg, Denmark, 2009).

[3] Sajavičius, S. On the stability of alternating direction method for two-dimensional parabolic equation with nonlocal integral conditions. In V. Kleiza et al. (ed.) *Proceedings of International Conference Differential Equations and their Applications (DETA'2009)*, 87–90 (Panevėžys, Lithuania, 2009).

[4] Sajavičius, S. On the stability of locally one-dimensional method for two-dimensional parabolic equation with nonlocal integral conditions. In J. C. F. Pereira et al. (ed.) *Proceedings of the V European Conference on Computational Fluid Dynamics (ECCOMAS CFD 2010)*, CD–ROM, 11 p. (Lisbon, Portugal, 2010).

[5] Sapagovas, M. P. On stability of fnite-difference schemes for one-dimensional parabolic equations subject to integral condition. *Obchysl. Prykl. Mat.* **92**, 77–90 (2005).